Structure and Chemical Durability of Glasses for High-Level Nuclear Waste Immobilization: A Solid-State Nuclear Magnetic Resonance Spectroscopy Study

by

Arun Krishnamurthy

A thesis submitted to the Faculty of Graduate Studies of the University of Manitoba in partial fulfillment of the requirements of the degree of

Doctor of Philosophy

Department of Chemistry

University of Manitoba

Winnipeg

Table of Contents

Abstract

Borosilicate and phosphate glasses function as immobilization matrices for high-level nuclear waste generated from the reprocessing of spent nuclear fuel rods. The waste is highly radioactive and chemically heterogeneous, with more than thirty elements present in their oxide forms, some in high oxidation states with phase-separation tendencies (for example, Mo^{6+} and S^{6+}). Phosphate glasses show high affinity for these troublesome cations but suffer from poor physical and chemical properties which can be improved by doping the glass with Al_2O_3 and B_2O_3. In this work, a detailed account of the network structure of Mo-doped aluminoborophosphate glasses and the mode of Mo incorporation in phosphate glasses is presented using multinuclear solid-state nuclear magnetic resonance spectroscopy and Pauling bond strength modeling. The above-mentioned cations are sparingly soluble in borosilicate melts, wherein they separate as water-soluble crystalline molybdates and sulfates by sequestering radionuclides from the glass. A new approach to improve their incorporation into the glass structure is presented, which relies on matching the field strengths of waste-cations with the glass network constituents. The utility of this cation field-strength matching principle in successfully vitrifying multiple high field-strength cations is demonstrated. The chemical durability of phosphate-doped borosilicate glasses with enhanced Mo incorporation is evaluated to discern their performance and applicability for waste remediation. Finally, the effect of alkali oxide content on the network structure of borosilicate glasses and their chemical durability is explored with the aim of determining the alkali-loading limit for silicate-based glasses targeted toward the vitrification of low- and intermediate-level nuclear waste.

Acknowledgements

I have been successful in my quest for knowledge only because of the support and encouragement I received from many people all these years. First and foremost, I would like to thank my supervisor Prof. Scott Kroeker for his immense help and support. His encouragement and guidance shaped my understanding of the subject and broadened my vision. I am forever indebted for his confidence in me, incubating new ideas and giving me many opportunities to see the world and present my work in several prestigious conferences. I thank my Ph.D. committee, Prof. Georg Schreckenbach, Prof. Mostafa Fayek, and Prof. David Herbert for guiding me constantly and offering new insights and directions all this time and helping me achieve my research goals. I am grateful to Dr. Kirill Levin for his mentorship during my initial days, his friendship and his cherishable ideas during our coffee breaks. I thank past and present Kroeker group members, Jordon Perillo, Daniel Padeanu, Lyle Walld, Emmalee Mosher, Tony Nguyen, Lucas Segato, Angela Lu, Clara Zwanziger, Katrina Bergmann, Aiden Farrant, Surani Weerasundarage and Mojtaba Abbasi for making my life blissful at the lab and wonderful scientific discussions. I am grateful to Dr. Kirk Marat and Dr. Dave Davidson for the access to the NMR facility and their help in running NMR experiments. I thank Ms. Debbie Armstrong, Mr. Ryan Sharpe, Dr. Ravinder Sidhu and Dr. Tom Ward for unfettered access to the analytical instruments, which immensely helped me to finish projects on time. I am grateful to Dr. James Xidos for helping me learn how to use the Gaussian program. Thanks to the Dept. of Chemistry and Faculty of Graduate Studies, University of Manitoba, for giving me this wonderful opportunity to study in Canada and the funding I have received over the years. I also thank Chemistry Graduate Student Association and the Faculty of Science, U of M, for travel grants. Finally, I want to thank my family and friends for their support and encouragement, without which I could not have been where I am today.

In the loving memory of my mother

List of Figures

List of Tables

List of Abbreviations and Units

gCO_2eqkWh^{-1}	grams of carbon dioxide equivalent per kilowatt-hour
EEU	Embodied energy use
Mwe	Megawatt electric
IAEA	International Atomic Energy Agency
EW	Exempt Waste
VSLW	Very short-lived waste
VLLW	Very low-level waste
LLW	Low-level waste
ILW	Intermediate-level waste
HLW	High-level waste
EC	Electron capture
IT	Isomeric transition
HLLW	High-level liquid waste
µSv/year	MicroSievert per year
mSv/year	MilliSievert per year
SLR	Short-lived radionuclides
LLR	Long-lived radionuclides
Bq/g	Becquerel per gram
TBq/m^3	Terabecquerel per cubic meter
T_L	Liquidus temperature
T_g	Glass-transition temperature
BO	Bridging oxygen

NBO	Non-bridging oxygen
S/V	Surface-area-to-volume ratio
μm	Micrometer/microns
Tc	Critical temperature or Upper consolute temperature
CFS	Cation field-strength
T_1	Spin-lattice relaxation or Longitudinal relaxation
T_2	Spin-spin relaxation or Transverse relaxation
RD	Recycle delay
NMR	Nuclear Magnetic Resonance
CT	Central transition
ST	Satellite transition
MAS	Magic angle spinning
PSD	Pre-scan delay
FID	Free induction decay
CPMAS	Cross-polarization magic angle spinning
G/L	Gaussian/Lorentzian
C_Q	Quadrupolar coupling constant
PXRD	Powder x-ray diffraction
XRD	X-ray diffraction
SEM	Secondary electron microscopy
SE	Secondary electron
BSE	Back-scattered electron
EDS	Energy-dispersive x-ray spectroscopy
ICP-OES	Inductively-coupled plasma optical-emission spectroscopy
ICP-MS	Inductively-coupled plasma mass spectrometry
CRN	Continuous random network
T_m	Melting temperature
PBS	Pauling bond strength
BV	Bond valence
MCC-1	Material characterization center-1

ICSD	Inorganic crystal structure database
1D	One dimensional
HT-NMR	High-temperature nuclear magnetic resonance
CEMHTI	Conditions Extrêmes et Matériaux: Haute Température et Irradiation
NL	Normalized loss
CP	Cross polarization
DP	Direct polarization

1 Radioactive waste and its classification

With the world population just shy of 8 billion, the need for sustainable energy has grown tremendously. Although a major share of the current energy requirement is met with hydropower and fossil fuels, the focus is slowly shifting towards renewable energy resources like wind and solar [1] due to hydro and fossil fuel's harsh ecological impacts. In the United States of America, the US energy information administration projects a decline in natural gas and coal usage from 37 to 36% and 24 to 13%, respectively, over the next few decades (**Figure 1.1**) [1]. However, the dependence on nuclear energy, which accounts for 19% of electricity generated in the US in 2020, will not wither and nuclear energy remains one of the main sources of energy in the foreseeable future. In fact, the international atomic energy agency (IAEA) reckons an increase in the world nuclear energy generation capacity from 396 gigawatts (GW) in 2018 to 496 GW in 2030 and 715 GW in 2050 [2]. **Figure 1.2** shows the share of nuclear energy (in %) in the electricity generated in different parts of the world in 2019 and the future projections [3], which unequivocally establishes, if not growing, a constant dependency on nuclear fuel through the mid-century. The per-unit life-cycle emissions calculated for the year 2050 using the global integrated *energy-economy-land-use-climate model* suggest a life-cycle emission of 78−100 grams of carbon dioxide equivalent per kilowatt-hour (gCO_2eqkWh^{-1}) for fossil-fuel and hydropower based electricity generation and substantially lower emission of 3.5−12 gCO_2eqkWh^{-1} for solar, wind, and nuclear energy [4]. This model is built on the *embodied energy use* (EEU) concept, where the energy spent in building the energy-harnessing infrastructure and its post-construction maintenance, including the fuel supply, are considered. The EEU of hydropower and fossil-fuel is *ca.* 12% of the total energy produced over the power-plant's lifetime whereas the non-carbon energies such as wind, solar and nuclear energy boast an EEU of just 5%, making them the most-sought energy sources to meet the mandates of the Paris agreement on climate change [5].

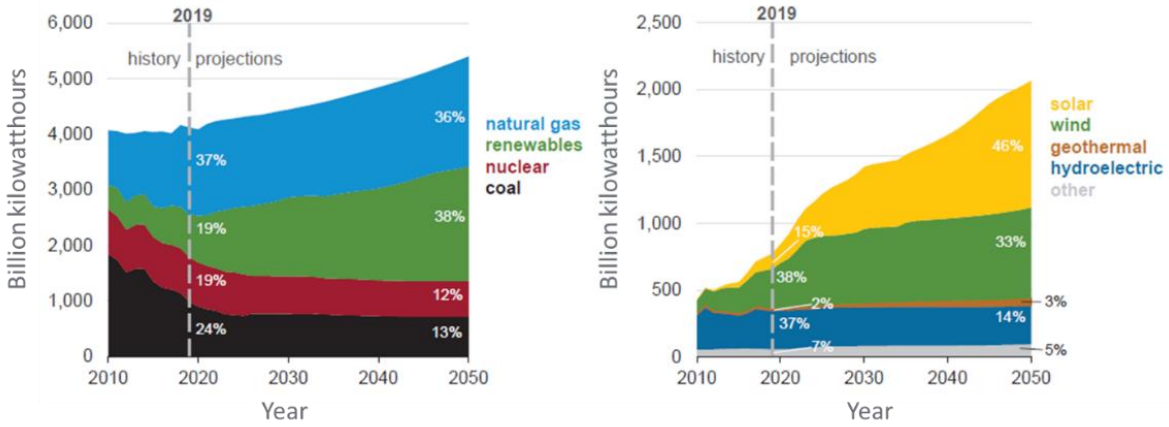

Figure 1.1. Amount of electricity generated from renewable and non-renewable energies in past decades and projection for the future decades. Source: U.S. Energy Information Administration (2020) [1].

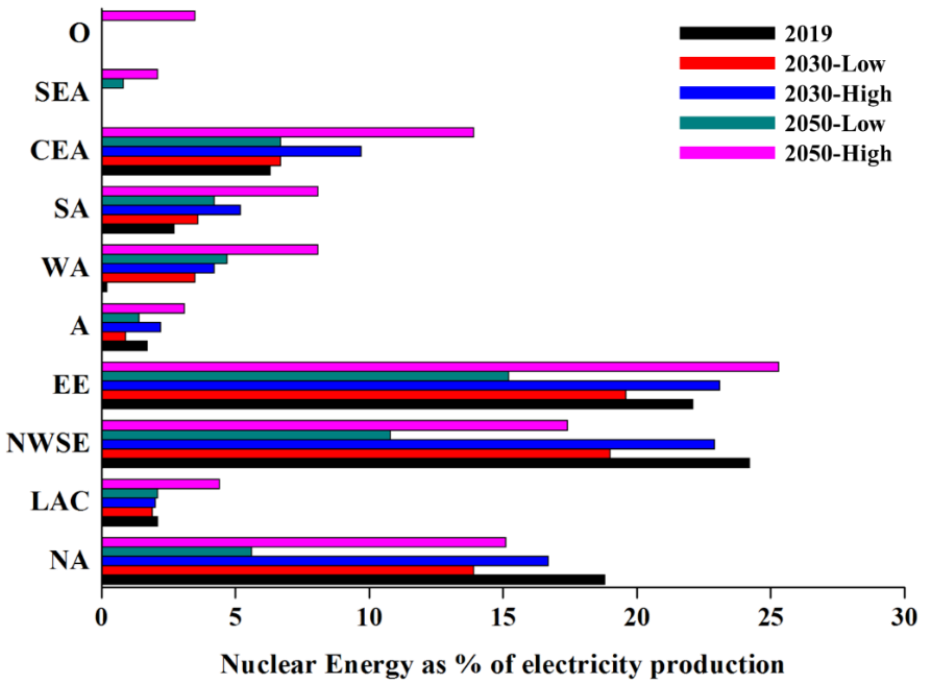

Figure 1.2. The percent of nuclear energy as an energy production source in 2019 and projections, both high and low for years 2030 and 2050. y-axis: NA, North America; LAC, Latin America, and the Caribbean; NWSE, Northern, Western and Southern Europe; EE, Eastern Europe; A, Africa; WA, Western Asia; SA, Southern Asia; CEA, Central-Eastern Asia; SEA, South-Eastern Asia; O, Oceania. Source: International Atomic Energy Agency [3].

1.1 Radioactive waste

Radioactive waste is generated at every stage of the nuclear energy harnessing process [7–13]. Different steps involved in nuclear power generation are shown in **Figure 1.3** and are classified as *front-end* or *back-end* processes [9,14]. While the mining, milling, and refining, fabrication of fuel-rods and nuclear fission are the *front-end* processes, the handling of spent fuel-rods and their reprocessing form the *back-end* process.

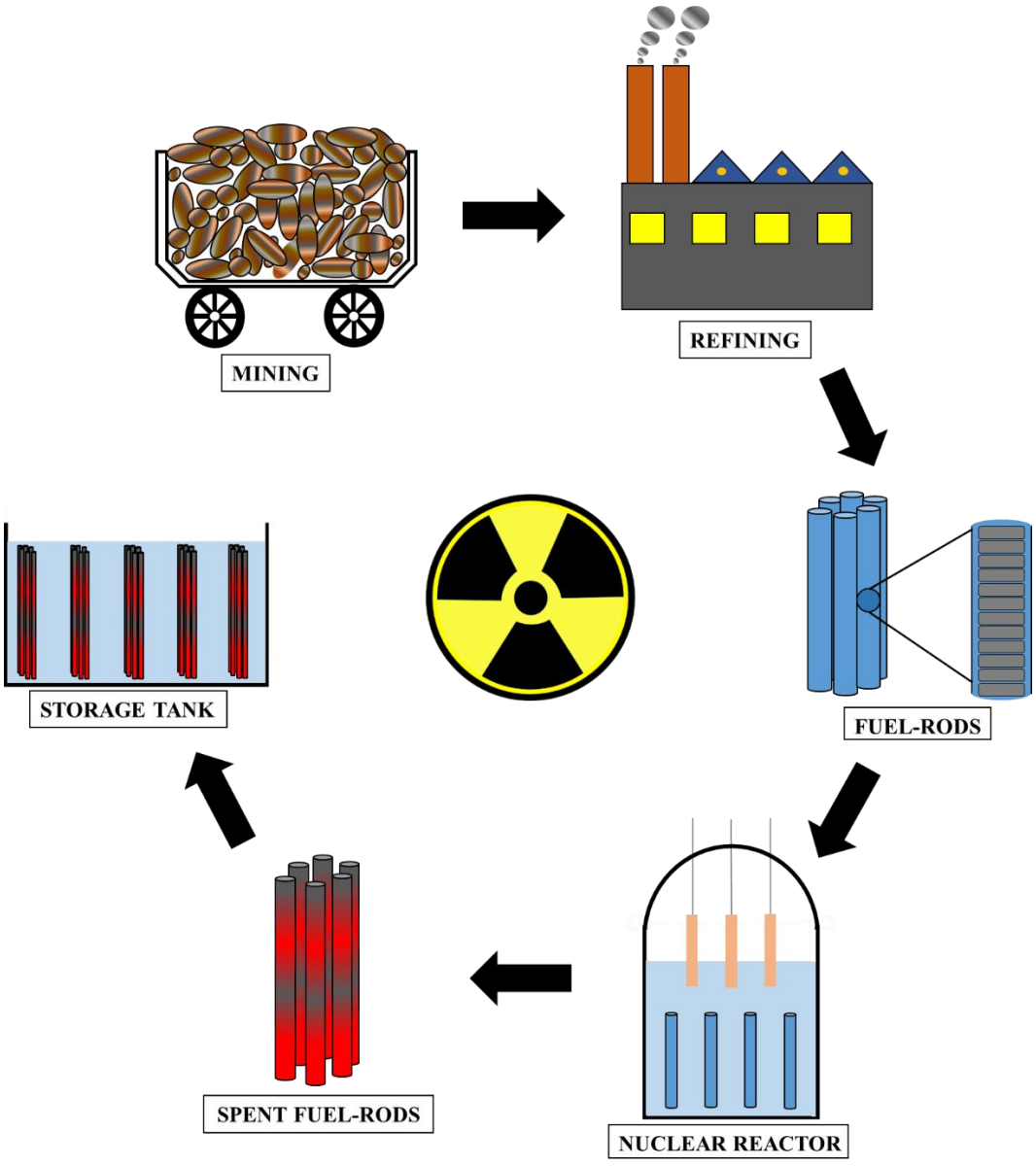

Figure 1.3. A pictorial representation of different steps involved in harnessing nuclear energy.

1.1.1 Mining and milling

Nuclear fuel-pellets are fabricated with UO_2 alone or with a mixture of UO_2 and PuO_2, called the *mixed-oxide fuel*. Uranium is an omnipresent lithophilic metal found in biotic and abiotic chemical forms and exists as a mixture of two primordial isotopes, ^{235}U (0.718%) and ^{238}U (99.28%), with half-lives ($t_{1/2}$) of 7.038 x 10^8 and 4.469 x 10^9 years, respectively [15]. The ^{234}U isotope (0.004%) is a ^{238}U radioactive decay-series product with a $t_{1/2}$ of 2.5 x 10^5 years. ^{235}U is a fissile radionuclide and ^{238}U is a fertile nuclide that can be converted to fissile ^{239}Pu by bombardment with thermal neutrons. Uranium is found in major rock-forming minerals such as quartz, feldspars, biotite, amphibolites, zircon, uraninite, apatite and sphene, and is known to concentrate in grain boundaries and fractures in non-crystalline phases formed by deuteric alteration of igneous rocks [15].

The mined ore is ground and blended at milling plants, and the uranium is extracted, which generates sand-like residues called *tailings* containing appreciable amounts of the above-mentioned radionuclides. Depending on the ore composition and the country where it is refined, either sulfuric acid or sodium carbonate is employed to extract the uranium in the form of uranyl sulfates or uranyl carbonates, respectively [16]. Further, the uranium salt solution is filtered via multi-stage counter-current decantation and purified by solvent extraction and ion exchange. Uranium is then precipitated from the solution as ammonium diuranate or as uranium peroxide and calcined into uranium oxide (U_3O_8), popularly called *yellowcake*. The yellowcake is only 70-90 percent U_3O_8 by weight and is refined by dissolving it in nitric acid forming uranyl nitrate solution, which is purified and converted to uranium trioxide (UO_3) [17]. Milling generates incinerable wastes such as scrap lumber, pallets, rags, paper, cardboard, rubber, plastic and compactible wastes like air filters, fiberglass, polyvinyl carbon ductwork, floor sweepings, sandblast sand, insulation, sample bottles, scrap metal anodes, radioactive drain waste and tailings [10].

1.1.2 ^{235}U enrichment and fuel fabrication

Due to low fractions of fissile ^{235}U (0.71%) [18], the yellowcake cannot be directly used to fabricate fuel pellets. Most of the world's power reactors are light water reactors that need ^{235}U-enriched fuel (3.5−4.5% ^{235}U) for operation [17]. In the enrichment process [18], the UO_3 is

converted to UO_2 ceramic powder and dissolved in the HF, forming uranium tetrafluoride (UF_4). The UF_4 is further converted to uranium hexafluoride (UF_6) by treating it with F_2 gas and shipped to enrichment plants where the $^{235}UF_6$ fraction is increased by gaseous diffusion, centrifugation and laser separation [17]. The ^{235}U-enriched uranium hexafluoride is converted to powder-form ceramic UO_2, which is pressed into pellets. The fuel rods are fabricated by encasing these pellets in metallic tubes called *cladding* [19]. In addition to incinerable and non-incinerable waste, these processes generate non-processable waste such as filters, light bulbs, cable, used equipment, metals, construction debris, absorbents such as sand vermiculite, sweeping compound and ion-exchange resins [17]. Processable liquids such as radioactive drain waste and chemical cleaning solutions also add to the waste stockpile [10]. Fuel fabrication generates small quantities of ^{234}Th and uranium-rich liquid waste, which is discharged into settling ponds [9].

1.1.3 Spent fuel rods

The fuel rods must be periodically replaced as the nuclear fission process decreases the ^{235}U fraction, making the chain reaction no longer sustainable. The spent fuel-rods that are removed from the reactor-core are dangerously rich in radioactive nuclides and are stored in-house in cooling tanks until the radionuclides with short half-lives have decayed. Some of the fuel rods mechanically fail and develop cracks through which the radionuclides such as ^{135}Cs, ^{137}Cs, and ^{90}Sr are released into the water. Since the rods are not completely depleted of ^{235}U isotope, they are reprocessed, and the fissile ^{235}U and ^{239}Pu radionuclides are extracted. The fuel rods are cut open, which releases the ^{131}I, ^{85}Kr, ^{135}Xe gaseous radionuclides and the ^{3}H as water vapor. The dissolution of fuel-pellets in nitric acid to extract fissile radionuclides generates a huge volume of liquid waste called *high-level waste*, rich in transuranic elements and other decay products with diverse half-lives and activity concentrations. The remains of the claddings are radioactive as well due to the neutron-dependent transmutation of the metal.

1.1.4 Other sources

Radiotherapy has emerged as one of the main cancer treatment methods wherein the radionuclides are used to administer localized dosage at the targeted tumor [20]. Besides, the radionuclides are in demand for radioimmunoassays in radiopharmaceuticals and diagnostic procedures [21]. Although the half-lives of most radionuclides used in the treatment are short (days), some with long half-lives (years) such as ^{3}H ($t_{1/2}$ = 12.5 years) and ^{137}Cs ($t_{1/2}$ = 30.17 years) are often used in radiotherapy. The solid and liquid discharges from the hospitals using therapeutic radionuclides are contaminated and have to be processed with strict waste-treatment regulations.

Research reactors are not intended for energy generation but function as a neutron source and are important for education and training, silicon doping, neutron activation analysis, radioisotope production, neutron radiography, material structural studies and neutron capture therapy [22]. These reactors consume less fuel than nuclear power plants, but the fuel needs to be enriched with ^{235}U up to 20%, referred to as *low-enriched fuel*. The type and volume of the waste generated depend on the reactor type, applications, and operational schedule. Solid wastes include ion-exchange resins used in water cleaning, high-efficiency particulate air filters used in the ventilation systems, iodine retention filters and reactor monitoring equipment. Coolant losses from the reactor pool, wash waters from maintenance and decontamination, water from sinks and showers within the controlled areas contribute to the liquid waste. Gaseous elements in the air are activated by neutron capture within the reactor and irradiation facilities. For example, ^{41}Ar is produced by $^{40}Ar(n,\gamma)^{41}Ar$ reaction where the ^{40}Ar captures a neutron and transmutates to ^{41}Ar emitting γ-radiation. The radioactive ^{14}C is generated by $^{17}O(n,\alpha)^{14}C$ and $^{14}N(n,p)^{14}C$ reactions. Radioactive noble gases like ^{85}Kr, ^{131}Xe, ^{133}Xe and iodine isotopes (^{131}I and ^{129}I) are also generated in small quantities.

During the height of the cold war, a huge volume of radioactive waste was generated from plutonium and weapon-grade uranium (>90% ^{235}U) production for nuclear warheads. Spent fuels from different reactor types contain a substantial amount of plutonium whose separation generates significant amounts of solid, liquid and gaseous radioactive wastes [23]. Due to non-proliferation agreements between several countries, the historical plutonium inventories are

being cleared up by fabricating mixed-oxide fuels consisting of Pu and U, thereby generating more waste.

Due to the complexity of the processes involved, decommissioning nuclear power plants and nuclear reactors that have completed or are nearing their lifespan of ca. 60 years poses a big challenge. The incinerable, non-processable, non-disposable wastes, both radioactive and non-radioactive, are generated in significant volumes when a reactor is dismantled [24]. For example, a modern light water reactor of 800–100 MWe capacity produces *ca.* 300,000 tonnes of radioactive and non-radioactive waste [25]. Materials and components of high radioactivity such as reactor-vessel internals, parts of biological shield, concrete surfaces, sand from off-gas filtering, piping in the reactor circuits and reactor building, filter sludge and ion-exchange resins from the decontamination operation [25] are generated.

1.2 Radioactive waste classification

The generation of an immense volume of radioactive waste contradicts the popular belief that nuclear-fission-based energy generation is relatively clean and eco-friendly. Depending on the radionuclide species present, the level of radioactivity in the waste may vary. The waste with short-lived radionuclides can be disposed of as normal industrial and domestic wastes, while others remain radioactive for millions of years. Classification of waste ensures the adoption of adequate safety measures and implementation of appropriate waste management strategies. It also helps in the design of waste management facilities, optimization of waste conditioning techniques, development of legislation, establishment of regulatory requirements, and the provision of a better understanding of potential hazards associated with various types of radioactive waste. An ideal waste classification scheme should cover a full range of waste types with a special emphasis on the degree of waste containment needed to ensure safety in the long term. It should clearly outline the interdependencies between the waste classes, be easy and straightforward to understand, and acceptable to all parties such as government agencies, regulators, and operators.

Radioactive waste is classified based on its physical state, point of origin, half-lives of the radionuclides, and radioactivity levels [7,13,23,26–29]. Waste classification schemes differ between countries [26–28] and are built in accordance with the waste classification scheme of

the International Atomic Energy Agency [7]. Although classification schemes are developed mainly for solid wastes, they are equally applicable to liquid and gaseous wastes as well. With disposal as the only criteria, the International Atomic Energy Agency (IAEA) classifies the radioactive waste into six different categories [7]. The boundaries between these are treated as transition zones, facilitating nuclear-waste agencies of countries to modify waste-class definitions based on the type of radioactive level of the waste generated. A conceptual illustration of waste classification based on the activity of the waste and the half-lives of radionuclides is shown in **Figure 1.4**, which establishes that the total radioactivity of the waste, referred to as *activity content* or *activity concentration*, plays a decisive role in waste categorization. A detailed list of the parameters used in the classification of waste is given in **Table 1.1**.

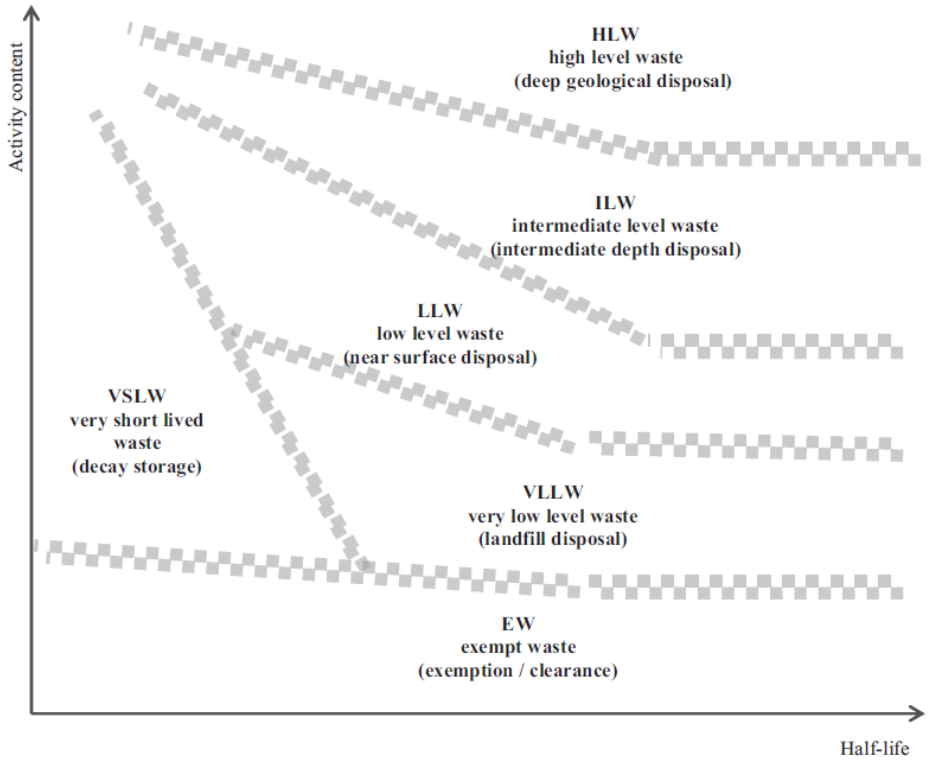

Figure 1.4. A conceptual graphic of waste classification based on the waste's radioactivity and the half-lives of the radionuclides present. Reproduced with permission [7].

Table 1.1. Parameters and properties used in the classification of radioactive wastes. Reproduced from reference [7].

Parameter	**Properties**
Origin	
Criticality	
Radiological	Half-lives of radionuclides Heat generation The intensity of penetrating radiation Activity concentration of radionuclides Surface contamination Dose factors of relevant radionuclides Decay products
Physical	Physical state Size and weight Compactibility Dispersibility Volatility Miscibility Free liquid content
Chemical	Chemical composition Solubility and chelating agents Potential chemical hazard Corrosion resistance/corrosiveness Organic content Combustibility and flammability Chemical reactivity and swelling potential Gas generation Sorption of radionuclides
Biological	Potential biological hazards Bio-accumulation
Other factors	Volume Amount arising per unit time Physical distribution

1.2.1 Exempt waste (EW)

Exempt waste does not require provisions for radiation protection and can be discharged in landfills or recycled as it contains little to no radionuclides. Analogously, gaseous effluents and liquids are discharged into the atmosphere and large water-bodies, respectively. To exempt this waste from containment, effective radiation dosage to individuals should be <10 μSv/year, and in accidents that are considered low-probability events, it should be < 1 mSv/year. In skin-exposure cases, the limit is set at <50 mSv/year [7].

1.2.2 Very short-lived waste (VSLW)

Very short-lived waste primarily consists of radionuclides with half-lives typically of 100 days or less such as ^{192}Ir and ^{99m}Tc [7,23]. Solid waste, liquid and gaseous effluents are stored on-site for a short period until the radionuclides decay and the activity concentration meets the regulatory requirements. The waste is then downgraded to exempt waste and disposed of accordingly.

1.2.3 Very low-level waste (VLLW)

Very-low level waste exhibits slightly higher activity than the exempt waste but does not need a high level of containment and hence is disposed of in engineered near-surface landfills. However, in contrast to the exempt waste, radiation protection and safety must be considered, but the regulatory provisions are not stringent. This class includes wastes from the decommissioning of nuclear facilities and the mining and processing of ores and minerals.

1.2.4 Low-level waste (LLW)

Materials contaminated with short-lived radionuclides (SLR) and long-lived radionuclides (LLR) fall into this category. The waste must be robustly contained and typically isolated for up to three hundred years [23]. The actual time of containment depends on the concentrations of SLR and LLR in the waste, activity concentration, and the heat dissipated. The SLR decay during the containment period after which, the waste is downgraded to the EW. Prior to disposal, liquid LLW is evaporated to concentrate the radionuclides and conditioned either by chemical

precipitation or ion-exchange methods. Solid waste is compacted and incinerated to reduce the volume and increase the waste's stability for disposal. Treated and untreated LLW is typically encapsulated in cement, bitumen and geopolymers and stored for the rest of the containment period in concrete containers and high-integrity containers made of steel or high-density polyethylene [23]. The contact dose rate for LLW should not exceed 2 mSv/h, and the activity concentration of LLW containing LLR (for example, ^{36}Cl, ^{93}Zr, ^{94}Nb, ^{129}I) should be 400 Bq/g on average and up to 4000 Bq/g in the case of individual packages [7].

1.2.5 Intermediate-level waste (ILW)

The LLR-rich waste with an activity concentration of up to 2 TBq/m^3 of α-activity and up to 800 TBq/m^3 of β- and γ-activity [13] is considered an intermediate-level waste. It should be completely isolated from the biosphere and is often disposed of in facilities at depths of a few hundred meters designed with effective natural and engineering barriers. No provisions for heat dissipation are necessary during the interim-storage and disposal as the waste has low concentrations of highly radioactive nuclides such as ^{135}Cs and ^{90}Sr. The ILW typically comprises irradiated reactor cores, graphite waste and fuel cladding waste from reprocessing facilities. Similar to the LLW, it is encapsulated in cement, bitumen and polymers before disposal.

1.2.6 High-level waste (HLW)

Spent fuel rods and the liquid waste generated from their reprocessing are classified as high-level waste as they have high concentrations of short- and long-lived radionuclides, including the fissile radionuclides and actinides. The HLW has a high activity concentration in the range of 10^4 to 10^6 TBq/m^3 [7] and hence demands a greater degree of containment and isolation compared to other waste classes. Moreover, heat dissipation is a big problem that needs to be taken into account when designing geological disposal facilities. Medical and military applications also generate waste with significant radioactivity, which is also considered HLW and appended to the waste stockpile for further processing and disposal. Although HLW is only a small fraction of the total radioactive waste generated, it accounts for 90 percent of the radioactivity associated with the back-end process of the nuclear fission business [9].

Due to the high radioactivity of HLW and the long half-lives of the radionuclides present, its isolation from the environment and its disposal are of utmost importance. The nuclear fission reaction generates more than 30 fission products in several isotopic forms, out of which many are radioactive. A comprehensive list of radionuclides present in the HLW is given in **Table 1.2**, which also lists their half-lives, principal mode of decay and specific activity [30]. The fission process is expressed as **equation 1.1** where N is a thermal neutron absorbed by the ^{235}U atom, A_1 and A_2 are the two daughter nuclei, and kN is the number of neutrons generated (k = 2.43±0.007) [30]. The daughter nuclei formed typically have a mass ratio of $(A_1/A_2) \sim 3/2$ and exhibit a distribution in the atomic masses, as shown in **Figure 1.5**.

$$N + {}^{235}U \rightarrow A_1 + A_2 + kN + 200\ MeV \qquad (1.1)$$

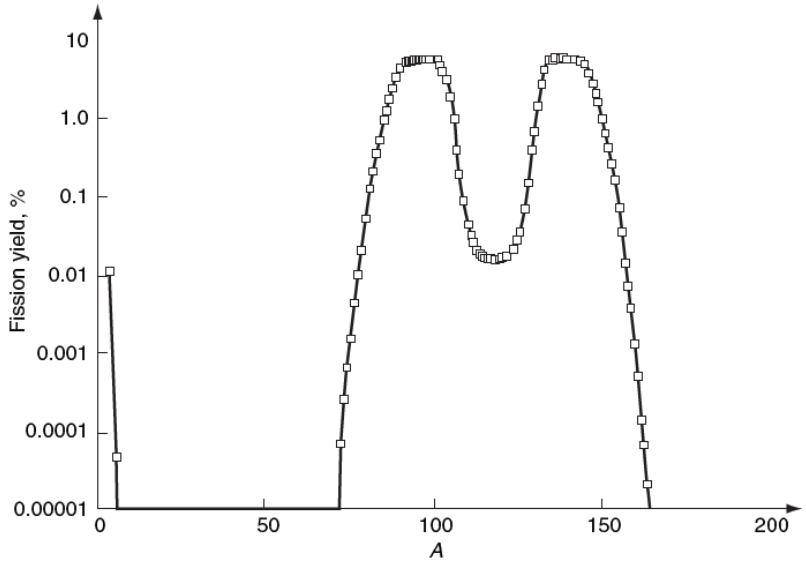

Figure 1.5. Distribution in the atomic masses of the fission products. Reproduced with permission [30].

The radioactive fission products decay into stable nuclides by emitting α- and β-particles or by γ-emission. In α-decay (**equation 1.2**), an alpha particle, identical to the helium nucleus (He^{2+}) is ejected and the parent atom transforms into a different element whose atomic mass (A) and atomic number (Z) are lower by 4 and 2, respectively. In β-decay, either a proton transmutes

to a neutron, emitting a positron (e^+) and a neutrino (ν_e) (β^+-decay, **equation 1.3**) or a neutron converts to a proton, emitting an electron (e^-) and an antineutrino ($\bar{\nu}_e$) (β^--decay, **equation 1.4**). In γ-decay (**equation 1.5**), atomic nuclei in an excited state relax to the ground state and dissipate excess energy as high-energy photons. Radionuclides that undergo γ-decay are generally the products of α- and β-decay and neutron capture reactions within the reactor. Electron capture (EC) is another mode of β-decay resembling β^+-decay wherein the nucleus captures an inner-shell electron and transmutates, emitting a positron and a neutrino. In a different process called isomeric transition (IT), the daughter nucleus from an α- or a β-decay emits gamma radiation without any changes in its atomic number or the atomic mass.

$$^{A}_{Z}X_N \rightarrow {}^{A-4}_{Z-2}Y_{N-2} + {}^{4}_{2}\alpha + 4.18 \text{ MeV} \quad (1.2)$$

$$^{A}_{Z}X_N \rightarrow {}_{Z-1}{}^{A}Y_{N+1} + e^+ + \nu_e + 10-1000 \text{ keV} \quad (1.3)$$

$$^{A}_{Z}X_N \rightarrow {}_{Z+1}{}^{A}Y_{N-1} + e^- + \bar{\nu}_e + 10-1000 \text{ keV} \quad (1.4)$$

$$^{A}_{Z}X^{*}_{N} \rightarrow {}^{A}_{Z}X_N + \gamma + \sim 1.3 \text{ MeV} \quad (1.5)$$

High-level liquid waste (HLLW) compositions (**Tables 1.3 and 1.4**) vary greatly amongst countries with different reactor technologies. Moreover, the extent of fuel burnup also contributes towards the gradient in waste compositions [31]. Many non-fission products are also present in HLLW due to various steps and limitations involved in fuel reprocessing [31,32]:

a. Unextracted U and Pu.
b. Radioactive isotopes of transuranic elements Np, Am, and Cm formed by neutron capture.
c. Alloying elements such as Mo, Fe, Cr, Al, Zr, and Si used to fabricate U-alloy fuel.
d. Fe, Ni, and Cr from the corrosion of stainless-steel reprocessing infrastructure.
e. Al, Zr, and Mg from the shearing of irradiated fuel-canisters.
f. Na, Fe, and sulfate salts added to HLLW for neutralization, catalysis, and redox control.
g. B and Gd as neutron poisons.

Table 1.2. Radionuclides present in the high-level waste, their half-lives, principal modes of decay and specific activity. Reproduced from reference [30].

Radionuclide	Half-life ($t_{1/2}$)[a]	Mode of decay	Specific activity (Ci/g)[b]
^{3}H	12.33 y	β	9650
^{14}C	5730 y	β	4.457
^{60}Co	5.271 y	β	1131
^{59}Ni	7.5×10^{4} y	EC[c]	8.079×10^{-2}
^{63}Ni	100.1 y	β	61.68
^{79}Se	$<6.5 \times 10^{4}$ y	–	6.966×10^{-2}
^{85}Kr	10.72 y	β	392.3
^{90}Sr	28.5 y	β	136.4
^{93m}Nb	13.6 y	IT[d]	282.6
^{94}Nb	2.03×10^{4} y	β	1.873×10^{-1}
^{93}Mo	3500 y	EC	1.10
^{99}Tc	2.13×10^{5} y	β	1.695×10^{-2}
^{106}Ru	1.020 y	β	3346
^{107}Pd	6.5×10^{6} y	β	5.143×10^{-4}
^{113}Cd	9.3×10^{15} y	β	3.402×10^{-13}
^{113m}Cd	13.7 y	β	216.8
^{126}Sn	1×10^{5} y	β	2.837×10^{-2}
^{125}I	60.14 d	EC	17370
^{129}I	1.57×10^{7} y	β	1.765×10^{-4}
^{134}Cs	2.062 y	β	1294
^{135}Cs	3.0×10^{6} y	–	1.151×10^{-3}
^{137}Cs	30.17 y	β	86.98
^{133}Ba	10.54 y	EC	250
^{146}Pm	5.53 y	EC	442.8
^{147}Pm	2.62 y	β	927.0
^{151}Sm	90 y	β	26.31
^{152}Eu	13.33 y	EC	172.9

Table 1.2. Continued

Radionuclide	Half-life ($t_{1/2}$)[a]	Mode of decay	Specific activity (Ci/g)[b]
^{226}Ra	1600 y	α	9.88×10^{-1}
^{227}Ac	21.77 y	β	72.33
^{229}Th	7340 y	α	2.12×10^{-1}
^{230}Th	7.54×10^{4} y	α	2.10×10^{-2}
^{232}Th	1.40×10^{10} y	α	1.09×10^{-7}
^{231}Pa	3.27×10^{4} y	α	4.72×10^{-2}
^{232}U	68.9 y	α	21.40
^{233}U	1.59×10^{5} y	α	9.68×10^{-3}
^{234}U	2.45×10^{5} y	α	6.24×10^{-3}
^{235}U	7.03×10^{8} y	α	2.16×10^{-6}
^{236}U	2.34×10^{7} y	α	6.46×10^{-5}
^{238}U	4.46×10^{9} y	α	3.36×10^{-7}
^{236}Np	1.55×10^{5} y	EC	1.31×10^{-2}
^{237}Np	$2.14 \times 10_{6}$ y	α	7.04×10^{-4}
^{236}Pu	2.85 y	α	531.3
^{238}Pu	87.74 y	α	17.12
^{239}Pu	2.41×10^{4} y	α	6.21×10^{-2}
^{240}Pu	6563 y	α	2.27×10^{-1}
^{241}Pu	14.4 y	β	103.0
^{242}Pu	3.76×10^{5} y	α	3.81×10^{-3}
^{244}Pu	8.26×10^{7} y	α	1.77×10^{-5}
^{241}Am	432.7 y	α	3.43
^{242m}Am	141 y	IT	9.71
^{243}Am	7380 y	α	1.99×10^{-1}
^{243}Cm	28.5 y	α	51.62
^{244}Cm	18.1 y	α	80.90
^{245}Cm	8500 y	α	1.71×10^{-1}
^{246}Cm	4730 y	α	3.07×10^{-1}

Table 1.2. Continued.

Radionuclide	Half-life ($t_{1/2}$)[a]	Mode of decay	Specific activity (Ci/g)[b]
^{247}Cm	1.56 x 10^{7} y	α	9.27 x 10^{-5}
^{248}Cm	3.4 x 10^{5} y	α	4.25 x 10^{-3}
^{252}Cf	2.64 y	α	537.8
^{154}Eu	8.8 y	β	269.9
^{155}Eu	4.96 y	β	465.1
^{153}Gd	241.6 y	EC	3526
^{157}Tb	150 y	EC	15.19
^{158}Tb	150 y	EC	15.08
^{187}Re	4.6 x 10^{10} y	β	3.82 x 10^{-8}
^{210}Pb	22.3 y	β	76.3
^{209}Po	102 y	α	16.8

[a]d - days; y - years
[b]Ci/g = 1 Ci = 3.7 · 10^{10} Bq, which is the activity of 1g of ^{226}Ra; 1 Bq = 1 decay/s
[c]Electron capture
[d]Isomeric transition

Table 1.3. A list of fission products and their concentrations in the high-level waste from a light water reactor with a fuel burnup of 33000 MW·d/t. Reproduced from reference [31].

Fission product element	Amount of oxide (g/L)
Rb	1.02
Sr	2.87
Y	1.60
Zr	13.92
Mo	14.87
Tc	2.91
Ru	8.37
Rh	1.29
Pd	4.07
Ag/Cd/In/Sn/Sb/Se	0.63
Te	1.99
Cs	8.54
Ba	4.96
La	4.13
Ce	8.20
Pr	3.85
Nd	13.16
Pm	0.22
Sm	2.45
Eu	0.63

Table 1.4. Composition of high-level liquid waste (in g/L) from different countries. Reproduced from reference [31].

Component	USA Hanford	Japan Tokai	France Marcoule	China Lanchow	UK Sellafield	Belgium	Germany
H^{+a}	–	2.5	1.5−2	1−2	1	2.3	5.3
Al	1.5	–	30−35	4.17−4.90	26	9.2	0.2
Na	4.1	44.5	19−23	28.54−33.22	–	45.9	16
K	–	–	–	0.50−0.66	–	–	0.4
Mg	0	–	4	–	20−40	–	0.2
Fe	6.1	8.4	15−17	12.52−14.47	13	22	5.2
Ni	0.6	2.2	1−2	2.74−2.97	1.4	6.3	1.2
Cr	0.1	2.2	1−2	1.18−1.30	1.6	3.5	1.3
Mn	–	–	–	–	–	7.3	0.17
Mo	0.2	–	–	0.65−0.68	10.8	–	–
Zr	3.4	–	–	0.73	11.8	–	–
Hg	–	–	–	–	–	–	–
F	–	–	8	–	–	14.1	0.06
Cl	0.1	–	–	–	–	–	0.04
SO_4	0.2	–	–	4.55−5.07	–	0.02	–
FPs[b]	<2.5	49	22−27	2.68−2.75	–	36.5	40.5
PO_4	–	–	–	–	1.9	0.5	–
Tc	4.3	0.8	–	–	0.8	4.8	–
TRU[c]	<0.05	12.6	3	16.10−19.60	~2	4.5	6.68

[a]In molar (M)
[b]Fission products
[c]Transuranic elements

1.3 High-level waste immobilization

The high radioactivity and the complex composition of HLW demand rigorous disposal considerations. Many types of solid matrices have been exhaustively studied for their efficacy in HLW containment. Materials such as cement [33,34], bitumen [35,36], minerals [37,38], ceramics [39,40], glass-ceramics [41] and glasses [42–44] are widely considered for nuclear waste immobilization and encapsulation. *Immobilization* is a process where the waste-components are chemically integrated into the host matrix, whereas in *encapsulation*, the waste material is physically surrounded by the candidate material with no chemical interactions between them [44]. Cementation, bitumenization and vitrification technologies have proven viable for waste containment on a large scale. Although factors such as the stability of the final wasteform, ease of handling, waste assimilation capacity, natural availability, cost of operation, packaging and logistics are important when choosing an optimal immobilization matrix [44–47], the long-term chemical durability of the wasteforms is the key criterion in selecting appropriate host candidates. Due to the excellent chemical durability of glasses compared to other wasteforms [44], vitrification trumps all other prevalent technologies and has been considered to be the best candidate for HLW immobilization. Due to sub-standard chemical durability, the bituminization and cementation techniques are utilized only to process low-level and intermediate-level wastes [44].

1.4 References

[1] U.S. Energy Information Administration, Electricity, 2020. URL: https://www.eia.gov/outlooks/aeo/pdf/AEO2020%20Electricity.pdf

[2] International Atomic Energy Agency, Energy, electricity and nuclear power estimates for the period up to 2050, Ref. Data Ser. No. 1. (2019).

[3] International Atomic Energy Agency, Energy, Electricity and nuclear power estimates for the period up to 2050, Ref. Data Ser. No 1. (2020).

[4] M. Pehl, A. Arvesen, F. Humpenöder, A. Popp, E.G. Hertwich, G. Luderer, Understanding future emissions from low-carbon power systems by integration of life-cycle assessment and integrated energy modelling, Nat. Energy. 2 (2017) 939–945.

[5] Adoption of the Paris agreement, 2015. URL: https://unfccc.int/resource/docs/2015/cop21/eng/l09r01.pdf

[6] International Energy Agency and Nuclear Energy Agency, Projected costs of generating electricity 2015 edition, 2015.

[7] International Atomic Energy Agency, IAEA safety standards: Classification of radioactive waste, IAEA- No. GSG-1. (2009).

[8] International Atomic Energy Agency, Handling and processing of radioactive waste from nuclear applications, Tech. Reports Ser. No. 402. (2001) 143.

[9] R.C. Ausness, High-level radioactive waste management : The nuclear dilemma, Wis. L. Rev. 707 (1979).

[10] Natural resources Canada, Inventory of radioactive waste in Canada, 2016.

[11] L.P. Sant'ana, T.C. Cordeiro, Management of radioactive waste: A review, Proc. Int. Acad. Ecol. Environemental Sci. 6 (2016) 38–43.

[12] S.M. Spearing, Materials issues in nuclear-waste management, JOM. 52 (2000) 26–29.

[13] L.E.J. Roberts, Radioactive waste management, Annu. Rev. Nucl. Part. Sci. 40 (1990) 79–112.

[14] M.I. Ojovan, W.E. Lee, Nuclear waste types and sources, M.I. Ojovan, W.E. Lee (Eds.) in: *An introduction to nuclear waste immobilization*, Elsevier, Oxford, UK, 2014: pp. 75–97.

[15] S. Dragović, M. Ćujić, J. Kovačević, Environmental radiological impact of uranium mining and milling operations, in: *Radionuclides sources*, Prop. Hazards, 2012: pp. 203–233.

[16] L.K. Kim, Uranium mining and milling, Lawrence Livermore National Laboratory, LLNL-TR-747582, (2018).

[17] D.P. Jackson, K.W. Dormuth, Uranium enrichment in Canada, C. Hurst and: Company, Nuclear Energy Future Paper no. 5 (2009).

[18] P. Harding, 12 - Uranium enrichment, I. Hore-Lacy (Ed.), in: *Uranium for nuclear power*, Woodhead Publishing, (2016): pp. 321–351.

[19] M. Lee, C. Wu, Conversion of UF_6 to UO_2: A quasi-optimization uranyl carbonate process of the ammonium, J. Nucl. Mater. 185 (1991) 190–201.

[20] R. Baskar, K.A. Lee, R. Yeo, K.W. Yeoh, Cancer and radiation therapy: Current advances and future directions, Int. J. Med. Sci. 9 (2012) 193–199.

[21] T. Chard, An introduction to radioimmunoassay and related techniques, Mir, USSR, 1981.

[22] Marques, J. G., A. Kling, Radioactive waste from research reactor operation and decommissioning, S. Yuan, W. Hidaka (Eds.) in: *Radioactive waste: Sources, types and management*, Nova Science Publishers, (2012), pp: 41–76.

[23] M.I. Ojovan, W.E. Lee, Waste processing schemes, M.I. Ojovan, W.E. Lee (Eds.) in: A*n introduction to nuclear waste immobilization*, Elsevier, Oxford, UK, (2014): pp. 117–134.

[24] H. Larsson, Å. Anunti, M. Edelborg, R-13-04 Decommissioning study of Oskarshamn NPP, (2013).

[25] P.-O. Nielsen, Waste from decommissioning of nuclear power plants., Ski Tech. Rep. 9217. (1992).

[26] Joint convention on the safety of spent fuel management and on the safety of radioactive

waste management, United States department of Energy-DOE/EM-0654, (2003).

[27] Management of radioactive waste in Australia, ANSTO, (2011).

[28] M.I. Hosan, Radioactive waste classification, management and environment, Eng. Int. 5 (2017) 53–62.

[29] Internationl Atomic Energy Agency, Disposal of radioactive waste. Safety Standards Series, SSR-5, (2011).

[30] M.I. Ojovan, W.E. Lee, Nuclear decay, M.I. Ojovan, W.E. Lee (Eds.), in: *An introduction to nuclear waste immobilization*, Elsevier, Oxford, UK, (2014): pp. 7–19.

[31] International Atomic Energy Agency, Design and operation of high level waste vitrification and storage facilities, Technical report series no. 339, Vienna, (1992).

[32] International Atomic Energy Agency, Techniques for the solidification of high -level wastes, Technical report series no. 176, Vienna, (1977).

[33] M. Atkins, F.P. Glasser, Application of portland cement-based materials to radioactive waste immobilization, Waste Manag. 12 (1992) 105–131.

[34] M.I. Ojovan, W.E. Lee, Immobilisation of radioactive wastes in cement, M.I. Ojovan, W.E. Lee (Eds.), in: *An introduction to nuclear waste immobilization*, Elsevier, Oxford, UK, (2014): pp. 205–232.

[35] M.I. Ojovan, W.E. Lee, Immobilisation of Radioactive Wastes in Bitumen, M.I. Ojovan, W.E. Lee (Eds.), in: *An introduction to nuclear waste immobilization*, Elsevier, Oxford, UK, (2014) Technical series no. 352, Vienna, (1993).

[36] Internation Atomic Energy Agency, Bituminization processes to condition radioactive wastes, Technical reports series no. 352, Vienna, 1993.

[37] R.C. Ewing, W.J. Weber, J. Lian, Nuclear waste disposal-pyrochlore ($A_2B_2O_7$): Nuclear waste form for the immobilization of plutonium and “minor” actinides, J. Appl. Phys. 95 (2004) 5949–5971.

[38] B.I. Omel’yanenko, T.S. Livshits, S. V. Yudintsev, B.S. Nikonov, Natural and artificial minerals as matrices for immobilization of actinides, Geol. Ore Depos. 49 (2007) 173–

193.

[39] M.I. Ojovan, W.E. Lee, New immobilising hosts and technologies, M.I. Ojovan, W.E. Lee (Eds.), in: *An introduction to nuclear waste immobilization*, Elsevier, Oxford, UK, (2014): pp. 283–305.

[40] R.C. Ewing, W. Lutze, High-level nuclear waste immobilization with ceramics, Ceram. Int. 17 (1991) 287–293.

[41] J.S. McCloy, A. Goel, Glass-ceramics for nuclear-waste immobilization, MRS Bull. 42 (2017) 233–238.

[42] W.J. Weber, A. Navrotsky, S. Stefanovsky, E.R. Vance, E. Vernaz, Materials science of high-level nuclear waste immobilization, MRS Bull. 34 (2009) 46–53.

[43] M.I. Ojovan, W.E. Lee, Immobilization of radioactive wastes in glass, M.I. Ojovan, W.E. Lee (Eds.), in: *An introduction to nuclear waste immobilization*, Elsevier, Oxford, UK, (2014): pp. 245–282.

[44] N.C. Hyatt, M.I. Ojovan, Special issue: Materials for nuclear waste immobilization, Materials (Basel). 12 (2019) 12–15.

[45] L.L. Hench, D.E. Clark, J. Campbell, High level waste immobilization forms, Nucl. Chem. Waste Manag. 5 (1984) 149–173.

[46] Donald I.W., B.L. Metcalfe, R.N.J. Taylor, Review: The immobilization of high level radioactive wastes using ceramics and glasses, J. Mater. Sci. 32 (1997) 5851–5887.

[47] E.R. Vance, B.D. Begg, D.J. Gregg, Immobilization of high-level radioactive waste and used nuclear fuel for safe disposal in geological repository systems, M.J. Apted and J. Ahn (Eds.), in: *Geological repository systems for safe disposal of spent nuclear fuels and radioactive waste*. Woodhead Publishing, (2017): pp. 269–295.

2 High-Level Waste Immobilization in Glasses

Vitrification of high-level waste has become a standard practice in many countries [1] owing to many favourable attributes of glasses. Despite the high investment and operational costs, including transportation and waste disposal expenditures, vitrification proves to be economically viable when the immensity of waste that needs to be contained is considered [2]. The high-throughput nature of the vitrification process and the reasonable glass-melting temperatures make the whole process economically viable. Although many glass systems such as metallic, chalcogenides, ionic, hydrogen-bonded and oxides are known [3], only borosilicate and phosphate glasses qualify for HLW immobilization as only they meet the waste-disposal regulations and fit the criteria of the final wasteform [2].

Glasses are topologically disordered materials with a three-dimensional network of interconnected structural units. The absence of long-range periodicity leads to a random distribution of waste cations in the glass network; therefore, higher waste-loading can be achieved, reducing the volume of the final wasteform. In broad strokes, the glass can be thought of as acting as a solvent for the HLW, as the waste components are completely assimilated into the glass network. The solubilities of various cations in silicate glasses are listed in **Table 2.1** [4].

Vitrification offers a high degree of flexibility as the composition of glasses can be tuned to suit the region-specific HLW compositions. While the radionuclides are immobilized in a glassy matrix, their decay produces significant heat output. The ^{90}Sr and ^{137}Cs radionuclides undergo β/γ-decay, emitting energetic β-particles and γ-radiation which generate heat in the wasteform [5]. The favourable thermal and mechanical properties of glasses equip them against this radiolytic heat [4]. The canister-core (*a.k.a* centerline) temperature, which is the resting temperature of HLW-immobilized glass poured into canisters, is *ca.* 400 °C [6]. However, the glass-transition temperature (see **section 2.1**) of candidates considered for HLW immobilization is 570 °C [7]; therefore radiolytic heating does not affect the network structure or the properties of the glasses. Electronic radiation damage such as covalent and ionic bond rupture, valence changes, changes in ionic mobility and localized electronic excitations [6], as well as atomic displacements due to ballistic collisions of the recoil nucleus from α-decay [5] are serious problems in wasteforms. However, the rapid quenching of the regions with ballistic collisions

into a new glassy state and the partial repair of the damaged regions by the electronic energy loss of the α-particle (He^{2+}) [8], contribute towards the self-healing capacity of glasses [9]. Furthermore, glasses exhibit excellent chemical durability compared to other candidate wasteforms [10], which is crucial for long-term storage in geological repositories.

Table 2.1. Approximate limits of element solubility in silicate glasses. Reproduced from reference [4].

Element	Solubility limit (wt %)
Al, Si, P, Pb	**>25**
Li, B, Na, Mg, K, Ca, Fe, Zn, Rb, Sr, Cs, Ba, Fr, Ra, U	**15–25**
Ti, Cu, F, La, Ce, Pr, Nd, Gd, Th, Bi, Zr, Pu, Th	**5–15**
Mn, Cr, Co, Ni, Mo	**3–5**
C, S, Cl, As, Se, Tc, Sn, Sb, Te, Np	**1–3**
H, He, N, Ne, Ar, Br, Kr, Ru, Rh, Pd, Ag, I, Xe,	**< 0.1**
Pt, Au, Hg, Rn	**< 0.1**
S	**0.5–1.4** [11]

2.1 Chemistry of glasses

Glasses are ubiquitous in the earth's crust, formed, for example, by the cooling of magma (e.g., obsidian) or by the amorphization of crystals due to the heat and pressure generated by meteorite impacts (tektites and impactites) [12]. The term "glass" is not specific to a chemical composition but refers to a particular arrangement of atoms in a condensed phase. Glasses can be organic, inorganic, or metallic, and can be synthesized by melt-cooling, sol-gel, vapor deposition, neutron irradiation of crystalline materials and many other methods [13].

The glass transition behaviour is best explained using an enthalpy vs. temperature diagram (**Figure 2.1**) [13,14]. Below the liquidus temperature (T_L), the atomic arrangement in the melt is a characteristic of the temperature at which the melt is held. If cooled slowly, the melt

crystallizes with a long-range periodic atomic arrangement with an abrupt change in the enthalpy. If the crystallization is bypassed by increasing the melt's cooling rate, the enthalpy changes gradually and the melt is considered to be in a supercooled state. As the melt is cooled, the viscosity increases drastically; therefore, the diffusivity of ions is reduced and they are inhibited from rearranging into a crystalline lattice. As a result, the enthalpy deviates from the equilibrium and the slope of the curve decreases, which will be a function of the heat capacity of the supercooled liquid [15]. The temperature region between the equilibrium enthalpy of a liquid and frozen solid is termed the *glass transformation region*. Since the deviation of the enthalpy from the equilibrium is viscosity-dependent, lower cooling rates increase viscosity less drastically, giving enough time for atoms to rearrange with a different microstructure. Evidently, the glass will have an atomic arrangement closer to the equilibrium (crystal) and a lower enthalpy. The glass transformation region is broad and cannot be represented by just one temperature. Tangents are drawn to the curve, and a single temperature value is derived, called the glass-transition temperature (T_g), which is widely adopted to define the physical properties of glasses.

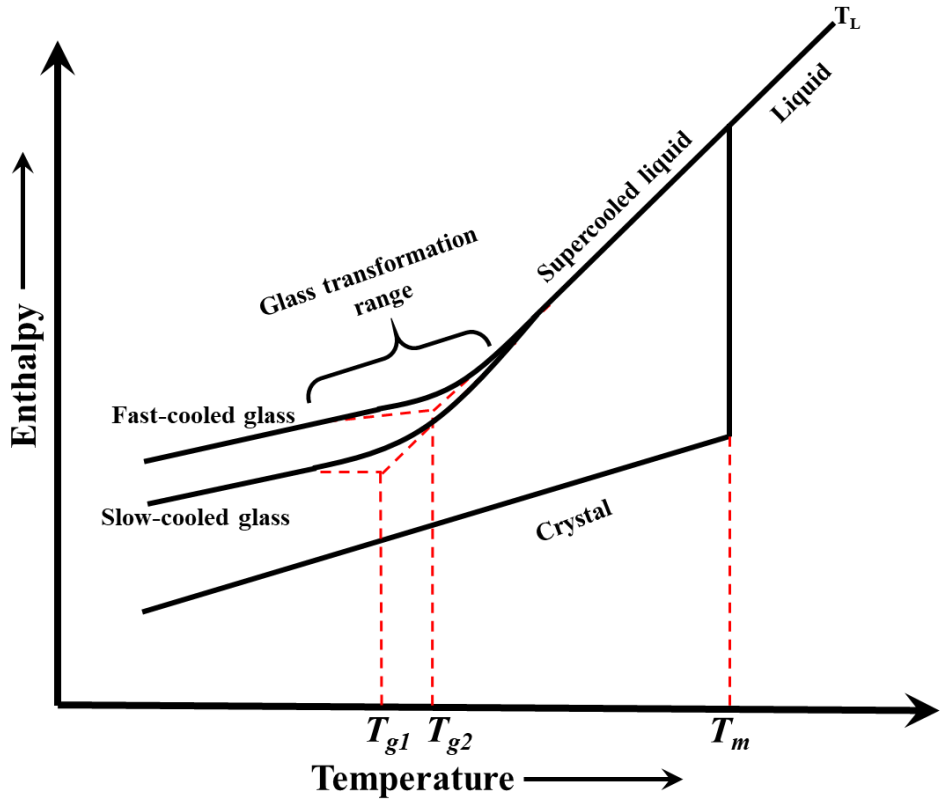

Figure 2.1. Enthalpy of a glass-forming melt as a function of its temperature. Adapted from [13].

2.2 Structure of glasses

Many theories have been put forward to explain the network structure of inorganic oxide-based glasses [16–19]. Goldschmidt proposed the first structural theory based on the radius-ratio of a cation and the oxide anion. He suggested that glasses of formula R_xO_y form most easily if the cation-anion radii ratio is 0.2–0.4, as it resembles the packing ratio of a tetrahedral geometry in crystal systems, where four oxygen atoms surround a cation [20]. Stanworth proposed a mixed-bond concept using the partial ionic character model of Pauling [21]. In this theory, cations are divided into three groups based on their electronegativity. Group I consists of cations that would bond to oxygens with up to 50% ionic character and are labeled as *network formers*. Cations that form bonds with more than 50% ionic character cannot form glasses on their own and are grouped as *intermediate network-formers*. The glassy network can host cations from the second group only if the network formers are present. The third group comprises cations that participate

in non-directional ionic bonding and are referred to as *network modifiers*. These cations do not form glasses on their own and affect the speciation of group I and II cations. In the model proposed by Sun, the strength of the cation-oxygen bonds was considered [22]. Accordingly, strong bonds prevent the transformation of melt structure to crystalline; therefore the disordered environment is conserved. Similar to Stanworth's model, the cations are grouped into three categories. Rawson proposed a variant of Sun's model wherein he suggested that materials with large single-bond strengths and low melting temperatures form good glasses compared to those with a smaller bond strength but a higher melting temperature [23].

Inspired by the Goldschmidt model, Zachariasen proposed a set of rules governing the structural topology in glasses [19]:

a. Oxygens cannot bond to more than two cations as the higher coordination number resembles that of oxygens in a crystalline environment. Moreover, high coordination numbers constrain the bond lengths and bond angles, preventing the formation of a disordered network.
b. Each cation must be bonded either to three or four oxygens.
c. Oxygen polyhedra can only be corner-shared and are not connected by edges or faces.
d. At least three corners must be shared for a three-dimensional network to be formed.

Based on these rules, a widely accepted model called the *continuous random network model* has been constructed in which the disordered structure of a glass network has been attributed to the distribution in the M−O−M bond angle [18,24]. For example, in silicate glasses, the Si−O−Si bond angle ranges from 120 to 180° with a mean bond angle of 144°. The tetrahedra in a glass network and a crystal are similar in structure, i.e., the internal bond lengths and bond angles are conserved to a great extent. The shortest Si−O and O−O distances in glasses are 0.162 and 0.265 nm, respectively [16], similar to crystalline SiO_2, which confirms that the structural characteristics of tetrahedral units are conserved. However, a distribution clustered around 0.312 nm is observed in the distance between silicon atoms in the centres of connected tetrahedra, attributed to a distribution in the Si−O−Si bond angles. The first coordination sphere of a cation is considered its *short-range order*, which always involves oxygen in oxide-based glasses and represents the cation's coordination number. The identity of next-nearest cations can sometimes be elucidated by experimental means, and this polyhedral

connectivity is referred to as *medium-range* or *intermediate-range order*. A distribution in the Si−O−Si bond angle in silicate glasses and Si−O−T (T = heteroatom) in multi-component silicate-based glasses, and the rotation of the polyhedra about the Si−O (also, T−O) prevents the existence of *long-range order* in glasses. The network structure of crystalline and amorphous SiO_2 is illustrated in **Figure 2.2**.

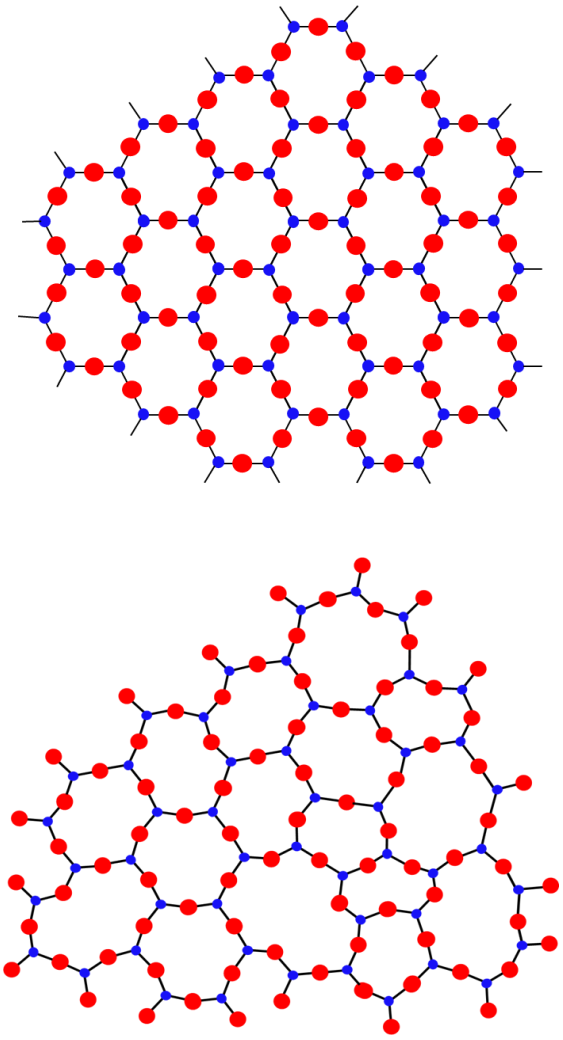

Figure 2.2. A two-dimensional representation of the network structure of crystalline (top) and amorphous (bottom) SiO_2.

2.3 Components of a glass network

Although all cations are bonded to oxygens in an oxide glass network, they are categorized into three groups based on factors such as coordination number, bond strength, and the ionic/covalent character of the bonds, as per the structural models discussed above.

2.3.1 Network formers

As per the models proposed by Stanworth and Sun, the ionicity of the bond between a network-former cation and the oxygen must be less than 50% and should meet the coordination requirements proposed by Zachariasen. Cations such as Si^{4+}, B^{3+} and P^{5+} fall into this category [16]. The polyhedra of network formers interconnect in a three-dimensional fashion and form the bulk of the glass network. Connectivity and dimensionality are two different aspects of a glass network. For example, in a silicate network (SiO_2), the Si^{4+} cations are in a tetrahedral geometry and form a three-dimensional glass network, whereas in a borate glass (B_2O_3), B^{3+} can exist in trigonal-planar geometry. Although the network is made of two-dimensional planar borate units, a three-dimensional network is formed by the predominance of non-zero dihedral angles (**Figure 2.3**). The extent of connectivity dictates the chemical and physical properties of glasses and depends on the fractions of bridging and non-bridging oxygens present in the network. If the oxygen is bonded to two cations (for example, Si−O−Si), it is called *bridging* (BO), and if bonded to a single cation ($Si-O^-$), it is called *non-bridging* (NBO).

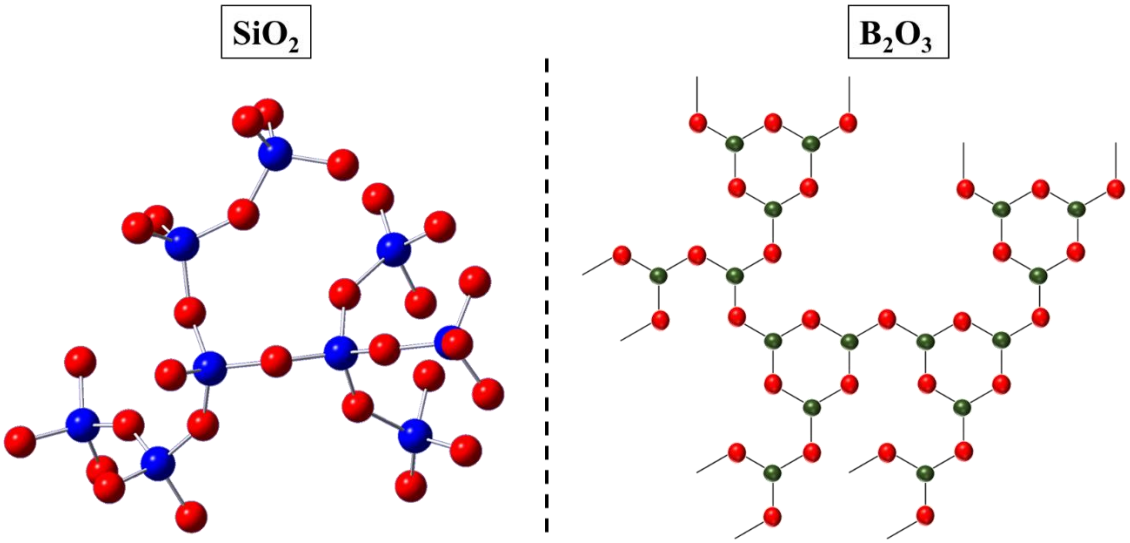

Figure 2.3. The three-dimensional network structure of the silicate glass (left) and a two-dimensional network structure of the borate glass (right). Blue, red and green balls represent Si, O and B atoms, respectively.

2.3.2 Network modifiers

Network modifiers have low electronegativity and participate in ionic interactions with the oxygens. They cannot form an extended three-dimensional network backbone of the glass and exist in high-coordinate environments. Alkali, alkaline-earth, transition metals and some heavy metals such as Pb function as network modifiers. When alkali or alkaline-earth oxides are introduced into a glass network, the oxygen anions are inserted into the network as non-bridging oxygens charge-balanced by modifier cations, therefore depolymerizing the glass network (**Figure 2.4**) [16]. In addition to charge-balancing the NBOs, network modifiers charge-compensate anionic structural units such as tetrahedral boron ($^{[4]}$B) and aluminum ($^{[4]}$Al). Since modifier oxides transform the glass network by changing the number of BO and NBO in the glass network, their concentration in the glass composition influences several properties of glasses [16].

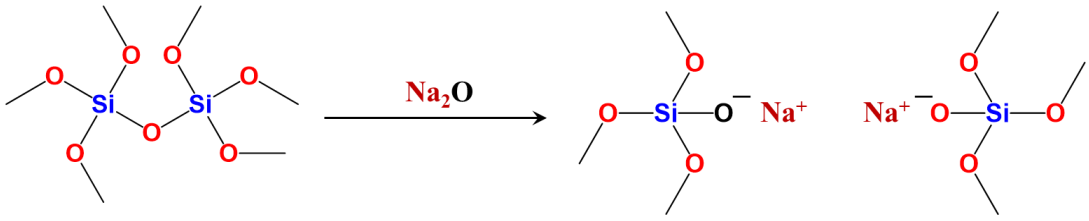

Figure 2.4. Depolymerization of the silicate network by the addition of Na_2O, a network-modifier oxide.

2.3.3 Intermediate network formers

Cations with electronegativities intermediate to network-formers, and -modifiers exhibit a median M−O bond ionicity. They cannot form a glassy network on their own but can integrate into the glass network either as network modifiers or network formers, depending on the glass composition. Ga^{3+} and Al^{3+} are good examples of intermediate network formers, as they can adopt coordination numbers of 4, 5 and 6. Their speciation is strongly dependent on the amount of modifier present in the network. In modifier-rich glasses (Na/Al(Ga)>1) , the Al and Ga units adopt tetrahedral geometry whereas under conditions where Na/Al(Ga)<1, a higher coordination number is evident (vide infra). This modifier-dependent structural adaptation of intermediate network formers helps in the tuning of the properties of many glass systems [25–27].

2.3.4 Network-forming structural units

2.3.4.1 Silicate speciation

Modifier cations depolymerize the silicate glass network by affecting the speciation of the silicate units. In a modifier-free silicate glass, the silicate units are fully connected with no NBOs present. As modifier oxide is introduced, Si−O−Si linkages are broken, forming NBOs bonded to the silicate units [$SiO_{3/2}$−O−$SiO_{3/2}$ + Na_2O → 2($SiO_{3/2}$−O^-Na^+) where, $O_{3/2}$ refers to three oxygens corner-shared with next-nearest silicate neighbours]. A progressive depolymerization of the glass network is observed with increasing modifier fraction [16], allowing silicate units to adopt five distinct configurations, represented by Q^n, where *n* represents the number of BOs per tetrahedron and can have a value from 0 to 4 (**Figure 2.5**). In multi-component silicate glasses,

such as borosilicates, aluminosilicates and aluminoborosilicates, the Si−O−T linkages (T = B, Al, etc.) are present in addition to Si−O−Si linkages.

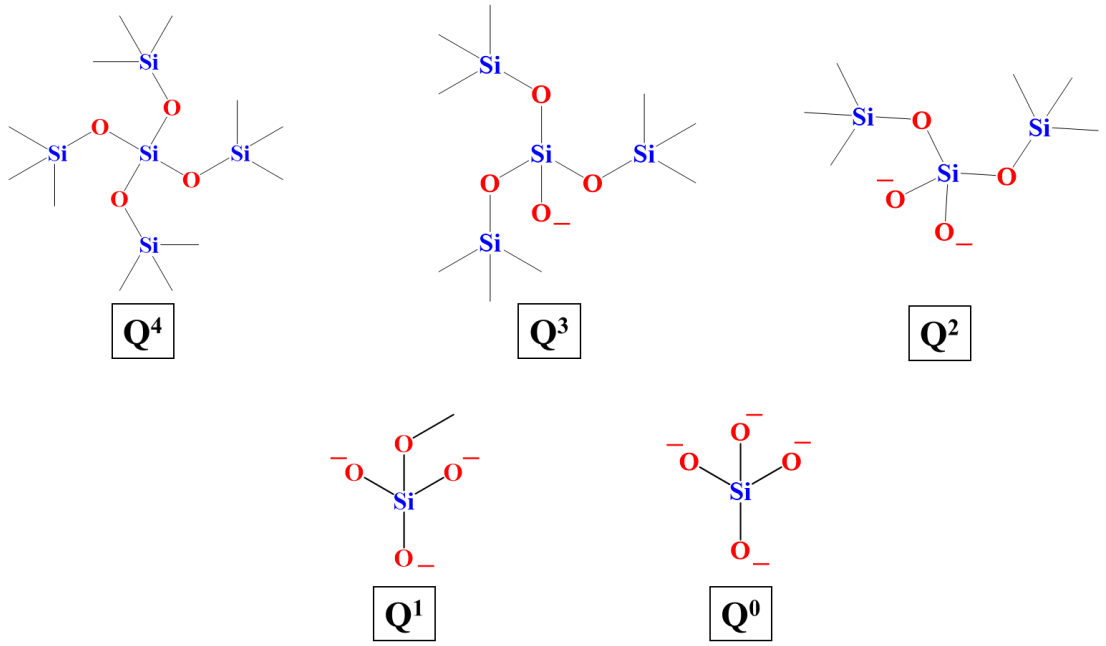

Figure 2.5. Chemically distinct silicate units present in silicate-based glasses.

2.3.4.2 Borate speciation

Boron can exist in three- and four-coordination due to its small cationic radius. In pure borates, B^{3+} exists in trigonal-planar geometry in a ring conformation called *boroxol rings* ($^{[3]}B_{ring}$) (**Figure 2.6**) [16]. As network modifiers are introduced, trigonal-planar borate units transform into tetrahedral units ($^{[4]}B$) with a delocalized negative charge, compensated by the modifier. Such a change increases the connectivity of the glass network. With increasing modifier fraction, the $^{[4]}B$ fraction saturates and with subsequent modifier loading, network depolymerization is observed with NBOs forming on the $^{[3]}B$ units [16]. This modifier-dependent balance between two different coordination geometries in borate glasses is referred to as the *borate anomaly* [16,28]. Trends in borate glass properties such as density [29], glass-transition temperature [30], thermal expansion [31], and thermal conductivity [28] follow the borate anomaly, which is an excellent example of a structure-property relationship. In multi-component borate glasses, the

$^{[3]}$B and $^{[4]}$B units bond to silicate, aluminate and phosphate structural units, generating an intricate network structure. **Figure 2.6** shows the bonding of $^{[3]}$B and $^{[4]}$B units to silicates. The nomenclature of $^{[n]}B_{mSi}$ is followed, where *n* and *m* represent the coordination number of B^{3+} and the number of next-nearest silicate neighbours, respectively.

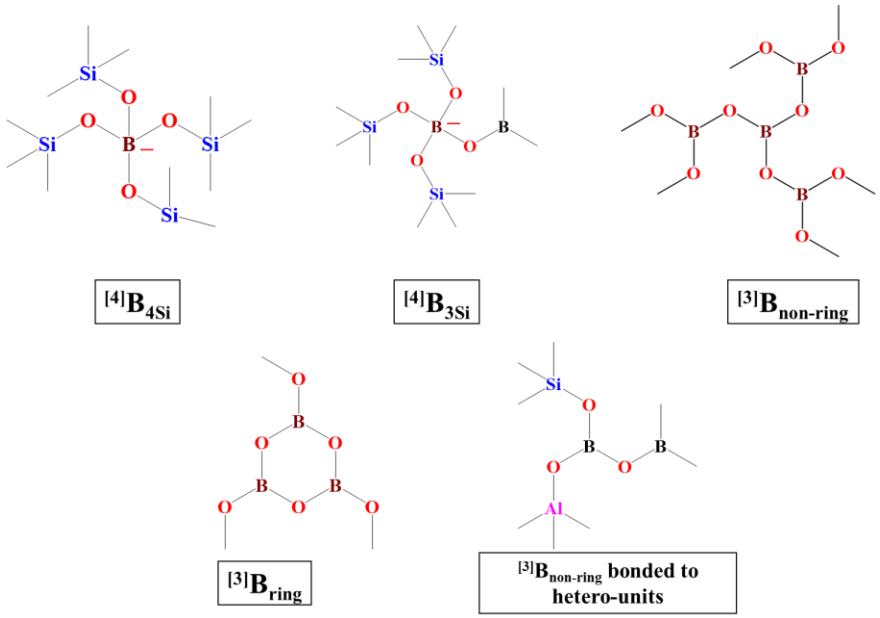

Figure 2.6. Examples of chemically distinct borate units present in borate-based glasses.

2.3.4.3 Aluminate and gallate speciation

Being an intermediate network former, Al^{3+} exists in three different coordination geometries, tetrahedral, penta-, and hexa-coordinated (**Figure 2.7**) [16]. Tetrahedral Al units are anionic and have a negative charge of -1, compensated by the modifier. The connectivity in aluminosilicate glasses generally follows Loewenstein's Al avoidance rule [32], which suggests that Si−O−Al linkages preferentially form over Al−O−Al linkages as the latter bond is energetically unfavourable. Since the tetrahedral Al units are negatively charged, bonding of two anionic units lowers the Al−O bond order, leading to destabilized structures. The same rule applies to borate glasses as well, where $^{[4]}$B−O−$^{[4]}$B linkages are not expected to form. The Ga units are isostructural to Al units and exist as four-, five- and six-coordinated polyhedra in glasses [16].

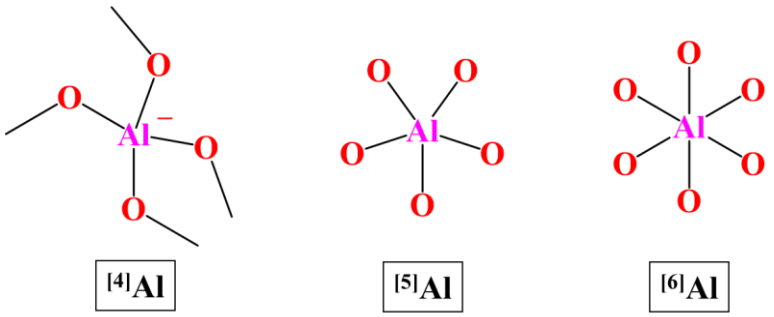

Figure 2.7. Chemically distinct aluminate units present in silicate-, borate- and phosphate-based glasses. The Ga units are isostructural to Al units shown here.

2.3.4.4 Phosphate speciation

The network structure of phosphate glasses consists of interconnected PO_4 tetrahedra, with phosphate units bonding to each other by sharing three bridging oxygens [33,34]. Phosphates exist in multiple conformations: as isolated units called *orthophosphates* (P^0), as dimers called *pyrophosphates* (P^1), in a chain conformation called *metaphosphates* or *polyphosphates* (P^2) and as three-dimensional structural units called *ultraphosphates* (P^3) (**Figure 2.8**) [34]. The term metaphosphate is generally reserved for cyclic phosphate anions $[(PO_3)^-_n]$. Although these structural terms originate from the stoichiometry of phosphates in crystalline alkali phosphate systems, they have become widely used in glass science to identify phosphate units with analogous chemical environments. The nomenclature of P^n is followed when labeling the phosphate units, where n refers to the number of BOs. In the case of multi-component phosphate glasses, the P^n_m labeling is followed, where *m* refers to the number of BOs shared between P and a heteroatom. An example of phosphate bonded to one borate unit (P^2_{1B}) is shown in **Figure 2.8**.

Adding network modifiers to pure phosphate glasses has the same effect as in silicate glasses. As the network-modifier fraction, x, increases, the glass network transforms in the order: $P^3 \rightarrow P^2 \rightarrow P^1 \rightarrow P^0$ [34]. At the modifier fraction of $0 \leq x < 0.5$, the phosphate network predominantly consists of ultraphosphates. As the modifier fraction approaches 0.5, the network is dominated by cyclic P^2 units, and at $x>0.5$, the network mainly consists of polyphosphate chains, terminated by P^1 units. As the x fraction further increases to 0.67, the phosphate dimers

emerge as a predominant network forming units. At x = 0.75, the network is dominated by orthophosphates, which have three NBOs.

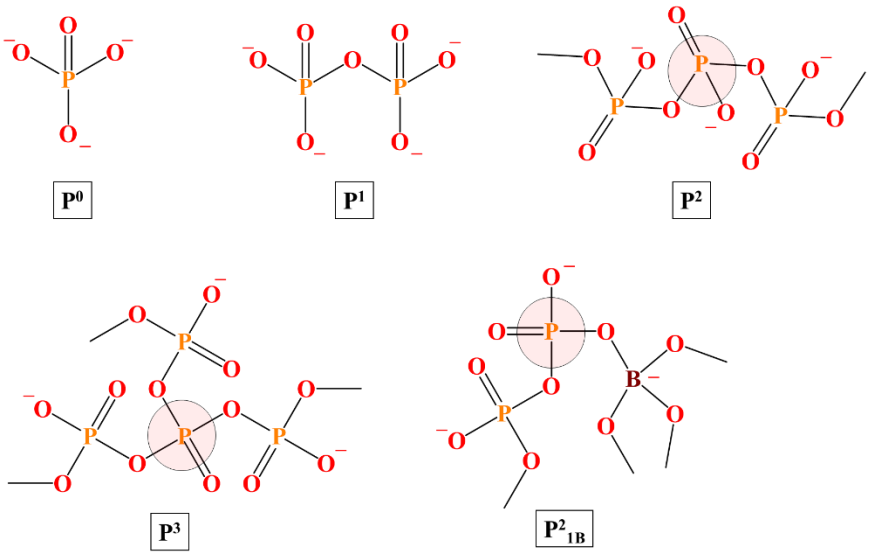

Figure 2.8. Chemically distinct phosphate units present in phosphate-based glasses.

2.4 Chemical durability

Due to the highly radioactive nature and long half-lives of the immobilized radionuclides, waste-immobilized glasses must be isolated from the environment over the geological timescale, typically for millions of years. Hence, underground repositories constituting low-water-permeable host rock, prone to low seismic activity and located below the water table, are chosen as disposal sites for glassy wasteforms [35]. Even though the wasteforms are embedded in multi-level engineering barriers [36], water ingress must always be considered due to the long time frames required. Chemical durability is not an intrinsic property of the glass but is a response to external stimuli and glass-water interactions. Factors such as temperature, near-field chemical conditions, pH, the concentration of various chemical species in water, and the chemical composition of glasses itself influence glass corrosion [37], potentially resulting in the leaching of immobilized radionuclides. Even though the chemical durability of nuclear waste glasses has been studied only for a few decades, rich information exists on the water-resistance capabilities of basaltic and obsidian glasses [35]. These studies suggest a dissolution mechanism common to

all silicate glasses which can be used to predict the long-term chemical durability of borosilicate glasses. Despite the heterogeneous compositions of waste-immobilized silicate glasses, their dissolution is governed by four reactions [35,37–41] (**Figure 2.9**).

2.4.1 Glass dissolution reactions

2.4.1.1 Ion exchange

Upon water contact, the network modifiers from the glass network are exchanged for H^+ ions from water instantaneously, hydrolyzing the glass at the glass-water interface. This process is also referred to as *interdiffusion*. The inward and outward flux of ions at the glass-water interface is driven by the difference in the electrochemical potential across the interface. In the ion-exchange mechanism, the interdiffusion of ions is expressed as [42]:

$$\widetilde{D} = \frac{D_M D_H}{C_M D_M + C_H D_H} \qquad (2.1)$$

where, $\widetilde{D}$ is the interdiffusion coefficient, D and C are the diffusion coefficient and mol fraction of the cations M and H, respectively. $C_M + C_H$ is always equal to 1. The ion-exchange reaction is coupled with the diffusion of molecular water, which immobilizes within the glass network through the following reaction [42]:

$$Si{-}O^-Na^+ + H_2O \rightarrow Si{-}O^-H^+ + OH^- + Na^+$$

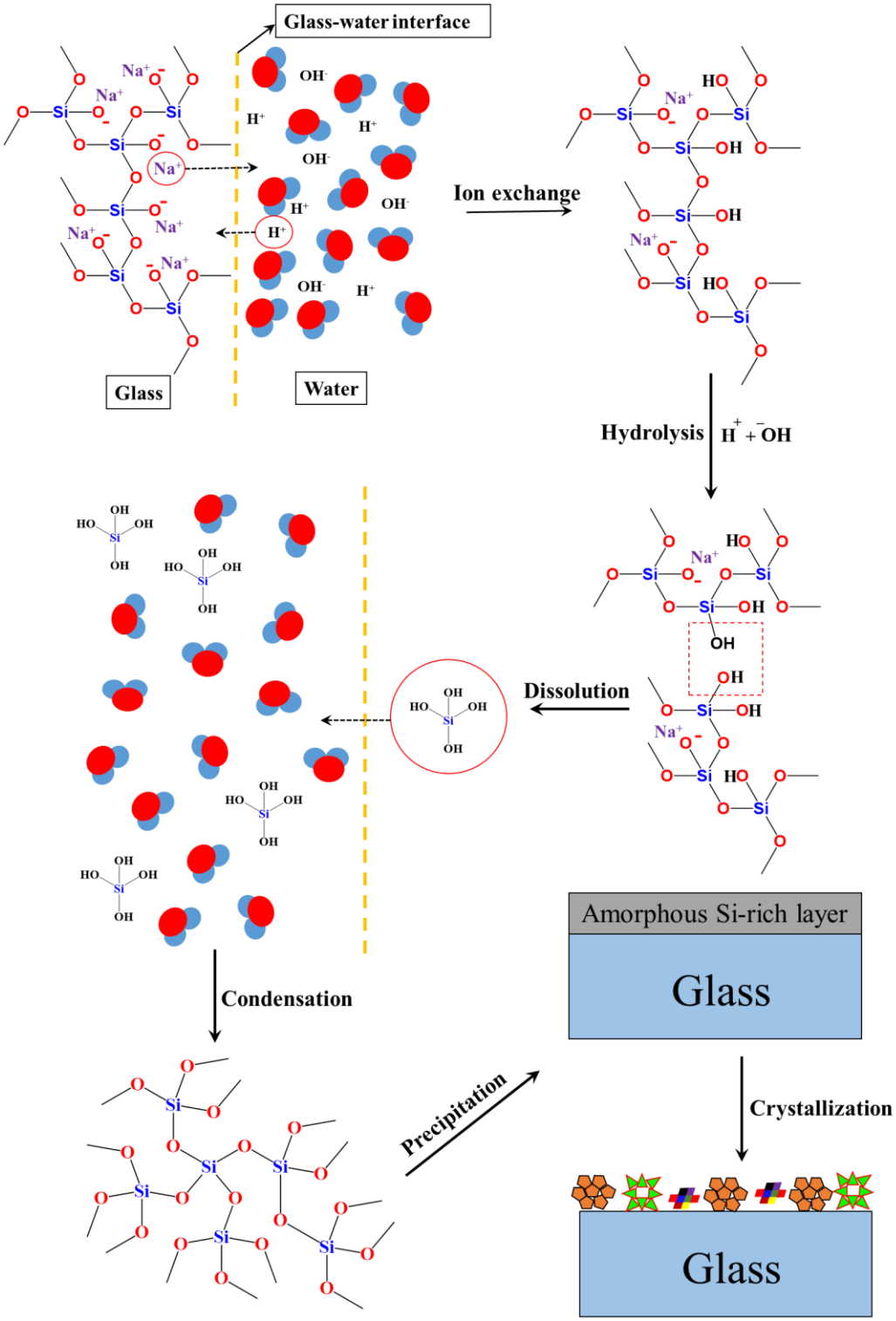

Figure 2.9. Different reactions involved in glass dissolution. The solid arrows represent different reactions, and the dashed-arrows represent the mobility of the chemical species across the glass-water interface.

2.4.1.2 Hydrolysis and dissolution

Hydrolysis is a nucleophilic substitution reaction wherein the nucleophile OH^- targets the Si−O−Si linkages and breaks Si-O bonds, generating silanol groups in the process [43].

$$\text{Si}-\text{O}-\text{Si} + OH^- \rightarrow \text{Si}-\text{OH} + \text{Si}-O^-$$

$$\text{Si}-O^- + H^+ \rightarrow \text{Si}-\text{OH}$$

$$\text{Si}-\text{O}-\text{Si} + OH^- + H^+ \rightarrow 2[\text{Si}-\text{OH}]$$

As the hydrolysis reaction proceeds, free silicic acid (H_4SiO_4) moieties form and diffuse into the water across the glass-water interface, marking the onset of the dissolution process. In multi-component silicate glasses, other cations from the structural framework such as B^{3+} (H_3BO_3), Al^{3+} ($Al(OH)_3$) and P^{5+} (H_3PO_4) can also be released. The compositional ratios of these cations will be similar in glass and water if the glass dissolution is congruent. Dissolution of the glass continues until the chemical potential across the glass-water interface becomes equal. Ion exchange, hydrolysis and dissolution are coupled reactions, occurring simultaneously.

2.4.1.3 Condensation

In static conditions such as in repositories, the continuous release of Si from the glass increases the Si concentration in the solution, and once the Si concentration reaches quasi-steady-state, the dissolution rate drops by several orders of magnitude. The steady-state Si concentration for the SON68 glass [44] with a surface-area-to-volume (S/V) ratio of 1500 m^{-1} at pH 9 and 90 °C is on the order of 50 ppm [45]. A thermodynamic equilibrium exists between the dissolving glass and the fluid composition [46,47], which is disrupted when the Si concentration in the solution reaches a steady state. The equilibrium is restored through a condensation reaction, which generates an amorphous silica-rich gel layer on the glass surface, called an *alteration layer* or a *passivation layer* [39]. The silicic acid moieties in the solution undergo condensation and form oligomers, which eventually polymerize and grow into a gel-like extended structure and precipitate on the glass surface.

$$2[H_4SiO_4] \rightarrow [(OH)_3Si-O-Si(OH)_3] + H_2O$$

$$[(OH)_3Si-O-Si(OH)_3] + H_4SiO_4 \rightarrow [(OH)_3Si-O-(OH)_2Si-O-Si(OH)_3] + H_2O$$

It should be noted that the steady-state concentration is not an intrinsic glass solubility limit, but only marks the onset of silica-gel layer formation as it is dependent on the temperature, pH and glass composition [48]. The alteration layer is transport-limiting as it cuts off water access to the glass surface, blocks ion exchange, and curtails hydrolysis and dissolution reactions. The low porosity (ca. 1 nm) of this layer contributes to its transport-limiting property [38]. The chemical durability of glass is restored once the passivation layer appears on the glass surface, which is generally 2−10 μm thick. The formation of the passivation layer can follow one of two different mechanisms [39].

I. Reorganization by hydrolysis and condensation

Once the Si concentration in the solution saturates, i.e., reaches a steady state, the kinetics of ion-exchange, hydrolysis and dissolution reactions decrease by several orders of magnitude. The similar chemical potential across the glass-water interface prevents detachment and dissolution of fresh silicate and other network-forming units and promotes condensation and reorganization of partially hydrolyzed silicate units into a Si-rich gel layer.

II. Interface-coupled dissolution-reprecipitation reaction

In this mechanism, the rates of glass dissolution and Si-gel formation are coupled. Dissolution proceeds congruently until a thin film of water at the glass-water interface becomes saturated with Si in the H_4SiO_4 form, which is in metastable equilibrium with the bulk of the solution across a solution boundary layer. Saturation of the solution boundary layer by H_4SiO_4 promotes the formation of silica colloids which polymerize into amorphous silica.

2.4.1.4 Crystallization

The metastable amorphous Si-gel layer transforms into thermodynamically stable crystalline silicate phases [38,41]. The minimization of the Gibbs free energy is the thermodynamic driver responsible for this phase change, as per *Ostwald's rule of stages* [49,50]. The rule states that all metastable systems phase-change into the energetically most favourable states but, through a series of intermediate stages wherein the conformer at each stage is slightly lower in Gibbs free energy than its predecessor. For example, If the Gibbs free energy of a metastable system and its corresponding crystalline phase is ΔG^* and ΔG ($\Delta G^* > \Delta G$), the transformation is represented as:

$$\Delta G^* \rightarrow \Delta G^*_A \rightarrow \Delta G^*_B \rightarrow \Delta G^*_C \rightarrow \Delta G^*_D \rightarrow \Delta G$$

The ΔG^*_X is the activation energy barrier for forming intermediate phases A, B, C and D during this phase change. The ΔG^*_A will always be the lowest activation barrier and can be overcome by atomic displacements caused by thermal fluctuations. As the transformation proceeds to later stages, the activation energy barriers increase, slowing the kinetics of phase change.

2.4.2 Stages of glass dissolution

Dissolution of silicate glasses occurs in three stages (**Figure 2.10**) [38]. In stage 1, also called the *forward rate regime,* the glass dissolves congruently due to the lack of solution feedback, and the rate at which the glass dissolves is referred to as the *forward dissolution rate*. The ion-exchange, hydrolysis and dissolution reactions all occur simultaneously in this regime. Eventually, due to the saturation of solution with Si or due to the formation of the solution layer boundary, the passivation layer precipitates on the surface marking the onset of stage 2. This is also called the *residual rate regime,* as the reactions active in stage 1 are subdued, and the glass dissolution stops, restoring its durability. Factors such as pH, temperature, and compositions of glass and the solution greatly impact the kinetics of stage 2 dissolution and its longevity. In stage 3, zeolites and other silicate phases crystallize from the amorphous Si layer, therefore depleting it of Si, and eventually resulting in the loss of the Si layer. This stage is marked by the loss of the protective property of the layer and the recurrence of glass dissolution. The water table in repositories has a large impact on the kinetics of these stages. In flowing conditions, stage 1 persists for a long time, whereas in static conditions, stage 2 is activated soon, typically in the first 30 days of water contact.

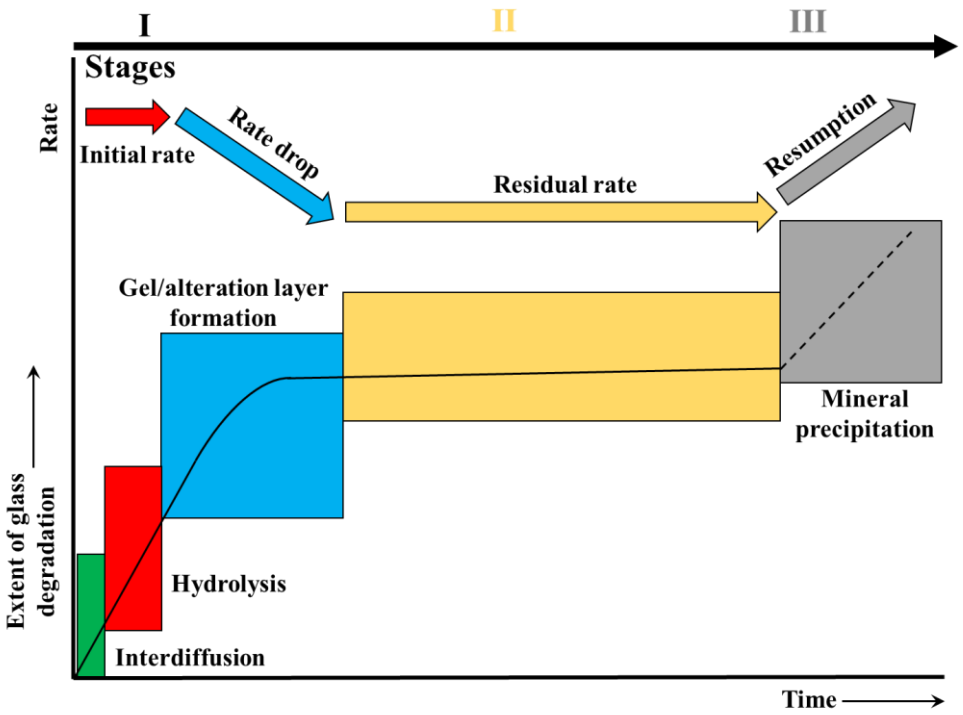

Figure 2.10. Stages of glass dissolution and the types of reactions occurring at each stage. Adapted from [38].

2.4.3 Dissolution of phosphate glasses

Unlike silicate glasses, phosphates lack the ability to form a passivation layer due to their altogether different composition and chemistry. Nevertheless, in some phosphate glasses, such as in barium iron phosphates, a 200 nm thick layer made of ferrihydrite and amorphous phases containing Fe and P has been observed [51] with transport-limiting property, similar to the amorphous silica-gel layer of silicate glasses. The layer formation is strictly a function of pH rather than the chemical potential that is at play in silicate glasses. The release of Ba increases the pH at the glass-water interface, thereby inducing the ferrihydrite layer formation. Only ion-exchange, hydrolysis and dissolution reactions are active in phosphate glasses wherein the P−O−P bonds are hydrolyzed. Under basic conditions, the kinetics of P−O−P bond hydrolysis is slower [52], which underscores the dependency of glass durability on the solution's pH. Phosphate glasses generally exhibit low chemical durability [53] except for some highly-specific compositions such as the iron phosphates [52,54–56], which have acceptable low dissolution rates and are being considered for waste-immobilization in a few countries. Moreover, phosphate

melts are highly corrosive and detrimental to the crucibles [57], an unattractive feature of phosphates in these applications.

2.5 Phase separation

Liquid-liquid phase separation is a common phenomenon in glasses wherein the melt differentiates into distinct glassy or crystalline phases with different microstructures upon cooling, depending on the melt composition and the cooling rate [17,58–63]. Driven by thermodynamic and kinetic energy barriers, phase separation can occur via two mechanisms: *spinodal decomposition* and *nucleation and growth* [60]. A solution of two liquids remains miscible above the liquidus temperature, also called *upper consolute temperature* or *critical temperature* (T_c), as the solution's free energy is lower than those of the two individual liquids. Their extent of miscibility depends on the free energy of mixing, which is given by the expression [17,58]:

$$\Delta G_m = \Delta H_m - T\Delta S_m \qquad (2.2)$$

where ΔG_m is the free energy of mixing, ΔH_m is the change in enthalpy, ΔS_m is the change in entropy of the system, and T is the temperature. The entropy is a function of the concentration of the two liquids and is given by:

$$\Delta S_m = -R[X_1 \ln X_1 + X_2 \ln X_2] \qquad (2.3)$$

where R is the universal gas constant and X_1 and X_2 are the mole fractions of the two liquids. The enthalpy is given by the expression:

$$\Delta H_m = \alpha X_1 X_2 \qquad (2.4)$$

$$\alpha = NZ[E_{AB} - \frac{1}{2}(E_{AA} + E_{BB})] \qquad (2.5)$$

where α is a constant corresponding to the energies of various bonds (E_{AA}, E_{BB} and E_{AB}), N is the Avogadro number, and Z is the number of nearest neighbours surrounding each atom.

Between T_c and T = 0, the enthalpy and entropy terms compete and result in a saddle point in the free energy of mixing vs. composition curve (**Figure 2.11**), wherein the inflection points a and b represent the free energies of two phase-separated liquids. At lower temperatures,

the mixture remains phase-separated, and the tangent connecting these two points is called a *tie-line*, and the points on the abscissa where the a and b intersect (c and d) represent the compositions of two liquids that have differentiated from the solution with similar chemical potentials. The tangent intersects the curve at different points at different free energies of mixing, and the corresponding points on the abscissa represent the compositions of liquids that are phase-separated. With increasing temperature, the two loci (a and b) on the curve merge at T_c, forming a homogeneous melt and resulting in a dome in the phase diagram (yellow dashed line). The curve representing this symmetric dome is called *binodal*, *immiscibility boundary* or the *phase boundary* [17,58]. The region encompassed by the dome is called the *immiscibility region* or the *miscibility gap* where phase separation occurs. In this zone, the liquid spontaneously phase-separates provided there is no kinetic barrier, i.e., the melt's viscosity is high enough to allow diffusion of ions.

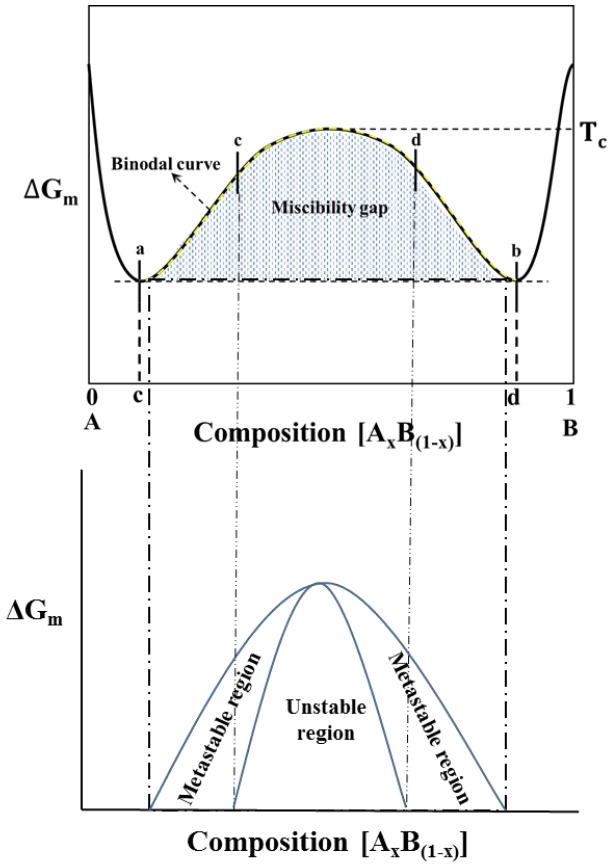

Figure 2.11. Thermodynamics of phase separation in glasses. Adapted from [59].

Although the free energy curve is beneficial in knowing the temperature at which phase separation occurs, no information on the phase separation mechanism can be obtained. The second-derivative ($\delta^2G/\delta x^2$) of the free energy curve's local curvature is determined to address this problem [17,61]. The second-derivative of the curvature is positive between points a, c and b, d, and is called the *metastable or immiscibility region*. The same is negative between points c and d and is called the *unstable region* as it is unstable to immiscibility. Two mechanisms, *nucleation and growth* [17,59,60] and *spinodal decomposition* [58–60], govern the phase-separation process and occur in the metastable and unstable regions, respectively.

2.5.1 Nucleation and growth

Compositional heterogeneity is often observed in melts, attributed to ionic diffusion, which is also considered the kinetic barrier in the phase separation process. Minute changes in composition in the metastable region increase the free energy, preventing phase separation of the melt. If the compositional change is significant, the free energy decreases substantially and the melt phase-separates into two liquids of distinct composition. This decrease in free energy is compensated by an increase in surface energy, which generates well-defined interfaces between the regions of different composition. Since the surface energy is lowest for a sphere, the second liquid appears as droplets dispersed within the first liquid, both with equilibrium compositions. Differentiation of the melt into glassy and crystalline phases follows the nucleation-and-growth mechanism. When the melt temperature and the crystallization temperature of the phase-separating crystal are similar, the droplet's critical radius is too large, inhibiting phase separation. This depends on the diffusion rate of ions, which is related to the melt's viscosity via the Stokes-Einstein relation (**Equation 2.6**). The critical radius decreases as the melt temperature is lowered; stable nucleation sites form homogeneously throughout the glass network upon which the crystallites grow. The lower viscosity of the melt reduces the kinetic barrier, and as a result, ions can diffuse faster, leading to a greater degree of phase separation. The composition of nucleation sites is invariant to the melt composition once they form.

$$D = kT / 3\pi\lambda\eta \qquad (2.6)$$

where D is the diffusion coefficient, k is the Boltzmann constant, T is the temperature, η is the melt's viscosity, and λ is the atomic jump distance.

2.5.2 Spinodal decomposition

Within the unstable region, spinodal decomposition begins with small fluctuations in the concentration which grow over time and result in two continuous interpenetrating phases [58–60]. As these changes are infinitesimally small, they occur spontaneously without any thermodynamic barriers. The free energy decreases until the compositional changes lead to the separation of two liquids with identical chemical potential. Both phases show a high degree of connectivity, and continuous pathways between the two phases exist across the material. The interface between the two phases will initially be diffuse and sharpen over time. Alternately, the matrix is first supersaturated with spherical droplets, which grow in size through long-range diffusion. Once the equilibrium composition is achieved, a coarsening process is observed wherein the smaller particles coalesce, forming larger particles. These droplets will grow into a continuous phase as it lowers the interfacial energy. Practical limitations in glassmaking lead to non-homogeneous cooling of the melt and develop a gradient in the cooling rate across the sample [64]. As a result, heterogeneous microstructures and properties are observed across the material. Due to differential cooling, a gradient exists in the melt viscosity, allowing ions to diffuse and form domains of heterogeneous compositions, both glassy and crystalline.

2.5.3 Phase separation in high-level waste immobilized glasses

A major drawback of borosilicate glasses in nuclear-waste applications is their low affinity for molybdenum, sulfur, rare-earth elements and platinoid elements (Ru, Rh, Pd), which are concentrated in calcined nuclear wastes [65]. Cations such as Mo^{6+} and S^{6+} have high field strengths and are distributed in the glass network as isolated tetrahedral molybdate and sulfate units at lower concentrations. Beyond their solubility limits, they phase-separate as crystalline molybdates and sulfates by sequestering alkali and alkaline-earth ions from the glass network for charge balance. The field strength of a cation is expressed as the ratio of the cation's charge to the square of mean cation-oxygen bond length.

$$\text{CFS} = \frac{n}{r(\text{M}-\text{O})^2} \qquad (2.7)$$

where *n* is the charge on the cation and *r(M−O)* is the mean cation-oxygen bond length. A list of cation field strengths for cations common in silicate-based glasses is given in **Table 2.2**. Cations

with high field-strengths induce strong ordering of the oxygen anions about the cations, leading to clustering, and ultimately to nucleation and crystallization of phases that separate from the glass.

Devitrification alters the structure and strength of these glasses and compromises their long-term performance. Mo^{6+} is a key concern because of its ability to sequester isotopes with very high radioactivity and long half-lives (e.g., ^{135}Cs and ^{90}Sr) to form complex molybdate assemblages known as the "yellow phase" [66]. These radioactive crystalline phases are highly soluble in water and could leach into the environment if they came into contact with water in a geological repository. MoO_3 is one of the limiting factors that controls nuclear-waste loading capacities in borosilicate glasses due to its low solubility. Homogeneous glasses without any phase separation can be achieved when the MoO_3 loading limit is less than 1.5 Mol% [67].

Table 2.2. Cation field-strengths of some HLW relevant cations. M−O bond lengths are obtained from [68–71].

Cations	**Mean bond length (Å)**	**Coordination number**	**Field-strength ($Z/Å^2$)**
Si^{4+}	1.625	4	1.51
B^{3+}	1.475	4	1.38
P^{5+}	1.537	4	2.13
Al^{3+}	1.746	4	0.99
Na^{+}	2.441	6	0.16
Cs^{+}	3.224	8	0.09
Mo^{6+}	1.764	4	1.92
S^{6+}	1.473	4	2.77

Like molybdenum, sulfate anions exhibit low solubility in borosilicate glasses (0.6 mol% or ~ <1 wt%) [72–74]. The sources of sulfate in a typical nuclear waste stream are ferrous sulfamate (used in the reduction of Pu^{4+} to Pu^{3+}) [75], waste liquors arising from the Purex process, and spent-ion-exchange resins [76]. Although the oxidation states of sulfur range from -2 to +6, in the oxidizing conditions of borosilicate glasses, they are predominantly found as hexavalent cations [75] with a coordination number of four (SO_4^{2-}). At low levels, isolated SO_4^{2-} tetrahedral units concentrate into voids in the borosilicate network [77]. Above the solubility limit of sulfur, a sulfate-rich salt layer is observed on top of the melt pool, which precipitates during melt cooling [73]. This phase-separated layer is called “gall” [75] and is prominent in borosilicate glasses used to immobilize high-level liquid wastes rich in sulfate, therefore limiting the waste-loading capacity of the glass. The main component in the gall layer is Na_2SO_4 [75], which is capable of sequestering radioactive isotopes of Cs, Sr, and Tc [72]. Phase separation and precipitation of the gall layer on top of the melt also has a detrimental effect on the crucible and furnace, as it is highly corrosive and, being a good conductor, makes the melting process less efficient [72]. The gall layer on the melt pool inhibits the release of gas bubbles, leading to swelling of the vitreous phase upon cooling [75]. The presence of sulfur in the waste stream also impacts the glass formation conditions, as sulfate decomposes at high temperatures, releasing SO_2 gas, which might be enriched with radioactive isotopes [78].

2.6 Vitrification

Vitrification [2] is a two-stage process (**Figure 2.12**) wherein the HLLW is calcined in a rotary or spray furnace [79], which is subsequently mixed with glass frit and melted in a joule-heated ceramic melter or an induction-heated melter. The melt is poured into stainless steel containers and either slow-cooled in an annealing furnace or not, depending on the reprocessing site's facilities. The calciner and melter are connected to off-gas purification systems to trap the radionuclide-rich aerosols and gases that are generated.

A variant of the two-stage technique called the one-pot process is also practiced wherein both calcination and melting are achieved in a single pot, which could either function as a crucible or is the wasteform container. The glass frit is mixed with the high-level liquid waste and fed to the melter in a paste-form, with due precautions for the aerosols. The melt is

homogenized by using baffles or bubbling air through the bottom of the crucible. The chemical composition of the French nuclear waste borosilicate glass called SON68 is listed in **Table 2.3** [44], which shows the complexity associated with these kinds of materials.

Table 2.3. SON68 nuclear waste glass composition (in wt%) [44].

Oxide	**wt%**
Li_2O	1.99
Na_2O	10.22
CaO	4.07
MoO_3	1.78
ZnO	2.53
B_2O_3	14.14
Al_2O_3	5.0
SiO_2	45.85
Fe_2O_3	3.03
MnO_2	0.39
P_2O_5	0.29
ZrO_2	2.75
Cs_2O	1.12
NiO	0.43
SrO	0.35
Cr_2O_3	0.53
Y_2O_3	0.20
Ag_2O	0.03
CdO	0.03
SnO_2	0.02
TeO_2	0.23
BaO	0.62
La_2O_3	0.93
Ce_2O_3	0.97
Pr_2O_3	0.46
Nd_2O_3	2.04

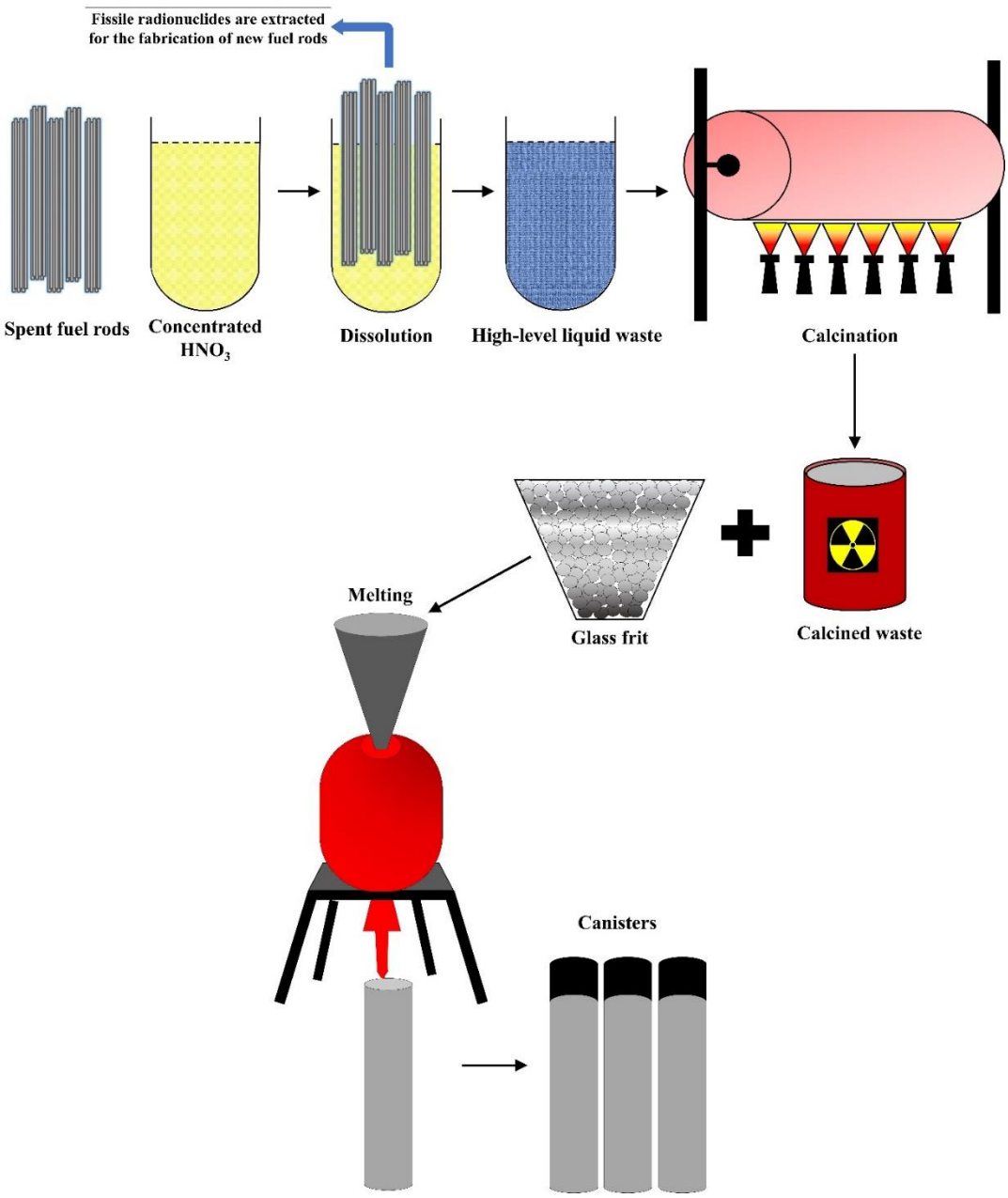

Figure 2.12. An illustration of the reprocessing of spent nuclear fuel and high-level waste vitrification stages.

2.7 References

[1] I.W. Donald, B.L. Metcalfe, R.N.J. Taylor, Review: The immobilization of high level radioactive wastes using ceramics and glasses, J. Mater. Sci. 32 (1997) 5851–5887.

[2] M.I. Ojovan, W.E. Lee, Glassy wasteforms for nuclear waste immobilization, in: Metall. Mater. Trans. A Phys. Metall. Mater. Sci., 2011: pp. 837–851.

[3] P. Gaskell, The local structure of oxide and metallic glasses, Nucl. Instruments Methods. 199 (1982) 45–60.

[4] M.I. Ojovan, W.E. Lee, Immobilisation of radioactive wastes in glass, in: *An introduction to nuclear waste immobilization*, Newnes, 2013.

[5] P. Rautiyal, G. Gupta, R. Edge, L. Leay, A. Daubney, M.K. Patel, A.H. Jones, P.A. Bingham, Gamma irradiation-induced defects in borosilicate glasses for high-level radioactive waste immobilisation, J. Nucl. Mater. 544 (2021) 152702.

[6] W.J. Weber, Radiation and thermal ageing of nuclear waste glass, Procedia Mater. Sci. 7 (2014) 237–246.

[7] T.C. Kaspar, J. V. Ryan, C.G. Pantano, J. Rice, C. Trivelpiece, N.C. Hyatt, C.L. Corkhill, C. Mann, R.J. Hand, M.A. Kirkham, C.L. Crawford, C.M. Jantzen, J. Du, X. Lu, M.T. Harrison, C. Cushman, M.R. Linford, N.J. Smith, Physical and optical properties of the International Simple Glass, Npj Mater. Degrad. 3 (2019).

[8] E.A. Maugeri, S. Peuget, D. Staicu, A. Zappia, C. Jegou, T. Wiss, Calorimetric study of glass structure modification induced by α-decay, J. Am. Ceram. Soc. 95 (2012) 2869–2875.

[9] T. Charpentier, L. Martel, A.H. Mir, J. Somers, C. Jégou, S. Peuget, Self-healing capacity of nuclear glass observed by NMR spectroscopy, Sci. Rep. 6 (2016) 1–6.

[10] N.C. Hyatt, M.I. Ojovan, Special issue: Materials for nuclear waste immobilization, Materials (Basel). 12 (2019) 12–15.

[11] B.A. Moyer, R. Custelcean, B.P. Hay, J.L. Sessler, K. Bowman-James, V.W. Day, S.O. Kang, A case for molecular recognition in nuclear separations: Sulfate separation from

nuclear wastes, Inorg. Chem. 52 (2013) 3473–3490.

[12] K.J. Rao, The world of inorganic glasses, in: *Structural chemistry of glasses*, Elsevier, 2002: pp. 1–8.

[13] J.E. Shelby, Introduction, in: *Introduction to glass science and technology*, 1st ed., Royal Society of Chemistry, 2005: pp. 1–7.

[14] K.J. Rao, The glass transition phenomenon, in: *Structural chemistry of glasses*, Elsevier, 2002: pp. 77–121.

[15] G.S. Henderson, G. Calas, J.F. Stebbins, The structure of silicate glasses and melts, Elements. 2 (2006) 269–273.

[16] J.E. Shelby, Structures of glasses, in: *Introduction to glass science and technology*, Royal Society of Chemistry, 2007: pp. 78–90.

[17] J.E. Shelby, Principles of glass formation, in: *Introduction to glass science and technology*, Royal Society of Chemistry, 2005: pp. 7–25.

[18] K.J. Rao, The glassy state, in: *Structural chemistry of glasses*, Elsevier, 2002.

[19] W.H. Zachariasen, The atomic arrangement in glass, J. Am. Chem. Soc. 54 (1932) 3841–3851.

[20] I.S. Gutzow, J.W. Schmelzer, General approaches in the description of the structure of glasses, in: *Vitreous state*, Springer, Berlin, Heidelberg, 2013: pp. 127–164.

[21] Stanworth J E, Tellurite glasses, Nature. (1952) 581–582.

[22] K. -H Sun, Fundamental condition of glass formation, J. Am. Ceram. Soc. 30 (1947) 277–281.

[23] G. de Leede, H. de Waal, Evaluation of glass formation criteria, J. Non-Cryst. Solids. 104 (1988) 45–51.

[24] R.J. Bell, P. Dean, The structure of vitreous silica : Validity of the random network theory, Philos. Mag. 25 (1972) 1381–1398.

[25] A. Ledieu, F. Devreux, P. Barboux, The role of aluminium in the durability of alumino-

borosilicate glasses, Phys. Chem. Glas. 46 (2005) 12–20.

[26] V.P. Klyuev, B.Z. Pevzner, The influence of aluminum oxide on the thermal expansion, glass transition temperature, and viscosity of lithium and sodium aluminoborate glasses, Glas. Phys. Chem. 28 (2002) 207–220.

[27] R.J. Eagan, J.C. Swearengen, Effect of composition on the mechanical properties of aluminosilicate and borosilicate glasses, J. Am. Ceram. Soc. 61 (1978) 27–30.

[28] S.S. Sørensen, H. Johra, J.C. Mauro, M. Bauchy, M.M. Smedskjaer, Boron anomaly in the thermal conductivity of lithium borate glasses, Phys. Rev. Mater. 3 (2019) 1–11.

[29] H. Doweidar, Consideration of the boron oxide anomaly, J. Mater. Sci. 25 (1990) 253–258.

[30] A. DeCeanne, A. Potter, K. Richter, D. Starkenburg, B. Perez, T. Munhollon, N. Barnes, E. Troendle, C. Flynn, M. Affatigato, S. Feller, E. Zanotto, O. Pietl, An anomaly in the glass transition width trends of alkali borate glasses at low modifier loadings, Phys. Chem. Glas. Eur. J. Glas. Sci. Technol. Part B. 58 (2017) 187–194.

[31] J.E. Shelby, Thermal expansion of alkali borate glasses., J. Am. Ceram. Soc. 66 (1982) 225–227.

[32] W. Loewenstein, The distribution of aluminum in the tetrahedra of silicates and aluminates, Am. Mineral. 39 (1954) 92–96.

[33] C.K. Loong, K. Suzuya, D.L. Price, B.C. Sales, L.A. Boatner, Structure and dynamics of phosphate glasses: From ultra- to orthophosphate composition, Phys. B Condens. Matter. 241–243 (1997) 890–896.

[34] R.K. Brow, Review: The structure of simple phosphate glasses, J. Non-Cryst. Solids. 263–264 (2000) 1–28.

[35] S. Gin, C. Guittonneau, N. Godon, D. Neff, D. Rebiscoul, M. Cabí, S. Mostefaoui, Nuclear glass durability: New insight into alteration layer properties, J. Phys. Chem. C. 115 (2011) 18696–18706.

[36] S.M. Spearing, Materials Issues in Nuclear-waste management, JOM. 52 (2000) 26–29.

[37] J.D. Vienna, J.J. Neeway, J. V. Ryan, S.N. Kerisit, Impacts of glass composition, pH, and temperature on glass forward dissolution rate, Npj Mater. Degrad. 2 (2018) 1–12.

[38] G.S. Frankel, J.D. Vienna, J. Lian, J.R. Scully, S. Gin, J. V. Ryan, J. Wang, S.H. Kim, W. Windl, J. Du, A comparative review of the aqueous corrosion of glasses, crystalline ceramics, and metals, Npj Mater. Degrad. 2 (2018).

[39] T. Geisler, A. Janssen, D. Scheiter, T. Stephan, J. Berndt, A. Putnis, Aqueous corrosion of borosilicate glass under acidic conditions: A new corrosion mechanism, J. Non-Cryst. Solids. 356 (2010) 1458–1465.

[40] C. Cailleteau, F. Angeli, F. Devreux, S. Gin, J. Jestin, P. Jollivet, O. Spalla, Insight into silicate-glass corrosion mechanisms, Nat. Mater. 7 (2008) 978–983.

[41] S. Gin, P. Jollivet, M. Fournier, F. Angeli, P. Frugier, T. Charpentier, Origin and consequences of silicate glass passivation by surface layers, Nat. Commun. 6 (2015).

[42] R.H. Doremus, Diffusion-controlled reaction of water with glass, J. Non-Cryst. Solids. 55 (1983) 143–147.

[43] M. V Landau, Sol-gel processing, in: *Synthesis of solid catalyst*s, Wiley-VCH Weinheim, 2009: pp. 83–109.

[44] P. Frugier, S. Gin, Y. Minet, T. Chave, B. Bonin, N. Godon, J.E. Lartigue, P. Jollivet, A. Ayral, L. De Windt, G. Santarini, SON68 nuclear glass dissolution kinetics: Current state of knowledge and basis of the new GRAAL model, J. Nucl. Mater. 380 (2008) 8–21.

[45] E. Vernaz, S. Gin, Apparent solubility limit of nuclear glass, Mater. Res. Soc. Symp. Proc. 663 (2001).

[46] E.M. Pierce, P. Frugier, L.J. Criscenti, K.D. Kwon, S.N. Kerisit, Modeling interfacial glass-water reactions: recent advances and current limitations, Int. J. Appl. Glas. Sci. 5 (2014) 421–435.

[47] P. Aagaard, H.C. Helgeson, Thermodynamic and kinetic constraints on reaction rates among minerals and aqueous solutions. I. Theoretical considerations., Am. J. Sci. 282 (1982) 237–285.

[48] J.J. Neeway, P.C. Rieke, B.P. Parruzot, J. V. Ryan, R.M. Asmussen, The dissolution behavior of borosilicate glasses in far-from equilibrium conditions, Geochim. Cosmochim. Acta. 226 (2018) 132–148.

[49] J.W.P. Schmelzer, A.S. Abyzov, How do crystals nucleate and grow: Ostwald's rule of stages and beyond, in Thermal physics and thermal analysis, Springer (2017), pp:195–211.

[50] T. Threlfall, Structural and thermodynamic explanations of Ostwald's rule, Org. Process Res. Dev. 7 (2003) 1017–1027.

[51] K. Joseph, T.R. Ravindran, R. Sudha, R. Asuvathraman, $BaO\text{-}Fe_2O_3\text{-}P_2O_5$ glasses: Understanding the thermal stability, J. Nucl. Mater. 517 (2019) 106–112.

[52] R.K. Brow, C.W. Kim, S.T. Reis, Iron polyphosphate glasses for waste immobilization, Int. J. Appl. Glas. Sci. 11 (2020) 4–14.

[53] T. Minami, J.D. Mackenzie, Thermal expansion and chemical durability of phosphate glasses, J. Am. Ceram. Soc. 60 (1977) 232–235.

[54] D. Kim, W. Buchmiller, M.J. Schweiger, J.D. Vienna, D.E. Day, C.W. Kim, D. Zhu, T.E. Day, T. Neidt, D.K. Peeler, I.A. Reamer, T.B. Edwards, R.J. Workman, Iron phosphate glass as an alternative waste-form for Hanford LAW, PNNNL-14251, Pacific Northwest Laboratory, Richland, WA, USA, 2003.

[55] S. V. Stefanovsky, O.I. Stefanovsky, M.B. Remizov, P. V. Kozlov, E.A. Belanova, R.A. Makarovsky, B.F. Myasoedov, Sodium–aluminum–iron phosphate glasses as legacy high level waste forms, Prog. Nucl. Energy. 94 (2017) 229–234.

[56] K. Joseph, M.C. Stennett, N.C. Hyatt, R. Asuvathraman, C.L. Dube, A.S. Gandy, K. V. Govindan Kutty, K. Jolley, P.R. Vasudeva Rao, R. Smith, Iron phosphate glasses: Bulk properties and atomic scale structure, J. Nucl. Mater. 494 (2017) 342–353.

[57] H. Cao, J.W. Adams, P.D. Kalb, Low temperature glasses for hanford tank wastes,BNL-52595, Brookhaven National Laboratory, Long Island, NY, USA, 1995.

[58] P.F. James, Liquid-phase separation in glass-forming systems, J. Mater. Sci. 10 (1975)

1802–1825.

[59] J.E. Shelby, Immiscibility/phase separation, in: *Introduction to glass science and technology*, Elseiver, 2005: pp. 51–71.

[60] B.R. Wheaton, A.G. Clare, Evaluation of phase separation in glasses with the use of atomic force microscopy, J. Non-Cryst. Solids. 353 (2007) 4767–4778.

[61] N. Kreidl, Phase separation in glasses, J. Non-Cryst. Solids. 129 (1991) 1–11.

[62] R.J. Charles, Phase separation in borosilicate glasses, J. Am. Ceram. Soc. 47 (1964) 559–563.

[63] G.F. Neilson, Phase separation in glass and glass-ceramic systems, Discuss. Faraday Soc. 50 (1970) 145–154.

[64] J.E.C. Wren, Application of nuclear magnetic resonance to the study of nuclear waste relevant molybdates at ambient and high temperatures, Ph.D. Thesis, University of Manitoba, 2014.

[65] N. Chouard, D. Caurant, O. Majérus, J.L. Dussossoy, S. Klimin, D. Pytalev, R. Baddour-Hadjean, J.P. Pereira-Ramos, Effect of MoO_3, Nd_2O_3, and RuO_2 on the crystallization of soda–lime aluminoborosilicate glasses, J. Mater. Sci. 50 (2015) 219–241.

[66] S. Kroeker, S. Schuller, J.E.C. Wren, B.J. Greer, A. Mesbah, ^{133}Cs and ^{23}Na MAS NMR spectroscopy of molybdate crystallization in model nuclear glasses, J. Am. Ceram. Soc. 99 (2016) 1557–1564.

[67] J.D. Vienna, Nuclear waste vitrification in the United States: Recent developments and future options, Int. J. Appl. Glas. Sci. 1 (2010) 309–321.

[68] O.C. Gagné, F.C. Hawthorne, Bond-length distributions for ions bonded to oxygen: Metalloids and post-Transition metals: Metalloids, Acta Crystallogr. Sect. B Struct. Sci. Cryst. Eng. Mater. 74 (2018) 63–78.

[69] O.C. Gagné, F.C. Hawthorne, Bond-length distributions for ions bonded to oxygen: Alkali and alkaline-earth metals, Acta Crystallogr. Sect. B Struct. Sci. Cryst. Eng. Mater. 72 (2016) 602–625.

[70] O.C. Gagné, F.C. Hawthorne, Bond-length distributions for ions bonded to oxygen: Results for the non-metals and discussion of lone-pair stereoactivity and the polymerization of PO_4: Results, Acta Crystallogr. Sect. B Struct. Sci. Cryst. Eng. Mater. 74 (2018) 79–96.

[71] O.C. Gagné, F.C. Hawthorne, Bond-length distributions for ions bonded to oxygen: Results for the transition metals and quantification of the factors underlying bond-length variation in inorganic solids, IUCrJ. 7 (2020) 581–629.

[72] D. Manara, A. Grandjean, O. Pinet, J.L. Dussossoy, D.R. Neuville, Sulfur behavior in silicate glasses and melts: Implications for sulfate incorporation in nuclear waste glasses as a function of alkali cation and V_2O_5 content, J. Non-Cryst. Solids. 353 (2007) 12–23.

[73] A.L. Billings, K.M. Fox, Retention of sulfate in savannah river site high-level radioactive waste glass, Int. J. Appl. Glas. Sci. 1 (2010) 388–400.

[74] L. Wu, J. Xiao, X. Wang, Y. Teng, Y. Li, Q. Liao, Crystalline phase, microstructure, and aqueous stability of zirconolite-barium borosilicate glass-ceramics of immobilization of sulfate bearing high-level liquid waste, J. Nucl. Mater. 498 (2018) 241–248.

[75] C.P. Kaushik, R.K. Mishra, P. Sengupta, A. Kumar, D. Das, G.B. Kale, K. Raj, Barium borosilicate glass - a potential matrix for immobilization of sulfate bearing high-level radioactive liquid waste, J. Nucl. Mater. 358 (2006) 129–138.

[76] P.A. Bingham, S. Vaishnav, S.D. Forder, A. Scrimshire, B. Jaganathan, J. Rohini, J.C. Marra, K.M. Fox, E.M. Pierce, P. Workman, J.D. Vienna, Modelling the sulfate capacity of simulated radioactive waste borosilicate glasses, J. Alloys Compd. 695 (2017) 656–667.

[77] D.A. Mckeown, I.S. Muller, H. Gan, I.L. Pegg, C.A. Kendziora, Raman studies of sulfur in borosilicate waste glasses: sulfate environments, J. Non-Cryst. Solids. 288 (2001) 191–199.

[78] M. Lenoir, A. Grandjean, S. Poissonnet, D.R. Neuville, Quantitation of sulfate solubility in borosilicate glasses using Raman spectroscopy, J. Non-Cryst. Solids. 355 (2009) 1468–1473.

[79] B.R. Wheeler, J.A. Buckham, J.A.Mcbride, A comparison of various calcination processes for processing high-level radioactive wastes, IDO-14622, Phillips Petroleum Co. Atomic Energy Div., National Reactor Testing Station Idaho, 1964.

3 Nuclear Magnetic Resonance Spectroscopy

3.1 Theory

The interaction between the *spin* of a nucleus, an intrinsic physical property, and an applied magnetic field is fundamental to NMR spectroscopy. Since one or more isotopic forms of more than 70% of known elements possess a nuclear spin [1], the technique may be applied to study a diverse class of materials with a broad range of chemical compositions. The nuclear spin is represented by the spin quantum number *I*, which has a value of $I = \frac{n}{2}$ (n = 1,2,3,4,…) and is quantized by 2*I*+1 *eigenstates*, labeled by the magnetic quantum number m_I [1-3]. The m_I can take any value between $[-I, -I+1, -I+2, \ldots +I]$ with integer steps between them. For example, a nucleus with spin $\frac{1}{2}$ has $-\frac{1}{2}$ and $+\frac{1}{2}$ spin states, whereas a nucleus with I = $\frac{5}{2}$ has a set of six spin states, $+\frac{5}{2}$, $+\frac{3}{2}$, $+\frac{1}{2}$, $-\frac{1}{2}$, $-\frac{3}{2}$, and $-\frac{5}{2}$. The spin quantum number is a function of the number of protons and neutrons a nucleus has: nuclei with an even number of protons and neutrons have a spin of zero and are not NMR active; nuclei with an odd number of protons and neutrons (integer spin, *I* = 1, 2,…) and nuclei with either odd number of neutrons or odd number of protons (half-integer spin, $I = \frac{1}{2}, \frac{3}{2}, \frac{5}{2}$,..), are NMR active. Due to their spin, nuclei have a nuclear spin angular momentum, $\hbar$I, and therefore a nuclear magnetic moment, $\vec{\mu}$, which are related by another intrinsic physical constant specific to each nucleus called the *gyromagnetic ratio* (γ) as expressed in **Equation 3.1**, where $\hbar$ is the Planck constant:

$$\vec{\mu} = \gamma \hbar I \qquad (3.1)$$

When an external magnetic field ($\vec{B}_0$) is applied, the degeneracy of the spin states is lifted, resulting in spin states with discrete energy differences (**Figure 3.1**). This phenomenon is referred to as the *Zeeman effect* [4]. The energy differences (ΔE) between these states increase as the strength of the applied magnetic field increases, which is given by,

$$\Delta E = \gamma \hbar \vec{B}_0 \qquad (3.2)$$

In addition to the splitting of the spin eigenstates, the Zeeman interaction is responsible for populating these spin states, according to the Boltzmann distribution (**Equation 3.3**)

$$\frac{N_{-\frac{1}{2}}}{N_{+\frac{1}{2}}} = e^{-\frac{\Delta E}{kT}} \qquad (3.3)$$

where $N_{+1/2}$ and $N_{-1/2}$ are the spin populations in $+\frac{1}{2}$ and $-\frac{1}{2}$ spin states, k is the Boltzmann's constant and T is the temperature. The population of the spin states is also influenced by the temperature, which increases as the temperature decreases. Since the spins in the $-\frac{1}{2}$ and $+\frac{1}{2}$ states have negative and positive nuclear magnetic moments (**Equation 3.1**), respectively, and as the $+\frac{1}{2}$ state has a slightly higher population relative to $-\frac{1}{2}$, a net positive magnetic moment persists. This excess population is very small, making the NMR a relatively insensitive technique; for example, only an excess of 3.2 x 10^{-3}% ^{1}H spins exist in the $+\frac{1}{2}$ state at a field of 9.4 T and room temperature, which are responsible for the observance of the NMR signal [1].

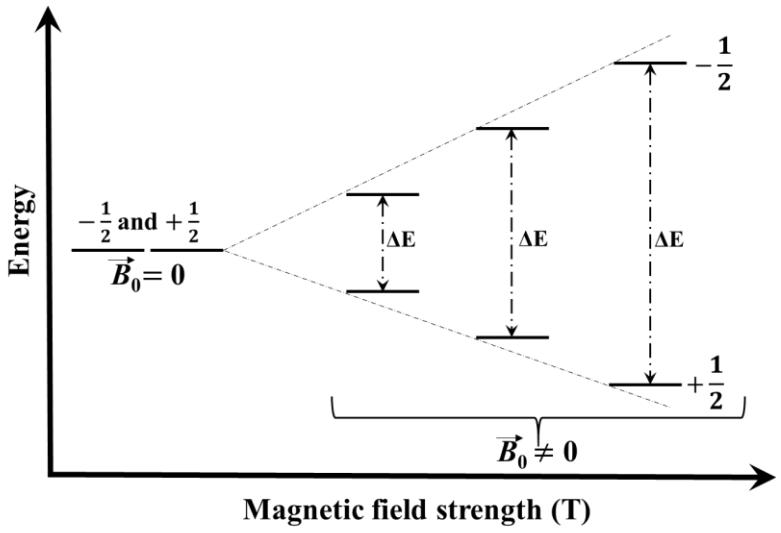

Figure 3.1. Zeeman splitting for a spin $\frac{1}{2}$ nucleus (for example, ^{1}H, ^{13}C, and ^{15}N) showing degenerate spin states in the absence of an external magnetic field ($\vec{B}_0$) and the splitting of the energy levels when the field is applied. The energy difference (ΔE) between the spin states increases with the strength of the magnetic field.

In the absence of $\vec{B}_0$, individual magnetic moments of the spins are randomly oriented, leading to zero net magnetization. When a field is applied along the z-axis in a laboratory frame of reference, the net magnetization, $\vec{M}_0$, which is a vectorial sum of all individual magnetic moments (**Equation 3.4**), aligns with the field (**Figures 3.2 and 3.3**).

$$\vec{M}_0 = \sum_i \vec{\mu}_i = \gamma I_i = \gamma \vec{J} \qquad (3.4)$$

where $\vec{\mu}_i$ and I_i are the magnetic moment and the spin quantum number of the i^{th} nucleus, respectively, γ is the gyromagnetic ratio, and $\vec{J}$ is the net angular momentum giving rise to $\vec{M}_0$. The equilibrium magnetization is given by [1],

$$\vec{M}_0 = \frac{N\gamma^2 \vec{B}_0 \hbar^2 I(I+1)}{3kT} \qquad (3.5)$$

where N is the population difference, $N = N_{+1/2} - N_{-1/2}$. The $\vec{B}_0$ exerts a torque on the net magnetization (**Equation 3.6**), $\vec{M}_0$, making it precess around the external magnetic field [3], and this precession frequency is called the *Larmor frequency* [5].

$$\vec{\tau} = \vec{\mu} \times \vec{B}_0 = \gamma \vec{J} \times \vec{B}_0 \qquad (3.6)$$

where, $\vec{\tau}$ is the torque.

For a nucleus with a positive gyromagnetic ratio, the Larmor frequency is negative (**Equation 3.7**) and vice versa.

$$\omega_0 = -\gamma \vec{B}_0 \qquad (3.7)$$

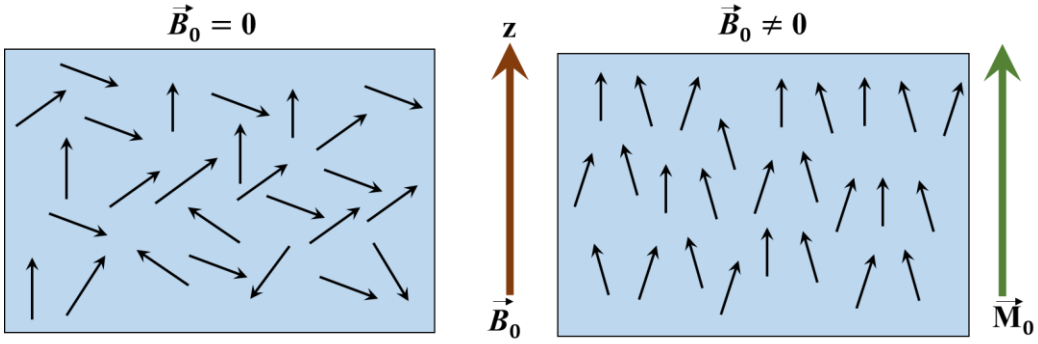

Figure 3.2. Pictorial representation of spins that are randomly oriented in the absence (left) and the presence (right) of $\vec{B}_0$. The net magnetization, $\vec{M}_0$, aligns with the applied magnetic field.

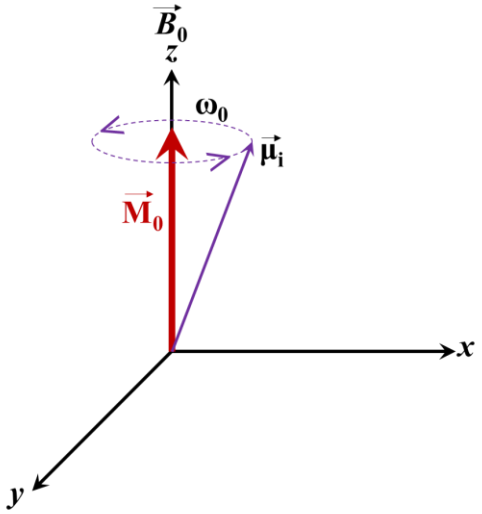

Figure 3.3. The nuclear magnetic moments ($\vec{\mu}_i$) precess around the $\vec{B}_0$ at their respective Larmor frequencies (ω_0), and the bulk magnetization $\vec{M}_0$ aligns with the external field along the z-axis.

3.2 Observing an NMR signal

Since the Larmor frequencies of all NMR-active nuclei fall in the radiofrequency (RF) region of the electromagnetic spectrum, radio waves with an oscillating magnetic field are employed to perturb the bulk magnetization. As the *Larmor* frequency is proportional to the gyromagnetic ratio of a nucleus and the strength of the magnetic field, nuclei with high γ will have high

Larmor frequencies, and for a given nucleus, the Larmor frequency increases with the strength of the static magnetic field. To observe the signal, an RF pulse oscillating at or near the Larmor frequency is applied using a coil mounted perpendicular (xy-plane) to the main field ($\vec{B}_0$, z-axis) to which the magnetization is aligned. The frequency of this oscillating field and the resultant magnetic field are labeled ω_{RF} and $\vec{B}_1$, respectively. The RF pulse rotates the bulk magnetization to the xy-plane ($\vec{M}_{xy}$), which precesses in the xy-plane and induces an electromotive force in the coil as per Faraday's law of induction [6]. The transmitting coil doubles as a receiving coil and measures the voltage of the current induced. Since the xy-plane is not the equilibrium position of the magnetization $\vec{M}_0$, it precesses and relaxes back to the z-axis. The voltage generated in the coil is time-dependent and gradually diminishes due to the relaxation processes (see **section 3.3**). This time-domain data are referred to as the *free induction decay* and are Fourier-transformed into frequencies [7] and plotted in the form of a spectrum (**Figure 3.4**). The electromotive force (ε), measured in volts, is given by the change in the magnetic flux with time and is expressed as,

$$\varepsilon = \frac{d\phi_B}{dt} \qquad (3.8)$$

where, ϕ_B is the magnetic flux.

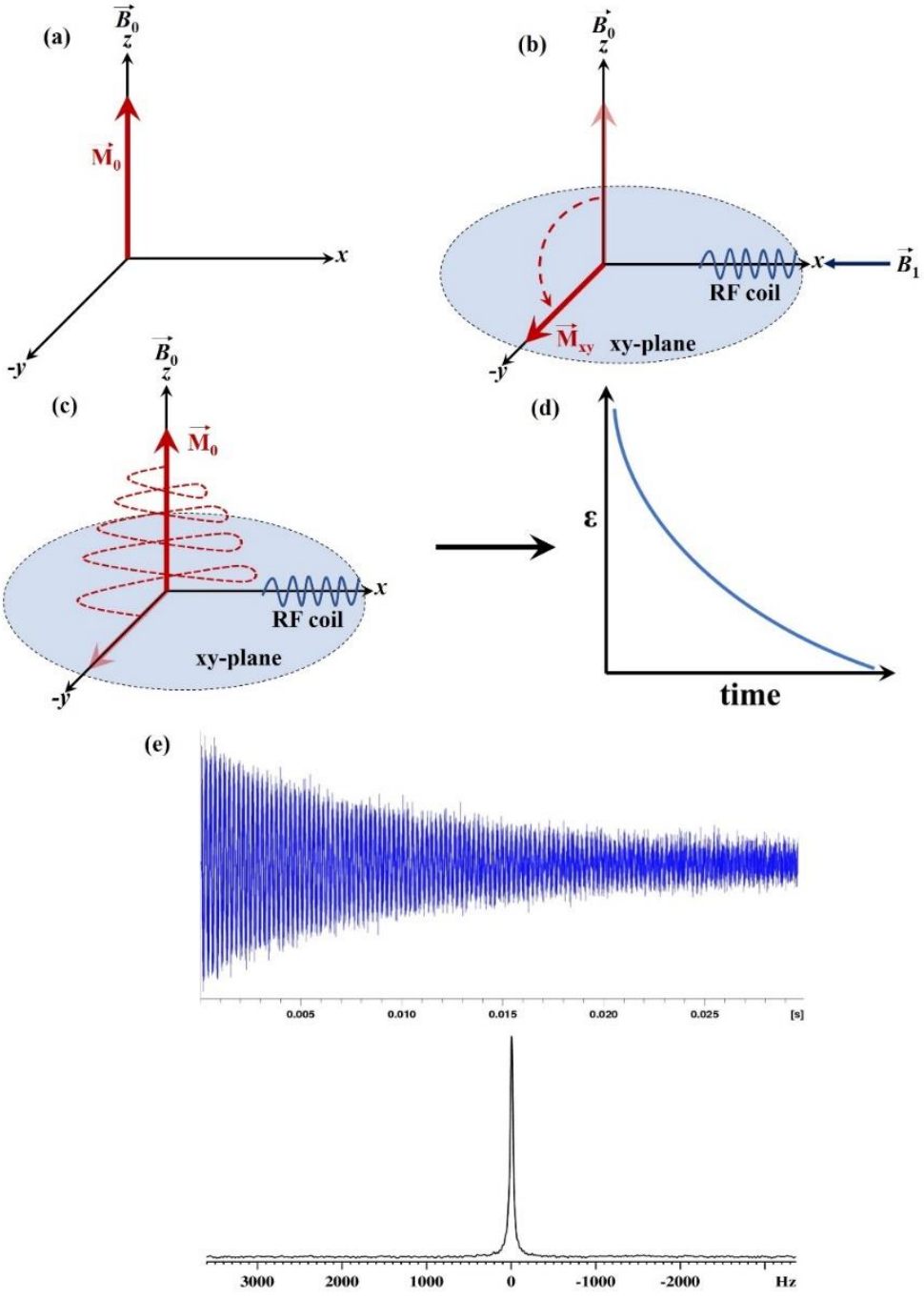

Figure 3.4. Pictorial representations of (a) magnetization ($\vec{M}_0$) along the z-axis, (b) perturbation of $\vec{M}_0$ by the RF pulse applied in the xy-plane, (c) relaxation of $\vec{M}_{xy}$ to its equilibrium position, (d) exponential decay of the electromotive force generated in the coil, (e) free induction decay recorded for ^{31}P using 85% H_3PO_4, and Fourier transformed ^{31}P NMR spectrum presented with a frequency axis.

The effect of an applied RF pulse on the bulk magnetization is best understood by transforming the laboratory frame to a rotating frame of reference, where $\vec{M}_0$ is stationary in a frame that is rotating at the Larmor frequency [2]. In this frame, the magnetization appears static, and its apparent Larmor frequency is zero. When the Larmor precession frequency (ω_0) and the frequency of an RF pulse applied along the x-axis, called the transmitter frequency (ω_{RF}), are similar but not exactly the same ($\omega_{RF} \neq \omega_0$), the Larmor precession is given by Ω_L where,

$$\Omega_L = \omega_0 - \omega_{RF} \qquad (3.9)$$

Since $\omega_o = -\gamma\vec{B}_0$ and $\omega_{RF} = -\gamma\vec{B}_1$,

$$\Omega = -\gamma(\vec{B}_0 - \vec{B}_1) \qquad (3.10)$$

$$\Omega = -\gamma\Delta\vec{B} \qquad (3.11)$$

$$\Delta\vec{B} = -\Omega/\gamma \qquad (3.12)$$

In the rotating frame, the apparent magnetic field $\Delta\vec{B}$ is along the z-axis and is called the *reduced field*. The reduced field $\Delta\vec{B}$ and the transmitter field $\vec{B}_1$ add vectorially to give an effective field $\vec{B}_{eff}$ (**Figure 3.5**), about which the magnetization precesses with a frequency of ω_{eff}.

$$\vec{B}_{eff} = (\vec{B}_1^2 + \Delta\vec{B}^2)^{1/2} \qquad (3.13)$$

$$\omega_{eff} = -\gamma\vec{B}_{eff} \qquad (3.14)$$

When the transmitter frequency matches the Larmor precession frequency ($\omega_{RF} = \omega_0$), the reduced field $\Delta\vec{B}$ will be zero, and the only field experienced by the bulk magnetization is $\vec{B}_1$, which is along the x-axis. Hence the net magnetization precesses about the $\vec{B}_1$ field, and $\vec{M}_0$ rotates to the xy-plane. The rotating frame helps in understanding why a relatively small field applied orthogonal to the static field ($\vec{B}_1 <<< \vec{B}_0$) has a strong influence on the bulk magnetization. The angle of magnetization rotation can be controlled by setting the time for which the pulse is applied. If τ_{RF} is the time duration for which an RF pulse of field $\vec{B}_1$ is applied, the angle of magnetization rotation (β) is given by,

$$\beta = \gamma\vec{B}_1\tau_{RF} \qquad (3.15)$$

Applying a 90° RF pulse along the x-axis flips the magnetization to the -y-axis. A 180° pulse flips the magnetization to the -z-axis, and a 270° pulse rotates the magnetization around to the +y-axis. A 360° pulse rotates the magnetization back to its equilibrium position. Since the detector is in the xy-plane, magnetization in -z and +z axes are not detected and are called null points, while the magnetization in the -y or +y axis generates positive and negative signals, respectively. The nutation curve generated for the ^{31}P signal from 85% H_3PO_4 is shown in **Figure 3.6**. In a typical NMR experiment, the magnetization is rotated to the xy-plane by applying a 90° RF pulse. It is then allowed to precess only under the external field influence, the vector component of which in the xy-plane decays exponentially.

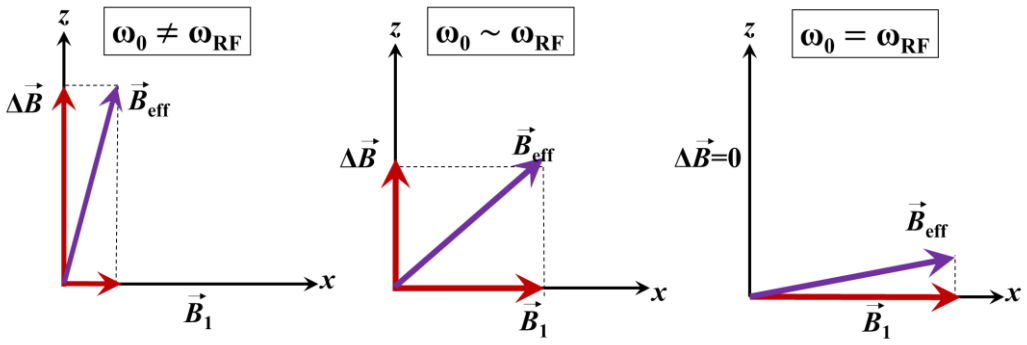

Figure 3.5. Illustration of the influence of $\vec{B}_0$ and $\vec{B}_1$ fields on the bulk magnetization, formation of the apparent reduced field, and the perturbation of $\vec{M}_0$ at different Larmor and transmitter frequency-matching conditions.

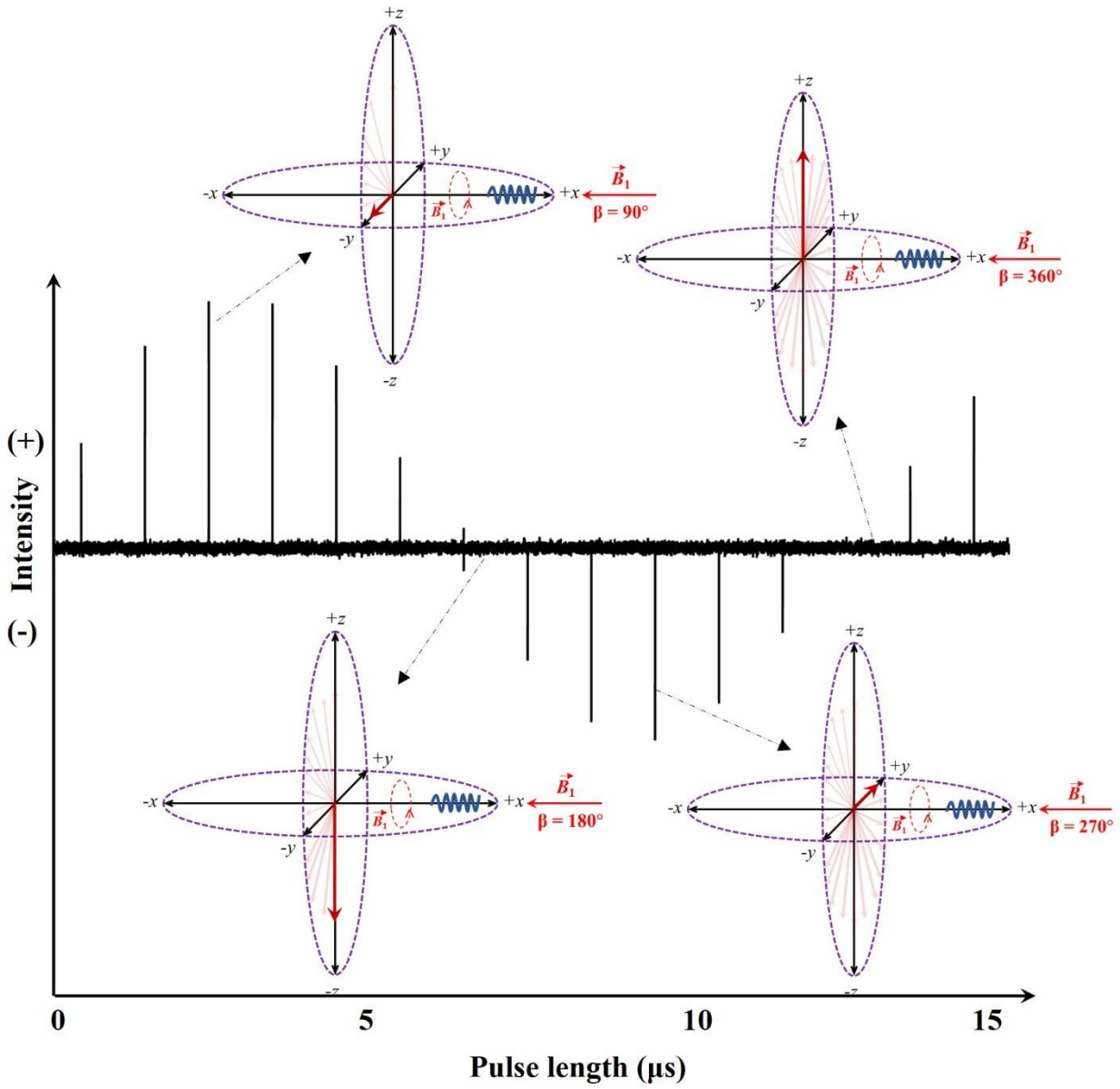

Figure 3.6. Nutation curve depicting the ^{31}P peak intensity as a function of the pulse duration. The magnetization's rotation angles and its position in the Cartesian coordinate system responsible for the peak intensities at different pulse lengths are shown in the inset.

3.3 Relaxation

The bulk magnetization achieved in the xy-plane by applying an RF pulse eventually returns to its equilibrium position along the z-axis, with exponential decay of the electromotive force generated in the receiver coil. This process is called relaxation and occurs via two separate mechanisms: *spin-spin* and *spin-lattice relaxation*, wherein the former refers to the loss of spin-coherence along the xy-plane and the latter refers to the reorientation of the bulk magnetization along the z-axis [1,3].

3.3.1 Transverse relaxation

In the spin-spin relaxation, also called transverse relaxation, the spins lose coherence and precess asynchronously in the xy-plane reducing the vector component of the bulk magnetization (**Figure 3.7**), decreasing the signal intensity. The Bloch equation of the transverse magnetization for an ensemble of spins in an external magnetic field is given by,

$$\vec{M}_{xy}(\mathrm{t}) = \vec{M}_0 \mathrm{e}^{-\frac{\mathrm{t}}{\mathrm{T}_2}} \qquad (3.16)$$

where, $\vec{M}_{xy}$ is the time-dependent magnetization in the transverse plane, and $\frac{1}{T_2}$ is the transverse relaxation rate. The spin-spin relaxation occurs mainly due to inhomogeneities in $\vec{B}_0$, and interactions between the spins, which changes their nuclear magnetic moments leading to different resonance frequencies and ultimately leading to the loss of coherence. A transition between nuclear spin states affects the local magnetic fields of nearby nuclei, stimulating an opposite transition, often called the *flip-flop transition*. These transitions conserve the system's total energy but change the nuclei's angular momentum, therefore altering their Larmor frequencies, ultimately leading to the loss of coherence. The transverse relaxation rate inclusive of the inhomogeneity in the static magnetic field and the spin-spin interactions is represented as $\frac{1}{T_2^*}$ and is given by,

$$\frac{1}{T_2^*} = \frac{1}{T_2} + \frac{1}{T_2'} \qquad (3.17)$$

where, $\frac{1}{T_2}$ is the decay of the magnetization due to spin-spin interactions and $\frac{1}{T_2'}$ is the decay of the magnetization due to field inhomogeneity.

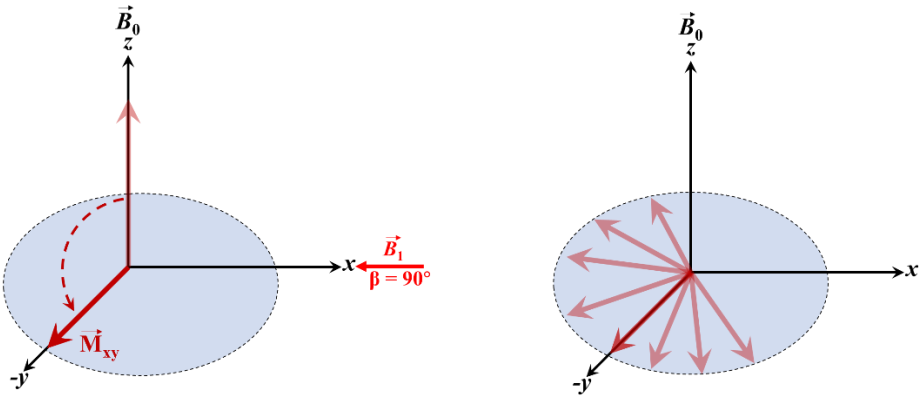

Figure 3.7. Pictorial representation of the rotation of bulk magnetization to the xy-plane by the applied RF pulse (left) and the loss of coherence over time due to spin-spin relaxation (right).

3.3.2 Longitudinal relaxation

Longitudinal relaxation, also referred to as *spin-lattice relaxation*, represents the rate of return of the bulk magnetization to its equilibrium position along the z-axis. The equation for the longitudinal relaxation rate is derived from the Bloch equation and is given as,

$$\vec{M}_z(\mathrm{t}) = \vec{M}_0(1 - \mathrm{e}^{-\frac{\mathrm{t}}{\mathrm{T}_1}}) \qquad (3.18)$$

where $\vec{M}_0$ is the equilibrium magnetization, $\vec{M}_z$ is the vector component of the magnetization present along the z-axis, and $\frac{1}{T_1}$ is the spin-lattice relaxation rate. Similar to $\frac{1}{T_2}$, the spin-lattice relaxation rate exhibits an exponential decay. It is caused by the fluctuations in the local magnetic field at the nucleus due to atomic motions, ionic hopping, molecular rotations, and atomic vibrations [1], which cause transitions between the stationary states of the nuclear spin system. The T_1 is inversely proportional to the square of the magnetic moment of the fluctuation field. Since the magnetic moment of an electron is 10^3 times greater than the nuclear magnetic moment, systems with paramagnetic impurities have extremely short T_1s [8]. This is an advantage in paramagnetic NMR as spectra with good signal-to-noise ratio can be acquired in a very short timeframe by rapid pulsing.

In a typical NMR experiment, multiple transients are collected with a pre-set delay called a *recycle delay* (RD) between them to allow complete relaxation of the magnetization. Incomplete relaxation of magnetization leads to a reduction in the intensity of the signal, and in cases where the spin-lattice relaxation rates are longer (for example, ^{29}Si and ^{31}P), the spectra suffer from a poor signal-to-noise ratio. To overcome this problem, the RD must be set to five times the spin-lattice relaxation rate constant T_1, as 99% of bulk magnetization will be restored in this timeframe. Since the restoration of bulk magnetization cannot proceed without the dephasing of spins in the transverse plane, T_1 must be $\geq T_2$. The line-width of NMR signals is a function of the relaxation time constants and is given by,

$$\nu_{\frac{1}{2}} = \frac{1}{2\pi T} \qquad (3.19)$$

where $\nu_{\frac{1}{2}}$ is the peak-width at half-height, and T is the relaxation time constant. Since $T_2 < T_1$ in most systems, this time constant will always be T_2. However, in cases where paramagnetic impurities exist, the peak-widths are governed by T_1 as well.

3.4 NMR interactions

So far, we have considered only the interaction of the nuclear spin with externally applied magnetic fields, $\vec{B}_0$ and $\vec{B}_1$. NMR spectra consist of information about all chemically distinct spins present in the system, the resonance frequencies of which are perturbed to a different extent by the external magnetic fields and internal interactions between the nuclei and their surroundings. Spins experiencing different types and ranges of interactions have distinct resonance frequencies, which imparts the analytical capability to the NMR spectroscopy technique. Fluctuations in the local magnetic field about the nucleus modify the field at the nucleus and perturb the energies of the spin eigenstates. Different interactions influence the energy levels differently and can be spectroscopically differentiated, and such spectral features provide a wealth of information on the structure and dynamics of molecules. The Zeeman interaction is often orders of magnitude greater than any other interactions (**Table 3.1**) and hence serves as the spins' main quantization axis, while internal interactions can be treated as perturbations to the quantized spin system. The Hamiltonian describing the interaction between a nuclear spin and any local magnetic field, B_{loc} is given by [3],

$$\hat{H}_{loc} = -\gamma \hat{I} \hbar \vec{B}_{loc} \qquad (3.20)$$

$$\vec{B}_{loc} = \bar{A}_{loc} \cdot \vec{Y} \qquad (3.21)$$

$$\hat{H}_{loc} = -\gamma \hat{I} \hbar \bar{A}_{loc} \cdot \vec{Y} \qquad (3.22)$$

where, $\hat{H}_{loc}$ is the Hamiltonian representing the internal interaction, $\hat{I}$ is the nuclear spin operator, $\bar{A}_{loc}$ is a 3×3 second-rank tensor, also called the coupling tensor, which describes the orientation dependence of the nuclear spin interaction, $\vec{Y}$ is the source of the $\vec{B}_{loc}$ magnetic field, which could be another nucleus, the main external field or the electronic environment of the nuclei. The Hamiltonian representing the total interaction is given by,

$$\hat{H}_{total} = \hat{H}_Z + \hat{H}_{RF} + \hat{H}_{loc} \qquad (3.23)$$

where, $\hat{H}_Z$ and $\hat{H}_{RF}$ are the Hamiltonians representing the interactions of nuclear spins with $\vec{B}_0$ and $\vec{B}_1$, respectively, and $\hat{H}_{loc}$ is the summation of individual internal interactions [1],

$$\hat{H}_{loc} = \hat{H}_D + \hat{H}_{CS} + \hat{H}_K + \hat{H}_J + \hat{H}_P + \hat{H}_Q^{(1)} + \hat{H}_Q^{(2)} + \cdots\cdots\cdots \qquad (3.24)$$

where, $\hat{H}_D$ is the through-space magnetic dipolar interaction between nuclei, $\hat{H}_{CS}$ is the perturbation of the local magnetic field at the nucleus due to the surrounding electrons, $\hat{H}_K$ is the interaction of the nuclear spin with conducting electrons, $\hat{H}_J$ is the change in the magnetic field due to indirect spin-spin coupling mediated through electrons, $\hat{H}_P$ is the interaction of unpaired electrons with the nuclear spins in a paramagnetic system, $\hat{H}_Q$ is the interaction between the nuclear electric quadrupole moment (eQ) and the electric field gradient (eq) at the nucleus in the case of nuclei with spin$>\frac{1}{2}$. $\hat{H}_Q$ is often expanded into its first- and second-order terms, $\hat{H}_Q^{(1)}$ and $\hat{H}_Q^{(2)}$, respectively. A table summarizing all these interactions and their typical sizes is given below. Three of these are specifically relevant to the work in this thesis:

a. Chemical shielding
b. Dipolar interaction
c. Quadrupolar interaction

Table 3.1. NMR interactions and their sizes [1].

Interaction Hamiltonians	Interaction	A_{loc}	J	Typical size (Hz)
$\hat{H}_Z$	Zeeman	Unitary	$\vec{B}_0$	10^7-10^9
$\hat{H}_{RF}$	RF	Unitary	$\vec{B}_1$	10^3-10^5
$\hat{H}_D$	Dipolar	D	I[a]	10^3-10^4
$\hat{H}_{CS}$	Chemical shielding	σ	$\vec{B}_0$	10^2-10^5
$\hat{H}_J$	Indirect spin	J	I	$1-10^3$
$\hat{H}_P$	Paramagnetic	P	S[b]	10^2-10^5
$\hat{H}_K$	Knight shielding	K	S	10^2-10^5
$\hat{H}_Q$	Quadrupolar	eq	I	10^3-10^7

[a]Nuclear spins; [b]Electrons

3.4.1 Chemical shielding

The electrons surrounding the nuclei produce a secondary magnetic field under the influence of the external magnetic field and contribute to the total magnetic field experienced by the nuclei. This phenomenon is called *chemical shielding* and is represented by the shielding constant σ [1−4,9−12]. The resonance frequencies are dictated by the total field experienced by the nuclei, and hence, nuclei in distinct electronic environments have unique resonance frequencies, making NMR spectroscopy an efficient analytical method for structural analysis. The electron-induced local magnetic field either reduces (shielding) or increases (deshielding) the net magnetic field experienced by the nuclei. The chemical shielding consists of diamagnetic and paramagnetic components, which account for shielding and deshielding aspects, respectively [9]. The diamagnetic contribution (σ^d) comes principally from the core electrons, while the paramagnetic portion (σ^p) arises from the mixing of ground state with various excited electronic states. Since the core electrons are responsible for the diamagnetic shielding, σ^d is fairly constant for an atom type, although the diamagnetic electron current generated by the neighbouring atoms also

contribute to the total diamagnetic shielding at the nucleus [3]. The paramagnetic contribution varies with the nuclear environment and depends on the degree of mixing of electronic excited and ground states.

$$\bar{\sigma} = \bar{\sigma}^{d} + \bar{\sigma}^{p} \qquad (3.25)$$

The chemical shielding Hamiltonian is given by,

$$\hat{H}_{CS} = -\gamma \hat{I} \hbar \bar{\sigma} \vec{B}_0 \qquad (3.26)$$

The electron current and the size of shielding depend on the orientation of a molecule in the $\vec{B}_0$ as the electron distribution around the nucleus is not spherically symmetric. Therefore the shielding is described using a second-rank tensor, represented by a 3×3 matrix with nine independent components describing the shielding interactions at the nucleus.

$$\bar{\sigma} = \begin{bmatrix} \sigma_{xx} & \sigma_{xy} & \sigma_{xz} \\ \sigma_{yx} & \sigma_{yy} & \sigma_{yz} \\ \sigma_{zx} & \sigma_{zy} & \sigma_{zz} \end{bmatrix}$$

The shielding tensor has symmetric and anti-symmetric components where the observable first-order response is symmetric ($\sigma_{ij} = \sigma_{ji}$; σ_{xx}, $\sigma_{yy,}$ and σ_{zz}) and the second-order shielding response ($\sigma_{ij} = ½(\sigma_{ij} + \sigma_{ji})$, σ_{xy}, σ_{xz},…), which is perpendicular to the applied field is never observed and is considered anti-symmetric. The symmetric portion of the chemical shift tensor is diagonalized into its own coordinate system called the principal axis system (PAS, $\bar{\sigma}_{PAS}$), wherein the diagonals are the principal values of the shielding tensor where $\sigma_{11} \leq \sigma_{22} \leq \sigma_{33}$.

$$\bar{\sigma}_{PAS} = \begin{bmatrix} \sigma_{XX} & 0 & 0 \\ 0 & \sigma_{YY} & 0 \\ 0 & 0 & \sigma_{ZZ} \end{bmatrix} = \begin{bmatrix} \sigma_{11} & 0 & 0 \\ 0 & \sigma_{22} & 0 \\ 0 & 0 & \sigma_{33} \end{bmatrix}$$

If the shielding tensor is pictured as an ellipsoid centered on the nucleus within a molecule, the principal components of the shielding tensor (σ_{11}, σ_{22}, and σ_{33}) coincide with the principal axes of the ellipsoid (X^{PAS}, Y^{PAS}, and Z^{PAS}), and the length of the principal axis is proportional to the principal value of the shielding tensor. For example, for a nucleus with axial symmetry wherein the principal component σ_{33} coincides with the Z^{PAS} principal axis of the ellipsoid, the principal tensor components are such that, $\sigma_{11} = \sigma_{22} \neq \sigma_{33}$. These three principal components form an

orthogonal three-dimensional basis wherein the σ_{11}, σ_{22}, and σ_{33} represent the directions of least, intermediate, and greatest shielding, respectively. Since only σ_{33} is aligned with $\vec{B}_0$, it is of particular interest, and the other two components make only second-order contributions, the Hamiltonian can be rewritten as,

$$\hat{\mathrm{H}}_{\mathrm{CS}} = -\gamma\hbar\hat{\mathrm{I}}_{\mathrm{z}}\sigma_{33}\vec{B}_0 \qquad (3.27)$$

The orientational dependence of σ_{33} on the $\vec{B}_0$ is given by,

$$\sigma_{33} = \sigma_{\mathrm{iso}} + \frac{\Delta\sigma}{2}[(3\cos^2\theta - 1) + \eta(\sin^2\theta\cos 2\phi)] \qquad (3.28)$$

where σ_{iso} is the isotropic shift (vide infra), θ and ϕ are the polar coordinates defining the orientation of the chemical shielding tensor with respect to $\vec{B}_0$, $\Delta\sigma$ is the shielding anisotropy and η is the shielding asymmetry where, $\Delta\sigma = \sigma_{33} - \sigma_{\mathrm{iso}}$ and $\eta = \frac{\sigma_{11}-\sigma_{22}}{\Delta\sigma}$.

For a single crystallite orientation, the resonance position changes with respect to $\vec{B}_0$, because the chemical shielding is intrinsically anisotropic. As powders are a collection of many crystallites and these could have all possible orientations in the field, the spectrum obtained from a powered sample will be a superposition of resonances from these individual crystallites. The chemical shielding has a direct dependence on the magnetic field strength, wherein the shielding anisotropy increases as the strength of the applied field increases.

In NMR experiments, the frequency of the sample (ν_{sample}) is referenced to the resonance frequency of a standard (ν_{ref}).

$$\delta_{sample} = 10^6\left(\frac{\nu_{sample}-\nu_{ref}}{\nu_{ref}}\right) \qquad (3.29)$$

The chemical shift and the chemical shielding are related by,

$$\delta = \left(\frac{\sigma_{ref}-\sigma_{sample}}{1-\sigma_{ref}}\right) \qquad (3.30)$$

Similar to chemical shielding, the chemical shift tensor in ppm can be defined by three principal components δ_{11}, δ_{22} and δ_{33}, which follow the order, $\delta_{11} \geq \delta_{22} \geq \delta_{33}$. While the rapid and random molecular tumbling averages the chemical shift anisotropy (CSA) in non-viscous solvents, the

CSA contributes significant line-broadening to the observed resonances in solid-state NMR. The breadth of the anisotropy called the span (Ω) is given by,

$$\Omega = \sigma_{33} - \sigma_{11} \approx \delta_{11} - \delta_{33} \qquad (3.31)$$

Anisotropy is a measure of the electronic symmetry of a molecule wherein the anisotropy of a highly symmetric molecule is small. The isotropic chemical shift (δ_{iso}) is the average of all three chemical shift components:

$$\sigma_{iso} = \frac{1}{3}(\sigma_{11} + \sigma_{22} + \sigma_{33}) \qquad (3.32)$$

$$\delta_{iso} = \frac{1}{3}(\delta_{11} + \delta_{22} + \delta_{33}) \qquad (3.33)$$

The degree of axial symmetry of the chemical shielding tensor is called skew (κ) and is given by,

$$\kappa = \frac{3(\sigma_{iso} - \sigma_{22})}{\Omega} \approx \frac{3(\delta_{22} - \delta_{iso})}{\Omega} \qquad (3.34)$$

Simulated powder patterns for a ^{31}P nucleus with a Ω of 250 ppm, δ_{iso} of -20 ppm and different degrees of axial symmetry are presented in Figure 3.8.

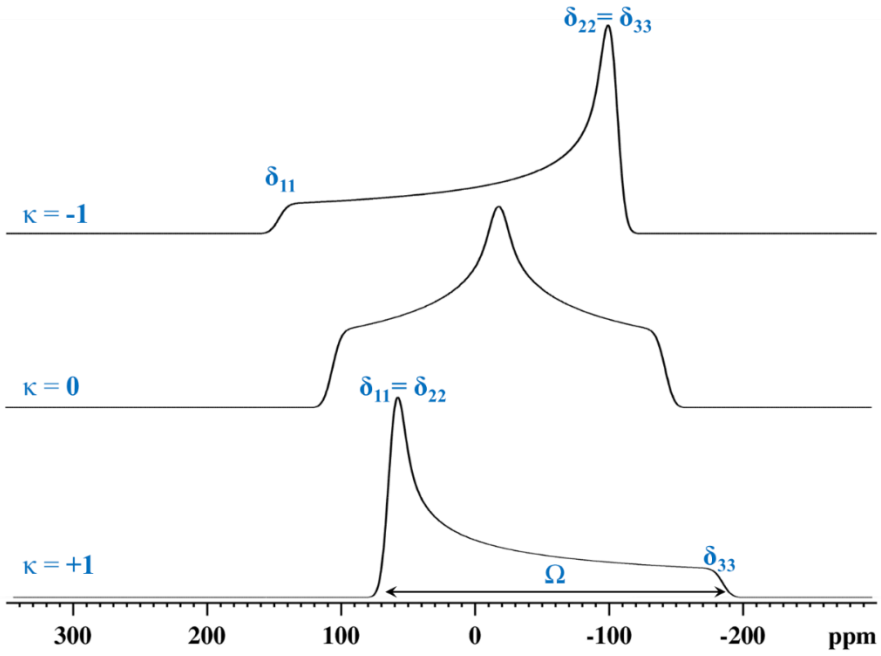

Figure 3.8. Simulated powder pattern for the ^{31}P nucleus with a span of 250 ppm, δ_{iso} of -20 ppm and different skew values.

3.4.2 Dipolar interaction

The magnetic field generated by the precession of nuclear spins can influence other nuclei in proximity through space. This distance-dependent coupling of spins is referred to as the *dipolar interaction* or *dipolar coupling* [1]. If two magnetic dipoles μ_1 and μ_2, which are the classical equivalents of the quantum mechanical nuclear spins, are separated by a distance *r* and are interacting through space (**Figure 3.9**), the energy of interaction is given by,

$$E_D = \frac{\mu_0}{4\pi}\left[\frac{\mu_1\mu_2}{r^3} - \frac{3(\mu_1 \cdot r)(\mu_2 \cdot r)}{r^5}\right] \qquad (3.35)$$

The quantum mechanical Hamiltonian for the interaction between two spins I and S is derived by substituting $\hat{\mu}_1$ and $\hat{\mu}_2$ magnetic moment operators with $\gamma_I\hbar\hat{I}$ and $\gamma_S\hbar\hat{S}$, respectively.

$$\hat{H}_D = \frac{\mu_0\gamma_I\gamma_S\hbar^2}{4\pi r^3}\left[\hat{I}\cdot\hat{S} - \frac{3(\hat{I}\cdot r)(\hat{S}\cdot r)}{r^5}\right] \qquad (3.36)$$

By expressing **equation 3.36** in spherical polar coordinates and expanding the scalar products, the "alphabet" expression for $\hat{H}_D$ is obtained:

$$\hat{H}_D = \frac{\mu_0\gamma_I\gamma_S\hbar^2}{4\pi r^3}(A + B + C + D + E + F) \qquad (3.37)$$

where,

$A = \hat{I}_z\hat{S}_z(3\cos^2\theta - 1)$

$B = -\frac{1}{4}[\hat{I}_+\hat{S}_- + \hat{I}_-\hat{S}_+](3\cos^2\theta - 1)$

$C = -\frac{3}{2}[\hat{I}_+\hat{S}_z + \hat{I}_z\hat{S}_+](\sin\theta\cos\theta)\exp(-i\phi)$

$D = -\frac{3}{2}[\hat{I}_-\hat{S}_z + \hat{I}_z\hat{S}_-](\sin\theta\cos\theta)\exp(+i\phi)$

$E = -\frac{3}{4}[\hat{I}_+\hat{S}_+]\sin^2\theta\exp(-2i\phi)$

$F = -\frac{3}{4}[\hat{I}_-\hat{S}_-]\sin^2\theta\exp(+2i\phi)$

$\hat{I}_Z$ is the z-component of the angular spin momentum, $\hat{I}_+$, $\hat{S}_+$, and $\hat{I}_-$, $\hat{S}_-$ are the raising and lowering operators acting on spins I and S which have values, $\hat{I}_X + i\hat{I}_Y$, $\hat{S}_X + i\hat{S}_Y$ and $\hat{I}_X - i\hat{I}_Y$, $\hat{S}_X - i\hat{S}_Y$, respectively. The terms A and B are time-independent and form the secular part ($\hat{H}_D^{sec}$) of the dipolar Hamiltonian. The terms C−F are time-dependent at frequencies ω_o and $2\omega_o$ and are the non-secular part ($\hat{H}_D^{non\text{-}sec}$) of the H_D, which are responsible only for the relaxation of spins to Boltzmann equilibrium, with no influence on the energy of the spin system. Since the frequency of the time-dependency of $\hat{H}_D^{non\text{-}sec}$ is much greater than that of $\hat{H}_D^{sec}$, its time average is zero and hence, can be neglected for spectroscopic purposes. The B-term is called the flip-flop

operator as it causes transitions between different spin-states in a coupled spin system. For example, if spin 'I' changes from m = $+\frac{1}{2} \rightarrow -\frac{1}{2}$, the other spin 'S' changes from $-\frac{1}{2}$ to $+\frac{1}{2}$. The probability of this transition is highest in the case of homonuclear spins (I = I_i and S = I_j), i.e., they are chemically the same, with a criterion of conservation of the energy of the system. In the case of a heteronuclear spin system ($\gamma_I \neq \gamma_S$), the flip-flop transitions are not energy-conserving, and hence, the B-term is zero.

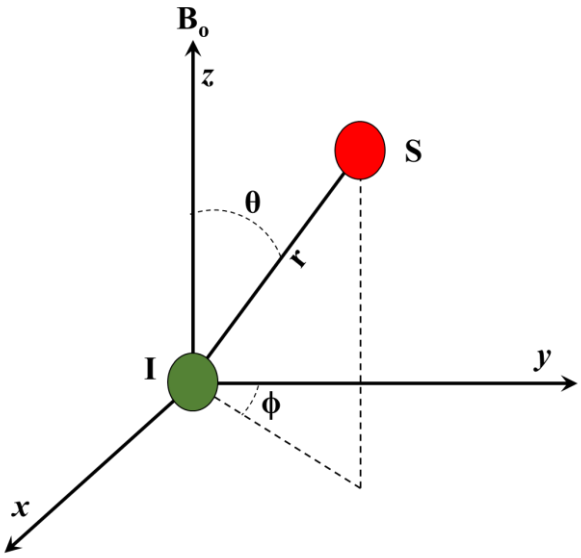

Figure 3.9. Orientation of the *I*−*S* internuclear vector in space and with respect to the external magnetic field present along the z-axis. The polar angles θ and ϕ specify the orientation.

The dipolar Hamiltonians for homo- ($\hat{H}_D^{IiIj}$) and hetero-nuclear ($\hat{H}_D^{IS}$) spin systems are expressed as,

$$\hat{H}_D^{IiIj} = \frac{\mu_0 \gamma^2 \hbar^2}{8\pi r^3}(2\hat{I}_{iz}\hat{I}_{jz} - \frac{1}{2}[\hat{I}_{i+}\hat{I}_{j-} + \hat{I}_{i-}\hat{I}_{j+}])(3\cos^2\theta_{ij} - 1) \quad (3.38)$$

$$\hat{H}_D^{IS} = \frac{\mu_0 \gamma_I \gamma_S \hbar^2}{8\pi r^3} 2\hat{I}_z\hat{S}_z(3\cos^2\theta_{IS} - 1) \quad (3.39)$$

The term $\frac{\mu_0 \gamma_I \gamma_S \hbar^2}{8\pi r^3}$ is known as the dipolar coupling constant (D) and has the unit of $rads^{-1}$, but is normally reported in Hz by multiplying D with the conversion factor 0.1591 ($rads^{-1} = \frac{1}{2\pi}$Hz). Due

to rapid and isotropic tumbling motions of molecules in solution, the A and B terms are averaged to zero, and hence, the dipolar coupling is not observed. However, in the NMR analysis of solids, non-averaging of these terms contributes significant line broadening.

3.4.3 Quadrupolar interaction

Quadrupolar nuclei (I >1/2), which have multiple energy levels (2I+1), represent more than 70% of the elements in the periodic table [13]. Due to their non-symmetric charge distribution, they possess an electric quadrupole moment which couples with the electric field gradient (eq) generated by the atoms present in their local chemical environment [1,3,4,13]. This affects the energies of the nuclear spin states, leading to broadened peaks in an NMR spectrum. The quadrupole moment is represented by the symbol eQ, where e is the elementary charge, and represents the shape of the ellipsoid of electric charge distribution of a nucleus, which can be an oblate (eQ < 0) or a prolate (eQ > 0). The Hamiltonian for the quadrupolar interaction is defined as [3,4],

$$\hbar\hat{\mathrm{H}}_{\mathrm{Q}} = \frac{\mathrm{eQ}}{6\mathrm{I}(2\mathrm{I}-\mathrm{I})}\sum\nolimits_{\alpha,\beta=\mathrm{x,y,z}} \mathrm{V}_{\alpha\beta}\left(\frac{3}{2}\left(\hat{\mathrm{I}}_{\alpha}\hat{\mathrm{I}}_{\beta} + \hat{\mathrm{I}}_{\beta}\hat{\mathrm{I}}_{\alpha}\right) - \delta_{\alpha\beta}\hat{\mathrm{I}}^{2}\right) \qquad (3.40)$$

with, $V_{\alpha\beta} = \left.\frac{\partial^2 U}{\partial\alpha\partial\beta}\right|_{r=0}$

where, $\delta_{\alpha\beta}$ is the Kronecker delta symbol, U is the electrostatic potential generated inside the nucleus by external charges, and $\mathrm{V}_{\alpha\beta}$ are the Cartesian components of the electric field gradient at the nucleus. Diagonalization of the EFG tensor into the principal axis system ($\overline{\Sigma_{PAS}}$) produces three traceless principal tensor components $\mathrm{V_{XX}}$, $\mathrm{V_{YY}}$ and $\mathrm{V_{ZZ}}$, which follow $|V_{ZZ}| \geq |V_{YY}| \geq |V_{XX}|$.

$$\bar{V} = \begin{bmatrix} \mathrm{V_{XX}} & 0 & 0 \\ 0 & \mathrm{V_{YY}} & 0 \\ 0 & 0 & \mathrm{V_{ZZ}} \end{bmatrix}$$

Since the EFG tensor follows the Laplace equation, only two out of three components need to be known to define the EFG tensor fully, and the largest tensor component is chosen to define the EFG.

$$V_{ZZ} = eq \qquad (3.41)$$

The Laplace equation confines the value of the asymmetry parameter η_Q to $1 \geq \eta_Q \geq 0$, which is expressed as,

$$\eta_Q = \frac{V_{XX} - V_{YY}}{V_{ZZ}} \qquad (3.42)$$

Two kinds of local symmetry at the nucleus govern the symmetry of the EFG tensor:

a. Cubic point symmetry, including the eightfold cubic, sixfold octahedral, and fourfold tetrahedral coordination result in $V_{XX} = V_{YY} = V_{ZZ}$; therefore eq = 0.
b. In cases where the nucleus lies on a threefold, fourfold, fivefold, or sixfold symmetry axis, the EFG is axial and hence, $\eta_Q = 0$.

In the $\overline{\Sigma_{PAS}}$, the quadrupole Hamiltonian is defined as [1],

$$\hbar\hat{H}_Q = \frac{e^2qQ}{4I(2I-1)}[3\hat{I}_z^2 - I(I+1) + \frac{1}{2}\eta(\hat{I}_+^2 + \hat{I}_-^2)] \qquad (3.43)$$

The term $\frac{e^2qQ}{\hbar}$ is defined as the *quadrupole coupling constant* (C_Q). The quadrupole Hamiltonian of a spin in a magnetic field is obtained by transforming the quadrupole Hamiltonian from the PAS to the lab frame by retaining the terms that commute with $\hat{I}_Z$ in the transformation. This process is called truncation and is applicable only when $\hat{H}_Q << \hat{H}_Z$. The quadrupole Hamiltonian is then defined as [1],

$$\hat{H}_Q = \frac{eQh}{4I(2I-1)}\left\{\sqrt{\frac{3}{2}}[3\hat{I}_z - \hat{I}^2]V_0 + [\hat{I}_z\hat{I}_+ + \hat{I}_z\hat{I}_+]V_{-1} - [\hat{I}_z\hat{I}_- + \hat{I}_-\hat{I}_z]V_1 + \hat{I}_+^2V_{-2} + \hat{I}_-^2V_2\right\} \qquad (3.44)$$

where V_i are the EFG elements in the PAS frame so that,

$V_0 = \sqrt{\frac{3}{2}}eq$

$V_{\pm 1} = 0$

$V_{\pm 2} = \frac{eq\eta}{2}$

3.4.4 Quadrupolar interaction as a perturbation of the Zeeman interaction

The quadrupolar interaction acts as a perturbation of the Zeeman interaction in the high-field limit ($\hat{H}_Q << \hat{H}_Z$), which splits the quadrupolar Hamiltonian into first- and second-order terms such that [1],

$$\hat{H}_Q = \hat{H}_Q^{(1)} + \hat{H}_Q^{(2)} \qquad (3.45)$$

In a strong magnetic field, the Zeeman interaction splits the energy levels of spin *I* into *2I+1* levels. 2I lines are observed in the spectrum of a quadrupolar nucleus wherein the transition between the $+\frac{1}{2}$ and $-\frac{1}{2}$ energy levels is called the *central transition* (CT), and the transitions between the energy levels m and m-1 are called the *satellite transitions* (ST). For example, for a nucleus with spin $\frac{5}{2}$, the central transition is $+\frac{1}{2} \leftrightarrow -\frac{1}{2}$ and the satellite transitions are $+\frac{5}{2} \leftrightarrow +\frac{3}{2}$, $+\frac{3}{2} \leftrightarrow +\frac{1}{2}$, $-\frac{1}{2} \leftrightarrow -\frac{3}{2}$ and, $-\frac{3}{2} \leftrightarrow -\frac{5}{2}$.

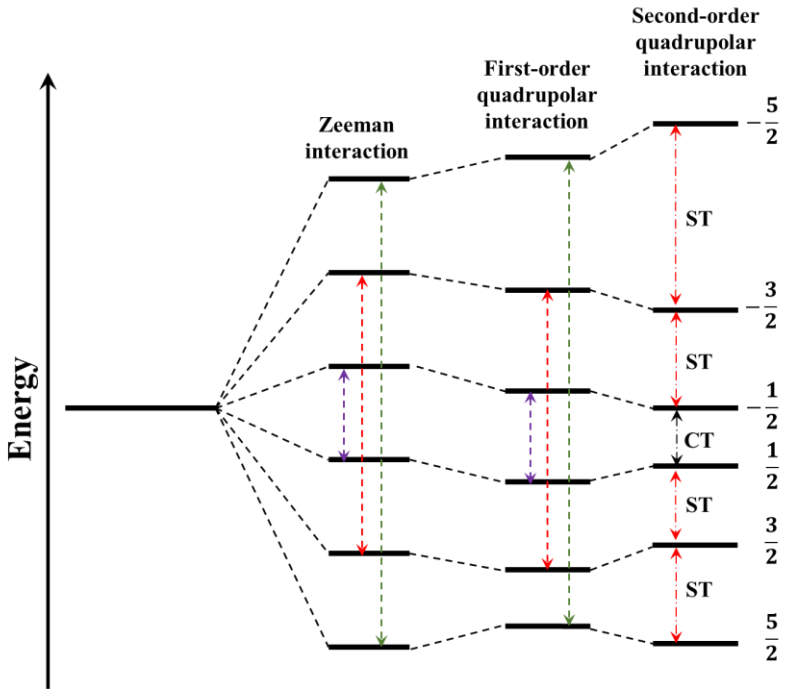

Figure 3.10. Energy level diagram of a spin $\frac{5}{2}$ nucleus showing the non-degenerate spin states in the presence of an external field (Zeeman interaction) and the effect of first- and second-order quadrupolar interactions on the energy levels.

The first-order quadrupolar interaction shifts the energy levels ±m by the same amount such that the energy difference between the spin states ±m is the same as their true Zeeman value (**Figure 3.10**). The first-order quadrupolar interaction affects only the single-quantum satellite transitions, with no effect on the m ↔ -m transition frequency. Therefore the central transition $+\frac{1}{2} \leftrightarrow -\frac{1}{2}$ is not affected by the first-order quadrupolar interaction. The first-order quadrupolar shift of the line position associated with the transition m−1 → m is [14],

$$\upsilon^{(1)}_{m-1,m} = \frac{3eQ}{4I(2I-1)\hbar}\frac{\sqrt{6}}{3}(1-2m)V_0 \qquad (3.46)$$

The second-order quadrupolar interaction affects both the central and the satellite transitions and shifts the energy levels of the spin states further. The contribution of the second-order quadrupolar interaction to the resonance position is [14],

$$\upsilon^{(2)}_{m-1,m} = -\frac{2}{\nu_0}\left(\frac{eQh}{4I(2I-1)}\right)^2 \times \left\{V_{-1}V_1[24m(m-1)-4I(I+1)+9] + \frac{1}{2}V_{-2}V_2[12m(m-1)-4I(I+1)+6]\right\} \qquad (3.47)$$

The polar coordinates θ and ϕ define the orientation of the B_o in the principal axis system of the EFG. The first-order quadrupolar shift of the Zeeman energy states due to the orientation dependence is given as [1],

$$E^{(1)} = \frac{C_Q h}{8I(2I-1)}[3\cos^2\theta - 1 + \eta\sin^2\theta\cos 2\phi](3m^2 - I(I+1)) \qquad (3.48)$$

For a powder sample of a non-integer quadrupolar nucleus, the entire powder pattern ($\Delta\nu_{full}$) is (**Figure 3.11**) [15],

$$\Delta\nu_{full} = (2I-1)\nu_Q \qquad (3.49)$$

where ν_Q is the nuclear quadrupolar frequency, which is equal to $3\chi_Q/2I(I-1)$.

The total breadth of the central transition for a powder sample is denoted by $\Delta\nu_{CT}$ and is calculated from equation [15],

$$\Delta\nu_{CT} = \frac{(25+\eta_Q+\eta_Q^2)a}{144} \qquad (3.50)$$

where, $a = \left(\frac{\nu_Q}{\nu_0}\right)^2 \left[I(I+1) - \frac{3}{4}\right]$

An estimate of the quadrupolar interaction can be obtained from the width of the central transition using the equation [1],

$$C_Q\sqrt{\eta_Q^2 + 22\eta_Q + 25} = 8I(2I-1)\sqrt{\frac{\nu_0\Delta\nu_{CT}}{\left(I(I+1)-\frac{3}{4}\right)}} \qquad (3.51)$$

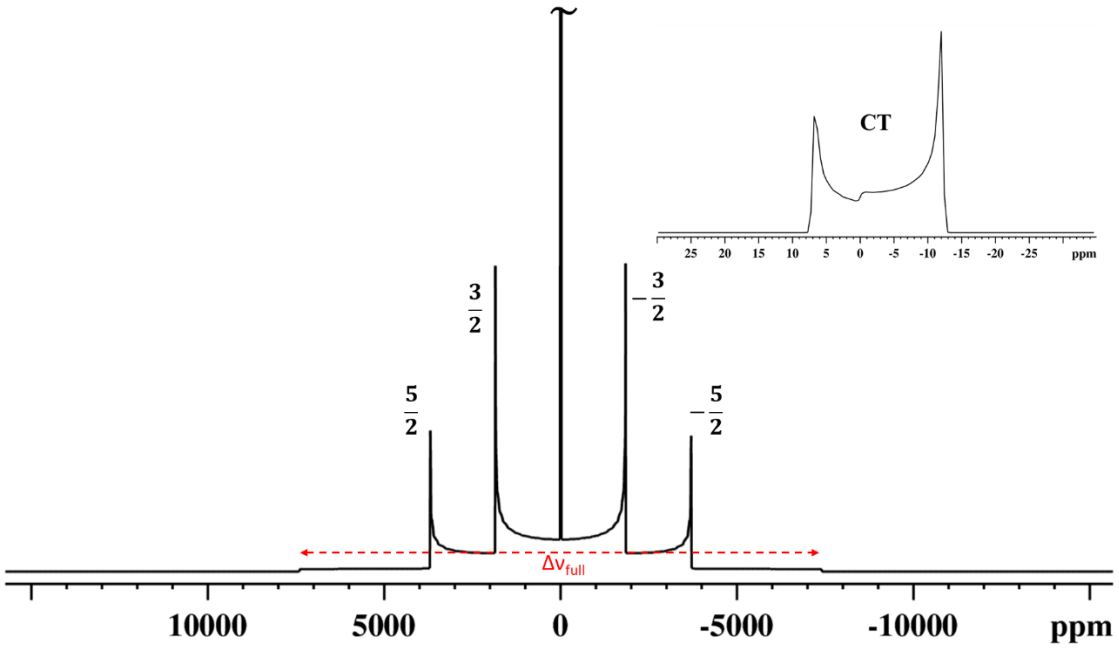

Figure 3.11. Powder pattern for an I = $\frac{5}{2}$ showing both the central and the satellite transitions. The central transition is off-scale in this spectrum and has been plotted as an inset. The $\Delta\nu_{full}$ represents the full width of the powder pattern.

3.5 Solid-state NMR spectroscopy

In liquids, the rapid and random tumbling motion of molecules averages the dipolar interaction and shielding anisotropy. As a result, sharp resonances with narrow peak widths and free of anisotropic contributions are observed in the NMR spectra. However, in the case of solids, due to the lack of motional averaging, all anisotropic interactions are active and contribute to the line-width, leading to the broadening of the peaks. Despite peak broadening being a major issue, accurate structural information can be obtained by studying the structure-dependent internal interactions. The dipolar interactions are useful in mapping interatomic distances, and the quadrupolar interactions are useful in determining the local site symmetries and local chemical environments. Solid-state NMR experiments can be performed on single crystals or powders. In the former case, sharp resonances (peak width governed by T_2) are observed, with the position dependent on the orientation of the crystal in the field. By changing the orientation and collecting successive spectra, the total anisotropy can be accurately determined. Although single-crystal NMR is used to determine the orientation of tensorial interactions relative to the molecular coordinate system, solid-state NMR of powders is more common. The powder is a collection of individual crystallites with all possible tensor orientations represented with respect to the external field. As a result, broad resonances are observed with chemical shielding, dipolar and quadrupolar contributions.

3.5.1 Magic angle spinning (MAS)

The chemical shift anisotropy, dipolar and quadrupolar interactions are anisotropic, i.e., the energies of the spin states and the corresponding resonance frequencies depend on the orientation of the tensor components with the external magnetic field [1,3]. This orientation dependence of chemical shielding, dipolar and quadrupolar interactions are given in equations 3.28, 3.38 and 3.48, respectively. If the sample is filled into a cylindrical rotor and spun about an axis inclined at a certain angle to the external field, the angles describing the tensorial orientation representing anisotropic interactions within the molecule vary with time. Each crystallite orientation acquires a modulation factor $\frac{1}{2}(3\cos^2\theta-1)$, and the average is [1],

$$\langle 3\cos^2\theta-1\rangle = \frac{1}{2}(3\cos^2\theta_R-1)(3\cos^2\beta-1) \qquad (3.52)$$

where θ is the angle between the Z^{PAS} axis of the tensor and the spinning axis R, θ_R is the angle between the external field and the spinning axis, and β is the angle between the Z^{PAS} axis and the external field (**Figure 3.12**).

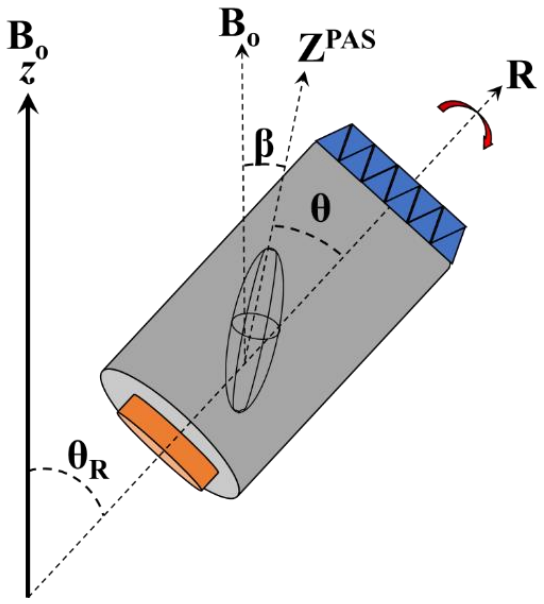

Figure 3.12. Pictorial representation of the magic angle setting where the cylindrical rotor is oriented at the magic angle (54.74°) with respect to the external field B_o. The shielding tensor is represented by the ellipsoid centered on the nucleus. θ is the angle between the Z^{PAS} axis of the tensor and the spinning axis R, θ_R is the angle between the external field and the spinning axis R, and β is the angle between the Z^{PAS} axis and the external field [3].

If θ_R is set to 54.74°, $3\cos^2\theta-1 = 0$ and therefore the $\langle 3\cos^2\theta-1\rangle$ term will also be zero. This angle is called the ***magic angle,*** and the spectrum collected with this setting will be free of anisotropic interactions and will be *solution-like*, with sharp resonances. However, this effect is true only for first-order effects. The second-order quadrupolar interaction can only be partially averaged (see **section 3.5.2**), and for this reason, the central transition of a quadrupolar nucleus

will have a second-order lineshape. For any anisotropic interaction to be averaged, the spinning frequency (ν_r) should be the same or higher than the interaction itself. If the spinning frequency is lower than the breadth of the powder pattern, a set of sharp peaks separated by the spinning frequency called the *spinning sidebands* flank the isotropic peak (**Figure 3.13**). In a polycrystalline sample, the orientation of each crystallite with respect to the external field is different, and hence, their resonance frequencies are also different, leading to rapid dephasing of magnetization after an RF pulse is applied. However, after one complete revolution, crystallites regain their phase coherence forming a rotational echo. At integer multiples of spinning frequency, all spin packets will experience the same set of orientations and will have undergone the same average precession. This generates rotational echoes in the time-domain data, which, upon Fourier transformation, yield spinning sidebands, the intensities of which provide information about the anisotropic interactions.

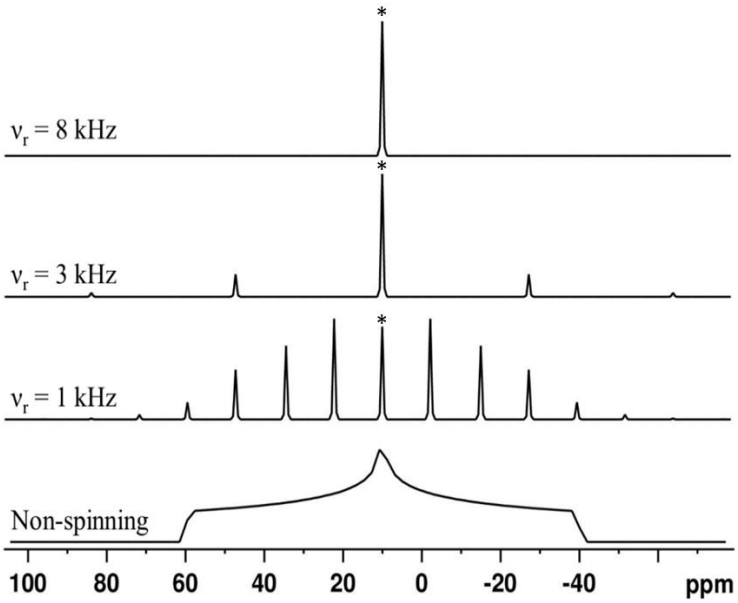

Figure 3.13. Effect of spinning a sample at the magic angle on the shielding anisotropy. At slow spinning speeds, the powder pattern is reduced to a set of sharp peaks, where spinning sidebands flank the isotropic peak, marked with an asterisk. At sufficiently high speeds, the anisotropy is completely averaged, leading to one sharp peak at the isotropic chemical shift position.

3.5.2 MAS NMR of quadrupolar nuclei

The second-order quadrupolar interaction dominates the line shape of the central transition in a static spectrum. It involves second-order and fourth-order Legendre polynomial terms, representing the isotropic and anisotropic parts of the second-order quadrupolar broadening, respectively [1]. These are given by,

$$P_2(\cos\theta) = \frac{1}{2}(3\cos^2\theta - 1) \qquad (3.53)$$

$$P_4(\cos\theta) = \frac{1}{8}(35\cos^4\theta - 30\cos^2\theta + 3) \qquad (3.54)$$

By spinning the sample at the magic angle, the isotropic part of the second-order broadening can be removed, but the anisotropic part of the broadening can be only partially averaged. Therefore the second-order quadrupolar broadening of the central transition can only be partially reduced, and the peak will have a characteristic second-order lineshape. The width of the central transition decreases when the sample is spun at the magic angle compared to the powder pattern but is governed by the incomplete averaging of the second-order quadrupolar interaction and hence will have residual broadening with a second-order lineshape. Complete removal of both parts of the second-order quadrupolar broadening is possible if the spinning axis is continually varied as a function of time (**Figure 3.14**). This is achieved by a technique called *double rotation*, which uses two rotors, one inside the other. The inner rotor moves bodily as a function of time, while the outer rotor is spun at the magic angle. The spinning axis of the inner rotor is tilted at $\theta = 30.6°$ with respect to the axis of the outer rotor [16]. The narrowing of the peak by spinning varies from 3.6 ($\eta = 0$) to 2.4 ($\eta = 1$) times, and the ratio of the overall line-width static to MAS is given by [1],

$$\frac{7(\eta^2+22\eta+25)}{2(6+\eta^2)} \qquad (3.55)$$

An important consequence of residual second-order quadrupolar broadening is that the isotropic shift of the peak does not coincide with its center-of-gravity (**Figure 3.15**). The isotropic second-order quadrupolar shift is given by [1],

$$\nu_{Q_{iso}}^{(2)}(I,m) = -\frac{3C_Q^2}{40\nu_0 I^2(2I-1)^2}[\mathrm{I(I+1)-9m(m-1)-3}]\left(1+\frac{\eta^2}{3}\right) \qquad (3.56)$$

The relation between the isotropic chemical shift (δ_{iso}) and the center-of-gravity shift (δ_{CG}) is given by [1],

$$\delta_{CG} = \delta_{iso} - \frac{3}{40}F(I)\frac{C_Q^2}{\nu_0^2}\left(1 + \frac{\eta^2}{3}\right) \qquad (3.57)$$

where F(I) is a spin-dependent factor and is given by [I, F(I)]: $(\frac{3}{2}, \frac{1}{3})$; $(\frac{5}{2}, \frac{2}{25})$; $(\frac{7}{2}, \frac{5}{147})$; $(\frac{9}{2}, \frac{1}{54})$.

The line-width of the central transition produced by the second-order quadrupolar effect is [1],

$$\Delta\nu_Q^{(2)} = F(I)\frac{C_Q^2(6+\eta)^2}{224\nu_0} \qquad (3.58)$$

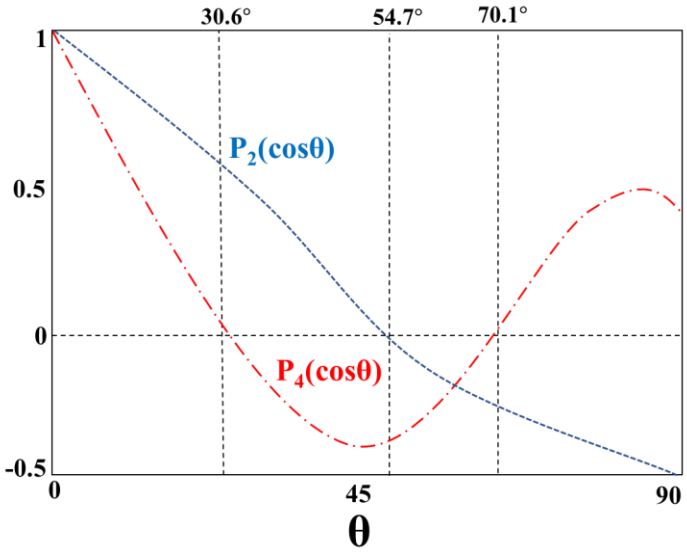

Figure 3.14. Graph showing the values of the Legendre functions $P_2(\cos\theta)$ and $P_4(\cos\theta)$ at different θ values. The second-order term is zero at θ = 54.74°, and the fourth-order term is zero at θ = 30.6 and 70.1°. Adapted from [1].

Partial averaging of the second-order quadrupolar broadening is observed in satellite transitions, but the breadth of the peak is governed by the first-order quadrupolar term, which is not averaged by the spinning as these transitions lack orientation dependence. Hence under magic angle spinning conditions, the breadth of the satellite transitions varies as a function of the

C_Q and are reduced to spinning sidebands. The breadth of the spinning sideband manifold will be the same as the overall width of the satellites.

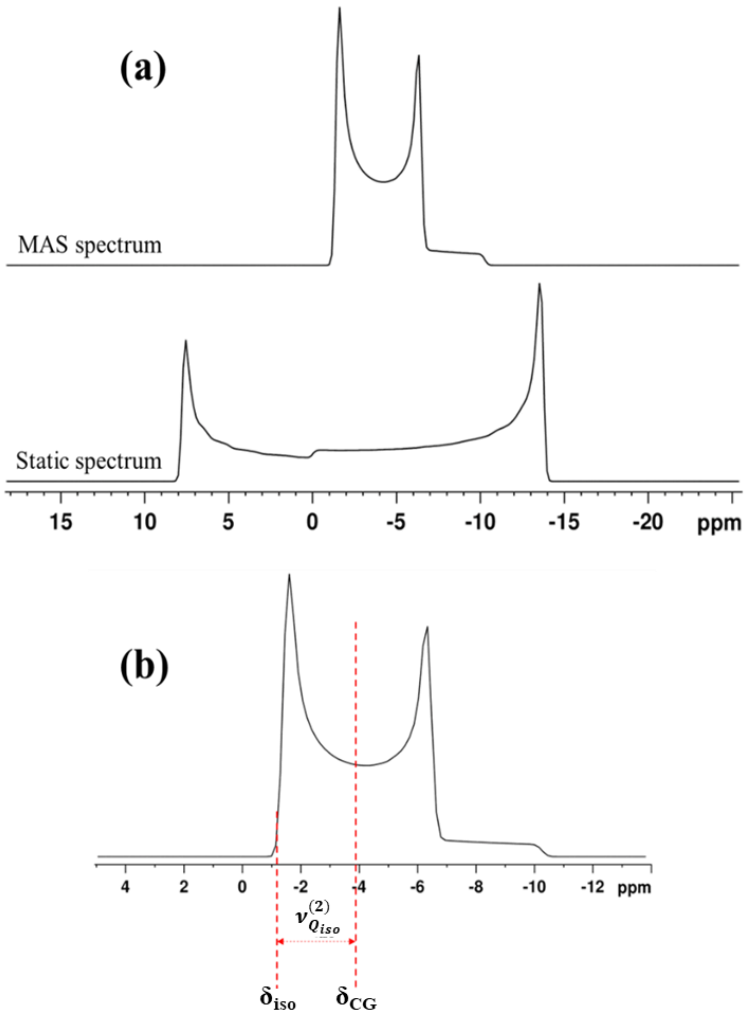

Figure 3.15. (a) The effect of magic-angle spinning on the breadth of the central transition; (b) The second-order quadrupole broadened centreband showing the isotropic chemical shift (δ_{iso}) and the center-of-gravity shift (δ_{CG}).

3.5.3 NMR lineshapes in crystalline versus glassy systems

Crystalline systems have long-range periodic atomic arrangements and tightly constrained structural parameters such as bond lengths and bond angles. As a result, no distribution in the anisotropic interactions exists, and resonances representing chemically distinct spins are

observed, with their peak widths governed by T_2. However, in oxide glasses, a range of M−O−M angles leads to a Gaussian distribution of the chemical shifts in I = $\frac{1}{2}$ nuclei such as ^{29}Si and the distribution of chemical shift and the quadrupolar coupling in quadrupolar nuclei such as ^{27}Al. To discern the structure of a disordered solid, it is often helpful to consider the NMR parameters of closely related crystalline analogues, with particular attention to the local geometry, such as the number of coordination atoms, the chemical identity of next-nearest neighbours and distribution in geometry parameters. The chemical shielding is susceptible to local chemical environments, and hence, distribution in geometry parameters will lead to dispersion in the isotropic chemical shifts, leading to broad resonances. For example, ^{29}Si chemical shifts of Si units with different next-nearest neighbours are distinct in crystalline systems but severely overlap in the case of amorphous solids (**Figure 3.16**). A qualitative understanding of silicate speciation from such spectra can be obtained by tightly constrained deconvolutions (see chapter 4: materials and methods).

In the case of quadrupolar nuclei, structural disorder produces a range of electric field gradients. If the isotropic shifts of these distinct sites arising from the structural disorder are similar, then the lineshape is stretched towards the lower frequency (**Figure 3.17**), often referred to as *tailing*. Since quadrupolar interaction is inversely related to the applied field strength, this feature can be removed, and the peak becomes more symmetric when the spectra are collected at sufficiently high fields. This is also called as *Czjzek distribution* [17,18], which can be defined by calculating the distribution function of the electric field gradient V_{zz} and the asymmetry parameter (η) by considering the structural randomness in terms of distribution of ionic angular positions in any coordination shell and the absence of any correlations between the distribution of ionic charges in different shells [17].

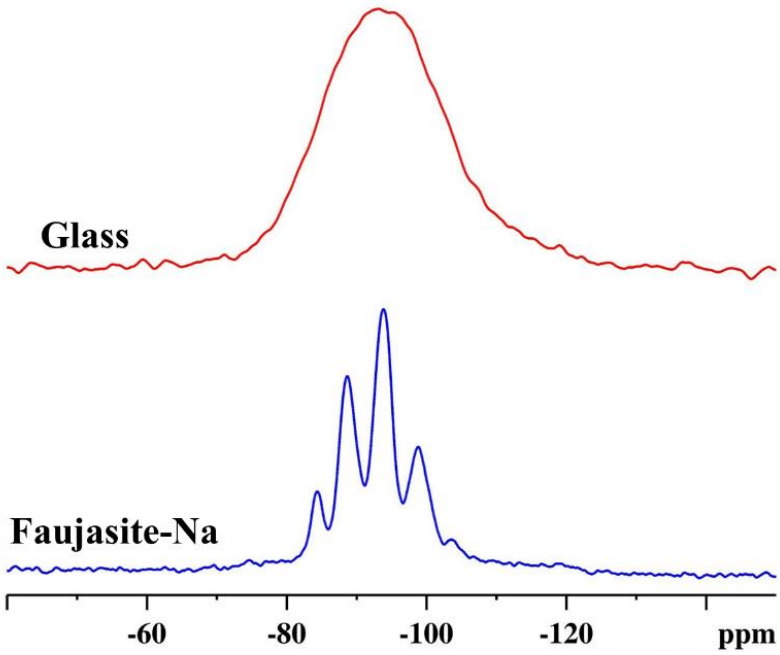

Figure 3.16. ^{29}Si MAS NMR spectra of a silicate glass (top) and a silicate-based zeolite faujasite-Na, which is a crystalline material. Well-resolved resonances in the zeolite spectrum corresponds to silicate units bonded to different numbers of next-nearest aluminate units.

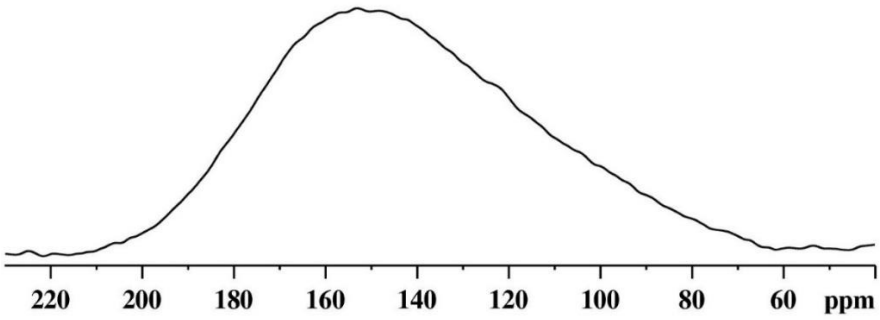

Figure 3.17. ^{71}Ga MAS NMR of a gallate glass exhibiting tailing towards the lower frequency, a characteristic of the distribution in quadrupolar coupling.

3.6 References

[1] K. J. D. MacKenzie and M. E. Smith, *Multinuclear solid-state nuclear magnetic resonance of inorganic materials*. Elsevier, 2002.

[2] J. Keeler, *Understanding NMR spectroscopy*. John Wiley & Sons, 2011.

[3] M. J. Duer, *Solid state NMR spectroscopy*, Blackwell Sci. Ltd., London, vol. 10, 2002.

[4] S. Kroeker, "Nuclear magnetic resonance spectroscopy of glasses," in: *Modern glass characterization*, M. Affatigato, Ed. Wiley Online Library, 2015, pp. 1–30.

[5] J. Larmor, "LXIII. On the theory of the magnetic influence on spectra; and on the radiation from moving ions," London, Edinburgh, Dublin Philos. Mag. J. Sci. 44 (1897) 503–512.

[6] P. Kinsler, "Faraday's law and magnetic induction: Cause and effect, experiment and theory," Physics, 2 (2020) 148–161.

[7] G. A. Morris, "NMR data processing," in *Encyclopedia of spectroscopy and spectrometry*, J. Lindon, G.E. Tanter, D. Koppenaal (Eds.), Academic Press, 2016, pp. 125–133.

[8] H. Günther, *NMR spectroscopy: basic principles, concepts and applications in chemistry*. John Wiley & Sons, 2013.

[9] C. M. Widdifield and R. W. Schurko, "Understanding chemical shielding tensors using group theory, MO analysis, and modern density-functional theory," Concepts Magn. Reson. Part A Bridg. Educ. Res. 34 (2009) 91–123.

[10] J. C. Facelli, "Chemical shift tensors: Theory and application to molecular structural problems," Prog. Nucl. Magn. Reson. Spectrosc. 58 (2011) 176–201.

[11] J. C. Facelli, "Calculations of chemical shieldings: Theory and applications," Concepts Magn. Reson. Part A Bridg. Educ. Res. 20 (2004) 42–69.

[12] C. J. Jameson and J. Mason, "The chemical shift," in *Multinuclear NMR*, J. Mason, Ed. Boston, MA: Springer US, 1987, pp. 51–88.

[13] R. E. Wasylishen, S. E. Ashbrook, and S. Wimperis, *NMR of quadrupolar nuclei in solid materials*. John Wiley & Sons, 2012.

[14] P. P. Man, “Quadrupolar interactions,” in: *NMR of quadrupolar nuclei in solid materials*, R. E. Wasylishen, S. E. Ashbrook, and S. Wimperis, Eds. Wiley Online Library, 2012, pp. 4–16.

[15] D. L. Bryce and R. E. Wasylishen, “Quadrupolar nuclei in solids: influence of different interactions on spectra,” in: *NMR of quadrupolar nuclei in solid materials*, R. E. Wasylishen, S. E. Ashbrook, and S. Wimperis, Eds. Wiley Online Library, 2012, pp. 63–74.

[16] B. Q. Sun, J. H. Baltisberger, Y. Wu, A. Samoson, and A. Pines, “Sidebands in dynamic angle spinning (DAS) and double rotation (DOR) NMR,” Solid State Nucl. Magn. Reson. 1 (1992) 267–295.

[17] G. Czjzek, J. Fink, F. Gotz, and H. Schmidt, “Atomic coordination and the distribution of electric field gradients in amorphous solids,” Phys. Rev. B, 23 (1981) 2513–2530.

[18] U. Werner-Zwanziger, A. L. Paterson, and J. W. Zwanziger, “The Czjzek distribution in solid-state NMR: Scaling properties of central and satellite transitions,” J. Non-Cryst. Solids, 550 (2020) 120383.

4 Materials and Methods

4.1 Synthesis of glasses

Glasses were synthesized in 1−4 g batches by mixing appropriate oxides and carbonates in stoichiometric ratios and melting the mixture at temperatures between 1100 and 1350 °C, depending on the glass composition. A Thermolyne® box furnace and a stage-operated Deltech® vertical-tube furnace (**Figure 4.1**) were employed to melt the glasses at temperatures 1100 °C and 1350 °C, respectively. The required amounts of oxides and carbonates were weighed and mixed in 95/5 Pt/Au crucibles and decarbonated at 650 °C for 12 hours, then melted for 1−2 hours with the lids on. The melt was then either slow-cooled at *ca.* 5 °C/min or quenched by dipping the crucible in water. For dissolution studies, the glasses were quenched in water, ground, re-melted for 1 hour to ensure homogeneity, and cooled in the air to obtain glass monoliths. These monoliths were cut into approximately rectangular pieces and stored in a desiccator before dissolution analysis, whereas the cut-off portions were used for NMR and powder x-ray diffraction analysis. Boron oxide (B_2O_3) was synthesized in the lab by heating boric acid (H_3BO_3) at 400, 650 and 800 °C for 15 minutes at each temperature, while other oxides and carbonates were used as received.

All batch compositions were calculated as follows: the mole fraction of each component is multiplied by its molecular weight, which is then totaled to determine the molecular weight of the glass. Each mole fraction is divided by molecular weight of the glass and multiplied by the amount of glass to be produced, to determine the mass of oxides/carbonates required. As the carbonates decompose to their respective oxide and CO_2, their mass is multiplied by the appropriate gravimetric factor. The obtained glasses were transferred into air-tight vials immediately after synthesis and stored in desiccators for further analysis. Since this thesis comprises studies on many different glass systems, the compositions are listed individually in relevant chapters.

A sample calculation for synthesizing three grams of $20Na_2O$-$20B_2O_3$-$60SiO_2$ glass (in mol%) is shown here [1]:

Molecular weights of components (in g/mol): Na_2O: 61.98; B_2O_3: 69.63; SiO_2: 60.09.

Molecular weight of glass (g/mol): $(0.20 \cdot 61.98) + (0.20 \cdot 69.63) + (0.60 \cdot 60.09) = 62.37$ g/mol.

Weight fraction of each component to synthesize three grams of glass:

Na_2O: $[(0.20 \cdot 61.98) \div 62.37] \cdot 3 = 0.59$ g

B_2O_3: $[(0.20 \cdot 69.63) \div 62.37] \cdot 3 = 0.66$ g

SiO_2: $[(0.60 \cdot 60.09) \div 62.37] \cdot 3 = 1.73$ g

Since Na_2O is added in a carbonate form (Na_2CO_3), the amount is multiplied by the gravimetric factor 1.70: $(0.59 \cdot 1.70) = 1.00$ g.

Total oxides and carbonate to be weighed to synthesize three grams of $20Na_2O$-$20B_2O_3$-$60SiO_2$ glass: Na_2CO_3: 1.00 g; B_2O_3: 0.66 g; SiO_2: 1.73 g.

Figure 4.1. The box furnace (left) and the stage-operated vertical-tube furnace (right).

4.2 NMR instrumentation and methodology

4.2.1 NMR instrumentation

Solid-state NMR experiments were conducted on several spectrometers operating at fields 9.4 T to 21.1 T, housed at several NMR facilities. The 400 (9.4 T), 500 (11.7 T) and 600 (14.1 T) MHz NMR spectrometers are located at the Prairie Regional NMR Facility, University of Manitoba, while the 850 (20 T) and the 900 (21.1 T) MHz NMR spectrometers are operational in the National Ultra-high Field NMR Facility for Solids, University of Ottawa, Canada and CEMHTI CNRS, Université d'Orléans, France, respectively. The single-pulse experiments were conducted on Bruker Avance II 400 and 500 MHz spectrometers and the Varian ^{UNITY}INOVA 600 MHz spectrometer. The ^{29}Si $\{^{1}H\}$ CPMAS NMR experiments were conducted on the Bruker Avance II 400 MHz spectrometer. The solid-echo experiments were conducted on Bruker Avance III 850 MHz and Bruker Avance II 900 MHz NMR spectrometers. Further information on the probe hardware and the experimental parameters is given in each chapter.

4.2.2 High-temperature NMR

The high-temperature MAS NMR experiments were conducted on a Bruker Avance II 400 MHz spectrometer. The rotor set includes an aluminum nitride or a boron nitride insert held inside a zirconia (ZrO_2) sheath using Macor® rings (**Figure 4.2**) [2]. The sheath is capped on one end and open on the other, through which a laser is directed at the insert for sample heating. A 50 W CO_2 laser is positioned on the floor orthogonal to the NMR probe, which is inserted into the superconducting magnet. A mirror at the end of the laser guide directs the laser into the probe and a second mirror inside the probe reflects the laser onto the sample. Dry N_2 is used as the bearing and driving gas to suspend and spin the rotor, respectively, and to cool the stator inside the probe, which houses the rotor and the RF coil. The temperature is calibrated using the ^{79}Br signal of potassium bromide (KBr), where the δ_{iso} changes at a rate of -0.0249 ± 0.0015 ppm/°C [3]. Single-pulse ^{23}Na and ^{31}P NMR experiments (vide infra) were acquired with pulse length and recycle delays of 0.4 μs (15° flip angle) and 1 s (^{23}Na), and 1 μs (30° flip angle) and 20 s (^{31}P).

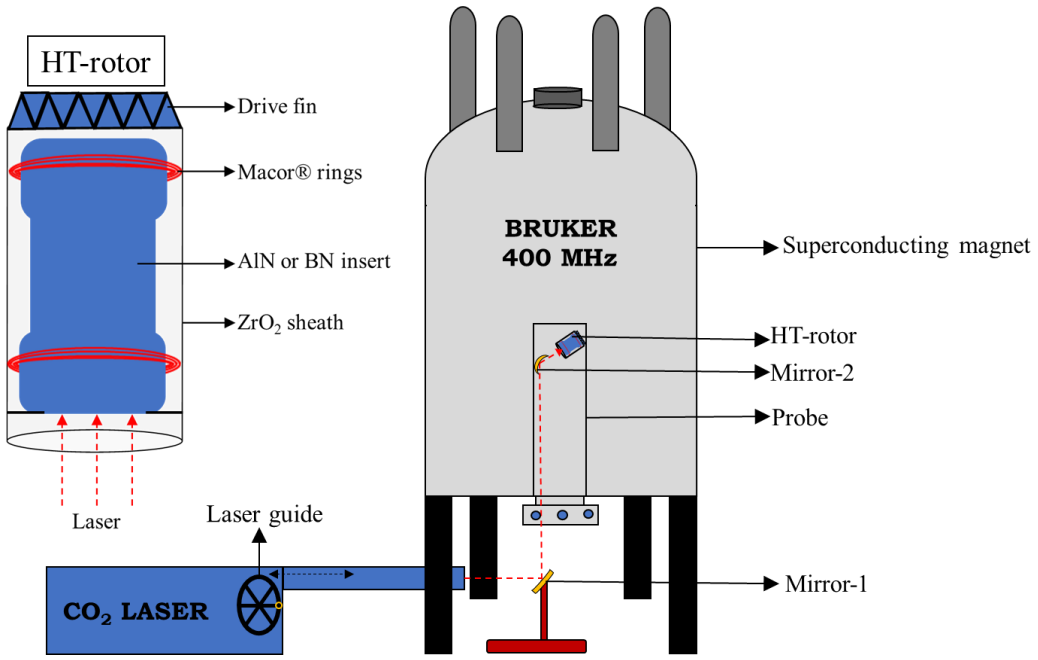

Figure 4.2. High-temperature rotor setup and experimental setup.

4.2.3 Solid-state NMR experiments

4.2.3.1 Single-pulse experiment

The single-pulse experiment, also called the Bloch-decay sequence [4], consists of a single radiofrequency pulse followed by an acquisition time during which the free-induction decay (FID) is recorded (**Figure 4.3**). A short delay exists between the pulsing and the acquisition time called the pre-scan delay, which is required to switch the function of the transmitting coil to a receiver. The RF pulse tips the magnetization to the x−y plane, and the degree of perturbation is called the *flip-angle* or *tip-angle*, set by changing the duration for which the pulse is applied. A set of one pulse, pre-scan delay and acquisition time is considered one scan, and a recycle delay is included in the sequence when several scans are involved in an experiment. This delay allows the magnetization to relax to its equilibrium position such that the magnetization perturbation achieved in each scan is maximized for a particular relaxation delay, which optimizes the signal-to-noise ratio of the spectrum. In cases where the spin-lattice relaxation rates are long, the RF pulse is applied for a shorter duration, which tips the magnetization just enough that short relaxation delays are sufficient to restore the magnetization between the scans. The flip-angle and the minimum necessary recycle delay show an exponential relationship [2]. For a spin with a

T_1 of 100 s, 50% of the maximum signal can be achieved by setting the flip-angle to 30−50°, and at 1/5th the recycle delay required to fully relax the magnetization [2].

In samples consisting of quadrupolar nuclei in more than one chemically distinct site, the response of nuclei to the applied RF pulse may differ (**Figure 4.4**) [5]. Due to different electric field gradients at each site, the quadrupolar coupling constants are different, and so are their nutation curves, so that care must be taken to ensure that the spectral intensities are quantitative. Similar pulse responses are observed in the linear regime of these nutation curves, which corresponds to short flip-angles. Generally, 15° flip-angles are used in the solid-state NMR experiments of samples consisting of quadrupolar nuclei, which are calculated (**Equation 4.1**) from the $\frac{\pi}{2}$(solid) pulse. The latter is calculated from the $\frac{\pi}{2}$ pulse length optimized for a reference solution [$\frac{\pi}{2}$(solution)] of the quadrupolar nucleus being studied.

$$\frac{\pi}{2}(\text{solid}) = \frac{\frac{\pi}{2}(\text{solution})}{(I+1/2)} \qquad (4.1)$$

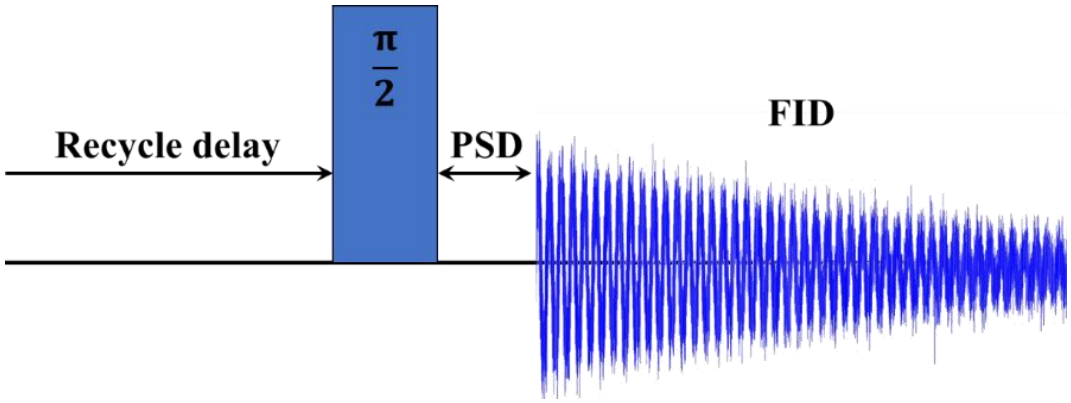

Figure 4.3. An illustration of the single-pulse experiment pulse sequence. (Prescan delay, PSD; free induction decay, FID)

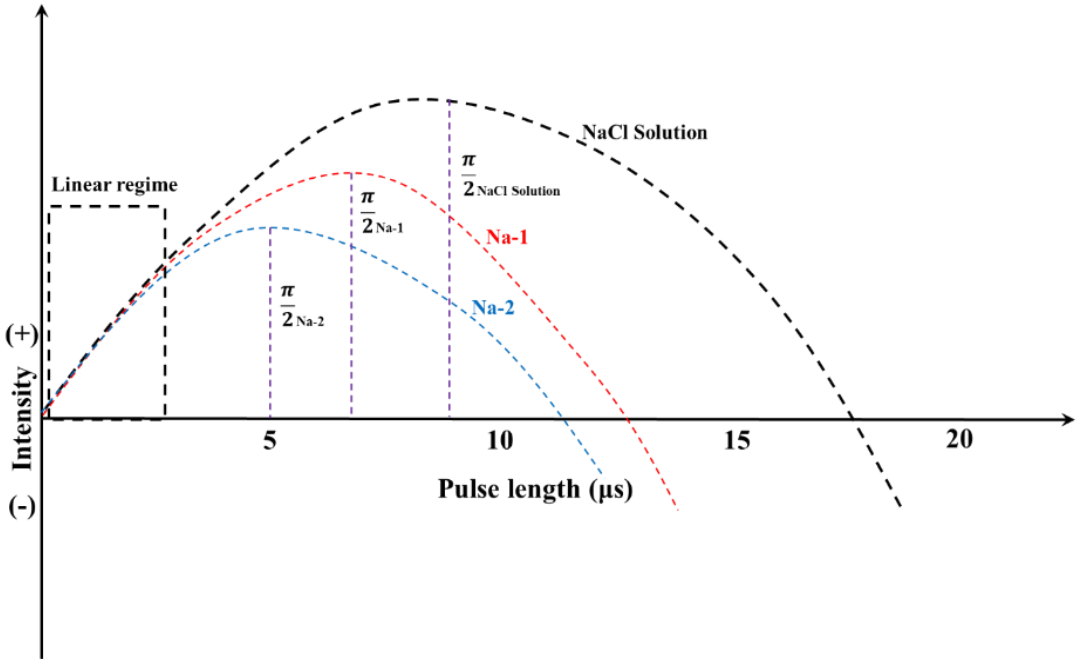

Figure 4.4. ^{23}Na nutation curves of an NaCl solution and Na^+ subject to different quadrupolar interactions. The linear regime where the pulse responses are similar is highlighted.

4.2.3.2 ^{29}Si{^{1}H} cross-polarization magic-angle spinning (CPMAS) NMR

Cross-polarization MAS NMR is a dipolar-based double resonance experiment mainly used to enhance the sensitivity of low-gamma and low natural abundance nuclei [5–7]. Here, the magnetization is transferred from an abundant spin (^{1}H) to the less abundant, lower-gamma spin (^{29}Si) by irradiating them at their respective Larmor frequencies, thereby fulfilling the Hartmann-Hahn condition. The pulse sequence of this experiment is given in **Figure 4.5**. First, the ^{1}H magnetization is created in the x−y plane, and spin-locked, i.e., the magnetization is not allowed to decay to zero by applying a second phase-shifted RF pulse of duration t ($T_2 << t < T_1$). The ^{29}Si spin system has no transverse magnetization. The transfer of magnetization from ^{1}H to ^{29}Si spins is achieved by applying a second B_1 field to the ^{29}Si spins for a specific time called the *contact time* such that,

$$\gamma_H B_{1H} = \gamma_{Si} B_{1Si} \qquad (4.2)$$

where γ_H and γ_{Si} are the gyromagnetic ratios of ^{1}H and ^{29}Si, B_{1Si} and B_{1H} are the magnetic fields experienced by the ^{29}Si and ^{1}H spins in the rotating frame. This is called the Hartmann-Hahn

matching condition and is achieved by varying the RF power levels until the nutation frequencies of ^{1}H and ^{29}Si match ($\omega_H = \omega_{Si}$). Once the Hartmann-Hahn condition is established, the magnetization is transferred from the ^{1}H to the ^{29}Si spins via their dipolar interaction. The FID is then recorded in the ^{29}Si channel with a decoupling pulse applied to the ^{1}H channel, if necessary. The theoretical gain in signal intensity relative to non-CP single-pulse experiment corresponds to γ_H/γ_{Si}, which is a factor of ~5. Since the RD in the experiment is governed by the T_1 of the protons in the rotating frame ($T_{1\rho}$), which is relatively short, more scans can be collected, also improving the signal-to-noise ratio for a given experimental time.

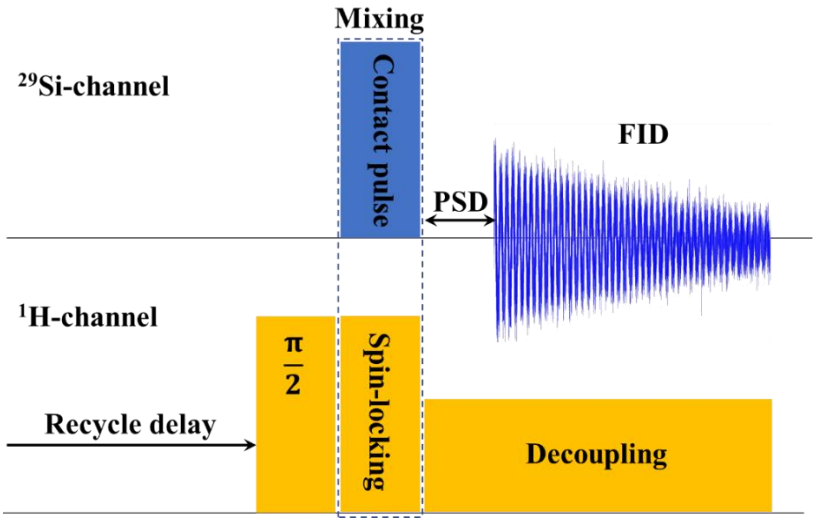

Figure 4.5. Pictorial representation of the $^{29}Si\{^{1}H\}$ CPMAS NMR pulse sequence. FID, free induction decay; PSD, pre-scan delay.

4.2.3.3 Spin-echo experiment

In solid-state NMR experiments involving nuclei with low Larmor frequency (low gyromagnetic ratio, γ) and, at conditions such as larger coil sizes and higher magnetic field, the spectra consist of spurious signals, attributed to large-amplitude acoustic ringing [8]. This phenomenon arises due to the electromagnetic generation of ultrasonic standing waves in metals surrounding the transmitter coil. In the presence of a static magnetic field, the applied RF pulse induces a radiofrequency current within the skin depth of the metal surface, generating a coherent

ultrasonic standing wave matching the frequency of the incident radiation. A reciprocal mechanism converts this acoustic energy into an oscillating magnetic field, which is picked up by the receiver coil and recorded as a spurious signal. The ringing impedes the observation of signals with short free-induction decays (i.e., broad peaks) and causes baseline distortions and phasing issues. Ringing artifacts can be removed by increasing the pre-scan delay set between the pulsing and signal acquisition but, this will deteriorate the signal-to-noise ratio of the spectrum as the amplitude of the FID is also lowered. It also compromises the quality of the data as the structural information encoded in the early part of the FID is lost. Furthermore, if the T_2 is very short, the signal may be completely lost within the pre-scan delay, and no peaks are observed in the collected spectrum. In these cases, a spin-echo pulse sequence, also called as the Hahn-echo can be employed [9]. This is a two-pulse sequence wherein the first 90° RF pulse generates magnetization in the transverse plane and the second 180° RF pulse applied after a time duration (τ) refocuses the magnetization (**Figure 4.6**). As the spurious signals are lost in the delay between the pulses, only the magnetization is refocused, and hence, the echo collected at the 2τ period will be free of any baseline and phasing problems. The delay τ must be set lower than the transverse relaxation rate ($\tau<T_2$).

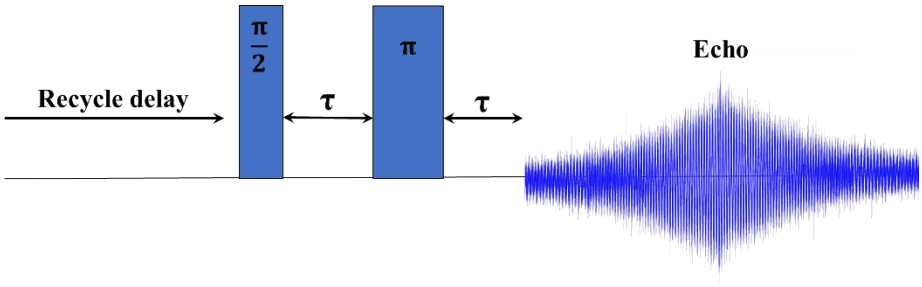

Figure 4.6. Pulse sequence of the Hahn-echo MAS NMR experiment.

4.2.3.4 Deconvolution of the MAS NMR spectra

The MAS NMR spectra were deconvolved using the DMFit [10] program. The program is designed for analyzing solid-state NMR spectra and functions as an excellent tool to deconvolve spectra of materials, ranging from ordered crystalline phases to disordered crystalline and

amorphous materials. Modules are available to simulate the spectra of spin-1/2 and quadrupolar nuclei, both non-spinning powder patterns and the spectra obtained under magic-angle spinning conditions. The program utilizes a mismatch criterion, a simple quadratic distance between the modeled and the experimental spectrum. The simulation starts with an approximate solution, and the parameters are changed until the mismatch criterion converges to a minimum.

The spectra of spin-1/2 nuclei such as ^{29}Si and ^{31}P are deconvolved using Gaussian lineshapes with some Lorentzian contributions (G/L) chosen to optimize the fit. The peak positions and peak widths are user-defined and are carefully selected to obtain reliable NMR parameters. The ^{11}B MAS NMR spectra mainly consist of two peaks, corresponding to borate units in trigonal-planar ($^{[3]}$B) and tetrahedral geometries ($^{[4]}$B). Due to the difference in $^{[3]}$B and $^{[4]}$B site-symmetries, they experience significantly different quadrupolar interactions and hence, have different quadrupolar coupling constants (C_Q), 2.6 and 0.4 MHz, respectively [11]. Due to a small C_Q, the $^{[4]}$B peak is symmetric and has the characteristics of a Gaussian lineshape. The $^{[3]}$B peak is broader and exhibits a second-order quadrupolar lineshape due to its larger C_Q. The $^{[4]}$B peak is deconvolved using G/L lineshapes, while the $^{[3]}$B peak is deconvolved using a DMFit module called *Quasar* [12], which simulates second-order quadrupolar lineshapes of the central transition. Since the central transition of the $^{[4]}$B peak overlaps with the centreband of the satellite transition, the intensity of the former peak must be corrected, which is done by subtracting the intensity of the first sideband from the $^{[4]}$B peak. The ^{23}Na NMR spectra of phase-separated glasses with sharp features are fitted using a combination of the Quasar module and G/L lineshapes, wherein the former simulates the peaks arising from crystalline inclusions and the latter represents the residual glass. The peaks are then integrated to determine the relative fractions of Na^+ ions in the crystalline and the glassy phases. Although ^{27}Al is a quadrupolar nucleus, symmetrical G/L lineshapes were used to fit the ^{27}Al NMR spectra as the observed peaks are symmetric and do not exhibit the tailing toward lower frequencies often seen for a distribution in quadrupolar couplings. The fitting parameter uncertainties were estimated by manually varying parameters - independently and in conjunction with other variations - until an acceptable fit could no longer be obtained.

4.3 Powder x-ray diffraction

Powder x-ray diffraction (PXRD) is a standard technique used to determine crystal structures and perform phase identification of crystalline minerals. While the diffractograms of crystalline phases consist of sharp Bragg peaks arising from different lattice planes in their crystal structures, no such peaks are observed in amorphous systems due to the absence of long-range periodic atomic arrangements and oriented lattice planes. The diffractograms of glasses consist of a featureless broad signal, referred to as *amorphous halo*. However, in the case of phase-separated glasses, the diffractogram features sharp Bragg peaks in addition to the halo, which can be used to identify the phases of the crystallites present. Hence, PXRD was used mainly to confirm the amorphous nature of the synthesized glasses and to determine the chemical identities of the crystalline phases present in phase-separated glasses. The phase identification process involves matching the Bragg peaks with a library of diffraction patterns calculated for a wide variety of crystalline systems.

X-ray diffraction analysis was done using a D4 Endeavor x-ray diffractometer (Bruker, Billerica, MA, USA). The samples were finely ground and mounted on polymer diffraction plates and subjected to Cu-Kα radiation generated at a voltage and current of 40 kV and 40 mA, respectively. The 2θ range was scanned between 10° and 50° with a step size of 0.02° and an acquisition time of 20 seconds, corresponding to 2000 steps. The sample was spun at 15 rpm during data acquisition to ensure homogeneous sampling. Phase identification was carried out using the *QualX* [13] program equipped with the crystallography open database library [14]. All possible combinations of elemental compositions were considered during the search-and-match procedure.

4.4 Electron microscopy

Electron microscopy [15,16] is a widely used technique for studying the surface characteristics of both organic and inorganic materials, and information such as external morphology, chemical composition, mesoporous architectures may be obtained. A beam of energetic electrons generated from a thermionic, Schottky or field-emission cathode is accelerated towards the sample held on a stage by applying a voltage difference of 0.1 to 50 keV between the anode and the cathode while the whole system is under vacuum. A series of electromagnetic lenses called

solenoids are used to focus the beam onto the sample and rastered across, generating a two-dimensional image of the sample surface in greyscale.

Specimen-electron beam interactions generate secondary electrons, back-scattered electrons, Auger electrons and characteristic x-rays, each of which provides different morphological information. Due to the ballistic nature of the incident electron beam, the electrons in the outer shells of atoms in the material are ejected, and these are referred to as *secondary electrons* (SE). These have energies between 0 and 50 eV and emerge from the shallow 'escape' region beneath the surface, ranging from 10−20 nm. The image produced from the detection of secondary electrons can provide spatial information up to 1 nm under optimized conditions. The *back-scattered electrons* (BSE), with an energy ranging from 50 eV to the energy of the incident electron beam (E_0), result from the elastic collisions of incident electrons with the atoms. The number of back-scattered electrons detected is a function of the atomic number, thus the BSE yield increases monotonically with atomic number, Z. As a result, BSE imaging, also called the *Z-contrast imaging*, is widely used in studying the chemical heterogeneity of the samples. The third important product of sample-electron interaction are the x-rays. The incident electron beam ejects an electron from the inner shell, and an electron from the outer shell fills the hole. In the process, x-rays matching the energy difference between these two shells are generated, the energies of which are specific to each element. The chemical compositions of the analyzed material can be precisely determined by registering the energies of these x-rays. This technique is called *energy-dispersive x-ray spectroscopy* (EDS) or *energy dispersive x-ray analysis* (EDXA or EDAX). Images can be acquired either in an environmental-SEM (e-SEM) mode, where the samples are analyzed in their native state, or the samples can be mounted in resins and polished. If the samples are not conducting, they must be either carbon- or gold-coated to prevent surface charging.

SE and BSE images of glass samples were acquired on a Quanta FEG 650 microscope (FEI, ThermoFisher, Oregon, USA) housed in the Manitoba Institute for Materials, University of Manitoba. Many thanks to Dr. Ravinder Sidhu for helping with the morphology analysis and the acquisition of SE and BSE images. Glass surfaces were imaged in "environmental" mode (low vacuum mode, 120 Pa) without mounting, polishing, or coating. Cross-section images of glasses after dissolution experiments were obtained by polishing the resin-mounted glass monoliths. A

large-field detector was used to acquire SE images with an accelerating voltage of 10 kV. A concentric higher-energy electron detector was used to acquire BSE images with an acceleration voltage of 10 kV. Energy-dispersive x-ray spectroscopy (EDS) and elemental mapping of glasses were carried out using the TEAM^{TM} EDS instrument (EDAX, Mahwah, NJ, USA). The EDS spectra were acquired with a takeoff angle of 33.3°, a live time of 10 s, an amplitude time of 7.6 μs and a resolution of 128 eV.

4.5 Inductively-coupled plasma-optical emission spectroscopy (ICP-OES) and -mass spectrometry (ICP-MS)

The inductively coupled plasma-optical emission spectroscopy (ICP-OES) [17,18] and -mass spectrometry (ICP-MS) [19] techniques are powerful analytical tools used to detect and quantify elements in aqueous solutions. Both methods employ inductively-coupled plasma to generate excited states of atoms, ions and charged ionic species, which are the detectable species in emission spectroscopy and mass spectrometry, respectively. The analyte solution is nebulized and passed through a high-temperature plasma torch (*ca.* 10,000 K) where the solution is atomized, and the atoms are further ionized. Collisional excitation of the analyte atoms and ions within the plasma promotes them to excited states, which relax to the ground state emitting photons. The wavelengths of these photons are element-specific, and hence, the chemical composition of the solution can be determined by observing them. By measuring their intensities, the elements present in the solution can be quantified.

While the mode of generating ions in ICP-MS is similar to the ICP-OES technique, the detection methods differ. The so-formed ions are extracted into a set of electrostatic lenses called *ion optics*, which focus and guide the ions into a quadrupole mass analyzer. The analyzer consists of four cylindrical metallic rods, and the electric field in the center is changed by applying direct- (DC) and alternating-currents (AC). Ions with a particular mass-to-charge (m/z) ratio will have stable flight trajectories through the analyzer at specific combinations of AC and DC fields; therefore, the ions can be separated and measured using a suitable detector.

ICP-MS analysis of aliquots collected from the dissolution of phosphate-doped borosilicate glasses (**Chapter 7**) was carried out using an Agilent 8900 triple-quad mass spectrometer equipped with a Seafast sample introduction system, housed at the Centre for Earth

Observation Science, University of Manitoba. Ms. Debbie Armstrong is acknowledged for analyzing the samples. Samples of 0.5 mL were introduced into a spray chamber with a nebulizer gas flow rate of 1 L/min of ultra-high purity Ar. Silicon analysis was run in H_2 gas mode; Al, B, Na, Cs, and Mo analyses were run in direct no-gas mode; and P was run in O_2 mode. The calibration curve (1000 ppm individual standards from Inorganic Ventures) was validated with NIST1640a trace elements in natural water and TM-27.4 natural water from Environment and Climate Change Canada Reference Material. Samples were analyzed in triplicate, and their relative standard deviation was included in the quantification plot as the instrumental error.

ICP-OES measurements of aliquots collected during the dissolution of sodium borosilicate glasses (**Chapter 9**) were done using a Varian 725-ES ICP optical emission spectrometer housed at the Manitoba Chemical Analysis Laboratory, University of Manitoba with radial-view plasma system. Dr. Tom Ward is acknowledged for his timely assistance in analyzing the solution samples. The aliquots of the leachate obtained at different time intervals were diluted from 0.25mL to 5mL with MiliQ water containing 2% analytical grade HNO_3 before the ICP-OES measurements. The calibration plots used for quantification were constructed using trace metal grade primary standards of sodium (999 ± 5 μg/mL, BDH), boron (997 ± 4 μg/mL, SCP Science), silicon (1000 ± 2 μg/mL, SCP Science) and, aluminum (999 ± 5 μg/mL, SCP Science).

4.6 Glass dissolution

Glass dissolution experiments were based on the MCC-1 test developed at the Materials Characterization Center (MCC), Pacific Northwest Laboratory, Richland, WA, USA [20]. The dissolution studies were carried out in polytetrafluoroethylene containers housed in stainless-steel Parr® digestion vessels at 90°C (**Figure 4.7**). Glass monoliths were cut into rectangular pieces with surface areas ranging from 400 to 800 mm^2. Since the glass monoliths were not perfectly rectangular in shape, the surface areas of each sample were estimated by averaging ten independent dimension measurements. These pieces were immersed in deionized water, and the volume of water was selected to obtain a surface-area-to-volume (SV) ratio of 25 and 11 m^{-1} for phosphate-doped borosilicate glasses and sodium borosilicate glasses, respectively. Milli-Q® water with a pH of 7.2 and a resistivity of 18.2 MΩ·cm (at 25 °C) was used as a dissolution

medium. Aliquots of 0.25 mL were collected at the same time of day on days 1, 2, 3, 6, 7, 14, and 28 and stored in a refrigerator for elemental analysis by ICP-OES or ICP-MS. After 28 days, the glass monoliths were pulled out of the containers, fragmented and the pieces were mounted in resin to obtain cross-section SEM images. The pH of the leachate on day 28 was measured using a Fisher Accumet® AB150 pH meter.

Figure 4.7. Digestion vessel and its components.

4.7 References

[1] J.E. Shelby, Glass melting, in: *Introduction to glass science and technology*, Royal Society of Chemistry, 2007: pp. 26–50.

[2] J.E.C. Wren, Application of Nuclear Magnetic Resonance to the study of nuclear waste relevant molybdates at ambient and high temperatures, Ph.D. thesis, University of Manitoba, 2013.

[3] K.R. Thurber, R. Tycko, Measurement of sample temperatures under magic-angle spinning from the chemical shift and spin-lattice relaxation rate of ^{79}Br in KBr powder, J. Magn. Reson. 196 (2009) 84–87.

[4] F. Bloch, W.W. Hansen, M. Packard, The Nuclear induction experiment, Phys. Rev. 70 (1946) 460–474.

[5] K.J.D. MacKenzie, M.E. Smith, *Multinuclear solid-state nuclear magnetic resonance of inorganic materials*, Elsevier, 2002.

[6] C.S. Yannoni, High-Resolution NMR in Solids: The CPMAS experiment, Acc. Chem. Res. 15 (1982) 201–208.

[7] M.J. Duer, *Solid state NMR spectroscopy*, Blackwell Sci. Ltd., London, (2002)

[8] E. Fukushima, S.B.W. Roeder, Spurious ringing in pulse NMR, J. Magn. Reson. 33 (1979) 199–203.

[9] E.L. Hahn, Spin echoes, Phys. Rev. 80 (1950) 580–594.

[10] D. Massiot, F. Fayon, M. Capron, I. King, S. Le Calvé, B. Alonso, J.O. Durand, B. Bujoli, Z. Gan, G. Hoatson, Modelling one- and two-dimensional solid-state NMR spectra, Magn. Reson. Chem. 40 (2002) 70–76.

[11] S. Kroeker, Nuclear Waste Glasses: Insights from Solid-State NMR, EMagRes. (2007).

[12] J.-P. Amoureux, Quasar, Lille, France, 2005.

[13] A. Altomare, C. Cuocci, C. Giacovazzo, A. Moliterni, R. Rizzi, QUALX: a computer program for qualitative analysis using powder diffraction data, J. Appl. Crystallogr. 41 (2008) 815–817.

[14] S. Gražulis, A. Daškevič, A. Merkys, D. Chateigner, L. Lutterotti, M. Quiros, N.R. Serebryanaya, P. Moeck, R.T. Downs, A. Le Bail, Crystallography Open Database (COD): an open-access collection of crystal structures and platform for world-wide collaboration, Nucleic Acids Res. 40 (2012) D420–D427.

[15] W.C. Nixon, The general principles of scanning electron microscopy, Trans. R. Soc. London. Ser. B. 261 (1971) 45–50.

[16] S. Amelinckx, D. Van Dyck, J. Van Landuyt, G. van Tendeloo, Electron microscopy: principles and fundamentals, John Wiley & Sons, 2008.

[17] X. Hou, R.S. Amais, B.T. Jones, G.L. Donati, Inductively coupled plasma optical emission spectrometry, Encycl. Anal. Chem. Appl. Theory Instrum. (2006) 1–25.

[18] Y. Morishige, A. Kimura, Ionization interference in inductively coupled plasma-optical emission spectroscopy, SEI Tech. Rev. (2008) 106–111.

[19] S.C. Wilschefski, M.R. Baxter, Inductively coupled plasma mass spectrometry: introduction to analytical aspects, Clin. Biochem. Rev. 40 (2019) 115–133.

[20] D.M. Strachan, Results from long-term use of the MCC-1 static leach test method, Nucl. Chem. Waste Manag. 4 (1983) 177–188.

5 Network Structure of Sodium Aluminoborophosphate Glasses from Solid-State NMR Spectroscopy and Pauling Bond Strengths

5.1 Introduction

Phosphate glasses have a variety of applications, such as solid-state electrolytes in batteries [1], lasers [2], ionic conductors [3], sealants [4,5], heterogeneous catalysts [6], and potential high-level nuclear waste (HLW) immobilization matrices [7,8]. Both Si and P are good glass formers, but phosphate glasses exhibit poor chemical durability [9] compared to silicates, which can be qualitatively explained using the Zachariasen rules of glass formation (**Chapter 2**) [10]. The physical and chemical properties of vitreous SiO_2 are superior to phosphate glass (P_2O_5), attributed to its cation-to-oxygen ratio of 1:2, which results in a fully-reticulated glass network. All of the oxygen anions are corner-shared by the Si tetrahedra, leading to rigid network connectivity. As a result, SiO_2 has a high melting temperature (T_m) and glass-transition temperature (T_g) [11]. The same ratio decreases to 1:2.5 in a pure phosphate glass [12], with each phosphate unit sharing three oxygens with neighbouring phosphate groups and one non-bridging oxygen (NBO), nominally represented by $(O{=}P{-}O_{3/2})_n$ [13]. This imparts some flexibility to the glass network, and consequently, the T_m and T_g are lower [14]. In an aluminophosphate, the cation-to-oxygen ratio changes to 1:2 (Al_2O_3:P_2O_5 = 4:8), yielding $AlPO_4$. $AlPO_4$ [15] is isostructural to SiO_2 with a three-dimensional network structure where the $[AlO_{4/2}]^-$ and $[PO_{4/2}]^+$ units alternate in the network. Likewise, the addition of B_2O_3, a glass former, also enhances the dimensionality of the phosphate network with the formation of BPO_4, a phase isostructural to $AlPO_4$ with alternating $[BO_{4/2}]^-$ and $[PO_{4/2}]^+$ units [16].

Al_2O_3- and B_2O_3-doped alkali and alkaline-earth phosphate glasses have garnered much attention due to their utility in diverse applications. The addition of Al_2O_3 to alkali phosphate glasses improves the corrosion resistance, increases T_g, and decreases thermal expansion [17]. A similar observation is made for B_2O_3 as well, where borophosphate glasses have improved network connectivity, higher T_g, stability against devitrification, thermal stability, and reduction in the hygroscopicity [18–20]. The network structures of aluminophosphate [21–24] and

borophosphate glasses [25–30] are well known as they have been extensively studied by solid-state nuclear magnetic resonance spectroscopy. Both Al and B bond to phosphate units through Al(B)−O−P bonds, forming an intricate network populated with different species of Al ($^{[4]}$Al, $^{[5]}$Al, and $^{[6]}$Al; $^{[n]}$Al, n = coordination number) or B ($^{[3]}$B and $^{[4]}$B; $^{[n]}$B, n = coordination number) and P (ortho-, P^0; pyro-, P^1; and metaphosphate, P^2; P^n, n = number of bridging oxygens (BO)). Since both Al^{3+} and B^{3+} cations improve several fundamental properties of phosphate glasses, it is strategic to design multi-network-former phosphate glasses involving B and Al. Although a few applications of aluminoborophosphate glasses are known [31–34], a complete picture of the network structure is still lacking due to the network complexity arising from the intra- and inter-connectivity of phosphate, aluminate, and borate units. A rigorous structural analysis of borophosphate, aluminophosphate, and the interconnectivity of borate and aluminate units in aluminoborate glasses [35–39] is required to model the connectivity in aluminoborophosphate glasses.

The lack of long-range periodic order in glasses contributes to significant deviations in bonding and, ultimately, structural parameters. Short-range order and non-periodicity in glasses lead to a Gaussian distribution in the bond lengths and bond angles, resulting in a topological disorder. As such, the network structure of glasses is better explained by the "continuous random network (CRN) model" developed by Zachariasen (**Section 2.2**) [10] and further substantiated by Warren [40]. The CRN model works best when the interatomic bonding in glasses is highly covalent and directional [41]. For glasses with non-directional bonding such as ionic, metallic, or van der Waals, the *random close packing model* [41–43] has been developed. While the CRN model best describes the topological disorder observed in glasses, several models have been formulated to explain the glass-forming abilities of oxides [41]. Factors such as cation field-strengths [44], coordination numbers [10], single bond strengths [45], mixed ionic and covalent character of bonds [46], electronegativity difference between cations and anions [47], orbital contributions [48], single-bond strength and temperature of the melt [49], and a thermodynamic approach [50] have been considered. Nevertheless, a sophisticated model explaining the complete network connectivity and topology of multi-component glasses with an emphasis on their total charge neutrality and preferred structural linkages is still a challenge to design.

The *Pauling bond strength* (PBS) [51–55] and *bond valence* (BV) [51,56–59] models are of great interest in crystallography and are commonly used to study the bonding arrangement in crystal systems. Pauling's study of a number of mineral structures led to the development of the ionic model and the principle of local charge neutrality [60], which involves the charge neutralization of each anion by the cations in its coordination sphere in an ionic structure. He introduced the concept of *bond strength*, a quotient of atomic valency and its coordination number, a simple yet effective concept to explain the network topology of crystals. He also stated that the valence of an anion matches the sum of bond strengths received from the coordinated cations. The strong correlation observed between the PBS and the bond length in crystals [61–63] led to the genesis of the *bond valence* [57,64], an empirical bond strength derived from experimental bond lengths. Since then, the empirical bond valence has been a standard parameter applied to explain bonding in crystal systems [59,65] and deduce the network structure in glasses [55,66,67]. Although the empirically derived bond valence is more accurate than the PBS, the latter can still provide useful insights into the bonding characteristics of a system, as it is a direct estimate of the electron density in the bond between the ion-pair [52]. Hence, a rigorous analysis of bonding characteristics in crystals and glasses can be performed provided the ion pairs have a small distribution in the bond lengths and no site distortions. In these cases, the theoretical bond strength and the empirical bond valences are similar, and hence, the PBS model can be conveniently applied to study the network structure of complicated systems such as aluminoborophosphate glasses. Moreover, PBS analysis can be adopted in conjunction with key experimental techniques to validate bond strength distribution statistics, which can point out key structural aspects of glassy systems. To date, there have been few studies on the derivation of network connectivity using Pauling bond strengths in conjunction with experimental results [55].

In this study, sodium-aluminophosphate, -borophosphate, and -aluminoborophosphate glasses are synthesized and their network structures are analyzed using Pauling bond strengths and multinuclear NMR spectroscopy. The $[(P_2O_5)_{0.4}(Na_2O)_{0.4}(B_2O_3)_{0.2-x}(Al_2O_3)_x$, x = 0, 0.05, 0.10, 0.15, and 0.20] glass series is synthesized by the melt-quench technique wherein the B_2O_3 and Al_2O_3 concentrations are proportionately varied to study their effect on the phosphate glass structure. A combination of ^{11}B, ^{31}P, ^{23}Na, and ^{27}Al MAS NMR spectroscopy is used to explore the inter-connectivity of these network formers and deduce the short- and medium-range order of

the network structure. The MAS NMR spectra are deconvolved, and different network-forming species are quantified. The phosphate units identified from the spectroscopic analysis are scrutinized using the Pauling bond strength approach to validate their presence in the glass network. Moreover, model glass networks for aluminophosphate, borophosphate, and aluminoborophosphate compositions are proposed in adherence to the Pauling bond strength concept and the obtained multinuclear NMR results.

5.2 Materials and Methods

5.2.1 Glass synthesis

Glasses of compositional series $[(P_2O_5)_{0.4}(Na_2O)_{0.4}(B_2O_3)_{0.2-x}(Al_2O_3)_x]$ were synthesized by the melt-quench technique, where *x* was varied from 0 to 20 mol% in increments of 5 mol%. B_2O_3 was synthesized by heating H_3BO_3 at 450, 650, and 800 °C for 30, 15, and 15 minutes, respectively. Analytical grade sodium hexametaphosphate $(NaPO_3)_6$, alumina (Al_2O_3), and laboratory-synthesized boron oxide (B_2O_3) were mixed in batches of 1 g as per the target compositions (**Table 5.1**) and melted at 1100 °C for one hour in platinum/gold crucibles. Melts were quenched by immersing the crucible bases in water, and the glasses were collected, ground, and stored in tight-capped glass vials in a desiccator. The samples are labelled as *BX* where *X* represents the mol% of B_2O_3 in the glass composition.

Table 5.1. Nominal compositions of glasses (in mol%).

	P_2O_5	Na_2O	Al_2O_3	B_2O_3
B0	40	40	20	0
B5	40	40	15	5
B10	40	40	10	10
B15	40	40	5	15
B20	40	40	0	20

5.2.2 Solid-state NMR spectroscopy

NMR analysis was carried out on Varian ^{UNITY}INOVA 600 MHz spectrometer equipped with a 3.2 mm double-resonance solid-state NMR probe from Chemagnetics. All samples were spun at the magic angle with a spinning speed of 14000(± 5) Hz. Bloch-decay experiments were carried out with pulse lengths and optimized relaxation delays of 0.35 μs and 4 s, respectively, for ^{11}B; 0.4 μs and 5 s for ^{23}Na; 0.3 μs and 2 s for ^{27}Al; 1.25 μs and 90 s for ^{31}P. For quadrupolar nuclei, the pulse lengths corresponded to a tip angle of 15° to equally excite sites with different quadrupolar coupling constants (C_Q). In ^{31}P MAS NMR, the pulse length used corresponded to a tip angle of 30°, due to the long T_1 values. The chemical shift references were 0.1 M H_3BO_3 [+19.6 ppm relative to $BF_3{\cdot}OEt_2$ (0 ppm)] 0.1 M NaCl (0 ppm), 1 M $Al(NO_3)_3$ (0 ppm) and 85% H_3PO_4 (0 ppm) for ^{11}B, ^{23}Na, ^{27}Al, and ^{31}P NMR, respectively.

Gaussian peaks with minor Lorentzian contributions as needed were used to fit ^{31}P and ^{27}Al MAS NMR spectra using the DMFit program [68]. In the ^{11}B MAS NMR spectra, the $^{[3]}$B peaks were fitted with Quasar [69], an external module in DMFit for modeling second-order quadrupolar lineshapes, while $^{[4]}$B signals were fit with mixed Gaussian/Lorentzian (G/L) lineshapes. The $^{[4]}$B peak intensities were corrected for the underlying satellite transitions by subtracting the intensity of the first sideband from the central peak.

5.3 Results

5.3.1 ^{11}B MAS NMR

Boron exists as tetrahedral ($^{[4]}$B) and trigonal-planar units ($^{[3]}$B) in glasses, which have characteristic C_Q of about 400 kHz and 2.6 MHz, respectively [70], due to their distinct local symmetries. As these units form B−O−P linkages in borophosphate glasses, the $^{[n]}B_{m\mathrm{P}}$ nomenclature is adopted to distinguish amongst different borate species, where *n* and *m* correspond to the coordination number of boron and the number of B−O−P bonds, respectively. The ^{11}B MAS NMR spectra (**Figure 5.1a**) consist of a broad peak at 16 ppm and partially resolved peaks positioned at *ca.* -0.5 and -2.6 ppm. The former is attributed to $^{[3]}$B and the latter peaks are assigned to $^{[4]}B_{2\mathrm{P}}$ [i.e., $B(OP)_2(OB)_2$] and $^{[4]}B_{3\mathrm{P}}$ [$B(OP)_3(OB)$] units, respectively [19,26,28,71]. Although the intensity of the $^{[4]}B_{3\mathrm{P}}$ peak increases relative to $^{[4]}B_{2\mathrm{P}}$ with an increasing B/Al ratio (**Table 5.2**), a plot of their absolute quantities (**Figure 5.1b**) indicates that

replacing Al by B increases the number of both $^{[4]}$B units, with $^{[4]}B_{2P}$ being the dominant species at all B/Al ratios.

Table 5.2. Parameters used in the deconvolution of ^{11}B MAS NMR spectra.

	$^{[4]}B_{3P}$		$^{[4]}B_{2P}$		$^{[3]}B^{a}$	
	δ_{iso} (ppm) ($\pm$0.1)	Int.(%)[b] ($\pm$1)	δ_{iso} (ppm) ($\pm$0.1)	Int.(%)[b] ($\pm$1)	δ_{iso} (ppm) ($\pm$0.1)	Int.(%)[b] ($\pm$1)
B5	-2.7	32	-0.5	59	16.8	9
B10	-2.9	36	-0.8	57	16.4	7
B15	-2.7	39	-0.7	56	16.7	5
B20	-2.8	39	-0.9	57	16.1	4

[a]C_Q = 2.6 MHz; η = 0.5
[b]Integrated intensity (%)

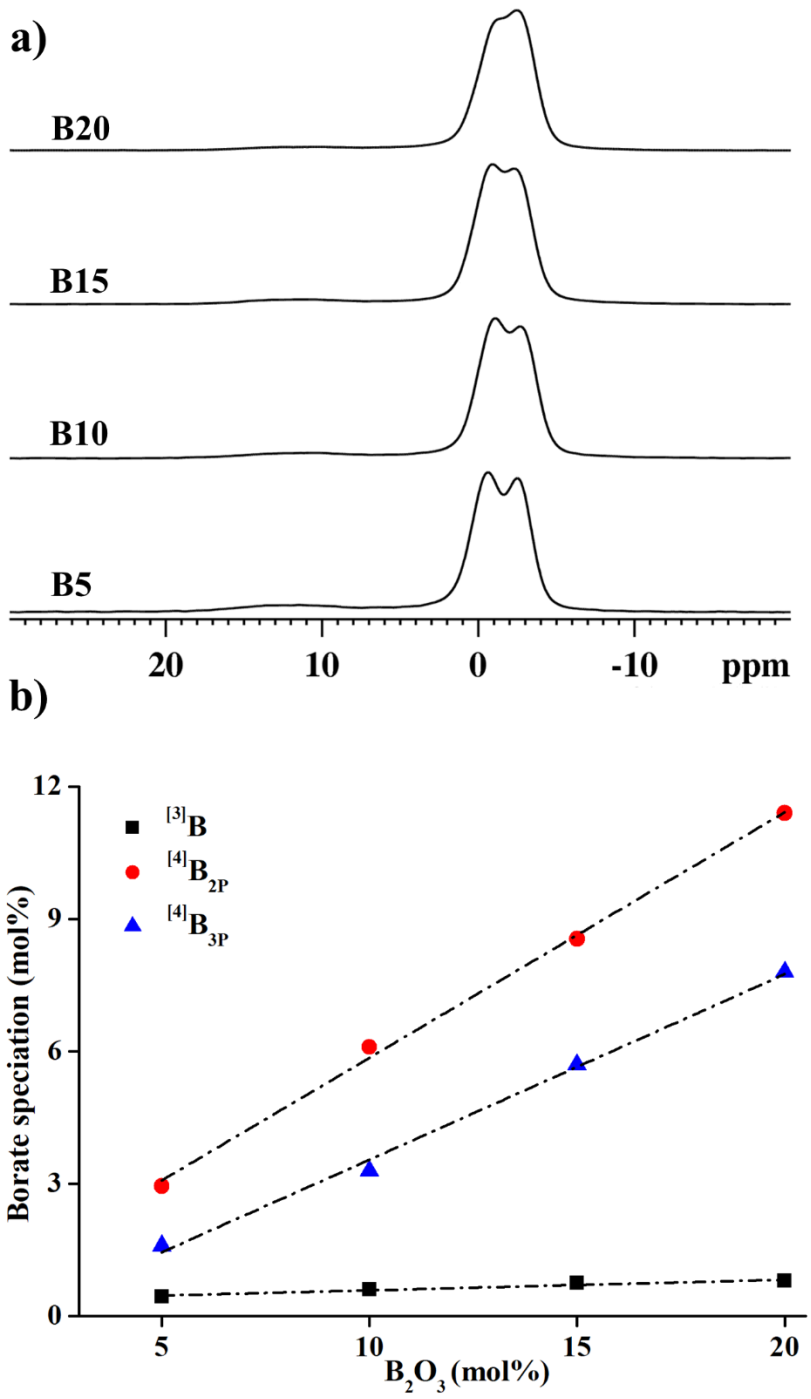

Figure 5.1. (a) ^{11}B MAS NMR spectra of glasses; **(b)** Absolute quantities of $^{[3]}$B and $^{[4]}$B units obtained from the deconvolution of ^{11}B MAS NMR spectra. The error bars are smaller than the size of the symbols.

5.3.2 ^{27}Al MAS NMR

The ^{27}Al MAS NMR spectra of glasses (**Figure 5.2a**) consist of three peaks with center-of-gravity shifts (δ_{CGS}) of 45, 12 and -14 ppm, assigned to different coordination environments of Al: four ($^{[4]}$Al), five ($^{[5]}$Al) and six ($^{[6]}$Al), respectively [21,72]. In the boron-free glass (B0), the integrated intensities of these species are 50, 18, and 32%, which are similar to aluminophosphate glasses with identical compositions [31,73]. The $^{[4]}$Al peak intensity increases at the expense of $^{[6]}$Al upon increasing the Al_2O_3 content (i.e., decreasing B/Al, **Table 5.3**) with minor changes in the $^{[5]}$Al peak intensity. When represented quantitatively in terms of the total Al species present in the glasses (**Figure 5.2b**), the fractions of $^{[4]}$Al and $^{[5]}$Al increase approximately linearly as the B/Al ratio decreases, whereas the $^{[6]}$Al fraction appears to plateau as Al is added.

Table 5.3. Parameters used in the deconvolution of ^{27}Al MAS NMR spectra.

	$^{[4]}$Al		**$^{[5]}$Al**		**$^{[6]}$Al**	
	δ_{CGS} [a] (±0.2)	Int.(%)[b] (±1)	δ_{CGS} [a] (±0.2)	Int.(%)[b] (±1)	δ_{CGS} [a] (±0.2)	Int.(%)[b] (±1)
B15	45.1	22	11.9	15	-14.6	63
B10	45.5	35	12.1	15	-14.4	50
B5	45.9	42	12.3	18	-14.2	40
B0	46.4	50	12.2	18	-14.3	32

[a]Center-of-gravity shift (ppm)
[b]Integrated intensity (%)

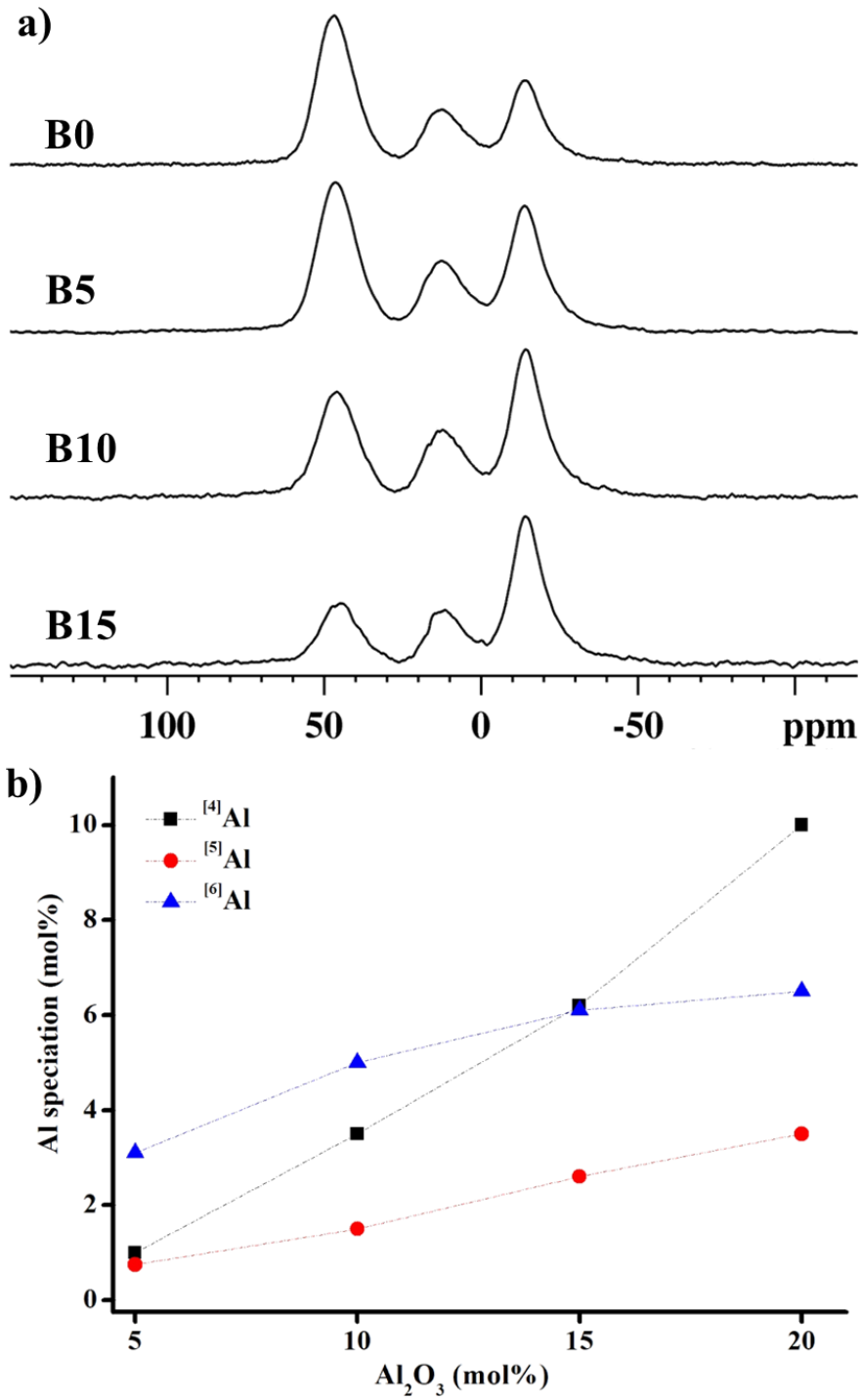

Figure 5.2. (a) ^{27}Al MAS NMR spectra of glasses normalized to the tallest peak. **(b)** Quantities of different Al species obtained from fitting the ^{27}Al MAS NMR spectra. The error bars are smaller than the size of the symbols.

5.3.3 ^{23}Na MAS NMR

The ^{23}Na MAS NMR spectra of glasses (**Figure 5.3)** consist of a single broad peak arising from the disordered environment of Na in the glass network [70,74]. These spectra lack any distinct features which might indicate the presence of separated Na-bearing crystalline phases in the synthesized samples. The peak maximum shifts towards lower frequency with the substitution of Al by B.

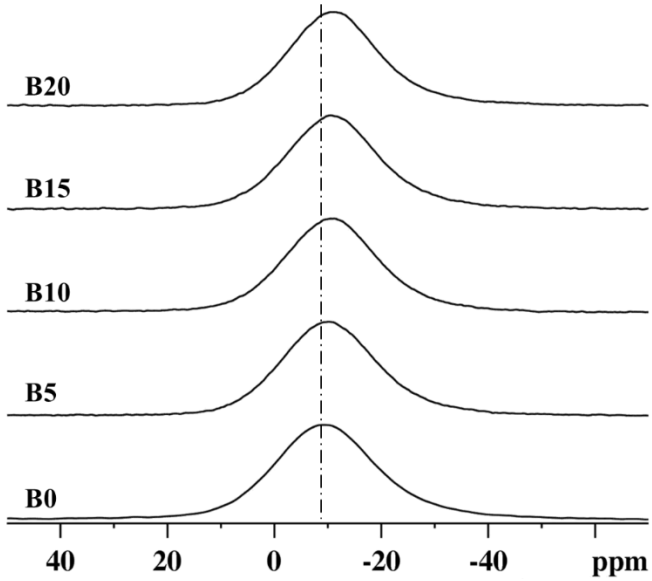

Figure 5.3. ^{23}Na MAS NMR spectra of glasses. The line is a guide for the eye.

5.3.4 ^{31}P MAS NMR

^{31}P MAS NMR resonances are broad and unresolved in these glasses due to the overlapping chemical shifts of different phosphate species. The ^{31}P NMR spectra of the glasses shown in **Figure 5.5** consist of broad asymmetric peaks, the deconvolution of which is impossible without a priori knowledge of the chemical shift ranges of phosphate units in aluminophosphate and borophosphate glasses. Since the composition of B0 glass is similar to known sodium aluminophosphate glasses [17,24,72], the phosphate speciation in these glasses serves as a guide for spectral deconvolution assignments of the P species. Using the P^n_m nomenclature - where *n* and *m* represent the number of BO and P−O−Al bonds per phosphate tetrahedron, respectively -

P^3_{2Al} and P^3_{3Al} units are identified in this composition (**Figure 5.4)**. Two linked P^3_{2Al} may be considered a phosphate dimer with four Al units in the next-nearest neighbouring (NNN) positions, whereas P^3_{3Al} is a branched phosphate bonded to three Al units.

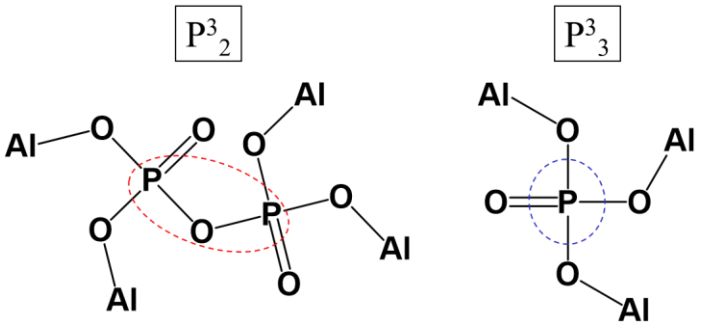

Figure 5.4. Structure of dimer (P^3_{2Al}) and branched phosphate (P^3_{3Al}) units present in the B0 glass.

To assign the ^{31}P spectrum of the B20 glass - i.e., Al-free borophosphate - an extensive survey of phosphate speciation in borophosphate glasses of similar compositions was conducted [19,25,27–30,71]. Analogous P^n_m nomenclature is used to label the phosphate units, where *n* and *m* represent the number of BO and P−O−B bonds per phosphate tetrahedron, respectively. A list of the different phosphate species observed in different borophosphate glasses is given in **Table 5.4**. The reported chemical shifts of identical phosphate units are combined into chemical shift ranges and plotted on the ^{31}P spectrum of B20 in **Figure 5.6**, which reveals the possible identities of phosphate species to be P^3_{nB} (n = 1, 2, 3) and P^2_{nB} (n = 0, 1, 2).

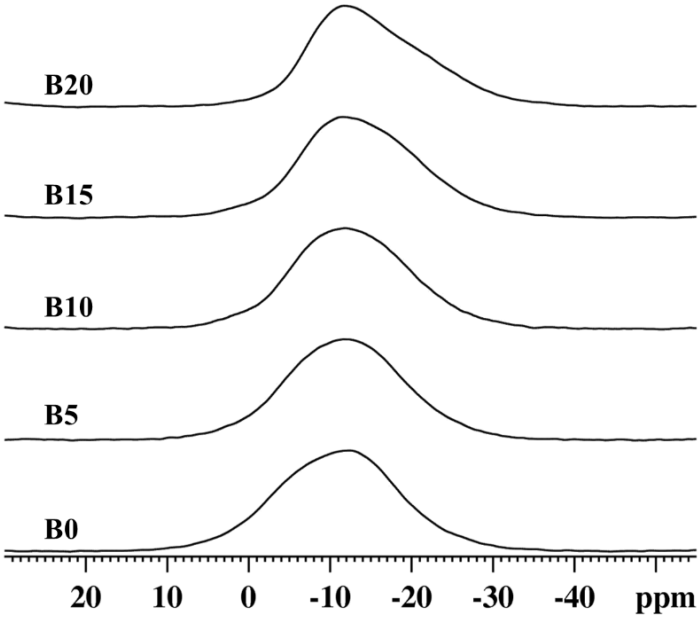

Figure 5.5. ^{31}P MAS NMR spectra of glasses.

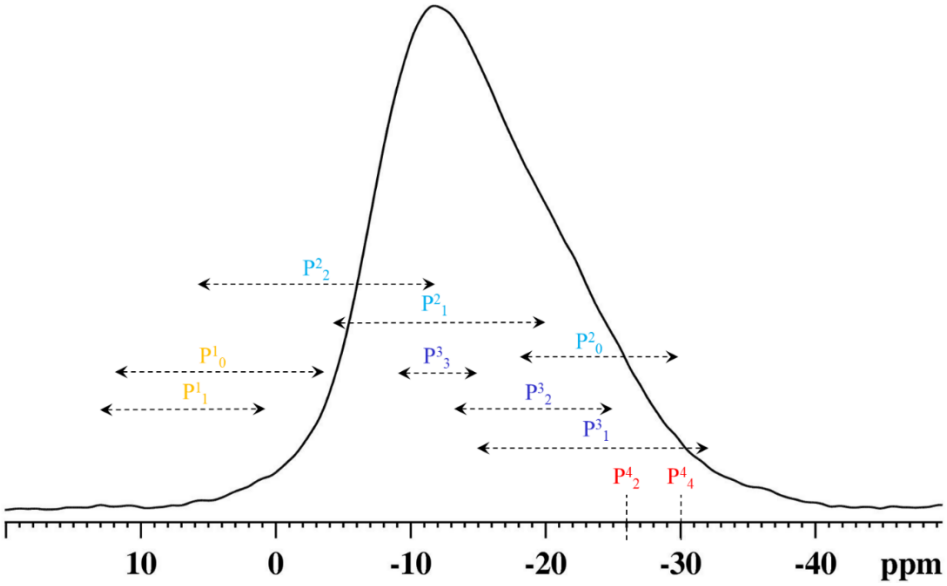

Figure 5.6. Chemical shift ranges of different phosphate units plotted on the ^{31}P MAS NMR spectrum of glass B20.

Table 5.4. Phosphate species reported in borophosphate glasses with compositions similar to the B20 glass.

Composition	x	Phosphate species (P^n_{mB})	δ(^{31}P)/ppm[a]	Int. (%)[b]	Ref
$50Ag_2O$-$50[(B_2O_3)_x(P_2O_5)_{1-x}]$	0.3	$P^3_1 + P^3_2$	-15.6	22.4	[71]
		$P^2_1 + P^2_2$	-4.8	60.1	
		P^1_0	+7.7	9.7	
		P^1_1	+12.4	7.8	
	0.4	P^3_2	-13.0	11.9	
		P^2_2	-2.2	59.1	
		$P^1_0 + P^2_2$	+6.1	13.0	
		P^1_1	+13.1	15.4	
$(P_2O_5)_{0.4}(B_2O_3)_x(Na_2O)_{0.6-x}$	0.2	P^2_1	-11.4	30.0	[19]
		$P^3_1 + P^3_2$	-18.4	70.0	
$(NaPO_3)_{1-x}(B_2O_3)_x$	0.2	P^2_1	-10.5	38.9	[25]
		$P^2_0 + P^3_2$	-18.0	55.5	
		P^4_4	-26.0	5.6	
$(Na_2O)_x(BPO_4)_{1-x}$	0.35	$P^2_1 + P^3_3$	-10.3	30	[27]
		P^3_2	-17.7	67	
		P^3_1	-26.6	3	
	0.4	$P^2_1 + P^3_3$	-9.0	77	
		P^3_2	-17.5	23	
	0.5	$P^1_0 + P^1_1$	+1.9	45	
		$P^2_1 + P^2_2$	-5.9	55	
$(Na_2O)_{0.4}[(B_2O_3)_x[P_2O_5)_{1-x})]_{0.6}$	0.3	$P^2_1 + P^2_2$	-10.4	43.7	[28]
		$P^2_1 + P^3_2$	-16.8	30.6	
		$P^3_1 + P^2_0$	-22.6	25.7	
	0.4	$P^2_1 + P^2_2$	-9.2	43.1	
		$P^3_2 + P^2_1$	-15.5	52.8	
		P^3_1	-22.2	4.1	

Table 5.4. Continued.

Composition	x	Phosphate species (P^n_{mB})	$\delta(^{31}P)$/ppm[a]	Int. (%)[b]	Ref
$(Na_2O)_{0.34}(B_2O_3)_{0.16}(P_2O_5)_{0.5}$		P^3_0	-42.6	2.0	[29]
		P^3_1	-32.1	29.0	
		P^2_0	-29.6	8.0	
		P^3_2	-24.2	31.0	
		P^2_1	-20.2	19.0	
		P^3_3	-15.7	7.0	
		P^2_2	-12.2	3.0	
$(Li_2O)_{0.45}[(B_2O_3)_x(P_2O_5)_{1-x}]_{0.55}$	0.36	P^1_0	-3.2	1.9	[30]
		P^4_2	-30.4	4.8	
		P^3_2	-21.6	17.1	
		P^1_1	+0.9	1.7	
		P^2_2	-11.7	71.5	

[a]Peak position
[b]Integrated intensity

With the substitution of Al by B, the ^{31}P NMR peak envelopes shift to lower frequencies and exhibit a change in their overall shape (**Figure 5.5**). The spectrum of B0 is fit using two peaks with chemical shifts of -4 and -13 ppm, representing P^3_{3Al} and P^3_{2Al} species, respectively, consistent with the analysis of Grigg *et al.* [31]. In B20, a peak appearing at the same position as P^3_{3Al} can be assigned to P^2_{1B}, P^2_{2B} or P^3_{3B}, or some combination of these (see **Figure 5.6**). Similarly, the peak appearing in the position of P^3_{2Al} may be attributed to some combination of P^2_{0B}, P^3_{1B} or P^3_{2B}. The relative fractions of these phosphate species and their likelihood of being present cannot be determined strictly from the ^{31}P NMR spectra due to their severely overlapping chemical shift ranges. Hence, a thorough Pauling bond strength analysis of borophosphate crystal structures was carried out to determine the likely identities of the phosphate species contributing to these signals (see **section 5.5.2**).

The assignment of phosphate species in glasses containing both B and Al (i.e., B5, B10 and B15) is not straightforward due to the severe spectral overlap and complex nature of bonding amongst borate, phosphate, and aluminate units. However, a qualitative understanding of phosphate speciation in these glasses has been obtained using the Pauling bond strength analysis of phosphate clusters (see **section 5.5.3**). Modeling the spectra, partially constrained by fixing the widths of the constituent peaks, reveals a gradual increase in the integrated intensity of the peak representing P^3_{3Al} in B0, and P^2_{1B} and/or P^2_{2B} in B20 glasses (**Table 5.5, Figure 5.7**). A shift toward lower frequency is observed for both peaks used in the fit as the B/Al ratio increases (see **section 5.3**).

Table 5.5. Parameters obtained from the deconvolution of ^{31}P MAS NMR spectra.

	Peak max.[c]	Int.(%)[d]	Peak max.[c]	Int.(%)[d]
	P^3_3[a]		P^3_2[b]	
B0	-4.5	24	-12.9	76
B5	-6.5	27	-13.9	73
B10	-8.2	37	-15.2	63
B15	-9.7	45	-17.1	55
	P^2_{1B} +/ P^2_{2B}		P^3_{2B}	
B20	-11.2	57	-20.1	43

[a]Full width at half-maximum (peak width) = 2.5 kHz
[b]Full width at half-maximum (peak width) = 3.4 kHz
[c]Peak maximum (ppm)
[d]Integrated intensity (%)

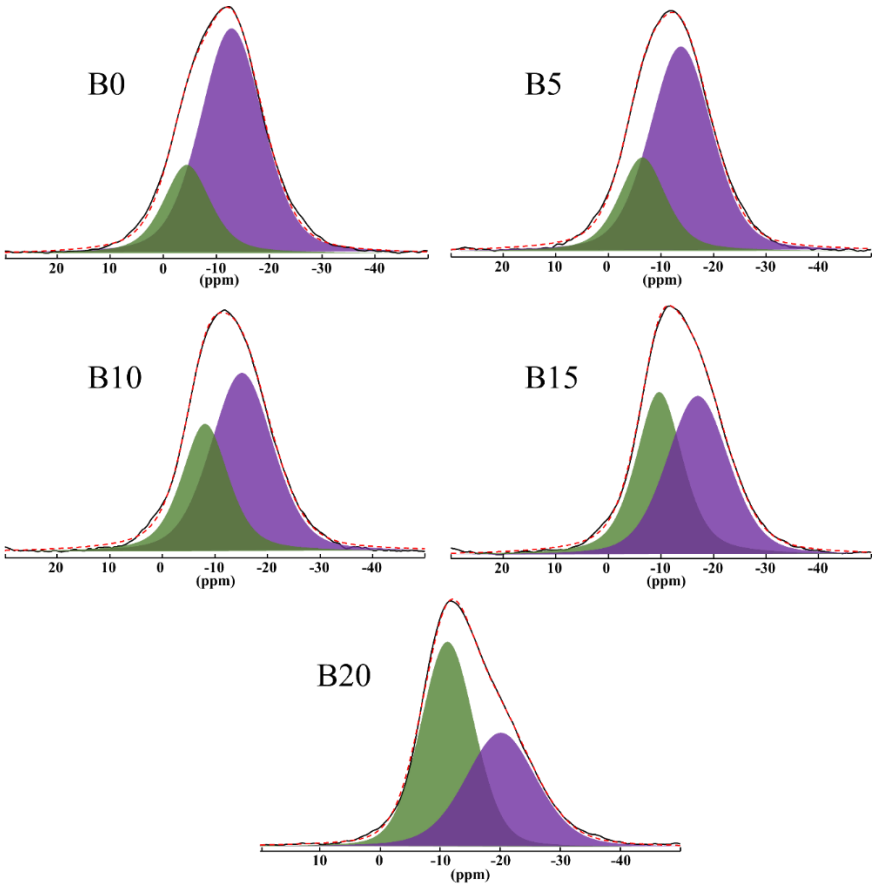

Figure 5.7. Deconvolution (red) of ^{31}P MAS NMR spectra (black). Green and purple peaks represent P^3_{3Al} and P^3_{2Al} species, respectively. In glass B20, the same green and purple peaks represent P^2_{1B}+/ P^2_{2B} and P^3_{2B} units, respectively (see text).

5.4 Pauling bond strengths and the bond-valence model

The stabilities of network structural clusters of aluminophosphate and borophosphate glasses were used to help identify the phosphate species present in B0 and B20 glasses. However, the lack of well-defined structural information for glass systems consisting of Al, B, and P makes it very difficult to precisely characterize the connectivity in B5, B10 and B15. Since the compositions of B0 and B20 glasses represent the extremes of the compositional series, the preferred connectivities between the aluminate and phosphate units in B0, and the borate and phosphate units in B20, are used as reference points to infer the network structures of glasses with intermediate compositions. As an additional constraint, the preferred linkages between aluminate and borate units in aluminoborate glasses are considered. A further complication

emerges with the interactions between borate and aluminate units in the presence of a predominant phosphate glass network. In the face of this challenge, we have used Pauling bond strengths [52] in conjunction with the multinuclear NMR results to guide our analysis.

Two concepts used to determine the atomic arrangements and structural topology in minerals are Pauling bond strength [51–55] and bond valence [51,55–59,65,75], both of which involve consideration of bond lengths, atomic valence, and coordination numbers. The former uses the ratio of the cation charge to its coordination number, whereas the bond-valence model is driven by the interdependence between bond length and bond valence (a.k.a., bond strength, bond flux, or valence strength) [56].

5.4.1 Pauling bond strength

One measure of the valency contribution of a cation to a neighbouring anion is called the Pauling bond strength (*s*), calculated from the charge of the cation (V_C) and its coordination number (N_C) [51]:

$$s = \frac{V_c}{N_c} \qquad (5.1)$$

Pauling's second rule, the *principle of local charge neutrality* or *electrostatic valence rule,* states that the valency of the anion is equal to the sum of Pauling bond strengths of coordinated cations:

$$V_A = \sum_i s_i \qquad (5.2)$$

where V_A is the valency of the anion, and *s* is the Pauling bond strength of the i^{th} cation bonded to the anion. The Pauling bond strengths derived for each cation in a glass network can be used to map out short- and medium-range bonding and provide guidelines to understand glass structure.

5.4.2 Bond-valence model

The bond-valence model relies on the correlation between bond length and bond valence. It has become valuable for predicting and interpreting bond lengths [58], calculating *a priori* bond valences and bond lengths in crystals [59], and studying network structure in glasses [55]. It can also be used as a validation tool in the determination of atomic arrangements in minerals and their structural topology. This model is governed by two fundamental rules called *network*

equations [51]. The *valency sum rule* states that the sum of bond valences around any ion, *i*, is equal to its valence, V_i [51]:

$$V_i = \sum_j S_{ij} \qquad (5.3)$$

where S_{ij} is the experimental bond valence between atoms i and j. The *equal valence* or *loop rule* holds that the sum of the directed bond valences around any circuit (closed path) of bonds in a structure is zero [59]:

$$0 = \sum_{loop} S_{ij} \qquad (5.4)$$

This rule dictates that the valency of each atom is distributed equally amongst its bonds and is subject to the constraints of **equation 5.3**. Both equations effectively calculate theoretical bond valences, *s*, if the valency of the cation and its coordination environment are known. It should be noted that the Pauling bond strength and the theoretical bond valence are equivalent in systems with well defined bond lengths and lacking lone-pair electrons and site distortions. The empirical relationship between bond length and bond valence is [55]:

$$S_{ij} = \exp\left[\frac{R_{ij} - d_{ij}}{B}\right] \qquad (5.5)$$

where R_{ij} is the bond-valence parameter for the atom pair *i* and *j*, d_{ij} is the associated bond length, and *B* is a parameterized constant, usually taken to be 0.37 Å. Since R_{ij} has been obtained from the statistical analysis of a huge number of crystal structures involving *i* and *j* atom pairs [58], this model must be considered empirical. The bond-valence parameter for each atom pair in a crystal structure is calculated according to [58]:

$$R_{ij} = B \ln\left[\frac{V_i}{\sum_j \exp(\frac{-d_{ij}}{B})}\right] \qquad (5.6)$$

The use of these approaches to predict and rationalize the polyhedral connectivity in glasses depends on the nature of the elemental constituents. For example, Pauling bond strengths do not account for bond-length distributions and would be inappropriate to study Pb-containing glasses due to uncertainty about the lead valency and associated Pb−O distances [51,56]. For more predictable cations such as B^{3+}, $Al^{3+,}$ and Na^{+}, the bond valences (*S*) and Pauling bond strengths (*s*) (**Table 5.6**) are very similar, deviating by less than 10%, making Pauling bond strengths suitable for deducing glass network connectivity. However, in phosphates, challenges

emerge for P^{5+}, where multiple maxima in the bond-length distribution of $^{[4]}P^{5+}-O^{2-}$ are observed due to different bond-valence constraints arising from different numbers of BO per P tetrahedron [76]. For example, P^{5+} cations in phosphate tetrahedra bearing zero, one, two, and three BO contribute bond valences of 1.25, 1.33, 1.5, and 2 to one or more P−O bonds, respectively [76]. In a phosphate unit, the P−O bond valence is contingent upon the number of BO, as well as the type of cation to which they are bonded. Hence, the valence of P cannot be simply constrained to 1.25, as in structures based on Pauling bond strengths. The PBS model has been successfully utilized in understanding the network connectivity of a wide variety of glassy systems, including lead gallate [55], zinc phosphate [77], aluminoborate [36], and aluminophosphate glasses [17,72]. However, its application to a more complex multi-component glass system like aluminoborophosphates in conjunction with NMR data is lacking.

Table 5.6. Pauling bond strengths, *s*, and bond valences, *S*, in valence units (v.u.), of cations present in an aluminoborophosphate glass network.

Cation	Charge	CN	*s* (v.u.)[a]	R_{ij} (Å)[b]	*B* (Å)[b]	*S* (v.u.)[c]
P^{5+}	5	4	1.25	1.624	0.399	1.25, 1.33, 1.5 and 2 (**see text**)[c] [76]
$^{[3]}B^{3+}$	3	3	1	1.372	0.357	1.0[d]
$^{[4]}B^{3+}$	3	4	0.75	1.372	0.357	0.745[e]
$^{[4]}Al^{3+}$	3	4	0.75	1.634	0.390	0.745(0.02)[c] [59]
$^{[6]}Al^{3+}$	3	6	0.5	1.634	0.390	0.47[c] [59]
Na^{+}	1	6	0.16	1.695	0.420	0.1(0.08)[c] [59]

[a]Theoretical Pauling bond strengths
[b]Obtained from reference [65]
[c]Experimental bond valences
[d]Calculated using equation 5; B−O bond length of 1.372 Å for $^{[3]}$B [78]
[e]Calculated using equation 5; B−O bond length of 1.475 Å for $^{[4]}$B [78]

5.5 Glass network connectivity

The network structures of B0 and B20 glasses have been analyzed with reference to the reported structures of aluminophosphate and borophosphate glasses. However, for phosphate glasses with both Al and B in the network (B5−B15), deducing the network connectivity is complicated by the compatibility of three network formers, which produces an enormous range of plausible connectivity patterns in homogeneous glasses. Our strategy is to establish a basis set of the preferred homopolar and heteropolar linkages by considering the bonding in binary aluminophosphate, borophosphate, and aluminoborate glasses, which are then tested against the NMR data and evaluated using Pauling bond strengths (PBS). The PBS-validated network structures of aluminophosphate (B0), borophosphate (B20), and aluminoborophosphate (B5−B15) glasses are discussed below. The following rules and constraints have been applied in the PBS analysis of different configurations of Al, B, and P clusters:

a. The PBS analysis of aluminophosphate clusters in B0 glass is strictly limited to crystalline phases observed along the $xAl_2O_3(1\text{-}x)NaPO_3$ join in the $Al_2O_3-NaPO_3$ system, and the spectral assignments reported in sodium aluminophosphate glasses of similar compositions [72,73].
b. The PBS structures must satisfy the oxygen valency (-2 v.u.), whereas the P−O bonds are allowed to have multiple bond strengths. For example, in a $^{[4]}$Al−O−P bond, $^{[4]}$Al donates 0.75 v.u. and P^{5+} donates 1.25 v.u.. However, in a $^{[6]}$Al−O−P bond, $^{[6]}$Al donates only 0.5 v.u., changing the bond strength contribution of P to 1.5 v.u., in accordance with **Equation 5.2**.
c. Since the Na^+ ions have high, variable and indeterminate coordination numbers in glasses and contribute about 0.20−0.12 v.u. (coordination number: 5−8) when bonded to oxygen anions, it is impractical to define PBS structures accounting for the full valence contributions of Na^+. Hence, these ions are confined to strictly balancing the deficit charges that may arise after accounting for valence contributions from B^{3+}, $P^{5+,}$ and Al^{3+}.
d. The impact of thermal motion on bond strength and the P−O−X bond angle, for example [57], has been ignored.

5.5.1 $(Na_2O)_{0.4}(Al_2O_3)_{0.2}(P_2O_5)_{0.4}$ glass (B0)

The Al speciation in aluminophosphate glasses is strongly dependent on their alumina content. At an Al_2O_3 mole fraction of 0.125, the glass network is dominated by high-coordinate Al (i.e., $^{[5]}$Al and $^{[6]}$Al), with tetrahedral Al becoming increasingly dominant as the Al fraction increases [72]. Moreover, the O/P ratio also directly influences the Al speciation, wherein $^{[6]}$Al is observed up to an O/P ratio of 3.5, the pyrophosphate composition. As the O/P ratio increases toward 4 (the orthophosphate composition), $^{[4]}$Al predominates [17,24,72,73]. Since the O/P ratio is 3.75 in this glass series, the glasses are expected to contain both $^{[4]}$Al and $^{[6]}$Al units, which is consistent with the ^{27}Al NMR results. The phosphate component of the glass network of B0 consists mainly of P^3_{3Al} and P^3_{2Al} phosphate units in a ratio of 1:3 [31], and the fractions of $^{[n]}$Al units match those of similar compositions [31,73]. The Al:P molar ratios associated with P^3_{2Al} and P^3_{3Al} units represent the compositions of $Na_6Al_2(P_2O_7)_3$ and $Na_3Al_2(PO_4)_3$, respectively, the crystalline phases observed along the $xAl_2O_3(1\text{-}x)NaPO_3$ join in the $Al_2O_3{-}NaPO_3$ system [72,73]. Up to an alumina content of 14.3 mol%, P^3_{2Al} units populate the network, beyond which P^3_{3Al} units become dominant. The phosphate dimer in $Na_6Al_2(P_2O_7)_3$ ($2P^3_{2Al}$) possesses one P−O−P bond and four P−O−$^{[6]}$Al bonds [73], and the branched phosphate unit in $Na_3Al_2(PO_4)_3$ (P^3_{3Al}) has two P−O−$^{[4]}$Al and one P−O−$^{[6]}$Al [72,73] (**Figure 5.8**). The bond between $^{[6]}$Al and the oxygen anion in the P−O−$^{[6]}$Al linkage is treated as ionic with respect to $^{[4]}$Al, as the valence contribution of the former is lower than the latter (0.5 vs. 0.75). Hence, the P^3_{2Al} units bonded to four $^{[6]}$Al units are treated as dimers rather than a fully reticulated phosphate unit. On the contrary, P^3_{3Al} may be considered a branched phosphate due to the higher valence contribution of $^{[4]}$Al, which contributes more covalent character to the $^{[4]}$Al−O−P bonds.

The P−O bond lengths in aluminophosphate crystals have been studied to test their dependency on the valence contribution of the P^{5+} cation in a P−O−Al bond [73]. The P−O bond lengths in a P−O−P, P−O−$^{[4]}$Al and P−O−$^{[6]}$Al are 1.577, 1.522, and 1.483 Å, with corresponding bond strength contributions from P^{5+} of 1.0, 1.25, and 1.5 v.u., respectively. Similarly, the $^{[4]}$Al−O and $^{[6]}$Al−O bond lengths are measured to be 1.694 and 1.857 Å in $AlPO_4$ [79] and Al_2O_3 [80], respectively, which correlate well with the bond strength contributions of Al^{3+}: 0.75 and 0.5 v.u., respectively. The P^3_{2Al} and P^3_{3Al} structures postulated from calculated Pauling bond strengths are given in **Figure 5.8**. The valency of oxygen is completely fulfilled in these two structures, confirming the credibility of the phosphate species assignment. The validity

of these structures is tested by replacing one of the P−O−[6]Al linkages with a P−O−[4]Al in P^3_{2Al} and checking for charge neutrality of the structure. This bonding generates an over-bonded BO (+2.25 v.u.) (**Figure 5.9**) and hence, the bonding in P^3_{2Al} is expected to be limited to P−O−[6]Al linkages. It should be noted that although the valency contribution to the BO in this scenario can be restricted to +2 by moving the excess charge to $P-O^-$ bond (1.25 v.u.), that would result in fractional charges on the NBO which cannot be compensated stoichiometrically by the Na^+ ions in the cluster (+2 vs. -1.75), leading to an excessive charge in the network.

Even though the Na^+ ions have high coordination numbers and are electrostatically bonded to multiple NBO sites in glasses, their actual coordination environments are not accounted for in these structural models, instead being shown to coordinate to a single NBO. As the P^3_{3Al} and P^3_{2Al} clusters are derived from crystalline compositions, the stoichiometry can be readily defined by building simplified connectivity schemes of these kinds. Large clusters simulating the actual coordination environments of Na^+ and the preferential connectivity between the phosphate and aluminate units are tedious to build, and require computational support. Even if such clusters can be constructed, the structural conclusions are little affected, as the ratio of Na^+ and the NBO mole fraction remain the same. Hence, we have refrained from building PBS structures of aluminophosphates with fractional charges on the NBO.

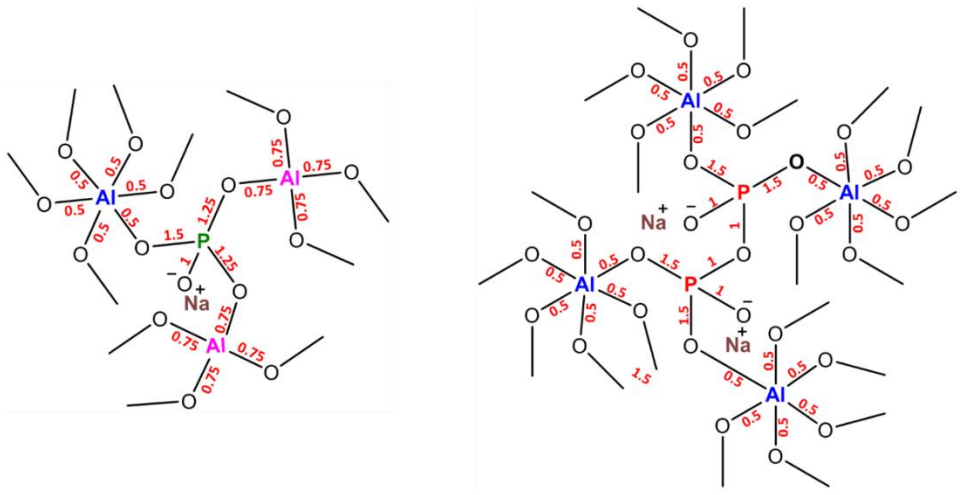

Figure 5.8. Bond-valence structures of branched (P^3_{3Al}) (left) and dimer phosphates ($2P^3_{2Al}$) (right) with next-nearest Al neighbours in different coordination environments.

Although $^{[5]}$Al has been consistently observed in many aluminophosphate systems, its structural role remains unclear. An attempt is made to understand its structural role and determine its bonding preferences using the Pauling bond strength concept. Structures with different combinations of phosphate and aluminate units are constructed and scrutinized for their ability to fulfill the oxygen valences (**Figure 5.10**). Substituting $^{[6]}$Al units by $^{[5]}$Al in P^3_{3Al} and P^3_{2Al} units increases the bond strength contribution to the BO in the $^{[5]}$Al−O−P bond to 2.1 (**Figure 5.10, a** and **b**), which is just a 5% deviation from the optimum value of 2.0. Hence, both P^3_{2Al} and P^3_{3Al} units can be expected to accommodate $^{[5]}$Al units, similar to $^{[6]}$Al. Furthermore, substituting one of the $^{[4]}$Al units in P^3_{3Al} by $^{[5]}$Al also seems plausible as the valence deficit is only 0.15 v.u. (**Figure 5.10c**), with a deviation of 7.5%. In scenarios where the branched phosphate is linked to all high-coordinate Al units, which is a sort of orthophosphate (**Figure 5.10d**), and a phosphate dimer bonded to both $^{[4]}$Al and $^{[5]}$Al (**Figure 5.10e**), the BO are severely under- and over-bonded, respectively, making the presence of such clusters highly unlikely.

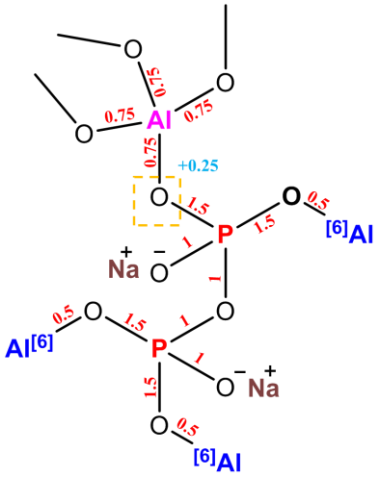

Figure 5.9. Bond valence structure of the P^3_{2Al} unit wherein one $^{[6]}$Al unit has been replaced with $^{[4]}$Al. The over-bonded BO (+2.25 v.u.) is marked in an orange square.

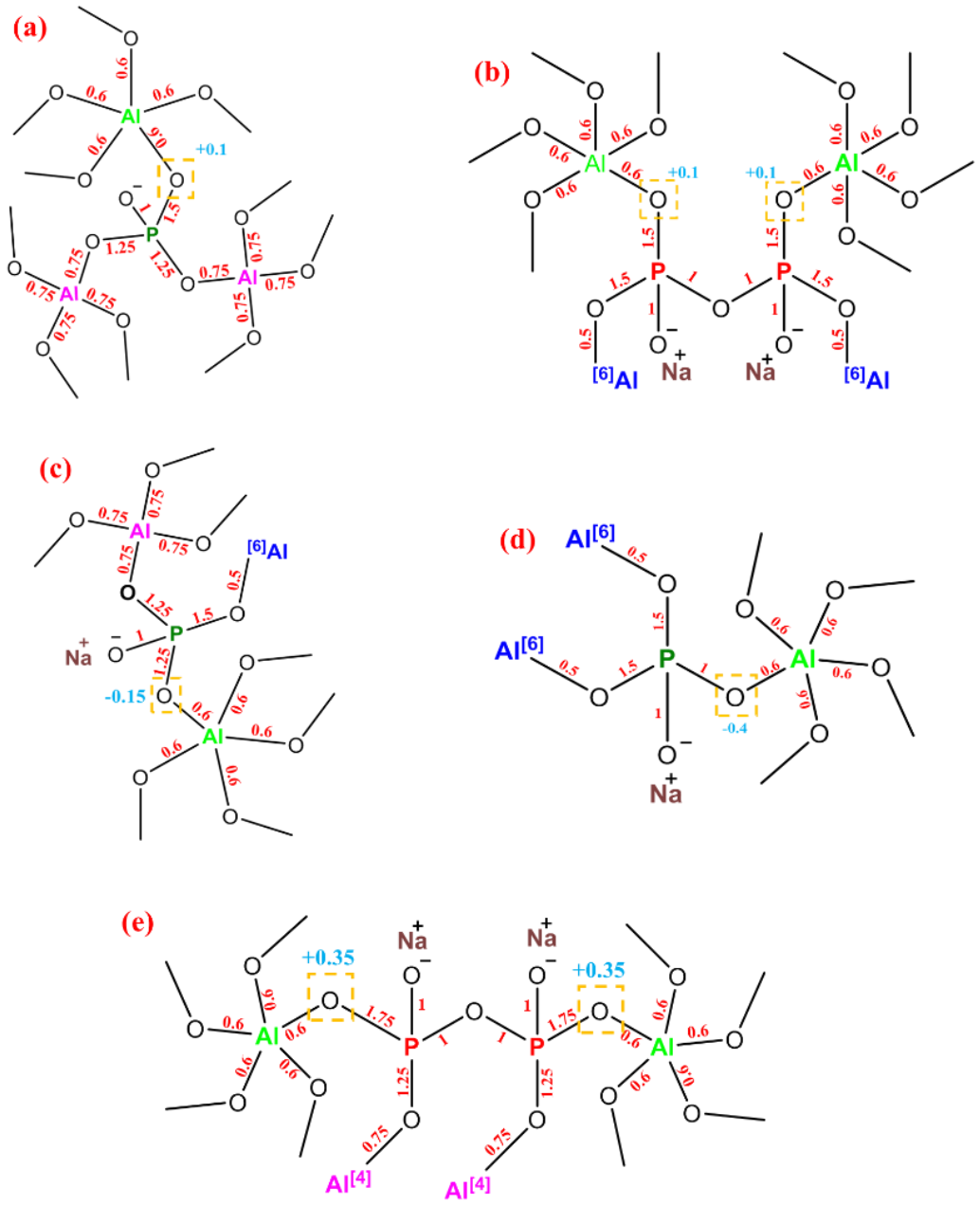

Figure 5.10. [5]Al bonded to branched (**a, c** and **d**) and dimeric phosphate units (**b** and **e**). The underbonded and overbonded BO are marked with orange squares along with their charge deficit or excess in light blue.

5.5.2 $(Na_2O)_{0.4}(B_2O_3)_{0.2}(P_2O_5)_{0.4}$ (B20) glass

Borophosphate glasses are one of the most extensively studied glass systems. The network structure of these glasses is very complex as the heteroatomic B−O−P linkages are preferred over B−O−B or P−O−P bonds [28], leading to the extensive interlinking of borate and phosphate structural units. Whereas the ability of Al to adopt multiple coordination environments contributes to some structural ordering in aluminophosphate glasses, borate units in a tetrahedral environment ($^{[4]}$B) promote the formation of multiple phosphate species with distinct configurations, leading to a proliferation of local structural arrangements and the randomization of the glass network (**Table 5.4**) [19,25,27–30,71,81]. Plotting the chemical shift ranges of the reported phosphate species on the ^{31}P NMR spectrum of B20 reveals the possible presence of six distinct phosphate units: P^3_{nB} (n=1−3) and P^2_{nB} (n≤2) (**Figure 5.11**). These units exhibit severely overlapping isotropic chemical shift ranges (**Table 5.4, Figure 5.6**), which make the spectral analysis ambiguous and preclude definite structural conclusions. Since the bond strength contributions of P^{5+} in these borophosphate configurations all fall within the acceptable range for plausibility, no clear distinction amongst the borophosphate clusters that might be present in the glass network is possible.

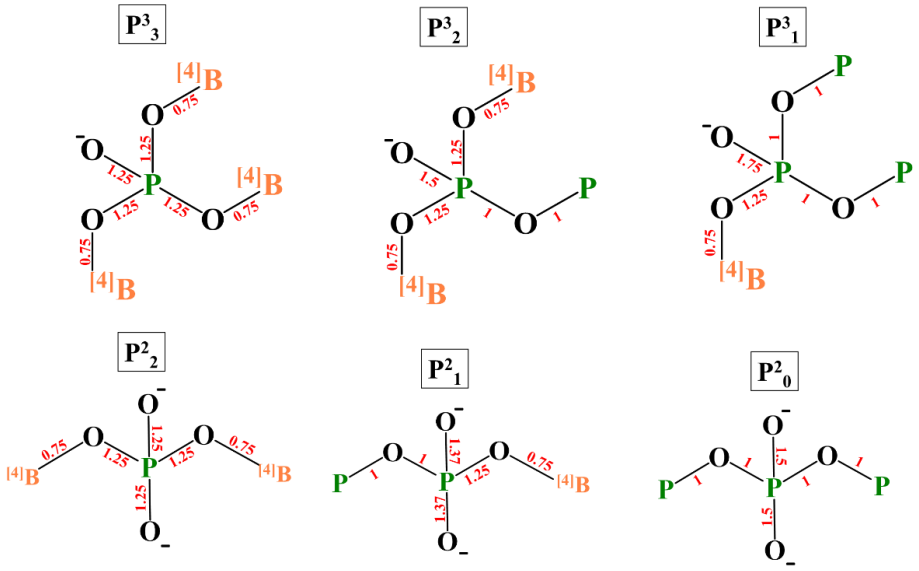

Figure 5.11. Pauling bond strength distribution maps and structures of phosphate units P^3_{nB} (n=1−3) and P^2_{nB} (n≤2).

Since the structural analysis of B0 glass was driven by the stoichiometry of Al to P in aluminophosphate crystals along the $NaPO_3-Al_2O_3$ join, a similar attempt was made to determine the dominant phosphate species present in the B20 glass by studying the network topology of borophosphate crystal systems. The Crystallographic Information Framework (CIF) files of borophosphate crystals with different B to P ratios were obtained from the Inorganic Crystal Structure Database (ICSD) (**Table 5.7**), and the phosphate and borate speciation was studied. The homo- and hetero-atomic connectivity between these two units are mapped using atomic-symbol-and-stick depictions, and the Pauling bond strength contributions of B^{3+} and P^{5+} to the BO and NBO are assigned based on conditions required to obtain charge-neutral BO. The summation of charge deficits on the NBO bonded to P^{5+} are matched to the total charge contributed by the modifier cations present in the system. To our knowledge, this is the first account of the application of Pauling bond strength criteria to explain the connectivity in crystalline borophosphates.

Table 5.7. Borophosphate crystalline phases with different B:P ratios, and the observed speciation of borate and phosphate units in the crystal structures.

Coll. Code[a]	BP crystalline phase	B:P	Borate speciation	$^{[4]}$B–O–P	$^{[4]}$B–O–$^{[4]}$B	$^{[4]}$B–O–$^{[3]}$B	Phosphate speciation
253941 [82]	$Li_3Cs_2BP_4O_{14}$	1:4	$^{[4]}B_{4P}$	4	—	—	P^2_{1B}
424282 [83]	$Li_3K_2BP_4O_{14}$	1:4	$^{[4]}B_{4P}$	4	—	—	P^2_{1B}
239629 [84]	$Li_3Cs_2Pb_2B_3P_6O_{24}$	1:2	$^{[4]}B_{4P}$	4	—	—	P^2_{2B}
248343 [85]	$Li_3BP_2O_8$	1:2	$^{[4]}B_{4P}$	4	—	—	P^2_{2B}
249929 [86]	$KSrBP_2O_8$	1:2	$^{[4]}B_{4P}$	4	—	—	P^2_{2B}
253356 [87]	$Li_3Cs_2Ba_2B_3P_6O_{24}$	1:2	$^{[4]}B_{4P}$	4	—	—	P^2_{2B}
291512 [88]	$Li_2NaBP_2O_8$	1:2	$^{[4]}B_{4P}$	4	—	—	P^2_{2B}
416727 [89]	$Na_3BP_2O_8$	1:2	$^{[4]}B_{4P}$	4	—	—	P^2_{2B}
410869 [90]	$KZnBP_2O_8$	1:2	$^{[4]}B_{4P}$	4	—	—	P^2_{2B}
410871 [90]	$CsZnBP_2O_8$	1:2	$^{[4]}B_{4P}$	4	—	—	P^2_{2B}
424283 [83]	$LiK_2BP_2O_8$	1:2	$^{[4]}B_{4P}$	4	—	—	P^2_{2B}
12621 [91]	$KNa_4B_2P_3O_{13}$	2:3	$^{[4]}B_{3P+1B}$	3	1	—	P^2_{2B}
401178 [92]	$Na_5B_2P_3O_{13}$	2:3	$^{[4]}B_{3P+1B}$	3	1	—	P^2_{2B}
244133 [93]	$Na_4CsB_2P_3O_{13}$	2:3	$^{[4]}B_{3P+1B}$	3	1	—	P^2_{2B}
55082 [94]	BPO_4	1:1	$^{[4]}B_{4P}$	4	—	—	P^4_{4B}
50875 [95]	$BaBPO_5$	1:1	$^{[4]}B_{2P+2B}$	2	2	—	P^2_{2B}
93598 [96]	$PbBPO_5$	1:1	$^{[4]}B_{2P+2B}$	2	2	—	P^2_{2B}
97675 [97]	$SrBPO_5$	1:1	$^{[4]}B_{2P+2B}$	2	2	—	P^2_{2B}
192496 [98]	$Li_2B_3PO_8$	3:1	$^{[4]}B_{2P+2B}$	2	—	2	P^2_{2B}
416726 [89]	$Na_3B_6PO_{13}$	6:1	$^{[4]}B_{1P+3B}$	1	1	2	P^2_{2B}

[a] Inorganic Crystal Structure Database collection code

In $Li_3Cs_2BP_4O_{14}$ (**Figure 5.12**, Coll. Code: 253941) and $Li_3K_2BP_4O_{14}$ (Coll. Code: 424282) crystal systems, B:P is 1:4, and the phosphate and borate structural units present are $P^2{}_{1B}$ and $^{[4]}B_{4P}$. The $P^2{}_{1B}$ is a heteroatom-bearing chain phosphate wherein each phosphate unit is bonded to a neighbouring phosphate (P−O−P), a tetrahedral borate unit (P−O− $^{[4]}$B), and two NBO (P−O^-). The $^{[4]}$B unit is bonded to four such phosphates ($^{[4]}B_{4P}$). The B^{3+} contributes 0.75 v.u. to each B−O bond, and the rest is compensated by the P^{5+} cation, which exhibits three distinct bond strength contributions. The bond strength contributions of P^{5+} for (P−O^-), P−O−B, and P−O−P linkages are 1.37, 1.25, and 1.0 v.u., respectively. The B−O bond length in the P−O−B linkage is 1.46 Å, and the length of the P−O bonds in (P−O^-), P−O−B, P−O−P linkages from the $Li_3Cs_2BP_4O_{14}$ crystalline phase are *ca.* 1.48, 1.55, 1.59 Å, respectively. The P−O bond lengths and the bond strength contributions from P^{5+} exhibit a linear relationship, emphasizing the compliance of the network structure with the Pauling bond strength contributions from B^{3+} and P^{5+}. The bond strengths (*S*) calculated for these experimental P−O bond lengths using **equation 5.5** are 1.43 v.u. for (P−O^-); 1.20 v.u. for P−O−B; and 1.08 for P−O−P. These values are within ±0.08 v.u. (error of 10%) from the proposed Pauling bond strength model of the crystal structure. Similarly, the calculated bond strength (*S*) of the B−O bond in P−O−B is 0.78 v.u., which agrees with the theoretical bond strength (*s*) proposed in the structure for $^{[4]}$B.

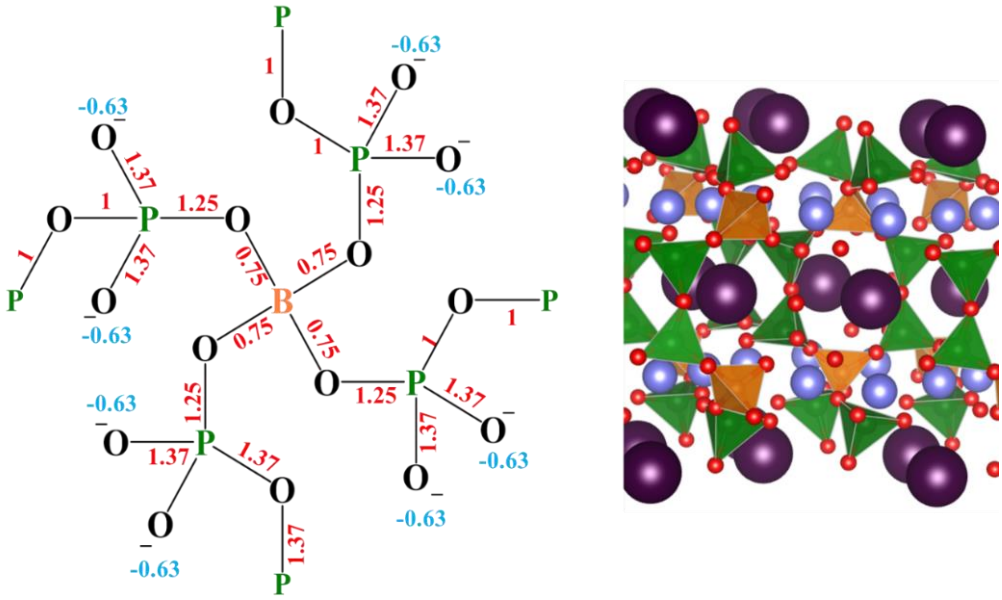

Figure 5.12. Pauling bond strength map (left) and the crystal structure of $Li_3Cs_2BP_4O_{14}$ with a B:P ratio of 1:4 (right). In the crystal structure, green and orange tetrahedra represent phosphate and borate units, respectively; purple and blue balls represent cesium and lithium ions, respectively.

Borophosphate crystalline phases with B:P = 1:2 consist of $P^2{}_{2B}$ phosphate units, which are chain phosphates bonded to two borate units. The network connectivity in $CsZnBP_2O_8$ (**Figure 5.13**) is analyzed to understand further the suitability of the Pauling bond strength model in studying structures with different network topologies. In $CsZnBP_2O_8$, the bond strength contribution of B^{3+} in the P−O−B linkage is 0.75 v.u. ($\bar{r}$(B−O) = 1.47 Å), and that of P^{5+} in (P−O^-) and P−O−B linkages is 1.25 v.u., with corresponding $\bar{r}$(P−O) bond lengths of 1.51 and 1.54 Å, respectively. A similar observation is made in other crystal structures with comparable B:P ratios, where a small distribution in the bond lengths is observed. The calculated v.u. contribution for these P−O bond lengths is 1.32 (P−O^-) and 1.23 (P−O−B) v.u., respectively, which are again within the allowed deviation of about 10%. The calculated v.u. contribution of B^{3+} to the B−O−P bonds is 0.76 v.u..

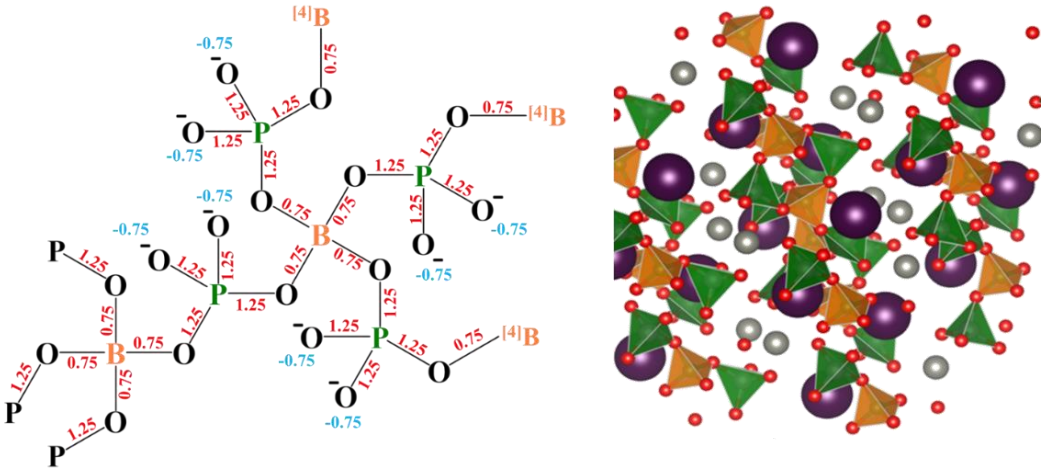

Figure 5.13. Pauling bond strength map (left) and the crystal structure of $CsZnBP_2O_8$ with a B:P ratio of 1:2 (right). In the crystal structure, green and orange tetrahedra represent phosphate and borate units, respectively; purple and grey balls represent cesium and zinc ions, respectively.

In BPO_4 (**Figure 5.14**, B:P = 1:1) the PBS contributions of B^{3+} and P^{5+} to the P−O−B bond are 0.75, and 1.25 v.u., respectively, and the corresponding bond lengths are 1.46 and 1.52 Å. These are similar to those observed in the previous two structures with similar bond strength contributions. The corresponding calculated bond strength contributions are 0.78 and 1.29 v.u., which agree with the observed bond length-bond strength trends in previously discussed crystal structures.

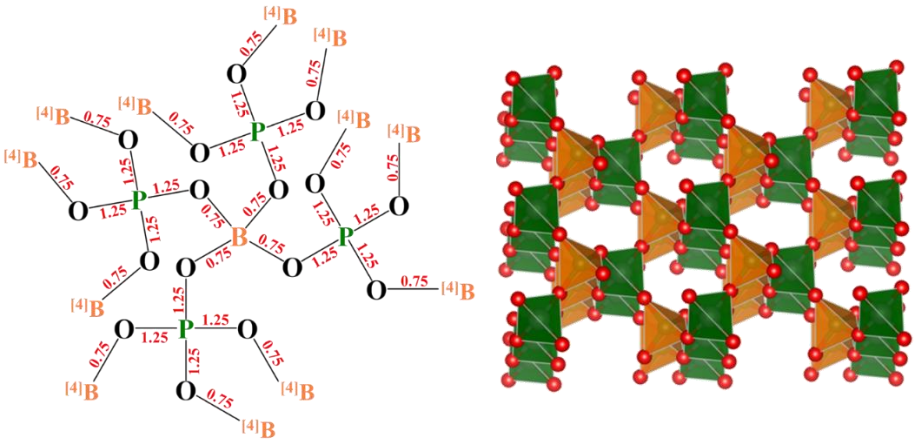

Figure 5.14. Pauling bond strength map (left) and the crystal structure of BPO_4 with a B:P ratio of 1:1 (right). In the crystal structure, green and orange tetrahedra represent phosphate and borate units, respectively.

The network connectivity in the BPO_4 system changes significantly upon the addition of a modifier oxide. $BaBPO_5$ (**Figure 5.15**) is one such example wherein $^{[4]}B$ has two $^{[4]}B$ units as next-nearest neighbours and two phosphate units in its medium-range chemical environment. As per the bond strength distribution map, B^{3+} contributes 0.5 v.u. to the $^{[4]}B-O-P$ bond and 1 v.u. to the $^{[4]}B-O-^{[4]}B$ bond, and P^{5+} contributes 1.5 v.u. to the $^{[4]}B-O-P$ and 1 v.u. to its NBO. A direct relation between the bond strength contribution and the bond lengths is observed wherein the B−O bond in the $^{[4]}B-O-^{[4]}B$ linkage is 1.38 Å and that in $^{[4]}B-O-P$ is 1.60 Å. The P−O bond length in the $^{[4]}B-O-P$ linkage is 1.47 Å and in $P-O^-$ is 1.57 Å. The bond strength contributions of B^{3+} calculated using the B−O bond lengths in $^{[4]}B-O-^{[4]}B$ and $^{[4]}B-O-P$ linkages are 0.98 v.u. and 0.53 v.u., respectively. The bond strength contributions of P^{5+} calculated using the P−O bond lengths in the $^{[4]}B-O-P$ linkage and $P-O^-$ are 1.46 v.u. and 1.13 v.u., respectively. A similar trend in bond lengths is observed in $PbBPO_5$, the structure of which is isostructural to $BaBPO_5$. The B−O bond in $^{[4]}B-O-^{[4]}B$ linkage is 1.42 Å and that in $^{[4]}B-O-P$ is 1.52 Å; the P−O bond length in the $^{[4]}B-O-P$ linkage is 1.42 Å and that in $P-O^-$ is 1.52 Å. The bond strength contributions of B^{3+} and P^{5+} calculated using these bond lengths are 0.87 and 0.66, 1.66 and 1.29, respectively. Yet again, full compliance of network structure with the Pauling bond strength distribution is evidenced.

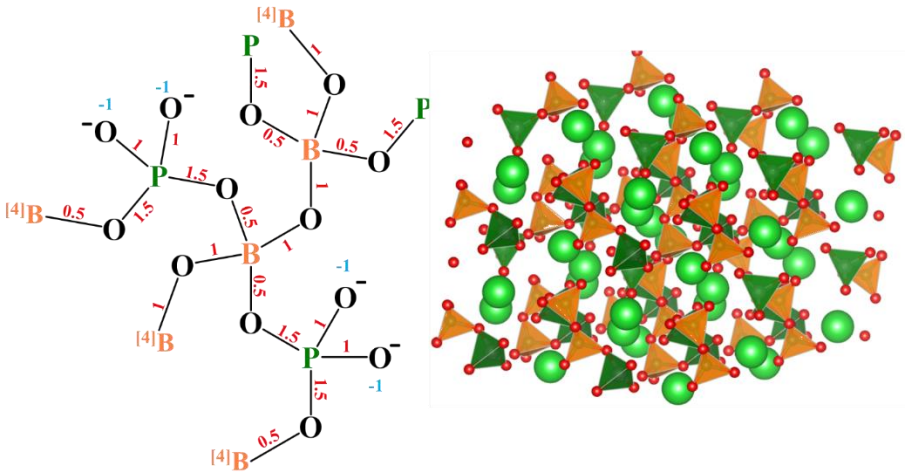

Figure 5.15. Pauling bond strength map (left) and the crystal structure of $BaBPO_5$ with a B:P ratio of 1:1 (right). In the crystal structure, green and orange tetrahedra represent phosphate and borate units, respectively, and the green balls represent barium ions.

For a valence contribution of 0.5 v.u., the coordination number of B^{3+} must be six according to the PBS theory, which is unlikely electronically and sterically; the chemical environment of B^{3+} in crystalline borates is well-defined and limited to trigonal-planar and tetrahedral geometries [99].[1] However, the contribution of B^{3+} is not 0.5 v.u. throughout as it contributes 1 v.u. to two $^{[4]}B-O-^{[4]}B$ bonds and 0.5 v.u. to two $^{[4]}B-O-P$ bonds.

Alternately, if B^{3+} distributes its valence equally across the four B−O bonds, the bond strength contribution will be 0.75 v.u. and the BO in the $^{[4]}B-O-^{[4]}B$ linkage will be underbonded by 0.5 v.u.. In these cases, the deficit charge can be compensated by the modifier ions [100,101], which are also responsible for balancing the charge on any NBO. While this might be true in the current case, the longer B−O bonds in $^{[4]}B-O-P$ linkages suggest a disparity in the B^{3+} bond strength contribution across its four B−O bonds such that the charge compensation role of the modifier cation is minimal and much of the charge deficit on the BO is compensated by P^{5+}, due to its capacity to adopt different bond strength contributions. In borophosphate systems, it can be postulated that the B^{3+} deviates largely from its optimum valency contribution of 0.75 v.u., mainly attributed to unconstrained P^{5+} bond strength contributions.

Finally, the utility of Pauling bond strengths for understanding bonding in borophosphates is demonstrated on a crystal structure with a high B:P ratio of 3:1, $Li_2B_3PO_8$ (**Figure 5.16**). The $^{[4]}B$ units are bonded to two phosphate units and two three-coordinate borate units ($^{[3]}B$), which are bonded to two more $^{[3]}B$. The phosphate units are bonded to two $^{[4]}B$, giving a configuration of $P^2{}_{2B}$. The B^{3+} cation in tetrahedral and trigonal-planar geometries contributes 1 v.u. to the B−O bond in $^{[3]}B-O-^{[3]}B$ and $^{[3]}B-O-^{[4]}B$ linkages and 0.5 v.u. in $^{[4]}B-O-P$ linkages. P^{5+} contributes 1.5 and 1 v.u. to the oxygen shared with the B^{3+} cation and the NBO, respectively. The $\bar{r}$(P−O) in $^{[4]}B-O-P$ and P−O- are 1.50 and 1.56 Å, and the calculated bond strength contributions are 1.36 and 1.17 v.u., respectively. The length of $^{[4]}B-O$ bonds ($\bar{r}$(B−O)) in $^{[4]}B-O-^{[3]}B$ and $^{[4]}B-O-P$ linkages is 1.46 Å, with a calculated bond strength of 0.78 v.u.. Finally, the average length of $^{[3]}B-O$ bonds in $^{[4]}B-O-^{[3]}B$ and

[1] A recent study has shown the presence of linear $[BO_2]^-$ molecules in borate crystals [104].

$^{[4]}$B−O−$^{[3]}$B linkages are 1.34 and 1.38 Å, with calculated bond strengths of 1.09 and 0.98 v.u., respectively.

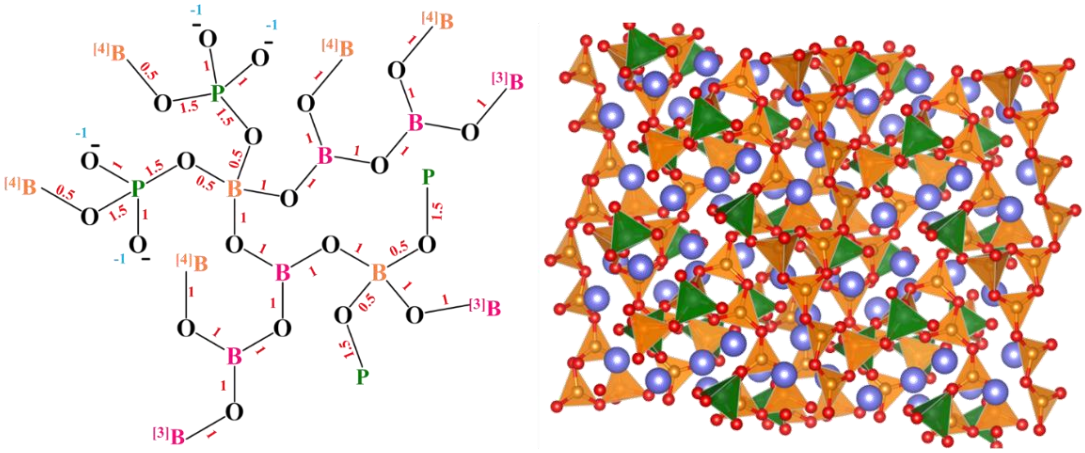

Figure 5.16. Pauling bond strength map (left) and the crystal structure of $Li_2B_3PO_8$ with a B:P ratio of 3:1 (right). In the crystal structure, green and orange polyhedra represent phosphate and borate units, respectively, and the blue balls represent lithium ions.

Detailed analyses of borophosphate crystal structures with different B:P ratios have identified reliable trends in the borate and phosphate speciation. In crystals with a B:P ratio of 1:4, the phosphate and borate speciation are P^2_{1B} and $^{[4]}B_{4P}$, respectively. As the ratio increases to 1:2, the phosphate speciation changes to P^2_{2B}, a borophosphate cluster with P^{5+} sharing the BO with two B^{3+} cations, while no change in the coordination environment of B^{3+} cations is observed. In borophosphate glasses, a progressive increase in the B fraction is known to decrease the number of P−O−P linkages in the network as heteroatomic B−O−P linkages are preferred over B−O−B and P−O−P homoatomic linkages [28]. Even at higher B:P ratios, the observed phosphate speciation is P^2_{2B}, which emphasizes the requirement of NBO in phosphate tetrahedra to effectively delocalize and distribute the bond strength contributions from P^{5+}. By contrast, the coordination environment of B^{3+} changes as $^{[4]}$B−O−$^{[4]}$B linkages and $^{[3]}$B appear in the network, which are exclusively bonded to other $^{[3]}$B and $^{[4]}$B units.

By plotting the chemical shift ranges of different phosphate units on the spectrum of B20 (**Figure 5.6**), the following phosphate species have been identified as candidates based solely on

NMR assignments: P^2_{2B}, P^2_{1B}, P^2_{0B}, P^3_{3B}, P^3_{2B} and, P^3_{1B} (**Figure 5.11**). The foregoing bond-strength analysis of crystalline borophosphates may be used to rule out the presence of some of these clusters based on unreasonable bonding characteristics. In P^3_{1B}, the bond strength contribution of P^{5+} to the NBO is 1.75, which is similar to the bond strength distribution of $^3P_0$ species in P_2O_5, where P^{5+} contributes 1 v.u. to its BO (P−O−P) and 2 v.u. to the NBO. Since the glasses studied here have a high fraction of Na^+ (40 mol%), such a high bond strength contribution to the NBO does not support the integration of Na^+ into the network as it leads to charge imbalance. In the crystal structures studied here (**Table 5.7**), P^3_{1B} was not found even in the phosphate-rich composition (B:P = 1:4), hence its presence in the glasses is unlikely. Pure phosphate units like P^2_0 are also not expected to be present in the glasses as the addition of B to a phosphate network preferentially forms heteroatomic B−O−P linkages and biases against the formation of phosphate-only clusters in the network. This is also supported by the speciation analysis of the crystalline borophosphates, where P-only clusters were not identified at any of the B:P ratios. P^3_{3B} units are not expected to be present according to the following analysis:

a. The bond strength distribution in P^3_{3B} clusters (**Figure 5.11**) is similar to P^4_{4B} in BPO_4, with P^{5+} contributing 1.25 v.u. to each P−O bond and forcing the B^{3+} to contribute 0.75 v.u. to each BO. Since the borate speciation in B20 is $^{[4]}B_{2P}$ and $^{[4]}B_{3P}$, there must be abundant $^{[4]}$B−O− $^{[4]}$B linkages, which cannot be justified through the bond strength distribution with phosphate units adopting the P^3_{3B} configuration and B^{3+} contributing 0.75 v.u. to BO.
b. The addition of a modifier oxide to BPO_4 (i.e., $BaBPO_5$) disrupts the B-P structural ordering, generating NBO on phosphate species along with charge-deficient $^{[4]}$B−O−$^{[4]}$B linkages (**Figure 5.15**). The phosphate units exist in the P^2_{2B} configuration, which provides enough flexibility in terms of bond strength contribution to support $^{[4]}$B−O−$^{[4]}$B linkages. Hence, two P−O−B bonds per phosphate tetrahedron must be the upper limit in terms of B-P intermixing in the B20 glass, ruling out the presence of P^3_{3B} units.
c. This species was not present in any of the crystalline borophosphates investigated.

The P^2_{2B}, $P^2_{1B,}$ and P^3_{2B} phosphate units are all plausible and are valid in terms of their bond strength distribution and configuration hence, these phosphate units can be expected to populate the B20 glass network. In fact, these species have been reported in a sodium

borophosphate glass of similar composition [28] wherein their relative fractions were deduced by tallying the modifier charge distribution between the anionic borate and phosphate units. However, the charge compensation of underbonded BO was not addressed, although a significant fraction of $^{[4]}$B units with fewer than four next-nearest phosphate neighbours ($^{[4]}B_{3P}$ and $^{[4]}B_{2P}$) were observed. A similar observation has been made here, where $^{[4]}B_{2P}$ and $^{[4]}B_{3P}$ dominate the network along with a small fraction of $^{[3]}$B, which is insufficient to prevent the formation of $^{[4]}B-O-^{[4]}B$ linkages, with BO that are underbonded by 0.5 v.u.. Such underbonded BO can be stabilized by Na^+, as implied by a recent double quantum-single quantum NMR study on $Na_2O-B_2O_3-SiO_2$ glasses over a wide compositional space in which ample $^{[4]}B-O-^{[4]}B$ were detected [100]. Although the stabilization of underbonded BO by high field-strength cations such as Ca^{2+} has been explored in binary borate glasses [101], a detailed account of how cations with relatively low field-strength such as Na^+ can stabilize such underbonded BO is lacking. Nevertheless, we believe that the flexibility of P^{5+} to contribute multiple bond strengths to its BO makes it capable of delocalizing its bond strength to underbonded BO, thereby stabilizing them and reducing the charge-compensation role of Na^+.

5.5.3 $(Na_2O)_{0.4}(B_2O_3)_{0.15-x}(Al_2O_3)_x(P_2O_5)_{0.4}$ (x = 0.05, 0.10 and 0.15) glasses

The structural analysis of aluminoborophosphate glasses is complicated by the extensive intermixing of Al, P, and B, leading to intricate glass networks with a multiplicity of contributing species. To gain insight into the network connectivity, the network topology in aluminophosphate and borophosphate glasses, along with the Al and B speciation and their bonding preferences in aluminoborate glasses, have been considered. Although the influence of B on Al speciation in aluminoborate glasses has been established [35,36,39], their interplay in phosphate glasses has not been defined. Upon substituting Al with B, the $^{[4]}$Al and $^{[5]}$Al fractions decrease monotonically, whereas the $^{[6]}$Al fraction plateaus, which is a dominant species in low-Al glasses (**Figure 5.2**). Upon comparing the Al fractions in our glasses with those of a sodium aluminophosphate glass series with 1:1 Na to P ratio [72] (**Figure 5.17**), some similarities are observed: the $^{[5]}$Al fraction is nearly identical, the $^{[4]}$Al content increases exponentially, and $^{[6]}$Al appears to plateau or approach a maximum with increasing Al_2O_3. However, the latter two differ

in detail, with the B-containing glass system possessing a higher $^{[4]}$Al fraction at the expense of $^{[6]}$Al, underscoring the effect of B on Al speciation in phosphate glasses.

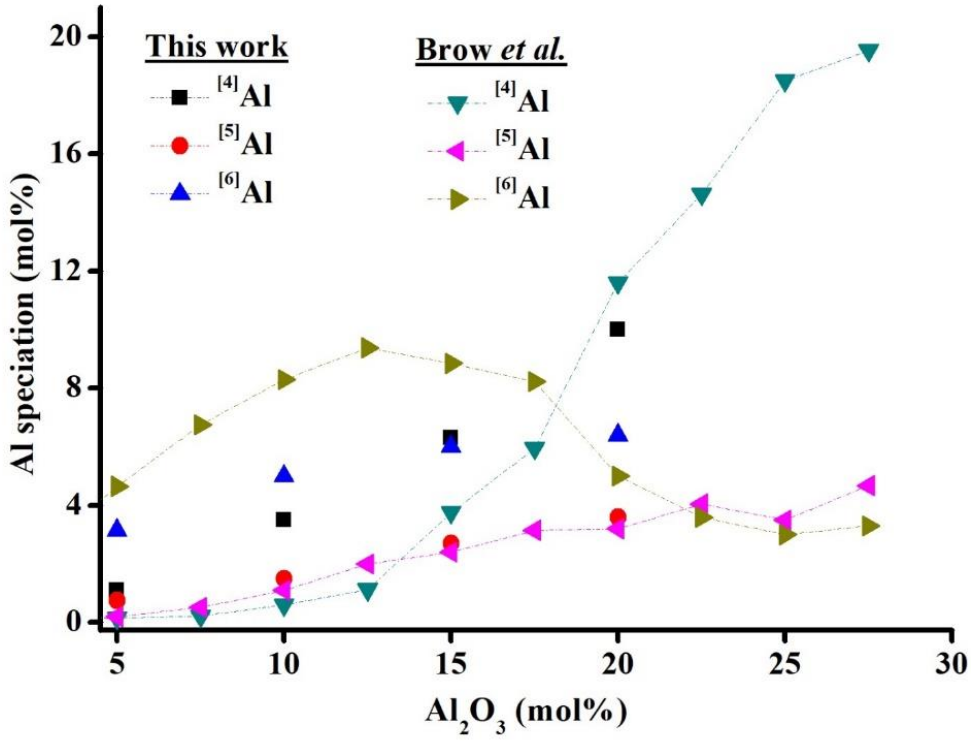

Figure 5.17. Quantification of Al species in sodium aluminophosphate and aluminoborophosphate glasses. The Al fractions shown with trend lines are adapted from reference [72].

The ^{11}B MAS NMR spectra of B5, B10 and B15 show the presence of $^{[4]}B_{2P}$ and $^{[4]}B_{3P}$ and only a trace of $^{[3]}$B, strongly suggesting the presence of $^{[4]}$B–O–$^{[4]}$B linkages in the network. The BO in these linkages will be underbonded, and their charge compensation in B20 has been attributed to the efficacy of P^{5+} in contributing multiple bond strengths to BO leading to a delocalization of bond strength to underbonded BO and the presence of Na^{+} in the vicinity of BO as a charge stabilizer. When Al is present however, high-coordinate Al can assist in compensating underbonded BO, by analogy with alkaline-earth borates, where the high field-strengths of A^{2+} enable them to charge-compensate underbonded BO [101]; the similar bond strengths of $^{[6]}$Al and divalent cations such as Mg^{2+} ($^{[4]}$Mg = 4; 0.5 v.u. [59]) supports this idea.

This has been observed experimentally where high-coordinate Al is in close proximity to $^{[4]}$B and is understood to have a stabilizing role [39]. Local-charge analysis of the $^{[4]}B_{3P}$ cluster bonded to different combinations of $^{[n]}$Al units is given in **Figure 5.18** wherein the Pauling bond strength approach is implemented to explain the charge compensation through bond strength contributions by $^{[5/6]}$Al. The underbonded BO have a charge deficit of 0.5 v.u., which can be compensated by either $^{[5]}$Al or $^{[6]}$Al units (**Figure 5.18, a and b**). In fact, stable $(^{[4]}B)_2-O-^{[6]}Al$ clusters are known to occur in crystalline $MgAlBO_4$ [36]. A surplus of 0.1 v.u. resulting from the $(^{[4]}B(Al))_2-O-^{[5]}Al$ cluster is within the acceptable limits of PBS analysis, hence such structures are considered to be valid. In scenarios where $^{[4]}$B bonds exclusively to high-coordinate Al ($^{[4]}B-O-(^{[5/6]}Al)_2$] (**Figure 5.18, c and d**), $^{[5]}$Al can comfortably charge-compensate the NBO, whereas $^{[6]}$Al bonding leads to a deficit of 0.25 v.u.. A combination of $^{[5]}$Al and $^{[6]}$Al units ($^{[4]}B-O-(^{[5]}Al+^{[6]}Al)$] (**Figure 5.18e**) can charge compensate the NBO with a physically reasonable valence deficit of 0.15 v.u.. Although such clusters are almost charge-neutral, the oxygen may be almost considered non-bridging due to the highly ionic nature of the $^{[5/6]}Al-O$ bond. Since it is known that the formation of NBO on $^{[4]}$B units is energetically unfavourable [102], these connectivities can be neglected despite satisfying the bond strength requirements.

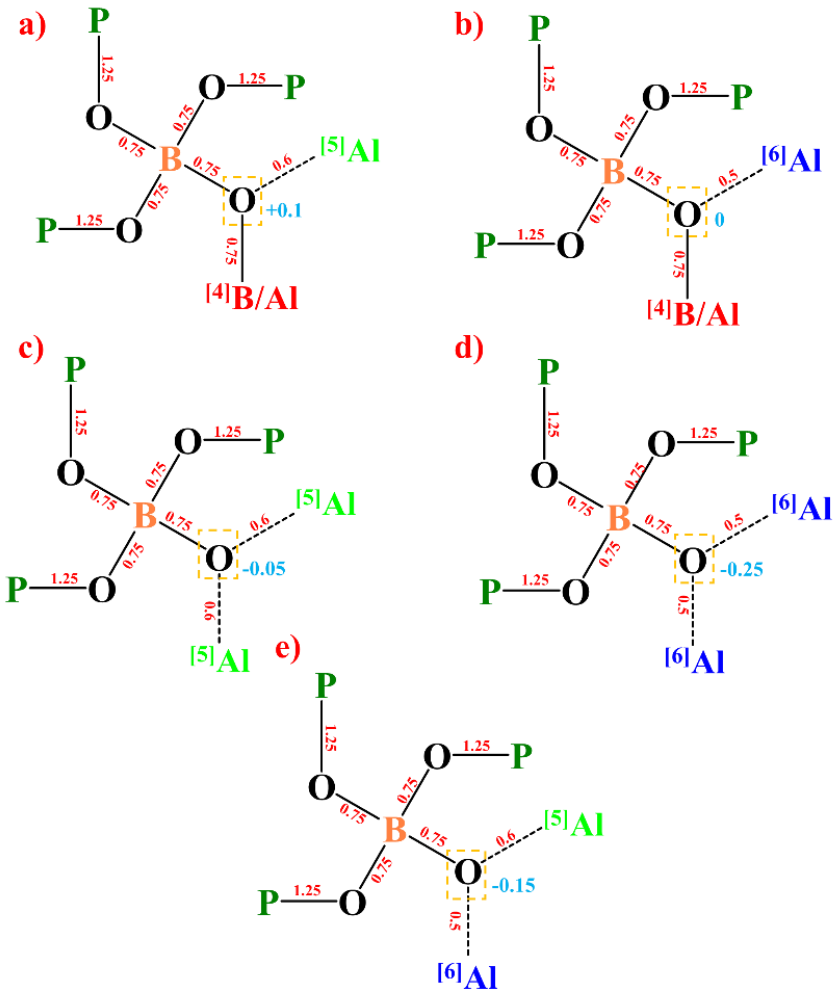

Figure 5.18. The structures of $^{[4]}B_{3P}$ with different combinations of $^{[4]}B$ and $^{[n]}Al$; over-bonded and underbonded BO are highlighted in orange squares: a) the underbonded BO charge-compensated by $^{[5]}Al$; b) the underbonded BO charge-compensated by $^{[6]}Al$; c) and d) NBO charge-compensated by either $^{[5]}Al$ or $^{[6]}Al$; e) NBO charge-compensated by both $^{[5]}Al$ and $^{[6]}Al$.

While this analysis does not permit a precise inventory of the phosphate units present in aluminoborophosphate glasses, it limits the range of possibilities and provides a qualitative understanding of the phosphate speciation assayed by NMR. The preference of high-coordinate Al to bond to phosphate dimers, and $^{[4]}Al$ bonding to branched phosphates is expected to dominate in pure aluminophosphate and low-B:P glasses. The addition of B diminishes this

structural ordering due to its strong tendency to form B−O−P linkages. As a result, the aluminoborophosphate network will consist of phosphate units in multiple configurations, including most of the species observed in B0 and B20. Since $^{[4]}$B and $^{[4]}$Al nominally have the same bond strengths (0.75 v.u.), their bonding in phosphate clusters will be analogous, hence $^{[4]}$Al and $^{[4]}$B can be expected to simultaneously bond to phosphate units. The trends in $^{[4]}$Al and $^{[6]}$Al fractions are quite distinct between the aluminophosphate and aluminoborophosphate glasses (**Figure 5.17**). Since it is known that $^{[6]}$Al dominates the glass network with low Al/P ratios, it is natural to observe a high $^{[6]}$Al fraction as the Al/P ratio decreases. However, the fraction of $^{[6]}$Al is lower compared to B-free analogues, which suggests that the addition of B induces the conversion of $^{[6]}$Al to $^{[4]}$Al. This might be due to the inaccessibility of $^{[6]}$Al-rich phosphate clusters to $^{[4]}$B units as the bonding leads to over-bonded BO (isostructural to $^{[4]}$Al**,** **Figure 5.9**). As $^{[4]}$Al and $^{[4]}$B have similar geometries and bond strength contributions, the $^{[6]}$Al→$^{[4]}$Al conversion might contribute toward a more homogenous glass network. Secondarily, $^{[6]}$Al can effectively charge compensate the underbonded BO, therefore its structural role is extended to charge compensation, and its complete conversion to $^{[4]}$Al upon increasing B/Al ratio is limited. A peakwidth-constrained deconvolution of ^{31}P MAS NMR spectra suggests a progressive increase in the integrated intensity of the peak representing P^3_{3Al} in B0 and P^2_{2B} +/ P^2_{1B} in B20 (**Table 5.4**), further substantiating this analysis.

Surprisingly, the fraction of $^{[5]}$Al is the same irrespective of whether boron is present in the glass system, suggesting that $^{[5]}$Al units are unaffected by the introduction of borate units into the glass network and do not interact with them. While the bond strength contributions of $^{[4]}$Al and $^{[6]}$Al are well defined (0.75 and 0.5 v.u., respectively), the intermediate bond strength of $^{[5]}$Al (0.6 v.u.) confers both $^{[4]}$Al and $^{[6]}$Al character to the $^{[5]}$Al unit. As a result, it might be expected to share phosphate units with the borates and stabilize the BO simultaneously, leading to subtle or no changes in its fraction. This further complicates the assignment of its structural role in the glass network, and its partitioning into $^{[4]}$Al/B- and $^{[6]}$Al-preferred phosphate clusters can not be differentiated.

In terms of bond strength distribution, phosphate units with P−O−P linkages are more effective in facilitating multiple bond strength contributions so that stable phosphate clusters with tetrahedral B and Al can form. Evidence of this is found in the peak shifts to lower frequencies with increasing B:P. In phosphate glasses, a low-frequency change in chemical shifts

is attributed to an increase in the number of P−O−P linkages [103], leading to the inference that the substitution of Al by B has a contrasting effect of forming P−O−P linkages compared to borophosphates, where the addition of B converts P−O−P to P−O−B linkages. This also agrees with the phosphate assignments in B0 and B20, where the former has fewer P−O−P linkages (P^3_{3Al} and P^3_{2Al} vs. P^2_{1B} and P^3_{2B}).

Finally, low-frequency shift of the ^{23}Na MAS NMR peak upon substitution of Al by B is attributed to an increase in the Na coordination number and mean Na−O bond length [74]. As Na^+ interacts significantly more strongly with phosphate units than with borates [29], the displacement of negative charge from $^{[4]}$B towards the P NBO results in a localized negative charge which functions as a "Coulomb trap" and contributes to the mobility of Na^+ ions [29]. This further substantiates the efficacy of P^{5+} in contributing bond strength to B−O−P linkages such that the charge deficits are localized on the phosphate unit.

5.6 Structural summary

The evaluation of network linkages using Pauling bond strengths allows for some degree of discrimination amongst possible bonding configurations which, in conjunction with NMR results, helps form a picture of how the network changes as a function of glass composition. The network of an aluminophosphate glass (B0) consists of branched phosphates linked to $^{[4]}$Al and phosphate dimers linked to $^{[6]}$Al. The structural role and connectivity of $^{[5]}$Al are ambiguous as its bond strength contribution is intermediate between $^{[4]}$Al and $^{[6]}$Al, imparting to it structural characteristics of both. Although such strong structural conclusions cannot be made for the sodium borophosphate network (B20), three distinct phosphate units with P−O−P and P−O−B linkages have been identified: P^2_{1B}, P^2_{2B} and P^3_{2B}. A high fraction of $^{[4]}$B−O−$^{[4]}$B linkages is expected to be present, which are stabilized by both Na^+ and P^{5+}, which contribute multiple bond strengths to BO, thereby delocalizing the bond strength to underbonded BO and stabilizing them. As a result, the bond-strength contribution of P^{5+} to the NBO decreases, further lowering its negative charge, increasing the NBO−Na^+ interaction and strongly affecting the Na−O bond length and the coordination number of Na^+. Due to NBO in phosphate groups functioning as Coulomb traps, the Na^+ ions are mainly associated with phosphate units, which improves their mobility, explaining the increased Na−O bond length or coordination number of Na.

The network structure of aluminoborophosphate glasses (B5−B15) is inherently complicated due to high compatibility between B, Al, and P units, leading to homogeneous glass systems. For aluminoborophosphate glasses with low and high B/Al ratios, the network structures are proposed to share structural features of B0 and B20 glasses, respectively, albeit with some characteristics of one another. The addition of B to an aluminophosphate glass reduces the structural ordering brought about by multiple Al coordination numbers and forces the conversion of $^{[6]}$Al to $^{[4]}$Al, as the latter is isostructural to $^{[4]}$B and helps in the formation of stable borophosphate clusters with B→Al site substitutions. Although high-coordinate Al units are exclusively bonded to phosphate dimers in aluminophosphate glasses, this structural preference is quenched in aluminoborophosphate glasses, where their structural role diversifies into charge-compensating the underbonded $^{[4]}$B−O−$^{[4]}$B. As a result, a stable and significant fraction of $^{[6]}$Al is maintained throughout the glass series. Although the addition of B to phosphate glasses leads to depolymerization of the pure phosphate network and the substitution of P−O−P with P−O−B linkages, increasing the B/Al ratio in aluminoborophosphate glasses increases the number of P−O−P linkages. This has been attributed to the efficacy of P−O−P rich phosphate clusters in simultaneously bonding to $^{[4]}$B(Al) units and stabilizing the underbonded BO originating from the $^{[4]}$B−O− $^{[4]}$B linkages through multiple bond strength contributions.

This work demonstrates the utility of the Pauling bond strength as a supporting tool to enhance the understanding of the speciation in multicomponent glasses which could not be obtained by 1D NMR alone.

5.7 References

[1] S. Lee, J. Kim, D. Shin, Modification of network structure induced by glass former composition and its correlation to the conductivity in lithium borophosphate glass for solid state electrolyte, Solid State Ionics. 178 (2007) 375–379.

[2] J.H. Campbell, T. I. Suratwala, Nd-doped phosphate glasses for high-energy/high-peak-power lasers, J. Non-Cryst. Solids. 236 & 264 (2000) 318–341.

[3] M.J.G. Jak, E.M. Kelder, Z.A. Kaszkur, J. Pielaszek, J. Schoonman, Li^+ ion conductivity of BPO_4–LiO_2; the relation between crystalstructure and ionic conductivity, Solid State Ionics. 119 (1999) 159–164.

[4] J.A. Wilder, Glasses and glass ceramics for sealing to aluminum alloys, J. Non-Cryst. Solids. 38–39 (1980) 879–884.

[5] R. Morena, Phosphate glasses as alternatives to Pb-based sealing frits, J. Non-Cryst. Solids. 263 (2000) 382–387.

[6] G.J. Hutchings, I.D. Hudson, D.G. Timms, Dehydration of 2-methylbutanal to isoprene using aluminium phosphate catalysts, Catal. Letters. 61 (1999) 219–224.

[7] Donald I.W. Donald, B.L. Metcalfe, R.N.J. Taylor, Review: The immobilization of high level radioactive wastes using ceramics and glasses, J. Mater. Sci. 32 (1997) 5851–5887.

[8] T. Lemesle, F.O. Méar, L. Campayo, O. Pinet, B. Revel, L. Montagne, Immobilization of radioactive iodine in silver aluminophosphate glasses, J. Hazard. Mater. 264 (2014) 117–126.

[9] T. Minamf, J.D. Mackenzie, Thermal Expansion and Chemical Durability of Phosphate Glasses, J. Am. Ceram. Soc. 60 (1977) 232–235.

[10] W.H. Zachariasen, The atomic arrangement in glass, J. Am. Chem. Soc. 54 (1932) 3841–3851.

[11] P. Richet, Y. Bottinga, Glass transitions and thermodynamic properties of amorphous SiO_2, $NaA1Si_nO_{2n+2}$ and $KAlSi_3O_8$, Geochim. Cosmochim. Acta. 48 (1984) 453–470.

[12] N.J. Kreidl, W.A. Weyl, Phosphates in Ceramic Ware: IV, Phosphate Glasses, J. Am.

Ceram. Soc. 24 (1941) 372–378.

[13] K. Suzuya, D.L. Price, C.K. Loong, S.W. Martin, Structure of vitreous P_2O_5 and alkali phosphate glasses, J. Non-Cryst. Solids. 232–234 (1998) 650–657.

[14] S.W. Martin, C.A. Angell, On the glass transition and viscosity of P_2O_5, J. Phys. Chem. 90 (1986) 6736–6740.

[15] L. Zhang, A. Bögershausen, H. Eckert, Mesoporous $AlPO_4$ glass from a simple aqueous sol-gel route, J. Am. Ceram. Soc. 88 (2005) 897–902.

[16] A. Adamczyk, M. Handke, The isotopic effect and spectroscopic studies of boron orthophosphate (BPO_4), J. Mol. Struct. 555 (2000) 159–164.

[17] R.K. Brow, Nature of alumina in phosphate glass: I, Properties of sodium aluminophosphate glass, J. Am. Ceram. Soc. 76 (1993) 913–918.

[18] J.F. Ducel, J.J. Videau, Physical and chemical characterizations of sodium borophosphate glasses, Mater. Lett. 13 (1992) 271–274.

[19] D. Carta, D. Qiu, P. Guerry, I. Ahmed, E.A. Abou Neel, J.C. Knowles, M.E. Smith, R.J. Newport, The effect of composition on the structure of sodium borophosphate glasses, J. Non-Cryst. Solids. 354 (2008) 3671–3677.

[20] H. Takebe, T. Harada, M. Kuwabara, Effect of B_2O_3 addition on the thermal properties and density of barium phosphate glasses, J. Non-Cryst. Solids. 352 (2006) 709–713.

[21] F. Behrends, H. Eckert, Mixed-alkali effects in aluminophosphate glasses: A re-examination of the system $[xNa_2O(1\text{-}x)Li_2O]_{0.46}[yAl_2O_3(1\text{-}y)P_2O_5]_{0.54}$, J. Phys. Chem. C. 115 (2011) 17175–17183.

[22] J.M. Egan, R.M. Wenslow, K.T. Mueller, Mapping aluminum/phosphorus connectivities in aluminophosphate glasses, J. Non-Cryst. Solids. 261 (2000) 115–126.

[23] D.P. Lang, T.M. Alam, D.N. Bencoe, Solid-state $^{31}P/^{27}AI$ and $^{31}P/^{23}Na$ TRAPDOR NMR investigations of the phosphorus environments in sodium aluminophosphate glasses, Chem. Mater. 13 (2001) 420–428.

[24] L. Zhang, H. Eckert, Short- And medium-range order in sodium aluminophosphate glasses: New insights from high-resolution dipolar solid-state NMR spectroscopy, J. Phys. Chem. B. 110 (2006) 8946–8958.

[25] D. Raskar, M.T. Rinke, H. Eckert, The mixed-network former effect in phosphate glasses: NMR and XPS studies of the connectivity distribution in the glass system $(NaPO_3)_{1-x}(B_2O_3)_x$, J. Phys. Chem. C. 112 (2008) 12530–12539.

[26] V.K. Michaelis, P. Kachhadia, S. Kroeker, Clustering in borate-rich alkali borophosphate glasses : a ^{11}B and ^{31}P MAS NMR study, Phys. Chem. Glas. Eur. J. Glas. Sci. Technol. B. 54 (2013) 20–26.

[27] M.T. Rinke, H. Eckert, The mixed network former effect in glasses: Solid state NMR and XPS structural studies of the glass system $(Na_2O)_x(BPO_4)_{1-x}$, Phys. Chem. Chem. Phys. 13 (2011) 6552–6565.

[28] D. Zielniok, C. Cramer, H. Eckert, Structure/property correlations in ion-conducting mixed-network former glasses: Solid-state NMR studies of the system Na_2O-B_2O_3-P_2O_5, Chem. Mater. 19 (2007) 3162–3170.

[29] L.M. Funke, H. Eckert, Charge compensation in sodium borophosphate glasses studied by $^{11}B\{^{23}Na\}$ and $^{31}P\{^{23}Na\}$ rotational echo double resonance spectroscopy, J. Phys. Chem. C. 120 (2016) 3196–3205.

[30] B. Raguenet, G. Tricot, G. Silly, M. Ribes, A. Pradel, Revisiting the “mixed glass former effect” in ultra-fast quenched borophosphate glasses by advanced 1D/2D solid state NMR, J. Mater. Chem. 21 (2011) 17693–17704.

[31] A.T. Grigg, A.J. Marsden, M. Mee, S. Feller, S.K. Fong, P.M. Mallinson, R. Dupree, D. Holland, Vitrification of β-tricalcium phosphate in sodium aluminoborophosphate glass and the effect of Ga^{3+} substitution, J. Solid State Chem. 231 (2015) 175–184.

[32] K. Kobayashi, Glasses and their applications to MOS capacitors, Mater. Sci. Eng. 55 (1998) 153–155.

[33] Y.K. Sharma, S.S.L. Surana, C.L. Gehlot, S.P. Tandon, Optical studies and laser parameters of various Pr^{3+} doped glass systems, Indian J. Eng. Mater. Sci. 10 (2003) 215–

218.

[34] B.I. Galagan, I.N. Glushchenko, B.I. Denker, Y.L. Kalachev, V.A. Mikhailov, S.E. Sverchkov, Influence of synthesis conditions on optical losses in aluminoborophosphate laser glass, Glas. Phys. Chem. 37 (2011) 258–262.

[35] L.S. Du, J.F. Stebbins, Site connectivities in sodium aluminoborate glasses: Multinuclear and multiple quantum NMR results, Solid State Nucl. Magn. Reson. 27 (2005) 37–49.

[36] B.C. Bunker, R.J. Kirkpatrick, R.K. Brow, Local structure of alkaline-earth boroaluminate crystals and glasses: I, crystal chemical concepts—structural predictions and comparisons to known crystal structures, J. Am. Ceram. Soc. 74 (1991) 1425–1429.

[37] L. Zuchner, J.C.C. Chan, W. Müller-Warmuth, H. Eckert, Short-range order and site connectivities in sodium aluminoborate glasses: I. Quantification of local environments by high-resolution ^{11}B, ^{23}Na, and ^{27}Al solid-state NMR, J. Phys. Chem. B. 102 (1998) 4495–4506.

[38] B.C. Bunker, R.J. Kirkpatrick, R.K. Brow, G.L. Turner, C. Nelson, Local structure of alkaline-earth boroaluminate crystals and glasses: II, ^{11}B and ^{27}Al MAS NMR spectroscopy of alkaline-earth boroaluminate glasses, J. Am. Ceram. Soc. 74 (1991) 1430–1438.

[39] J.C.C. Chan, M. Bertmer, H. Eckert, Site connectivities in amorphous materials studied by double-resonance NMR-of quadrupolar nuclei: High-resolution $^{11}B \leftrightarrow ^{27}Al$ spectroscopy of aluminoborate glasses, J. Am. Chem. Soc. 121 (1999) 5238–5248.

[40] B.E. Warren, H. Krutter, O. Morningstar, Fourier analysis of x-ray patterns of vitreous SiO_2 and B_2O_3, J. Am. Ceram. Soc. 19 (1936) 202–206.

[41] K.J. Rao, The glassy state, In: *Structural chemistry of glasses*, Elsevier, 2002.

[42] R. Kurita, E.R. Weeks, Experimental study of random-close-packed colloidal particles, Phys. Rev. E. 82 (2010) 1–9.

[43] J.D. Bernal, A geometrical approach to the structure of liquids, Nature. 183 (1959) 141–147.

[44] A. Dietzel, Die Kationenfeldstärken und ihre Beziehungen zu Entglasungsvorgängen, zur Verbindungsbildung und zu den Schmelzpunkten von Silikaten, Z. Elektrochem. angew. phys. chemie. 48 (1942) 9–23.

[45] K.-H. Sun, Fundamental condition of glass formation, J. Am. Ceram. Soc. 30 (1947) 277–281.

[46] A. Smekal, On the structure of glass, J. Soc. Glas. Technol. 35 (1951) 392–394.

[47] Stanworth J E, Tellurite glasses, Nature. (1952) 581–582.

[48] Y.S. Bobovich, T.P. Tulub, J.M. Valentine, S.C. Curran, Raman spectra and structure of certain inorganic types of glasses, Physics-Uspekhi. 1 (1958) 1–28.

[49] E.A. Chechetkina, Rawson's criterion and intermolecular interactions in glass-forming melts, J. Non-Cryst. Solids. 128 (1991) 30–47.

[50] N. Boubata, A. Roula, I. Moussaoui, Thermodynamic and relative approach to compute glass-forming ability of oxides, Bull. Mater. Sci. 36 (2013) 457–460.

[51] I.D. Brown, Recent developments in the methods and applications of the bond valence model, Chem. Rev. 109 (2009) 6858–6919.

[52] G. V. Gibbs, N.L. Ross, D.F. Cox, K.M. Rosso, B.B. Iversen, M.A. Spackman, Pauling bond strength, bond length and electron density distribution, Phys. Chem. Miner. 41 (2014) 17–25.

[53] I.D. Brown, The ionic bond, In: *The Chemical bond in inorganic chemistry*, Oxford University Press, 2002: p. 13.

[54] I.D. Brown, Anion and Cation Bonding Strengths, in: *The Chemical bond in inorganic chemistry*, Oxford University Press, 2002: p. 43.

[55] A.C. Hannon, Bonding and structure in network glasses, J. Non-Cryst. Solids. 451 (2016) 56–67.

[56] V.S. Urusov, Semi-empirical groundwork of the bond-valence model, Acta Crystallogr. Sect. B. 51 (1995) 641–649.

[57] I.D. Brown, R.D. Shannon, Empirical bond-strength–bond-length curves for oxides, Acta Crystallogr. Sect. A. 29 (1973) 266–282.

[58] N.E. Brese, M. O'Keeffe, Bond-valence parameters for solids, Acta Crystallogr. Sect. B. 47 (1991) 192–197.

[59] O.C. Gagné, P.H.J. Mercier, F.C. Hawthorne, A priori bond-valence and bond-length calculations in rock-forming minerals, Acta Crystallogr. Sect. B Struct. Sci. Cryst. Eng. Mater. 74 (2018) 470–482.

[60] L. Pauling, The principles determining the structure of complex ionic crystals, J. Am. Chem. Soc. 51 (1929) 1010–1026.

[61] W.H. Zachariasen, H.A. Plettinger, Crystal chemical studies of the 5f-series of elements. XXV. The crystal structure of sodium uranyl acetate, Acta Crystallogr. 12 (1959) 526–530.

[62] W.H. Zachariasen, Crystal chemical studies of the 5 f -series of elements. XXIII. On the crystal chemistry of uranyl compounds and of related compounds of transuranic elements , Acta Crystallogr. 7 (1954) 795–799.

[63] W.H. Baur, Bond length variation and distorted coordination polyhedra in inorganic crystals, Trans. Am. Crystallogr. Assoc. 6 (1970) 129–155.

[64] G. Donnay, R. Allmann, How to recognize O^{2-}, OH^{-}, and H_2O in crystal structures determined by X-rays, Am. Mineral. 55 (1970) 1003–1015.

[65] O.C. Gagné, F.C. Hawthorne, Comprehensive derivation of bond-valence parameters for ion pairs involving oxygen, Acta Crystallogr. Sect. B Struct. Sci. Cryst. Eng. Mater. 71 (2015) 562–578.

[66] S. Adams, J. Swenson, Determining ionic conductivity from structural models of fast ionic conductors, Phys. Rev. Lett. 84 (2000) 4144–4147.

[67] S. Adams, J. Swenson, Pathway models for fast ion conductors by combination of bond valence and reverse Monte Carlo methods, Solid State Ionics. 154–155 (2002) 151–159.

[68] D. Massiot, F. Fayon, M. Capron, I. King, S. Le Calvé, B. Alonso, J.O. Durand, B. Bujoli,

Z. Gan, G. Hoatson, Modelling one- and two-dimensional solid-state NMR spectra, Magn. Reson. Chem. 40 (2002) 70–76.

[69] J.P. Amoureux, C. Fernandez, “QUASAR—Solid-State NMR Simulation for Quadrupolar Nuclei.,” 2005.

[70] S. Kroeker, Nuclear waste glasses: Insights from solid-state NMR, Encycl. Magn. Reson. (2011) 453–466.

[71] S. Elbers, W. Strojek, L. Koudelka, H. Eckert, Site connectivities in silver borophosphate glasses: New results from $^{11}B\{^{31}P\}$ and $^{31}P\{^{11}B\}$ rotational echo double resonance NMR spectroscopy, Solid State Nucl. Magn. Reson. 27 (2005) 65–76.

[72] R.K. Brow, R.J. Kirkpatrick, G.L. Turner, Local structure of $xAl_2O_3(1\text{-}x)NaPO_3$ glasses: An NMR and XPS study, J. Am. Ceram. Soc. 73 (1990) 2293–2300.

[73] R.K. Brow, R.J. Kirkpatrick, G.L. Turner, Nature of alumina in phosphate glass: II, structure of sodium aluminophosphate glass, J. Am. Ceram. Soc. 76 (1993) 919–928.

[74] X. Xue, J.F. Stebbins, ^{23}Na NMR Chemical Shifts and Local Na Coordination Environments in Silicate Crystals , Melts and Glasses, Phys. Chem. Miner. 20 (1993) 297–307.

[75] I.D. Brown, The bond valence model, In: *The chemical bond in inorganic chemistry*., Oxford University Press, 2002: p. 26.

[76] O.C. Gagné, F.C. Hawthorne, Bond-length distributions for ions bonded to oxygen: Results for the non-metals and discussion of lone-pair stereoactivity and the polymerization of PO_4, Acta Crystallogr. Sect. B Struct. Sci. Cryst. Eng. Mater. 74 (2018) 79–96.

[77] R.K. Brow, D.R. Tallant, S.T. Myers, C.C. Phifer, The short-range structure of zinc polyphosphate glass, J. Non-Cryst. Solids. 191 (1995) 45–55.

[78] O.C. Gagné, F.C. Hawthorne, Bond-length distributions for ions bonded to oxygen: Metalloids and post-Transition metals: Metalloids, Acta Crystallogr. Sect. B Struct. Sci. Cryst. Eng. Mater. 74 (2018) 63–78.

[79] H.N. Ng, C. Calvo, X-ray study of the alpha-beta transformation of berlinite ($AlPO_4$), Can. J. Phys. 54 (1976) 638–647.

[80] S. Di Mo, W.Y. Ching, Electronic and optical properties of theta-Al_2O_3 and comparison to alpha-Al2O3, Phys. Rev. B - Condens. Matter Mater. Phys. 57 (1998) 15219–15228.

[81] M. Schuch, C. Trott, P. Maass, Network forming units in alkali borate and borophosphate glasses and the mixed glass former effect, RSC Adv. 1 (2011) 1370–1382.

[82] M.A. Khan, Y.Y. Li, S.X. Huang-Fu, H. Chen, L.J. Zhang, P.F. Liu, J.S. Yu, R.H. Duan, L. Chen, Synthesis and characterization of mixed alkali borophosphate with a new 1D chain: $Li_3Cs_2BP_4O_{14}$, Inorganica Chim. Acta. 466 (2017) 174–179.

[83] Y. Wang, S. Pan, Y. Shi, Further examples of the P-O-P connection in borophosphates: Synthesis and characterization of $Li_2Cs_2B_2P_4O_{15}$, $LiK_2BP_2O_8$, and $Li_3M_2BP_4O_{14}$ (M=K, Rb), Chem. - A Eur. J. 18 (2012) 12046–12051.

[84] L.J. Zhang, Y.Y. Li, P.F. Liu, L. Chen, $Li_3Cs_2M_2B_3P_6O_{24}$ (M = Pb, Sr): borophosphates with double six-membered ring of $[BP_2O_8]^{3-}$, Dalt. Trans. 45 (2016) 7124–7130.

[85] T. Hasegawa, H. Yamane, Synthesis, crystal structure and lithium ion conduction of $Li_3BP_2O_8$, Dalt. Trans. 43 (2014) 2294–2300.

[86] D. Zhao, W.D. Cheng, H. Zhang, S.P. Huang, Z. Xie, W.L. Zhang, S.L. Yang, $KMBP_2O_8$ (M = Sr, Ba): A new kind of noncentrosymmetry borophosphate with the three-dimensional diamond-like framework, Inorg. Chem. 48 (2009) 6623–6629.

[87] M.A. Khan, Y.Y. Li, H. Lin, L.J. Zhang, P.F. Liu, H.J. Zhao, R.H. Duan, J.Q. Wang, L. Chen, Syntheses of six and twelve membered borophosphate ring structure with nonlinear optical activity, J. Solid State Chem. 243 (2016) 259–266.

[88] T. Hasegawa, H. Yamane, Synthesis and crystal structure analysis of $Li_2NaBP_2O_8$ and $LiNa_2B_5P_2O_{14}$, J. Solid State Chem. 225 (2015) 65–71.

[89] D.B. Xiong, H.H. Chen, X.X. Yang, J.T. Zhao, Low-temperature flux syntheses and characterizations of two 1-D anhydrous borophosphates: $Na_3B_6PO_{13}$ and $Na_3BP_2O_8$, J. Solid State Chem. 180 (2007) 233–239.

[90] R. Kniep, G. Schäfer, H. Engelhardt, I. Boy, K [$ZnBP_2O_8$] and A [$ZnBP_2O_8$](A= NH_4^+, Rb^+, Cs^+): zincoborophosphates as a new class of compounds with tetrahedral framework structures, Angew. Chemie Int. Ed. 38 (1999) 3641–3644.

[91] Y. Yang, P. Gong, Q. Huang, G. Song, X. Liu, Z. Lin, $KNa_4B_2P_3O_{13}$: A deep-ultraviolet transparent borophosphate exhibiting second-harmonic generation response, Inorg. Chem. 58 (2019) 8918–8921.

[92] C. Hauf, T. Friedrich, R. Kniep, Crystal structure of pentasodium catena-(diborato-triphosphate), $Na_5[B_2P_3O_{13}]$, Zeitschrift Für Krist. Cryst. Mater. 210 (1995) 446.

[93] C. Wu, L. Li, G. Yang, J. Song, B. Yan, M.G. Humphrey, L. Zhang, J. Shao, C. Zhang, Low-temperature-flux syntheses of ultraviolet-transparent borophosphates $Na_4MB_2P_3O_{13}$ (M = Rb, Cs) exhibiting a second-harmonic generation response, Dalt. Trans. 46 (2017) 12605–12611.

[94] M. Schmidt, B. Ewald, Y. Prots, R. Cardoso-Gil, M. Armbrüster, I. Loa, L. Zhang, Y. Huang, U. Schwarz, R. Kniep, Growth and characterization of BPO_4 single crystals, Zeitschrift Für Anorg. Und Allg. Chemie. 630 (2004) 655–662.

[95] Y. Shi, J. Liang, H. Zhang, Q. Liu, X. Chen, J. Yang, W. Zhuang, G. Rao, Crystal structure and thermal decomposition studies of barium borophosphate, $BaBPO_5$, J. Solid State Chem. 135 (1998) 43–51.

[96] A. Ben Ali, E. Antic-Fidancev, B. Viana, P. Aschehoug, M. Taibi, J. Aride, A. Boukhari, Crystal structure of $ABPO_5$ and optical study of Pr^{3+} embedded in these compounds, J. Phys. Condens. Matter. 13 (2001) 9663.

[97] S. Pan, Y. Wu, P. Fu, G. Zhang, Z. Li, C. Du, C. Chen, Growth, structure, and properties of single crystals of $SrBPO_5$, Chem. Mater. 15 (2003) 2218–2221.

[98] T. Hasegawa, H. Yamane, The crystal structure of $Li_2B_3PO_8$ with the 2D-linkage of BO_3, BO_4 and PO_4 groups, Dalt. Trans. 43 (2014) 14525–14528.

[99] F.C. Hawthorne, P.C. Burns, J.D. Grice, The crystal chemistry of boron, Rev. Mineral. 33 (1996) 41–115.

[100] Y. Yu, B. Stevensson, M. Edén, Direct experimental evidence for abundant BO_4-BO_4 motifs in borosilicate glasses from double-quantum ^{11}B NMR spectroscopy, J. Phys. Chem. Lett. 9 (2018) 6372–6376.

[101] J. Wu, J.F. Stebbins, Cation field strength effects on boron coordination in binary borate glasses, J. Am. Ceram. Soc. 97 (2014) 2794–2801.

[102] M. Zeyer-Düsterer, L. Montagne, G. Palavit, C. Jäger, Combined ^{17}O NMR and ^{11}B-^{31}P double resonance NMR studies of sodium borophosphate glasses, Solid State Nucl. Magn. Reson. 27 (2005) 50–64.

[103] L. Montagne, G. Palavit, R. Delaval, ^{31}P NMR in (100-x)($NaPO_3$)-xZnO glasses, J. Non-Cryst. Solids. 215 (1997) 1–10.

[104] C. Huang, M. Mutailipu, F. Zhang, K.J. Griffith, C. Hu, Z. Yang, J.M. Griffin, K.R. Poeppelmeier, S. Pan, Expanding the chemistry of borates with functional $[BO_2]^-$ anions, Nat. Commun. 12 (2021) 1–8.

6 Effect of Mo Incorporation on the Network Structure of Sodium Aluminoborophosphate Glasses

6.1 Introduction

The practical utility of borosilicate glasses as high-level (HLW) and low-level nuclear waste (LLW) immobilization matrices is compromised by their high processing temperatures, which lead to the volatilization of radioactive nuclides such as ^{99}Tc, ^{131}I, ^{135}Cs, ^{137}Cs, and others [1,2]. In addition, certain cations in high oxidation states such as Mo^{6+} [3,4] and S^{6+} [5,6] exhibit low solubilities in borosilicate glasses due to their strong nucleating properties. The success of phosphate glasses in immobilizing cations with phase-separation tendencies like Mo^{6+}, S^{6+}, Cr^{6+} and W^{6+} [5,7–10], emphasizes their potential applicability as wasteforms for immobilizing chemically heterogeneous HLW calcines. Furthermore, phosphate glasses have lower processing temperatures than borosilicates, which eliminates the problem of radionuclide volatilization and makes them more suitable for nuclear-waste immobilization applications [11,12]. Since the compositions of these glasses vary widely, with phosphate being the only constant, their efficacy in incorporating troublesome cations into their network is mainly attributed to the structural role played by the phosphate units. However, phosphate glasses are mechanically weaker than borosilicates, as their network is populated by diverse phosphate species - isolated units (PO_4^{3-}, orthophosphate), dimers ($P_2O_7^{4-}$, pyrophosphate) and chains ($P_3O_{10}^{5-}$, metaphosphate) [13] - leading to lower network reticulation and hence, poor physical and chemical properties [14]. Their corrosion resistance can be improved by densifying the network through the addition of Al_2O_3 [15] or B_2O_3 [16–18], which form Al(B)−O−P linkages and increase the dimensionality of the glass network. Due to the synergistic effect of Al and B in improving the network reticulation and therefore chemical durability, aluminoborophosphate glasses qualify as matrices for immobilizing HLW and LLW wastes. The network structure of aluminoborophosphate glasses is important for understanding and predicting their chemical durability but has not been explored in detail. Here, we use multinuclear solid-state NMR spectroscopy and Pauling bond strength principles to analyze the network topology of a series of aluminoborophosphate glasses.

Mo is present in high concentrations in some HLW such as the Collins-CLT waste stream [19], and as a result, the overall extent of waste-loading in glasses is limited by their capacity to incorporate Mo. Borosilicate glasses exhibit low Mo solubility of about 1.5 mol% [20] but some phosphate glasses can integrate up to 70 mol% Mo without the separation of crystalline molybdates [9,21–23]. The low solubility of Mo in silicate systems may be attributed to the disparity in the Si^{4+} and Mo^{6+} *field strengths*, the ratio of the cation oxidation number to the square of the average cation−oxygen bond length [24]. The field strengths of Si^{4+}, P^{5+} and Mo^{6+} calculated for M−O bond lengths of 1.625 Å [25], 1.537 Å [26] and 1.764 Å [27] in tetrahedral geometries, respectively, are 1.51, 2.11 and 1.92 $Å^{-2}$. The mismatch in the field strengths of Mo^{6+} and Si^{4+} leads to the formation of isolated molybdate units dispersed within the silicate network through the preferential formation of Mo−O bonds, and eventually to the phase separation of crystalline molybdates. By contrast, the similarity in the field strengths of P^{5+} and Mo^{6+} leads them both to compete effectively for oxygen, resulting in more covalent P−O−Mo linkages. This CFS compatibility allows Mo to exhibit different bonding characteristics in phosphate glasses, wherein Mo^{6+} adopts octahedral geometry [9,21–23] .

Nuclear magnetic resonance (NMR) spectroscopy (**Chapter 3**) is a versatile technique to study the short-range and medium-range order in the network structures of disordered systems such as glasses [28,29]. In principle, ^{95}Mo NMR should be an effective method to probe the local chemical environment of Mo, however it is not NMR-friendly due to its low natural abundance and low gyromagnetic ratio. Mo has two NMR-active isotopes, ^{95}Mo and ^{97}Mo, of which the latter is normally favoured for NMR observation due to its higher natural abundance and smaller quadrupole moment [30]. ^{95}Mo NMR measurements often require high magnetic fields and isotopic enrichment of the samples, therefore only a few studies involving direct detection of Mo in glasses have been reported. In silicate glasses, these studies have confirmed the Mo coordination environments to be tetrahedral [4,31–33], whereas in phosphates, ^{95}Mo NMR results are ambiguous, with reported coordination environments ranging from tetrahedral [34] to a mixture of tetrahedral and octahedral Mo [8] to completely octahedral [35]. These results are limited to simple phosphate systems, and no information about the coordination of Mo in multicomponent glasses such as aluminoborophosphates has been reported.

The vitrification process involves melting a mixture of glass frit and calcined waste, and pouring the melt into metal canisters [36], which are then cooled and processed for long-term disposal. The canister-core (a.k.a. "centerline") temperature can reach up to 673 K due to radiolytic heating [37], hence the glassy wasteform must tolerate the heat and not undergo any structural changes which might compromise its physical and chemical properties. High-temperature NMR (HT-NMR) spectroscopy is an ideal technique to study temperature-induced changes in the network structure and test for phase separation. In the past, HT-NMR experiments have been conducted on silicate and phosphate melts to determine atomic-scale diffusive processes, chemical exchange, thermodynamic and transport properties, structural relaxation processes, devitrification, and the fictive-temperature dependence of melts [38–47].

This study involves two series of sodium aluminoborophosphate glasses. The first series builds upon chapter 5 by adding a fixed amount of Mo to the base-glass compositions described there to study the effect of Mo addition on the sodium aluminoborophosphate glass structure at different B/Al ratios. The second series investigates the Mo loading capacity in glasses with constant B and Al mole fractions by progressively increasing the Mo content. These glasses are characterized by multinuclear solid-state NMR spectroscopy to discern the structural changes occurring due to Mo incorporation. ^{95}Mo NMR of two ^{95}Mo-enriched sodium aluminoborophosphate glasses with varying Mo fractions is observed to study the coordination environment of Mo. High-temperature ^{23}Na and ^{31}P MAS NMR experiments simulating canister-centerline conditions (*ca.* 400 °C) are carried out to determine the heat tolerance of the glasses and to track possible changes in the network connectivity. Crystalline phosphomolybdates with different Mo and P mole fractions are examined using the Pauling bond strength concept (**Chapter 5**) to develop an understanding of the nature of P−O−Mo bonding. The Pauling bond strength models supported by the NMR results are developed to explain the mode of Mo incorporation into sodium aluminoborophosphate glasses.

6.2 Experimental details

6.2.1 Synthesis

Two series of glasses were synthesized wherein MoO_3, a HLW simulant, was added in wt% to base glasses, consistent with the general practice of vitrification where the calcine is mixed with a glass frit of fixed composition and melted. The compositions of series 1 and 2 glasses are $[(Na_2O)_{0.4}(P_2O_5)_{0.4}(B_2O_3)_x(Al_2O_3)_{0.2-x} + 13MoO_3]$ (x = 0, 0.05, 0.10, 0.15 and 0.20) and $[(Na_2O)_{0.4}(P_2O_5)_{0.4}(B_2O_3)_{0.1}(Al_2O_3)_{0.1} + zMoO_3]$ (z = 3 to 28 wt%), respectively (**Table 6.1**). B_2O_3 was synthesized by heating H_3BO_3 at 450 °C, 650 °C, and 800 °C for 30, 15, and 15 minutes, respectively. Reagent-grade sodium hexametaphosphate $(NaPO_3)_6$, aluminum oxide (Al_2O_3), molybdenum oxide (MoO_3), and laboratory-synthesized boron oxide (B_2O_3) were mixed, melted at 1100 °C for 1 hour in lidded Pt/Au crucibles and water-quenched. The batches were formulated by combining the oxides required to obtain a one-gram batch of glass "frit", followed by the addition of MoO_3 in wt% (**Equation 6.1**), to simulate the procedure followed in waste vitrification plants:

$$\text{Wt\%} = \frac{Grams\ of\ \text{MoO3}}{Grams\ of\ glass + Grams\ of\ MoO3} \qquad (6.1)$$

The glass samples were transferred to tight-capped glass vials and stored in a desiccator for NMR and XRD analysis. Two glasses from series 2 containing 8 and 21 wt% MoO_3 were enriched in ^{95}Mo using 95% $^{95}MoO_3$ (Cortecnet, France) in their synthesis. The samples are labeled according to their boron content as *B-*X_{MoY}, where *X* and *Y* correspond to the mol% of B_2O_3 and wt% of MoO_3, respectively.

Table 6.1. Nominal compositions of glasses (MoO_3 is in wt% while the rest of the oxides are in mol%).

	P_2O_5	Na_2O	Al_2O_3	B_2O_3	MoO_3
Series 1					
B-0$_{Mo13}$	40	40	20	0	13
B-5$_{Mo13}$	40	40	15	5	13
B-10$_{Mo13}$	40	40	10	10	13
B-15$_{Mo13}$	40	40	5	15	13
B-20$_{Mo13}$	40	40	0	20	13
Series 2					
B-10$_{Mo0}$	40	40	10	10	0
B-10$_{Mo3}$	40	40	10	10	3
B-10$_{Mo8}$	40	40	10	10	8
B-10$_{Mo13}$	40	40	10	10	13
B-10$_{Mo17}$	40	40	10	10	17
B-10$_{Mo21}$	40	40	10	10	21
B-10$_{Mo24}$	40	40	10	10	24
B-10$_{Mo28}$	40	40	10	10	28

6.2.2 Solid-state MAS NMR spectroscopy

^{11}B, ^{23}Na, ^{27}Al, and ^{31}P MAS NMR spectra were acquired on a ^{UNITY}INOVA Varian 600 spectrometer operating at 14.1 T, equipped with a 3.2 mm double-resonance Chemagnetics solid-state MAS NMR probe with a sample spinning speed of 14000($\pm$5) Hz. Bloch-decay experiments were carried out with pulse lengths and recycle delays, respectively, of 0.35 μs and 4 s for ^{11}B, 0.39 μs and 4 s for ^{23}Na, 0.21 μs and 2 s for ^{27}Al. The pulse lengths in all these cases corresponded to a tip angle of 15° to ensure uniform excitation of sites with different quadrupolar coupling constants (C_Q). In ^{31}P NMR experiments, a pulse length of 1.25 μs (30° flip angle) and a recycle delay of 30 s were used.

Rotor-synchronized Hahn-echo [48] ^{11}B and ^{95}Mo MAS NMR experiments were conducted on a Bruker Avance III 850 MHz spectrometer (CEMHTI, Orléans, France). The samples were spun at the magic angle at 20 kHz. ^{11}B spectra were collected with a 90° pulse length of 12 μs, recycle delay of 4 s, and the signal was averaged over 16 scans. ^{95}Mo NMR spectra were collected with a 90° pulse length of 4.7 μs, recycle delay of 0.2 s, and the signal was averaged over 16384 scans.

6.3 Results

6.3.1 ^{95}Mo MAS NMR

Due to the low gyromagnetic ratio and low natural abundance of ^{95}Mo, NMR experiments were done at a high magnetic field on ^{95}Mo-enriched samples in order to obtain spectra with adequate signal-to-noise ratios. The ^{95}Mo MAS NMR spectra of two glasses from the second series with low and high Mo fractions (B-10$_{Mo8}$ and B-10$_{Mo21}$) are shown in **Figure 6.1**. A single broad peak with a peak maximum of *ca.* -110 ppm is observed in both spectra, which is assigned to six-coordinate Mo (vide infra).

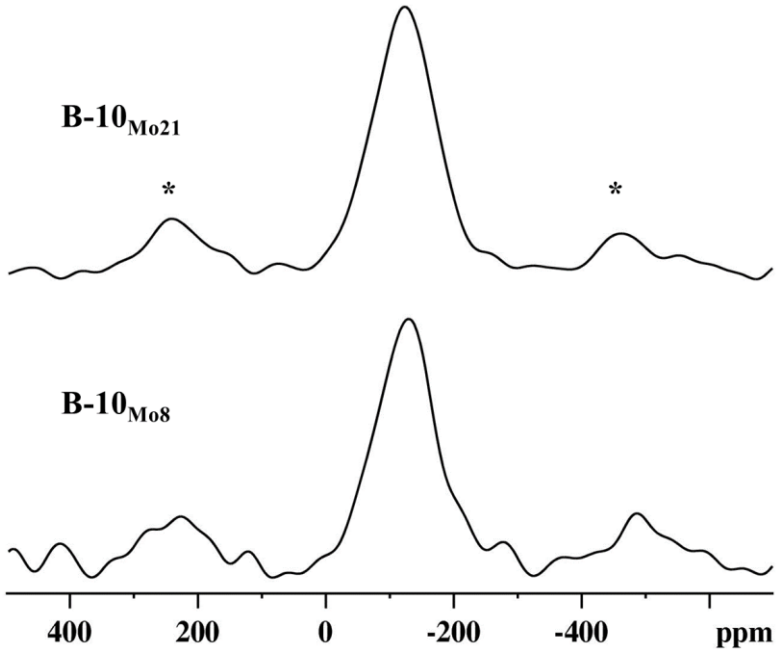

Figure 6.1. Hahn-echo ^{95}Mo MAS NMR spectra of ^{95}Mo-enriched glasses B-10$_{Mo8}$ and B-10$_{Mo21}$ collected at 20 T. Asterisks denote spinning sidebands.

6.3.2 ^{11}B MAS NMR

The ^{11}B MAS NMR spectra of glasses from the first series (**Figure 6.2**) consist of two partially-resolved peaks centered at ca. -2.3 and -0.1 ppm, attributed to tetrahedral borate units in two distinct chemical environments, and a low-intensity second-order quadrupolar broadened peak at ca. 15 ppm, representing borate units in trigonal-planar geometry. The borate species are labelled as $^{[n]}B_{mP}$, where *n* and *m* represent the number of bridging oxygens and next-nearest phosphate neighbours, respectively. The two $^{[4]}$B peaks at -0.1 and -2.3 ppm are assigned to $^{[4]}B_{2P}$ and $^{[4]}B_{3P,}$ respectively [49]. Substitution of Al by B increases the fraction of $^{[4]}$B in the network, $^{[4]}B_{2P}$ and $^{[4]}B_{3P}$ both increasing disproportionately, with $^{[4]}B_{2P}$ being the most-favoured network species at all compositions (**Table 6.2**). The fractions of $^{[n]}B_{mP}$ and $^{[3]}$B (in mol%) in series-1 glasses obtained from the deconvolution of the ^{11}B NMR spectra are plotted along with those of the base glasses for comparison in **Figure 6.3**. Compared to the base glasses, the series-1 glasses exhibit a lower N_4 ratio, $^{[4]}B/(^{[4]}B+^{[3]}B)$, along with higher fractions of $^{[4]}B_{2P}$ and $^{[3]}$B and a lower number of $^{[4]}B_{3P}$.

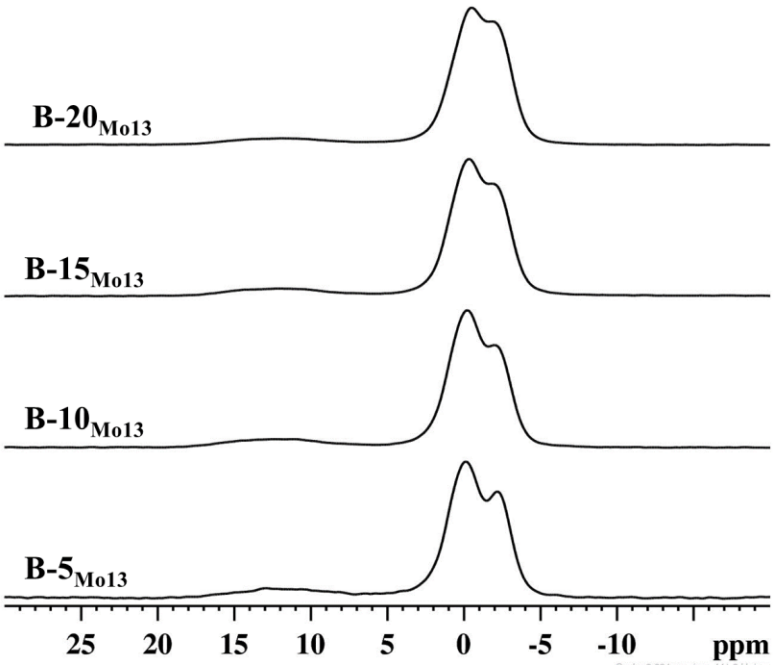

Figure 6.2. ^{11}B MAS NMR spectra of glasses from series 1.

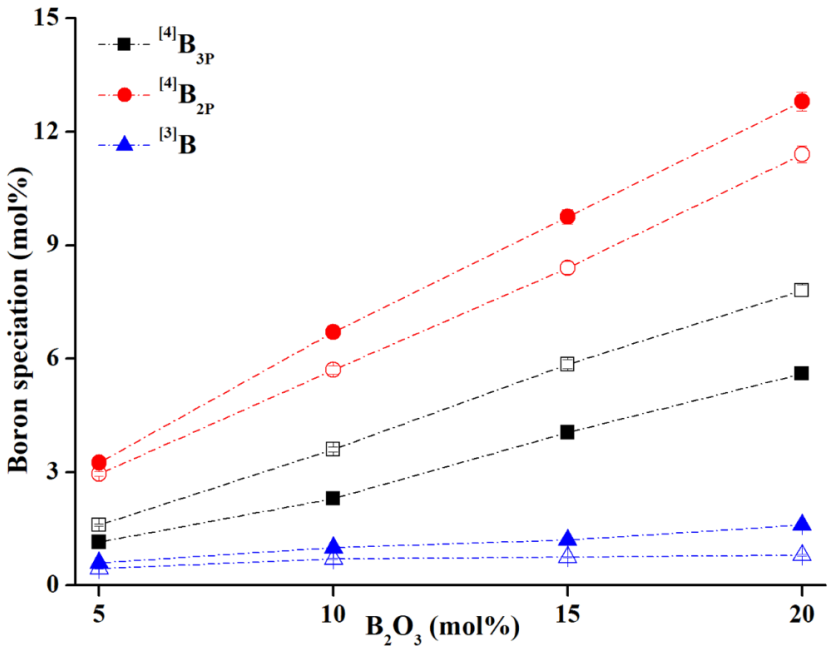

Figure 6.3. The total fractions of different borate species (in mol%) in series-1 glasses plotted as a function of their B_2O_3 content. The borate speciation in base glasses (**Chapter 5**) are plotted for comparison in open symbols. Error bars are smaller than symbol size.

Table 6.2. Integrated intensities (in %) of $^{[n]}B_{mP}$ and $^{[3]}B$ peaks obtained from the deconvolution of ^{11}B MAS NMR spectra of series-1 glasses.

	$(^{[4]}B_{3P})^a$ (±1)	$(^{[4]}B_{2P})^b$ (±1)	$(^{[3]}B)^c$ (±1)
B-5_{Mo13}	23	65	12
B-10_{Mo13}	23	67	10
B-15_{Mo13}	27	65	8
B-20_{Mo13}	28	64	8

[a]Peak maximum = -2.3(±0.3) ppm; Peak width = 0.4(±0.05) kHz
[b]Peak maximum = -0.1(±0.3) ppm; Peak width = 0.5(±1) kHz
[c]δ_{iso} = 16.5(±0.5) ppm; C_Q = 2.6(±0.1) MHz; η = 0.5

The ^{11}B MAS NMR spectra of series-2 glasses with fixed B and Al fractions and varying Mo content are plotted in **Figure 6.4**. The addition of Mo results in a concomitant increase in the $^{[3]}$B and $^{[4]}B_{2P}$ fractions at the expense of $^{[4]}B_{3P}$ (**Table 6.3, Figure 6.5**). Overall, a linear reduction in the N_4 fraction is observed. The $^{[4]}B_{2P}$ peak broadens with increasing Mo content (example, B-10$_{Mo8}$ vs. B-10$_{Mo21}$), suggesting the presence of additional chemically distinct $^{[4]}$B units. Hence, ^{11}B spectra of B-10$_{Mo21}$ were collected at a higher magnetic field (20 T) (**Figure 6.6**), which show additional intensity on the high-frequency side of the $^{[4]}$B peak, the position of which is *ca.* +0.8 ppm and may be assigned either to $^{[4]}B_{1P}$ [49] or $^{[4]}$B bonded to Mo through B−O−Mo linkages ($^{[4]}B_{xMomP}$, where x and m are the numbers of B−O−Mo and B−O−P linkages, respectively) [34]. Due to reasons discussed in **section 6.4.1**, the peak is assigned to $^{[4]}B_{1P}$. Since the dataset at high field is incomplete, the presence of $^{[4]}B_{1P}$ could not be determined for the remainder of the compositions. As a result, the remaining spectra were fit with only three peaks, representing $^{[3]}$B, $^{[4]}B_{2P,}$ and $^{[4]}B_{3P}$, the deconvolution parameters and integrated intensities of which are listed in **Table 6.3**. In broad strokes, it can be concluded that the number of phosphate units bonded to $^{[4]}$B decreases with Mo addition, and the fraction of $^{[3]}$B increases.

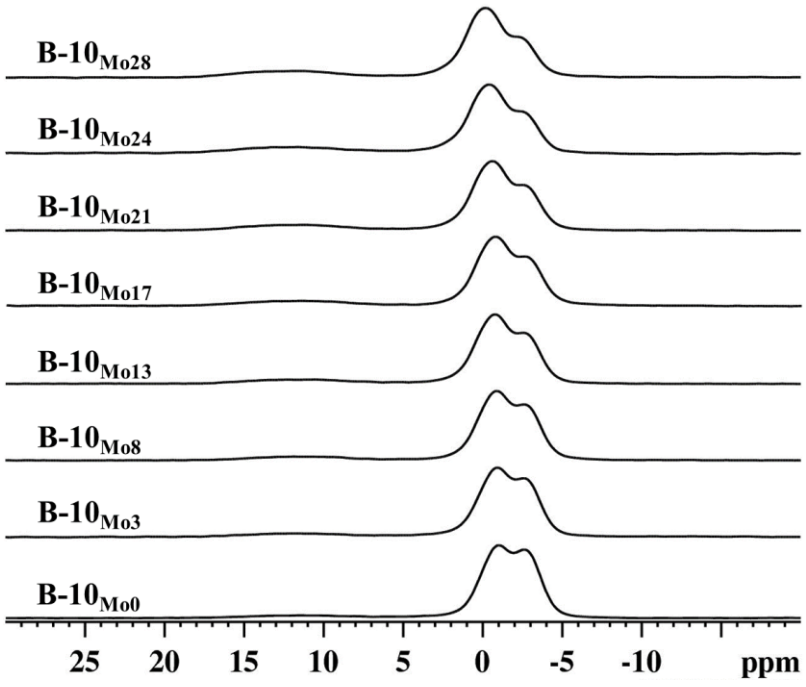

Figure 6.4. ^{11}B MAS NMR spectra of glasses from series 2.

Table 6.3. Integrated intensities (in %) of $^{[n]}B_{mP}$ and $^{[3]}B$ peaks obtained from the deconvolution of ^{11}B MAS NMR spectra of series-2 glasses.

	$(^{[4]}B_{3P})^a$ (±1)	$(^{[4]}B_{2P})^b$ (±1)	$(^{[3]}B)^c$ (±1)
B-10$_{Mo0}$	33	61	6
B-10$_{Mo3}$	29	63	8
B-10$_{Mo8}$	29	63	8
B-10$_{Mo13}$	25	65	10
B-10$_{Mo17}$	24	64	12
B-10$_{Mo21}$	21	66	13
B-10$_{Mo24}$	16	70	14
B-10$_{Mo28}$	18	67	15

[a]Peak maximum = -2.3(±0.3) ppm; Peak width = 0.4(±0.05) kHz
[b]Peak maximum = -0.1(±0.3) ppm; Peak width = 0.5(±1) kHz
[c]δ_{iso} = 16.5(±0.5) ppm; C_Q = 2.6(±0.1) MHz; η = 0.5

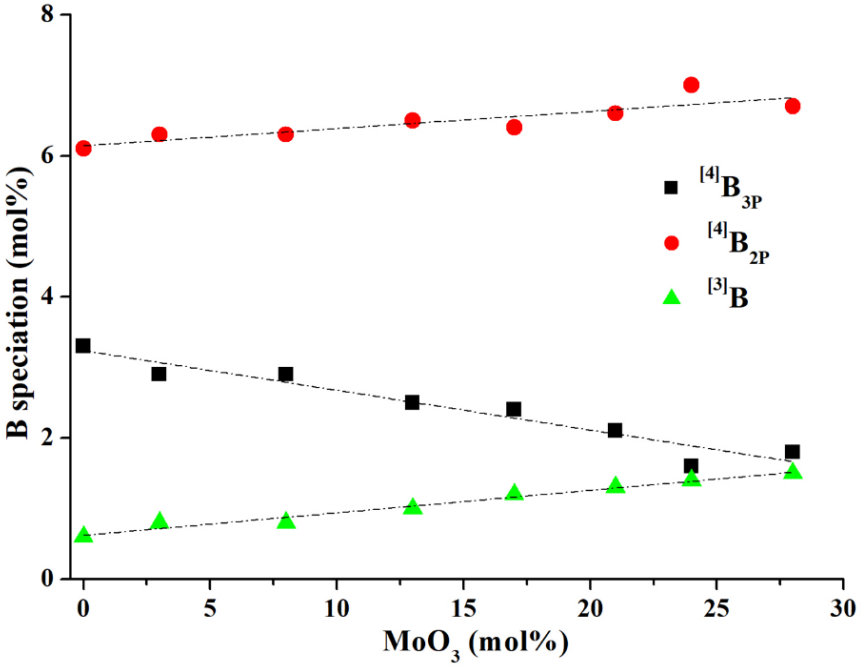

Figure 6.5. Changes in the total boron speciation in series-2 glasses as a function of their MoO_3 content. Error bars are smaller than the symbol size.

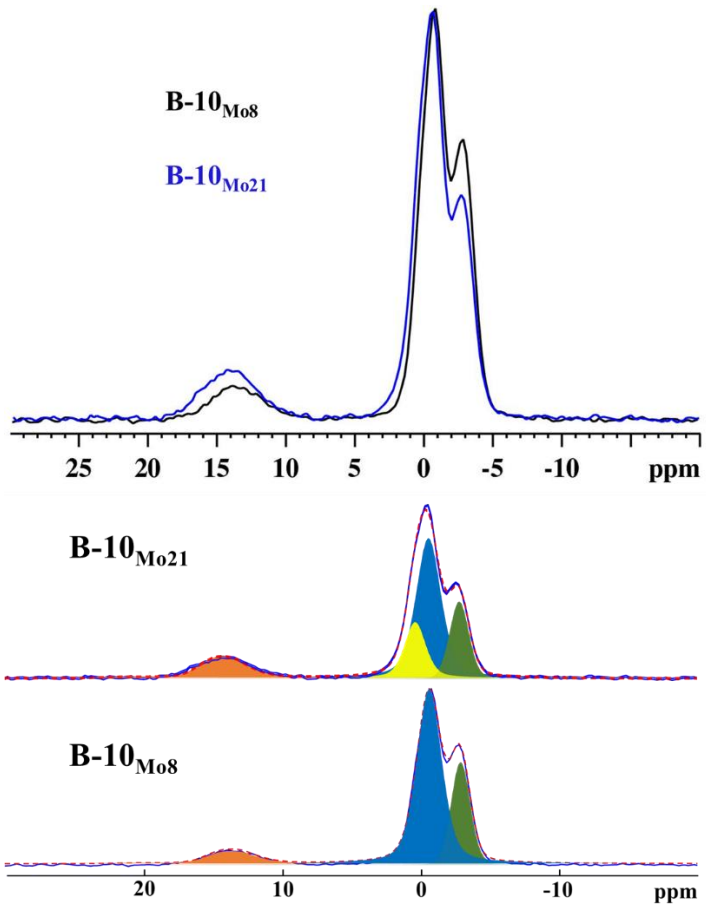

Figure 6.6. ^{11}B MAS NMR spectra of B-10$_{Mo8}$ and B-10$_{Mo21}$ glasses acquired at 20 T (top) and their deconvolution (bottom). The peaks in green, blue, orange and yellow correspond to $^{[4]}B_{3P}$, $^{[4]}B_{2P}$, $^{[3]}B$, and $^{[4]}B_{1P}$ species.

6.3.3 ^{27}Al MAS NMR

The ^{27}Al MAS NMR spectra of series-1 and series-2 glasses consist of three peaks with center-of-gravity shifts of ca. +45, +13, and -12 ppm (**Figure 6.7**), representing Al^{3+} coordinated to four ($^{[4]}$Al), five ($^{[5]}$Al) and six ($^{[6]}$Al) oxygens, respectively [50,51]. A sharp peak observed at +42 ppm in the spectrum of B-0$_{Mo13}$ has been assigned to crystalline $AlPO_4$ [52,53]. The x-ray diffractogram of this sample consists of Bragg peaks corresponding to the crystalline $AlPO_4$ phase [54], further confirming its crystallization from glass (**Figure 6.8**). The addition of Mo induces the phase-separation of $AlPO_4$ in the aluminophosphate glass (B-0$_{Mo13}$), which is inhibited by substituting 5 mol% of Al by B. Upon increasing B/Al, the $^{[6]}$Al fraction increases at

the expense of $^{[4]}$Al, with subtle changes in the $^{[5]}$Al fraction (**Table 6.4**). Comparison of the relative fractions of $^{[n]}$Al species from series-1 glasses with the base glasses reveals that the former glasses have higher $^{[4]}$Al and lower $^{[6]}$Al fractions (**Figure 6.9**). Interestingly, the fraction of $^{[5]}$Al does not change upon Mo addition.

With the addition of Mo to glasses with fixed B and Al mole fractions, a gradual transformation of $^{[6]}$Al to $^{[4]}$Al is observed with subtle changes in the $^{[5]}$Al fraction (**Figures 6.10 and 6.11, Table 6.5**). At 28 wt% Mo loading, a sharp peak appears at ca. +42 ppm from phase-separated $AlPO_4$, marking the upper limit of Mo solubility in the aluminoborophosphate glasses studied in this work.

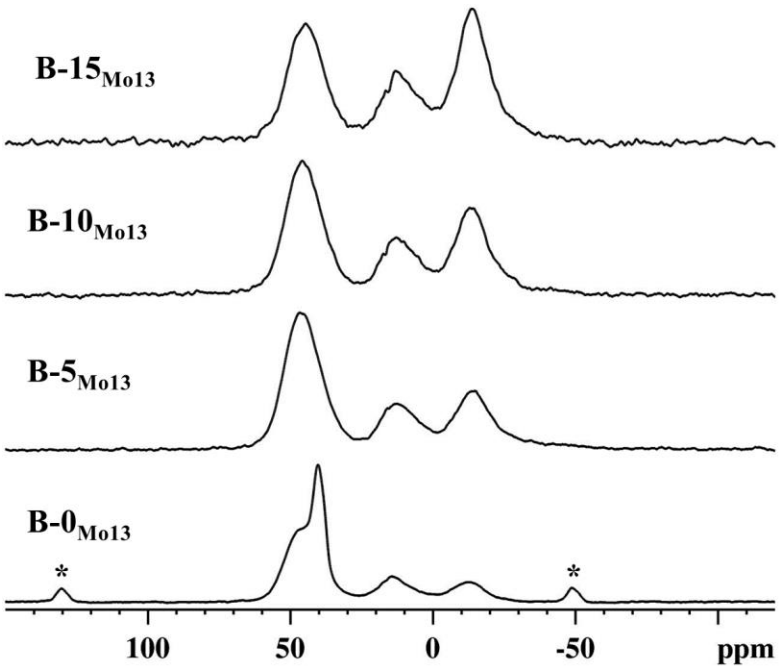

Figure 6.7. ^{27}Al MAS NMR spectra of series-1 glasses. Asterisks denote spinning sidebands.

Table 6.4. Integrated intensities (in %) of $^{[n]}$Al peaks obtained from the deconvolution of ^{27}Al MAS NMR spectra of series-1 glasses.

	$^{[4]}$Al[a] (±2)	$^{[5]}$Al[b] (±2)	$^{[6]}$Al[c] (±2)	$AlPO_4$[d] (±1)
B-0_{Mo13}	45	18	14	23
B-5_{Mo13}	53	18	29	
B-10_{Mo13}	46	19	35	
B-15_{Mo13}	34	21	45	

[a]δ_{CGS}, center-of-gravity shift (ppm) = 45 (±1) ppm
[b]δ_{CGS} = 13 (±1) ppm
[c]δ_{CGS} = -12 (±1) ppm
[d]δ_{iso} = +42 ppm; C_Q = 3.3 MHz; η = 0.5

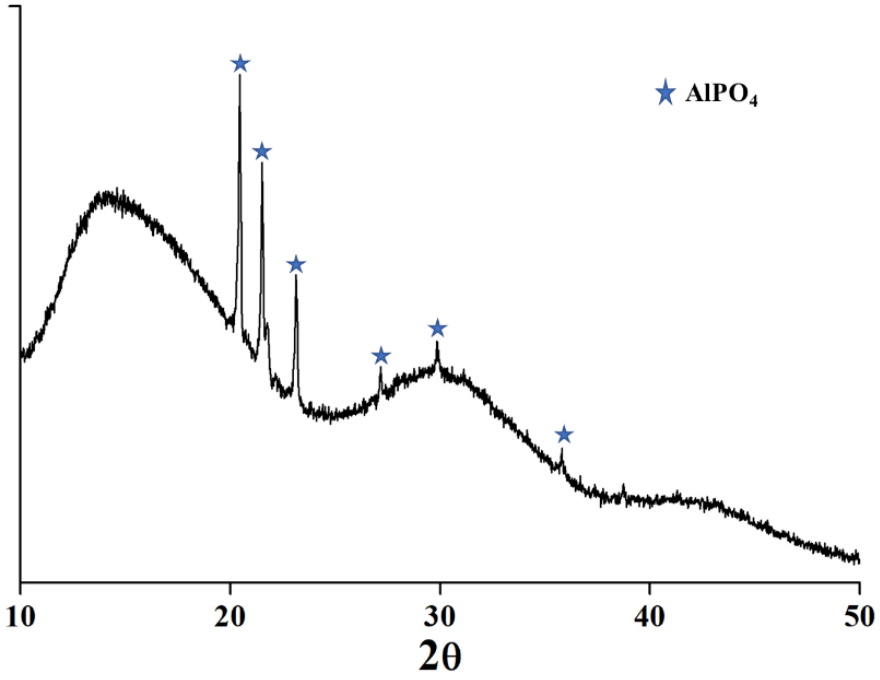

Figure 6.8. X-ray diffractogram of B-0_{Mo13}.

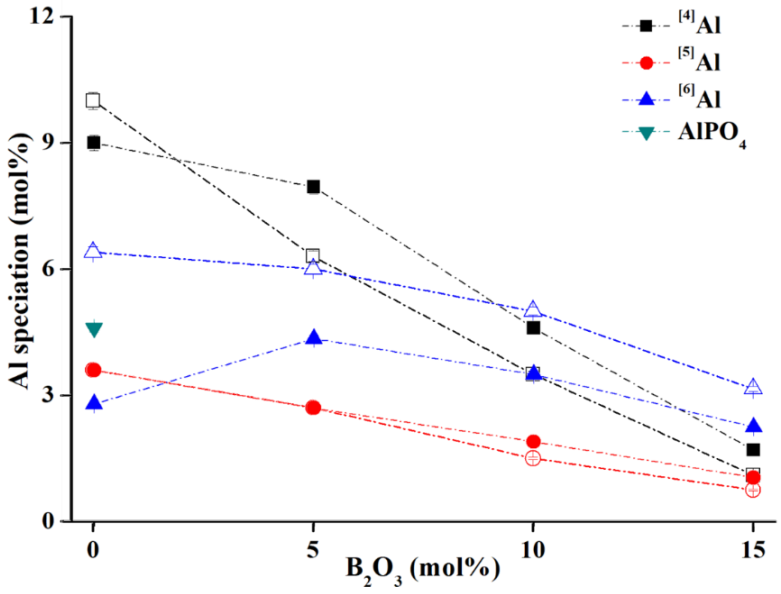

Figure 6.9. The fractions of $^{[n]}$Al species (in mol%) in series-1 glasses plotted as a function of their B_2O_3 content. The fractions of the same aluminate species observed in base glasses (**Chapter 5**) are plotted in open symbols for comparison. Error bars are smaller than the symbol size.

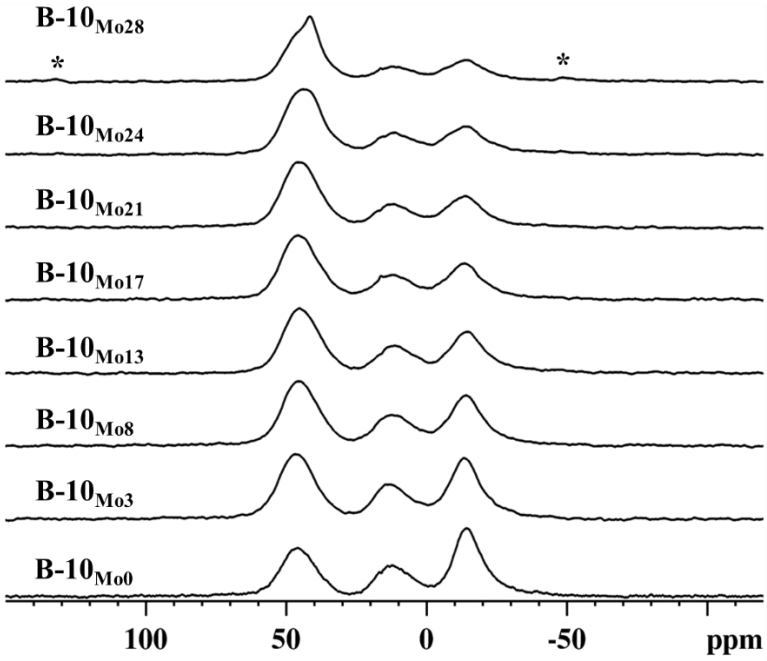

Figure 6.10. ^{27}Al MAS NMR spectra of glasses from series 2. Asterisks denote spinning sidebands.

Table 6.5. Integrated intensities (in %) of $^{[n]}$Al peaks obtained from the deconvolution of ^{27}Al MAS NMR spectra of series-2 glasses.

	$^{[4]}$Al^{a} (±2)	$^{[5]}$Al^{b} (±2)	$^{[6]}$Al^{c} (±2)	AlPO$_4$^{d} (±1)
B-10$_{Mo0}$	35	15	50	
B-10$_{Mo3}$	40	20	40	
B-10$_{Mo8}$	42	21	37	
B-10$_{Mo13}$	45	20	35	
B-10$_{Mo17}$	49	19	32	
B-10M$_{o21}$	52	18	30	
B-10$_{Mo24}$	55	18	27	
B-10$_{Mo28}$	51	17	26	6

$^{a}\delta_{CGS}$ = 46 (±1) ppm
$^{b}\delta_{CGS}$ = 13 (±1) ppm
$^{c}\delta_{CGS}$ = -13.5 (±1) ppm
$^{d}\delta_{iso}$ = +42 ppm; C_Q = 3.3 MHz; η = 0.5

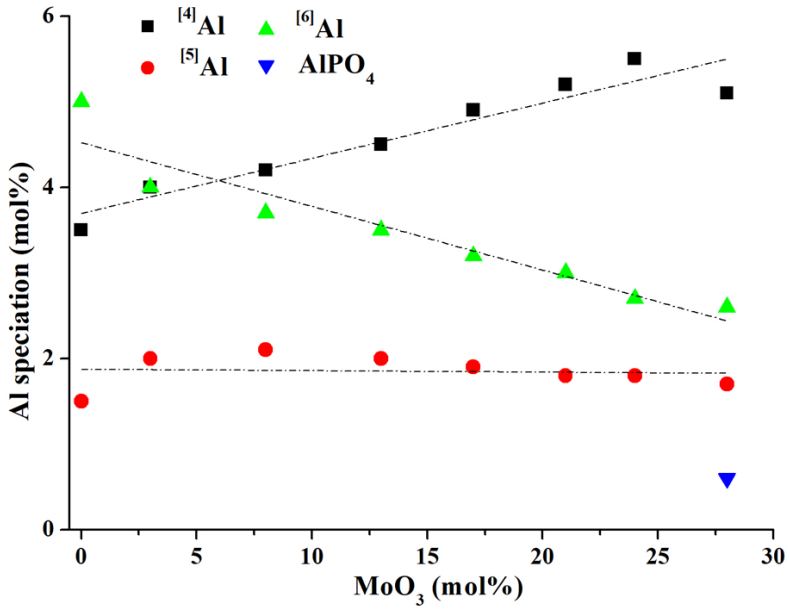

Figure 6.11. Changes in the Al speciation in series-2 glasses as a function of their MoO_3 content. Error bars are smaller than symbol size.

6.3.4 ^{31}P MAS NMR

The ^{31}P MAS NMR spectra of series-1 glasses exhibit broad featureless peaks (**Figure 6.12**), similar to the corresponding base glasses. B-0_{Mo13} exhibits a small peak at *ca.* -27 ppm, attributed to crystalline $AlPO_4$ [52]. Based on the speciation analysis of borophosphate and aluminophosphate glasses using Pauling bond strengths (**Chapter 5**), the phosphate species present in base-glass analogues of B-0_{Mo13} and B-20_{Mo13} have been identified to be P^3_{3Al}, P^3_{2Al} and P^2_{1B}, P^2_{2B} and P^3_{2B}, respectively (P^n_m, *n* = number of bridging oxygens; *m* = number of heteroatoms bonded to the phosphate unit). Briefly, the P^0_{3Al} and P^1_{2Al} predominantly consist of $^{[4]}$Al and $^{[6]}$Al species, respectively, whereas no such structural constraints are observed in borophosphates as $^{[4]}$B bonds to all phosphate units non-preferentially. The glasses with intermediate compositions have been proposed to consist of combinations of these species, with structural characteristics similar to aluminophosphate (B0) or borophosphate glasses (B20) depending on the B and Al mole fractions. With the addition of Mo to glasses possessing different B and Al mole fractions, the peak shifts slightly to higher frequencies with no appreciable changes in the peak shape. (**Figure 6.12**). The bonding of Mo to P is known to induce high-frequency shifts in ^{31}P NMR spectra [8,9,21,34]. Hence the observed shift in the peak position to higher frequencies in Mo-doped glasses vis-à-vis base glasses is strong evidence for the formation of P−O−Mo linkages.

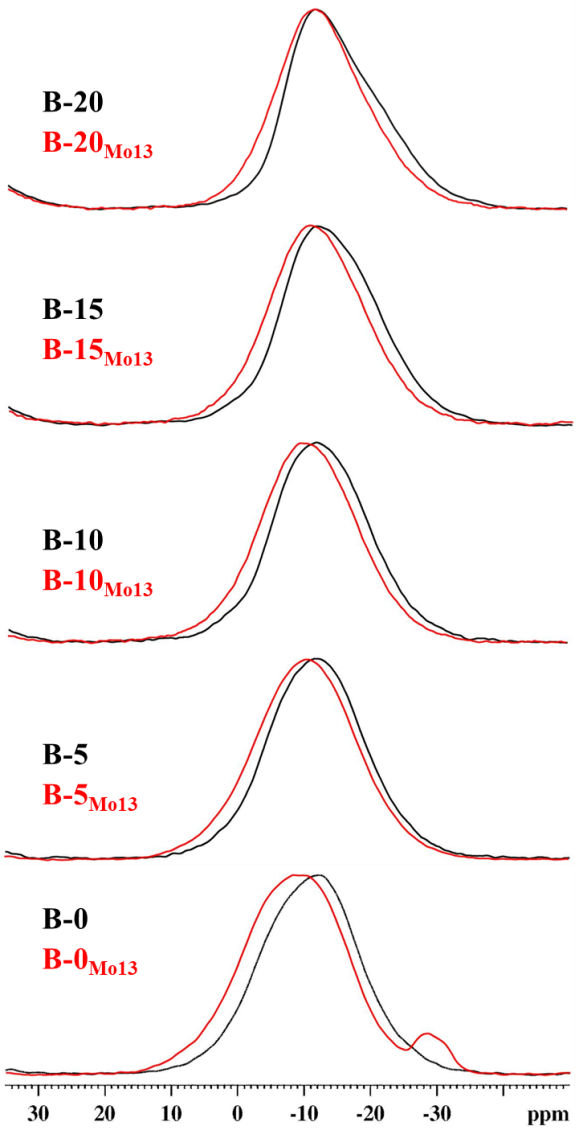

Figure 6.12. ^{31}P MAS NMR spectra of base glasses (black) and the Mo-loaded glasses (red).

The spectra of series-2 glasses are shown in **Figure 6.13** where it can be seen that the peak shifts progressively to higher frequencies with increasing Mo loading, representing the formation of P−O−Mo linkages, consistent with other Mo-bearing phosphate glasses [8,9,21,22,34,35]. In the spectrum of B-10$_{Mo28}$, a low-intensity peak at *ca.* -26 ppm representing crystalline $AlPO_4$ is observed. Since no appreciable peak shape changes are observed in this series, we have refrained from attempting to fit these spectra to estimate the relative populations of different phosphate units.

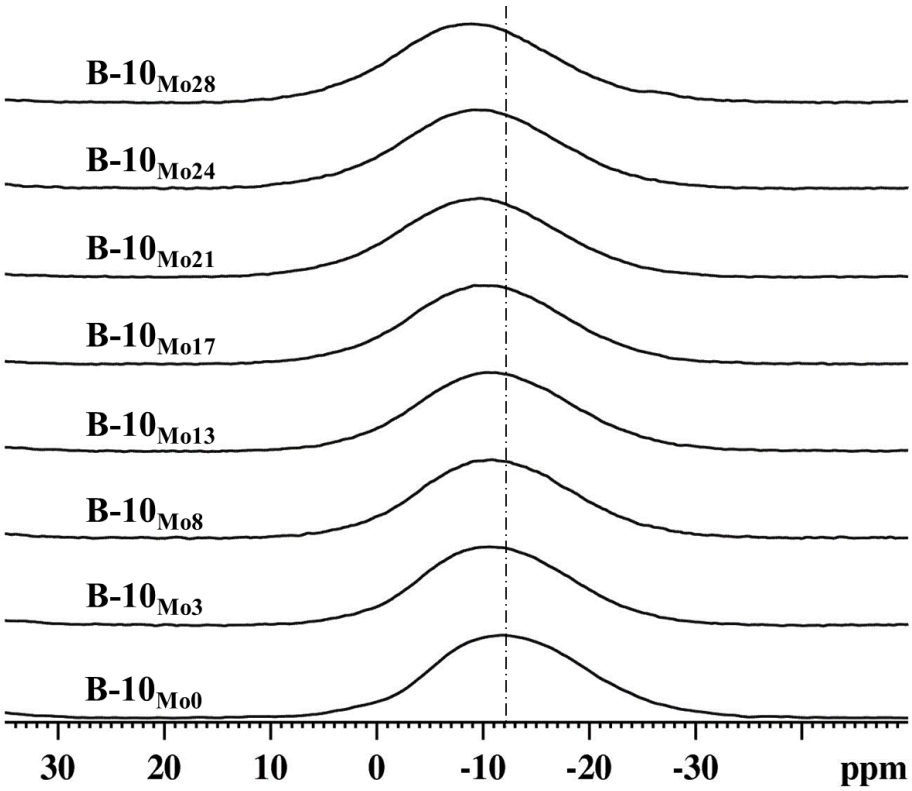

Figure 6.13. ^{31}P MAS NMR spectra of series-2 glasses. A line is drawn to guide the eye.

6.3.5 High-temperature MAS NMR

To assess the effect of canister-centerline temperature (*ca.* 400 °C) on the network structure of glasses and their tendency to phase separate, a sample with high Mo was chosen from the second series for variable-temperature NMR analysis. ^{23}Na MAS NMR spectra of B-10$_{Mo21}$ at different temperatures are displayed in **Figure 6.14**, which show significant changes over the temperature range probed. The peak shifts to lower frequency and its width narrows as the temperature of the sample is increased. The low-frequency shift suggests an increase in the coordination number of Na or an increase in the mean Na-O bond lengths, or both [47]. Narrowing of the peak is observed at higher temperatures, attributed to thermally induced motions of Na atoms, which leads to the coalescence of the NMR signals [40,44] which are otherwise dispersed due to the disordered chemical environment of Na^+ in glasses. No sign of devitrification of sodium-bearing crystalline phases is observed, which would likely manifest in the spectrum as a new peak with a

distinct isotropic shift and peak shape. As the temperature is decreased, the peak characteristics completely recover, matching the original spectrum (25 °C).

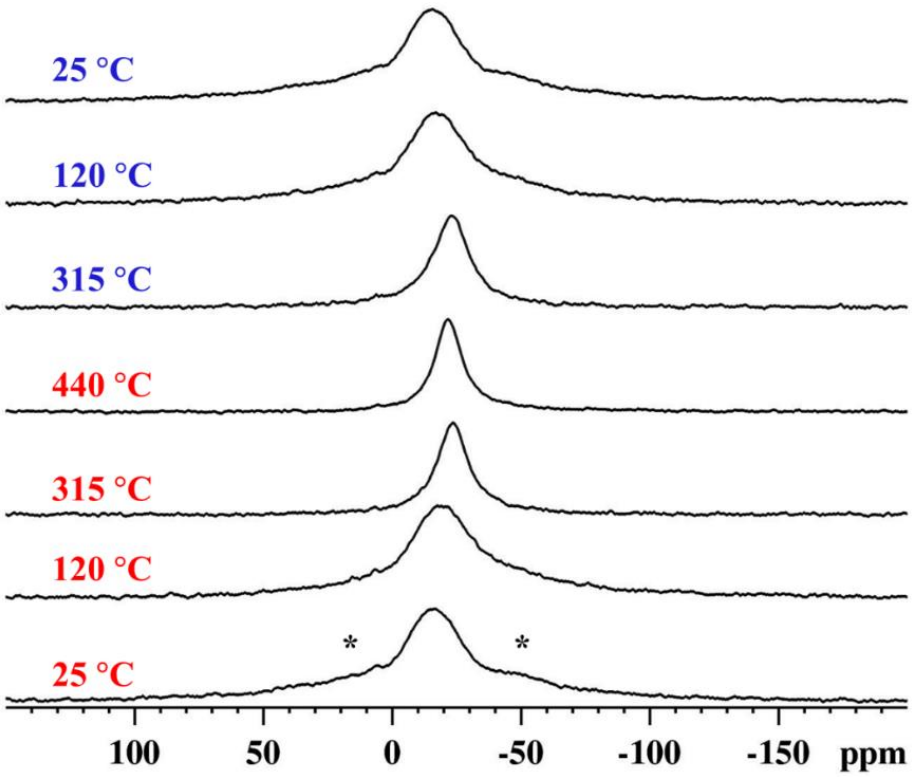

Figure 6.14. ^{23}Na MAS NMR spectra of B-10$_{Mo21}$ acquired at different temperatures. Temperatures during the heating (red) and cooling (blue) cycles at which the spectra were acquired are listed. Asterisks denote spinning sidebands.

^{31}P NMR spectra of the same sample obtained at different temperatures are plotted in **Figure 6.15**, which show no changes in the spectral features. In order to aid the fitting of these spectra and to determine the principal components of the chemical shift tensor, the spectrum obtained at a higher field with a faster spinning speed (14 T and 14 kHz, respectively) was deconvolved, yielding an isotropic shift (δ_{iso}) of -9.5 ppm, a span (Ω) of 151 ppm and a skew (κ) of 0.19 (**Figure 6.16**). These parameters were used to fit the lower-field spectra obtained at variable temperatures, an example of which is given in **Figure 6.16**. Whereas under normal circumstances, slower-spinning spectra should provide a more accurate measurement of the

chemical shift tensor components, repeated temperature cycling can cause magic-angle misalignment, consequently altering the relative intensities of the spinning sidebands and introducing errors into the fitting parameters. Although the fit does not exactly replicate the spectrum, negligible changes were observed in the fitting parameters for the spectra obtained at different temperatures, implying that no substantial structural changes occurred during heating.

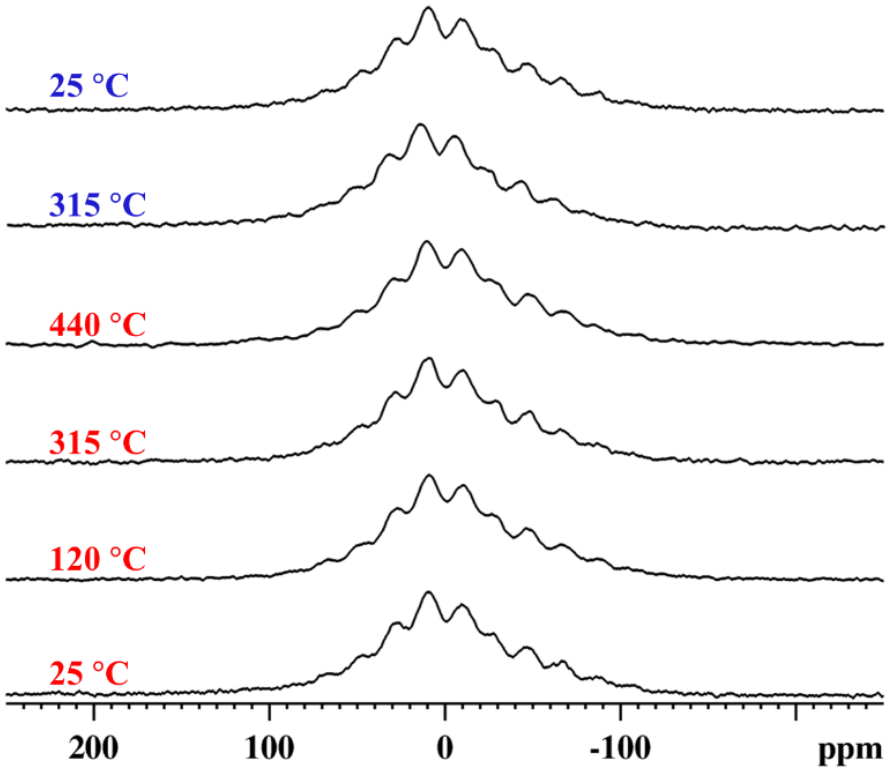

Figure 6.15. ^{31}P MAS NMR spectra of sample B-10$_{Mo21}$ at different temperatures. The top two spectra were acquired during the cooling cycle of the experiment.

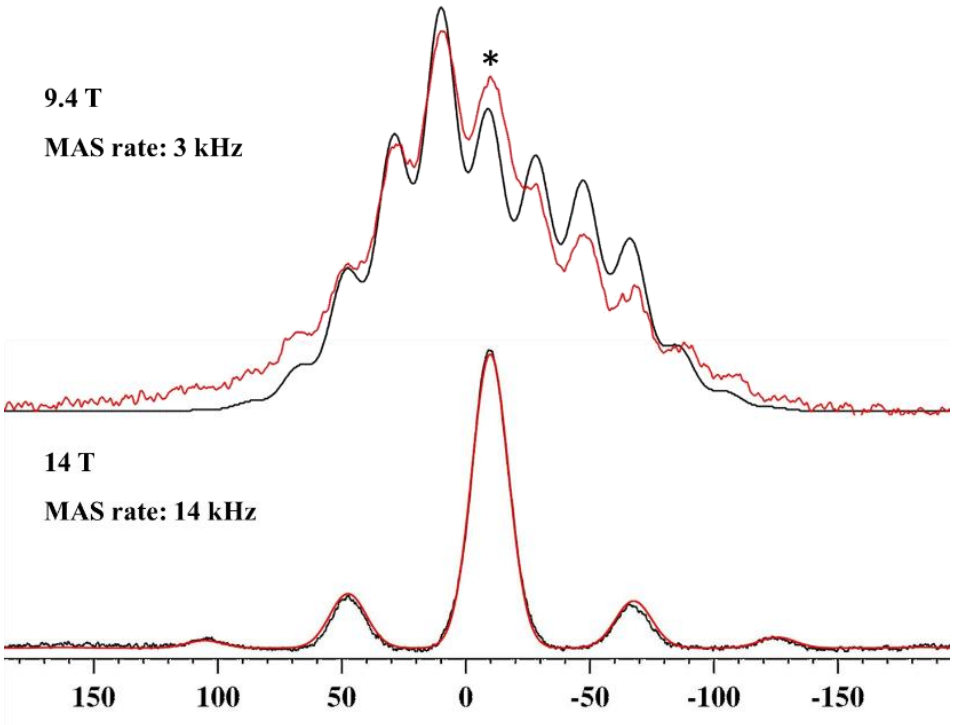

Figure 6.16. ^{31}P MAS NMR spectra of B-10$_{Mo21}$ (black) obtained at 9.4 T (top) and 14 T (bottom), and their deconvolutions (red) (δ_{iso} = -9.5 ppm; Ω = 151 ppm; κ = 0.19). The isotropic peak is marked with an asterisk.

6.4 P-O-Mo connectivity in crystalline and glassy phosphomolybdate systems

6.4.1 Crystalline phosphomolybdates

To better understand the nature of the bonding involving Mo and P, the network topology in alkali and alkaline-earth phosphomolybdates and binary phosphomolybdates is studied using the principles of the Pauling bond strength (PBS) model [55,56]. The chemical environment of Mo in aluminophosphate systems is also explored through aluminophosphomolybdate crystal structures. An attempt was made to include borophosphomolybdates in the analysis, but a search of the ICSD database returned only three matches, each of which possessed complex structural formulae and partial occupancies for the elements of interest; hence these compounds were not included in the analysis. The phosphomolybdates and aluminophosphomolybdates analyzed in terms of Pauling bond strengths are listed in **Table 6.6,** along with the phosphate speciation, the Mo oxidation states and coordination numbers, and the number of oxygens shared between P^{5+}

and Mo^{6+}, which represents the number of P−O−Mo linkages in the structure. The phosphate speciation is represented as $P^{n}_{x\mathrm{Mo}}$ in the case of phosphomolybdates and $P^{n}_{x\mathrm{Mo}y\mathrm{Al}}$ in aluminophosphomolybdates, where *n* is the number of total bridging oxygens per phosphate tetrahedron, *x* and *y* are the numbers of bridging oxygens shared by P with Mo and Al, respectively. Pauling bond strength distribution maps of selected crystal structures with Mo in different oxidation states (+3, +5, and +6) are presented in **Figure 6.17**. Since the MoO_6 octahedra ($^{[6]}$Mo) are distorted in most of these structures, the summation of the PBS distribution about the Mo−O bond represents the total valency contribution of Mo^{n+}; it does not accurately correspond to specific Mo−O bond lengths but results in an agreeable trend. Although this can be achieved by calculating the experimental bond valences using the reported bond lengths, the purpose of this structural analysis is to understand the P−O−Mo connectivity for different P/Mo ratios and Mo^{n+} oxidation states rather than demonstrating the validity of the PBS model.

Table 6.6. Phosphomolybdate and aluminophosphomolybdate crystal systems used in the analysis of the nature of bonding between phosphate and molybdate units.

Coll. Code[a]	**Structural formula**	$\mathbf{P^n_{xMo_yAl}}$	$\mathbf{(Mo^{n+})}$[b]	**P−O−Mo**[c]	**Mo−O−Mo**[d]	$\mathbf{^{[n]}Al}$[e]
17319 [57]	$LiK(MoPO_6)_2$	P^4_{4Mo}	+6	4		—
17747 [58]	$KCsMoP_2O_9$	P^3_{2Mo}	+6	4		—
24894 [59]	$MoPO_5$	P^4_{4Mo}	+5	4	2	—
63258 [60]	$Cs_2Mo_4P_6O_{26}$	P^4_{3Mo} + P^4_{4Mo}	+5	5		—
68469 [61]	$KMo_2P_3O_{13}$	P^4_{3Mo} + P^4_{4Mo}	+5	5		—
260578 [62]	$Mo_2P_4O_{15}$	P^4_{3Mo}	+5	5		—
75086 [63]	MoP_3O_9	P^4_{2Mo}	+3	6		—
49919 [64]	$CsMoP_2O_7$	P^4_{3Mo}	+3	6		—
67221 [65]	$MoAlP_2O_9$	P^4_{2Mo2Al}	+5	4	2	$^{[4]}Al$
79375 [66]	$Cs_9Mo_9Al_3P_{11}O_{59}$	P^4_{3Mo1Al}	+5	3	2	$^{[4]}Al$
80895 [67]	$K_2Cs_7Mo_9Al_3P_{11}O_{59}$	P^4_{3Mo1Al}	+5	3	2	$^{[4]}Al$
68501 [68]	$K_{0.5}Mo_{0.75}Al_{0.25}P_2O_7$	$P^4_{3Mo/Al}$		5		$^{[6]}Al$

[a]Inorganic Crystal Structure Database collection code
[b]Oxidation state of Mo
[c]Number of P−O−Mo linkages per MoO_6 octahedron
[d]Number of Mo−O−Mo linkages per MoO_6 octahedron
[e]Coordination number of Al^{3+}

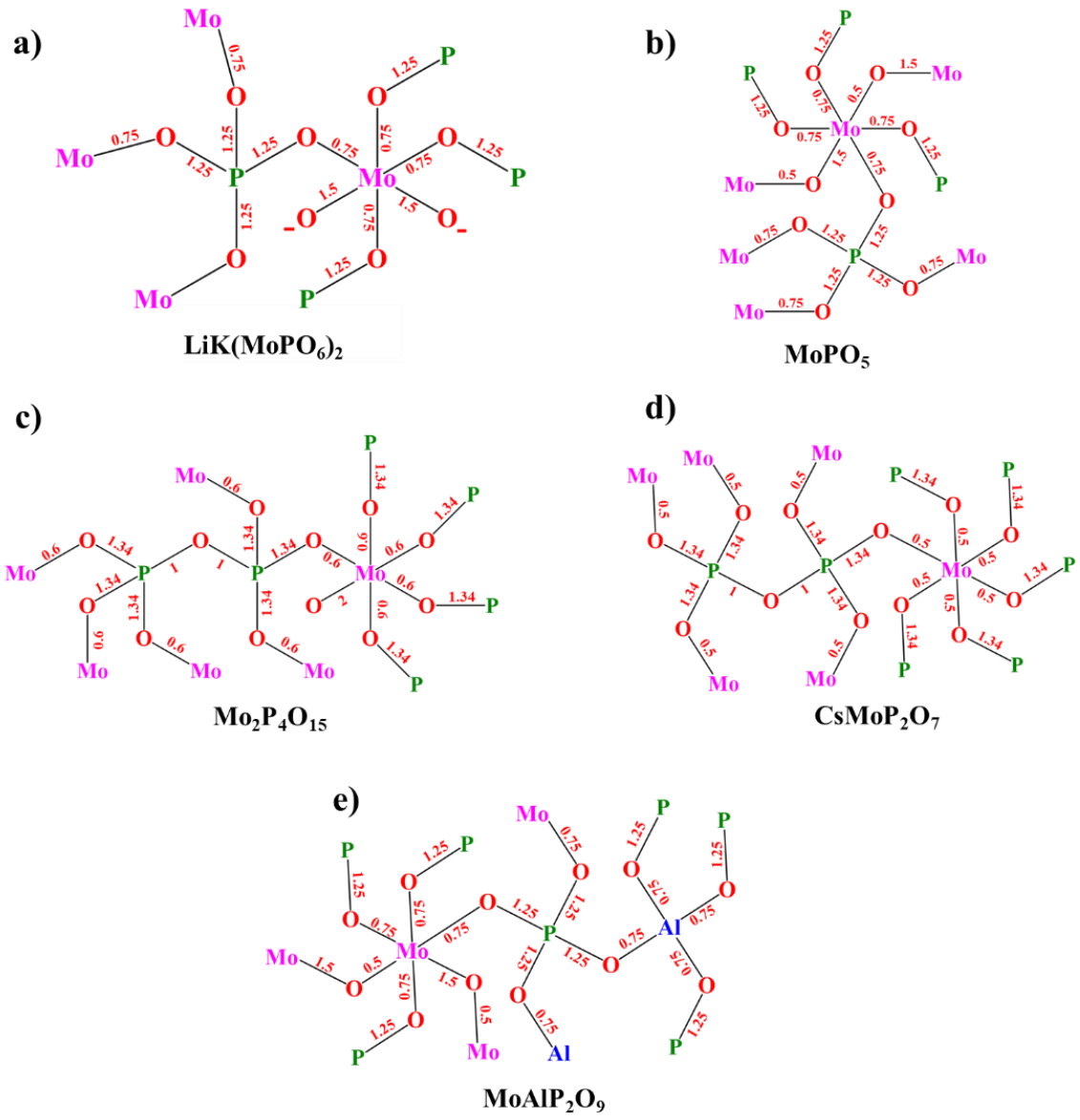

Figure 6.17. Pauling bond strength distribution maps of phosphomolybdate crystals and their network topologies.

Mo^{6+}: In ($LiK(MoPO_6)_2$ (**Figure 6.17a**), the Mo/P mole ratio is 1. All four oxygens of the phosphate tetrahedra are corner-shared with the MoO_6 octahedra, which share oxygens with four phosphate tetrahedra in total and consist of two non-bridging oxygens (NBO) that are charge-compensated by the modifier cations. When the ratio changes to 1:2 ($KCsMoP_2O_9$), P−O−P linkages appear in the network, with no change in the coordination environment of Mo.

Mo^{5+}: In modifier-free phosphomolybdates with a Mo:P ratio of 1 ($MoPO_5$, **Figure 6.17b**), each phosphate unit shares four oxygens with MoO_6 octahedra; Mo^{5+} is bonded to four phosphate tetrahedra and shares two oxygens with octahedral Mo units (Mo−O−Mo). The bond-valence contribution of Mo to each of its two Mo−O bonds in the Mo−O−Mo linkage is listed as 0.5 and 1 v.u., in accordance with the observed bond lengths of 2.64 and 1.65 Å, respectively. The valence contribution of Mo^{5+} to four P−O−Mo bonds is 0.75 v.u., consistent with the invariant Mo−O bond length of 1.97 Å. Upon introducing modifiers and increasing the Mo/P ratio (1:1.5) ($Cs_2Mo_4P_6O_{26}$ and $KMo_2P_3O_{13}$), two different phosphate species are observed which are bonded to Mo: PO_4 and P_2O_7. The MoO_6 octahedra consist of five P−O−Mo linkages and one NBO. At a Mo/P ratio of 1:2 ($Mo_2P_4O_{15}$, **Figure 6.17c**), only pyrophosphate groups are observed, with no change in the coordination environment of Mo.

Mo^{3+}: In phosphomolybdates with trivalent Mo, each phosphate unit is bonded to another phosphate group yielding the pyrophosphate configuration, which corner-shares oxygens with three MoO_6 octahedra ($CsMoP_2O_7$, **Figure 6.17d**). The Mo^{3+} shares six oxygens with P^{5+} and contributes 0.5 v.u. to each P−O−Mo linkage. The bridging oxygens are slightly underbonded, which is compensated by the modifier cations present in the network.

Aluminophosphomolybdates: In aluminophosphomolybdates ($MoAlP_2O_9$, **Figure 6.17e**), the Al^{3+} adopts a tetrahedral geometry with four phosphate units as the next-nearest neighbours. Each phosphate unit is bonded to two Al^{3+} and two Mo^{5+}. Each MoO_6 octahedron consists of four P−O−Mo and two Mo−O−Mo linkages. In alkali aluminophosphomolybdates ($Cs_9Mo_9Al_3P_{11}O_{59}$ and $K_2Cs_7Mo_9Al_3P_{11}O_{59}$), the coordination environments of P and Al remain the same but the number of P−O−Mo linkages decreases to three, and an NBO forms in the MoO_6 octahedra. In the crystal structure of $K_{0.5}Mo_{0.75}Al_{0.25}P_2O_7$, each MoO_6 octahedron is surrounded by six PO_4 tetrahedra, which are in turn bonded to three MoO_6 octahedra and one PO_4 tetrahedron. Two octahedral sites have been identified, wherein one site is occupied only by

Mo, and in the second site, Mo and Al are randomly distributed. Mo in Mo-only octahedral sites is tetravalent and is trivalent in the Al-substituted sites.

6.4.2 Coordination environment of Mo in phosphate glasses

The chemical environment of Mo and the nature of its bonding to phosphate units have been studied in phosphate glasses over wide compositional ranges [8,9,72–77,21–23,34,35,69–71], with most of these compositions capable of incorporating high fractions of MoO_3. The coordination number of Mo is subject to composition and bonding environment in glasses [75,77]. However, in the oxidizing conditions of phosphate glasses, Mo is predominantly hexavalent and is known to occupy octahedral sites in phosphate glasses and bond to phosphate units through P−O−Mo linkages [8,21–23,34,35]. Electron paramagnetic resonance studies of Mo-bearing phosphate glasses suggest that less than 2% of total Mo atoms are pentavalent [23,34], which sit in highly distorted MoO_6 octahedral sites, analogous to a square-pyramidal site with five-coordinated oxygens [23,74]. Upon adding MoO_3 to phosphate glasses, MoO_6 octahedra insert into metaphosphate chains wherein the Mo^{6+} bonds to the NBO of metaphosphate units, resulting in extensive crosslinking of the network due to P−O−Mo linkages [8,21,34,35]. The octahedral environment of Mo^{6+} is found to be invariant to the glass composition, with phosphate-only neighbours at lower Mo loading; beyond 40 mol%, Mo−O−Mo linkages are observed due to the clustering of molybdate polyhedra [8,35]. The addition of Cs_2O to phosphomolybdate glasses has been shown to have little effect on the length of the phosphate chains and phosphate anion distributions, as the modifier oxide is utilized in the formation of MoO_6 polyhedra and the Cs^+ ions associate with the Mo−O^- bonds (Mo−O^- Cs^+) [23]. A similar observation has been made in $NaPO_3$-MoO_3 glasses using $^{23}Na\{^{31}P\}$ rotational-echo double-resonance experiments, where the Na-P dipolar interaction is found to diminish with the MoO_3 addition, suggesting a partial transfer of Na^+ from phosphate to molybdate structural units and leading to partial repolymerization of the phosphate network [8]. Adding high fractions of MoO_3 to phosphate glasses depolymerizes the phosphate network and progressively transforms it in the order: metaphosphates → pyrophosphates → orthophosphates [21,22,34].

6.5 Discussion

6.5.1 Mo addition to glasses with different B/Al ratios

Despite a thorough understanding of Mo chemical environments in pure phosphate glasses, a clear interpretation of its local bonding environment in multicomponent phosphate glasses is lacking. Clues can be obtained from studying the P−Mo connectivity in crystalline phosphomolybdates and the structural information obtained from several phosphomolybdate glassy systems. Since Mo is predominantly hexavalent in phosphate glasses, the chemical environment of Mo can be expected to resemble that of $LiK(MoPO_6)_2$ and $KCsMoP_2O_9$ crystal systems where Mo^{6+} is bonded to PO_4 and P_2O_7 groups, respectively. In both cases, the MoO_6 consist of two NBO, with four oxygens corner-shared with neighbouring phosphate tetrahedra. The bond valence contribution of Mo^{6+} to bridging oxygens and NBO are 0.75 and 1.5 v.u., respectively, with the latter oxygen species charge-compensated by nearby modifier cations. This structural configuration holds for multicomponent glasses as well since the Mo bond only to phosphates, as observed in aluminophosphomolybdate crystal systems. In the crystal structures studied, Mo−O−Mo linkages are observed only in modifier-free systems ($MoPO_5$) and those with pentavalent Mo or higher-P mole fractions (P/Mo > 1). Although Mo−O−Mo linkages are observed in glasses with high Mo fractions, they are not expected in phosphate glasses studied here due to the higher oxidation state of Mo(VI) and low Mo:P mole ratio.

The glass series discussed in this chapter encompass aluminophosphate, borophosphate, and aluminoborophosphate glasses, the network structures of which have been characterized using multinuclear NMR spectroscopy, with Pauling bond strengths as a guide to select likely local structural units. Since the Al and P mole fractions in the base glasses of chapter 5 are similar to those discussed here and are meant to function as glass frits for Mo incorporation, the structural conclusions formed in the previous chapter are extended to the $B\text{-}X_{Mo13}$ glasses to discern the changes in network connectivity upon Mo incorporation.

The network of the sodium aluminophosphate glass (B0) consists of branched phosphates linked to $^{[4]}Al$ (P^3_{3Al}) and phosphate dimers linked to $^{[6]}Al$ (P^3_{2Al}) (**Figure 6.18**). The addition of Mo to B0 ($B\text{-}0_{Mo13}$) drives the conversion of $^{[6]}Al$ to $^{[4]}Al$ and the crystallization of $AlPO_4$. Pauling bond strength analysis of P^3_{3Al} and P^3_{2Al} bonded to $^{[6]}Mo$ reflects the fact that Mo polyhedra are inserted between the phosphate units and interact with the NBO, leading to the

transfer of Na^{+} from phosphate to molybdate polyhedra. Mo^{6+} contributes 0.75 v.u. to the P−O−Mo bond and 1.5 v.u. to the NBO in MoO_6, whereas P^{5+} donates 1.25 v.u. to the P−O−Mo bond and 1 v.u. to the P−O−P linkage (**Figure 6.18e**). The bonding of $^{[6]}Mo$ to P^{3}_{2Al} and P^{3}_{3Al} generates underbonded bridging oxygens (**Figures 6.18b and 6.18e**), but if $^{[6]}Al$ transforms to $^{[4]}Al$, the demand for bond-valence contribution from P^{5+} decreases from 1.5 to 1.25 v.u. leading to stable structures (**Figures 6.18c and 6.18f**). Hence, the fraction of $^{[4]}Al$ and increases upon Mo addition, which ultimately leads to the crystallization of $AlPO_4$, a modifier-free charge-neutral phase with alternating $[AlO_{4/2}]^{-}$ and $[PO_{4/2}]^{+}$ structural units [78].

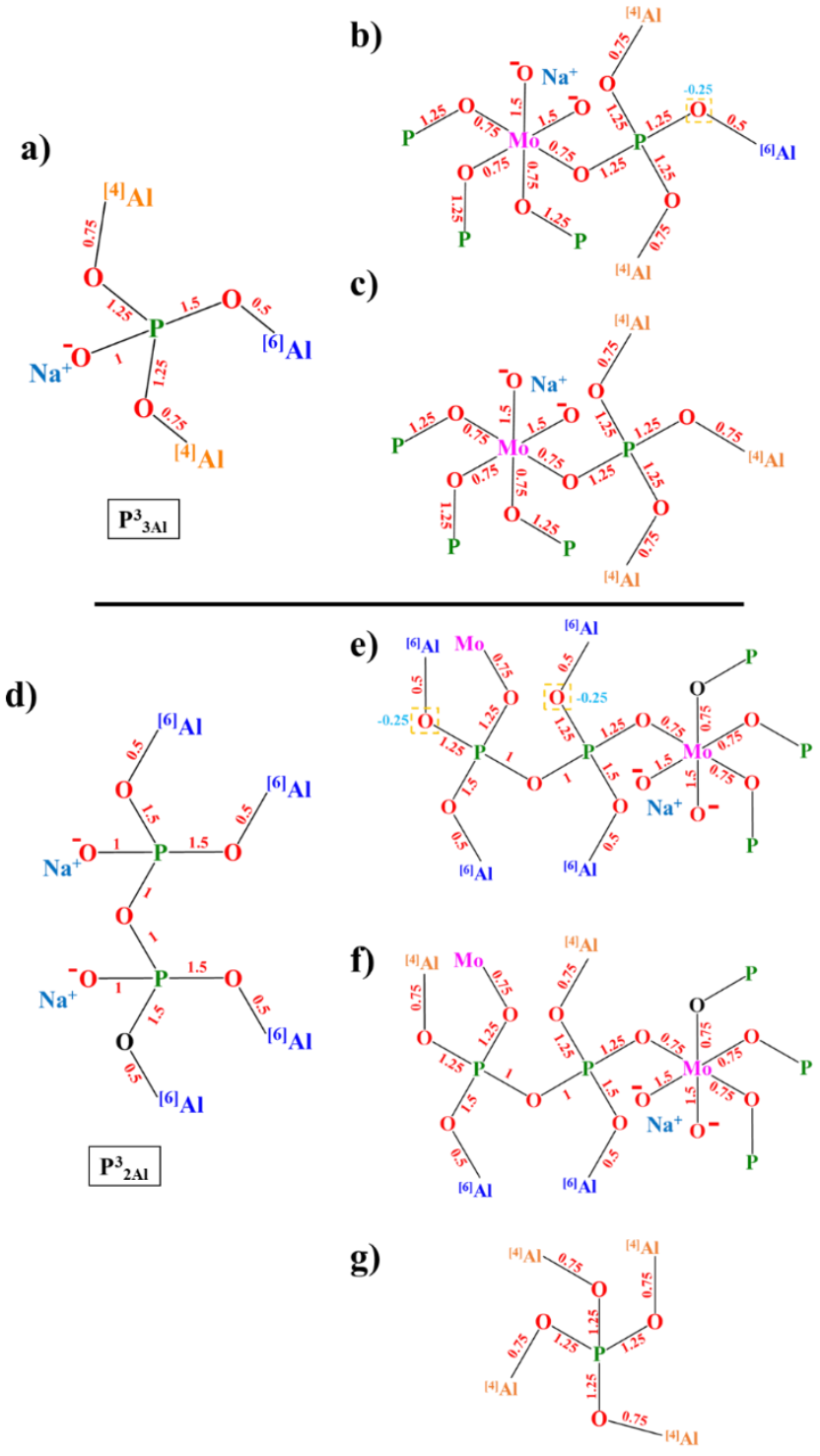

Figure 6.18. Pauling bond strength distribution maps of aluminophosphate and aluminophosphomolybdate clusters.

The addition of B_2O_3 to aluminophosphate glass (B5−B15**, Chapter 5**) reduces the structural ordering brought about by multiple Al coordination numbers and forces the conversion of $^{[6]}$Al to $^{[4]}$Al, as the latter is isostructural to $^{[4]}$B and helps in the formation of stable aluminoborophosphate clusters. This effect is further amplified by the addition of Mo, as bond-valence constraints do not allow the bonding of high-coordinate Al to phosphate clusters containing $^{[4]}$B (**Figure 6.19a**) or $^{[6]}$Mo (**Figure 6.18e**). Furthermore, Mo promotes the bonding of $^{[4]}$B to the pyrophosphate groups (**Figure 6.19c**), which is generally not favoured due to the excess valence contributions to the bridging oxygens. Substituting 5 mol% of Al_2O_3 with B_2O_3 (B-5_{Mo13}) quenches the crystallization of $AlPO_4$, which can be attributed to the disruption in the ordering of $[AlO_{4/2}]^-$ and $[PO_{4/2}]^+$ structural units by $[BO_{4/2}]^-$ in the network (**Figure 6.19b**). Since both $^{[4]}$Al and $^{[4]}$B contribute 0.75 v.u. to the Al(B)−O−P bonds, $[AlO_{4/2}]^-$ can be easily substituted by $[BO_{4/2}]^-$. A similar effect of boron on nepheline crystallization in aluminosilicate glasses is observed, wherein the trigonal-planar borate units intercalate between $[AlO_{4/2}]^-$ and $SiO_{4/2}$ and inhibit crystallization by disrupting the structural ordering [79]. The addition of Mo decreases the number of $^{[4]}B_{3P}$ and increases the fraction of $^{[4]}B_{2P}$. This reflects the similar bond-valence contributions of $^{[6]}$Mo and $^{[4]}$B (0.75 v.u.) as $^{[6]}$Mo can readily substitute for $^{[4]}$B in the network, thereby decreasing the average number of next-nearest borate neighbours in the local chemical environment of phosphates.

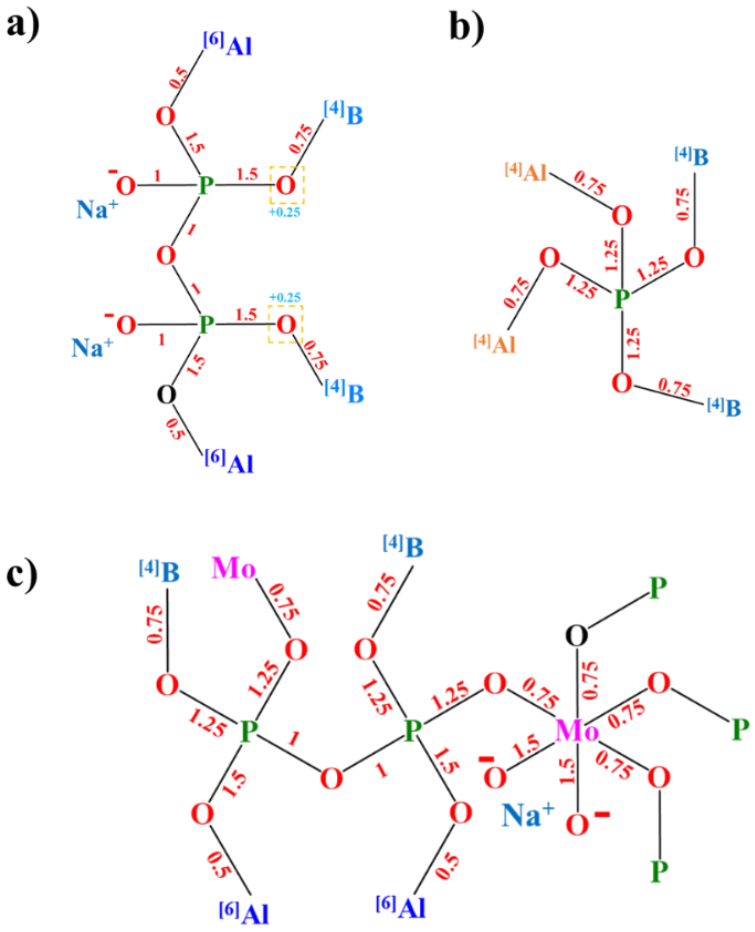

Figure 6.19. Pauling bond strength distribution maps showing the incorporation of borate units into phosphate clusters bonded to Al and Mo units.

Information on Mo chemical environments in borophosphates glasses is scant, with those few studies involving Mo-doped borophosphates postulating the presence of B−O−Mo linkages [9,34]. Due to the lack of borophosphomolybdate crystal structures, a qualitative assessment of the presence of such linkages using Pauling bond strengths cannot be made. Instead, it may be assumed that the coordination environment of B is generally the same as Al in aluminophosphomolybdates, since both network formers have the same bond strength contributions (0.75 v.u.) and form tetrahedral structural units. The absence of B−O−Mo linkages at low Mo fractions and the conditions required for their formation at high Mo loading can be explained based on the bond-strength analysis of B-bearing phosphomolybdate structures

(**Figure 6.20**). Substituting one P−O−Mo with a $^{[4]}$B−O−Mo linkage leads to severe underbonding of the bridging oxygen and hence the formation of such clusters is energetically unfavourable (**Figure 6.20a**). However, if one of the NBO in MoO_6 becomes bridging and is shared between two $^{[6]}$Mo, a case observed in glasses with high Mo fractions, the bond-valence contribution of Mo^{6+} to the B−O−Mo linkage increases, thereby stabilizing the clusters (**Figure 6.20b**). Nevertheless, the presence of Mo−O−Mo linkages is crucial for B−O−Mo bonds to form in the network. In such cases, Mo^{6+} may function similarly to P^{5+}, as both contribute 1.25 v.u. to the X−O−B linkages, which may translate spectroscopically as low-frequency shifts for $^{[4]}$B. Hence, the ^{11}B MAS NMR assignments made in previous works [9,34] postulating the formation of $^{[4]}B(OP)_{4-x}(OMo)_x$ units can be deemed incorrect wherein a new peak was observed at higher frequencies upon Mo addition. Therefore the peak observed at +0.8 ppm in the high field (20 T) ^{11}B MAS NMR spectrum of B-10_{Mo21} is assigned to $^{[4]}B_{1P}$.

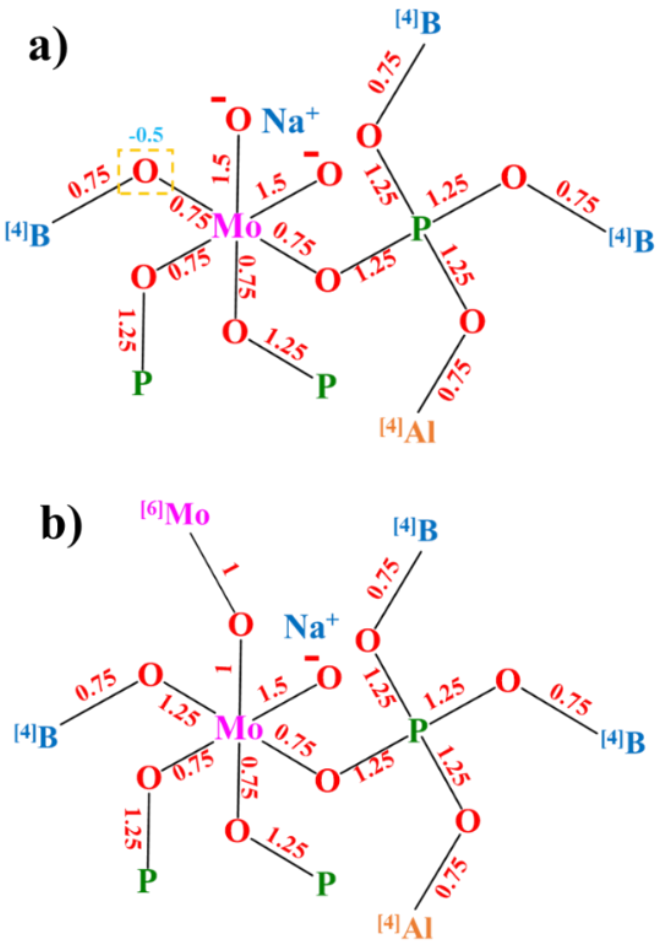

Figure 6.20. Bond-strength distribution scenarios required for the formation of B−O−Mo linkages in the glass network.

In the base glasses, the ^{31}P MAS NMR peak shift to lower frequencies with the substitution of Al_2O_3 by B_2O_3 was attributed to the formation of P−O−P linkages (**chapter 5**), as phosphate clusters stabilize the underbonded bridging oxygens in $^{[4]}$B−O−$^{[4]}$B linkages through multiple bond strength contributions. A similar observation has been made for Mo-bearing glasses, although the shift is subtle compared to the base glasses. In phosphomolybdate glasses, the addition of Mo is known to substitute P−O−P with P−O−Mo linkages, which shifts the ^{31}P NMR peaks to higher frequencies [8,9,21,34]. The Al and B speciation in aluminophosphate [80] and borophosphate [81] glasses is known to be composition dependent as it changes with the B(Al):P mole ratio and influences the ^{31}P shift significantly. Due to the high

phosphate content of the series 1 and 2 glasses, the phosphate network can be expected to host enough binding sites (NBO) for Mo incorporation, without leading to the substitution of P−O−P bonds with P−O−Mo, at least at lower Mo loading. Aluminoborophosphate glasses from the two series studied here show significant changes in the B and Al speciation upon Mo addition and hence may contribute to the changes in ^{31}P shifts. Therefore the observed differences in the ^{31}P NMR shifts between the base glasses and their Mo-containing analogues can be attributed to changes in the B and Al speciation and the formation of P−O−Mo linkages, with the substitution of P−O−P with P−O−Mo taking effect only at high-Mo loading.

^{95}Mo MAS NMR is an attractive method to study the coordination environment of Mo in glasses, and several articles on the geometry of Mo sites in silicate glasses have been published which show that Mo exclusively adopts tetrahedral coordination in silicate glasses [4,31–33] and crystalline molybdates [82]. However, studies employing ^{95}Mo NMR to determine the coordination environment of Mo in phosphate glasses are scarce and the assignments are ambiguous [8,34,35]. Santagneli *et al.* [8] originally suggested that Mo predominantly adopts tetrahedral geometry along with some octahedral Mo in $NaPO_3$-MoO_3 glasses, an interpretation which was subsequently revised to specify solely octahedral Mo based on $AgPO_3$-MoO_3 glasses [35]. In work by Tricot *et al.* [34], the ^{95}Mo spectra of Mo-bearing borophosphate glasses were interpreted as tetrahedral Mo based on the earlier work of Santagneli *et al.* [8]. From the structural analysis of crystalline and glassy phosphomolybdate systems, it can be inferred that Mo is incorporated into phosphate glasses as octahedral structural units. The observed shifts in the ^{95}Mo MAS NMR spectra acquired for two samples appear at lower frequencies with respect to the four-coordinate molybdates found in crystalline molybdates and silicate systems. Hence the broad peak centered at *ca.* -110 ppm in the ^{95}Mo MAS NMR spectra of 8 and 21 wt% MoO_3 loaded glasses is attributed to Mo^{6+} coordinated to six oxygens, unlike in the work of Tricot *et al.* [34], where the CPMG spikelet with a center-of-gravity shift of ca. -150 ppm was assigned to tetrahedral Mo.

6.5.2 Mo loading limit

The maximum Mo loading capacity of aluminoborophosphate glasses is tested in the second series wherein the B-to-Al ratio is fixed and Mo added in increments up to 28 wt%. Progressive addition of Mo leads to a decrease in the $^{[6]}$Al fraction with a concomitant increase in the number of $^{[4]}$Al in the network. This has been attributed to the inability of $^{[6]}$Mo to bond to phosphate clusters with high-coordinate Al due to bond-strength constraints (vide supra). Furthermore, the peaks in the ^{31}P MAS NMR spectra shift to higher frequencies with Mo addition, which signifies the formation of P−O−Mo linkages. Mo incorporation affects the boron speciation profoundly wherein the fraction of $^{[4]}B_{3P}$ decreases constantly with a concomitant increase in the $^{[4]}B_{2P}$ and $^{[3]}$B fraction. Due to the favourable bonding of Mo to phosphate units, the increased addition of Mo scavenges all possible binding sites on phosphates, leading to a reduction in the number of phosphate units bonded to $^{[4]}$B. As a result, the fraction of $^{[4]}B_{3P}$ decreases and those bonded to fewer phosphate units (i.e., $^{[4]}B_{2P}$ and $^{[3]}$B) increase.

Crystallization of $AlPO_4$ is observed at 28 wt% Mo loading, even in the presence of boron, reaching the limit of boron's ability to inhibit crystallization and marking the upper Mo loading limit in multicomponent aluminoborophosphate glasses with equal moles of B and Al. This loading limit is much lower than that of binary phosphomolybdate glasses, which can be attributed to competition with borate and aluminate units for phosphate binding sites. Although no crystalline molybdate phases were observed, devitrification of $AlPO_4$ limits the amount of Mo that can be added, as phase-separated glasses are not ideal for waste-immobilization applications.

For a glass to be considered as a waste-immobilization matrix, the glass-transition temperature (T_g) and the crystallization temperatures (T_c) of possible devitrification products must be higher than the canister-centerline temperatures so that the network structure remains intact even during radiolytic heating. In-situ high-temperature NMR studies of several alkali aluminophosphate [42,45,46] and zinc phosphate [43] glasses have been reported wherein the evolution of the aluminophosphate network structure has been tracked through ^{31}P MAS NMR as a function of temperature. The T_g of these glass systems is in the range of 200 to 350 °C, beyond which crystallization of aluminophosphate phases has been observed spectroscopically [45,46]. Beyond the T_g, the network of these glasses undergoes reorganization due to the breakage and formation of the P−O−P and P−O−Al bonds, leading to dynamic phosphate speciation at higher

temperatures. High-temperature ^{23}Na NMR has been used to characterize Na-bearing silicate systems where low-frequency shifts in the peak position are attributed to the mobility of the cation, resulting in an increase in the Na−O bond length and the coordination number [47]. Higher temperatures reduce the peak widths, which has been attributed to the averaging of distinct chemical environments, leading to the coalescence of peaks arising from these environments into sharp resonances. ^{23}Na relaxation rates and diffusive and vibrational motions of Na^+ at high temperatures have been well characterized in silicate systems [39,40,44]. The vibrational motion refers to the rattling of Na^+ at constricted sites and diffusive motion involves non-periodic motion of the cation in the network with a cooperative motion of network constituent atoms, representative of changes in the network structure. At low temperatures ($T<T_g$), vibrational motion dominates, which is limited to the rattling of the cation in its coordination shell, whereas at higher temperatures, diffusion takes over [44].

Negligible changes are observed in the ^{31}P MAS NMR spectra of the B-10_{Mo21} at higher temperatures, which implies that there is no major reorganization of the phosphate network. Since structural modifications occur beyond the T_g of the glasses, the HT-NMR results suggest that the aluminoborophosphate glasses have a T_g higher than 400 °C, which may be attributed to the strengthening of the network due to B−O−P and Al−O−P linkages vis-à-vis binary phosphate glasses. Although the peak width decreases and the peak shifts to lower frequencies in the ^{23}Na NMR spectra with increasing temperature, spectroscopic evidence of Na present in multiple distinct chemical environments is not observed. This further implies that the aluminoborophosphate glasses resist devitrification of Na-bearing crystalline phases at canister-centerline temperatures, underscoring the suitability of aluminoborophosphate glasses as hosts for nuclear waste immobilization.

6.6 Structural summary

Due to the strong tendencies of borate, aluminate, and phosphate units to intermix, the network structure of aluminoborophosphate glasses is highly intricate. The structural conclusions made for aluminoborophosphate glasses using multinuclear NMR spectroscopy and Pauling bond strength models in the previous chapter provide valuable insight on the preferred connectivity between the structural units and their composition-dependent speciation. These are used to

discern the structural changes occurring upon the incorporation of Mo, and its mode of integration into the glass network.

Structural analysis of phosphomolybdate and Mo-bearing phosphate glasses provides a clear understanding of Mo coordination environments in phosphate systems, which show a dependence on both oxidation state and the Mo:P ratio. The PBS analysis of phosphomolybdate crystal structures and the reported network structures of Mo-bearing glasses suggest that Mo is predominantly hexavalent in phosphate glasses and is incorporated into the phosphate network as octahedral units. Mo interacts with the NBO of phosphate units, inserting through P−O−Mo linkages and drawing the charge-compensating cations into its coordination shell. In alkali phosphomolybdate crystals and glasses, the Mo octahedra include non-bridging oxygens, which are charge-compensated by alkali cations sequestered from phosphate units. If the glass network is phosphate- and alkali-rich, the influence of Mo on the phosphate speciation is weak, as there are more than enough binding sites available for Mo. But at lower P/Mo ratios, the replacement of P−O−P linkages by P−O−Mo is observed, which may be interpreted as depolymerization of the phosphate network, despite the fact that the fraction of bridging oxygens will not decrease. The ^{95}Mo MAS NMR spectral comparison between silicate and phosphate systems reveals striking differences, with the peak in phosphate glasses appearing at a diagnostically lower frequency with respect to that of the tetrahedral molybdates found in silicates, substantiating the octahedral environment of Mo. Further, the breadth of the peaks (**Figure 1**) imply a large geometrical distribution of sites and anisotropic shielding effects, consistent with the observations made for octahedral Mo with four bridging and two non-bridging oxygens [35].

The addition of Mo to glasses with different B/Al mole ratios (series 1) shows a profound effect on the speciation of the glass network constituents compared to the Mo-free base glasses. The Mo-doped glasses exhibit a greater conversion of $^{[6]}$Al to $^{[4]}$Al compared to the base glasses, and a lower number of next-nearest phosphate neighbours in the local environment of $^{[4]}$B. Crystallization of $AlPO_4$ is observed in the B-free glass and at high Mo loading. Pauling bond strength analysis of aluminoborophosphate clusters bearing Mo provides valuable insights into the observed changes in the speciation, wherein the formation of underbonded bridging oxygens is expected in the clusters bearing $^{[6]}$Al. Hence $^{[6]}$Al is converted to $^{[4]}$Al, the fraction of which in the network increases leading to the crystallization of $AlPO_4$. Interestingly, addition of B inhibits

this crystallization, which has been attributed to the interruption in the $[AlO_{4/2}]^-$ and $[PO_{4/2}]^+$ structural ordering brought about by the insertion of $[BO_{4/2}]^-$, which is isostructural to $[AlO_{4/2}]^-$. In the second series, crystallization of $AlPO_4$ is observed at 28 wt% Mo loading, even in the presence of boron, reaching the limit of boron's ability to inhibit crystallization and marking the upper Mo loading limit. This limit is lower than that of binary phosphate glasses and may be attributed to competition with borate and aluminate units for phosphate binding sites. The bonding of Mo to phosphate groups replaces some of the B−O−P linkages with Mo−O−P and decreases the number of next-nearest phosphate neighbours in the local chemical environment of $^{[4]}B$. As a result, the fraction of $^{[4]}B_{2P}$ increases, with a parallel increase in $^{[3]}B$. Using Pauling bond strength models of clusters involving B, Mo and P, the existence of B−O−Mo linkages proposed by few recent studies was tested, showing that the presence of Mo−O−Mo linkages is required to favour the bonding of borate and molybdate units, possible only in high-Mo glasses where Mo−O−Mo clustering exists. Since this conclusion contradicts earlier NMR-based structural models, a reinterpretation of previous NMR data has been proposed using the bond-strength contributions of B, P and Mo, to rationalize the observed $^{[4]}B$ chemical shifts.

The presence of B−O−P and Al−O−P linkages in aluminoborophosphate glasses increases the overall network reticulation relative to binary phosphate systems, increasing their T_g values. This is reflected in NMR data recorded at canister-centerline temperatures, where no evidence of changes to the network structure is observed, and the glasses are found to be resistant to devitrification. Further, the addition of Mo is also expected to contribute to the strengthening of the aluminoborophosphate glass network through the formation of P−O−Mo bonds, consistent with the observation that Mo-loaded phosphate glasses have higher glass-transition temperatures [8].

6.7 References

[1] S. Gin, P. Jollivet, M. Tribet, S. Peuget, S. Schuller, Radionuclides containment in nuclear glasses: An overview, Radiochim. Acta. 105 (2017) 927–959.

[2] D. Kim, A.A. Kruger, Volatile species of technetium and rhenium during waste vitrification, J. Non-Cryst. Solids. 481 (2018) 41–50.

[3] G. Calas, M. Le Grand, L. Galoisy, D. Ghaleb, Structural role of molybdenum in nuclear glasses: An EXAFS study, J. Nucl. Mater. 322 (2003) 15–20.

[4] B.J. Greer, S. Kroeker, Characterisation of heterogeneous molybdate and chromate phase assemblages in model nuclear waste glasses by multinuclear magnetic resonance spectroscopy, Phys. Chem. Chem. Phys. 14 (2012) 7375–7383.

[5] P.A. Bingham, R.J. Hand, Sulphate incorporation and glass formation in phosphate systems for nuclear and toxic waste immobilization, Mater. Res. Bull. 43 (2008) 1679–1693.

[6] J.D. Vienna, D.S. Kim, I.S. Muller, G.F. Piepel, A.A. Kruger, Toward understanding the effect of low-activity waste glass composition on sulfur solubility, J. Am. Ceram. Soc. 97 (2014) 3135–3142.

[7] D. Boudlich, L. Bih, M. El Hassane Archidi, M. Haddad, A. Yacoubi, A. Nadiri, B. Elouadi, Infrared, Raman and electron spin resonance studies of vitreous alkaline tungsten phosphates and related glasses, J. Am. Ceram. Soc. 85 (2002) 623–630.

[8] S.H. Santagneli, C.C. De Araujo, W. Strojek, H. Eckert, G. Poirier, S.J.L. Ribeiro, Y. Messaddeq, Structural studies of $NaPO_3$-MoO_3 glasses by solid-state nuclear magnetic resonance and Raman spectroscopy, J. Phys. Chem. B. 111 (2007) 10109–10117.

[9] J. Šubčík, L. Koudelka, P. Mošner, L. Montagne, B. Revel, I. Gregora, Structure and properties of MoO_3-containing zinc borophosphate glasses, J. Non-Cryst. Solids. 355 (2009) 970–975.

[10] W. Huang, D.E. Day, C.S. Ray, C.W. Kim, A. Mogus-Milankovic, Vitrification of high chrome oxide nuclear waste in iron phosphate glasses, J. Nucl. Mater. 327 (2004) 46–57.

[11] T. Lemesle, F.O. Méar, L. Campayo, O. Pinet, B. Revel, L. Montagne, Immobilization of radioactive iodine in silver aluminophosphate glasses, J. Hazard. Mater. 264 (2014) 117–126.

[12] I.W. Donald, B.L. Metcalfe, R.N.J. Taylor, Review: The immobilization of high level radioactive wastes using ceramics and glasses, J. Mater. Sci. 32 (1997) 5851–5887.

[13] R.K. Brow, Review: the structure of simple phosphate glasses, J. Non-Cryst. Solids. 263–264 (2000) 1–28.

[14] N.J. Kreidl, W.A. Weyl, Phosphates in ceramic ware: IV, Phosphate glasses, J. Am. Ceram. Soc. 24 (1941) 221–225.

[15] R.K. Brow, Nature of alumina in phosphate glass: I, Properties of sodium aluminophosphate glass, J. Am. Ceram. Soc. 76 (1993) 913–918.

[16] J.F. Ducel, J.J. Videau, Physical and chemical characterizations of sodium borophosphate glasses, Mater. Lett. 13 (1992) 271–274.

[17] D. Carta, D. Qiu, P. Guerry, I. Ahmed, E.A. Abou Neel, J.C. Knowles, M.E. Smith, R.J. Newport, The effect of composition on the structure of sodium borophosphate glasses, J. Non-Cryst. Solids. 354 (2008) 3671–3677.

[18] H. Takebe, T. Harada, M. Kuwabara, Effect of B_2O_3 addition on the thermal properties and density of barium phosphate glasses, J. Non-Cryst. Solids. 352 (2006) 709–713.

[19] J.H. Hsu, J. Bai, C.W. Kim, R.K. Brow, J. Szabo, A. Zervos, The effects of crystallization and residual glass on the chemical durability of iron phosphate waste forms containing 40 wt% of a high MoO_3 Collins-CLT waste, J. Nucl. Mater. 500 (2018) 373–380.

[20] J.D. Vienna, Nuclear waste vitrification in the United States: Recent developments and future options, Int. J. Appl. Glas. Sci. 1 (2010) 309–321.

[21] L. Koudelka, I. Rösslerová, J. Holubová, P. Mošner, L. Montagne, B. Revel, Structural study of PbO-MoO_3-P_2O_5 glasses by Raman and NMR spectroscopy, J. Non-Cryst. Solids. 357 (2011) 2816–2821.

[22] J. Šubčík, L. Koudelka, P. Mošner, L. Montagne, G. Tricot, L. Delevoye, I. Gregora,

Glass-forming ability and structure of ZnO-MoO_3-P_2O_5 glasses, J. Non-Cryst. Solids. 356 (2010) 2509–2516.

[23] J. Bai, J. Hsu, P. Sandineni, C.W. Kim, R.K. Brow, The structure and properties of cesium loaded Mo-Fe-phosphate glasses, J. Non-Cryst. Solids. 510 (2019) 121–129.

[24] G.E. Brown, F. Farges, G. Calas, X-Ray scattering and X-Ray spectroscopy studies of silicate melts, in: *Structure, dynamics, and properties of silicate melts*, J.F. Stebbins, P.F. McMillan, D.B. Dingwell (Eds.), De Gruyter, Berlin, Germany, 1995: pp. 317–410.

[25] O.C. Gagné, F.C. Hawthorne, Bond-length distributions for ions bonded to oxygen: Metalloids and post-Transition metals: Metalloids, Acta Crystallogr. Sect. B Struct. Sci. Cryst. Eng. Mater. 74 (2018) 63–78.

[26] O.C. Gagné, F.C. Hawthorne, Bond-length distributions for ions bonded to oxygen: Results for the non-metals and discussion of lone-pair stereoactivity and the polymerization of PO_4, Acta Crystallogr. Sect. B Struct. Sci. Cryst. Eng. Mater. 74 (2018) 79–96.

[27] O.C. Gagné, F.C. Hawthorne, Bond-length distributions for ions bonded to oxygen: Results for the transition metals and quantification of the factors underlying bond-length variation in inorganic solids, IUCrJ. 7 (2020) 581–629.

[28] S. Kroeker, Nuclear waste glasses: Insights from solid-state NMR, Encycl. Magn. Reson. (2011) 453–466.

[29] S. Kroeker, Nuclear Magnetic Resonance spectroscopy of glasses, in: *Modern glass characterization*, M. Affatigato (Ed.), John Wiley & Sons, Inc., 2015: pp. 315–344.

[30] K.J.D. Mackenzie, M.E. Smith, NMR of low-gammanuclides, in: R.W. Cahn (Ed.), Multinucl. Solid-State NMR Inorg. Mater., Pergamon m, Elsevier, Oxford, UK, 2002: pp. 461–526.

[31] S. Kroeker, I. Farnan, S. Schuller, T. Advocat, ^{95}Mo NMR study of crystallization in model nuclear waste glasses, Mater. Res. Soc. Symp. Proc. 53 (2009) 1124.

[32] C. Martineau, V.K. Michaelis, S. Schuller, S. Kroeker, Liquid-liquid phase separation in

model nuclear waste glasses: A solid-state double-resonance NMR study, Chem. Mater. 22 (2010) 4896–4903.

[33] M. Magnin, S. Schuller, C. Mercier, J. Trébosc, D. Caurant, O. Majérus, F. Angéli, T. Charpentier, Modification of molybdenum structural environment in borosilicate glasses with increasing content of boron and calcium oxide by ^{95}Mo MAS NMR, J. Am. Ceram. Soc. 94 (2011) 4274–4282.

[34] G. Tricot, K. Ben Tayeb, L. Koudelka, P. Mosner, H. Vezin, Insertion of MoO_3 in borophosphate glasses investigated by magnetic resonance spectroscopies, J. Phys. Chem. C. 120 (2016) 9443–9452.

[35] S.H. Santagneli, J. Ren, M.T. Rinke, S.J.L. Ribeiro, Y. Messaddeq, H. Eckert, Structural studies of $AgPO_3$-MoO_3 glasses using solid state NMR and vibrational spectroscopies, J. Non-Cryst. Solids. 358 (2012) 985–992.

[36] M.I. Ojovan, W.E. Lee, Immobilisation of radioactive wastes in glass, in: *An Introduction to nuclear waste immobilization*, 2nd ed., Elsevier, Oxford, UK, 2005: pp. 213–248.

[37] S.C. Slate, W.A. Ross, W.L. Partain, Reference commerical high-level waste glass and canister definition, Richland, Washington, USA, 1981.

[38] J.F. Stebbins, J.B. Murdoch, E.Scheider, I.S.E. Carmichael, A. Pines, A high-temperature high-resolution NMR study of ^{23}Na, ^{27}Al and ^{29}Si in molten silicates, Nature. 314 (1985) 1984–1986.

[39] S.B. Liu, A. Pines, M. Brandriss, J.F. Stebbins, Relaxation mechanisms and effects of motion in albite ($NaAlSi_3O_8$) liquid and glass: A high temperature NMR study, Phys. Chem. Miner. 15 (1987) 155–162.

[40] X. Xue, J.F. Stebbins, ^{23}Na NMR chemical shifts and local Na coordination environments in silicate crystals, melts and glasses, Phys. Chem. Miner. 20 (1993) 297–307.

[41] J.F. Stebbins, S.E. Ellsworth, Temperature effects on structure and dynamics in borate and borosilicate liquids: High-resolution and high-temperature NMR results, J. Am. Ceram. Soc. 79 (1996) 2247–2256.

[42] S. Wegner, L. Van Wüllen, G. Tricot, Network dynamics and species exchange processes in aluminophosphate glasses: An in situ high temperature magic angle spinning NMR view, J. Phys. Chem. B. 113 (2009) 416–425.

[43] L. Muñoz-Senovilla, S. Venkatachalam, F. Muñoz, L. Van Wüllen, Relationships between fragility and structure through viscosity and high temperature NMR measurements in Li_2O-ZnO-P_2O_5 phosphate glasses, J. Non-Cryst. Solids. 428 (2015) 54–61.

[44] S.B. Liu, J.F. Stebbins, E. Schneider, A. Pines, Diffusive motion in alkali silicate melts: An NMR study at high temperature, Geochim. Cosmochim. Acta. 52 (1988) 527–538.

[45] S. Wegner, L. van Wüllen, G. Tricot, The structure of phosphate and borosilicate glasses and their structural evolution at high temperatures as studied with solid state NMR spectroscopy: Phase separation, crystallisation and dynamic species exchange, Solid State Sci. 12 (2010) 428–439.

[46] L. Van Wüllen, S. Wegner, G. Tricot, Structural changes above the glass transition and crystallization in aluminophosphate glasses: An in situ high-temperature MAS NMR study, J. Phys. Chem. B. 111 (2007) 7529–7534.

[47] H. Maekawa, T. Nakao, S. Shimokawa, T. Yokokawa, Coordination of sodium ions in $NaAlO_2$-SiO_2 melts: A high temperature ^{23}Na NMR study, Phys. Chem. Miner. 24 (1997) 53–65.

[48] E.L. Hahn, Spin echoes, Phys. Rev. 80 (1950) 580–594.

[49] D. Larink, H. Eckert, M. Reichert, S.W. Martin, Mixed network former effect in ion-conducting alkali borophosphate glasses: Structure/property correlations in the system $[M_2O]_{1/3}[(B_2O_3)_x(P_2O_5)1_{-x}]_{2/3}$ (M = Li, K, Cs), J. Phys. Chem. C. 116 (2012) 26162–26176.

[50] L. Zhang, H. Eckert, Short- and medium-range order in sodium aluminophosphate glasses: New insights from high-resolution dipolar solid-state NMR spectroscopy, J. Phys. Chem. B. 110 (2006) 8946–8958.

[51] E.E. Metwalli, R.K. Brow, F.S. Stover, Cation effects on anion distributions in aluminophosphate glasses, J. Am. Ceram. Soc. 84 (2001) 1025–1032.

[52] M. Kanzaki, X. Xue, Structural characterization of moganite-type $AlPO_4$ by NMR and powder X-ray diffraction, Inorg. Chem. 51 (2012) 6164–6172.

[53] R. Jelinek, B.F. Chmelka, Y. Wu, P.J. Grandinetti, A. Pines, P.J. Barrie, J. Klinowsk, Study of the aluminophosphates $A1PO_4$-21 and $AlPO_4$-25 by ^{27}Al double-rotation NMR, J. Am. Chem. Soc. 113 (1991) 4097–4101.

[54] H. Graetsch, Two forms of aluminium phosphate tridymite from X-ray powder data, Acta Crystallogr. Sect. C Cryst. Struct. Commun. 56 (2000) 401–403.

[55] L. Pauling, The principles determining the structure of complex ionic crystals, J. Am. Chem. Soc. 51 (1929) 1010–1026.

[56] G. V. Gibbs, N.L. Ross, D.F. Cox, K.M. Rosso, B.B. Iversen, M.A. Spackman, Pauling bond strength, bond length and electron density distribution, Phys. Chem. Miner. 41 (2014) 17–25.

[57] H. Liu, H. Wu, H. Yu, Z. Hu, J. Wang, Y. Wu, Effect of Mo/P ratios on dimensions: syntheses, structures, and properties of three new molybdophosphates, Inorg. Chem. 59 (2020) 5742–5750.

[58] T. Baiheti, S. Han, A. Tudi, Z. Yang, S. Pan, Alignment of polar moieties leading to strong second harmonic response in $KCsMoP_2O_9$, Chem. Mater. 32 (2020) 3297–3303.

[59] P. Kierkegaard, J.M. Longo, A refinement of the crystal structure of $MoOPO_4$, Acta Chem. Scand. 24 (1970) 427–432.

[60] K.H. Lii, R.C. Haushalter, Layer and tunnel structures in new molybdenophosphates: $Cs_2Mo_4P_6O_{26}$ and $M_4Mo_8P_{12}O_{52}$ (M = Cs, Rb, K, Tl), J. Solid State Chem. 69 (1987) 320–328.

[61] A. Leclaire, M.M. Borel, A. Grandin, B. Raveau, Structure of a molybdenum(V) phosphate β-$KMo_2P_3O_{13}$, Acta Crystallogr. Sect. C Cryst. Struct. Commun. 46 (1990) 2009–2011.

[62] S.E. Lister, I.R. Evans, J.S.O. Evans, Complex superstructures of $Mo_2P_4O_{15}$, Inorg. Chem. 48 (2009) 9271–9281.

[63] I.M. Watson, M.M. Borel, J. Chardon, A. Leclaire, Structure of the trivalent molybdenum metaphosphate $Mo(PO_3)_3$, J. Solid State Chem. 111 (1994) 253–256.

[64] K.H. Lii, R.C. Haushalter, $CsMoP_2O_7$: a molybdenopyrophosphate containing isolated Mo^{3+} cations, Acta Crystallogr. Sect. C Cryst. Struct. Commun. 43 (1987) 2036–2038.

[65] A. Leclaire, M.M. Borel, A. Grandin, B. Raveau, $MoAlP_2O_9$ molybdenum(V) aluminophosphate isostructural with $VSiP_2O_9$, Zeitschrift Für Krist. Mater. 190 (1990) 135–142.

[66] A. Guesdon, M.M. Borel, A. Leclaire, A. Grandin, B. Raveau, An aluminophosphate of molybdenum (V) with a tunnel structure: $Cs_9Mo_9Al_3P_{11}O_{59}$, J. Solid State Chem. 114 (1995) 451–458.

[67] A. Guesdon, A. Leclaire, M.M. Borel, B. Raveau, Significant structural disorganization in alkaline molybdenum(V) aluminophosphates, Chem. Mater. 7 (1995) 1873–1878.

[68] A. Leclaire, M.M. Borel, A. Grandin, B. Raveau, $K_2Mo_3AlP_8O_{28}$: A tunnel structure isotypic with $Na_{0.5}MoP_2O_7$, Acta Crystallogr. Sect. C Cryst. Struct. Commun. 46 (1990) 1368–1370.

[69] M. Szumera, Molybdenum modified phosphate glasses studied by ^{31}P MAS NMR and Raman spectroscopy, Spectrochim. Acta - Part A Mol. Biomol. Spectrosc. 137 (2015) 111–115.

[70] L. Koudelka, O. Kupetska, P. Kalenda, P. Mošner, L. Montagne, B. Revel, Crystallization of sodium molybdate-phosphate and tungstate-phosphate glasses, J. Non-Cryst. Solids. 500 (2018) 42–48.

[71] Y. Wang, F. Wang, J. Zhou, H. Zhu, Q. Liao, L. Li, Y. Zhu, Y. Yuan, J. Zhang, Effect of molybdenum on structural features and thermal properties of iron phosphate glasses and boron-doped iron phosphate glasses, J. Alloys Compd. 826 (2020).

[72] A. Moguš-Milanković, A. Šantić, A. Gajović, D.E. Day, Spectroscopic investigation of MoO_3-Fe_2O_3-P_2O_5 and SrO-Fe_2O_3-P_2O_5 glasses. Part I, J. Non-Cryst. Solids. 325 (2003) 76–84.

[73] J. Bai, J. Hsu, R.K. Brow, C.W. Kim, J. Szabo, A. Zervos, Structure and properties of Mo-Fe-phosphate glasses, Phys. Chem. Glas. Eur. J. Glas. Sci. Technol. Part B. 60 (2019) 62–69.

[74] O. Cozar, D.A. Magdas, I. Ardelean, EPR study of molybdenum-lead-phosphate glasses, J. Non-Cryst. Solids. 354 (2008) 1032–1035.

[75] G. Poirier, F.S. Ottoboni, F.C. Cassanjes, Á. Remonte, Y. Messaddeq, S.J.L. Ribeiro, Redox behavior of molybdenum and tungsten in phosphate glasses, J. Phys. Chem. B. 112 (2008) 4481–4487.

[76] U. Selvaraj, K.J. Rao, Characterization studies of molybdophosphate glasses and a model of structural defects, J. Non-Cryst. Solids. 72 (1985) 315–334.

[77] Y. Dimitriev, R. Iordanova, Non-traditional molybdate glasses, Phys. Chem. Glas. Eur. J. Glas. Sci. Technol. Part B. 50 (2009) 123–132.

[78] L. Zhang, A. Bögershausen, H. Eckert, Mesoporous $AlPO_4$ glass from a simple aqueous sol-gel route, J. Am. Ceram. Soc. 88 (2005) 897–902.

[79] A. Krishnamurthy, V.K. Michaelis, S. Kroeker, Network formation in borosilicate glasses with aluminum or gallium: implications for nepheline crystallization, J. Phys. Chem. C. 125 (2021) 8815–8824.

[80] R.K. Brow, R.J. Kirkpatrick, G.L. Turner, Nature of alumina in phosphate glass: II, structure of sodium alurninophosphate glass, J. Am. Ceram. Soc. 76 (1993) 919–928.

[81] D. Zielniok, C. Cramer, H. Eckert, Structure/property correlations in ion-conducting mixed-network former glasses: Solid-state NMR studies of the system Na_2O-B_2O_3-P_2O_5, Chem. Mater. 19 (2007) 3162–3170.

[82] J.E.C. Wren, B.J. Greer, V.K. Michaelis, C.S. Higman, S. Kroeker, Multinuclear magnetic resonance investigation of crystalline alkali molybdates, Inorg. Chem. 54 (2015) 9853–9861.

7 Network Structure and Dissolution Properties of Phosphate-Doped Borosilicate Glasses

7.1 Introduction

The immobilization of high-level radioactive waste using borosilicate glasses is a mature technology based on decades of research [1–3]. Borosilicate glasses are relatively resistant to chemical degradation and can accommodate a wide array of cations with different chemical properties into their network structure [4]. However, high-field-strength cations such as Mo^{6+} and S^{6+} are not easily incorporated into the glass network structure due to their ability to compete with other network formers for oxygens [5]. Hence, they exhibit low solubility in typical borosilicate glasses, phase-separating from the glass above about 1 mol% as anionic units [$(MoO_4)^{2-}$ and $(SO_4)^{2-}$], which sequester alkali and alkaline-earth cations into crystalline inclusions [6–8]. These mixed-alkali molybdates separate as droplets in the melt, and after cooling, are distributed throughout the glass in non-uniformly sized spheroids [9]. Prominent among the fission products that constitute high-level nuclear waste are cesium (^{137}Cs) and strontium (^{90}Sr), which are ß-emitters with short half-lives and high specific activities, and ^{135}Cs, with a half-life of over 2 million years [10,11]. The Cs and Sr molybdates that may be formed as a result of phase separation are hygroscopic and will dissolve readily in any water that might breach the canister over time, releasing the radionuclides into the environment. As a major component in most borosilicate glasses, sodium ions are also sequestered by molybdate anions to form Na_2MoO_4 or, in conjunction with Cs, other mixed-alkali phases such as $CsNaMoO_4$, $Cs_3Na(MoO_4)_2$ and their hydrated phases [8,12]. Although Na is not radioactive, the hygroscopic nature of Na_2MoO_4 compromises the durability and chemical integrity of a waste-loaded glass. In practice, the low solubility of Mo^{6+} and S^{6+} in borosilicate glasses limits the total amount of waste that can be incorporated into a glass. As a result, the immobilization of high-level radioactive waste rich in Mo, such as Collins-CLT waste [13]. may generate immense amounts of waste-loaded glass at high energy and materials costs, while increasing pressure on repositories. Increasing the solubility of these high field-strength fission products would have

economic and ecological benefits by increasing the overall loading capacities of glasses and thereby reducing the volume of waste glass generated.

Unlike borosilicates, phosphate glasses can incorporate high amounts of Mo without phase separation [14] due to competitive ordering effects on oxygens by the comparably high field-strength Mo^{6+} and P^{5+} [15,16], resulting in the successful integration of molybdenum into the phosphate network through P−O−Mo bonds [16]. Despite this attractive property, these glasses generally suffer from low chemical durability with respect to borosilicate glasses [17], making them unfit for long-term nuclear waste immobilization. Nevertheless, this favourable bonding motif may prove to be key to improving Mo incorporation in borosilicate glasses [18] and glass-ceramics [19], provided low levels of phosphate doping does not unduly compromise the chemical durability or lead to other types of phase separation. Whereas the dissolution of phosphate-doped silicate glasses in simulated body fluid has been thoroughly explored in the context of bioactive glasses for bone regeneration [20], much less is known about phosphate connectivity and dissolution behaviour in borosilicate glasses relevant to nuclear waste disposal [18,19,21,22].

This work focuses on phosphate-doped borosilicate glasses designed to represent nuclear-waste glasses. Multinuclear solid-state nuclear magnetic resonance spectroscopy is used to study the network structure of these glasses before and after standardized dissolution tests. One glass in this series is additionally doped with molybdenum to assess the effectiveness of phosphate for improving Mo incorporation, and how it impacts the glass performance in the presence of water. Ion-release profiles are analyzed in terms of the dissolution mechanism, supported by scanning-electron microscopy for visualizing morphological changes on the glass surface, and energy dispersive x-ray spectroscopy to generate elemental maps.

7.2 Experimental details

7.2.1 Synthesis

Five glasses were prepared with SiO_2 incrementally substituted by P_2O_5 from 1-4 mol% (**Table 7.1**). In a sixth sample, 3 mol% of Na_2O was replaced by MoO_3. Glasses were synthesized in three-gram batches by weighing appropriate amounts of SiO_2, B_2O_3, Na_2CO_3, Cs_2CO_3, $(NaPO_3)_6$, Al_2O_3 and MoO_3. The oxides and carbonates were mixed in 95/5 Pt/Au crucibles and decarbonated at 650°C for 12 hours, then melted at 1100°C for 2 hours with the lids on. The

resulting glasses were quenched in water, ground using a mortar and pestle, re-melted at 1100°C for 1 hour to ensure homogeneity, and cooled in air to obtain glass monoliths. Visual inspection suggested some degree of phase separation in the high-P-bearing samples. Monoliths were cut into approximately rectangular pieces and stored in a desiccator prior to dissolution analysis, whereas the cut-off portions were used for NMR analysis, and to confirm the amorphous nature of the samples by powder x-ray diffraction.

Table 7.1. Nominal composition of glasses (mol%)

Sample	**P0**	**P1**	**P2**	**P3**	**P4**	**P4-Mo3**
SiO_2	58.5	57.5	56.5	55.5	54.5	54.5
Na_2O	18.2	18.2	18.2	18.2	18.2	15.2
B_2O_3	16.3	16.3	16.3	16.3	16.3	16.3
Al_2O_3	4.0	4.0	4.0	4.0	4.0	4.0
P_2O_5	0	1.0	2.0	3.0	4.0	4.0
Cs_2O	3.0	3.0	3.0	3.0	3.0	3.0
MoO_3	0	0	0	0	0	3.0

7.2.2 Solid-state Nuclear Magnetic Resonance spectroscopy (NMR)

NMR analyses of ^{11}B, ^{23}Na and ^{27}Al were carried out on a Varian ^{UNITY}INOVA 600 MHz spectrometer equipped with a Chemagnetics 1.6 mm triple-resonance solid-state NMR probe. All samples were spun at the magic angle with a spinning speed of 30 kHz (±5 Hz). Bloch-decay experiments were carried out with pulse lengths of 0.4 μs, corresponding to tip angle of ca. 15°, which is essential to equally excite sites with different quadrupolar coupling constants (C_Q). The MAS NMR signal was averaged over 1024, 2048, and 2048 transients for ^{11}B, ^{23}Na, and ^{27}Al isotopes, respectively, with optimized relaxation delays of 2 s, 1 s, and 1 s. ^{29}Si and ^{31}P MAS NMR spectra were acquired at 9.4 T on a Bruker Avance III spectrometer using a double-resonance 4 mm solid-state NMR probe. To acquire ^{29}Si MAS NMR, a 30° tip angle was used, which corresponded to a pulse length of 1 μs; 2048 scans were acquired with a relaxation delay of 20 s. ^{31}P MAS NMR spectra were acquired with a pulse length of 2.5 μs (30° tip angle), an

optimized relaxation delay of 15 s, and averaged over 256 scans. Chemical shift references for ^{23}Na, ^{11}B, ^{27}Al, ^{31}P and ^{29}Si NMR were 0.1 M NaCl (0 ppm), 0.1 M H_3BO_3 (+19.6 ppm relative to $BF_3{\cdot}OEt_2$ (0 ppm)), 0.1 M $Al(NO_3)_3$ (0 ppm), 85% H_3PO_4 (0 ppm) and hexamethyldisiloxane (+6.68 ppm relative to TMS (0 ppm)), respectively.

The MAS NMR spectra were fit using the DMFit program [24] to determine the relative concentrations of different network-forming species. Symmetrical lineshapes with mixed Gaussian/Lorentzian character were used to fit ^{27}Al, ^{29}Si and ^{31}P MAS NMR spectra, whereas a combination of Gaussians and the Czjzek model was used to fit the spectra of ^{11}B and ^{23}Na using Quasar, an external module incorporated into DMFit which simulates the NMR spectra of quadrupolar nuclei with distributions in the characteristic second-order quadrupolar lineshapes [25]. Although ^{27}Al is a quadrupolar nucleus, the peaks were fit using gaussians, as the observed peaks were symmetric and did not exhibit the tailing towards lower frequencies symptomatic of a distribution in quadrupolar couplings. In the case of ^{11}B MAS NMR spectra, the symmetric $^{[4]}$B peaks were fit with gaussians, and the $^{[3]}$B peak with second-order quadrupole broadening was fit using the Quasar module. In order to correct the $^{[4]}$B peak intensity for the underlying satellite transition, the intensity of the first spinning sideband of the $^{[4]}$B peak was shifted by the spinning frequency and subtracted from the original spectrum.

7.3 Results

7.3.1 Solid-state NMR spectroscopy

7.3.1.1 ^{11}B MAS NMR

The ^{11}B MAS NMR spectra of these glasses (**Figure 7.1**) consist of two main peaks arising from boron with different coordination numbers. The broad peak centered around 15 ppm represents planar BO_3 units ($^{[3]}$B), and the narrow peak at *ca*. -2 ppm represents tetrahedral BO_4^- units ($^{[4]}$B) [27,28]. The $^{[3]}$B units experience significantly larger quadrupolar interactions compared to $^{[4]}$B, and hence, the peak is broadened and possesses a second-order quadrupolar lineshape. The C_Q for $^{[4]}$B and $^{[3]}$B units are about 0.6 and 2.6 MHz, respectively [29]. Replacement of Si by P results in a progressive decrease in the overall fraction of $^{[4]}$B (N_4) [30], indicating lower overall connectivity of B in the glass (**Table 7.2**). The addition of Mo to glass P4 induces an abrupt

reduction in N_4 [$^{[4]}$B/($^{[4]}$B+$^{[3]}$B)] from 0.60 to 0.47, indicating a substantial rearrangement of the borate network.

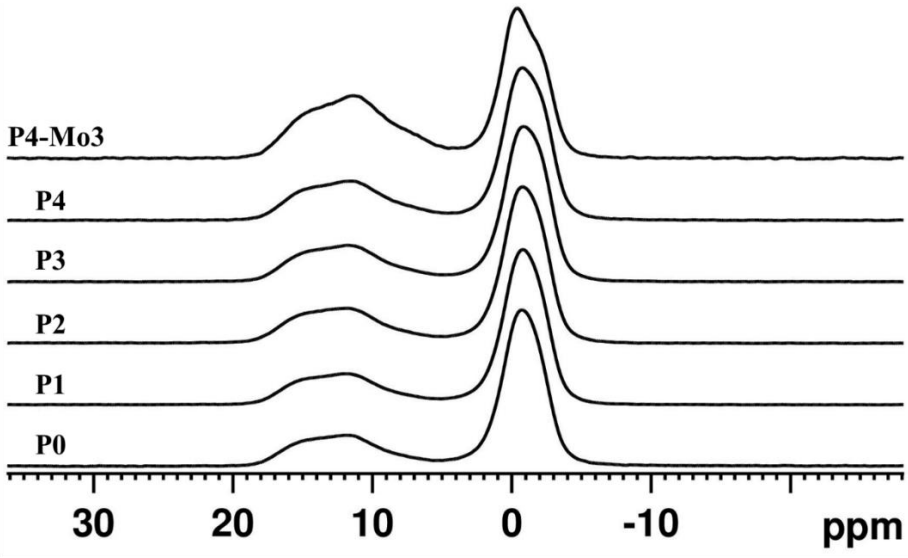

Figure 7.1. ^{11}B MAS NMR spectra of glasses.

Each of these signals can be deconvoluted into at least two distinct environments: the $^{[4]}$B peak arises from overlapping sites with chemical shifts of -0.1 and -1.7 ppm, attributed to $^{[4]}$B with four ($^{[4]}B_{4Si}$) and three ($^{[4]}B_{3Si}$) silicate neighbours, respectively [31–33]. The $^{[3]}$B peak can be decomposed into sites with a C_Q of 2.65 MHz, $\eta = 0-0.2$, and isotropic chemical shifts of ca. 17 and 15 ppm, which are attributed to $^{[3]}$B units present in the form of boroxol ring ($^{[3]}B_{ring}$) and non-ring ($^{[3]}B_{non\text{-}ring}$) structures, respectively [31–34] (**Table 7.2, Figure 7.2**). Changes in the concentrations of the subspecies comprising the three- and four-coordinate boron are subtle, and fall within the estimated uncertainties of the intensity measurements for the five Mo-free glasses. With the introduction of Mo, the non-ring BO_3 fraction doubles and the $^{[4]}B_{4Si}$ concentration drops, reflecting substantial changes to the borate network. Concomitantly, the chemical shifts of these components appear to trend toward greater shielding (i.e., lower frequencies).

Table 7.2. Chemical shifts and integrated intensities used in the deconvolution of ^{11}B MAS NMR spectra.

	$^{[3]}B_{ring}$[a]		$^{[3]}B_{non\text{-}ring}$[a]		$^{[4]}B_{3Si}$[b]		$^{[4]}B_{4Si}$[b]		N_4[c]
	δ_{iso} (ppm) (±0.5)	Int. (%)[d]	δ_{iso} (ppm) (±0.5)	Int. (%)[d]	δ_{iso} (ppm) (±0.1)	Int. (%)[d]	δ_{iso} (ppm) (±0.1)	Int. (%)[d] (±2)	
P0	17.7	26(5)	15.5	8(2)	-0.12	37	-1.67	29	0.66
P1	17.7	27(6)	15.4	7(4)	-0.15	36	-1.72	30	0.66
P2	17.7	28(4)	15.4	8(3)	-0.14	35	-1.76	29	0.64
P3	17.6	29(5)	15.2	9(3)	-0.24	34	-1.90	28	0.62
P4	17.5	30(7)	14.9	10(5)	-0.24	34	-1.97	26	0.60
P4-Mo3	17.4	33(4)	14.8	20(4)	-0.15	30	-2.02	17	0.47

[a]C_Q = 2.65 MHz; η = 0.0-0.2
[b]Mixed gaussian/lorentzian peaks with widths of 0.4 kHz
[c]N_4 = $^{[4]}$B/($^{[4]}$B+$^{[3]}$B)
[d]Integrated intensity

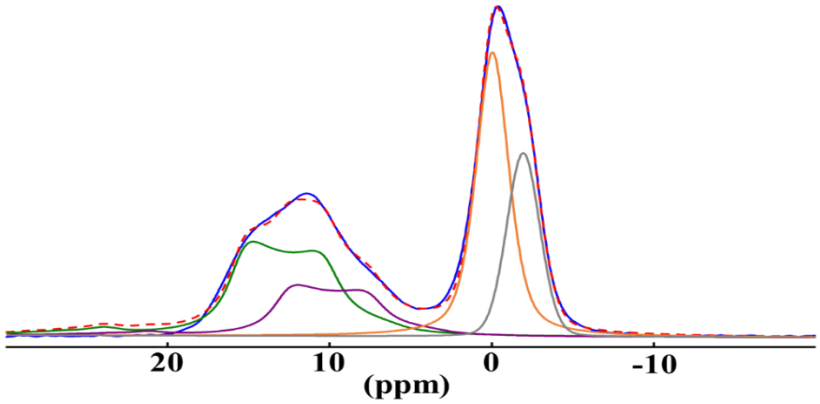

Figure 7.2. Deconvolution of ^{11}B MAS NMR spectrum of sample P0. Green, magenta, orange, and grey components represent $^{[3]}B_{non\text{-}ring}$, $^{[3]}B_{ring}$, $^{[4]}B_{3Si}$ and $^{[4]}B_{4Si}$ units, respectively.

7.3.1.2 ^{23}Na MAS NMR

The ^{23}Na MAS NMR spectra of the glasses are shown in **Figure 7.3a**. One broad symmetric peak with a peak maximum of ca. -10 ppm is observed in all cases, except for the one with the highest P content (P4), which has an asymmetric lineshape. The peaks are broad due to a substantial C_Q subject to a geometrical distribution typical of the highly disordered environment in glasses (~3 MHz) [32]. While it is difficult to extract reliable NMR parameters from such featureless peaks, the comparison between P3 and P0, P1 and P2 shows signs of additional broadening hinting a second distinct Na environment (**Figure 7.3b**). By increasing the P content to 4 mol%, evidence of crystallinity may be observed in the same position, implying that the beginning of crystallization of a sodium-bearing phase occurs in P3. Deconvolution of this spectrum using that of P2 as a reference suggests a poorly crystalline phase with δ_{iso} = +2.5 ppm, C_Q = 2.5 MHz and $\eta \sim 0.6$, representing about 13% of the total integrated intensity (**Table 7.3, Figure 7.4**). Crystalline $Na_4P_2O_7$ possesses four distinct Na sites with C_Q values in this range, and a peak envelope similar to the one used in the deconvolution [35]. Furthermore, a high-P glass sample prepared as part of a separate study showed x-ray diffraction peaks assignable to $Na_4P_2O_7$, providing support for this hypothesis (**unpublished results**). Lacking more precise NMR parameters or clear peaks in the x-ray diffractogram, it is only possible to conclude that this phase is probably a poorly crystalline or freshly nucleated phase with very small particle sizes. For P4-Mo3, a small peak with a chemical shift of -1 ppm on the shoulder of the broad,

major peak is observed. The chemical shift of this peak is in line with that of $Na_2MoO_4 \cdot 2H_2O$ [12], but its low intensity precludes confident deconvolution of the spectrum. The x-ray diffractogram of this sample lacks diffraction peaks corresponding to the above-mentioned phase, implying that any crystalline phase must be present only in very minute quantities.

Table 7.3. ^{23}Na MAS NMR fitting parameters for sample P4.

δ_{iso} (ppm)	C_Q (MHz)	η_Q	Int. (%)[c]
2.46(0.3)	2.54(0.05)	0.6(0.2)	13(5)
-11.3(0.2)[a]	28.3(1)[b]		87(5)

[a]Peak position (ppm)
[b]Peak width (ppm)
[c]Integrated intensity

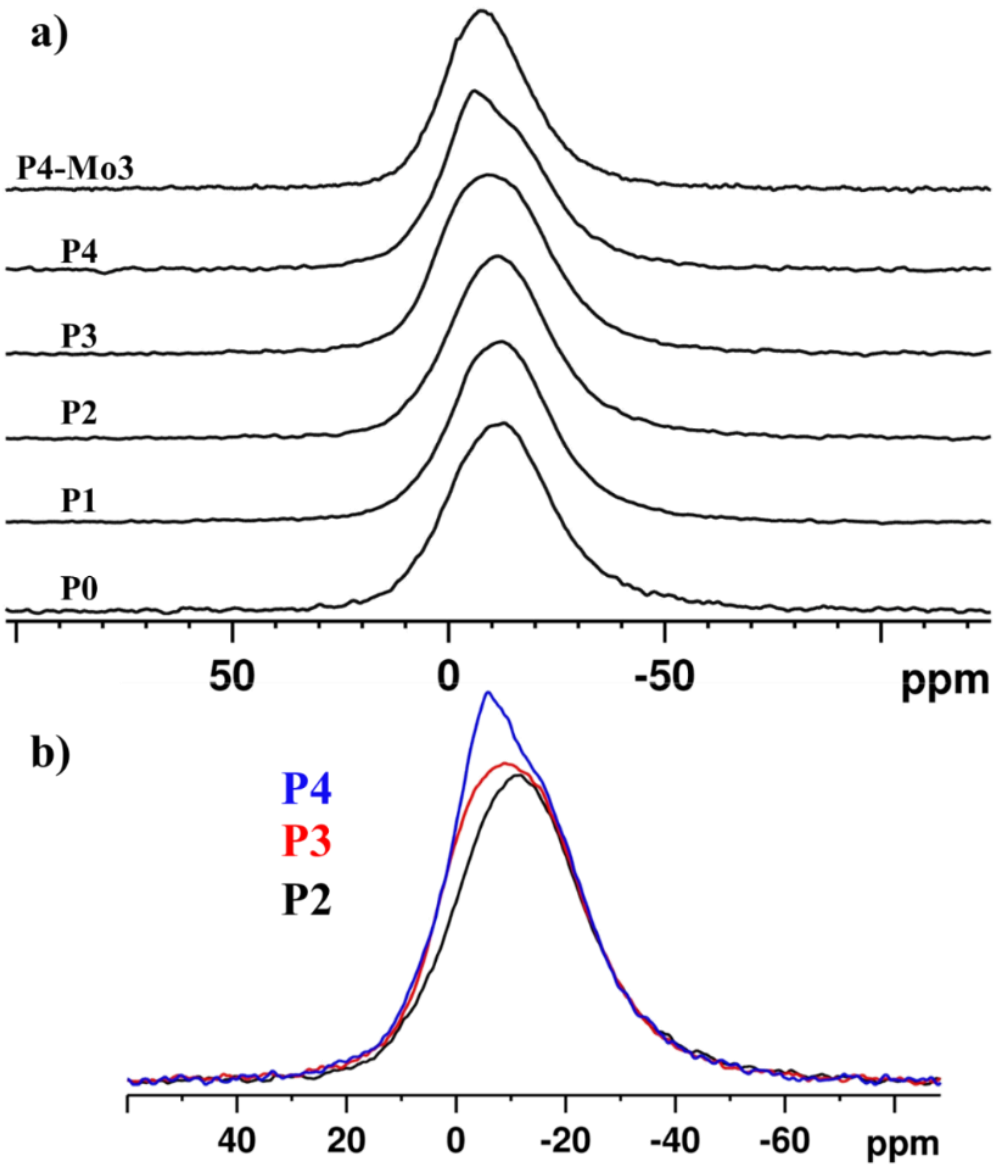

Figure 7.3. a) ^{23}Na MAS NMR spectra of glasses; b) overlay of ^{23}Na NMR spectra of glasses P2, P3, and P4.

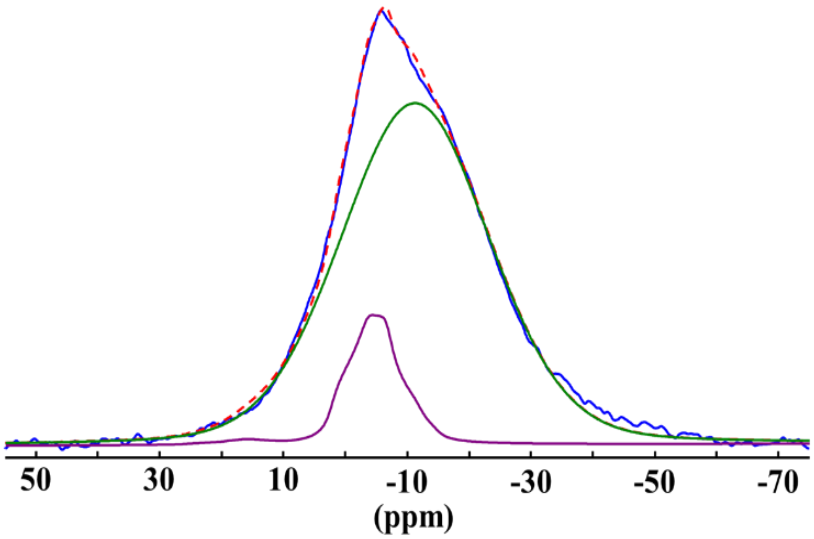

Figure 7.4. Deconvolution of the ^{23}Na MAS NMR spectrum of P4 representing glassy (green) and poorly-crystalline $Na_4P_2O_7$ (magenta) phases.

7.3.1.3 ^{31}P MAS NMR

The ^{31}P MAS NMR spectra are shown in a stacked plot in **Figure 7.5**, and their absolute intensities overlaid in **Figure 7.6**. Due to peak overlap, the spectra were deconvolved according to documented spectral assignments (**Figure 7.7, Table 7.4**). The glass containing the lowest phosphate content (P1) was fit with three components having peak positions of 15.8, 3.4 and -6.6 ppm, where the components with chemical shifts around 15 and 3.5 ppm correspond to ortho- (P^0) and pyro- (P^1) phosphate units [36–38]. The chemical shift of a metaphosphate unit (P^2) in a pure phosphate chain is known to be ca. -20 ppm [37], and that of a P^2 where one or two of the neighbouring network species is a borate unit has a chemical shift between -5 and -15 ppm [36–39]. Hence the third component with a chemical shift of *ca.* -6 ppm is assigned to a metaphosphate unit bonded to one or two borate units, P^2_{nB}. Since both borate and aluminate units can bond to phosphates, and have a similar influence on the ^{31}P chemical shift trends, the P^2_{nB} unit may be dubbed a $P^2_{nB(Al)}$ to reflect this ambiguity. A quantitative plot of these phosphate units as a function of phosphate content in these glasses is shown in **Figure 7.8**. Terminal P^1 units are the dominant species, increasing regularly with increasing P content and implying the presence of phosphate dimers. Isolated orthophosphate P^0 species also increase in concentration with phosphate content. At 3 mol% P (P3), evidence of two peaks appears in the P^1 region, one

of which (ca. +5 ppm) may be attributed to the poorly crystalline $Na_4P_2O_7$ phase detected in ^{23}Na MAS NMR; the ^{31}P NMR chemical shift of pyrophosphate in $Na_4P_2O_7$ is +2.3 ppm [40] which is very close to the observed value. At 4 mol% P, the concentration of P^1, both in the glassy phase and in $Na_4P_2O_7$, increases at the expense of P^0, while the overall content of $P^2_{nB(Al)}$ increases modestly. When Mo is added to the P4 glass (P4-Mo3), the P^1 and P^2 peaks shift to lower frequencies, implying that Mo associates with these phosphate species. While this shift introduces uncertainty into the lineshape deconvolution, it appears that the fraction of chain phosphate (P^2) increases, whereas the P^0 and $Na_4P_2O_7$ fractions diminish.

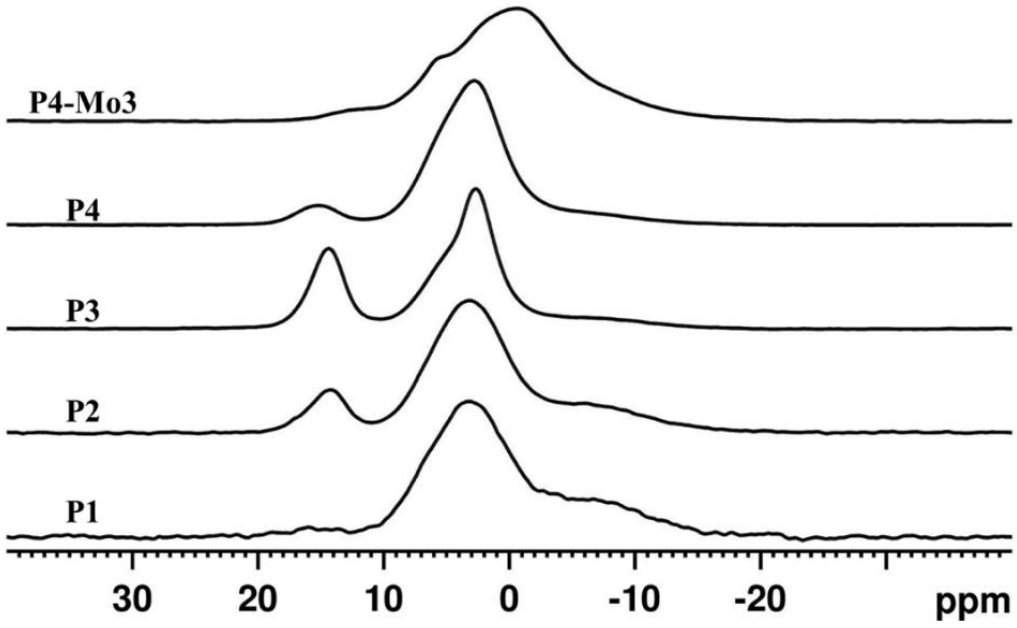

Figure 7.5. ^{31}P MAS NMR spectra of glasses.

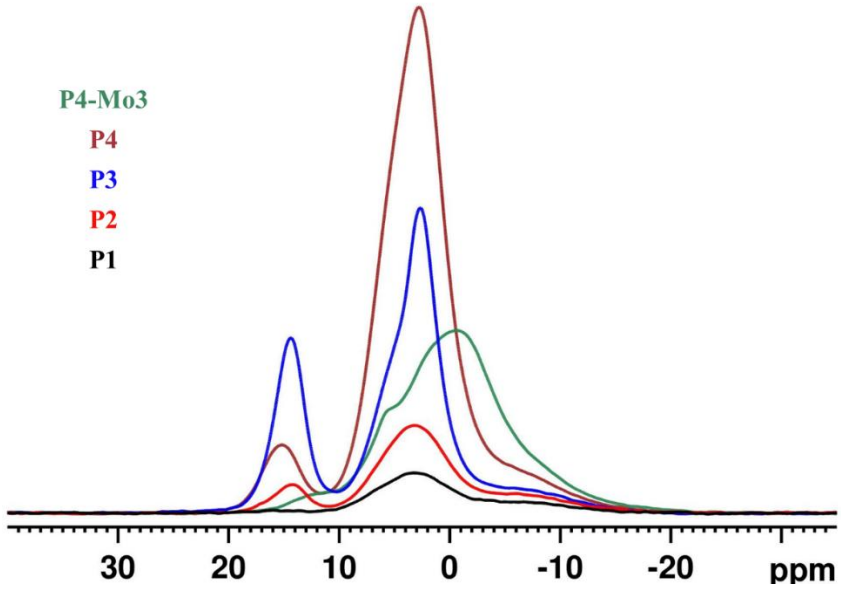

Figure 7.6. ^{31}P MAS NMR spectra of glasses in absolute intensity mode.

Table 7.4. Fitting parameters used in the deconvolution of ^{31}P MAS NMR spectra

	P^0			P^1			$P^2_{nB(Al)}$			$Na_4P_2O_7$		
	δ_{iso} (ppm) (±0.5)	PW[a] (±1)	(%)[b]	δ_{iso} (ppm) (±0.5)	PW[a] (±2)	(%)[b]	δ_{iso} (ppm) (±2)	PW[a] (±3)	(%)[b]	δ_{iso} (ppm) (±1)	PW[a] (±2)	(%)[b]
P1	15.7	3.6	2(1)	3.4	7.4	69(5)	-6.5	10.3	29(5)	—	—	—
P2	14.5	3.6	11(2)	3.3	7.2	68(3)	-6.7	10.4	21(3)	—	—	—
P3	14.5	3.1	24(2)	2.6	3.1	51(8)	-6.5	10.4	9(4)	5.6	3.1	16(6)
P4	15.3	3.5	6(2)	2.4	4.9	65(15)	-6.3	10.4	8(4)	5.6	4.2	21(10)
P4-Mo3	12.3	4.4	3(2)	-0.1	8.1	64(20)	-6.2	11.3	19(15)	5.8	4.9	13(8)

[a]Peak Width (ppm); [b]Integrated intensity (%)

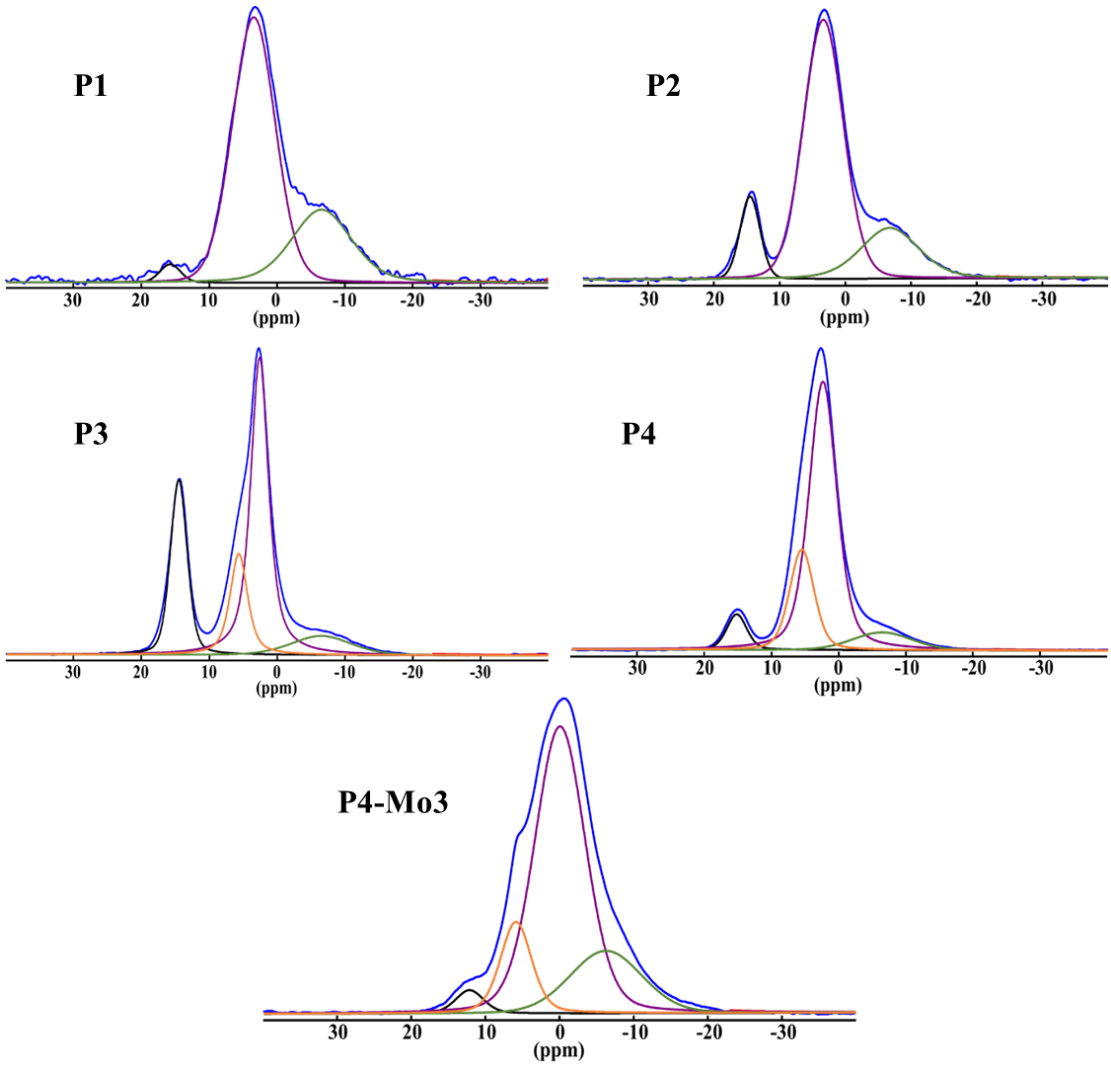

Figure 7.7. Deconvolution of ^{31}P MAS NMR spectra. Blue is the experimental spectrum and components in black, orange, purple and green represent P^0, P^1, $P^2_{nB(Al)}$ and poorly crystalline $Na_4P_2O_7$, respectively.

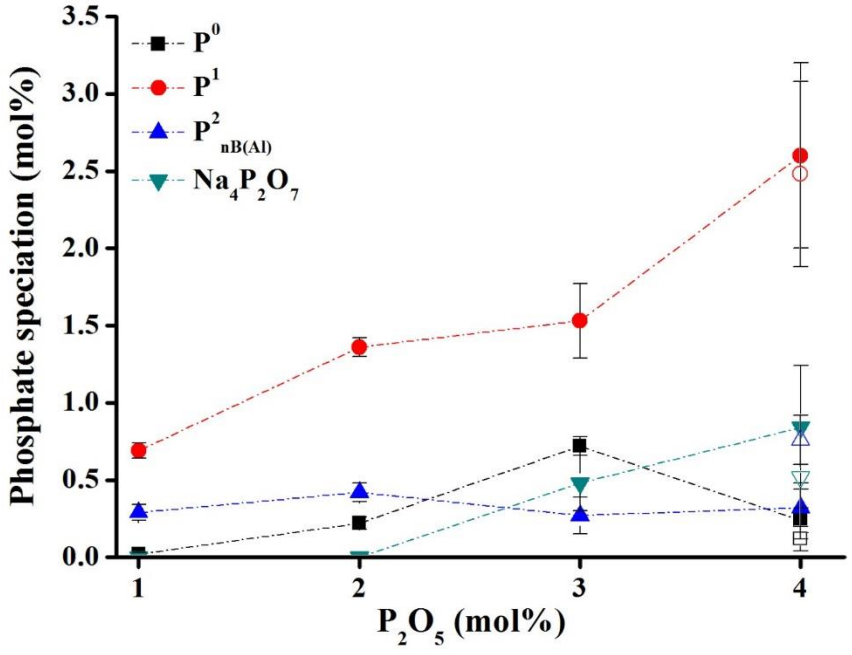

Figure 7.8. Absolute quantities of phosphate units obtained from the deconvolution of the ^{31}P MAS NMR spectra. Open symbols represent sample P4-Mo3.

7.3.1.4 ^{27}Al MAS NMR

The ^{27}Al MAS NMR spectra are substantially similar, exhibiting peaks in the four-coordinate (+56 ppm) and five-coordinate (+14 ppm) regions [41,42] (**Figure 7.9**). Slight changes in their relative intensities are observed as the P content is varied, with $^{[4]}$Al appearing to increase at the expense of $^{[5]}$Al for P0 to P3, only to decrease when P_2O_5 = 4 mol% (**Table 7.5**). A slight broadening and shift to lower frequency is observed in the $^{[4]}$Al peak as Si is replaced by P. With the introduction of Mo to P4, some of the $^{[4]}$Al is converted to six-coordinate Al to give about 6% $^{[6]}$Al (**Figure 7.9**).

Table 7.5. ^{27}Al MAS NMR fit parameters.

	$^{[4]}$Al			$^{[5]}$Al			$^{[6]}$Al		
	δ_{iso} (ppm) (±0.2)	FWHM[a] (±0.1)	Int. (%)[b]	δ_{iso} (ppm) (±0.2)	FWHM[a] (±0.05)	Int. (%)[b]	δ_{iso} (ppm) (±0.2)	FWHM[a] (±0.15)	Int. (%)[b]
P0	56.9	2.1	81(3)	14.3	0.9	19(3)	—	—	—
P1	56.3	2.1	84(2)	14.4	0.9	16(2)	—	—	—
P2	56.2	2.2	84(2)	14.4	0.9	16(2)	—	—	—
P3	56.4	2.2	90(1)	14.6	0.9	10(1)	—	—	—
P4	54.9	2.2	84(2)	14.1	0.9	16(2)	—	—	—
P4-Mo3	54.2	2.3	79(2)	14.4	0.9	15(1)	-6.1	2.3	6(2)

[a]Full-width half maximum (kHz)
[b]Integrated intensity

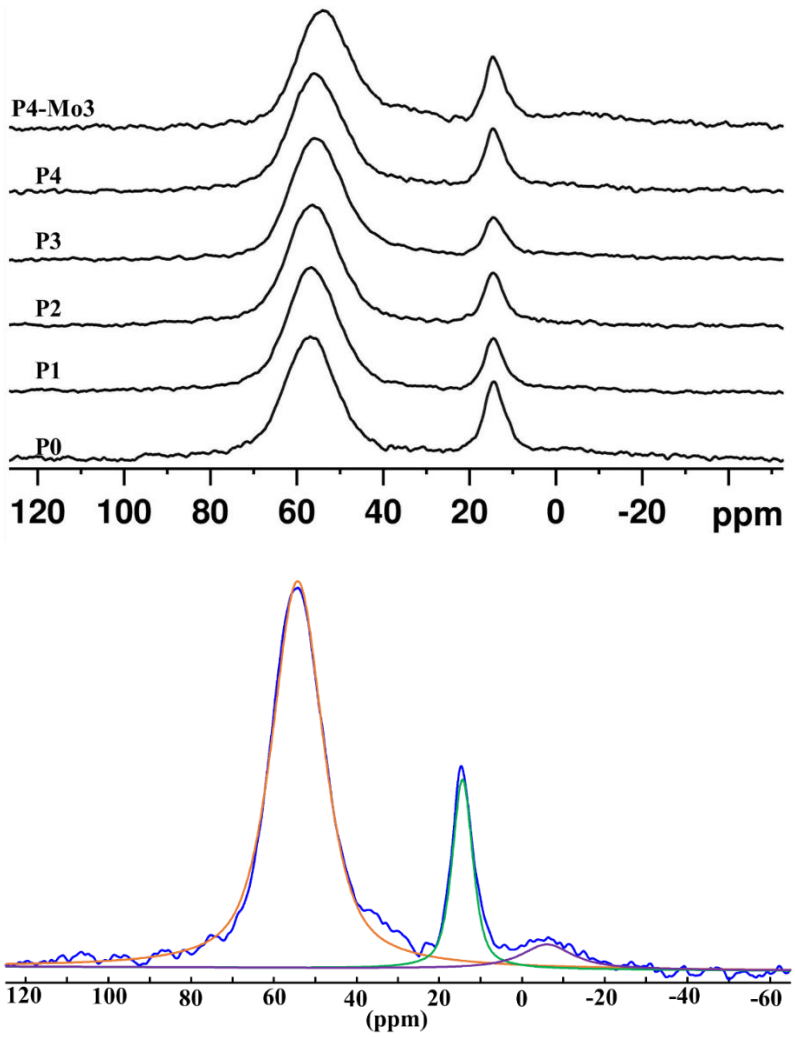

Figure 7.9. ^{27}Al MAS NMR spectra of glasses (top) and deconvolution of ^{27}Al MAS NMR spectrum of P4-Mo3, where orange, green and purple components represent $^{[4]}$Al, $^{[5]}$Al and $^{[6]}$Al units, respectively.

7.3.1.5 ^{29}Si MAS NMR

^{29}Si MAS NMR spectra of selected samples are shown in **Figure 7.10**, where the broad peaks common for silicate glasses may be seen. Due to the heterogeneous chemical environments of silicates in mixed-network-former glasses such as these, wide chemical-shift ranges for different Q^n species have been documented, where *n* represents the number of Si−O−T bonds (T = B, Al, Si). In binary silicates and alkali borosilicates, the mean chemical shifts of Q^1, Q^2, Q^3, and Q^4 species appear around -70, -80, -93 and -104 ppm, respectively [5,32,43–49]. Using these

chemical shifts as a guide, the spectra were deconvoluted using width-constrained Gaussian/Lorentzian peaks representing Q^3 and Q^4 silicate units with chemical shifts of about -90 and -102 ppm, (**Figure 7.11, Table 7.6**) to obtain the integrated intensities shown in **Figure 7.12**. The P-free aluminoborosilicate glass appears to be dominated by Q^3 units, with Q^4 also present in a significant quantity. Upon replacement of Si by 2 mol% P (P2), the peak envelope shifts towards lower frequency indicating an increase in the Q^4 fraction. With the addition of more phosphorus, the peak shifts to more negative frequencies in P4, reducing the Q^3 fraction drastically in favour of Q^4 species. The addition of Mo to P4 shifts the peak to an even more negative chemical shift and may be fit with a single Q^4 peak at -105 ppm.

Table 7.6. ^{29}Si MAS NMR fit parameters.

	Q^3		Q^4	
	Peak max (ppm)	Int. (%)[a]	Peak max (ppm)	Int. (%)[a]
P0	-89(2)	63(17)	-101(3)	37(17)
P2	-92(5)	41(14)	-102(3)	59(14)
P4	-93(2)	10(10)	-102(1)	90(10)
P4-Mo3	—	—	-105	100

[a]Integrated Intensity

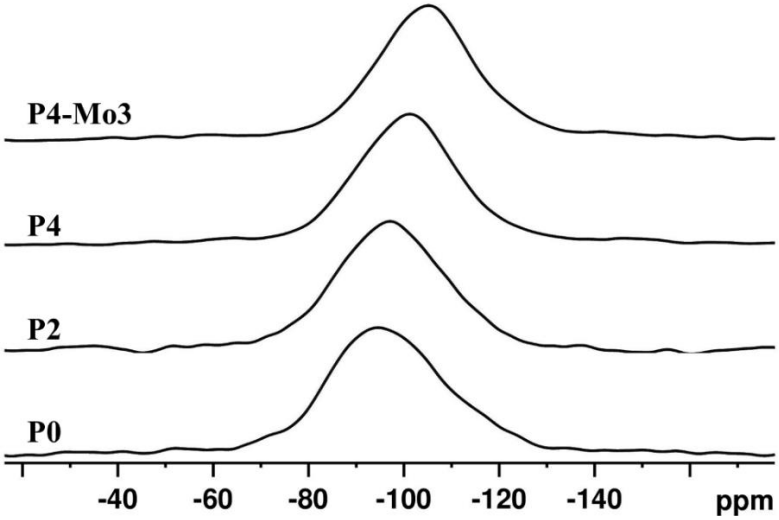

Figure 7.10. ^{29}Si MAS NMR spectra of glasses.

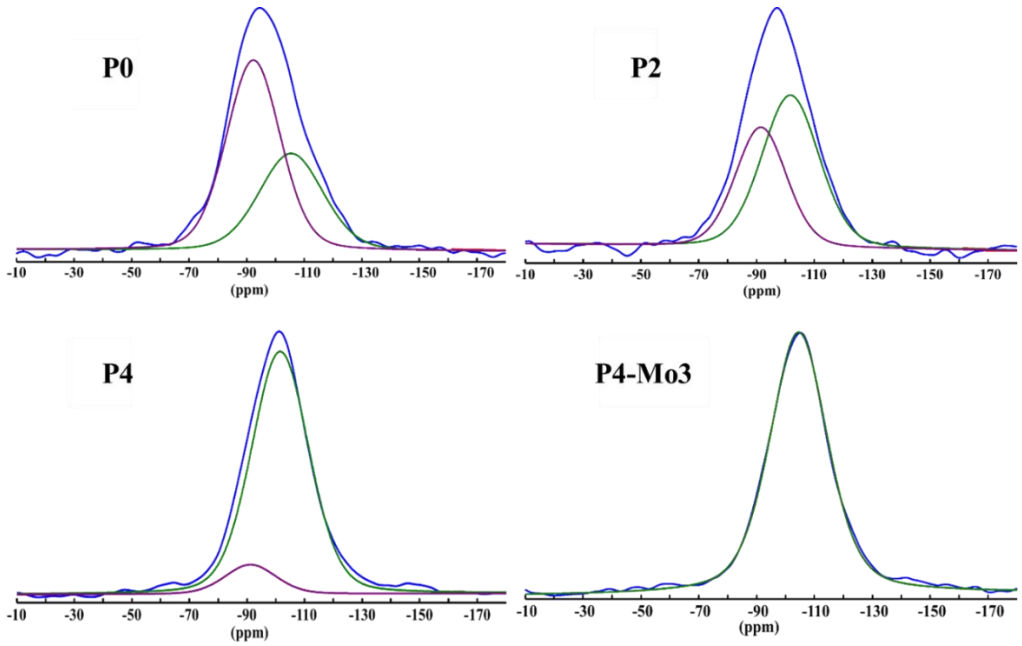

Figure 7.11. Deconvolution of ^{29}Si MAS NMR spectra. The subspectral components in purple and green represent Q^3 and Q^4 units, respectively.

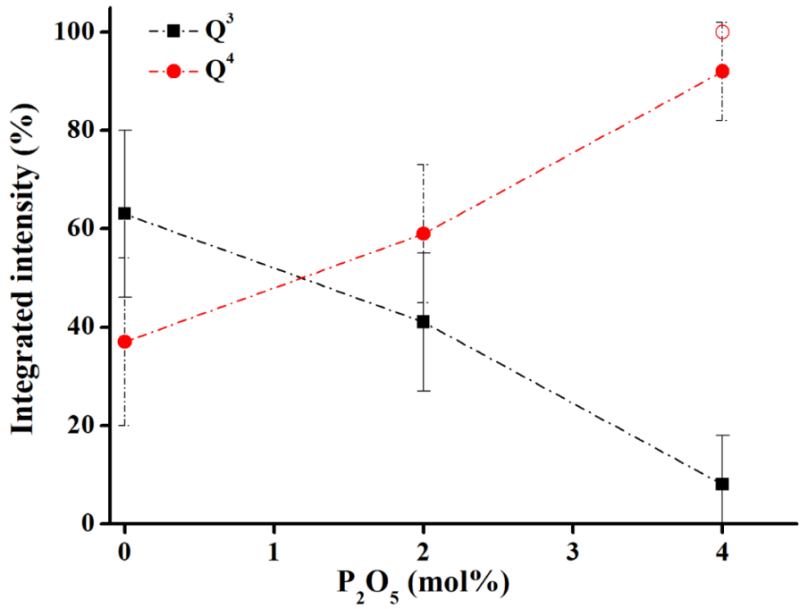

Figure 7.12. Quantification of Si species obtained from the deconvolution of the ^{29}Si MAS NMR spectra. Open circle represents sample P4-Mo3.

7.3.1.6 NMR spectroscopy on samples after dissolution

NMR spectra collected on the samples after the 28-day dissolution experiments are substantially similar to those of the pristine glass samples in most cases. For example, before and after ^{27}Al, ^{23}Na and ^{11}B NMR spectra of P3 are essentially identical (**Figure 7.13**). Similarly, ^{29}Si NMR spectra are unchanged by the dissolution experiments (**Figure 7.14**). However, some subtle but structurally significant differences may be observed. **Figure 7.15** shows ^{31}P MAS NMR spectra of all P-bearing glasses before and after the MCC-1 test, where it can be seen that the orthophosphate fraction around 15 ppm is reduced in P1 and P2, but increased in P3, P4 and P4-Mo3. Whereas the pyro- and metaphosphate spectral regions are the same for P2, P3 and P4, a significant sharpening of the P^1 and P^2 peak is observed after dissolution for sample P1. While the integrated intensity remains roughly the same, the narrowing suggests increased structural order about the P^1 units. Spectral changes in the P^1 and P^2 regions for P4-Mo3 are also notable, revealing increases in the P^1 signal at +5 ppm and the P^2 signal near -10 ppm, implying significant changes in the phosphate speciation upon dissolution.

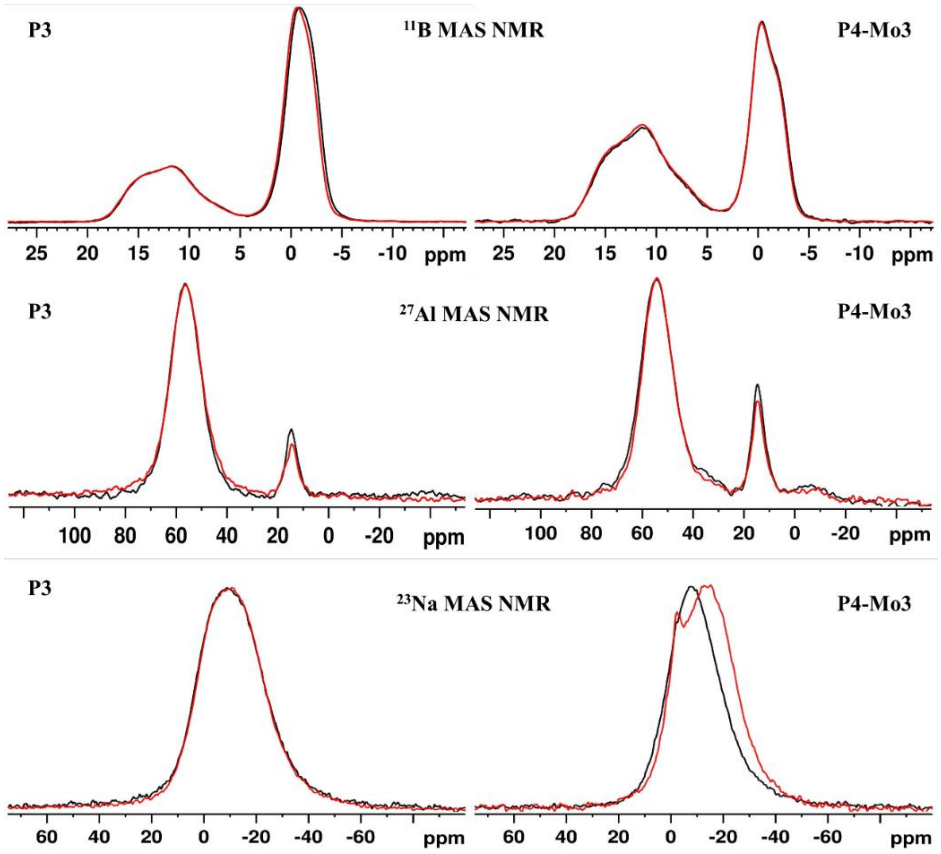

Figure 7.13. ^{11}B, ^{27}Al and ^{23}Na MAS NMR spectra of P3 and P4-Mo3 before (black) and after (red) dissolution.

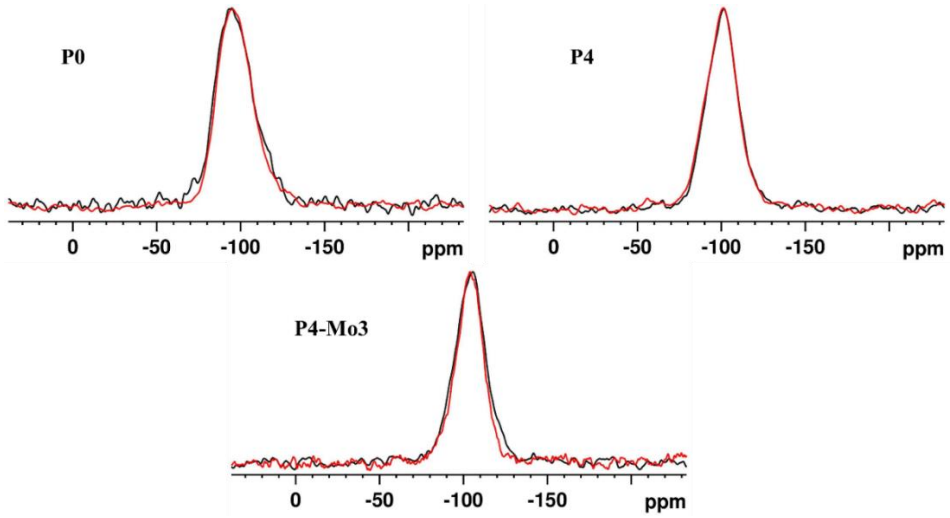

Figure 7.14. ^{29}Si MAS NMR spectra before (black) and after (red) dissolution.

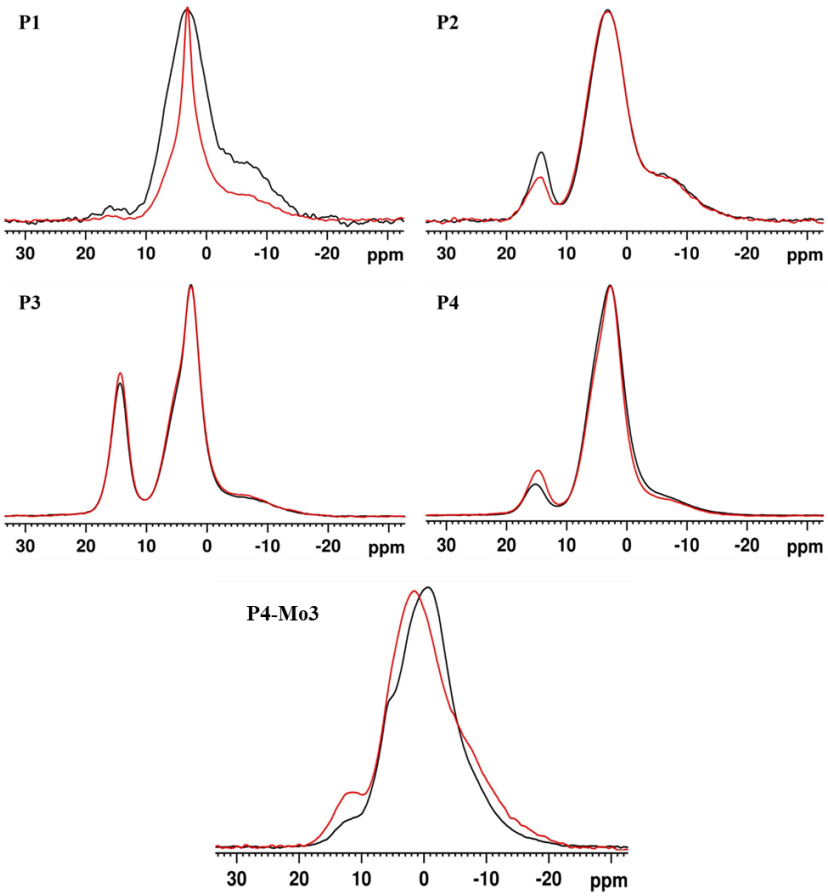

Figure 7.15. An overlay of ^{31}P MAS NMR spectra before (black) and after (red) the dissolution.

These changes are reflected in the ^{23}Na MAS NMR spectrum of P4-Mo3 (**Figure 7.13**), where the major glassy peak shifts significantly to lower frequency, and the signature of a crystalline Na-bearing phase becomes apparent at 0 ppm, consistent with the NMR parameters of Na_2MoO_4 [12]. Interestingly, x-ray diffraction does not show any evidence of Na_2MoO_4, or indeed any Na-, Mo- or P-bearing phases, the only peaks being attributable to minor SiO_2 contribution in P3 and P4-Mo3 (entry numbers 00-101-1097 and 00-101-0938) (**Figure 7.16**). This implies that any crystalline phases observed by ^{31}P or ^{23}Na NMR are either at a very low level or poorly crystalline, or both, escaping detection by XRD. Positive identification of crystalline SiO_2 by NMR is difficult in this case, particularly for small quantities which may have a very long spin-lattice relaxation times relative to that of the glassy phase. A final difference in the NMR spectra is the observation that the $^{[5]}$Al fraction is consistently reduced relative to $^{[4]}$Al after the dissolution for all samples (**Figure 7.13**).

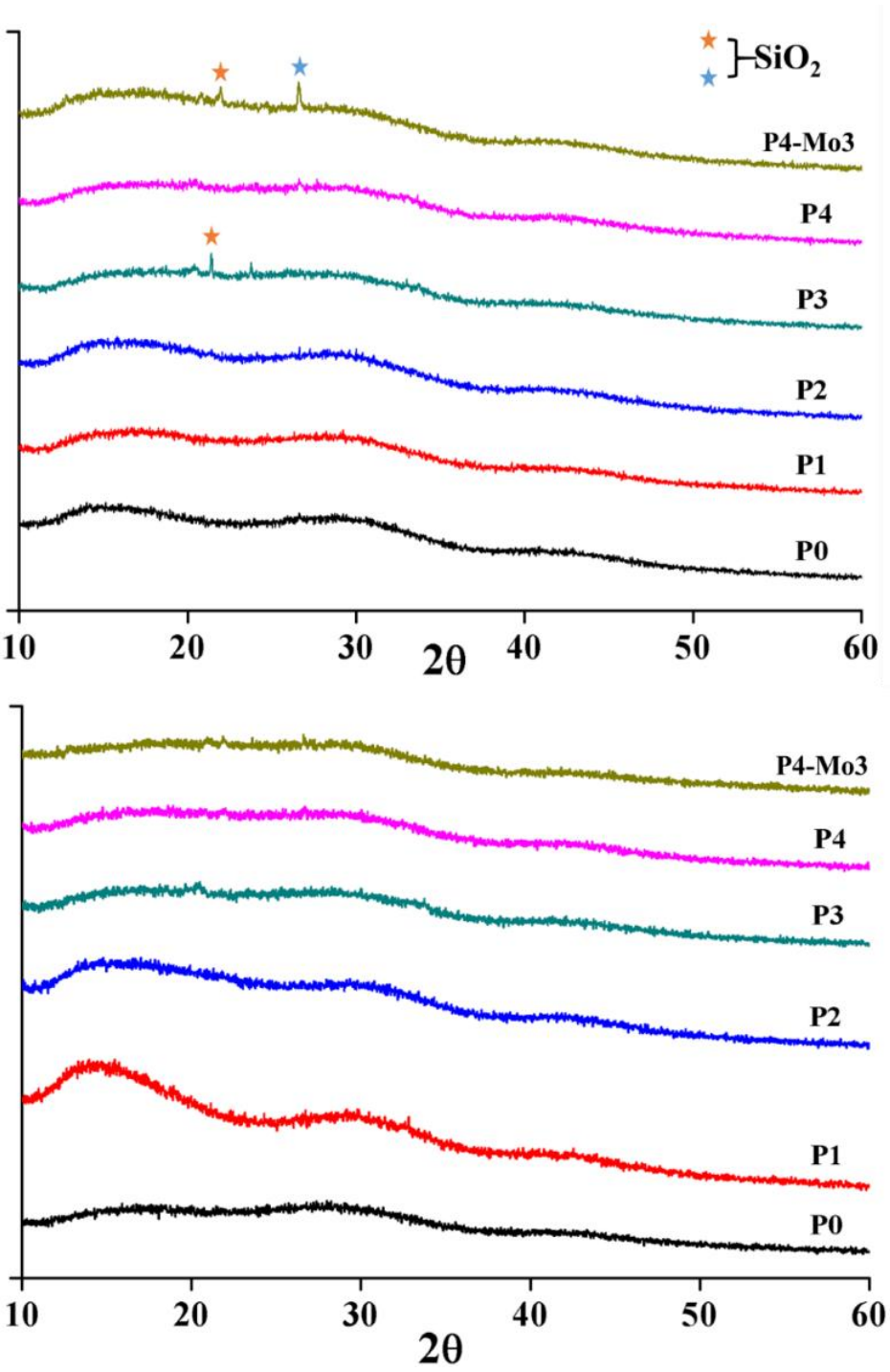

Figure 7.16. X-ray diffractograms before (top) and after (bottom) dissolution. The orange and blue stars represent peaks from the SiO_2 phases, cristobalite and quartz, respectively.

7.3.2 Dissolution behaviour

Leachates were sampled at regular intervals and subjected to ICP-MS analysis to quantify the elements released over each period of time. The element profiles of all glasses are plotted in **Figure 7.17**. The concentrations of all elements in the leachate were normalized according to the compositions of the glasses [50]:

$$NL = \frac{C_i}{f_i * SV} \qquad (8.1)$$

where the normalized loss (NL, g m^{-2}) is related to the concentration of the element in the leachate as determined from ICP-MS analysis (C_i, ppm), the fraction of the element present in the bulk glass (f_i, atomic %), and the surface-area-to-volume ratio (SV), chosen to be 25 m^{-1}.

The beneficial effect of doping the glasses with phosphate is illustrated in the Si release data: as the phosphate content of the glass increases, Si release into the solution decreases, suggesting a reduction in the extent of glass dissolution and corresponding increase in chemical durability. Moreover, the Si concentration in the leachate of all Mo-free glasses has dropped drastically by day 28, a clear indication that Si from the leachate is being redeposited onto the glass surface as new layer [51]. The dissolution behaviour of the Mo-bearing glass (P4-Mo3) is distinct from the others, showing significant retention of Si over the time course of this study; even after 28 days, the Si release is lower than the Mo-free analogue, and it is unlikely that it has reached the “saturation” point.

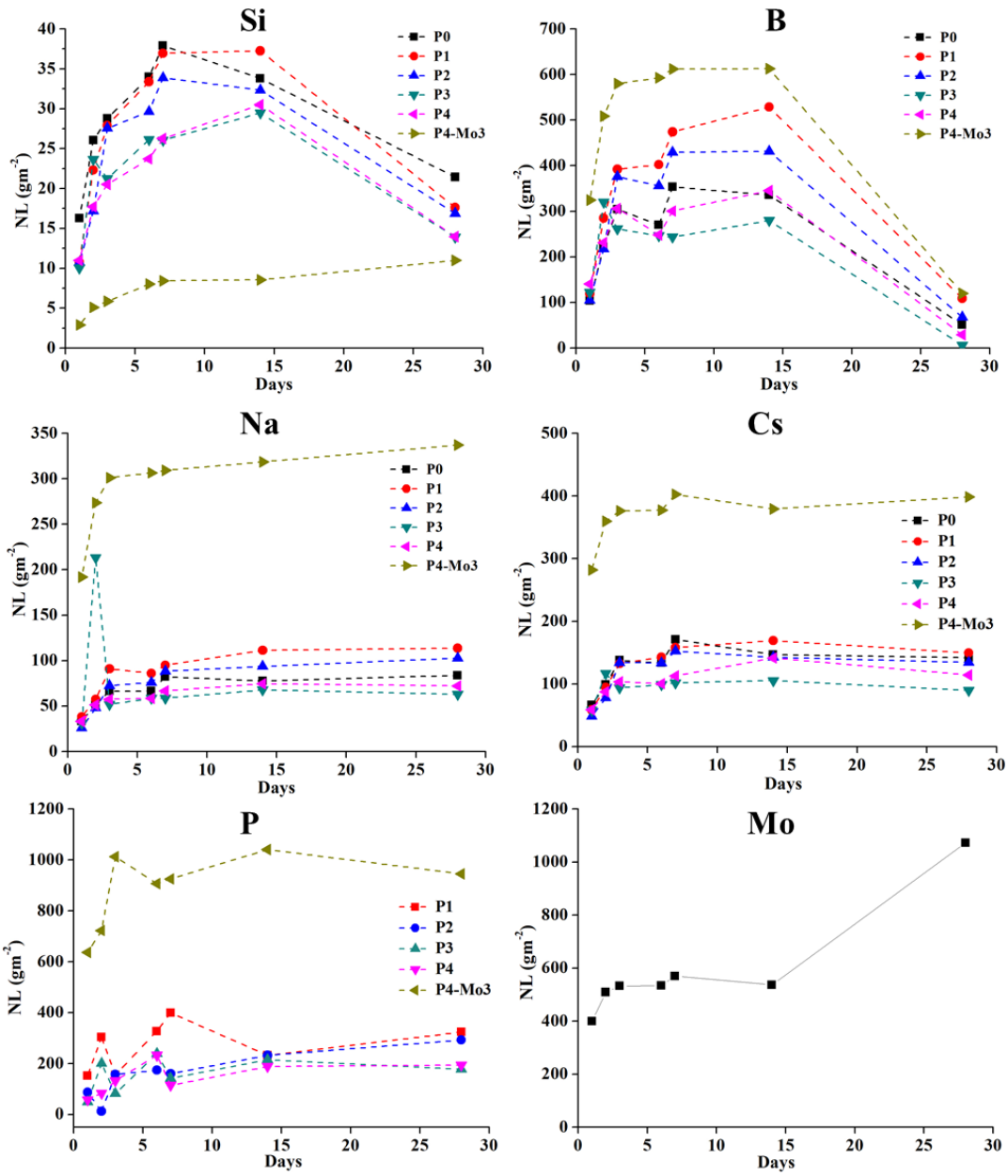

Figure 7.17. Normalized loss of elements leached from glasses over 28 days of dissolution, as measured by ICP-MS. The error bars are smaller than the size of the symbols.

The B release data appear similar to the Si data: both profiles rise quickly in the first week, followed by a plateau and then a precipitous decline by the end of the test period. Like Si, B leaching is retarded by the addition of P. Differences include the much higher overall release of B vis-à-vis Si — more than an order of magnitude despite its lower concentration in the glass

— and a more pronounced discontinuity in the first week. The drop in B concentration after 28 days implies that, like Si, B redeposits on the glass surface, possibly along with Si in a gel-like alteration layer. The dissolution behaviour of the Mo-bearing glass also departs from that of Si, exhibiting substantially higher B release than the Mo-free glasses, suggesting that Mo incorporation induces incongruent dissolution of the glass network formers.

The Na and Cs release plots show similarities, which emphasize their common role as glass-network modifiers. Consistent with what is observed for Si and B, increased P content appears to reduce the loss of these ions from the glass, with the maximum release reached around the one-week point. Unlike the network formers, the concentrations of Na and Cs do not change in the last two weeks, suggesting that these cations do not participate in the re-deposition or alteration layer. Like B, the incorporation of Mo into the P4 glass significantly increases the Cs and Na release into solution, most likely due to the phase separation observed by EDS (vide infra). It is interesting to note that the overall loss of Cs and Na is comparable, despite their vastly different concentrations in the pristine glass: 3 mol% Cs_2O and 18 mol% Na_2O.

Phosphorus release into the solution is generally similar to that of the other elements, with lower dissolution associated with higher P contents. Although there is no reduction in P release at long times, the release profile of the first week appears more complex than the other elements. P release from the Mo-bearing glass is substantially greater than any of the Mo-free glasses, and also any of the other elements, despite its relatively low concentration in the pristine glass. A continuous increase in the Mo leaching is observed in the case of P4-Mo3.

7.3.3 Scanning electron microscopy

Backscattered-electron (BSE) and secondary-electron (SE) SEM images of pristine Mo-free glasses appear homogeneous at 500x magnification (**Figure 7.18**), with energy-dispersive x-ray spectroscopy (EDS) showing elemental profiles as expected for these compositions (**Figure 7.19**). With the introduction of Mo (P4-Mo3), however, evidence of phase-separated regions is observed on the surface under 2000x magnification, EDS of which reveals enrichment in P, Na, and Mo in these areas, and the near-exclusion of silicon (**Figure 7.20a**). These microscopic observations confirm visual inspection of the as-made glasses, where the opacity of the glasses increased progressively from transparent (P0) to partially opaque (P4), and fully opaque in P4-Mo3.

To better understand the phase separation in P4-Mo3, SEM images of a freshly fractured surface were collected. The inset in **Figure 7.20b** shows bright regions in the BSE image, ranging from the sub-micron to millimeter scale, their brightness suggesting enrichment by heavy Mo. Indeed, EDS analyses (**Figures 7.20b and c**) confirm that the droplets are rich in Mo, Na, and P, whereas the bulk glass has an elemental signature similar to that of P4. Significantly, the bulk glass contains small but non-negligible amounts of P and Mo, indicating that the aluminoborosilicate glass network incorporates some amount of both elements. Element maps of P4-Mo3 indicate a high degree of uniformity across the two distinct regions: the bulk glass is predominantly sodium boroaluminosilicate, whereas the inclusion is mainly sodium phosphate with molybdenum, and possibly some aluminum (**Figure 7.21**). Subtle patchiness observed in the Si map hints at the possibility of the separation of a Si-rich region.

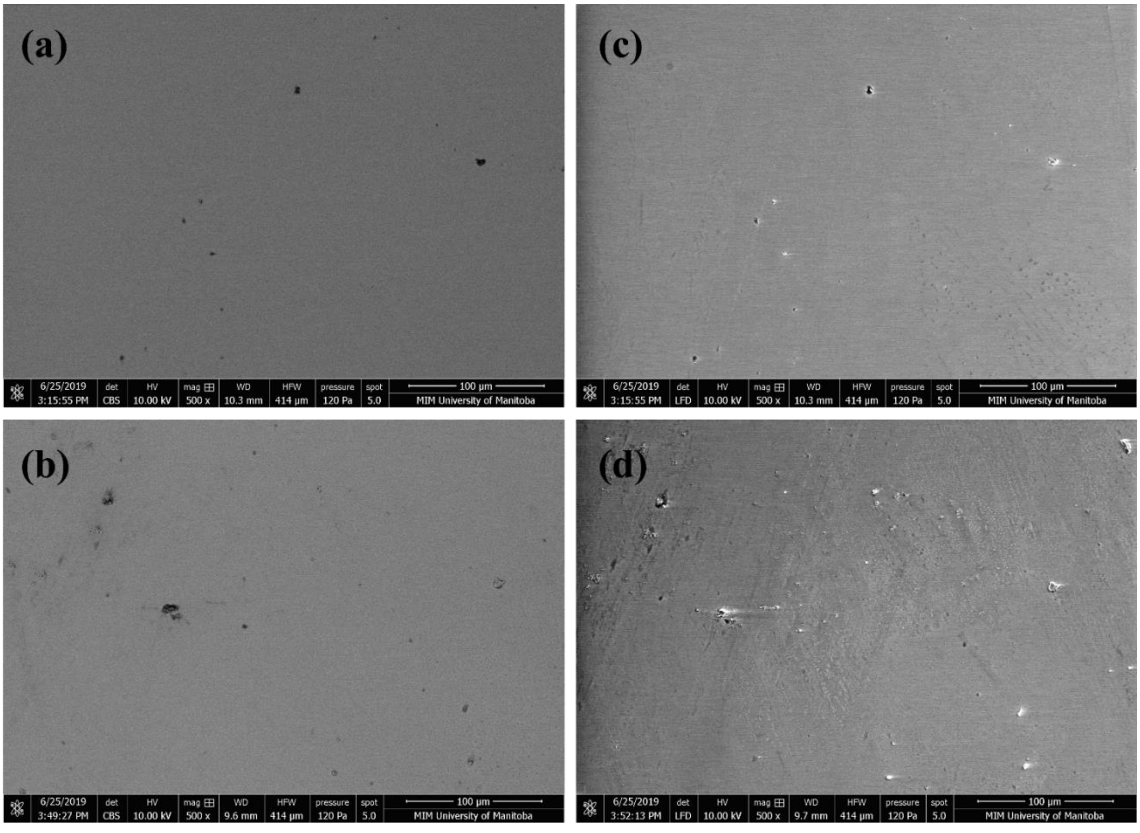

Figure 7.18. SEM images (500x magnification) of glasses prior to dissolution: (a) BSE image of P0, (b) BSE image of P4, (c) SE image of P0, (d) SE image of P4.

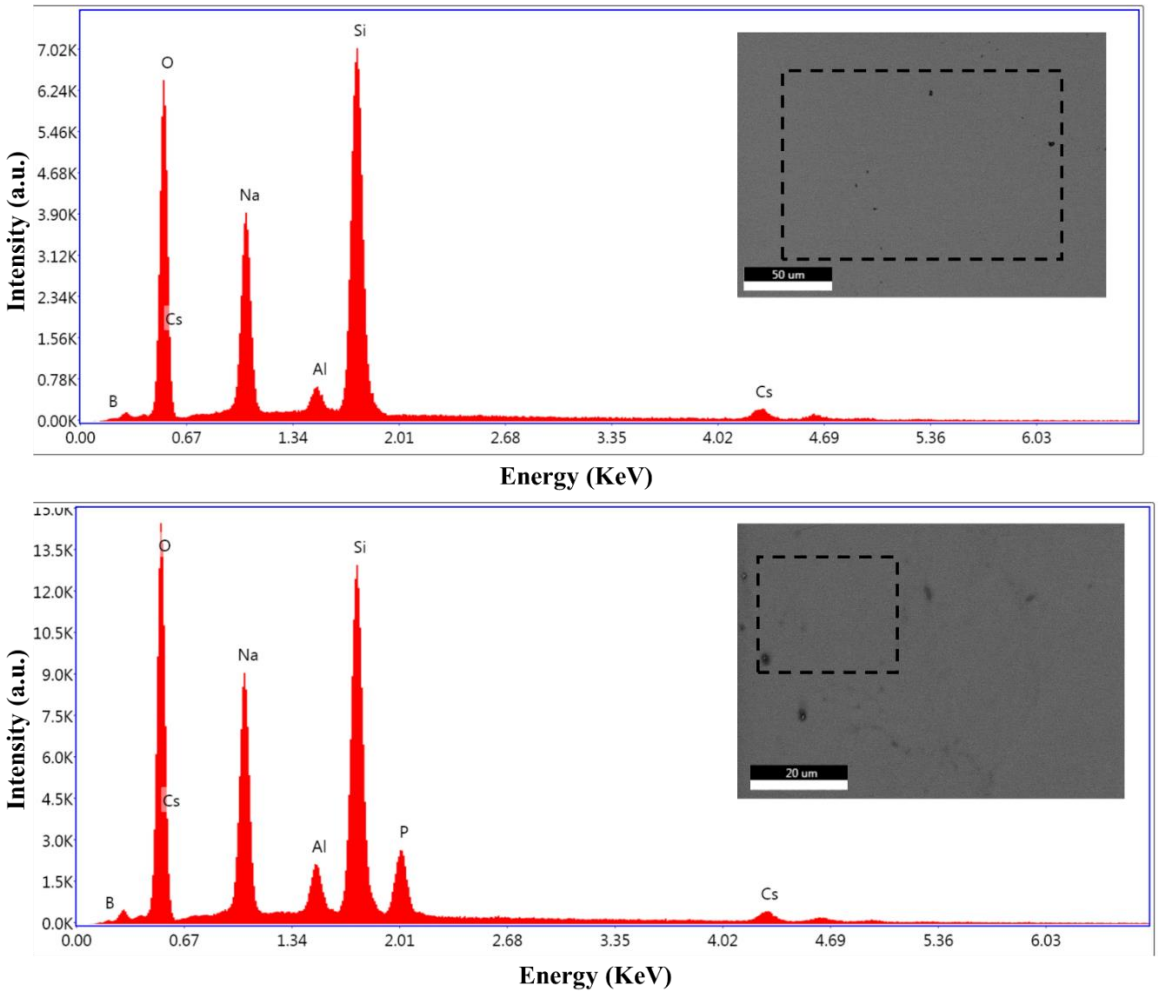

Figure 7.19. EDS spectra of glasses P0 and P4 with their corresponding BSE images. The dotted rectangles show the analyzed areas.

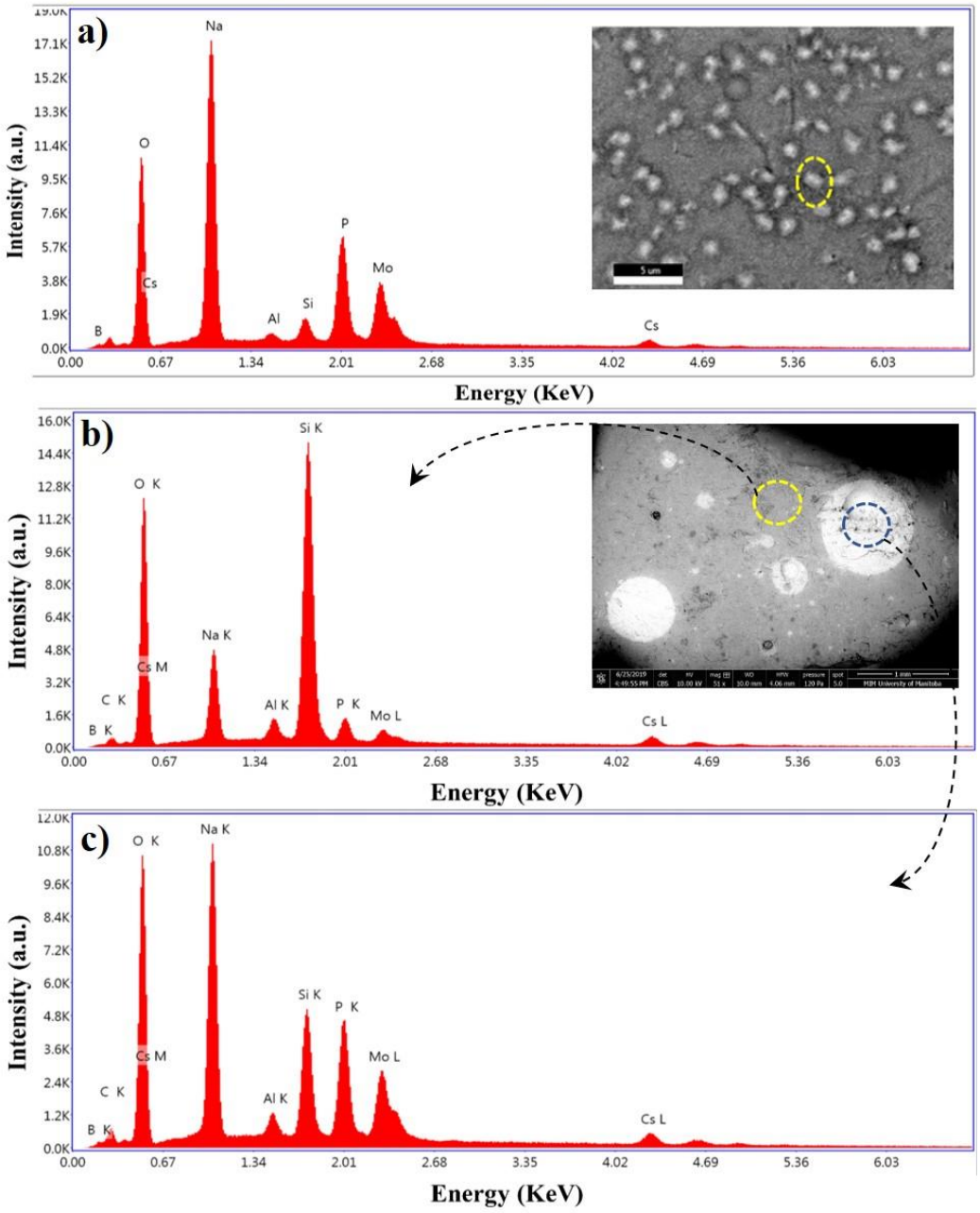

Figure 7.20. (a) EDS spectrum of the surface of sample P4-Mo3; (b) EDS spectrum of the dark region (yellow circle) within the BSE image of a cross-section of P4-Mo3 (inset); (c) EDS spectrum of the bright region (blue circle).

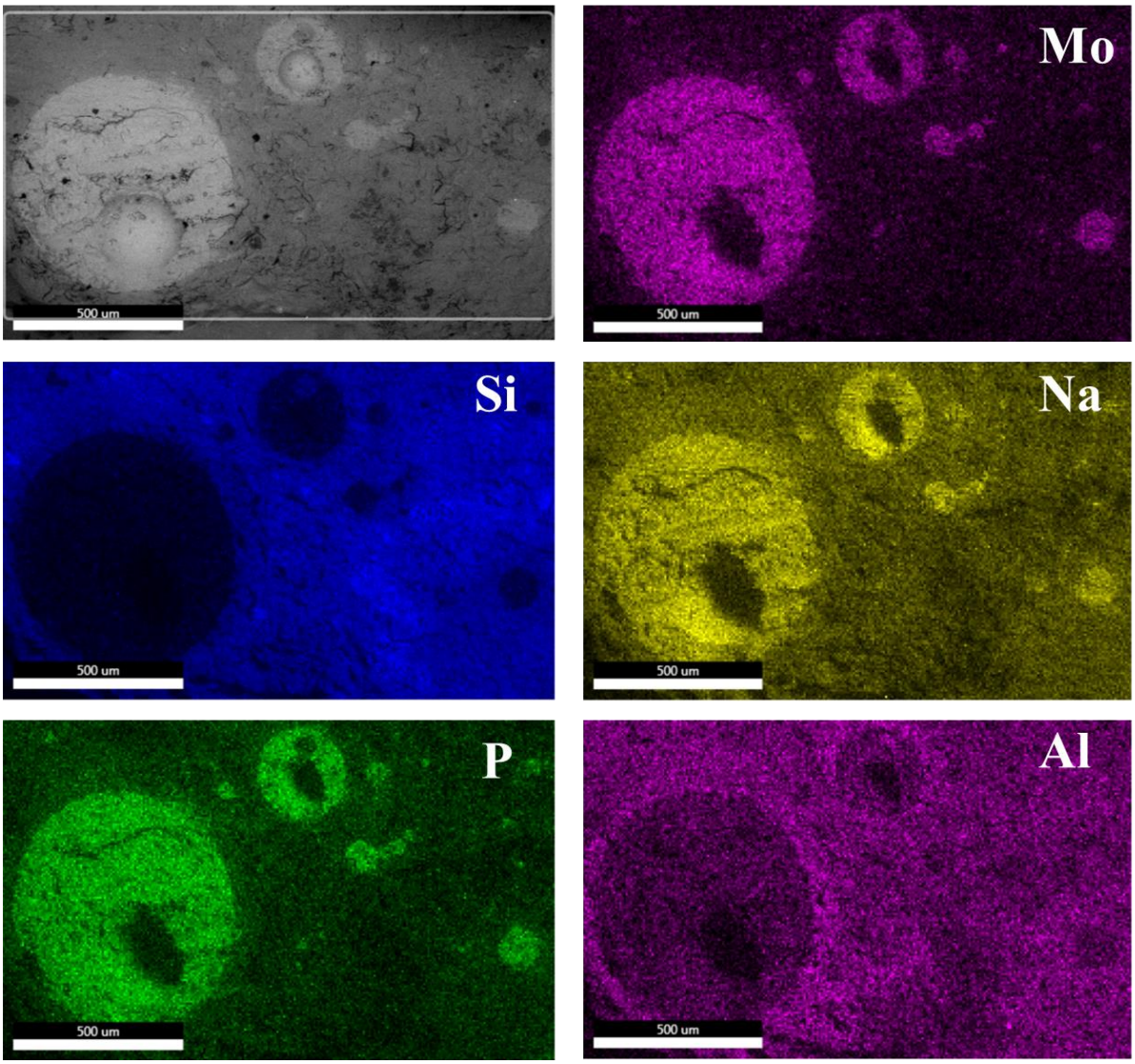

Figure 7.21. BSE image of a cross-section of P4-Mo3 and the element maps showing the distribution of elements in the mapped area.

After the dissolution experiments, images of the glass surfaces reveal substantial alteration with respect to the pristine glasses. For example, both P4 and P4-Mo3 surfaces appear to be altered by a smooth amorphous layer (**Figure 7.22**) enriched in Si and Al, and depleted in P, Na and Mo (**Figure 7.23**) relative to the pristine glasses (**Figures 7.19**). A direct comparison of the EDS spectra of the P4 sample surface before and after dissolution is shown in **Figure 7.24**, confirming the formation of a Si- and Al-rich layer post-dissolution vis-à-vis the pristine glass. A

BSE image of a cross-section of P4 after dissolution confirms the presence of 10-µm thick Si-rich layer on the glass surface, enriched in Si and Al and devoid of P and Na (**Figure 7.25**).

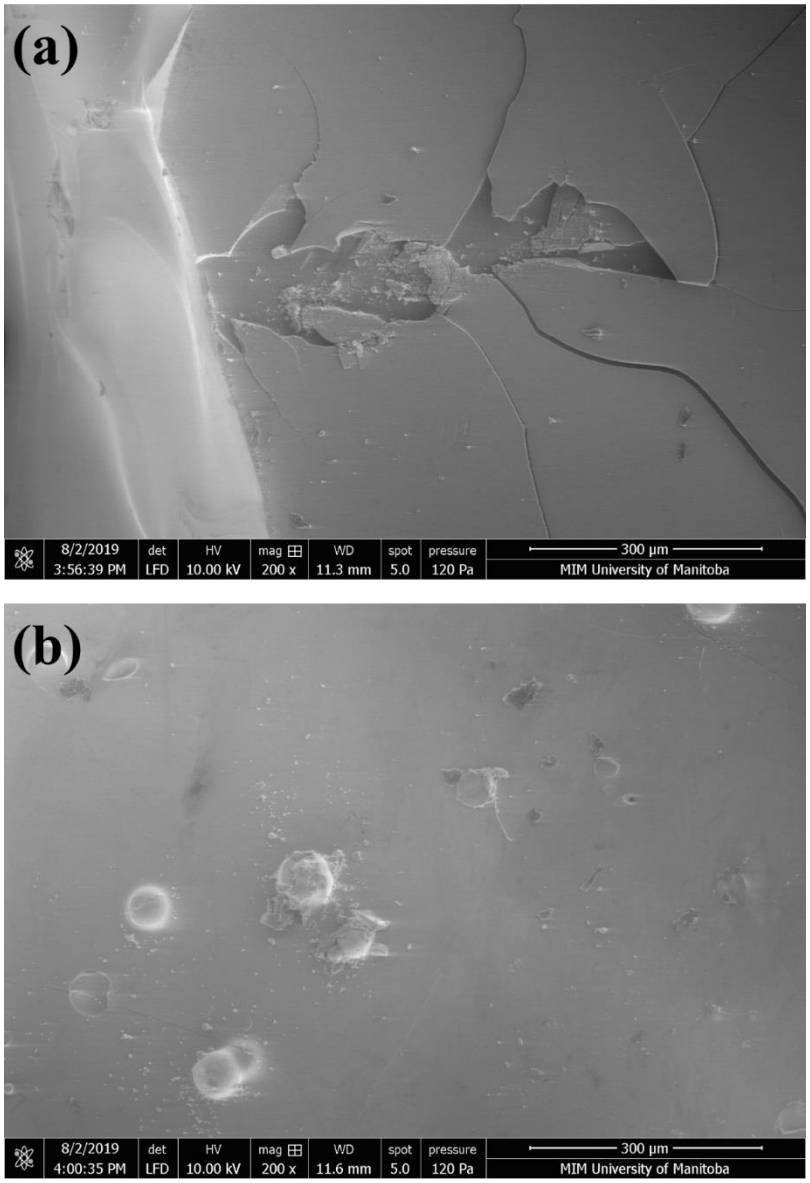

Figure 7.22. BSE images of the surfaces of (a) P4 and (b) P4-Mo3 after dissolution.

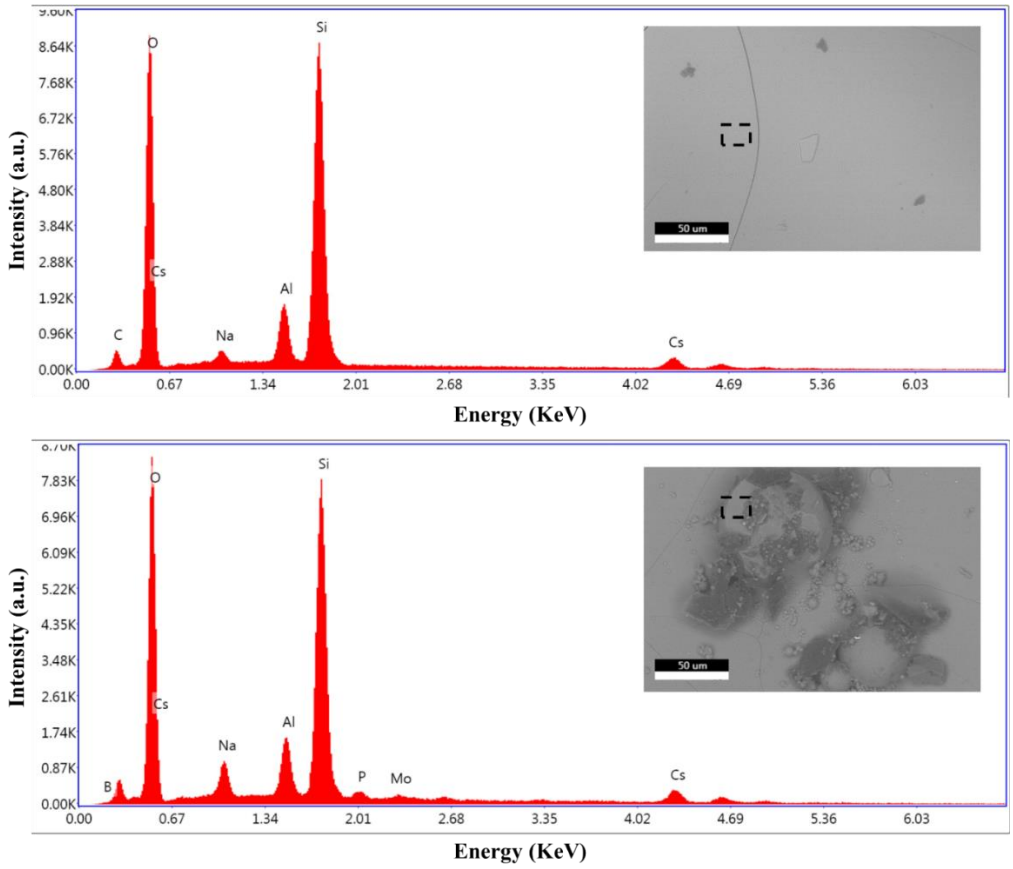

Figure 7.23. EDS spectra of the surfaces of glasses P4 (top) and P4-Mo3 (bottom) after dissolution. The analyzed areas are marked with a dotted rectangle in the BSE images shown.

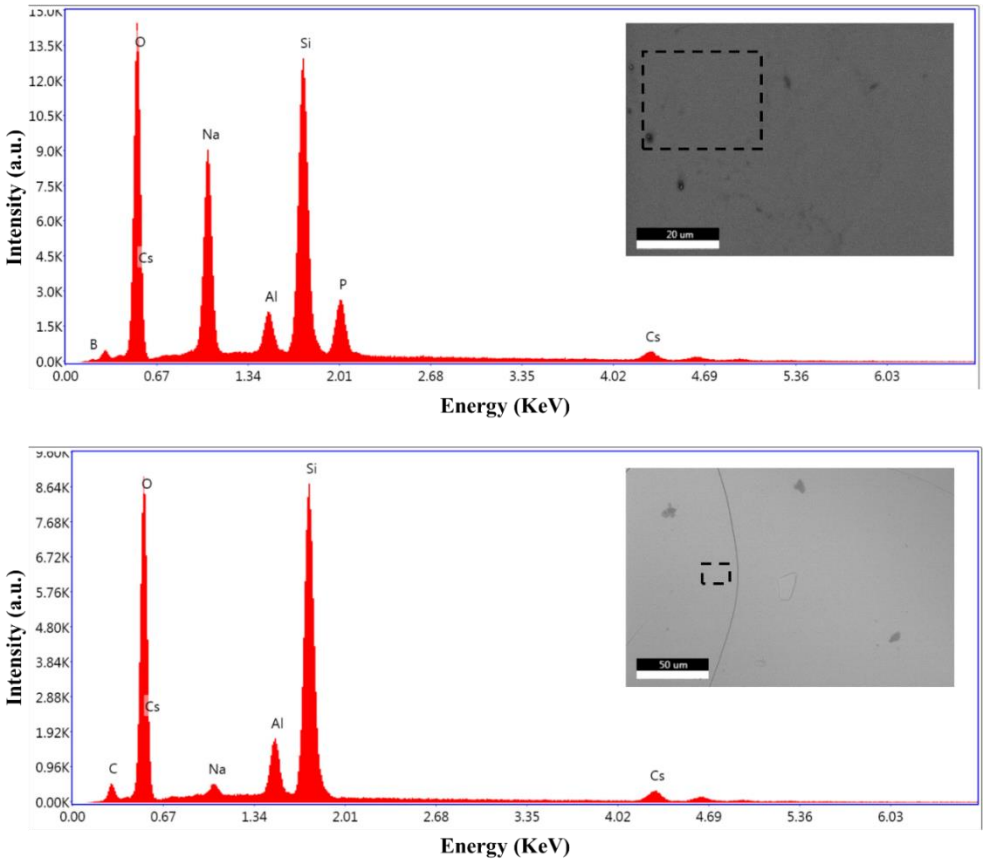

Figure 7.24. EDS spectra of the surface of sample P4 before (top) and after (bottom) dissolution. The BSE images are provided in the inset with the analyzed areas marked using dotted rectangles.

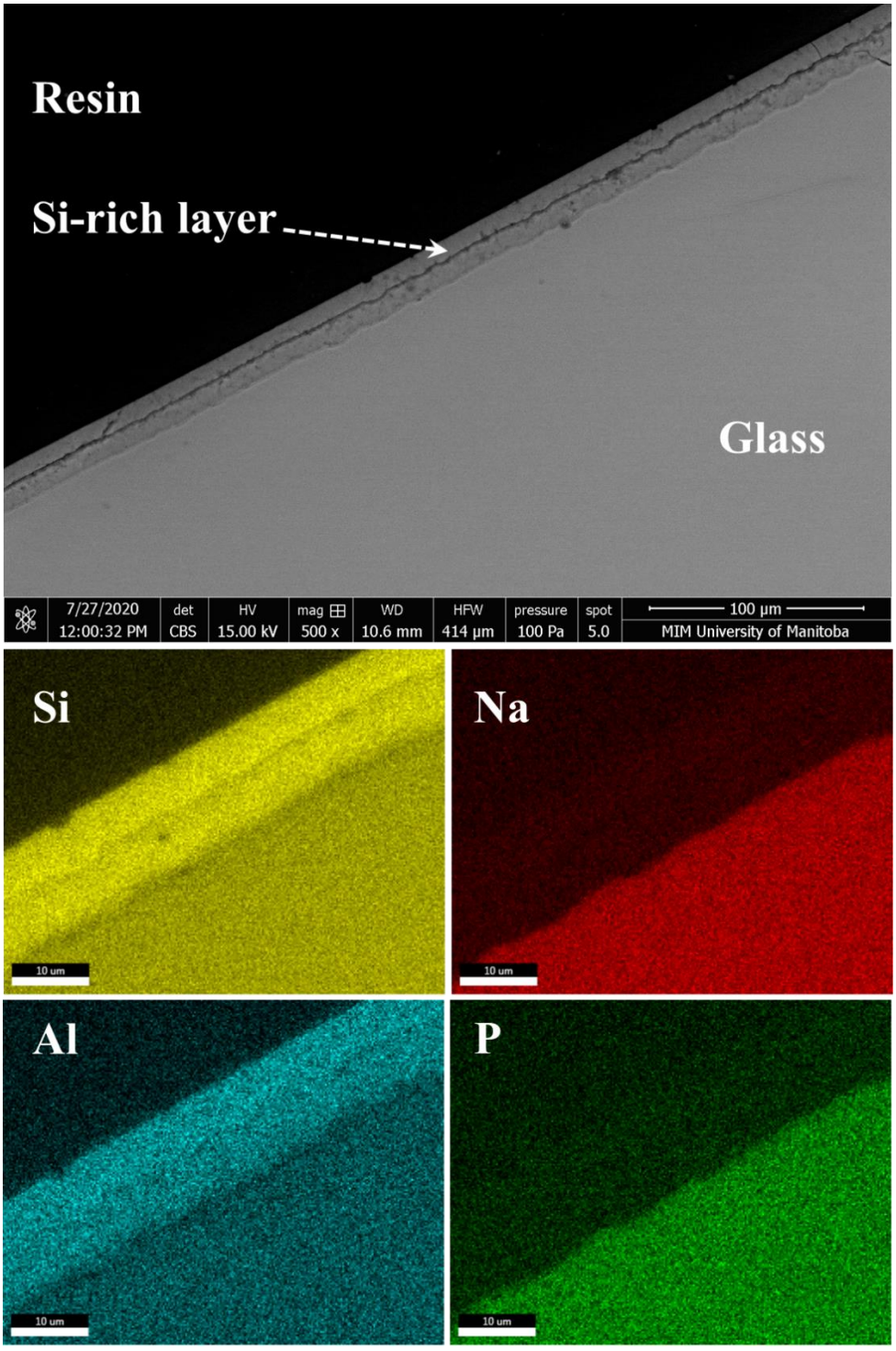

Figure 7.25. Back-scattered electron image of a cross-section of sample P4 after dissolution, and element maps of the Si-rich layer deposited on the glass surface.

7.4 Discussion

7.4.1 Glass network structure

Multinuclear magnetic resonance spectroscopy is particularly well suited for the study of glass network structure. Most of the constituent elements in these multicomponent materials can be conveniently probed by NMR in the solid state, providing valuable information about their local chemical environments which can be assembled into a comprehensive model of glass structure. In combination with XRD, NMR can also be used to confirm the amorphous nature of the samples and identify any crystalline inclusions. At the macroscopic level, maps generated by EDS illustrate the elemental distributions throughout the materials, revealing the presence of chemical heterogeneity which is essential to understanding their dissolution behaviour. Combining these techniques, a structural model showing how phosphorus and molybdenum are assimilated into the aluminoborosilicate network can be constructed.

The P-free aluminoborosilicate glass structure is much the same as previously documented for similar compositions [33,42,52]. The silicate network is highly reticulated and consists of appreciable amounts of fully connected tetrahedral silicate units, Q^4 (37%), and silicate species with one non-bridging oxygen, Q^3 (63%). Likewise, most of the boron is in fourfold coordination (66%), bonded to three or four silicate units, with about one-third present as fully-coordinated $BO_{3/2}$ species. The small amount of aluminum in the framework is mostly four-coordinated, with about 20% AlO_5. Mass- and charge-balance calculations confirm that there are enough sodium and cesium cations to account for the Si non-bridging oxygens and the anionic aluminum and boron species.

Phosphorus enters this network mainly as dimers, with a small fraction appearing to be connected to boron or aluminum in chains ($P^2_{nB(Al)}$) for glasses containing 1 and 2 mol% P_2O_5. The anionic phosphate species scavenge alkali cations, lowering the $BO_{4/2}$ and Q^3 populations in favour of their neutral counterparts, $BO_{3/2}$ and Q^4. A subtle low-frequency shift in the $BO_{4/2}$ peak position hints at the formation of B−O−P at the expense of B−O−Si linkages, consistent with the ^{31}P NMR data. A slight increase in peak width and a low-frequency shift in the four-coordinate ^{27}Al resonance is consistent with the formation of a small quantity of Al−O−P bonds. At 3 mol% P_2O_5, evidence of clustering can be observed as poorly crystalline $Na_4P_2O_7$ in the ^{23}Na and ^{31}P NMR spectra, accounting for the onset of a translucent appearance in the bulk glass. Further nucleation is evident at 4 mol% P_2O_5, where a distinct ^{23}Na NMR signal can be

observed, and the preferential association of alkali cations with phosphate dimers depletes the aluminoborosilicate network of charge-balancing cations, inducing increased reticulation of the major glassy phase. This picture coheres with early NMR work on the incorporation of phosphorus into alkali silicate glasses [53–55].

Introducing 3 mol% MoO_3 into the P4 composition causes substantial structural changes, both on the micro- and macro-scale. Whereas only subtle spectral changes are observed for most nuclei, the ^{31}P MAS NMR spectrum is significantly altered (**Figure 7.6**). The shift in peak maximum implies either the formation of more metaphosphate groups, or that bonding to Mo increases the ^{31}P shielding of pyrophosphate groups, either explanation indicating that Mo interacts predominantly with the small fraction of phosphate present in the glass. ^{29}Si NMR provides evidence for only Q^4 species, while ^{11}B NMR shows a reduction in tetrahedral boron, both consistent with the formation of a borosilicate glass phase low in alkali cations. These observations can be explained by phase separation into an amorphous alkali-phosphate-rich phase which binds most of the molybdenum, and a borosilicate glass phase. Aluminum appears to partition into both phases, with hexacoordinate aluminum in the phosphate-rich phase, as previously observed [53,56]. Since high-coordinate Al is considered a network modifier in aluminophosphates, the formation of $^{[6]}$Al upon Mo addition seems to be a structural requirement for charge-balancing purposes. The higher cation field strength of Mo^{6+} with respect to P^{5+} allows it to preferentially associate with the alkali cations, forcing the phosphate units to generate $^{[6]}$Al for charge balance.

7.4.2 Macroscopic phase separation

Up to 3 mol% P_2O_5 can be added to this aluminoborosilicate glass without phase separation. At 4 mol% P_2O_5, the glass appears translucent; NMR detects the beginning of clustering in the form of a partially ordered sodium-phosphate phase, despite the absence of any such features in XRD or SEM, highlighting the importance of local spectroscopic probes in complex materials. However, the addition of Mo to P4 induces glass-in-glass phase separation, with droplet sizes measuring from a few microns to mm in SEM (**Figure 7.20**). Maps generated using EDS clearly distinguish the elemental partitioning between the two phases, revealing the droplets to be rich in Na, P and Mo, with the rest of the matrix predominantly Si, and presumably B, which is too electron-poor to be observed by EDS. Aluminum is present in both phases, consistent with

inferences from NMR (see above). Within the dominant Si-rich phase, the Si distribution does not appear to be homogeneous, with patchy areas rich in Si which could be an indication of further immiscibility within the borosilicate matrix [57]. The clustering of P and Mo into droplet-like regions within the glassy matrix underscores the bonding preferences of these cations, as implied by the NMR results.

In view of the original objective of this research to improve Mo solubility in borosilicate glasses without molybdate devitrification, the incorporation of small amounts of phosphate has proven successful. The element maps of P4-Mo3 (**Figure 7.21**) show that the borosilicate-rich matrix is not entirely devoid of P and Mo, suggesting that phase separation occurs only once their respective solubility limits are reached. A molecular-style diagram illustrates this schematically in **Figure 7.26**, showing the main bonding features determined from NMR. The droplet phase is rich in phosphorus dimers, charge-balanced by sodium and hexa-coordinate molybdenum, and anchored to the dominant aluminoborosilicate phase through borate and aluminate tetrahedra. The small fraction of orthophosphate units observed in ^{31}P NMR is shown as isolated tetrahedra randomly distributed throughout the silicate network, as well as some isolated molybdate units expected also to be present there [58]. In broad strokes, this depiction represents the encapsulation of a phosphate-rich glass phase within a silicate-rich glass phase; any molybdenum loading beyond its solubility limit in the borosilicate phase is taken up by the phosphate glass phase.

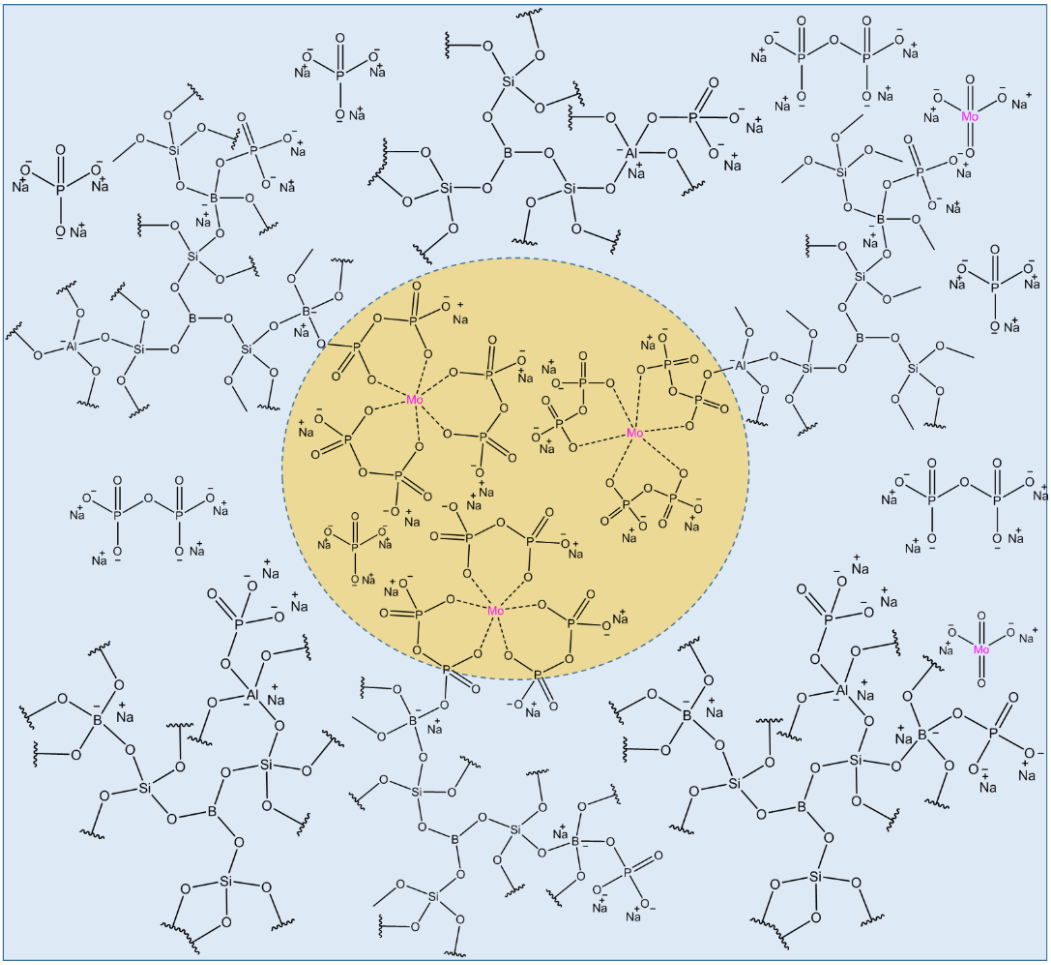

Figure 7.26. A structural schematic of the network structure of glass P4-Mo3. The blue and orange regions represent two glassy phases observed in the BSE image of the glass.

7.4.3 Dissolution behaviour

Despite the success of phosphorus for inhibiting the crystallization of molybdates, the larger issue is the overall chemical durability of these materials. Standardized dissolution experiments reveal that in Mo-free glasses, elemental release generally decreases as the P_2O_5 content is increased from 1 to 4 mol%, indicating that phosphate additives on their own do not degrade the durability of these model glasses (**Figure 7.17**). Analytical data show few changes before and after dissolution, except for the ^{31}P NMR data, discussed above.

More interesting is the behaviour of the Mo-bearing glass, which exhibits vastly different characteristics than the Mo-free glasses. The high initial release rate of P, Na, Cs and Mo is clear

evidence that the phase-separated phosphate-rich regions suffer from low durability and are accessible to the solvent, dissolving rapidly under the conditions of the test. The comparatively low Si release rate confirms that the silicate-rich glassy phase has a higher degree of network connectivity, as observed by NMR, and a correspondingly higher chemical durability.

An encouraging factor in terms of potential value to the nuclear industry is the formation of a solid silicate layer during exposure to water. Such layers - whether due to direct alteration or redeposition - are thought to act as a barrier preventing the interdiffusion of ions between the glass and water, thereby preventing further leaching of radionuclides.[51,59] Since glass composition is the key parameter controlling the growth of these layers, we were interested in determining whether the addition of phosphate would influence their formation. The appearance in SEM images of layered depositions on the glass monoliths after dissolution, and EDS spectra indicating enhanced Si and Al contents (**Figures 7.22 and 7.23**), confirm that the added phosphorus does not prevent their formation. Although the thicknesses of these layers could not be measured with the tools at hand, the thickness of a passivation layer formed on an international simple glass (ISG) composition was found to be ca. 2 μm [60]. Further, albeit indirect, evidence for the protective role of the passivation layers is that the P, Na and Cs release profiles level off around the same time as Si begins redeposition, indicating that the glass durability is restored.

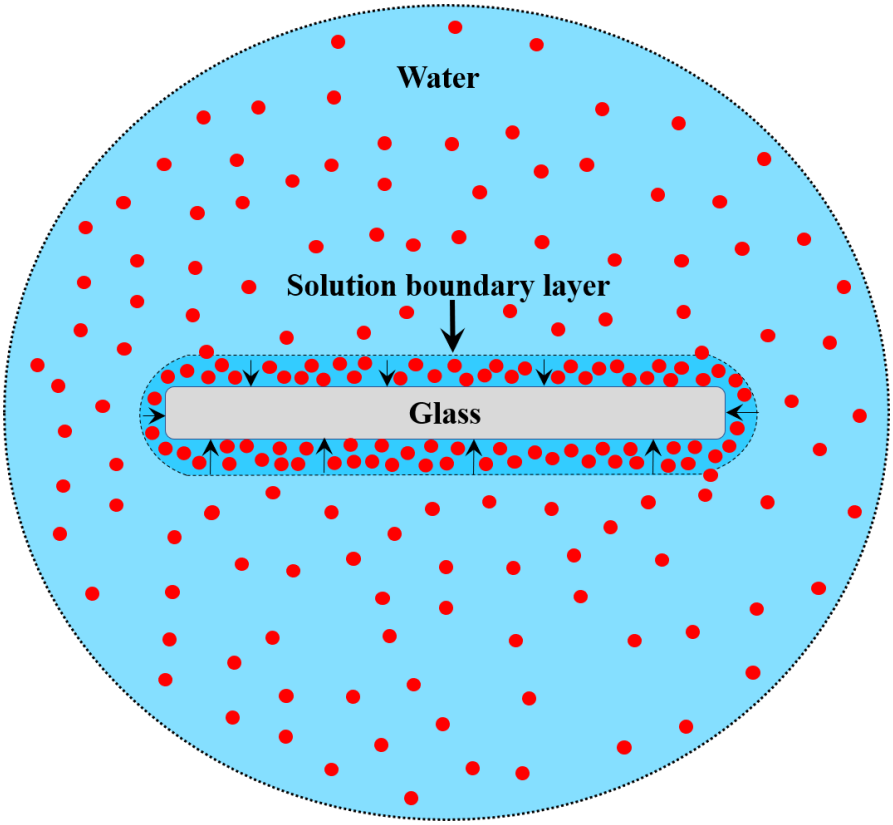

Figure 7.27. Schematic depiction of the formation of a nanometer-thick Si-saturated film of water near the glass surface. The arrows depict the motion of the water film towards the sample during dissolution.

The formation of such passivation layers is thought to occur by one of two mechanisms [61]: a localized nanoscale layer of Si-saturated water at the glass surface leading to eventual silicate precipitation[62] (**Figure 7.27**), or the simultaneous removal of modifier cations by ion exchange and silicon by Si-O hydrolysis, resulting in saturation of the solution preventing further dissolution [63]. The latter mechanism is more likely to occur in cases where the surface-area-to-volume ratio is much higher, such as in cracks or bubbles, and it is improbable that the current dissolution experiments are capable of saturating the leachate with silicon. Hence, the first mechanism, featuring coupled glass dissolution and silicate precipitation rates, may explain the drop in the concentration of Si in the leachate. In this *interface-coupled dissolution-reprecipitation reaction* [62], dissolution proceeds congruently until a thin film of water near the surface of the dissolving glass becomes saturated with silicon in the form of orthosilicic acid,

which is in metastable equilibrium with the bulk of the solution across a solution boundary layer. Polymerization into colloidal silica is followed by aggregation to form amorphous silica, which matures into an alteration layer.

The EDS spectra of post-dissolution glasses P4 and P4-Mo3 share the same features, implying that alteration layers form on both glasses (**Figure 7.23**); however, close inspection reveals that the P4-Mo3 surface has P and Mo peaks of very low intensity, suggesting that the layer formed on P4-Mo3 may not have matured as quickly as that of P4. This is most likely due to the slow Si release profile in P4-Mo3, which is still increasing after 28 days (**Figure 7.17**) and may not have reached a high enough local concentration to begin redeposition. This explanation would be consistent with effect of glass-in-glass phase separation resulting in a more durable - and hence, slower dissolving - high-silica glassy phase.

A surprising result is that the boron release profiles match those of silicon, decreasing over time for all samples (**Figure 7.17**). Boron's typically modifier-like dissolution behaviour has led to the use of B as a glass-alteration tracer [64], on the assumption that it is not incorporated into the alteration layer [61]. The clear decrease in leachate B concentration over time challenges this assumption and suggests that boron may be implicated in the alteration layer, or at least redeposits on the monolith surface as part of a solid layer. As there is no indication of the formation of crystalline borates in the post-dissolution ^{11}B MAS NMR spectra, and boron is too light to be reliably probed by EDS, the chemical nature of the redeposited boron cannot be readily determined. The incorporation of boron into the alteration layer could be consistent with the interface-coupled dissolution-reprecipitation mechanism and would involve the co-condensation of aqueous borate and silicate species near the surface of the glass under static conditions, with the concomitant depletion of B from the leachate. However, saturation of the bulk solution followed by B redeposition is not possible under these experimental conditions (i.e., glass composition, B release and water volume), indicating that the boron dissolution profiles may be interpreted to identify the glass corrosion mechanism at play.

7.5 Conclusion

The strategy of doping nuclear-waste glasses with phosphate to improve Mo incorporation without compromising chemical durability has been explored by studying the structure and dissolution properties of P-doped borosilicate glasses. This work has confirmed that up to 3 mol% P_2O_5 can be incorporated into the borosilicate glass network before the onset of clustering and phase separation, even appearing to improve the chemical durability of the materials in water, based on static dissolution tests. A borosilicate glass with 4 mol% P_2O_5 can accommodate 3 mol% MoO_3 without devitrification, more than doubling the Mo solubility in P-free borosilicate glasses, but at the expense of segregation into a water-soluble amorphous alkali-phosphate phase containing most of the molybdenum. Nevertheless, the formation of a protective Si-rich solid layer significantly reduces ion release from the glass monolith after seven days, arresting further dissolution of network modifiers such as Cs. Interestingly, the boron dissolution profile mirrors that of Si, implying that B participates in this layer, and calling into question the reliability of boron as an alteration tracer. Considering that the concentrations of Mo, Cs and P in this model system are much higher than typical nuclear glasses such as SON-68 [63], it is anticipated that the strategy of doping borosilicate glasses with low (<4 mol%) levels of P_2O_5 will more than double their capacity for molybdenum, and to the extent that Mo solubility limits total waste loading, P doping may permit significant increases in overall waste loading. If these observations prove sufficiently general under further testing with more complex glasses and waste components, minor compositional adjustments may serve to permit improved waste-loading capacities within existing industrial process streams, providing economic and ecological benefits.

7.6 References

[1] S. Gin, A. Abdelouas, L.J. Criscenti, W.L. Ebert, K. Ferrand, T. Geisler, M.T. Harrison, Y. Inagaki, S. Mitsui, K.T. Mueller, J.C. Marra, C.G. Pantano, E.M. Pierce, J. V. Ryan, J.M. Schofield, C.I. Steefel, J.D. Vienna, An international initiative on long-term behavior of high-level nuclear waste glass, Mater. Today. 16 (2013) 243–248.

[2] M.J. Plodinec, Borosilicate glasses for nuclear waste imobilisation, Glas. Technol. 41 (2000) 186–192.

[3] M.I. Ojovan, W.E. Lee, Glassy wasteforms for nuclear waste immobilization, *Metall. Mater. Trans. A Phys. Metall. Mater. Sci.*, 2011: pp. 837–851.

[4] R.C. Ewing, W.J. Weber, Nuclear-waste management and disposal, in: *Fundamentals of materials for energy and environment sustainability*, D.S. Ginley, D. Cahen (Eds.), Cambridge University Press, 2012: pp. 178–193.

[5] D. Caurant, O. Majérus, E. Fadel, A. Quintas, C. Gervais, T. Charpentier, D. Neuville, Structural investigations of borosilicate glasses containing MoO_3 by MAS NMR and Raman spectroscopies, J. Nucl. Mater. 396 (2010) 94–101.

[6] J.D. Vienna, D.S. Kim, I.S. Muller, G.F. Piepel, A.A. Kruger, Toward understanding the effect of low-activity waste glass composition on sulfur solubility, J. Am. Ceram. Soc. 97 (2014) 3135–3142.

[7] P.A. Bingham, R.J. Hand, Sulphate incorporation and glass formation in phosphate systems for nuclear and toxic waste immobilization, Mater. Res. Bull. 43 (2008) 1679–1693.

[8] S. Kroeker, S. Schuller, J.E.C. Wren, B.J. Greer, A. Mesbah, ^{133}Cs and ^{23}Na MAS NMR Spectroscopy of Molybdate Crystallization in Model Nuclear Glasses, J. Am. Ceram. Soc. 99 (2016) 1557–1564.

[9] B.J. Greer, S. Kroeker, Characterisation of heterogeneous molybdate and chromate phase assemblages in model nuclear waste glasses by multinuclear magnetic resonance spectroscopy, Phys. Chem. Chem. Phys. 14 (2012) 7375–7383.

[10] B.C. Russell, I.W. Croudace, P.E. Warwick, Determination of ^{135}Cs and ^{137}Cs in environmental samples: A review, Anal. Chim. Acta. 890 (2015) 7–20.

[11] R.J. Budnitz, Strontium-90 and Strontium-89: A review of Measurement Techniques in Environmental Media, Berkeley, 1974.

[12] J.E.C. Wren, B.J. Greer, V.K. Michaelis, C.S. Higman, S. Kroeker, Multinuclear magnetic resonance investigation of crystalline alkali molybdates, Inorg. Chem. 54 (2015) 9853–9861.

[13] J.H. Hsu, J. Bai, C.W. Kim, R.K. Brow, J. Szabo, A. Zervos, The effects of crystallization and residual glass on the chemical durability of iron phosphate waste forms containing 40 wt% of a high MoO_3 Collins-CLT waste, J. Nucl. Mater. 500 (2018) 373–380.

[14] M.H. Hekmat-Shoar, C.A. Hogarth, G.R. Moridi, A study of the electrical properties of molybdenum phosphate glasses, J. Mater. Sci. 20 (1985) 889–894.

[15] J.A. Duffy, M.D. Ingram, An interpretation of glass chemistry in terms of the optical basicity concept, J. Non-Cryst. Solids. 21 (1976) 373–410.

[16] G. Tricot, K. Ben Tayeb, L. Koudelka, P. Mosner, H. Vezin, Insertion of MoO_3 in borophosphate glasses investigated by magnetic resonance spectroscopies, J. Phys. Chem. C. 120 (2016) 9443–9452.

[17] T. Minamf, J.D. Mackenzie, Thermal expansion and chemical durability of phosphate glasses, J. Am. Ceram. Soc. 60 (1977) 232–235.

[18] A.D. Prakash, M. Singh, R.K. Mishra, T.P. Valsala, A.K. Tyagi, A. Sarkar, C.P. Kaushik, Studies on modified borosilicate glass for enhancement of solubility of molybdenum, J. Non-Cryst. Solids. 510 (2019) 172–178.

[19] O. Pinet, J.F. Hollebecque, I. Hugon, V. Debono, L. Campayo, C. Vallat, V. Lemaitre, Glass ceramic for the vitrification of high level waste with a high molybdenum content, J. Nucl. Mater. 519 (2019) 121–127.

[20] D.S. Brauer, Bioactive glasses - Structure and properties, Angew. Chemie - Int. Ed. 54 (2015) 4160–4181.

[21] O. Pinet, J.L. Dussossoy, C. David, C. Fillet, Glass matrices for immobilizing nuclear waste containing molybdenum and phosphorus, J. Nucl. Mater. 377 (2008) 307–312.

[22] S. Schuller, O. Pinet, A. Grandjean, T. Blisson, Phase separation and crystallization of borosilicate glass enriched in MoO_3, P_2O_5, ZrO_2, CaO, J. Non-Cryst. Solids. 354 (2008) 296–300.

[23] D.M. Strachan, R.P. Turcotte, B.O. Barnes, Mcc-1: A Standard leach test for nuclear waste forms., Nucl. Technol. 56 (1980) 306–312. doi:10.13182/nt82-a32859.

[24] D. Massiot, F. Fayon, M. Capron, I. King, S. Le Calvé, B. Alonso, J.O. Durand, B. Bujoli,

Z. Gan, G. Hoatson, Modelling one- and two-dimensional solid-state NMR spectra, Magn. Reson. Chem. 40 (2002) 70–76.

[25] J.P. Amoureux, C. Fernandez, QUASAR—Solid-State NMR Simulation for Quadrupolar Nuclei, Univ. Lille, Lille, Fr. (2005).

[26] A. Altomare, N. Corriero, C. Cuocci, A. Falcicchio, A. Moliterni, R. Rizzi, QUALX2.0: a qualitative phase analysis software using the freely available database POW_COD, J. Appl. Crystallogr. 48 (2015) 598–603.

[27] P.M. Aguiar, S. Kroeker, Boron speciation and non-bridging oxygens in high-alkali borate glasses, J. Non-Cryst. Solids. 353 (2007) 1834–1839.

[28] V.K. Michaelis, P.M. Aguiar, S. Kroeker, Probing alkali coordination environments in alkali borate glasses by multinuclear magnetic resonance, J. Non-Cryst. Solids. 353 (2007) 2582–2590.

[29] S. Kroeker, Nuclear Waste Glasses: Insights from solid-state NMR, Encycl. Magn. Reson. (2011) 453–466.

[30] W.J. Clarida, J.R. Berryman, M. Affatigato, S.A. Feller, S.C. Kroeker, J. Ash, J.W. Zwanziger, B. Meyer, F. Borsa, S.W. Martin, Dependence of N_4 upon alkali modifier in binary borate glasses, Phys. Chem. Glas. 44 (2003) 215–217.

[31] L.S. Du, J.F. Stebbins, Site preference and Si/B mixing in mixed-alkali borosilicate glasses: A high-resolution ^{11}B and ^{17}O NMR study, Chem. Mater. 15 (2003) 3913–3921.

[32] C. Martineau, V.K. Michaelis, S. Schuller, S. Kroeker, Liquid-liquid phase separation in model nuclear waste glasses: A solid-state double-resonance NMR study, Chem. Mater. 22 (2010) 4896–4903.

[33] L.-S.S. Du, J.F. Stebbins, Solid-state NMR study of metastable immiscibility in alkali borosilicate glasses, J. Non-Cryst. Solids. 315 (2003) 239–255.

[34] S. Kroeker, J.F. Stebbins, Three-coordinated boron-11 chemical shifts in borates, Inorg. Chem. 40 (2001) 6239–6246.

[35] G. Engelhardt, A.P.M. Kentgens, H. Koller, A. Samoson, Strategies for extracting NMR parameters from ^{23}Na MAS, DOR and MQMAS spectra. A case study for $Na_4P_2O_7$, Solid State Nucl. Magn. Reson. 15 (1999) 171–180.

[36] C. Rong, K.C. Wong-Moon, H. Li, P. Hrma, H. Cho, Solid-state NMR investigation of phosphorus in aluminoborosilicate glasses, J. Non-Cryst. Solids. 223 (1998) 32–42.

[37] H. Gan, P.C. Hess, R.J. Kirkpatrick, Phosphorus and boron speciation in K_2O-B_2O_3-SiO_2-P205 glasses, Geochim. Cosmochim. Acta. 58 (1994) 4633–4647.

[38] F. Muñoz, L. Montagne, L. Delevoye, A. Durán, L. Pascual, S. Cristol, J.F. Paul, Phosphate speciation in sodium borosilicate glasses studied by nuclear magnetic resonance, J. Non-Cryst. Solids. 352 (2006) 2958–2968.

[39] M. Reichert, S.W. Martin, Mixed network former effect in ion-conducting alkali borophosphate glasses: Structure/property correlations in the system $[M_2O]_{1/3}[(B_2O_3)_x(P_2O_5)_{1-x}]_{2/3}$ (M = Li, K, Cs), J. Phys. Chem. C. 116 (2012) 26162–26176.

[40] S. Dusold, J. Kümmerlen, A. Sebald, A ^{31}P NMR Study of Solid Compounds $M_xP_2O_7$, J. Phys. Chem. A. 101 (1997) 5895–5900.

[41] S. Kapoor, X. Guo, R.E. Youngman, C.L. Hogue, J.C. Mauro, S.J. Rzoska, M. Bockowski, L.R. Jensen, M.M. Smedskjaer, Network glasses under pressure: permanent densification in modifier-free Al_2O_3- B_2O_3- P_2O_5-SiO_2 systems, Phys. Rev. Appl. 7 (2017) 1–16.

[42] E.I. Morin, J.F. Stebbins, Separating the effects of composition and fictive temperature on Al and B coordination in Ca, La, Y aluminosilicate, aluminoborosilicate and aluminoborate glasses, J. Non-Cryst. Solids. 432 (2016) 384–392.

[43] D.C. Kaseman, A. Retsinas, A.G. Kalampounias, G.N. Papatheodorou, S. Sen, Q-speciation and network structure evolution in invert calcium silicate glasses, J. Phys. Chem. B. 119 (2015) 8440–8445.

[44] T. Ohkubo, R. Monden, Y. Iwadate, S. Kohara, K. Deguchi, S. Ohki, T. Shimizu, Structural investigation of aluminoborosilicate glasses containing Na_2MoO_4 crystallites by solid state NMR, Phys. Chem. Glas. Eur. J. Glas. Sci. Technol. Part B. 56 (2015) 138–144.

[45] E. Nicoleau, S. Schuller, F. Angeli, T. Charpentier, P. Jollivet, A. Le Gac, M. Fournier, A. Mesbah, F. Vasconcelos, Phase separation and crystallization effects on the structure and durability of molybdenum borosilicate glass, J. Non-Cryst. Solids. 427 (2015) 120–133.

[46] S. Prasad, T.M. Clark, T.H. Sefzik, H.T. Kwak, Z. Gan, P.J. Grandinetti, Solid-state multinuclear magnetic resonance investigation of Pyrex®, J. Non-Cryst. Solids. 352 (2006) 2834–2840.

[47] H. Maekawa, T. Maekawa, K. Kawamura, T. Yokokawa, The structural groups of alkali silicate glasses determined from ^{29}Si MAS-NMR, J. Non-Cryst. Solids. 127 (1991) 53–64.

[48] F. Angeli, O. Villain, S. Schuller, S. Ispas, T. Charpentier, Insight into sodium silicate glass structural organization by multinuclear NMR combined with first-principles calculations, Geochim. Cosmochim. Acta. 75 (2011) 2453–2469.

[49] P. Zhang, P.J. Grandinetti, J.F. Stebbins, Anionic species determination in $CaSiO_3$ glass using two-dimensional ^{29}Si NMR, J. Phys. Chem. B. 101 (1997) 4004–4008.

[50] T.L. Gout, M.T. Harrison, I. Farnan, Relating Magnox and international waste glass, J. Non-Cryst. Solids. 524 (2019) 119647.

[51] G.S. Frankel, J.D. Vienna, J. Lian, J.R. Scully, S. Gin, J. V. Ryan, J. Wang, S.H. Kim, W. Windl, J. Du, A comparative review of the aqueous corrosion of glasses, crystalline ceramics, and metals, Npj Mater. Degrad. 2 (2018).

[52] L.S. Du, J.F. Stebbins, Network connectivity in aluminoborosilicate glasses: A High-resolution ^{11}B, ^{27}Al and ^{17}O NMR study, J. Non-Cryst. Solids. 351 (2005) 3508–3520.

[53] R. Dupree, D. Holland, M.G. Mortuza, Six-coordinated silicon in glasses, Nature. 328 (1987) 416–417.

[54] R. Dupree, D. Holland, M.G. Mortuza, The role of small amounts of P_2O_5 in the structure of alkali disilicate glasses, Phys. Chem. Glas. 29 (1988) 18–21.

[55] R.J. Kirkpatrick, R.K. Brow, Nuclear magnetic resonance investigation of the structures of phosphate and phosphate-containing glasses: A review, Solid State Nucl. Magn. Reson. 5 (1995) 9–21.

[56] F. Behrends, H. Eckert, Mixed-alkali effects in aluminophosphate glasses: A re-examination of the system $[xNa_2O(1 - x)Li_2O]_{0.46}[yAl_2O_3(1 - y)P_2O_5]_{0.54}$, J. Phys. Chem. C. 115 (2011) 17175–17183.

[57] C. Martineau, V.K. Michaelis, S. Schuller, S. Kroeker, Liquid-liquid phase separation in model nuclear waste glasses: A solid-state double-resonance NMR study, Chem. Mater. 22 (2010) 4896–4903.

[58] S. Kroeker, I. Farnan, S. Schuller, T. Advocat, ^{95}Mo NMR Study of Crystallization in Model Nuclear Waste Glasses, Mater. Res. Soc. Symp. Proc. 1124 (2009).

[59] C. Cailleteau, F. Angeli, F. Devreux, S. Gin, J. Jestin, P. Jollivet, O. Spalla, Insight into silicate-glass corrosion mechanisms, Nat. Mater. 7 (2008) 978–983.

[60] D. Ngo, H. Liu, N. Sheth, R. Lopez-Hallman, N.J. Podraza, M. Collin, S. Gin, S.H. Kim, Spectroscopic ellipsometry study of thickness and porosity of the alteration layer formed on international simple glass surface in aqueous corrosion conditions, Npj Mater. Degrad. 2 (2018).

[61] S. Gin, P. Jollivet, M. Fournier, F. Angeli, P. Frugier, T. Charpentier, Origin and consequences of silicate glass passivation by surface layers, Nat. Commun. 6 (2015).

[62] T. Geisler, A. Janssen, D. Scheiter, T. Stephan, J. Berndt, A. Putnis, Aqueous corrosion of borosilicate glass under acidic conditions: A new corrosion mechanism, J. Non-Cryst. Solids. 356 (2010) 1458–1465.

[63] P. Frugier, S. Gin, Y. Minet, T. Chave, B. Bonin, N. Godon, J.E. Lartigue, P. Jollivet, A. Ayral, L. De Windt, G. Santarini, SON68 nuclear glass dissolution kinetics: Current state of knowledge and basis of the new GRAAL model, J. Nucl. Mater. 380 (2008) 8–21. d

[64] M. Fournier, T. Ducasse, A. Pérez, A. Barchouchi, D. Daval, S. Gin, Effect of pH on the stability of passivating gel layers formed on International Simple Glass, J. Nucl. Mater. 524 (2019) 21–38.

8 Improving Molybdenum and Sulfur Vitrification in Model Nuclear Waste Borosilicate Glasses using Phosphorus: Structural Insights from NMR

8.1 Introduction

Spent fuel rods from nuclear power plants are reprocessed to extract residual fissile materials which enter a new cycle of the nuclear fission process [1,2]. The waste from this reprocessing step is rich in radioactive fission products and must be carefully handled to prevent harmful environmental exposure. The best way to protect the biosphere from these radioactive wastes is to immobilize them in materials possessing extremely high chemical durability, allowing them to decay to safe levels while locked in a robust material. The most widely used material for this purpose is glass, due to its many favorable properties. Borosilicate-based glasses are especially useful for nuclear waste immobilization and have been adopted worldwide [3−5]. However, despite their ability to simultaneously incorporate high levels of a large range of waste ions into the glass structure, borosilicate glass has a low affinity for molybdenum, sulfur, rare-earth elements and platinoid elements (Ru, Rh, Pd) which can be concentrated in calcined nuclear wastes [6]. The high cation field-strengths of these fission products [7] induce ordering of oxygen anions about the cations, leading to clustering, and ultimately to the nucleation and crystallization of phases which separate from the glass.

Molybdenum is one such problem element which tends to sequester alkali (A^{+}) and alkaline-earth metal ions (A^{2+}) from waste-immobilized glasses in the form of crystalline molybdates (A_2MoO_4 and $AMoO_4$) [8]. This devitrification alters the composition, structure and strength of these glasses, compromising their long-term performance. Mo^{6+} is a key concern because of its propensity to sequester isotopes with very high radioactivity and long half-lives (e.g., ^{135}Cs, ^{137}Cs and ^{90}Sr) to form complex molybdate assemblages known as "yellow phase" [9]. These radioactive crystalline phases are highly soluble in water and could leach into the environment if they came into contact with water in a geological repository. MoO_3 is one of the limiting factors which restricts nuclear waste loading capacities in borosilicate glasses owing to

its low solubility; homogeneous glasses without separated crystalline phases can typically be achieved only when the MoO_3 loading limit is less than 1.5 mol% [10].

Like molybdates, sulfate anions in radioactive waste have low solubility in borosilicate glasses (0.6 mol% or ~ <1 wt%) [11–13]. Sources of sulfate in typical nuclear waste streams include ferrous sulfamate (used in the reduction of Pu^{4+} to Pu^{3+}) [14], waste liquors arising from the Purex process, and spent ion-exchange resins [15]. Although the oxidation states of sulfur range from -2 to +6, they are predominantly found as hexavalent cations in the oxidizing conditions of borosilicate glasses [16], with a coordination number of four (SO_4^{2-}). At low levels, isolated SO_4^{2-} tetrahedral units concentrate into interstitial spaces in the borosilicate network [16]. Above the solubility limit, a sulfate-rich salt layer is observed on top of the melt pool, which precipitates during melt cooling [12]. This phase-separated layer is called "gall" [14] and must be avoided in the immobilization of high-level liquid waste by limiting the overall waste loading according to the sulfate content. The main component of the gall layer is Na_2SO_4 [14], which is capable of sequestering radioactive isotopes of Cs, Sr, and Tc [11,12,14,17]. Phase separation and precipitation of the gall layer on top of the melt also has a detrimental effect on the crucible and furnace, as it is highly corrosive and, being a good conductor, makes the melting process less energy-efficient [11]. The gall layer on the melt pool inhibits the release of gas bubbles, leading to swelling of the vitreous phase upon cooling [14]. The presence of sulfur in the waste stream also impacts the glass formation conditions, as sulfate decomposes at high temperatures, releasing SO_2 gas in a reaction which may be enriched with volatile radioactive isotopes [18,19].

The chemical environment of molybdate in borosilicate glass is similar to that of sulfate: molybdate units are present as isolated tetrahedra concentrated in depolymerized regions rich in alkali and alkaline-earth ions [20]. This concentration leads to clustering and nucleation, with the eventual sequestration of charge-balancing alkali ions by the phase-separating molybdate units when Mo is loaded above its solubility limit [21]. Separated molybdate phases are distributed in borosilicate glasses as nano- and micrometer spherical droplets formed by nucleation and growth [9]. Owing to the fact that both Mo^{6+} and S^{6+} are high-field-strength cations distributed throughout the borosilicate glass network as isolated tetrahedral units, a reasonable starting assumption is that they follow similar alkali-ion sequestration and phase-separation mechanisms.

Increasing the solubilities of MoO_3 and SO_3 in borosilicate glasses would reduce the volume of waste glass generated and lead to more efficient and economical immobilization processes. The development of new borosilicate glass compositions which can melt at lower temperatures, yielding homogeneous glasses and incorporating higher amounts of MoO_3 and SO_3 than currently possible could have a significant impact on the safety and feasibility of nuclear waste disposal worldwide.

Phosphate glasses are known to incorporate higher amounts of MoO_3 [22] and SO_3 [23] than silicates. Although phosphate glasses have higher SO_3 loading capacities in general, the binary Fe_2O_3-P_2O_5 glass, which has been proposed as a potential glass composition for nuclear waste immobilization due to its high chemical durability, has very low SO_3 solubility (<0.1 mol%) [24,25]. Other phosphate glass systems designed to improve on this poor sulfate solubility tend to have much lower chemical durability with respect to both iron-phosphate and borosilicate glasses.

An alternate approach is to use phosphorus as an additive to existing borosilicate-based nuclear glasses as a means to increase the solubility of high field-strength cations without compromising chemical durability. The presence of both phosphorus and molybdenum in some radioactive waste streams has prompted investigation into the behaviour of silicate glasses loaded with both cations. Molybdenum phase separation was studied in calcium-sodium silicate glasses which contained 3.6 wt% of phosphorus and 12 wt% of molybdenum under different glass-cooling conditions such as water quenching, steel-plate quenching and slow cooling [26], all of which led to the phase separation of crystalline phases such as $Na_2MoO_4{\cdot}2H_2O$, $CaMoO_4$ and $NaCaPO_4$, which formed droplets 100 nm to 200 μm in size. In another study, molybdenum incorporation was evaluated in silicate-phosphate glasses [27]. Molybdenum solubility between 4.4 and 5.7 mol% was measured in a silicon-rich glass containing 6 mol% P_2O_5, however the glass also contained ~45 mol% alkali and alkaline-earth oxides [A_2O + AO], making it wholly inappropriate for nuclear waste immobilization. The lack of boron in this system also makes it less relevant to the industry standard borosilicate glasses. A 13-component borosilicate glass system possessing 2 mol% P_2O_5 was studied by Raman spectroscopy and rheological measurements [28,29]. Even with the fastest quench rates, phases with similar compositions separated from the glass by the nucleation-and-growth mechanism and coalesced into larger

regions. The immiscibility range for this glass system was found to be between 1150 °C and 1200 °C, in which phases rich in Ca, Mo, P, O and Nd separated from a residual matrix enriched in Si, Al, Zn, O and Zr. Unfortunately, the fate of Na^+ was not discussed, which might have provided insight into the structural roles of the highly radioactive ^{135}Cs and ^{137}Cs isotopes. The phase diagram of a six-component borosilicate glass with molybdenum and phosphorus was studied in detail by Pinet *et al.* [30]. A wide range of compositions was examined, with silica contents of 32 to 44 wt%. Glasses with the highest aluminum and lowest phosphorus concentrations were found to be homogeneous, while low aluminum and high phosphorus glasses yielded stratified materials consisting of two layers, one rich in phosphorus and the other rich in silica. The homogeneous glasses contained lower amounts of Si than what is normally used for nuclear waste immobilization, which could prove detrimental to their chemical durability. Since only the high-alumina glasses were homogeneous, the required melting temperatures were very high due to its high refractory content, making the process less economical and incompatible with current melter technology. Finally, a glass-ceramic developed to immobilize Mo- and P-rich waste originating from the reprocessing of legacy UMo spent fuel [31] comprised a vitreous borosilicate phase encapsulating Si-deficient secondary phases containing Nd, Mo, P, Zn and Ca, ranging in size from a few nanometers to hundreds of micrometers, depending on the melt-cooling profile.

Whereas these studies treat molybdenum and phosphorus as waste components, two very recent reports use phosphorus specifically as a strategy to improve Mo solubility in borosilicate glasses relevant to nuclear glass compositions [32,33]. In one, up to 4 mol% of Mo was immobilized in a sodium borophosphosilicate glass containing 5 mol% of P, which was reported to have a homogeneous distribution of Mo throughout the glass network [32]. Our own work (**Chapter 7**) focused on the structural role of phosphorus in borosilicate glasses, showing that the progressive addition of phosphorus increases the silicate network polymerization and results in improved glass chemical durability, however at the expense of homogeneity for higher P contents [33]. Molybdenum was added to one such composition to test the efficacy of P for keeping Mo from crystallizing, revealing that Mo concentrates in amorphous alkali-phosphate regions of the glass, likely forming six-coordinate polyhedra with phosphate dimers and chains. The success of this strategy was attributed to the high cation field-strength of P^{5+}, which is capable of competing effectively with the similarly high field-strength Mo^{6+} for oxygens,

resulting in more oxygen-sharing in the network, instead of clustering and crystallization, as is observed in borosilicates [21,34].

Whereas the emphasis of our previous work was on the incorporation of phosphorus in borosilicate glasses, this work focuses specifically on the inhibition of Mo and S crystallization by investigating Mo-loaded model nuclear glasses based on the SON68 nuclear glass reference composition [35] with increasing P content. Sulfur is added to some compositions to test its integration into the glass in the absence and presence of molybdenum and phosphorus, simulating a more realistic nuclear-waste containment scenario. X-ray diffraction and solid-state nuclear magnetic resonance (NMR) spectroscopy are used complementarily to identify any devitrification products, characterize the glass network structures, and infer insight about the Mo and S binding sites in the glass.

8.2 Experimental details

8.2.1 Synthesis

The glasses listed in **Table 8.1** were synthesized by mixing SiO_2, Al_2O_3, MoO_3, Na_2CO_3, Cs_2CO_3, $(NaPO_3)_6$, anhydrous Na_2SO_4 and B_2O_3 in two-gram batches according to the target composition. They were decarbonated at 650 °C for 12 hours and melted at 1100 °C for one hour in loosely covered Pt/Au crucibles, before cooling at *ca.* 5 °C/min. The glasses were ground and remelted at 1100 °C for 60 minutes to ensure homogeneous mixing of oxides, and slow-cooled again. B_2O_3 was synthesized by heating H_3BO_3 at 450 °C, 650 °C and 800 °C for 30, 15 and 15 minutes, respectively. All other reagents were used as received from commercial sources. The final glass samples were placed in tight-capped glass vials and stored in a desiccator prior to analysis. Sample labels indicate the P_2O_5 mole fraction (P-*X*) with subscripts specifying the mole fraction of MoO_3 and/or SO_3 (Mo*X*/S*X*). Glass P-0_{S3} was synthesized twice, and the gall layer formed on the glass surface was harvested for further characterization. To aid the assignment of the ^{23}Na MAS NMR spectrum of the gall layer, a hydrated form of Na_2SO_4 was prepared by evaporating 10 mL of 0.7 M Na_2SO_4 solution.

Table 8.1. Nominal compositions of glasses (in mol%).

Sample	SiO_2	Na_2O	B_2O_3	Cs_2O	MoO_3	Al_2O_3	P_2O_5	SO_3
P-0$_{Mo3}$	56.5	18.0	16.5	2.0	3.0	4.0	0	0
P-0$_{S3}$	56.5	18.0	16.5	2.0	0	4.0	0	3.0
P-2.5$_{Mo3}$	54.0	18.0	16.5	2.0	3.0	4.0	2.5	0
P-5$_{Mo3}$	51.5	18.0	16.5	2.0	3.0	4.0	5.0	0
P-5$_{Mo3/S3}$	48.5	18.0	16.5	2.0	3.0	4.0	5.0	3.0
P-7.5$_{Mo4}$	48.0	18.0	16.5	2.0	4.0	4.0	7.5	0
P-10$_{Mo4}$	45.5	18.0	16.5	2.0	4.0	4.0	10	0
P-10$_{Mo5}$	44.5	18.0	16.5	2.0	5.0	4.0	10	0

8.2.2 Solid-state NMR spectroscopy

The NMR analysis was carried out on a Varian ^{UNITY}INOVA 600 MHz NMR spectrometer equipped with a 1.6 mm H(F)-X-Y magic-angle spinning (MAS) NMR probe. All samples were spun at the magic angle with a spinning speed of 30,000 ± 5 Hz. At a magnetic field of 14.1 T, the resonance frequencies of ^{11}B, ^{23}Na, ^{27}Al, ^{31}P, and ^{133}Cs are 192.39, 158.63, 156.25, 242.75 and 78.66 MHz, respectively. Bloch-decay experiments were carried out with pulse lengths and optimized relaxation delays, respectively, of 0.35 μs and 2 s (^{11}B), 0.39 μs and 4 s (^{23}Na), 0.275 μs and 4 s (^{27}Al), 1 μs and 30 s (^{31}P), 0.3 μs and 15 s (^{133}Cs). For ^{11}B, ^{27}Al, ^{23}Na and ^{133}Cs, these pulse lengths corresponded to a tip angle of 15°, which will equally excite sites with different quadrupolar coupling constants (C_Q). The ^{31}P MAS NMR spectra were collected with tip angle set to 30° to maximize the signal intensity for a given acquisition time. The time-domain signals were averaged over 1024, 1024, 512, 128 and 2048 transients for ^{11}B, ^{23}Na, ^{27}Al, ^{31}P and ^{133}Cs NMR experiments, respectively. ^{31}P spin-lattice relaxation times were measured in selected samples using inversion recovery [36] on a Bruker Avance 400 MHz NMR spectrometer. The ^{23}Na, ^{11}B, ^{27}Al, ^{31}P and ^{133}Cs MAS NMR spectra were referenced using aqueous solutions of 0.1 M NaCl (0 ppm), 0.1 M H_3BO_3 (+19.6 ppm relative to $BF_3{\cdot}OEt_2$ (0 ppm)), 0.1 M $Al(NO_3)_3$ (0 ppm), 85% H_3PO_4 (0 ppm) and 1 M CsCl (0 ppm). ^{29}Si MAS NMR spectra were acquired using a Bruker Avance 400 MHz NMR spectrometer, corresponding to a ^{29}Si resonance frequency of

79.49 MHz. The samples were spun with a spinning speed of 14 kHz. Bloch-decay experiments were carried out with a pulse length of 1.2 μs (30° tip angle) and a recycle delay of 30 s. A total of 1024 transients were collected and the spectra were referenced using hexamethyldisiloxane (+6.68 ppm relative to TMS (0 ppm)).

Spectral fitting was carried out using the DMFit software developed by Massiot *et al.* [37]. In the case of ^{11}B MAS NMR spectra, four-coordinate borons ($^{[4]}$B) were fit with a mixed Gaussian/Lorentzian (G/L) peak shape, and three-coordinated borons ($^{[3]}$B) were fit using the Quasar [38] module incorporated into DMFit to properly model the second-order quadrupolar lineshapes in amorphous solids. The $^{[4]}$B peak integration was adjusted for overlapping satellite transition intensity by subtracting the first spinning sideband after shifting the spectrum by the spinning frequency. For the ^{23}Na MAS NMR spectra, the Quasar model was used to fit the sharp peaks originating from crystalline phases, and a G/L lineshape was used to fit the broad symmetrical peak associated with sodium in the glassy phase. The ^{31}P and ^{27}Al MAS NMR spectra were fit using G/L peak shapes.

8.3 Results

8.3.1 Solid-state NMR spectroscopy

Multinuclear magnetic resonance data are analyzed both to identify any devitrification products present in the glasses, and to follow the evolution of glass structure at the molecular level with increasing phosphorus content. Scanning electron microscopy is used to characterize the macroscopic phase separation and elemental distribution present in one glass containing phosphorus, molybdenum, and sulfur.

8.3.1.1 ^{23}Na MAS NMR

The ^{23}Na MAS NMR spectra of glasses illustrating the effectiveness of phosphorus in inhibiting the growth of Na-bearing crystalline phases are shown in **Figure 8.1**. The spectra are broad in general, indicating a disordered chemical environment around the sodium ions. The spectrum of P-0_{Mo3}, containing 3 mol% of MoO_3, shows sharp peaks overlapping the broad glassy peak which originate from sodium-bearing crystalline phases. The spectrum was fit to obtain the identities and quantities of the crystalline phases (**Table 8.2**), revealing them to be Na_2MoO_4 and

$Na_2MoO_4 \cdot 2H_2O$ based on previously documented NMR parameters [39]. Deconvolution showed that 5% of the sodium ions (*ca.* 0.9 mol%) are associated with crystalline molybdates, while the rest of the Na^+ is in the glassy phase. Based on the Na:Mo stoichiometric ratios of the oxide starting materials and Na_2MoO_4, about 1 mol% of Mo is estimated to be phase-separated, which establishes the upper limit of Mo solubility in this glass to be 2 mol%. This value is slightly higher than the accepted value of 1.5 mol%, possibly due to the formation of cesium molybdates often found as devitrification products [9]. The x-ray diffractogram of P-0_{Mo3} (**Figure 8.2**) confirms the presence of sodium molybdate phases.

Table 8.2. ^{23}Na MAS NMR fitting parameters for P-0_{Mo3}, P-0_{S3} and the gall layer.

Phase	δ_{iso} (ppm)	C_Q (MHz)	η	Int. (%)[a]
		P-0_{Mo3}		
Na_2MoO_4[b]	+3.5(±0.3)	2.59 (±0.05)	0	3(±2)
$Na_2MoO_4 \cdot 2H_2O$[b]	-0.9(±0.3)	0.88(±0.05)	0.2	1(+1)
	+4.3(±0.3)	2.68(±0.05)	0.1	1(+1)
Glass	-13.5[c]	3.9[d]		95(±2)
		P-0_{S3}		
Na_2SO_4[d]	-8.5	2.6	0.7	4(+2)
Hydrated Na_2SO_4	-0.6	0.7	0.5	6(+1)
Glass	-13.5[c]	3.9[d]		90(+2)
		Gall layer		
Na_2SO_4[e]	-8.6	2.6	0.7	43
Hydrated Na_2SO_4	-0.8	0.7	0.5	56

[a]Integrated intensity
[b]NMR parameters taken from reference 40
[c]Peak maximum (±0.5)
[d]Full width at half-maximum in kHz (±0.15)
[e]NMR parameters taken from reference 59

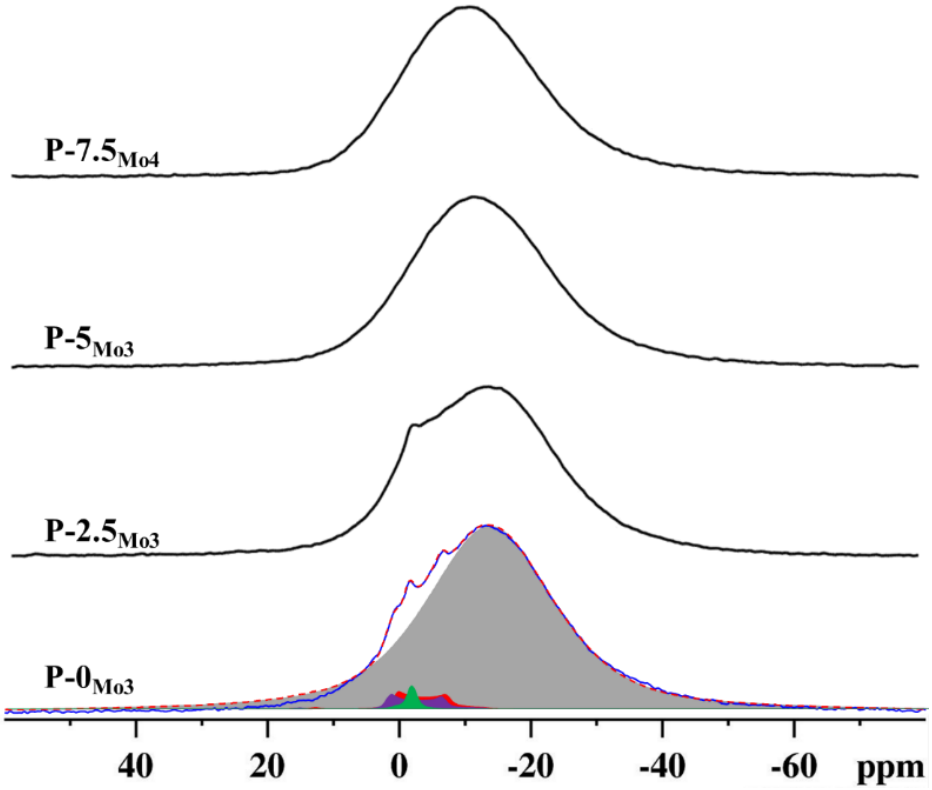

Figure 8.1. ^{23}Na MAS NMR spectra of Mo-bearing glasses with increasing P_2O_5 content. The P-0_{Mo3} spectrum (blue line) is deconvolved (dashed red line) to show the presence of crystalline phases Na_2MoO_4 (red) and $Na_2MoO_4{\cdot}2H_2O$ (green and purple). Fit parameters are listed in **Table 8.2.**

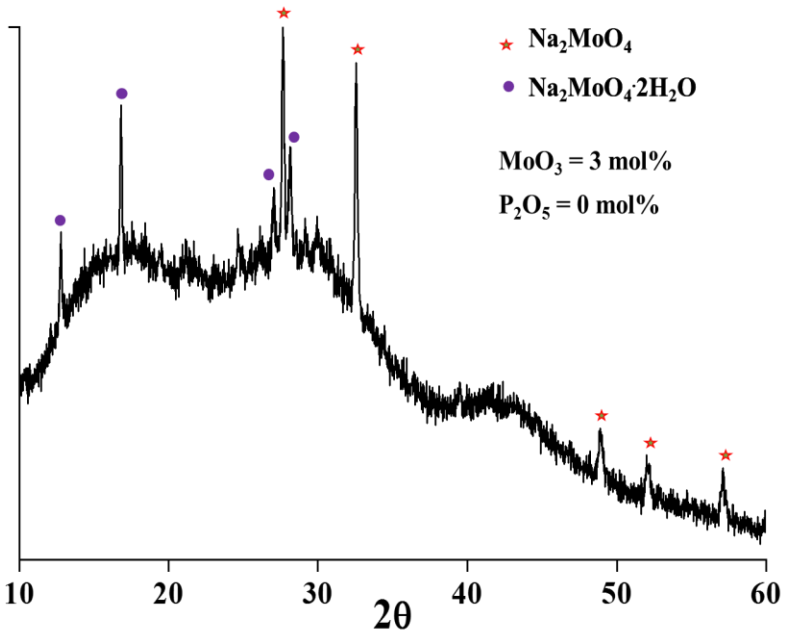

Figure 8.2. X-ray diffractogram of P-0_{Mo3} showing sharp peaks from the crystalline phases and the halo from the glassy phase. The peaks are assigned to sodium molybdate in both hydrated and dehydrated forms.

When 2.5 mol% of SiO_2 is replaced by P_2O_5 (P-2.5_{Mo3}), the sharp ^{23}Na NMR peaks are reduced to just one very small peak (*ca.* -2 ppm) on the shoulder of the broad peak, indicating a drastic reduction in the crystallization of Na-bearing phases. The spectrum of P-5_{Mo3} is devoid of sharp peaks, suggesting the presence of Na^+ ions only in the glassy phase. After establishing the minimum amount of P_2O_5 required to immobilize 3 mol% of MoO_3, the amounts of P_2O_5 and MoO_3 were increased to 7.5 and 4 mol%, respectively, to test whether a higher concentration of MoO_3 can be immobilized within the glassy phase; no evidence of devitrification is observed for P-7.5_{Mo4} in ^{23}Na NMR. ^{23}Na MAS NMR spectra comparing the ability of 10 mol% P_2O_5 to prevent crystallization of 4 and 5 mol% MoO_3 are shown in **Figure 8.3**. Broad featureless peaks confirm that there are no sodium-bearing crystalline phases present in P-10_{Mo4} and P-10_{Mo5}. X-ray diffraction of the latter shows no evidence of molybdate phases, but there are peaks representing a small amount of SiO_2 (vide infra, **Figure 8.4**).

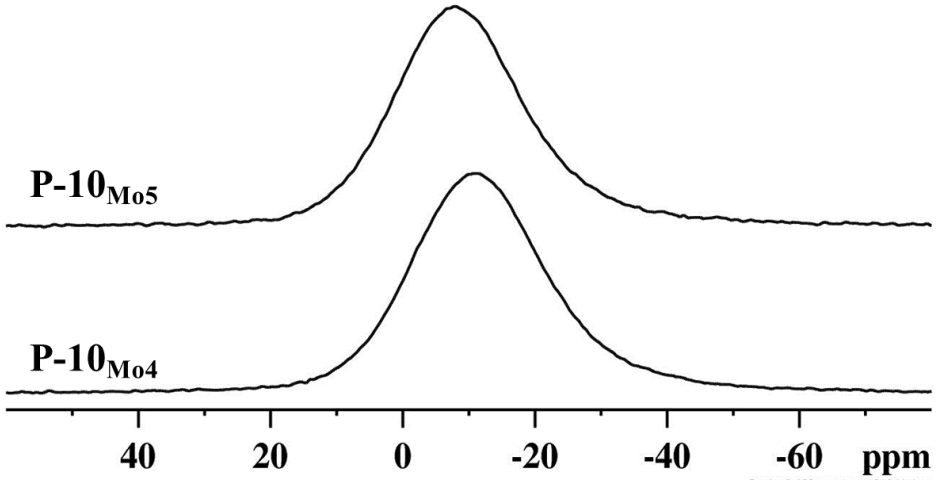

Figure 8.3. ^{23}Na MAS NMR spectra of P-10$_{Mo4}$ and P-10$_{Mo5}$.

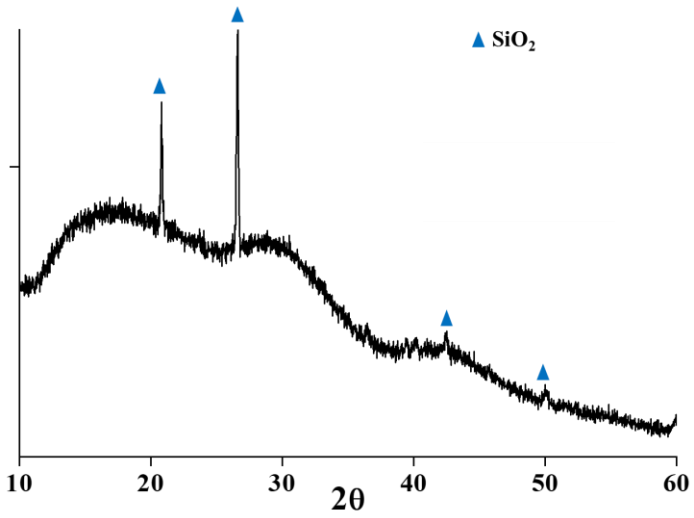

Figure 8.4. X-ray diffractogram of P-10$_{Mo5}$ showing the halo from the glassy phase and sharp peaks from SiO_2. No crystalline molybdate phases are observed.

The ^{23}Na MAS NMR spectra of glasses prepared to assess the effectiveness of phosphorus additives for sulfur vitrification are shown in **Figure 8.5.** P-0$_{S3}$, loaded with 3 mol% SO_3 but without phosphorus or molybdenum, yields strong sodium sulfate signals, highlighting the poor solubility of sulfate in conventional nuclear waste glasses. Deconvolution of the spectrum (**Table 8.2**) shows that *ca.* 10% of the Na^+ ions (*ca.* 1.8 mol% in the entire glass) are

associated with the crystalline sulfate phase. Considering the Na:S stoichiometric ratios of the starting materials and Na_2SO_4 (thenardite), the upper limit of sulfate solubility in P-0_{S3} is estimated to be about 1.2 mol%, confirming that S is less soluble than Mo in these aluminoborosilicates. This value is expected to be overestimated due to the presence of an unknown amount of sulfur in the gall layer (vide infra). By contrast, a comparison of the ^{23}Na MAS NMR spectra of P-5_{Mo3} (**Figure 8.1**) and P-$5_{Mo3/S3}$ (**Figure 8.5**) shows no evidence of molybdate or sulfate devitrification when SO_3 is added to a 5 mol% P_2O_5 glass already containing 3 mol% MoO_3; this is supported by x-ray diffraction (**Figure 8.6**). The peak shape cannot be perfectly modeled by a symmetric peak but requires two strongly overlapping peaks to match the experimental lineshape, implying distinct disordered Na^+ environments. Replacing just 5 mol% of SiO_2 with P_2O_5 successfully immobilizes 3 mol% each of Mo and S in the glassy phase.

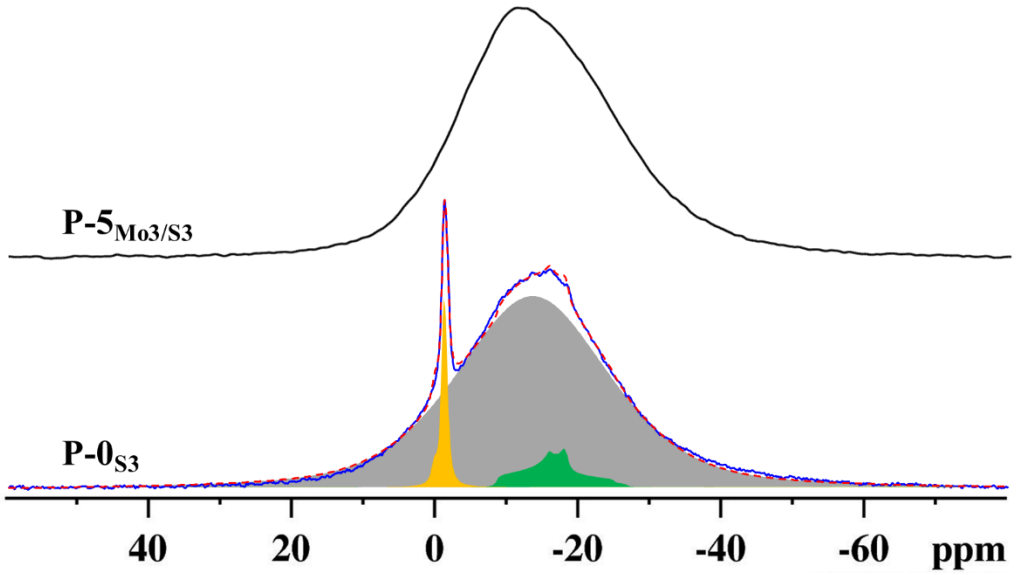

Figure 8.5. ^{23}Na MAS NMR spectra of S-bearing glasses. The P-0_{S3} spectrum (blue line) is deconvolved (dashed red line) to show the presence of crystalline phases Na_2SO_4 (green) and hydrated sodium sulfate ($Na_2SO_4 \cdot nH_2O$, yellow). Fit parameters are listed in **Table 8.2.**

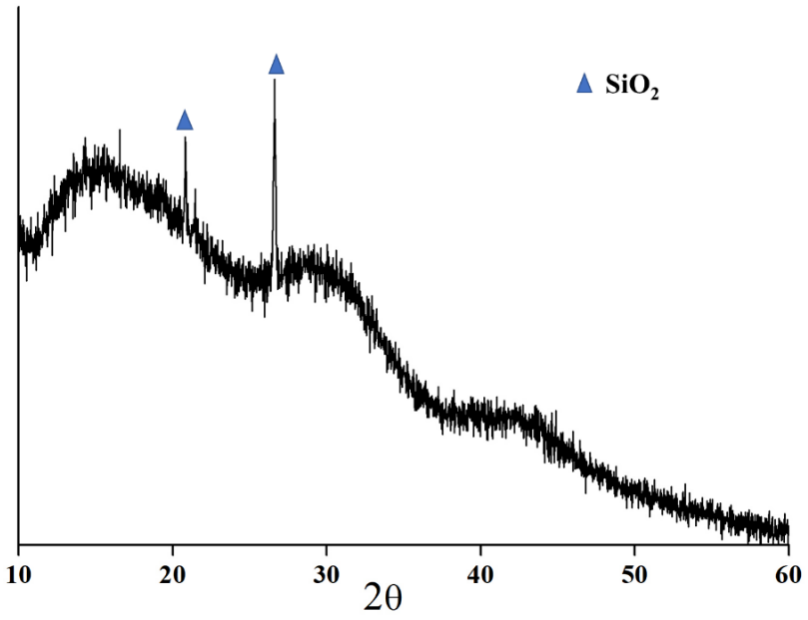

Figure 8.6. X-ray diffractogram of P-$5_{Mo3/S3}$, which is devoid of peaks from crystalline molybdate or sulfate phases.

8.3.1.2 ^{31}P MAS NMR

The ^{31}P MAS NMR spectra of Mo-loaded glasses are plotted in absolute-intensity (**Figure 8.7)** and normalized formats (**Figure 8.8**)**,** illustrating the spectral changes associated with increasing P_2O_5. Spectral deconvolution with three components based on documented ^{31}P chemical shifts [40–42] of species expected to be present in mixed-network glasses of similar compositions are shown in **Figure 8.9**, tabulated in **Table 8.3** and plotted as a function of phosphate concentration in **Figure 8.10**. Isolated orthophosphate species (P^0, where the superscript refers to the number of bridging oxygens) appear around 10-13 ppm, chain-terminus pyrophosphates (P^1) are expected to appear around 1−4 ppm, and chain metaphosphates (P^2) have been reported around -20 ppm [33]. However, the mixed-network nature of these glasses implies that some nominally "metaphosphate" units are likely to be bonded to other network formers, which may modify the diagnostic ^{31}P chemical shifts. For example, a metaphosphate group wherein one phosphate neighbour is replaced by a borate unit (P^2_{1B}, **Figure 8.11**) has been observed at a chemical shift of -10 ppm [41,42]. The chemical shift of one of the components observed in these spectra (-5.8 ppm) falls between that of a pure pyrophosphate and a pure metaphosphate, closer to that

expected for a P^2_{1B} unit; thus, it has been attributed to $P^2_{1B/Al}$, [33] a species which may alternately be described as a pyrophosphate anchored to a borate or an aluminate unit.

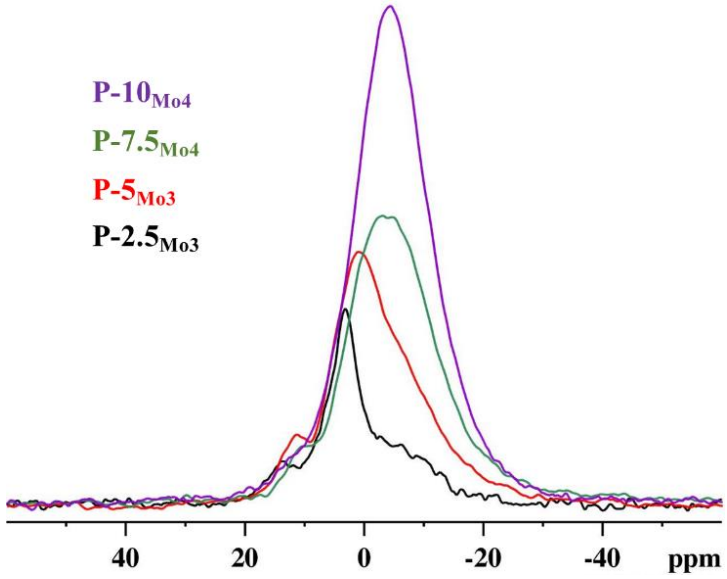

Figure 8.7. ^{31}P MAS NMR spectra of Mo-bearing glasses with increasing P_2O_5 content overlaid in absolute-intensity mode for comparison.

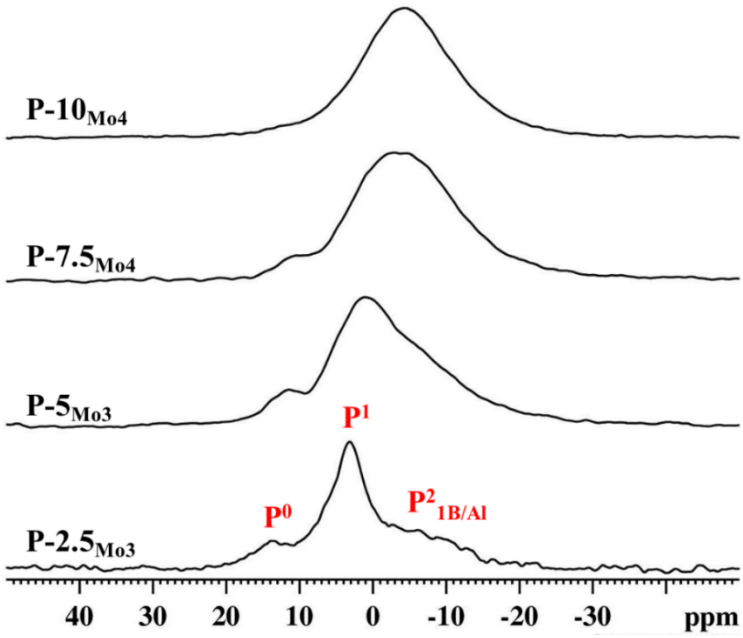

Figure 8.8. ^{31}P MAS NMR spectra of glasses with increasing P_2O_5 content.

Table 8.3. ^{31}P MAS NMR fitting parameters and relative intensities of phosphate units.

	P^0			P^1			$P^2_{1B/Al}$		
	δ_{iso} (ppm)	FWHM[a] (kHz)	Int. (%)[b]	δ_{iso} (ppm)	FWHM[a] (kHz)	Int. (%)[b]	δ_{iso} (ppm)	FWHM[a] (kHz)	Int. (%)[b]
P-2.5$_{Mo3}$	13(1)	1.4(0.2)	9(1)	+3.3(0.1)	1.6(0.1)	57(6)	-6.1(0.5)	3.2(0.3)	34(6)
P-5$_{Mo3}$	12(1)	1.1(0.2)	5(1)	+1.5(0.2)	2.1(0.5)	42(6)	-6.4(0.5)	3.9(0.3)	53(5)
P-5$_{Mo3/S3}$	12(1)	1.3(0.2)	6(1)	+1.2(0.2)	1.8(0.5)	60(3)	-8.9(0.5)	4.1(0.3)	35(4)
P-7.5$_{Mo4}$	10(1)	1.4(0.2)	3(1)	-0.5(0.6)	1.7(0.4)	28(10)	-7.6(1.5)	3.2(0.3)	69(9)
P-10$_{Mo4}$	4(1)	1.4(0.2)	3(1)	-1.5(1.2)	1.7(0.4)	23(9)	-6.9(1.5)	3.2(0.5)	74(10)
P-10$_{Mo5}$	4(1)	1.4(0.2)	4(1)	-1.5(1.2)	1.7(0.4)	23(9)	-6.9(1.5)	3.2(0.5)	74(10)

[a]Full width at half-maximum; [b]Integrated intensity

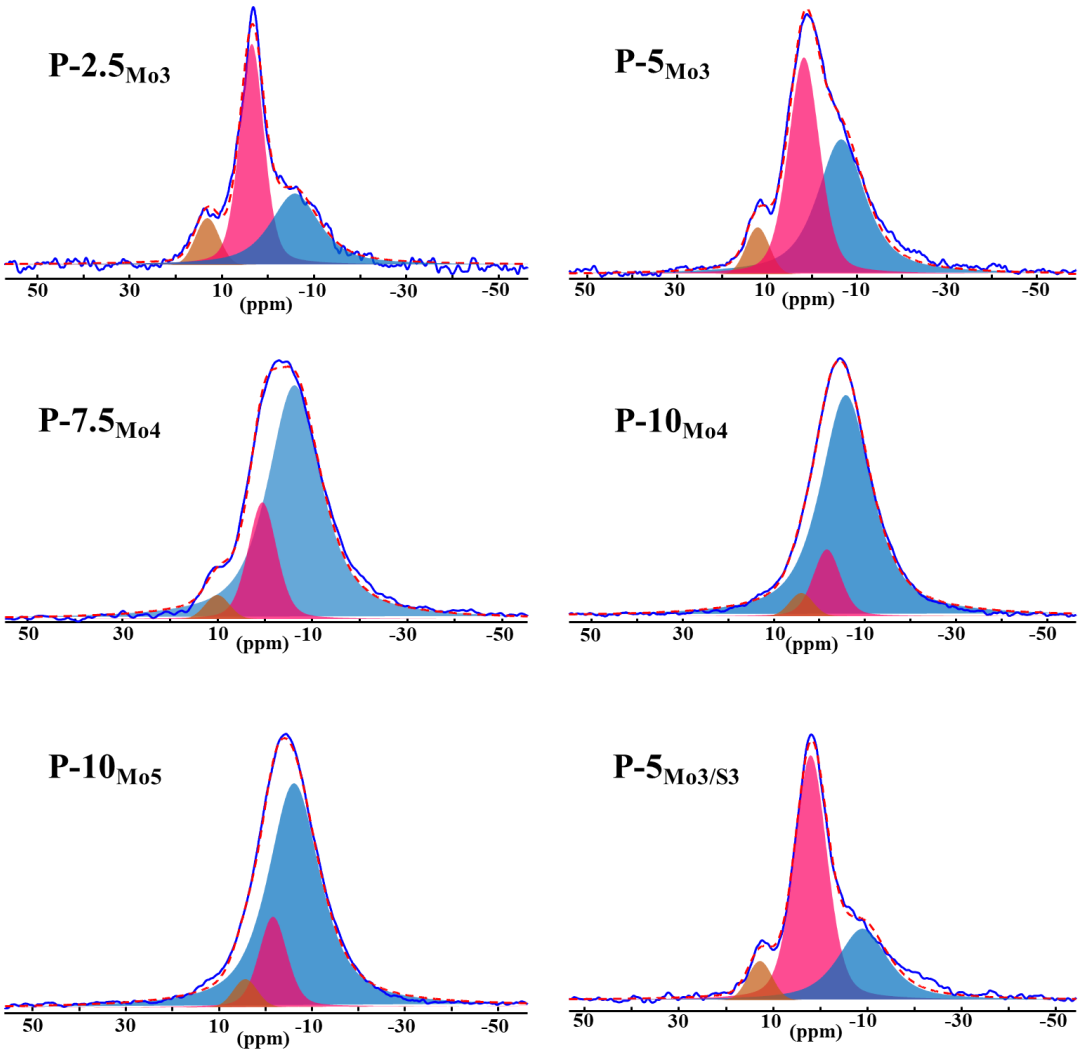

Figure 8.9. Deconvolution of the ^{31}P MAS NMR spectra of glass samples. The dotted red line represents the overall envelope from the fitting components. The brown, pink, and blue peaks represent P^0, P^1 and $P^2_{1B/Al}$ units, respectively.

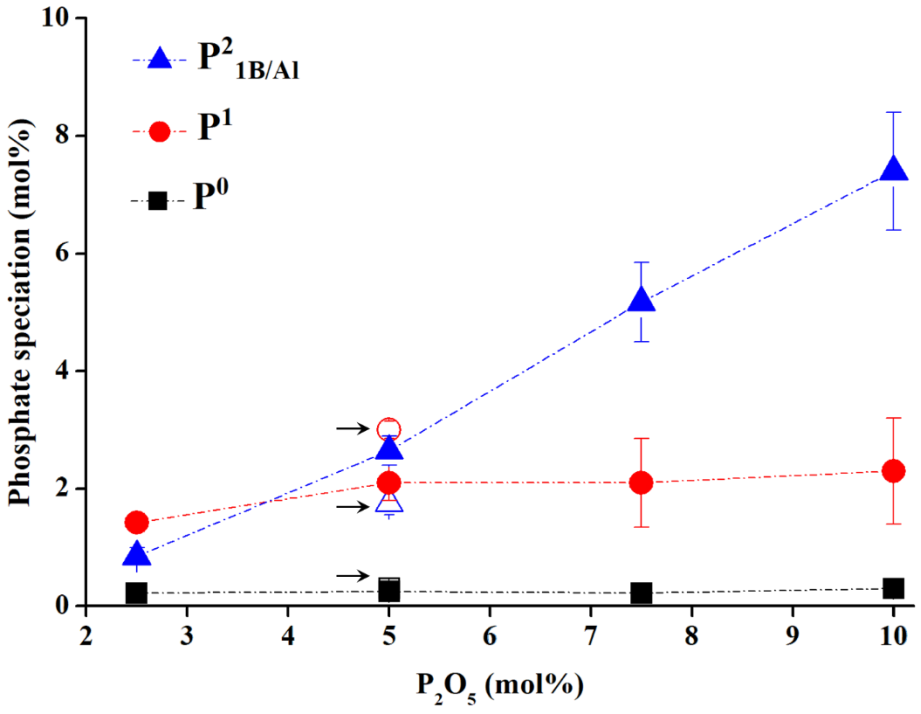

Figure 8.10. Absolute concentrations of phosphate units. Open symbols represent the phosphate speciation in P-$5_{Mo3/S3}$, marked with arrows.

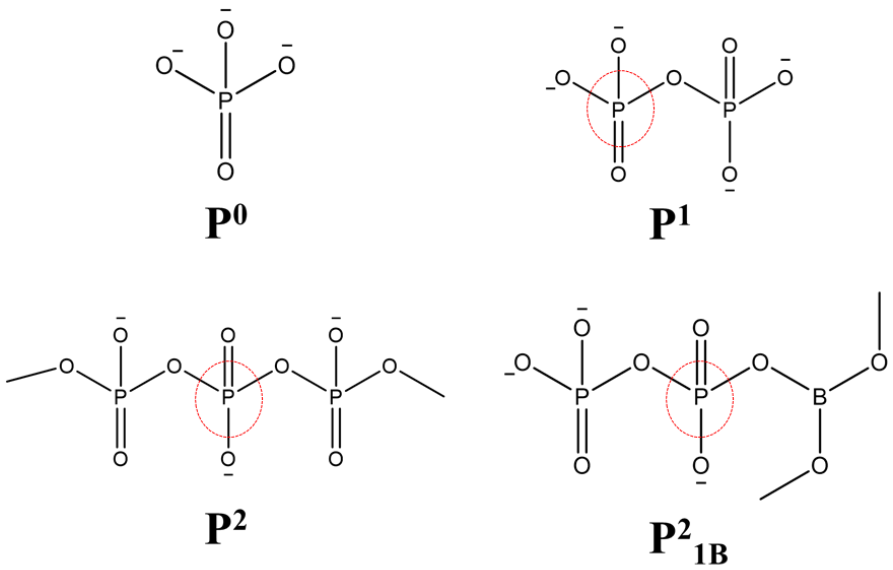

Figure 8.11. Structures of different phosphate units.

With the progressive substitution of SiO_2 by P_2O_5, the total numbers of orthophosphate and pyrophosphate species remain roughly constant, while the number of metaphosphate species ($P^2_{1B/Al}$) increases (**Figure 8.10**), reflecting the formation of longer phosphate chains. Spin-lattice relaxation times (T_1) measured for P-5_{Mo3} are 17±2 s for ortho- and metaphosphate peaks, while the pyrophosphate peak has a distinctly shorter T_1 of 12±1 s. Considering the phase separation into a P-rich glassy domain observed by SEM in P-$5_{Mo3/S3}$ (vide infra) and a glass with similar composition (P-4_{Mo3}, ref 33), the difference in T_1 values implies that the majority of the metaphosphates are in a different phase than the pyrophosphate dimers. The linear increase in chain phosphates with P_2O_5 loading suggests that the phosphate-rich separated phase comprises mainly chain phosphates near the metaphosphate composition (Na/P = 1; O/P = 3) [43]. If it may be assumed that phosphorus is mainly found as P^0 and P^1 dimers in silicate glasses [44], then the formation of longer phosphate chains appears to be related to the uptake of Mo in the glassy phase. The addition of 3 mol% SO_3 to a Mo-loaded glass containing phosphate (P-$5_{Mo3/S3}$) results in a marked reduction in the intensity in the region assigned to $P^2_{1B/Al}$ (**Table 8.3, Figure 8.12, Figure 8.13**). The T_1 values for all phosphate species in this glass are 13±2 s.

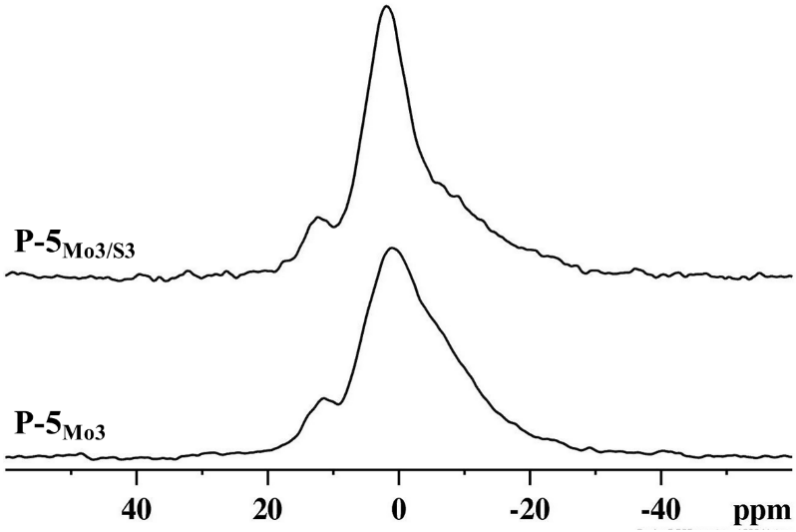

Figure 8.12. ^{31}P MAS NMR spectra of glasses with and without SO_3.

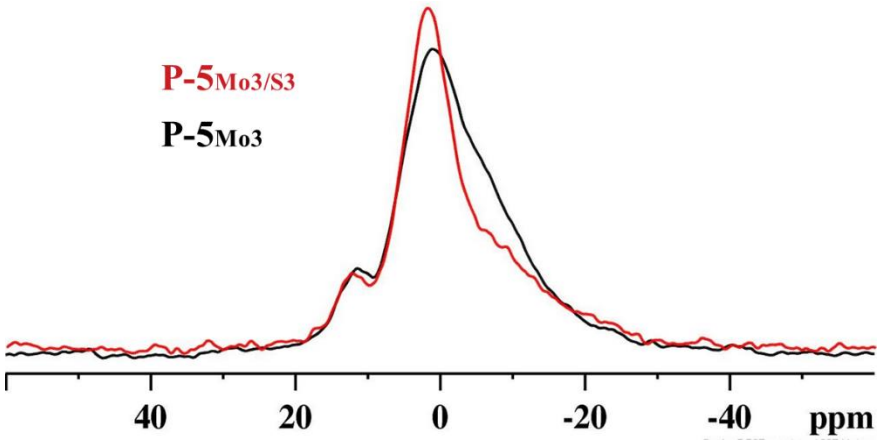

Figure 8.13. ^{31}P MAS NMR spectra of glasses P-5$_{Mo3}$ and P-5$_{Mo3/S3}$ presented as absolute intensities.

8.3.1.3 ^{11}B MAS NMR

The ^{11}B MAS NMR spectra of glasses with increasing P content are shown in **Figure 8.14**. The spectra consist of two main peaks: three-coordinate boron ($^{[3]}$B) appears between 10 and 20 ppm, and four-coordinate boron ($^{[4]}$B) appears between -4 and 5 ppm [45]. The spectra were fit using well-documented ranges [45] of δ_{iso} and C_Q for $^{[3]}$B and δ_{iso} for $^{[4]}$B to obtain the best agreement with the experimental lineshapes and the most accurate integrated intensities of $^{[3]}$B and $^{[4]}$B. Whereas the lineshape features of P-0$_{Mo3}$ support the presence of at least two structurally distinct $^{[4]}$B species (see below), the two $^{[3]}$B sites used in the fitting procedure do not necessarily correspond to distinct, structurally identifiable trigonal boron units (**Figure 8.15)**.

With increasing phosphate, the total fraction of tetrahedral borate units (N_4) decreases steadily (**Table 8.4)**. To understand these changes, it is necessary to identify the connectivity of the four-coordinate borons. Whereas two distinct $^{[4]}$B units are observed for P-0$_{Mo3}$, their unambiguous assignment is complicated by the multiplicity of possible $^{[4]}$B species when next-nearest neighbours (e.g., B, Si, P, Al) are considered. For reasons presented more comprehensively in **section 8.4.2**, we attribute these peaks to $^{[4]}$B bonded to four silicon neighbours ($^{[4]}$B$_{4Si}$, -1.7 ppm) and to three silicon neighbours ($^{[4]}$B$_{3Si}$, -0.1 ppm) over this compositional range [33]. With the substitution of Si by P, the $^{[4]}$B signal shifts toward higher frequencies, along with a subtle evolution in the overall peak shape (**Figure 8.14**). The $^{[4]}$B spectral regions were deconvolved using peaks representing $^{[4]}$B$_{2Si}$, $^{[4]}$B$_{3Si}$ and $^{[4]}$B$_{4Si}$, as appropriate. The gradual substitution of Si

by P decreases N_4 and decreases the number of next-nearest Si neighbours: $^{[4]}B_{4Si}$ → $^{[4]}B_{3Si}$ → $^{[4]}B_{2Si}$ (**Figure 8.16**).

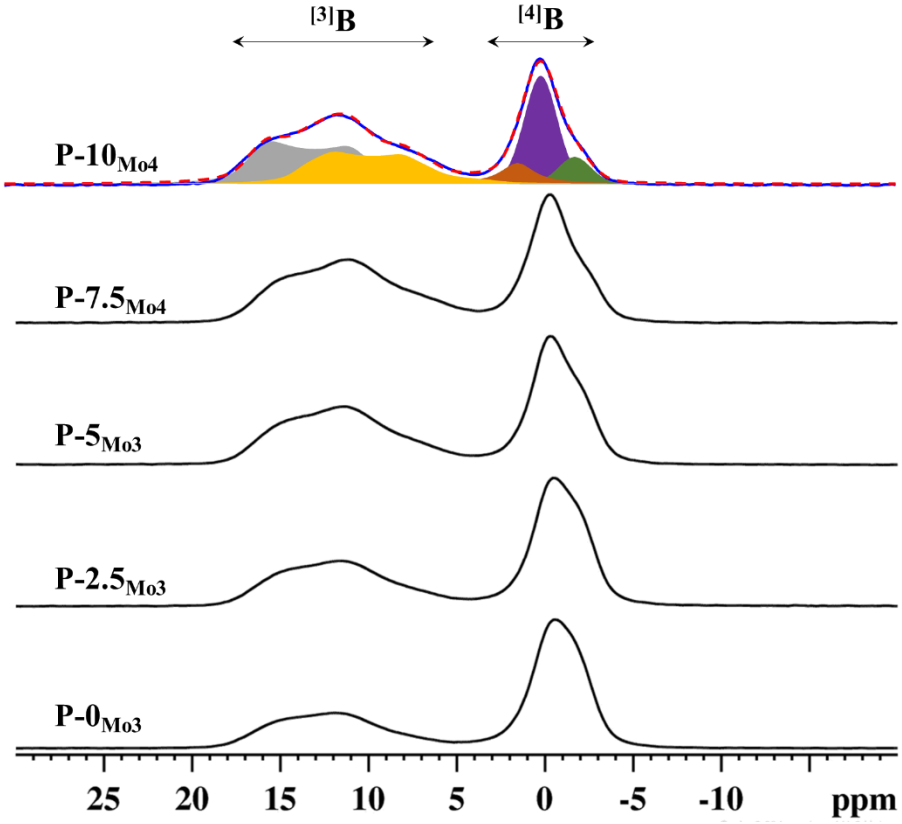

Figure 8.14. ^{11}B MAS NMR spectra of Mo-bearing glasses with increasing P_2O_5 content. The deconvolution (dashed red line) of P-10_{Mo4} spectrum (blue line) is shown, with $^{[3]}B$ components represented by orange and grey subspectra, and $^{[4]}B_{2Si}$, $^{[4]}B_{3Si,}$ and $^{[4]}B_{4Si}$, represented by brown, purple and green, respectively.

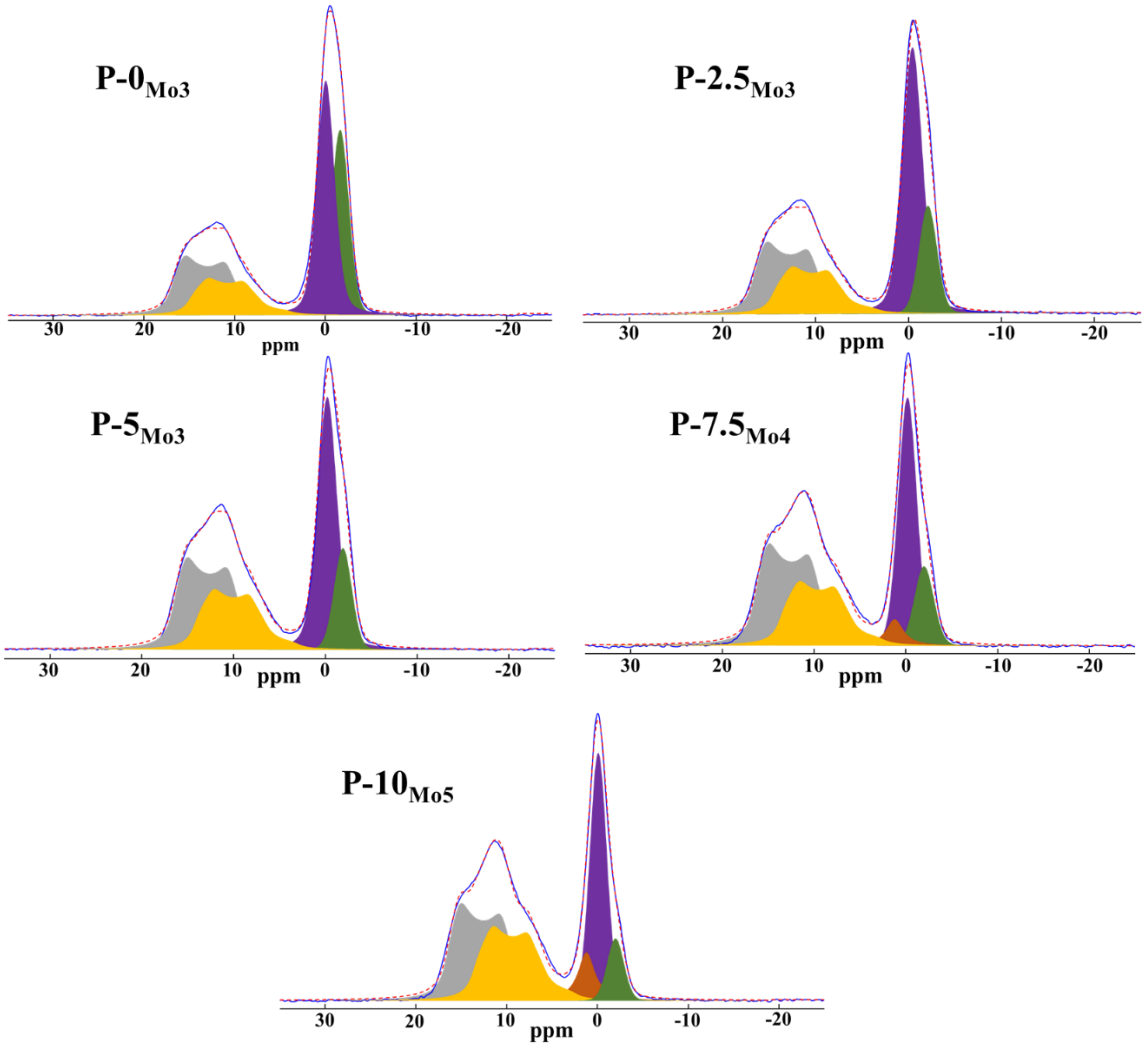

Figure 8.15. Deconvolution of the ^{11}B MAS NMR spectra of glass samples. The dotted red line represents the envelope from the fitting components. Orange and grey components represent $^{[3]}$B units, and green, purple, and brown components represent $^{[4]}B_{4Si}$, $^{[4]}B_{3Si,}$ and $^{[4]}B_{2Si}$, respectively.

Table 8.4. ^{11}B MAS NMR fitting parameters and relative intensities of borate units.

	$^{[4]}B_{2Si}$	$^{[4]}B_{3Si}$	$^{[4]}B_{4Si}$	$^{[3]}B$	
	Int. (%)[a]	Int. (%)[a]	Int. (%)[a]	Int. (%)[a]	N_4[b] ($\pm$0.03)
P-0$_{Mo3}$	—	35(5)	23(5)	42(3)	0.58
P-0$_{S3}$	—	36(5)	22(5)	42(3)	0.58
P-2.5$_{Mo3}$	—	35(4)	15(4)	50(3)	0.50
P-5$_{Mo3}$	—	34(3)	10(3)	56(3)	0.44
P-5$_{Mo3/S3}$	—	35(3)	10(3)	55(3)	0.45
P-7.5$_{Mo4}$	2(1)	28(3)	10(3)	57(3)	0.43
P-10$_{Mo4}$	8(2)	26(2)	6(2)	60(3)	0.40
P-10$_{Mo5}$	9(2)	25(2)	6(2)	60(3)	0.40

[a]Integrated intensity

[b]N_4 = ($^{[4]}$B)/[($^{[4]}$B)+($^{[3]}$B)]

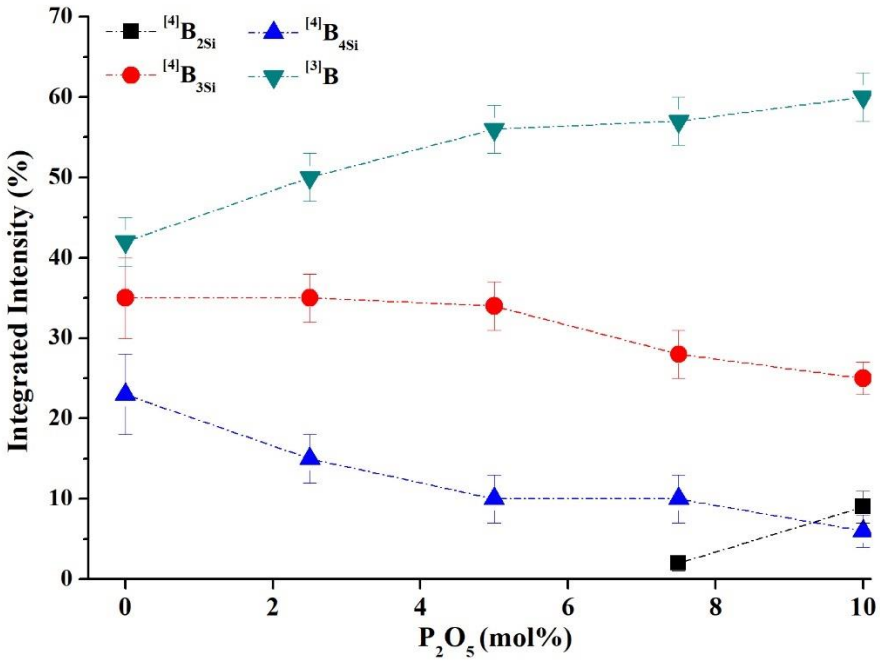

Figure 8.16. Integrated intensities of different boron species present in glasses as a function of P_2O_5 content. Mo and S contents have a negligible influence on the boron speciation (see **Table 8.4**).

The ^{11}B MAS NMR spectra of 10 mol% P_2O_5 containing glasses with 4 and 5 mol% Mo (**Figure 8.17**) are very similar to each other, indicating that with a sufficiently high amount of phosphorus, small increases in the amount of Mo have little influence on the borate portion of the glass network. Likewise, the ^{11}B MAS NMR spectra of the P-0 glasses examined here are similar in appearance and speciation, irrespective of S or Mo loading (**Figure 8.17, Table 8.4**). Upon addition of 5 mol% P_2O_5, similar reductions in N_4 are observed for Mo-loaded ($P\text{-}5_{Mo3}$) and Mo- and S-loaded glasses ($P\text{-}5_{Mo3/S3}$), suggesting that the boron network is affected mainly by changes in the network composition and not by waste-ion loading.

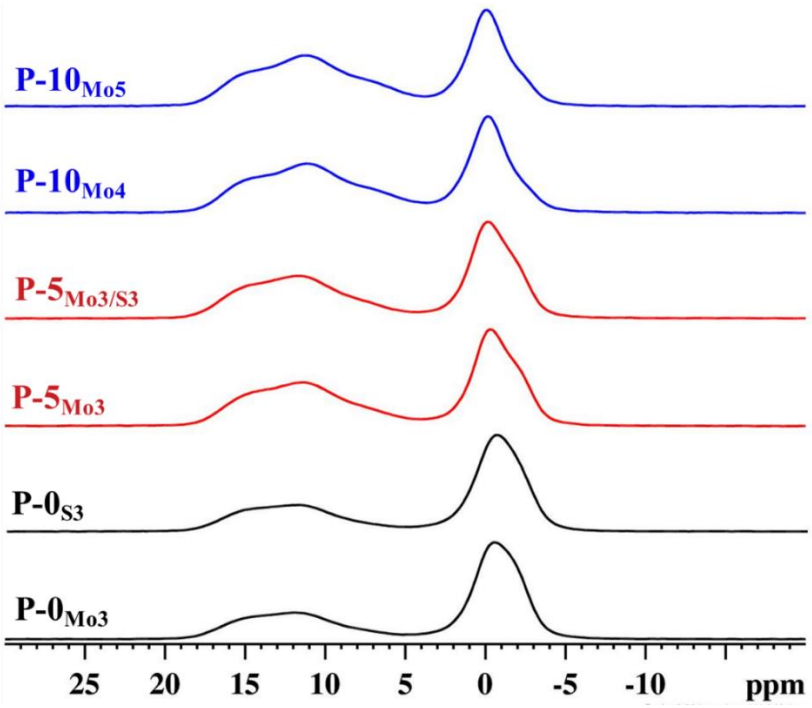

Figure 8.17. ^{11}B MAS NMR spectra of glasses with different P_2O_5, MoO_3 and SO_3 contents. The spectra with similar P_2O_5 contents are colour-coded.

8.3.1.4 ^{29}Si MAS NMR

Two samples with considerably different compositions were selected for ^{29}Si MAS NMR spectroscopy (**Figure 8.18**). $P\text{-}0_{Mo3}$, devoid of phosphorus and containing 3 mol% MoO_3, gives a single broad peak centered around -97 ppm, whereas $P\text{-}10_{Mo5}$ yields a peak shifted to lower

frequency by 10 ppm, at -107 ppm. These signals were fit according to well-established silicate chemical shift ranges: Q^2 (-80 to -95 ppm), Q^3 (-88 to -100 ppm) and Q^4 (< -98 ppm) [33,45,47−52] where the superscript in Q^n indicates the number of bridging oxygens. As precise quantitative populations are difficult to ascertain from poorly differentiated peaks, charge-balance calculations were used to constrain the relative concentrations of Q^3 and Q^4 units (**Table 8.5, Figure 8.19**). The spectrum of P-10_{Mo5} was deconvolved using two peaks with positions of -99 and -109 ppm, both assigned to neutral Q^4 units, in accordance with charge-balance constraints.

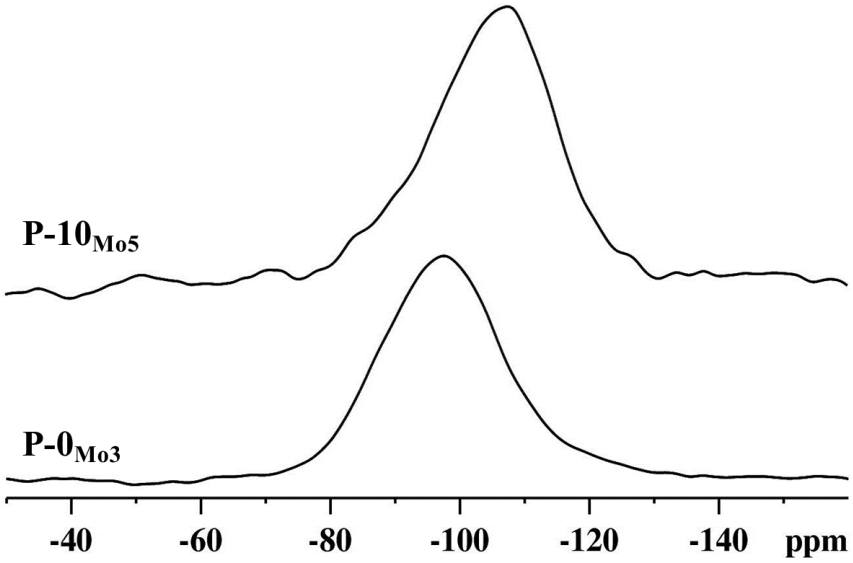

Figure 8.18. ^{29}Si MAS NMR spectra of glasses with 0 and 10 mol% P_2O_5.

Table 8.5. Qualitative deconvolution of the ^{29}Si MAS NMR spectra and relative intensities of silicate units.

	Q^3			Q^4		
	δ_{iso} (ppm)	FWHM[a] (kHz)	Int. (%)[b]	δ_{iso} (ppm)	FWHM[a] (kHz)	Int. (%)[b]
P-0$_{Mo3}$	-88	1.3	15	-99	1.4	85
P-10$_{Mo5}$	—	—	—	-99	1.6	30
				-109	1.4	70

[a]Full width at half-maximum
[b]Integrated intensity

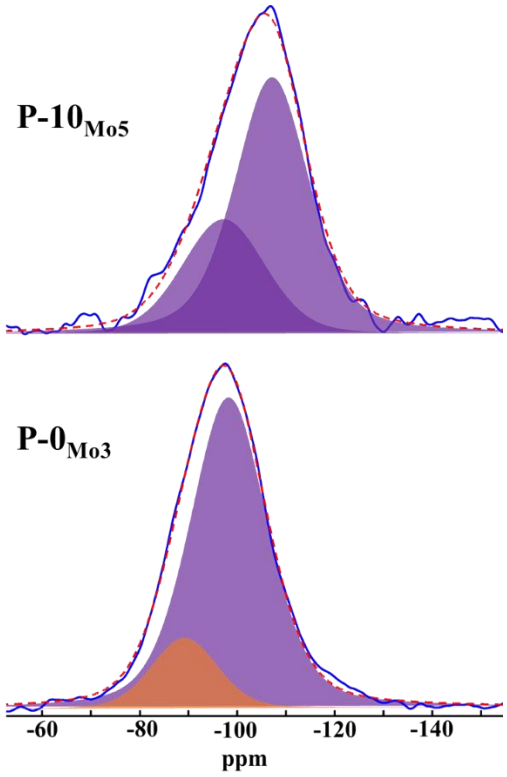

Figure 8.19. Deconvolution of the ^{29}Si MAS NMR spectra of glasses P-0$_{Mo3}$ and P-10$_{Mo5}$. Purple and brown peaks represent peaks represent Q^4 and Q^3 species, respectively (see text).

8.3.1.5 ^{27}Al MAS NMR

Selected ^{27}Al MAS NMR spectra are shown in **Figure 8.20,** and the corresponding NMR fit parameters listed in **Table 8.6**. Glasses with less than 10 mol% P_2O_5 show peaks centred at ~55 and ~13 ppm which can be assigned to four- ($^{[4]}$Al) and five-coordinate ($^{[5]}$Al) aluminum, respectively [33,52,53]. With increasing P_2O_5 content, the average Al coordination number tends to increase due to more $^{[5]}$Al, and even evidence of $^{[6]}$Al at -10 ppm [52,54,55] in P-10$_{Mo4}$. Increasing phosphate content also results in an increase in the tetrahedral aluminum peakwidths and a shift toward lower frequency.

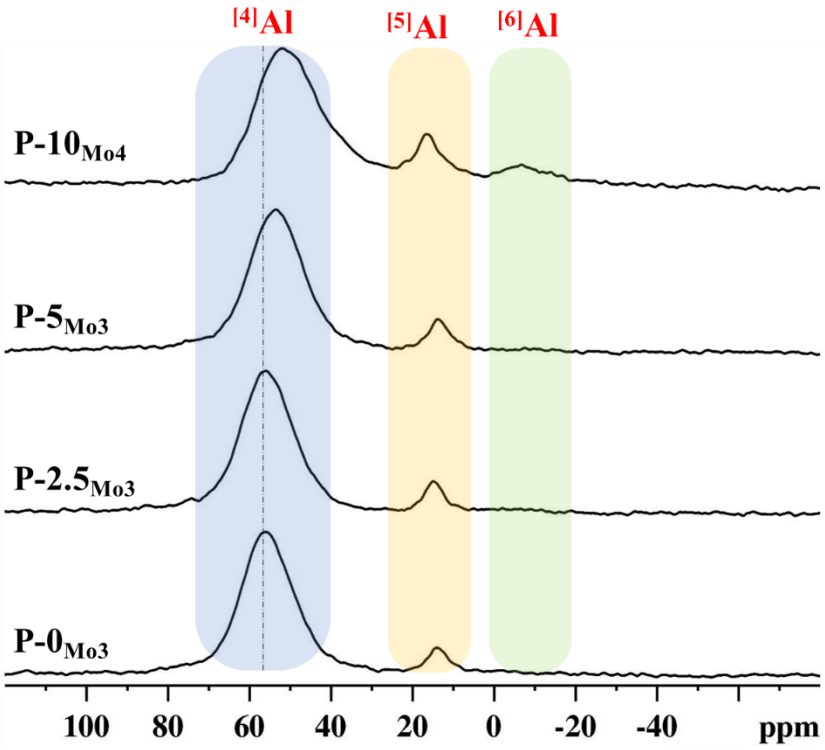

Figure 8.20. ^{27}Al MAS NMR spectra of glasses with increasing P_2O_5 content.

Table 8.6. ^{27}Al MAS NMR fitting parameters and relative intensities of aluminate units.

	$^{[4]}$Al			$^{[5]}$Al			$^{[6]}$Al		
	δ_{iso} (ppm) (±0.3)	FWHM[a] (kHz) (±0.1)	Int. (%)[b] (±2)	δ_{iso} (ppm) (±0.3)	FWHM[a] (kHz) (±0.05)	Int. (%)[b] (±2)	δ_{iso} (ppm) (±0.3)	FWHM[a] (kHz) (±0.1)	Int. (%)[b] (±2)
P-0$_{Mo3}$	55.7	2.2	92	13.6	1.0	8	—	—	—
P-0$_{S3}$	55.6	2.3	92	12.1	1.0	8	—	—	—
P-2.5$_{Mo3}$	55.7	2.3	92	14.6	0.9	8	—	—	—
P-5$_{Mo3}$	53.4	2.4	92	13.3	0.9	8	—	—	—
P-5$_{Mo3/S3}$	52.5	2.4	94	11.9	0.8	6	—	—	—
P-7.5$_{Mo4}$	53.9	2.6	89	16.5	1.1	11	—	—	—
P-10$_{Mo4}$	50.2	2.8	80	15.6	1.7	14	-9.3	2.1	6
P-10$_{Mo5}$	50.5	2.8	74	16.5	1.7	16	-7.1	2.3	10

[a]Full width at half-maximum; [b]Integrated intensity

8.3.2 Characterization of the gall layer

The x-ray diffractogram of the gall layer which formed on the surface of P-0_{S3} consists of peaks attributable to Na_2SO_4 and Cs_2SO_4 (**Figure 8.21**). Its ^{133}Cs MAS NMR spectrum possesses sharp peaks at 100 and 68 ppm in a 1:1 ratio, corresponding to the two crystallographically inequivalent Cs sites with nine- and eleven-fold coordination, respectively (**Figure 8.22)** [56,57]. The ^{23}Na MAS NMR spectrum exhibits two peaks with different quadrupolar coupling constants (**Figure 8.22, Table 8.2**). The second-order quadrupolar broadened peak (δ_{iso} = -8.5, C_Q = 2.6 MHz, η = 0.56) is assigned to anhydrous Na_2SO_4 [58], whereas the sharp peak with a negligible C_Q at -1.7 ppm probably arises from a hydrated sodium sulfate phase [59,60] in which water mobility averages the electric field gradient around Na^+ (**Figure 8.23**). These latter phases are efflorescent [60], and will transform into anhydrous phases unless stored in sealed containers, potentially explaining the absence of diffraction peaks corresponding to hydrates, as the sample mounted on the diffraction plates was exposed to air during a 10-hour scan.

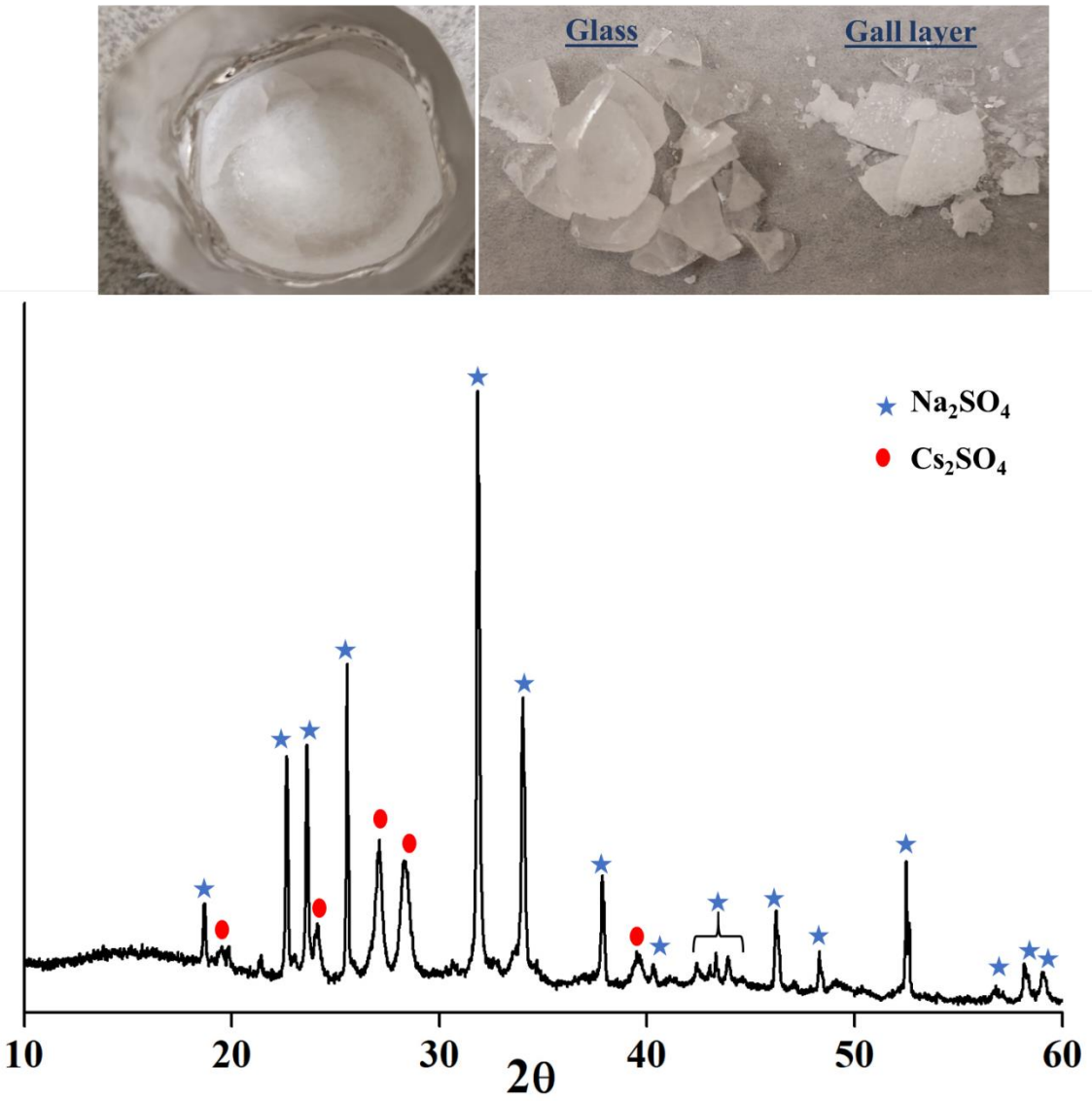

Figure 8.21. Photographs of P-0_{S3} with intact and separated gall layer (**top**). The x-ray diffractogram of the gall layer with identified crystalline phases (**bottom**).

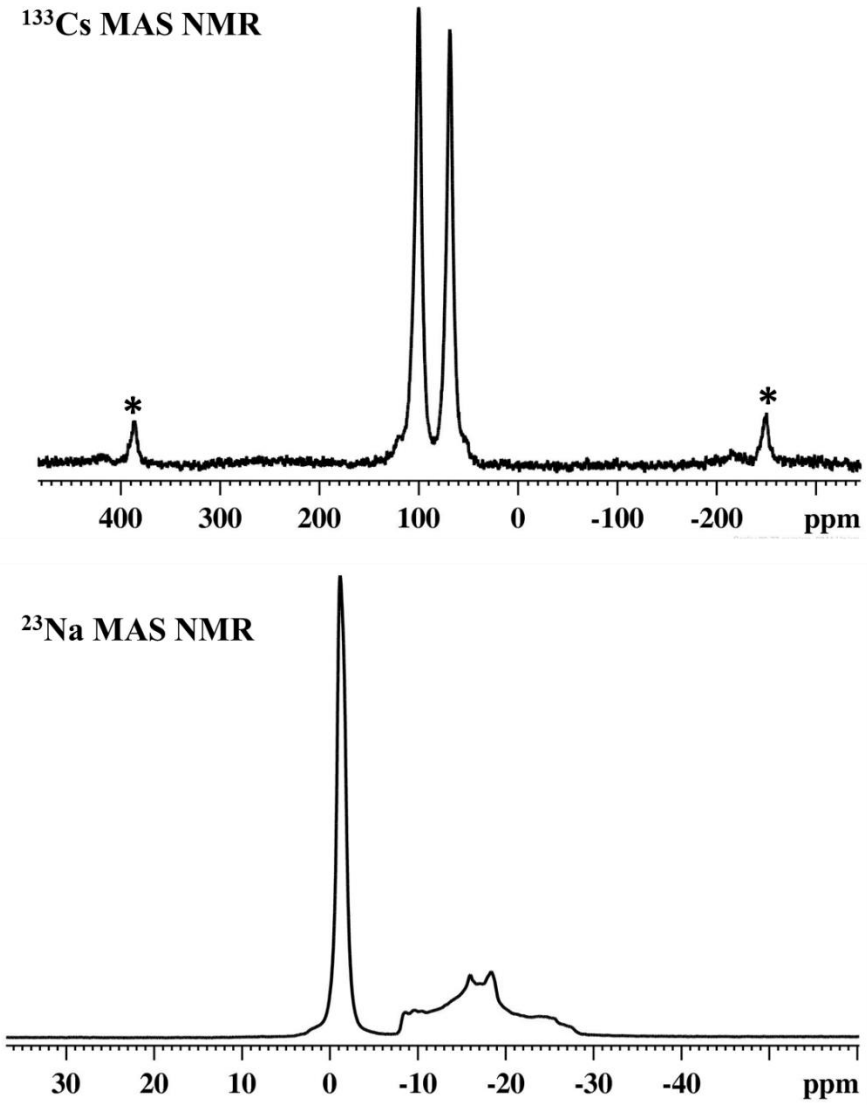

Figure 8.22. ^{133}Cs (top) and ^{23}Na MAS NMR (bottom) spectra of the gall layer. The asterisks denote spinning sidebands.

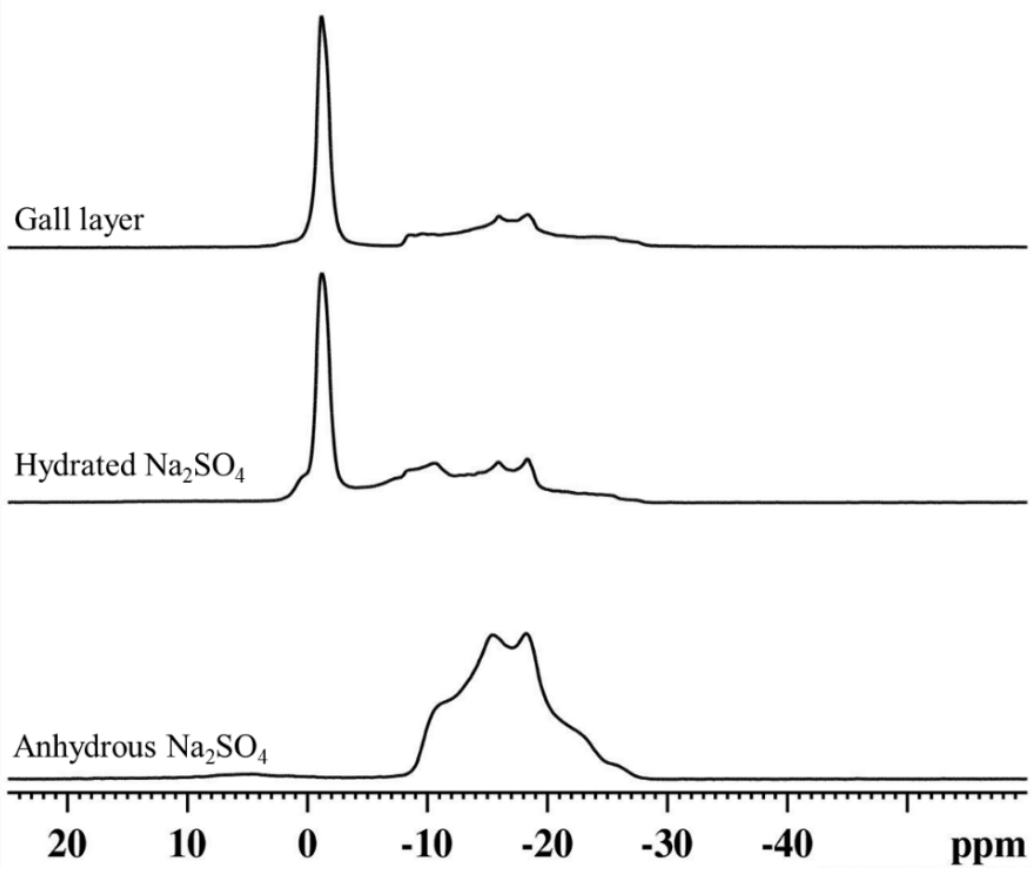

Figure 8.23. ^{23}Na MAS NMR spectra of anhydrous Na_2SO_4, a hydrated form of sodium sulfate, and the gall layer.

8.3.3 Electron microscopy

The back-scattered electron image of a cross-section of P-$5_{Mo3/S3}$ reveals spherical regions with diameters up to 500 μm homogeneously distributed throughout the glass matrix (**Figure 8.24**). The difference in the contrast between the matrix and the droplets suggests very different chemical compositions, with the spherical regions rich in elements with high atomic masses. Energy dispersive x-ray spectroscopic analysis indicates that the droplets are enriched in P, Mo, S and Na, while the matrix is rich in silicon (**Figure 8.24**). Since the energies of the Kα and the Lα lines of S (2.307 KeV) and Mo (2.293 KeV) are similar [61], a single peak representing both elements is observed from the spherical regions and they cannot be independently quantified by

this method. The Si-rich matrix has negligible intensity in this region, confirming the depletion of Mo and S in the bulk glass. These results indicate a droplet-type phase separation wherein a phase rich in P, Na, Mo, and S has separated from the silicate melt. While aluminum is observed to be present in both regions, the distribution of B cannot be ascertained by this technique due to its low atomic mass.

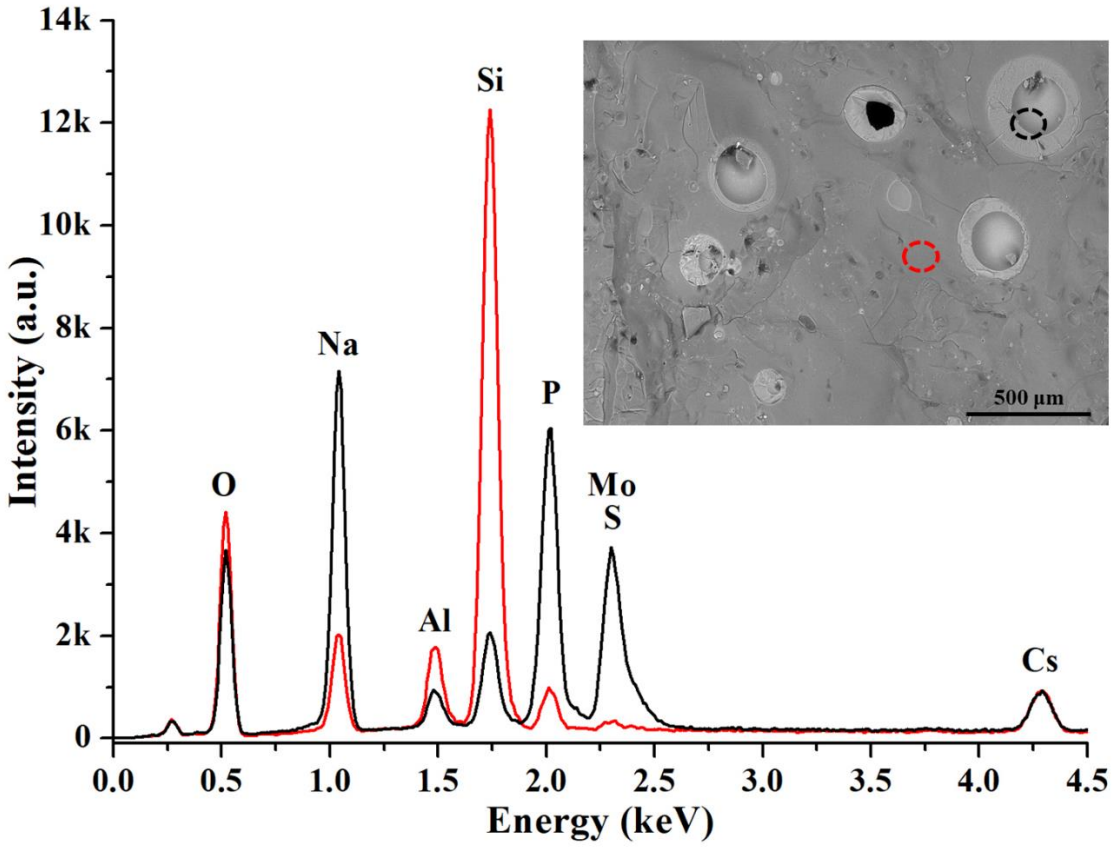

Figure 8.24. EDS spectra of dark (red circle) and bright (black circle) regions within the BSE image (inset) of a cross-section of sample P-$5_{Mo3/S3}$.

8.4 Discussion

8.4.1 Mo retention

The notoriety of Mo as a problem element in nuclear waste vitrification has inspired various approaches to improve its incorporation into a durable glass matrix. The propensity of Mo to devitrify as molybdates and the effect of glass composition on this process has been studied in detail using the phase specificity and quantitative accuracy of NMR spectroscopy [8,9,39,45,62]. The borosilicate glass without phosphorus (P-0_{Mo3}) exhibits diagnostic peaks in ^{23}Na NMR and x-ray diffraction corresponding to sodium molybdate phases. The presence of both anhydrous and hydrated forms of Na_2MoO_4 reflects the affinity of alkali molybdates for atmospheric water. Despite subjecting the devitrified glass to x-ray diffraction analysis immediately after grinding the sample on the benchtop, the anhydrous sodium molybdate apparently adsorbed water from the air and partially transformed into the hydrated form. This hygroscopic behaviour underscores the importance of preventing molybdate crystallization in materials intended for long-term nuclear waste immobilization.

In previous work, glass compositions containing cesium consistently yielded Cs-bearing molybdates such as Cs_2MoO_4, $Cs_2Mo_2O_7$ or the Na/Cs-bearing phases, $CsNaMoO_4.2H_2O$ and $Cs_3Na(MoO_4)_2$ [9,39,45], demonstrating that mixed-alkali molybdates are common devitrification products in overloaded borosilicate glasses. Owing to the presence of a small amount of cesium in the glasses in this work (2 mol%), such cesium molybdate phases might also be present below detection limits. Studies on similar glass compositions showed that whereas sodium molybdate was the only separated phase identifiable by x-ray diffraction, ^{133}Cs NMR revealed sharp peaks diagnostic of cesium in crystalline environments [63]. In general, it can be assumed that cesium-containing molybdate phases are also present in conjunction with sodium molybdates, raising concern about the mobilization of radioactive (i.e. ^{135}Cs and ^{137}Cs) molybdates.

Glasses in which a small amount of phosphate replaces a portion of the silicate are better able to resist devitrification of molybdate phases. For example, only 2.5 mol% P_2O_5 substantially reduces the amount of crystallinity in the glass, as measured by ^{23}Na MAS NMR. However, the presence of a small NMR peak on the shoulder of the dominant signal corresponding to the glassy phase in P-2.5_{Mo3} suggests that this amount of phosphorus is not adequate to completely immobilize 3 mol% Mo. Considering the *ca.* 1.5 mol% Mo loading limit of typical nuclear

glasses [10], this may be viewed as a significant improvement. Glasses with higher fractions of phosphorus show no evidence of crystallinity in NMR or XRD, indicating that all Mo is present in purely glassy environments.

To further probe the effectiveness of P addition for vitrifying Mo in an aluminoborosilicate glass, the Mo content was raised to 5 mol% in a glass containing 10 mol% P_2O_5 (P-10_{Mo5}). Neither ^{23}Na MAS NMR (**Figure 8.3**) nor XRD (**Figure 8.4**) show any evidence of molybdate crystallization, despite the presence of nearly four times the Mo solubility limit in borosilicate glasses [9]. Although XRD reveals the presence of a small amount of crystalline SiO_2 (vide supra), this underscores the value of P to inhibit molybdate formation, even when other crystalline phases are present to serve as nucleation sites. Likewise, the ^{31}P MAS NMR spectrum (not shown) is almost indistinguishable from that of P-10_{Mo4}, implying that the glass can accommodate 25% more Mo without undergoing further structural changes involving phosphorus. It may be reasonably concluded that there are ample phosphate sites available for bonding to Mo. Molybdenum incorporation beyond 5 mol% was not tested as such high concentrations of Mo are rarely found in typical nuclear waste streams. To understand the structural role of phosphorus in improving Mo solubility in borosilicate glasses, a detailed analysis of the multinuclear NMR results was carried out.

8.4.2 Glass structure

8.4.2.1 Aluminoborosilicate glasses

An aluminoborosilicate glass overloaded with 3 mol% Mo (P-0_{Mo3}) consists mainly of silicon tetrahedra bridging through oxygen to borate and aluminate units. Three chemically distinct $^{[4]}$B units have been identified in such glasses that are bonded to two ($^{[4]}B_{2Si}$), three ($^{[4]}B_{3Si}$) and four Si units ($^{[4]}B_{4Si}$), the other linkages being to $^{[3]}$B. Although more than one chemically distinct $^{[3]}$B species has been found [64], a detailed analysis of the specific nature of multiple $^{[3]}$B species is beyond the scope of this report and is not expected to impact the conclusions.

Aluminum is observed predominantly in fourfold coordination, bonded to Si tetrahedra through bridging oxygens to form an integral part of the glass network. Since these $^{[4]}$Al are negatively charged ($[AlO_4]^-$), the general consensus is that they are not bonded to other $^{[4]}$Al units according to Loewenstein's aluminum avoidance rule [65]; likewise, they are also not

expected to bond to negatively charged $^{[4]}B$ units ($[BO_4]^-$) [66]. However, $^{[4]}Al$ readily bonds to $^{[3]}B$ [66,67], accounting for the presence of $^{[3]}B$ in the glass network. A small but significant fraction of $^{[5]}Al$ is also observed in these glasses, which can function to stabilize anionic borate and aluminate tetrahedra [66].

Two distinct Si species have been identified in this glass, Q^3 and Q^4, which are expected to be bonded to $^{[4]}B$, $^{[3]}B$ and $^{[4]}Al$. The ^{29}Si chemical shift ranges of Q^3 and Q^4 depend on the identities of the neighbouring polyhedra. For example, replacing one silicate tetrahedron bonded to a Q^4 with $^{[3]}B$ or $^{[4]}B$ leads to Q^4 chemical shifts of -106 and -98 ppm, respectively [68], whereas a Q^4 bridging to four $^{[4]}B$ has a chemical shift of -92 ppm [48]. Similar effects have been documented for Q^4 bonding to Al [48]. This sensitivity to next-nearest-neighbours makes more detailed assignments of Q^n species speculative. However, simply balancing the expected positive and negative charges for a given composition confirms the NMR analysis showing a small amount of Q^3 in P-0_{Mo3}.

In borosilicate glasses, Mo is known to aggregate in depolymerized regions of the glass as isolated molybdate anions ($[MoO_4]^{2-}$), sequestering alkali and alkaline-earth cations to form the respective molybdates [20]. The observation of separated sodium molybdates in P-0_{Mo3} confirms this understanding. A two-dimensional pictorial representation of the network structure is shown in **Figure 8.25** with a corresponding bonding summary.

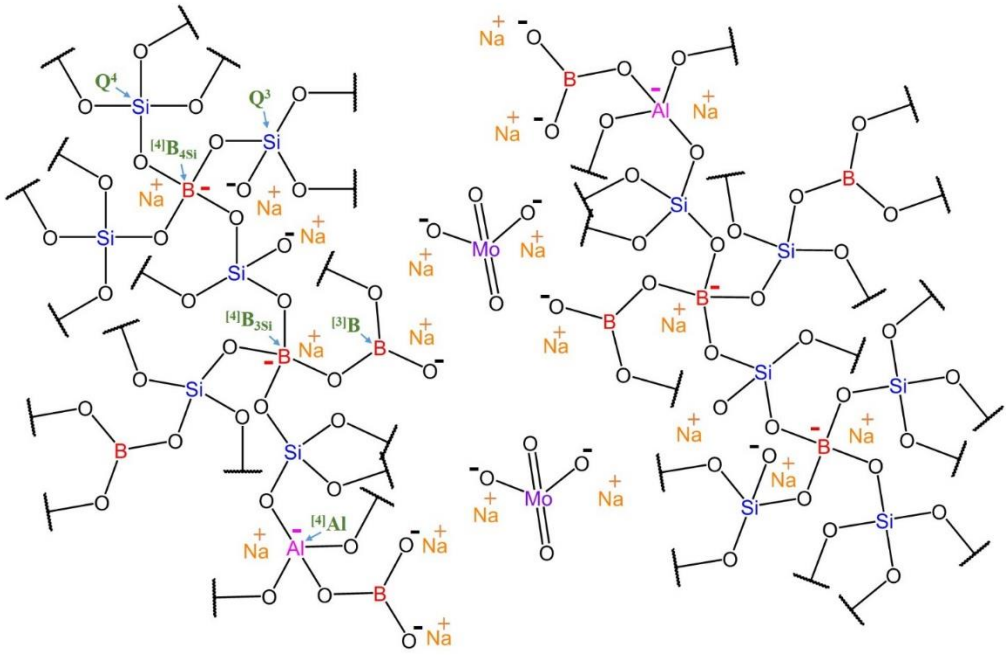

Figure 8.25. Pictorial representation of the network structure of a molybdate-bearing aluminoborosilicate glass. Q^4 and Q^3 Si units are bonded to $^{[4]}B$, $^{[3]}B$ and $^{[4]}Al$ units. $^{[4]}B_{4Si}$ units are bonded to four Si units; $^{[4]}B_{3Si}$ units are bonded to three Si and one $^{[3]}B$. $^{[3]}B$ may be bonded to Q^4, Q^3 and $^{[4]}Al$ units. $^{[4]}Al$ are bonded to Q^3, Q^4 and $^{[3]}B$ units. Mo is present as isolated $[MoO_4]^{2-}$ unit in alkali-rich areas of the glass, also called depolymerized regions.

8.4.2.2 Phosphorus in aluminoborosilicate glasses

At low levels, phosphorus has been reported to distribute as isolated orthophosphate units in silicate glasses [69,70]. Our previous work showed that monomeric and dimeric phosphates are the dominant species present in borosilicate glasses containing up to 3 mol% P [33]. In the presence of molybdenum, ^{31}P MAS NMR indicates that about 10% of the phosphorus in P-2.5$_{Mo3}$ is present as orthophosphates, whereas more than half of the phosphorus exists as pyrophosphate units (**Table 8.3)**. The latter may be dimers or the termini of short chains, as nearly 35% of the phosphorus is present in chains (P^2). Doubling the phosphate content to 5 mol% increases the chain lengths, as signified by the increase in metaphosphate species relative to pyrophosphates, and tripling it to 7.5 mol% results in nearly 70% of the phosphorus located in chains. Another way to analyze the data is to calculate the total amount of each phosphate unit in the glass, where

it may be seen that the overall concentration of isolated orthophosphates is small and relatively constant with increasing phosphorus content (**Figure 8.10**). Likewise, the concentration of P^1 units appears to be generally stable, with the major change in the phosphorus speciation being a dramatic increase in chain metaphosphates. An overlay of all the spectra from the series clearly highlights the overall transformation of the phosphate network with a gradual increase in the phosphorus content of the glass (**Figure 8.7**).

The P speciation must be understood in the context of a phase-separated glass, where amorphous droplets enriched in alkali phosphate can be seen using SEM (**Figure 8.24**). In addition to Mo, these separated phases appear to contain Al, making them alkali aluminophosphates, which readily incorporate Mo. Based on the glass chemistry, it is possible that B is also present in this phase, however this cannot be readily confirmed as B is invisible to EDS, and scant evidence for $^{[4]}$B-O-P linkages may be found in the ^{11}B MAS NMR data. Thus, the ^{31}P MAS NMR data represent the species present in both the silicate-rich matrix and the phosphate-rich droplets. The different spin-lattice relaxation times measured for chain phosphates and pyrophosphates in P-5_{Mo3} suggest that these species are present in different phases. This would be consistent with studies showing that dimers (i.e., linked P^1 units) are the dominant phosphate species in silicate glasses at low P loadings [44], beyond which phosphate-rich phases segregate. Accordingly, the growing proportion of chain phosphates would be found mainly in the droplets, implying that this phase is near the metaphosphate composition (i.e., Na:P $\approx$ 1, O/P $\approx$ 3) [43], a composition which has been shown to readily incorporate Mo [22]. In contrast to a recent report asserting homogeneity in P- and Mo-loaded borosilicate glasses [32], the phase separation documented here appears to play an important role in the ability of phosphorus to enhance Mo loading in borosilicate glasses.

Boron plays an essential role in optimizing nuclear waste glass properties. It is an excellent network former and forms glasses when added to silicate and phosphate glasses due to favourable B−O−Si [45] and B−O−P [71] bonds. Boron is also known to bond well to intermediate network formers like aluminum via B−O−Al bonds [72], and may possibly connect to molybdenum through bridging oxygens, forming B−O−Mo bonds [22]. Like aluminum [30], boron can also be expected to interconnect silicon and phosphorus within the same glass network, improving homogeneity with respect to B-free compositions. Moreover, a boron-rich aluminoborosilicate glass should alleviate the problems associated with high-refractory glasses

by reducing melting temperatures, mitigating the loss of radioisotope volatility, and making the melting process more economical. As the phosphorus content increases, tetrahedral boron might be expected to have phosphate units as next-nearest neighbours in addition to silicate units, yielding $^{[4]}B_{2Si/P}$, $^{[4]}B_{3Si/P}$ and $^{[4]}B_{4Si/P}$ configurations. Density functional theory (DFT) calculations have revealed that $^{[4]}B$ in a borophosphate glass network bonded to four neighbouring phosphate units ($^{[4]}B_{4P}$) has a chemical shift of ~ -4 ppm, whereas $^{[4]}B$ units bonded to fewer than four phosphate units (e.g., $^{[4]}B_{2/3P}$, where the remaining linkage is to a trigonal boron) have chemical shifts ranging between -2 and -3 ppm [73]. Since the chemical shifts of the components used in deconvolution are greater than -2 ppm, $^{[4]}B_{(2-4)P}$ units do not appear to be present. While it may be possible for the chemical shift of $^{[4]}B_{1P}$ to overlap with those of the above-mentioned $^{[4]}B$ species, leading to $^{[4]}B_{1Si+1P}$, $^{[4]}B_{2Si+1P}$ and $^{[4]}B_{3Si+1P}$, the peak shift towards higher frequencies with increasing P mitigates against the presence of $^{[4]}B-O-P$ bonds, as bonding to P would be expected to shift them toward lower frequencies [74,75]. In borosilicate glasses, fewer neighbouring silicate units - and more $^{[3]}B$ units - around $^{[4]}B$ pushes their chemical shifts to higher frequencies [76], and the chemical shift difference between $^{[4]}B_{4Si}$, $^{[4]}B_{3Si}$ and $^{[4]}B_{2Si}$ units is found to be ~ 1.8 ppm [77]. This serves as a basis for the constraints used in our fitting procedure to determine possible $^{[4]}B$ connectivities. Since the chemical shift difference between $^{[4]}B_{4Si}$ and $^{[4]}B_{3Si}$ units in P-0_{Mo3} is ~1.5 ppm, the peaks used to model the other experimental spectra were constrained to a difference of approximately 1.5 ppm between them. Accordingly, the chemical shifts of $^{[4]}B_{4Si}$, $^{[4]}B_{3Si}$ and $^{[4]}B_{2Si}$ units were set to -1.7, -0.1 and 1.3 ppm, respectively, with an allowed deviation of ± 0.2 ppm. The peak widths were constrained to 2.3 ± 0.2 ppm, commensurate with which is generally observed for well-resolved $^{[4]}B$ peaks representing distinct coordination environments.

In the substitution of SiO_2 by P_2O_5, two P^{5+} are introduced for every Si^{4+}, which has a decisive impact on the borate speciation in the glass. Since P^{5+} exists predominantly as ortho- ($[PO_4]^{3-}$) and pyrophosphates ($[P_2O_7]^{4-}$), the demand for charge-balancing Na^+ ions increases significantly. As a result, phosphate units target the Na^+ ions which are charge-compensating anionic $[BO_4]^-$, effectively converting them into $^{[3]}B$ and accounting for the significant decrease in N_4 as Si is replaced by P. This effect becomes even more pronounced with the formation of separate alkali aluminophosphate droplets, sequestering the alkali cations and driving boron in the silicate matrix toward neutral $^{[3]}B$ species.

In the ^{27}Al MAS NMR spectra (**Figure 8.20, Table 8.6**), the $^{[4]}$Al peak shift toward lower frequencies with increasing P reflects the formation of Al−O−P bonds in addition to the original Al−O−Si bonds, as $^{[4]}$Al units bonded to phosphorus have lower chemical shifts [55,78] than do $^{[4]}$Al bonded to silicon [79,80]. The observed increase in the peak widths suggests the overlap of signals arising from both $^{[4]}$Al−O−Si and $^{[4]}$Al−O−P, the latter of which may located in the separated glassy phase. At higher phosphorus contents, $^{[6]}$Al is also observed, which is common to aluminophosphate glasses [55] and substantiates the presence of Al in the phosphate phase. It can be generalized that the chemical environment around the aluminate units incrementally transforms from that of aluminosilicate to aluminophosphate, as evidenced by gradual changes in the positions and widths of the peaks. These results support the designation of metaphosphate units as $P^2_{Al/B}$. As such, the number of metaphosphates available to bond with borate units is reduced, with the result that $^{[4]}$B are bonded primarily to $^{[3]}$B, further explaining the $^{[4]}$B peak shift to higher frequency. These observations point toward the conclusion that when Si is initially replaced by P, B−O−Si bonds are mainly replaced by B−O−$^{[3]}$B bonds, with the added phosphorus present predominantly as isolated orthophosphates and pyrophosphate dimers. With increasing P, $^{[3]}$B−O−P and Al−O−P bonds start to form, interconnecting the borate, aluminate, and phosphate networks and leading to a mixed-network-former glass.

Increasing silicate network connectivity with increasing P and Mo is evident in the ^{29}Si NMR spectra (**Figures 8.18 and 8.19**). This has been attributed to the alkali-scavenging property of phosphorus: at lower phosphate contents, P enters the silicate network predominantly as orthophosphate along with some pyrophosphate dimers, these anionic species sequestering alkali ions for charge balance and forcing the transformation of Q^3 to Q^4 units [70]. Further addition of phosphorus leads to the formation of chain phosphates and induces glass-in-glass phase separation, driven both by the charge-balancing demands of the P^0 and P^1 species in the silicate phase, and the sequestering of alkali ions into the phosphate phase [33]. At still higher P fractions, the silicate network is dominated by Q^4 units, along with the separation of crystalline SiO_2, as supported by XRD (**Figure 8.4**). Although the ^{29}Si NMR deconvolution of P-10_{Mo5} suggests the presence of two chemically distinct Q^4, their respective sources could not be determined due to chemical heterogeneity of the sample.

The NMR data lead to a structural picture in which a low level of isolated orthophosphate and pyrophosphate dimers can be accommodated within the aluminoborosilicate network,

followed by the separation of predominantly chain phosphate units with bonding to trigonal boron and tetrahedral aluminum at higher P content. In this context, the ability to load more Mo into phosphate-bearing glasses may be understood as deriving from favourable bonding interactions with the available phosphate species, with which it may form neutral $^{[6]}Mo^{6+}$ species bonded to the glass network [81], rather than charged $^{[4]}Mo^{6+}$ species [39] which require further alkali charge-balancing, driving molybdate clustering and crystallization.

8.4.2.3 Cation field-strength matching

The favourable interaction between P^{5+} and Mo^{6+} may be partly explained by their similar field strengths. The field strength of a cation can be defined as the ratio of its charge, Z, to the square of the average cation-oxygen bond distance in Å: $Z/[r(M\text{-}O)]^2$ [7]. The mean P−O bond length is 1.53 Å [82], Mo^{6+} has mean bond lengths of 1.76 Å ($^{[4]}Mo$) and 1.97 Å ($^{[6]}Mo$) [83], and the mean bond length of Si−O in silicates in tetrahedral coordination is 1.62 Å [84], leading to field strengths of 1.52 (Si^{4+}), 2.13 (P^{5+}), 1.94 ($^{[4]}Mo^{6+}$) and 1.54 $Å^{-2}$ ($^{[6]}Mo^{6+}$). The higher field strength of $^{[4]}Mo^{6+}$ than Si^{4+} gives it a more control over the shared oxygen in a hypothetical Mo−O−Si bond, resulting in the formation of stable MoO_4^{2-} species unconnected to the silicate network, nucleating into crystalline molybdates with charge-balancing alkali cations and leaving behind more highly polymerized silicate regions [51,85]. In phosphate glasses the comparable field strengths of Mo^{6+} and P^{5+} lead to a more equitable competition for oxygen in which P−O−$^{[6]}$Mo bonds are stable and facilitate the integration of Mo into the phosphate glass network. This is borne out by the association of Mo with P^1 and P^2 units in phosphosilicate glasses [33] and to chain phosphates in low-Mo borophosphate glasses [22]. The increase in P^2 units with increasing phosphate content shown in the present work ensures that Mo is more effectively incorporated into the glassy phosphate network.

8.4.2.4 The incorporation of sulfur into P-containing glasses

Due to the detrimental effects of the gall layer on the vitrification process and the potential incorporation of radioactive Cs^+ into water-soluble sulfate phases (see **section 8.3.6**), it is vital to avoid the formation of crystalline sulfates during waste vitrification. Similarities in the dissolution properties of S^{6+} and Mo^{6+} in borosilicate glasses suggest that the cation field

strength matching principle may also be applied to immobilize S^{6+} in the glassy phase. The average $^{[4]}S^{6+}-O$ bond length is 1.47 pm [82], which results in a cation field strength of 2.77 $Å^{-2}$, even higher than those of $^{[4]}Mo^{6+}$ and P^{5+}. High-phosphate glasses have been shown to be effective for sulfate incorporation [24,86], but they suffer from poor chemical durability. Sulfur segregates as isolated tetrahedral sulfate units in borosilicate glasses surrounded by charge-balancing cations [16], a chemical environment similar to that of Mo. Despite this similarity, there do not appear to be any crystalline compounds containing high-coordinate S^{6+} or P−O−S bonds, suggesting that the difference in cation field strengths is sufficiently large to prevent equal sharing of oxygen in a bridging arrangement. Nevertheless, phosphorus does seem to improve sulfur solubility, and structural insight is needed to understand and utilize this as a design principle.

The ^{23}Na NMR spectra (**Figure 8.5**) of aluminoborosilicate glasses containing sulfate alone and with both sulfate and phosphorus highlight the benefit of doping a borosilicate glass with phosphorus. Whereas the P-free glass (P-0_{S3}) has a prominent sodium-sulfate signature, the phosphorus-doped glass (P-$5_{Mo3/S3}$) does not exhibit any peak which can be attributed to sodium-bearing crystalline phases; nor does XRD feature any peaks from sulfate phases (**Figure 8.6**). It should be noted that P-$5_{Mo3/S3}$ also contains 3 mol% of Mo, showing that this particular glass composition can simultaneously incorporate both the high field-strength ions which tend to phase-separate in conventional borosilicate glasses. The asymmetric peak shape of P-$5_{Mo3/S3}$ may be deconvolved into two peaks representing different amorphous sodium environments, possibly due to the presence of Na^+ in distinct glassy phases. However, it is challenging to assign these peaks to specific chemical environments due to their multiple roles of charge balancing both bridging and non-bridging oxygens on four network-forming cations (aluminate, borate, silicate, and phosphate). It is interesting to note that the ^{23}Na NMR peak shape of P-5_{Mo3}, which contains no sulfur, is symmetrical, suggesting that sulfate has a substantial influence on Na^+ which is reflected in its chemical shift.

The ^{11}B MAS NMR spectrum of P-0_{S3} differs in interesting ways from that of P-$5_{Mo3/S3}$ (**Figure 8.17**). Both P-0_{Mo3} and P-0_{S3} have similar N_4 fractions (**Table 8.4**) and undergo devitrification, underscoring the similarity in the chemical properties of Mo^{6+} and S^{6+}, and their similar interactions with the borate network. The spectral features of P-$5_{Mo3/S3}$ are similar to P-5_{Mo3}, suggesting that in the presence of phosphate, the borate network is hardly affected by the

addition of sulfate. In contrast, the addition of sulfate to a Mo-containing glass led to a significant reduction in the metaphosphate fraction, as shown in the ^{31}P MAS NMR spectra (**Figures 8.12 and 8.13**). Moreover, a sharp reduction in the T_1 of metaphosphates is observed in P-$5_{Mo3/S3}$, which further substantiates the interaction between the added sulfate and the chain phosphates. If P^2 is indicative of the degree of alkali phosphate droplet formation, this implies that phase separation is less pronounced in the S-bearing glass. Alternately, this could represent depolymerization of phosphate chains, as reported in some phosphate glasses upon addition of Mo [87]. Either way, this observation implies that S has a significant impact on the phosphate speciation which appears to be distinct from that of Mo.

While NMR spectroscopy and x-ray diffraction shed light on the glass network connectivity and the identities of any crystalline phases formed, electron microscopy provides information on the chemical heterogeneity and elemental distributions within the materials. Adding Mo to a P-doped aluminoborosilicate glass induces glass-in-glass phase separation, producing spherical droplets of a phase rich in P, Na and Mo within a silicate-rich glass matrix [33]. A similar observation is made in P-$5_{Mo3/S3}$, where both S and Mo strongly partition into an alkali aluminophosphate glassy phase (**Figure 8.24**). In combination with the spectroscopic results, the concentration of Mo, S and P in phase-separated droplets provides further support for the direct interaction of phosphate species with sulfur. These results underscore the similarities in the chemical properties and bonding preferences of Mo^{6+} and S^{6+} in silicate and phosphate glass networks, providing compelling evidence for the preferential bonding of S^{6+} and Mo^{6+} to phosphate units through P−O−Mo and P−O−S interactions.

8.5 Conclusions

The substitution of phosphate for a small fraction of silicate network formers in glasses related to those used for radioactive waste disposal results in a significantly enhanced capacity for Mo^{6+} and S^{6+} within the glass network. NMR spectroscopy, supported by x-ray diffraction, reveals that only at the lowest P concentrations do crystalline molybdates form, whereas the solubility of Mo in the glass melt is increased by at least four-fold with respect to the P-free aluminoborosilicate nuclear glasses currently in use worldwide. Sulfur incorporation is also substantially improved, even in the presence of Mo, suggesting that ample binding sites are involved in vitrification.

Multinuclear magnetic resonance spectroscopy provides clues about the specific bonding locations of Mo^{6+} and S^{6+} within the glassy network, indicating that phosphate chains are key to their enhanced solubility. The effectiveness of phosphorus appears to be related to its high cation field strength, which enables more equal sharing of oxygens with Mo^{6+} and S^{6+} than the lower field-strength silicon, boron, and aluminum, while remaining connected to the glass network through aluminate and borate linkages. Matching the cation field strengths with appropriate additives to optimize the assimilation of selected cations may prove to be a valuable design principle in the development of better materials for radioactive waste immobilization.

8.6 References

[1] D.D. Sood, S.K. Patil, Chemistry of nuclear fuel reprocessing: Current status, J. Radioanal. Nucl. Chem. 203 (1996) 547–573.

[2] R.S. Herbst, P. Baron, M. Nilsson, Standard and advanced separation: PUREX processes for nuclear fuel reprocessing, In: *Advanced separation techniques for nuclear fuel reprocessing and radioactive waste management*; Nash K. L.; Lumetta G. J., Eds.; Woodhead Publishing Limited, Elsevier, Amsterdam, **2011**. pp 141–175

[3] I.W. Donald, R.N. Metcalfe, J. Taylor, Review: The immobilization of high level radioactive wastes using ceramics and glasses, J. Mater. Sci. 32 (1997) 5851–5887.

[4] M.I. Ojovan, W.E. Lee, Glassy wasteforms for nuclear waste immobilization, *Metall. Mater. Trans. A Phys. Metall. Mater. Sci.*, 2011: pp. 837–851.

[5] M.J. Plodinec, Borosilicate glasses for nuclear waste imobilisation, Glas. Technol. 41 (2000) 186–192.

[6] N. Chouard, D. Caurant, O. Majérus, J.L. Dussossoy, S. Klimin, D. Pytalev, R. Baddour-Hadjean, J.P. Pereira-Ramos, Effect of MoO_3, Nd_2O_3, and RuO_2 on the crystallization of soda–lime aluminoborosilicate glasses, J. Mater. Sci. 50 (2015) 219–241.

[7] G.E. Brown, F. Farges, G. Calas, X-Ray Scattering and X-Ray Spectroscopy Studies of Silicate Melts, in: *Structure, dynamics, and properties of silicate melts*, J.F. Stebbins, P.F. McMillan, D.B. Dingwell (Eds.), De Gruyter, Berlin, Germany, 1995: pp. 317–410.

[8] B.J. Greer, S. Kroeker, Characterisation of heterogeneous molybdate and chromate phase assemblages in model nuclear waste glasses by multinuclear magnetic resonance spectroscopy, Phys. Chem. Chem. Phys. 14 (2012) 7375–7383.

[9] S. Kroeker, S. Schuller, J.E.C. Wren, B.J. Greer, A. Mesbah, ^{133}Cs and ^{23}Na MAS NMR spectroscopy of molybdate crystallization in model nuclear glasses, J. Am. Ceram. Soc. 99 (2016) 1557–1564.

[10] J.D. Vienna, Nuclear waste vitrification in the United States: Recent Developments and future options, Int. J. Appl. Glas. Sci. 1 (2010) 309–321.

[11] D. Manara, A. Grandjean, O. Pinet, J.L. Dussossoy, D.R. Neuville, Sulfur behavior in silicate glasses and melts: Implications for sulfate incorporation in nuclear waste glasses as a function of alkali cation and V_2O_5 content, J. Non-Cryst. Solids. 353 (2007) 12–23.

[12] A.L. Billings, K.M. Fox, Retention of sulfate in savannah river site high-level radioactive waste glass, Int. J. Appl. Glas. Sci. 1 (2010) 388–400.

[13] L. Wu, J. Xiao, X. Wang, Y. Teng, Y. Li, Q. Liao, Crystalline phase, microstructure, and aqueous stability of zirconolite-barium borosilicate glass-ceramics of immobilization of sulfate bearing high-level liquid waste, J. Nucl. Mater. 498 (2018) 241–248.

[14] C.P. Kaushik, R.K. Mishra, P. Sengupta, A. Kumar, D. Das, G.B. Kale, K. Raj, Barium borosilicate glass - a potential matrix for immobilization of sulfate bearing high-level radioactive liquid waste, J. Nucl. Mater. 358 (2006) 129–138.

[15] O.J. McGann, P.A. Bingham, R.J. Hand, A.S. Gandy, M. Kavčič, M. Žitnik, K. Bučar, R. Edge, N.C. Hyatt, The effects of γ-radiation on model vitreous wasteforms intended for the disposal of intermediate and high level radioactive wastes in the United Kingdom, J. Nucl. Mater. 429 (2012) 353–367.

[16] D.A. Mckeown, I.S. Muller, H. Gan, I.L. Pegg, C.A. Kendziora, Raman studies of sulfur in borosilicate waste glasses: sulfate environments, J. Non-Cryst. Solids. 288 (2001) 191–199.

[17] B.J. Riley, J.S. McCloy, A. Goel, M. Liezers, M.J. Schweiger, J. Liu, C.P. Rodriguez, D.S. Kim, Crystallization of rhenium salts in a simulated low-activity waste borosilicate glass, J. Am. Ceram. Soc. 96 (2013) 1150–1157.

[18] M. Lenoir, A. Grandjean, S. Poissonnet, D.R. Neuville, Quantitation of sulfate solubility in borosilicate glasses using Raman spectroscopy, J. Non-Cryst. Solids. 355 (2009) 1468–1473.

[19] W.L. Ebert, S.D. Rosine, A.J. Bakel, Gas evoution during vitrification of sodium sulfate and silica ANL/CTD/PP--86307, Argonne National Laboratory, Illinois, 1997.

[20] G. Calas, M. Le Grand, L. Galoisy, D. Ghaleb, Structural role of molybdenum in nuclear glasses: An EXAFS study, J. Nucl. Mater. 322 (2003) 15–20.

[21] D. Caurant, O. Majérus, E. Fadel, M. Lenoir, C. Gervais, O. Pinet, Effect of molybdenum on the structure and on the crystallization of SiO_2-Na_2O-CaO-B_2O_3 glasses, J. Am. Ceram. Soc. 90 (2007) 774–783.

[22] G. Tricot, K. Ben Tayeb, L. Koudelka, P. Mosner, H. Vezin, Insertion of MoO_3 in borophosphate glasses investigated by magnetic resonance spectroscopies, J. Phys. Chem. C. 120 (2016) 9443–9452.

[23] P.A. Bingham, A.J. Connelly, R.J. Hand, N.C. Hyatt, P.A. Northrup, Incorporation and speciation of sulphur in glasses for waste immobilisation, Glas. Technol. Eur. J. Glas. Sci. Technol. Part A. 50 (2009) 135–138.

[24] P.A. Bingham, R.J. Hand, Sulphate incorporation and glass formation in phosphate systems for nuclear and toxic waste immobilization, Mater. Res. Bull. 43 (2008) 1679–1693.

[25] P.A. Bingham, R.J. Hand, S.D. Forder, A. Lavaysierre, S.H. Kilcoyne, I. Yasin, Preliminary studies of sulphate solubility and redox in $60P_2O_5$-$40Fe_2O_3$ glasses, Mater. Lett. 60 (2006) 844–847.

[26] S. Schuller, F. Bart, Phase separation and crystallization induced by the addition of Mo and P to a calcium-sodium silicate glass, Glas. Odyssey 6th ESG Conf. (2002).

[27] M. Szumera, I. Wačawska, Effect of molybdenum addition on the thermal properties of silicate-phosphate glasses, J. Therm. Anal. Calorim. 109 (2012) 649–655.

[28] S. Schuller, O. Pinet, B. Penelon, Liquid-liquid phase separation process in borosilicate liquids enriched in molybdenum and phosphorus oxides, J. Am. Ceram. Soc. 94 (2011) 447–454.

[29] S. Schuller, O. Pinet, A. Grandjean, T. Blisson, Phase separation and crystallization of borosilicate glass enriched in MoO_3, P_2O_5, ZrO_2, CaO, J. Non-Cryst. Solids. 354 (2008) 296–300.

[30] O. Pinet, J.L. Dussossoy, C. David, C. Fillet, Glass matrices for immobilizing nuclear waste containing molybdenum and phosphorus, J. Nucl. Mater. 377 (2008) 307–312.

[31] O. Pinet, J.F. Hollebecque, I. Hugon, V. Debono, L. Campayo, C. Vallat, V. Lemaitre, Glass ceramic for the vitrification of high level waste with a high molybdenum content, J. Nucl. Mater. 519 (2019) 121–127.

[32] A.D. Prakash, M. Singh, R.K. Mishra, T.P. Valsala, A.K. Tyagi, A. Sarkar, C.P. Kaushik, Studies on modified borosilicate glass for enhancement of solubility of molybdenum, J. Non-Cryst. Solids. 510 (2019) 172–178.

[33] A. Krishnamurthy, T. Nguyen, M. Fayek, B. Shabaga, S. Kroeker, Network structure and dissolution properties of phosphate-doped borosilicate glasses, J. Phys. Chem. C. 124 (2020) 21184–21196.

[34] K.B. Patel, B. Boizot, S.P. Facq, S. Peuget, S. Schuller, I. Farnan, Impacts of composition and beta irradiation on phase separation in multiphase amorphous calcium borosilicates, J. Non-Cryst. Solids. 473 (2017) 1–16.

[35] R. Bouakkaz, A. Abdelouas, Y. El Mendili, B. Grambow, S. Gin, SON68 glass alteration under Si-rich solutions at low temperature (35–90 °C): kinetics, secondary phases and isotopic exchange studies, RSC Adv. 6 (2016) 72616–72633.

[36] E.L. Hahn, An accurate nuclear magnetic resonance method for measuring spin-lattice relaxation times, Phys. Rev. 76 (1949) 145.

[37] D. Massiot, F. Fayon, M. Capron, I. King, S. Le Calvé, B. Alonso, J.O. Durand, B. Bujoli, Z. Gan, G. Hoatson, Modelling one- and two-dimensional solid-state NMR spectra, Magn. Reson. Chem. 40 (2002) 70–76.

[38] J.P. Amoureux, C. Fernandez, QUASAR—Solid-State NMR simulation for quadrupolar nuclei, Univ. Lille, Lille, Fr. (2005).

[39] J.E.C. Wren, B.J. Greer, V.K. Michaelis, C.S. Higman, S. Kroeker, Multinuclear magnetic resonance investigation of crystalline alkali molybdates, Inorg. Chem. 54 (2015) 9853–9861.

[40] H. Gan, P.C. Hess, Phosphate speciation in potassium aluminosilicate glasses, Am. Mineral. 77 (1992) 495–506.

[41] F. Muñoz, L. Montagne, L. Delevoye, A. Durán, L. Pascual, S. Cristol, J.F. Paul, Phosphate speciation in sodium borosilicate glasses studied by nuclear magnetic resonance, J. Non-Cryst. Solids. 352 (2006) 2958–2968.

[42] H. Gan, P.C. Hess, R.J. Kirkpatrick, Phosphorus and boron speciation in K_2O-B_2O_3-SiO_2-P_2O_5 glasses, Geochim. Cosmochim. Acta. 58 (1994) 4633–4647.

[43] R.J. Kirkpatrick, R.K. Brow, Nuclear magnetic resonance investigation of the structures of phosphate and phosphate-containing glasses: A review, Solid State Nucl. Magn. Reson. 5 (1995) 9–21.

[44] R. Dupree, D. Holland, M.G. Mortuza, Six-coordinated silicon in glasses, Nature. 328 (1988) 416–417.

[45] C. Martineau, V.K. Michaelis, S. Schuller, S. Kroeker, Liquid-liquid phase separation in model nuclear waste glasses: A solid-state double-resonance NMR study, Chem. Mater. 22 (2010) 4896–4903.

[46] T. Nanba, M. Nishimura, Y. Miura, A theoretical interpretation of the chemical shift of ^{29}Si NMR peaks in alkali borosilicate glasses, Geochim. Cosmochim. Acta. 68 (2004) 5103–5111.

[47] F. Angeli, O. Villain, S. Schuller, S. Ispas, T. Charpentier, Insight into sodium silicate glass structural organization by multinuclear NMR combined with first-principles calculations, Geochim. Cosmochim. Acta. 75 (2011) 2453–2469.

[48] S. Prasad, T.M. Clark, T.H. Sefzik, H.T. Kwak, Z. Gan, P.J. Grandinetti, Solid-state multinuclear magnetic resonance investigation of Pyrex®, J. Non-Cryst. Solids. 352 (2006) 2834–2840.

[49] H. Maekawa, T. Maekawa, K. Kawamura, T. Yokokawa, The structural groups of alkali silicate glasses determined from ^{29}Si MAS-NMR, J. Non-Cryst. Solids. 127 (1991) 53–64.

[50] P. Zhang, P.J. Grandinetti, J.F. Stebbins, Anionic species determination in $CaSiO_3$ glass using two-dimensional ^{29}Si NMR, J. Phys. Chem. B. 101 (1997) 4004–4008.

[51] D. Caurant, O. Majérus, E. Fadel, A. Quintas, C. Gervais, T. Charpentier, D. Neuville,

Structural investigations of borosilicate glasses containing MoO_3 by MAS NMR and Raman spectroscopies, J. Nucl. Mater. 396 (2010) 94–101.

[52] S. Kapoor, X. Guo, R.E. Youngman, C.L. Hogue, J.C. Mauro, S.J. Rzoska, M. Bockowski, L.R. Jensen, M.M. Smedskjaer, Network glasses under pressure: Permanent densification in modifier-free Al_2O_3-B_2O_3- P_2O_5-SiO_2 Systems, Phys. Rev. Appl. 7 (2017) 1–16.

[53] E.I. Morin, J.F. Stebbins, Separating the effects of composition and fictive temperature on Al and B coordination in Ca, La, Y aluminosilicate, aluminoborosilicate and aluminoborate glasses, J. Non-Cryst. Solids. 432 (2016) 384–392.

[54] R.K. Brow, R.J. Kirkpatrick, G.L. Turner, Nature of alumina in phosphate glass: II, structure of sodium alurninophosphate glass, J. Am. Ceram. Soc. 76 (1993) 919–928.

[55] L. Zhang, H. Eckert, Short- And medium-range order in sodium aluminophosphate glasses: New insights from high-resolution dipolar solid-state NMR spectroscopy, J. Phys. Chem. B. 110 (2006) 8946–8958.

[56] S. Mooibroek, R.E. Wasylishen, R. Dickson, G. Facey, B.A. Pettitt, Simultaneous observation of shielding anisotropies and quadrupolar splittings in solid state ^{133}Cs NMR spectra, J. Magn. Reson. 66 (1986) 542–545.

[57] H.J. Weber, M. Schulz, S. Schmitz, J. Granzin, H. Siegert, Determination and structural application of anisotropic bond polarisabilities in complex crystals, J. Phys. Condens. Matter. 1 (1989) 8543–8557.

[58] H. Koller, G. Engelhardt, A.P.M. Kentgens, J. Sauer, ^{23}Na NMR spectroscopy of solids: Interpretation of quadrupole interaction parameters and chemical shifts, J. Physial Chem. 98 (1994) 1544–1551.

[59] I.D.H. Oswald, A. Hamilton, C. Hall, W.G. Marshall, T.J. Prior, C.R. Pulham, In situ characterization of elusive salt hydrates-the crystal structures of the heptahydrate and octahydrate of sodium sulfate, J. Am. Chem. Soc. 130 (2008) 17795–17800.

[60] H.W. Ruben, D.H. Templeton, R.D. Rosenstein, I. Olovsson, H.W. Ruben, D.H. Templeton, R.D. Rosenstein, I. Olovsson, Crystal Structure and entropy of sodium sulfate

decahydrate, J. Am. Chem. Soc. 83 (1961) 820–824.

[61] D.E. Newbury, N.W.M. Ritchie, Performing elemental microanalysis with high accuracy and high precision by scanning electron microscopy/silicon drift detector energy-dispersive X-ray spectrometry (SEM/SDD-EDS), J. Mater. Sci. 50 (2014) 493–518.

[62] S. Kroeker, I. Farnan, S. Schuller, T. Advocat, ^{95}Mo NMR study of crystallization in model nuclear waste glasses, MRS Online Proc. Libr. Arch. 1124 (2008).

[63] S. Kroeker, C.S. Higman, V.K. Michaelis, N.B. Svenda, S. Schuller, Precipitation of mixed-alkali molybdates during HLW vitrification, Mater. Res. Soc. Symp. Proc. 1265 (2010) 95–101.

[64] S. Kroeker, J.F. Stebbins, Three-coordinated boron-11 chemical shifts in borates, Inorg. Chem. 40 (2001) 6239–6246.

[65] W. Loewenstein, M. Lowenstein, The distribution of aluminum in the tetrahedra of silicates and aluminates, Am. Mineral. 39 (1954) 92–96.

[66] J.C.C. Chan, M. Bertmer, H. Eckert, Site connectivities in amorphous materials studied by double-resonance NMR-of quadrupolar nuclei: High-resolution ^{11}B ↔ ^{27}Al spectroscopy of aluminoborate glasses, J. Am. Chem. Soc. 121 (1999) 5238–5248.

[67] A. Krishnamurthy, V.K. Michaelis, S. Kroeker, Network formation in borosilicate glasses with aluminum or gallium: implications for nepheline crystallization, J. Phys. Chem. C. 125 (2021) 8815–8824.

[68] E. Nicoleau, S. Schuller, F. Angeli, T. Charpentier, P. Jollivet, A. Le Gac, M. Fournier, A. Mesbah, F. Vasconcelos, Phase separation and crystallization effects on the structure and durability of molybdenum borosilicate glass, J. Non-Cryst. Solids. 427 (2015) 120–133.

[69] R.M. Baltzar Stevensson Mattias Edén, Assessing the phosphate distribution in bioactive phosphosilicate glasses by ^{31}P solid-state nmr and molecular dynamics simulations., *J. Phys. Chem. B.* 118 (2014) 8863–8876.

[70] R. Dupree, D. Holland, M.G. Mortuza, J.A. Collins, M.W.G. Lockyer, An MAS NMR study of network - cation coordination in phosphosilicate glasses, J. Non-Cryst. Solids.

106 (1988) 403–407.

[71] L.M. Funke, H. Eckert, Charge compensation in sodium borophosphate glasses studied by $^{11}B\{^{23}Na\}$ and $^{31}P\{^{23}Na\}$ rotational echo double resonance spectroscopy, J. Phys. Chem. C. 120 (2016) 3196–3205.

[72] S. Sen, P. Yu, V.P. Klyuev, B.Z. Pevzner, Atomic structure of beryllium boroaluminate glasses : A multi-nuclear NMR spectroscopic study, J. Non-Cryst. Solids. 354 (2008) 4005–4011.

[73] V.K. Michaelis, P. Kachhadia, S. Kroeker, Clustering in borate-rich alkali borophosphate glasses: A ^{11}B and ^{31}P MAS NMR study, Phys. Chem. Glas. Eur. J. Glas. Sci. Technol. Part B. 54 (2013) 20–26.

[74] D. Zielniok, C. Cramer, H. Eckert, Structure/property correlations in ion-conducting mixed-network former glasses: Solid-state NMR studies of the system $Na_2O{-}B_2O_3{-}P_2O_5$, Chem. Mater. 19 (2007) 3162–3170.

[75] D. Larink, H. Eckert, M. Reichert, S.W. Martin, Mixed network former effect in ion-conducting alkali borophosphate glasses: Structure/property correlations in the system $[M_2O]_{1/3}[(B_2O_3)_x(P_2O_5)_{1-x}]_{2/3}$(M = Li, K, Cs), J. Phys. Chem. C. 116 (2012) 26162–26176.

[76] Y. Yu, M. Edén, Structure-composition relationships of bioactive borophosphosilicate glasses probed by multinuclear ^{11}B, ^{29}Si, and ^{31}P solid state NMR, RSC Adv. 6 (2016) 101288–101303.

[77] L.S. Du, J.F. Stebbins, Site preference and Si/B mixing in mixed-alkali borosilicate glasses: A high-resolution ^{11}B and ^{17}O NMR study, Chem. Mater. 15 (2003) 3913–3921.

[78] S. Wegner, L. van Wüllen, G. Tricot, The structure of aluminophosphate glasses revisited: Application of modern solid state NMR strategies to determine structural motifs on intermediate length scales, J. Non-Cryst. Solids. 354 (2008) 1703–1714.

[79] E.I. Morin, J. Wu, J.F. Stebbins, Modifier cation (Ba, Ca, La, Y) field strength effects on aluminum and boron coordination in aluminoborosilicate glasses: The roles of fictive temperature and boron content, Appl. Phys. A Mater. Sci. Process. 116 (2014) 479–490.

[80] L.M. Thompson, J.F. Stebbins, Non-stoichiometric non-bridging oxygens and five-coordinated aluminum in alkaline earth aluminosilicate glasses: Effect of modifier cation size, J. Non-Cryst. Solids. 358 (2012) 1783–1789.

[81] J. Bai, J. Hsu, P. Sandineni, C.W. Kim, R.K. Brow, The structure and properties of cesium loaded Mo-Fe-phosphate glasses, J. Non-Cryst. Solids. 510 (2019) 121–129.

[82] O.C. Gagné, F.C. Hawthorne, Bond-length distributions for ions bonded to oxygen: Results for the non-metals and discussion of lone-pair stereoactivity and the polymerization of PO_4, Acta Crystallogr. Sect. B Struct. Sci. Cryst. Eng. Mater. 74 (2018) 79–96.

[83] O.C. Gagné, F.C. Hawthorne, Bond-length distributions for ions bonded to oxygen: Results for the transition metals and quantification of the factors underlying bond-length variation in inorganic solids, IUCrJ. 7 (2020) 581–629.

[84] O.C. Gagné, F.C. Hawthorne, Bond-length distributions for ions bonded to oxygen: Metalloids and post-Transition metals, Acta Crystallogr. Sect. B Struct. Sci. Cryst. Eng. Mater. 74 (2018) 63–78.

[85] F. Farges, R. Siewert, G.E.J. Brown, A. Guesdon, Structural environments around molybdenum in silicate glasses and melts.I. Influence of composition and oxygen fugacity on the local structure of molybdenum, Can. Mineral. 44 (2006) 731–753.

[86] K. Ghosh, G.K. DasMohapatra, N. Soodbiswas, Glass formation in K_2SO_4-CaO-P_2O_5 system, Phys. Chem. Glas. 44 (2003) 313–318.

[87] M. Szumera, Molybdenum modified phosphate glasses studied by ^{31}P MAS NMR and Raman spectroscopy, Spectrochim. Acta - Part A Mol. Biomol. Spectrosc. 137 (2015) 111–115.

9 The Effect of Network-Modifier Content on the Chemical Durability of Borosilicate Glasses

9.1 Introduction

The chemical durability of borosilicate glasses and the mechanism of glass dissolution have been extensively studied due to their suitability as nuclear-waste immobilization matrices [1–13]. The water-resistant capabilities of basaltic and obsidian glasses [14] are a rich source of information, suggesting that a dissolution mechanism common to all silicate glasses can be used to predict the long-term chemical durability of borosilicate glasses. Despite the variable compositions of waste-immobilized silicate glasses, their dissolution is governed by four reactions: ion exchange, hydrolysis, dissolution, and condensation [13,15]. These reactions ultimately lead to the formation of a Si-rich amorphous layer on the glass surface called an *alteration layer* or a *passivation layer* [14–16], which has transport-limiting properties due to its low porosity. The dissolution of silicate glasses may be partitioned into three stages, according to *Ostwald's rule of stages* [13,15]. In stage 1, also called the *forward rate regime*, the glass dissolves congruently due to a lack of solution feedback at the *forward dissolution rate*. The ion exchange, hydrolysis, and dissolution reactions occur simultaneously in this regime. Eventually, due to the saturation of the solution with Si, or to the formation of the solution boundary layer, an amorphous passivation layer forms on the surface, marking the onset of stage 2. This is also called the *residual rate regime*, as the reactions active in stage 1 are quenched and glass dissolution slows to a negligible rate, effectively restoring its durability. Stage 2 determines the long-term durability of waste-immobilized glasses and factors such as pH [4,6,7,11], temperature [2,6,11], and the glass composition [6,12,17,18] greatly impact the kinetics and duration of stage 2 dissolution. In stage 3, zeolites and other silicate phases crystallize from the amorphous Si layer, depleting it of Si and reducing its protective properties. Glass dissolution resumes.

Sodium is present in all high-level and low-level waste streams, often in high concentrations in its oxide form [19]. In glass science, the sodium and other alkali ions are categorized as charge compensators and network modifiers since they are responsible for balancing negative charges on the anionic structural units and non-bridging oxygens (NBO) in the glass network [20]. The addition of Na_2O to a silicate glass forms NBO on silicon by

breaking Si−O−Si linkages and inserting oxide anions (O^{2-}) into the network, leading to a progressive change in the Si speciation from $Q^4 \rightarrow Q^3 \rightarrow Q^2 \rightarrow Q^1$ (Q^n, quaternary silicon species, where *n* represents the number of Si−O−Si bonds per Si tetrahedron) [20–22]. Alkali oxides affect boron speciation differently, initally adding oxygen to convert neutral trigonal-planar borate units ($^{[3]}$B) into anionic four-coordinate boron ($^{[4]}$B) species, which are charge compensated by Na^+. At higher alkali oxide contents, NBO begin to form on $^{[3]}$B, altering the speciation from $T^3 \rightarrow T^2 \rightarrow T^1 \rightarrow T^0$ (T^n, ternary boron, where *n* represents the number of bridging oxygens). This compositional relationship between the $^{[4]}$B fraction and the alkali content is popularly known as the "boron anomaly" [23]. At high alkali oxide contents, a high fraction of NBO bonded to $^{[3]}$B can appear in the network, decreasing the network reticulation. The speciation of Al in silicate glasses also exhibits a strong dependence on alkali content, wherein anionic tetrahedral Al units ($^{[4]}$Al) are observed in alkali-rich glasses (Na/Al ≥ 1), and high-coordinate Al ($^{[5]}$Al and $^{[6]}$Al) are found in peraluminous compositions (Na/Al < 1) [24].

The chemical durability of glass is a bulk property and depends on its network structure, which is a function of its alkali content. As Na_2O controls the extent of network reticulation and the speciation of all constituent structural units, understanding the effect of alkali oxide content on the glass network and the corresponding durability will aid in the design of glass compositions suitable for synthesizing durable wasteforms for long-term storage. Network depolymerization resulting from increased Na_2O content may compromise the chemical durability of the loaded glasses. Although the relationship between the physical properties of borosilicate and silicate glasses and their alkali contents has been well-established [25–29], systematic studies of the effect of alkali content on their resistance to aqueous corrosion are scarce. The durability studies conducted so far [1–13] have focused only on isolated target compositions rather than broad compositional ranges, which limits the ability to draw general conclusions about the effect of alkali content on the durability of glasses over a wide compositional space. Furthermore, the effect of alkali fraction on the instigation of different glass dissolution stages, and therefore the kinetics of forward and residual dissolution rates, have not been explored. To bridge this gap, a compositional series wherein SiO_2 is progressively substituted by Na_2O has been designed for structural characterization and dissolution studies.

In this work, a sodium aluminoborosilicate glass series with Na/Si ratios spanning a high-sodium range has been prepared to explore the effect of Na fraction on the network structure of

glasses using multinuclear solid-state NMR spectroscopy. The glasses are subjected to MCC-1 type [30] dissolution tests to determine the effect of the Na/Si ratio on the durability of the glasses, wherein the glasses are immersed in deionized water at 90 °C for 28 days with periodic sampling of the leachate. Solid-state NMR analysis of the altered samples is carried out to determine network modifications caused due to water corrosion. The elemental concentrations in the collected leachate aliquots are analyzed using inductively-coupled plasma optical emission spectroscopy (ICPOES) to produce elemental release profiles. The samples were analyzed by x-ray diffraction to confirm their amorphous nature and to track the formation of crystalline phases after dissolution. These multiscale measurements are used to relate Na loading to glass dissolution behaviour and the speciation of individual network formers.

9.2 Experimental details

9.2.1 Synthesis

Glasses of composition $(Na_2O)_{21+x}(Al_2O_3)_4(B_2O_3)_{16.5}(SiO_2)_{58.5-x}$, where *x* is varied from 5 to 25 in increments of 5 mol%, were synthesized by mixing SiO_2, Al_2O_3, Na_2CO_3, and B_2O_3 in three-gram batches according to the target composition (**Table 9.1**). B_2O_3 was synthesized by heating H_3BO_3 at 450 °C, 650 °C, and 800 °C for 30, 15, and 15 minutes, respectively. All other reagents were used as received. The samples were doped with 0.1 wt% of cobalt oxide to reduce the spin-lattice relaxation time of ^{29}Si NMR for NMR data acquisition. The oxides and carbonates were weighed and decarbonated at 650 °C for 12 hours and melted at 1100 °C for one hour in lidded Pt/Au crucibles. The crucibles were removed from the furnace and air-cooled to obtain glass monoliths. The monoliths were cut into approximately rectangular pieces and stored in a desiccator before the dissolution study, whereas the cutoff pieces were confirmed to be x-ray amorphous and used for NMR analysis. The composition of this glass series is shown on the $Na_2O-SiO_2-B_2O_3$ phase diagram, which also includes the immiscibility region (**Figure 9.1**) [31,32].

Table 9.1. Batch compositions of glasses (in mol%), designated by the mole % of Na_2O.

	Na-21	Na-26	Na-31	Na-36	Na-41	Na-46
SiO_2	58.5	53.5	48.5	43.5	38.5	33.5
B_2O_3	16.5	16.5	16.5	16.5	16.5	16.5
Al_2O_3	4.0	4.0	4.0	4.0	4.0	4.0
Na_2O	21.0	26.0	31.0	36.0	41.0	46.0
K'^a	2.85	2.60	2.36	2.12	1.87	1.63
R'^b	1.02	1.26	1.51	1.75	2.0	2.24

[a]$K' = [SiO_2/(B_2O_3+Al_2O_3)]$
[b]$R' = [Na_2O/(B_2O_3+Al_2O_3)]$

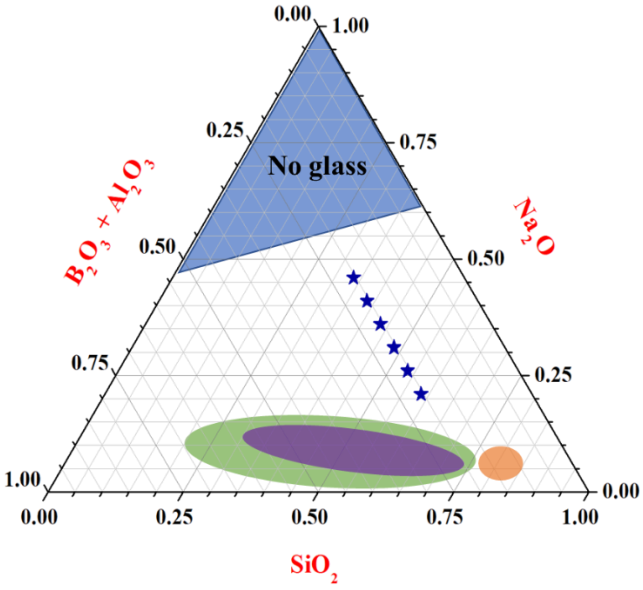

Figure 9.1. $Na_2O-B_2O_3-SiO_2$ ternary phase diagram with glass compositions marked with stars and the immiscibility, Vycor and Pyrex regions are marked in green, purple and orange, respectively [31,32]. The region of the phase diagram where a glass cannot be obtained is marked in blue.

9.2.2 Solid-state NMR spectroscopy

Solid-state magic-angle spinning (MAS) NMR analysis of pristine and altered glasses was conducted on a Varian ^{UNITY}INOVA 600 MHz NMR spectrometer equipped with a 1.6 mm H(F)-X-Y solid-state MAS probe. All samples were spun at the magic angle with a spinning speed of 25000±5 Hz. Bloch-decay [33] ^{11}B, ^{23}Na, and ^{27}Al MAS NMR experiments were carried out with a pulse length of *ca*. 0.4 μs, corresponding to a flip-angle of 15° for equal excitation of sites with different quadrupolar coupling constants (C_Q) and a relaxation delay of 2 s. One-pulse ^{29}Si MAS and ^{29}Si{^{1}H} cross-polarization MAS (CP-MAS) NMR spectra were acquired using a Bruker Avance 400 MHz NMR spectrometer equipped with a 4 mm double-resonance probe and a sample spin-rate of 8 kHz. Bloch-decay ^{29}Si experiments were carried out with a pulse length of 1.2 μs corresponding to a 30° tip angle, and a recycle delay of 10 s. A total of 1024 transients was collected and the spectra were referenced using hexamethyldisiloxane (+6.68 ppm relative to tetramethylsilane (0 ppm)). In the ^{1}H→^{29}Si CPMAS NMR experiment, a $\pi/2$ pulse of 4.3 μs was applied on the ^{1}H channel, and a recycle delay of 2 s was used. 16000 transients were collected at a spinning speed of 6 kHz, with high-power ^{1}H decoupling and a contact time of 4 ms.

9.3 Results

9.3.1 Characterization of pristine glasses

9.3.1.1 ^{11}B MAS NMR

The ^{11}B MAS NMR spectra of glasses (**Figure 9.2**) consist of a broad and a narrow peak centered at ca. 15 and 0 ppm, representing $^{[3]}$B and $^{[4]}$B, respectively [34–37] . The near-symmetric tetrahedral geometry of $^{[4]}$B results in a small quadrupolar broadening of the peak, with a C_Q of *ca.* 400 kHz. The trigonal-planar geometry of the $^{[3]}$B unit leads to an appreciable electric field gradient around the boron nucleus resulting in a much larger quadrupolar broadening characterized by a C_Q of 2.6 MHz [38,39]. Two G/L lineshapes with δ_{iso} of -1.5 and -0.2 ppm are used to fit the $^{[4]}$B peak in the Na-21 spectrum, attributed to $^{[4]}$B bonded to four ($^{[4]}B_{4Si}$) and three Si units ($^{[4]}B_{3Si}$), respectively [34–37]. The $^{[3]}$B peak is deconvolved with two second-order quadrupolar lineshapes with a C_Q of 2.6 ($\pm$0.2) MHz and an η of 0.2−0.5, with unconstrained isotropic chemical shifts. These parameters are characteristic of $^{[3]}$B units in ring

($^{[3]}B_{ring}$) and non-ring ($^{[3]}B_{non\text{-}ring}$) conformations [36,38,40], and their integrated intensities are added to represent the total $^{[3]}B$ present in the network. With increasing Na/Si, a high-frequency shift of the $^{[4]}B$ peak is observed. In high-Na glasses, the $^{[4]}B$ peak is fit again with two subspectra, but with δ_{iso} of -0.2 and +1.5 ppm, representing $^{[4]}B$ bonded to three ($^{[4]}B_{3Si}$) and two ($^{[4]}B_{2Si}$) silicate neighbours, respectively [36,41]. The fraction of $^{[4]}B$ in the glass network, represented by N_4 [$N_4 = {}^{[4]}B/({}^{[3]}B+{}^{[4]}B)$], increases slightly from 0.65 to 0.67 (**Table 9.2**) as the Na_2O mole fraction increases to 26 mol%. Further substitution of SiO_2 with Na_2O results in a sharp decline in N_4, consistent with the Yun and Bray [42,43] and Dell, Bray and Xiao [44] structural models for borosilicate glasses. In addition to an increase in the intensity, the left edge of $^{[3]}B$ peak shifts to higher frequencies with the Si→Na substitution. The formation of NBO on $^{[3]}B$ is known to shift the $^{[3]}B$ peak to higher frequencies [38,45]. Hence, a significant fraction of NBO can be expected to be associated with $^{[3]}B$ in high-Na glasses, and can be calculated for a given K (molar ratio of SiO_2 and B_2O_3) using these models as "asymmetric $^{[3]}B$" ($^{[3]}B_A$), and its fraction represented by N_{3A}.

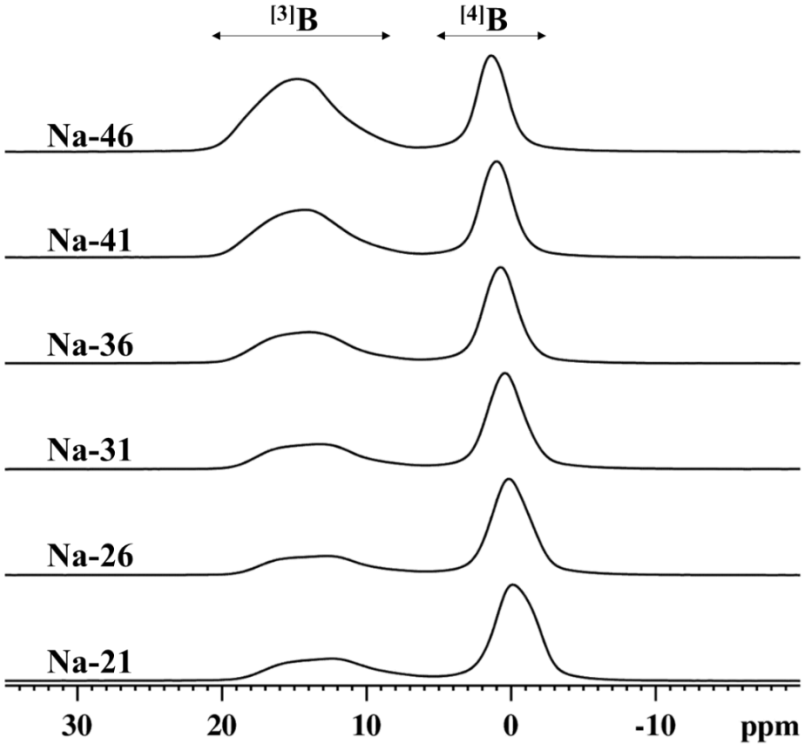

Figure 9.2. ^{11}B MAS NMR spectra of glasses.

Table 9.2. Integrated intensities of $^{[n]}B_{xSi}$ units and the N_4 fraction obtained from the deconvolution of the ^{11}B MAS NMR spectra.

	$^{[4]}B_{4Si}$[a]	$^{[4]}B_{3Si}$[b]	$^{[4]}B_{2Si}$[c]	$\Sigma^{[4]}B$	
	Int. I. (%)[d] (±3)	**Int. I. (%)[d] (±3)**	**Int. I. (%)[d] (±3)**	**Int. I. (%)[d] (±1)**	**N_4[e] (±0.01)**
Na-21	27	38	—	65	0.65
Na-26	25	42	—	67	0.67
Na-31	—	19	42	61	0.61
Na-36	—	18	36	54	0.54
Na-41	—	20	21	41	0.41
Na-46	—	12	21	33	0.33

[a]δ_{iso} = -1.5(±0.2) ppm; peak width = 4.3(±0.05) kHz
[b]δ_{iso} = -0.2(±0.5) ppm; peak width = 4.3(±0.05) kHz
[c]δ_{iso} = +1.3(±0.3) ppm; peak width = 4.3(±0.05) kHz
[d]Integrated intensity (%)
[c]$N_4 = {}^{[4]}B/({}^{[4]}B+{}^{[3]}B)$

9.3.1.2 ^{23}Na NMR

The ^{23}Na MAS NMR spectra of glasses (**Figure 9.3**) consist of a broad featureless peak, characteristic of Na ions present in a disordered chemical environment [22,34]. The spectra lack sharp peaks, confirming the absence of sodium-bearing crystalline phases in these glasses. The peak shifts to higher frequency with increasing Na/Si, with a difference in the peak maxima of *ca.* 10 ppm observed between samples with the lowest and highest Na fractions.

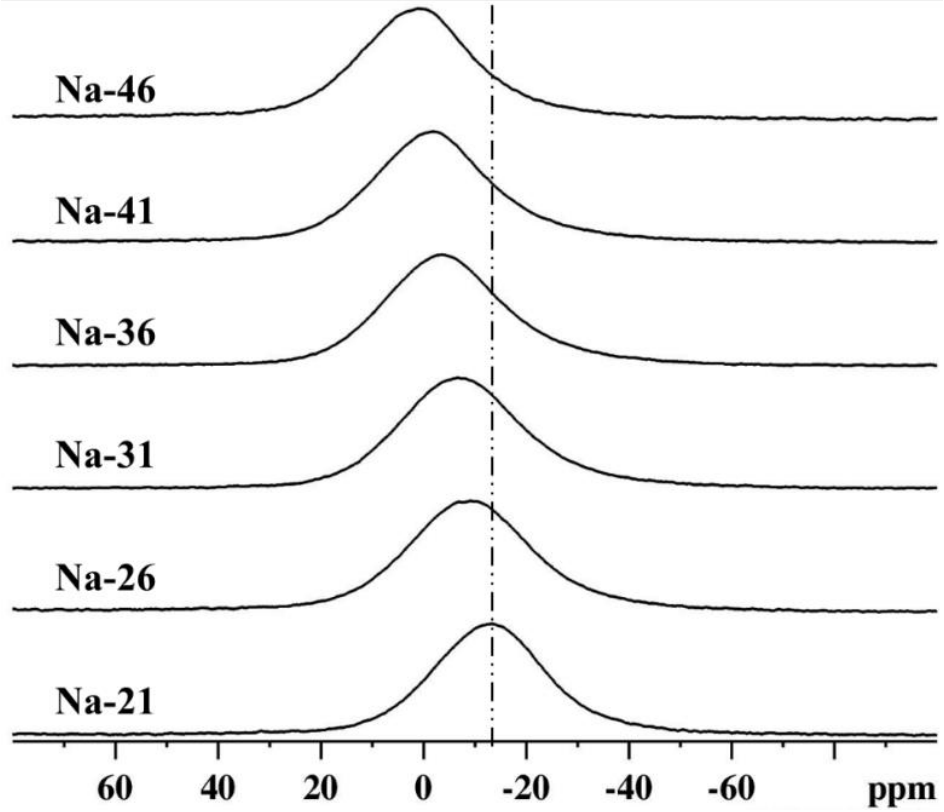

Figure 9.3. ^{23}Na MAS NMR spectra of glasses, with dotted line as a guide for the eye.

9.3.1.3 ^{27}Al MAS NMR

The ^{27}Al MAS NMR spectra of glasses (**Figure 9.4)** consist of two broad, symmetric peaks with maxima of *ca.* 57 and 14 ppm, assigned to tetrahedral ($^{[4]}$Al) and penta-coordinated ($^{[5]}$Al) Al, respectively [46,47]. The $^{[4]}$Al peak shifts to higher frequencies with the alkali content of glasses. The $^{[5]}$Al peak intensity also includes background signal from an alumina impurity in the ZrO_2 NMR rotors used to hold the samples. Although the intensity contribution from $^{[5]}$Al to the peak cannot be determined accurately due to the rotor background, the intensity of the peak appears to increase with the Na_2O content of the glass, hinting the possible presence of $^{[5]}$Al in high-Na glasses.

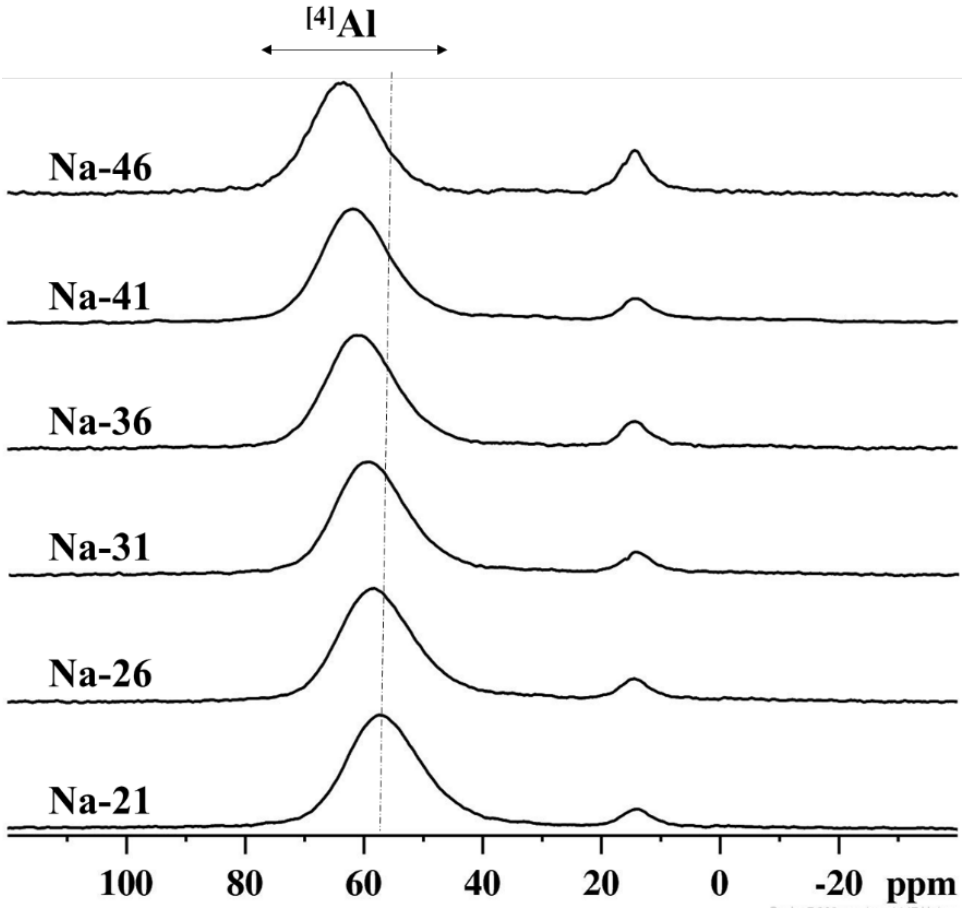

Figure 9.4. ^{27}Al MAS NMR spectra of glasses, with dotted line as a guide for the eye. The peak at *ca.* 14 ppm comes from the rotor background, and possibly an unquantifiable amount of $^{[5]}$Al in the samples.

9.3.1.4 ^{29}Si MAS NMR

Chemically distinct silicate units exhibit a large distribution in their isotropic shifts, often severely overlapping and making spectral analysis complicated and generally qualitative. Silicate species are designated using the Q^n nomenclature, where *n* represents the number of bridging oxygens (BO) in the Si tetrahedron. In ^{29}Si NMR, peaks shift toward higher frequencies as BO are converted to NBO. Accordingly, the reported chemical shift ranges of Si units are: Q^0 (-60 to -70 ppm); Q^1 (-70 to -80 ppm); Q^2 (-78 to -90 ppm); Q^3 (-83 to -100 ppm) and Q^4 (-90 to -115 ppm) [21,34,35,48–59]. Within these ranges, the chemical identity of next-nearest neighbours has a significant influence on the observed chemical shifts. For example, a tetrahedral Si unit

with four next-nearest Si neighbours has a chemical shift of -110 ppm [55,57], whereas a Si unit bonded to three Si units and one $[BO_4]^-$ or $[AlO_4]^-$ unit has a shift of *ca.* -100 ppm (Q^4) [35,48]. On the other hand, the bonding of Si units to $^{[3]}$B does not induce any detectable changes in the chemical shift [57] as $^{[3]}$B and Si have similar bond-overlap populations [52]. The observed susceptibility of the chemical shielding to changes in the nature of oxygens and network neighbours underscores the difficulty associated with the analysis of the ^{29}Si NMR spectra in multicomponent glasses. The ^{29}Si NMR spectra of glasses (**Figure 9.5**) consist of a broad peak, the attributes of which, such as peak shape and position, change significantly with increasing Na/Si ratio. The peak shifts to higher frequency and becomes asymmetric at higher Na/Si. These spectra originally contained a broad peak at ca. 115 ppm from the probe components, which was corrected by subtracting the signal of an empty spinning rotor from the original spectra to yield only the spectra of the glass samples (**Figure 9.6**).

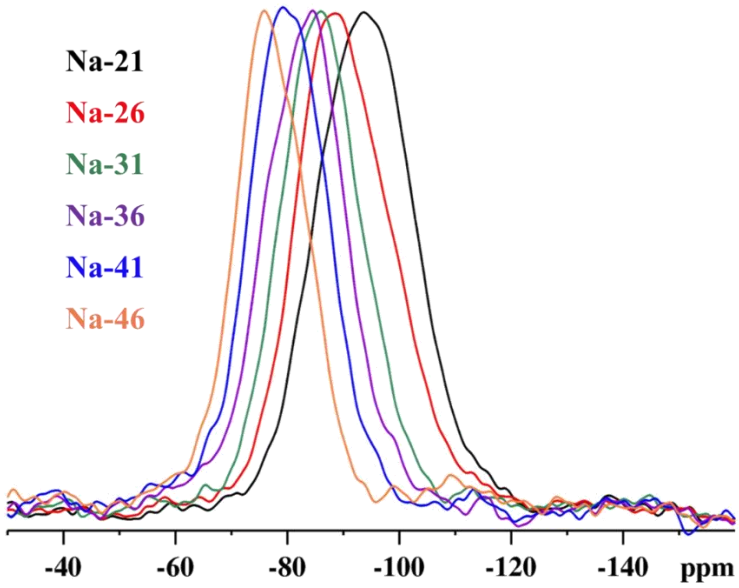

Figure 9.5. ^{29}Si MAS NMR spectra of the glass samples with the probe background signal subtracted.

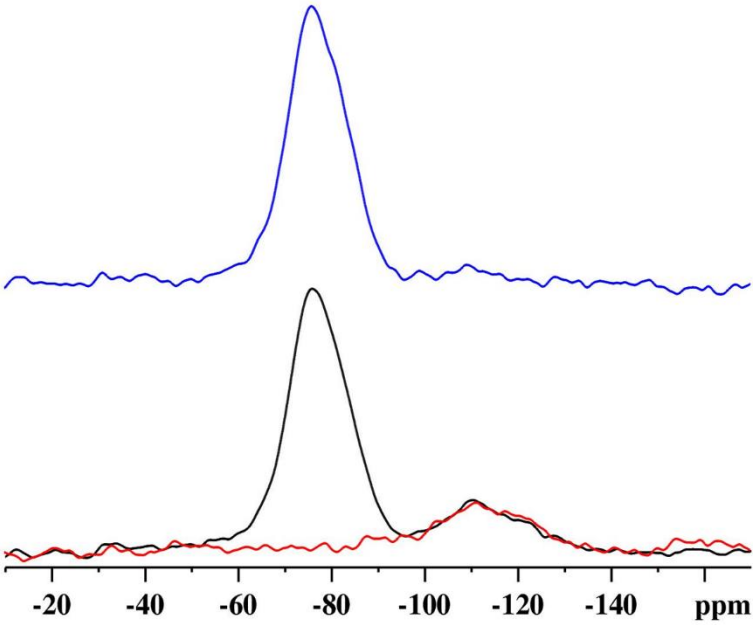

Figure 9.6. ^{29}Si MAS NMR spectrum of Na-46 (black) overlaid upon the background signal (red) from probe components. The subtracted spectrum is plotted in blue.

To understand changes in the silicate network and determine the Si species present in different compositions, the spectra were deconvolved using multiple subspectra, guided by the structural models proposed by Bray *et al.* [42–44], Dupree *et al.* [49,54]. and others [51,52]. Additional constraints on spectral fitting were generated by tallying the net charges in the system to estimate the fractions of anionic silicate species. In this calculation, the fractions of $^{[4]}$B and $^{[4]}$Al (in mol%) are calculated using the NMR results and are treated as negative charge contributors. Na_2O is the lone positive-charge contributor in this glass series. The N_{3A} fraction is obtained from the N_{3A} vs. R (molar ratio of Na_2O and B_2O_3) plot for different K values reported for sodium borosilicate glasses by Bray *et al.* [42–44] and is considered as a negative charge contributor. The R and K values are corrected for the presence of $^{[4]}$Al in the system (K' and R' respectively, $K' = [(SiO_2)/(B_2O_3+Al_2O_3)]$; $R' = [Na_2O/(B_2O_3+Al_2O_3)]$), as per the *modified Dell and Bray model* proposed by Du and Stebbins [60]. The charges are tabulated for each glass composition in **Table 9.3**, and the charge difference (Δ) is taken to represent the excess positive charge in the system, which corresponds to Na^+ charge-balancing anionic silicate units in the network.

Table 9.3. Determination of the total anionic Si unit fraction in the glass network by tallying the net charge in the system.

	$(N_4)^a$ (±0.01)	$(C_{[4]B})^b$ (-ve)	$(C_{[4]Al})^c$ (-ve)	$(N_{3A})^d$	$(C_{[3]B})^e$ (-ve)	$(C_{Na})^f$ (+ve)	$\Sigma(\text{-ve})^g$	$(\Delta)^h$
Na-21	0.65	21	8	0	0	42	29	13
Na-26	0.67	22	8	0.05	2	52	32	20
Na-31	0.61	20	8	0.16	5	62	33	29
Na-36	0.54	18	8	0.28	9	72	35	37
Na-41	0.41	13	8	0.45	15	82	36	46
Na-46	0.33	11	8	0.58	19	92	38	54

[a] $N_4 = {}^{[4]}B/({}^{[4]}B+{}^{[3]}B)$ (**Table 9.2**)
[b] $C_{[4]B} = N_4 \cdot B_2O_3 \cdot 2$ (in mol%)
[c] $C_{[4]Al} = Al_2O_3 \cdot 2$ (in mol%)
[d] N_{3A} - see text
[e] $C_{[3]B} = N_{3A} \cdot B_2O_3 \cdot 2$ (in mol%)
[f] $C_{Na} = (M \cdot Na_2O) \cdot 2$; M is the charge contributed by each Na^+ ion
[g] $\Sigma(\text{-ve}) = [C_{[4]B} + C_{[4]Al} + C_{[3]B}]$
[h] $\Delta = [C_{Na} - \Sigma(\text{-ve})]$
B_2O_3, Al_2O_3, and Na_2O are in mol%; $C_{[4]B}$, $C_{[3]B}$, $C_{Na,}$ and $C_{[4]Al}$ are doubled as these oxides introduce two cations per oxide molecule (X_2O_3 and Na_2O).

As a further refinement, the fractions of Q^4, $Q^{3,}$ and Q^2 silicate units are calculated from the Na fraction predicted to be associated with the anionic Si units (Δ, **Table 9.4**), and the molar ratios of Q^n units are used as a guide to deconvolve the ^{29}Si MAS NMR spectra. As Δ represents the fraction of anionic Si units present in the network, the difference between Δ and the total SiO_2 (both in mol%) gives the fraction of charge-neutral Q^4 units. This calculation is constrained by the assumption that the formation of Q^n species is sequential, and the network is populated with Q^n and Q^{n-1} units for any given composition, which agrees with the Si trends observed in silicate-based glasses [21,50]. While the conversion of a charge-neutral species to a singly-charged anionic species ($Q^4 \rightarrow Q^3$) is easy to track in this charge calculation model, and the calculated Q^3 and Q^4 fractions are reliable, the balance of Q^3 and Q^2 units is more difficult to determine as both are negatively charged. In related glasses matching the alkali content of Na-41

and Na-46 samples [21,49,54] , the Q^3/Q^2 intensity ratios have been reported as $2-4$ and ≤ 1, respectively. Hence, for charge calculation purposes, the Q^3/Q^2 ratios have been constrained to *ca.* 4 and 0.5 in Na-41 and Na-46 glasses, respectively. Finally, using these theoretical Q^n fraction predictions, the ^{29}Si spectra are deconvolved and the integrated intensities are listed in **Table 9.5** and the fits are plotted in **Figure 9.7**. While the theoretical Q^4/Q^3 ratios and the integrated intensities from the fits agree well for samples with Na_2O content from 21 to 36 mol%, the Q^3/Q^2 ratios in the Na-41 and Na-46 fits deviate significantly and represent the uncertainty associated with calculating the fractions of these two anionic units theoretically.

Table 9.4. Calculation of relative fractions of different types of anionic Si units from the total anionic Si fraction, Δ.

	(Δ)[a]	(SiO_2)[b]	(fQ^3)[c]	(fQ^4)[d]	(fQ^2)[e]	(%Q^2)[f]	(%Q^3)[g]	(%Q^4)[h]
		Mol%	Mol%	Mol%	Mol%			
Na-21	13	58.5	13	45.5	—	—	23	77
Na-26	20	53.5	21	32.5	—	—	39	61
Na-31	29	48.5	30	18.5	—	—	61	39
Na-36	37	43.5	38	5.5	—	—	87	13
Na-41	46	38.5	30.5	—	8	20	80	—
Na-46	54	33.5	11.5	—	22	66	34	—

[a] Δ - Na_2O (in mol%)/2; $\Delta = [fQ^3 + (fQ^2 \cdot 2)]$
[b] Si content in glass
[c] fraction of Q^3 (in mol%) = (Δ)
[d] fraction of Q^4 (in mol%) = ($SiO_2 - fQ^3$)
[e] fraction of Q^2 (in mol%): see text
[f] $(fQ^2/SiO_2) \cdot 100$
[g] $(fQ^3/SiO_2) \cdot 100$
[h] $(fQ^4/SiO_2) \cdot 100$

Table 9.5. Q^n speciation obtained from the deconvolution of the ^{29}Si MAS NMR spectra, with the calculated values in parentheses.

	$(Q^4)^a$	$(Q^3)^b$	$(Q^2)^c$
	Int. I. (%)	Int. I. (%)	Int. I. (%)
Na-21	76(77)	24(23)	—
Na-26	63(61)	37(39)	—
Na-31	38(39)	62(61)	—
Na-36	15(13)	85(87)	—
Na-41	—	73(80)	27(20)
Na-46	—	27(34)	72(66)

[a]peak maximum = -93(±3) ppm; peak width = 1.3(±0.3) kHz
[b]peak maximum = -85(±3) ppm; peak width = 1.1(±0.1) kHz
[c]peak maximum = -75(±3) ppm; peak width = 1.1(±0.1) kHz

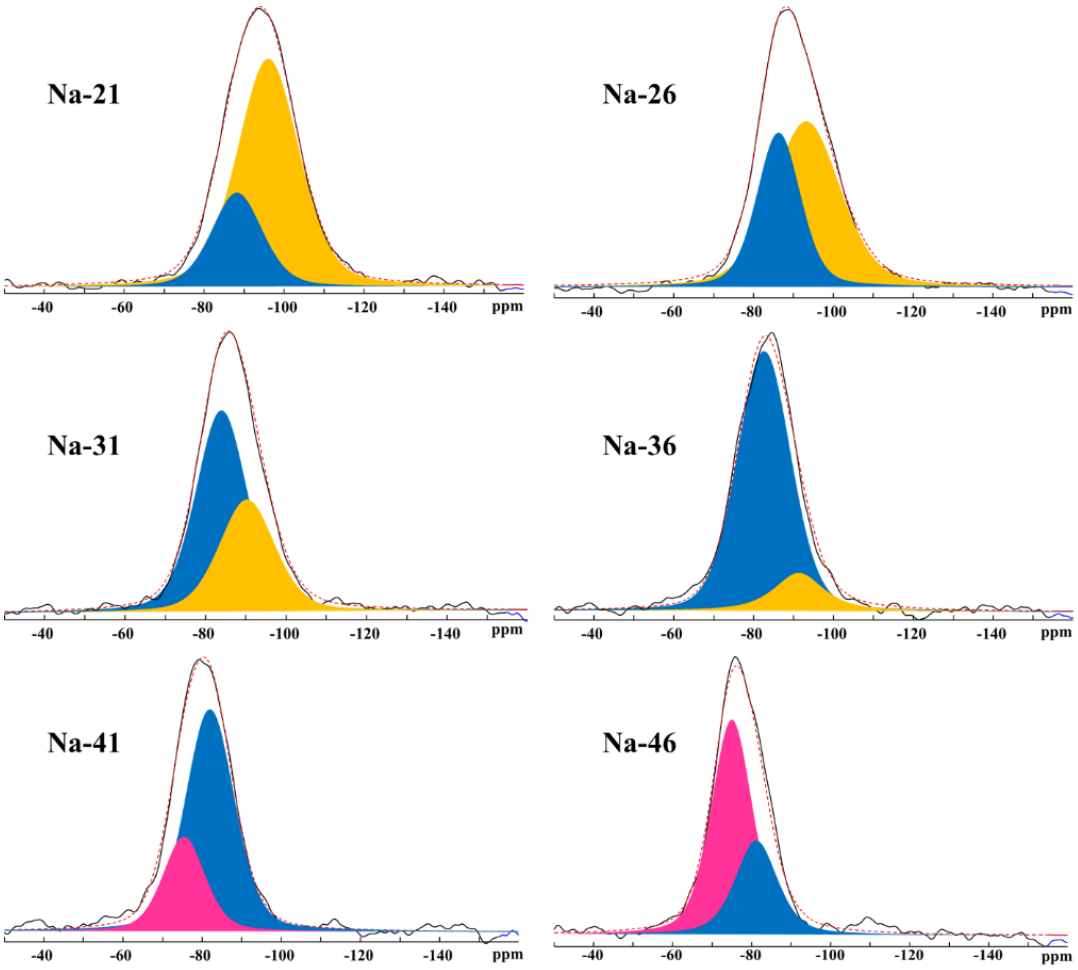

Figure 9.7. Deconvolution of the ^{29}Si MAS NMR spectra. Orange, blue and pink peaks represent Q^4, $Q^{3,}$ and Q^2 silicate units, respectively.

9.3.2 Characterization of altered glasses

9.3.2.1 X-ray diffraction

Whereas the x-ray diffractograms of the pristine glasses lack Bragg peaks, thereby confirming their amorphous nature (not shown), the altered glasses exhibit evidence of crystallinity. While the diffractograms of altered samples Na-21, Na-26, and Na-31 show only the amorphous "halo" (**Figure 9.8**), the diffractogram of sample Na-36 consists of peaks at 22° and 25° from crystalline SiO_2 in cristobalite [SiO_2, entry number 00-101-0954] and quartz [SiO_2, entry number 00-101-1097] forms. The diffractograms of Na-41 and Na-46 specimen show sharp peaks for which a matching pattern could not be retrieved from the library embedded in the QualX; hence, Xpert

HighScore Plus software (Malvern Panalytical, Malvern, UK) [61] was used to identify the phase as having the faujasite structure [entry number 00-012-0228] (**Figure 9.9**) with a chemical formula of $Na_2Al_2Si_{3.3}O_{10.6}{\cdot}7H_2O$, a hydrated aluminosilicate mineral belonging to the zeolite family. Some of the peaks in these two diffractograms could not be assigned due to their low intensity, which might represent one or more additional silicate or aluminosilicate crystalline phases.

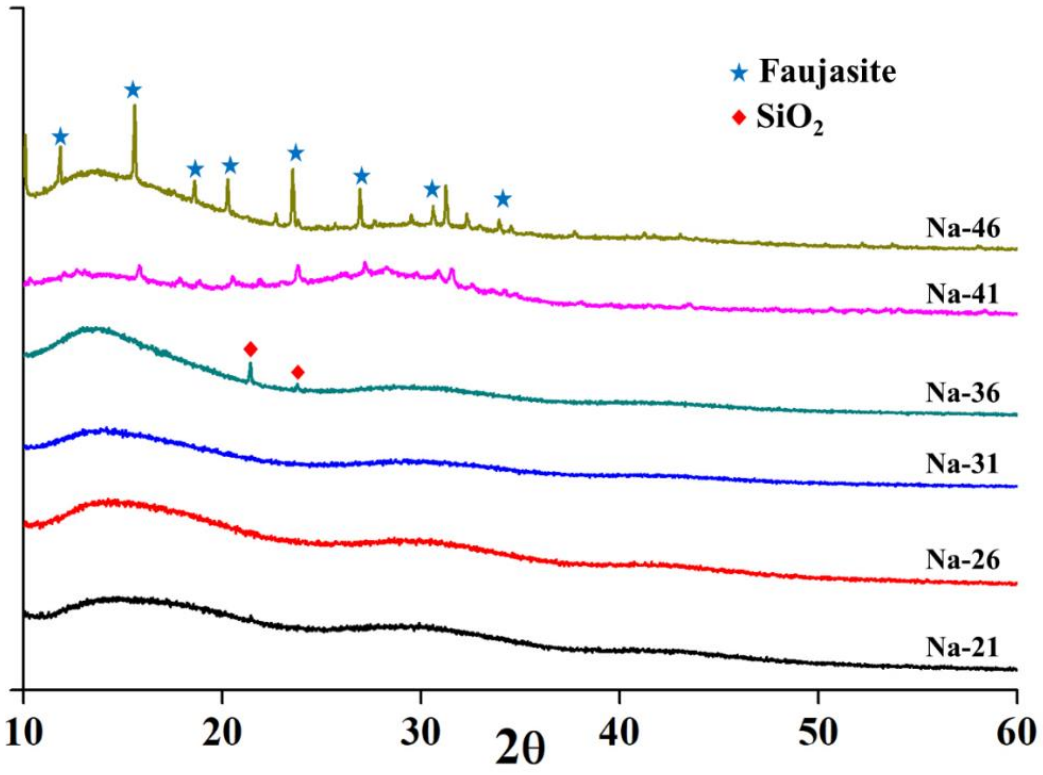

Figure 9.8. X-ray diffractograms of samples post-dissolution.

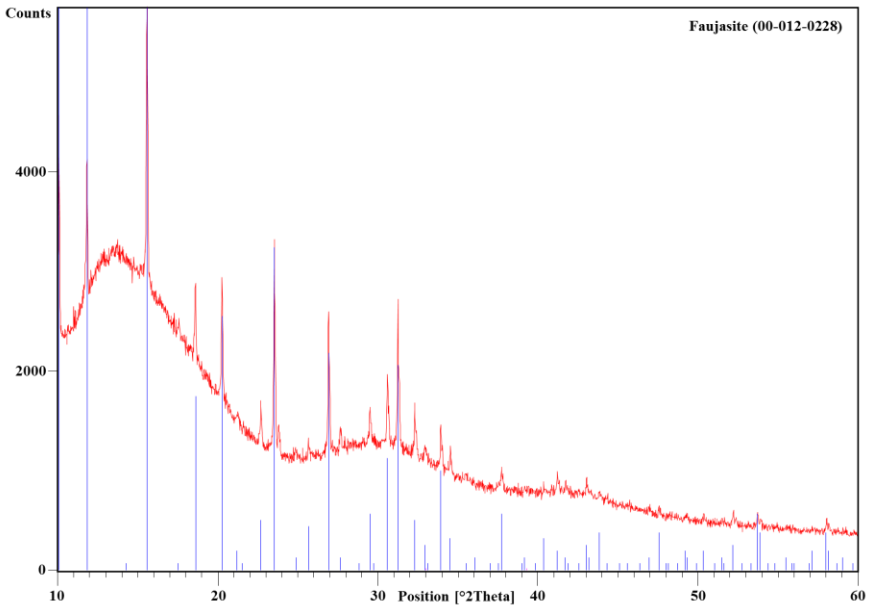

Figure 9.9. Assignment of the Bragg peaks observed in the diffractogram of the altered Na-46 sample to a crystalline phase with faujasite structure.

9.3.2.2 Solid-state NMR spectroscopy

^{11}B MAS NMR spectra of pristine and altered glasses are compared in **Figure 9.10,** and the N_4 values obtained from deconvolving these spectra are listed in **Table 9.6**. The absolute $^{[3]}$B and $^{[4]}$B peak intensities decrease progressively with Na loading, indicating extensive dissolution of the borate portion of the glass network. At low Na fractions, the intensities of $^{[4]}$B and $^{[3]}$B peaks decrease proportionately and no change in N_4 is detected. However, at higher Na loadings, the fraction of $^{[4]}$B in the solid collected after dissolution is augmented with respect to that of the pristine glass, the changes becoming more prominent with higher Na fractions. Since the NMR experiments were acquired on the total sample retrieved from the dissolution vessels, they represent signals from both the altered surface as well as the (presumably) unaltered glass from the interior of the glass coupon; hence, changes in speciation due to alteration will be difficult to quantify for less-altered materials. In Na-41, the $^{[4]}$B peak shifts slightly to lower frequency, and in Na-46, a significant reduction in the intensity of the $^{[4]}B_{3Si}$ peak and a narrowing of the $^{[4]}B_{2Si}$ peak are observed.

Table 9.6. N_4 values of pristine and altered glasses obtained from the deconvolution of the ^{11}B MAS NMR spectra.

	PG[a] (±0.01)	**AG[b] (±0.01)**
Na-21	0.65	0.65
Na-26	0.67	0.67
Na-31	0.61	0.61
Na-36	0.54	0.56
Na-41	0.41	0.71
Na-46	0.33	0.55

[a] Pristine glasses
[b] Altered glasses

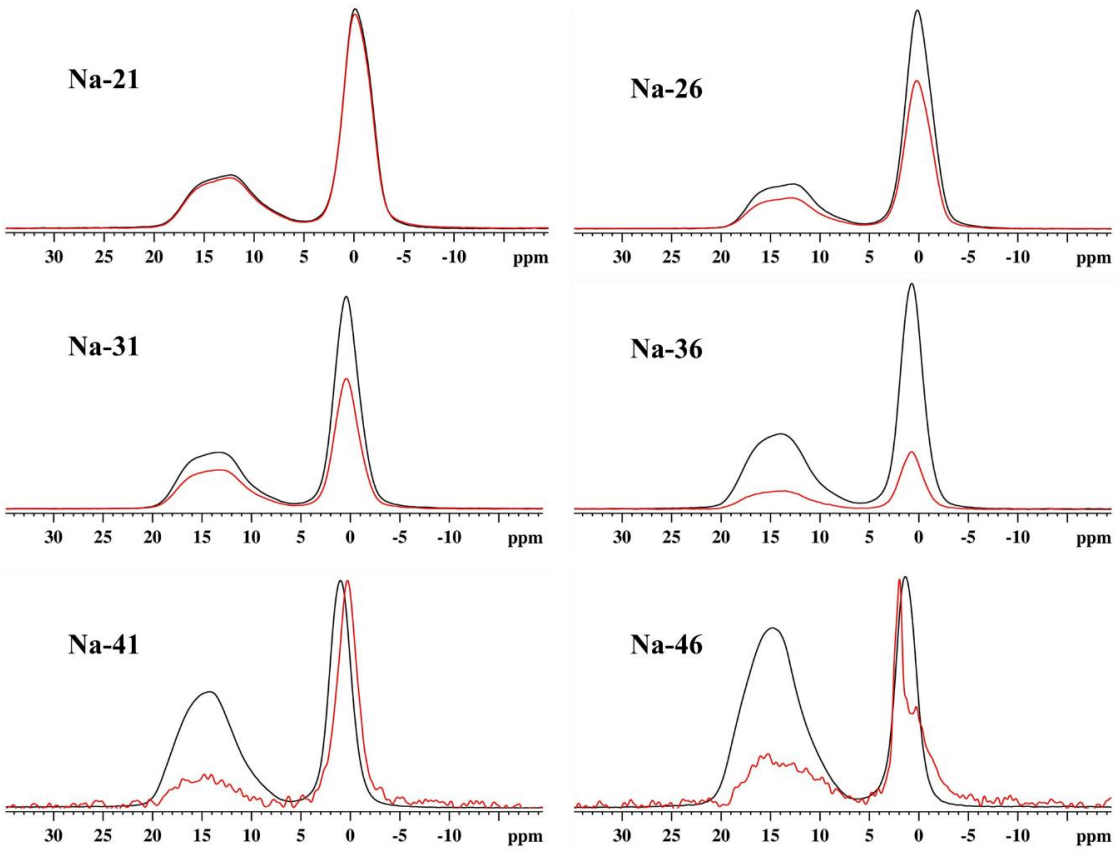

Figure 9.10. Comparison of the ^{11}B MAS NMR spectra of pristine (black) and altered (red) glasses. The spectra of Na-21, Na-26, Na-31, and Na-36 samples are plotted in absolute-intensity mode, whereas the peak intensities are normalized to the $^{[4]}$B peak in Na-41 and Na-46 for ease of viewing.

While the ^{23}Na NMR spectrum of altered Na-21 is identical to the pristine sample, the spectra of Na-26 and Na-31 change marginally, wherein a broad, low-intensity peak may be detected on the shoulder of the broad glassy peak at *ca.* 6 ppm (**Figure 9.11**). This peak may be fit with a C_Q of 2.9 MHz and η of 0.7, (**Figure 9.12**) which might represent the Na^+ ions in a poorly crystalline chemical environment, as no Bragg peaks are observed in the diffractogram of this sample. As the Na_2O fraction in the glass increases, the overall peak width decreases, which may be interpreted as a progressive conversion of sodium from amorphous to crystalline environments. (**Table 9.7, Figure 9.12**). Based on x-ray diffraction (**Figure 9.8**), the second-order quadrupolar lineshape appearing in Na-41 and Na-46 can be assigned to the zeolite

faujasite. Generally, zeolites have a wide range of ^{23}Na C_Q, η, and δ_{iso} values [62,63] which depend on the stoichiometric ratios of Na to other cations and their occupancies within the crystal structure; hence it is not straightforward to precisely identify the chemical composition of the phase from NMR alone, as the peak could easily represent multiple Na sites with small distributions in their isotropic shifts and quadrupolar interaction parameters, arising from one or more crystalline phases. However, the NMR parameters are consistent with those of faujasite [64]. As in the ^{23}Na NMR spectra, no changes are observed in the ^{27}Al NMR spectra of pristine and altered Na-21 (**Figure 9.13**). However, as the Na fraction increases, the $^{[4]}$Al peak width decreases, and a shift toward lower frequency is observed.

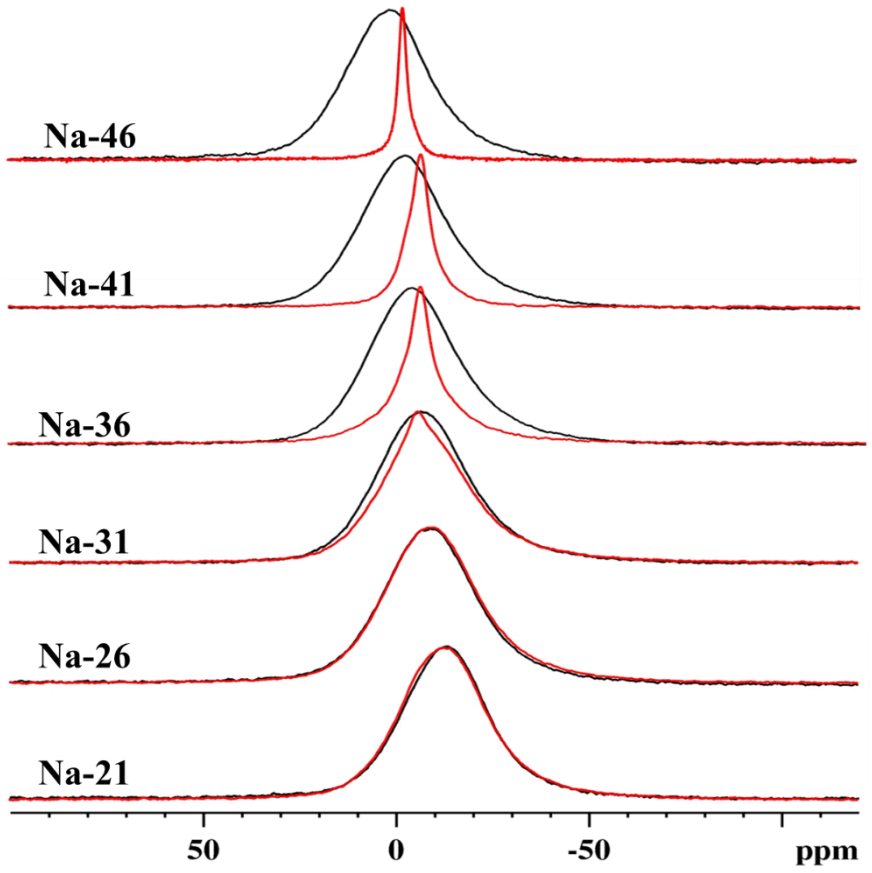

Figure 9.11. ^{23}Na MAS NMR spectra of pristine (black) and altered (red) samples plotted with intensities normalized to the highest peak.

Table 9.7. Fitting parameters obtained from the deconvolution of the ^{23}Na MAS NMR spectra of altered samples.

	Glass			Aluminosilicate phase			
	Peak max.[a] (±0.5)	**FWHM**[b] (±0.2)	**Int. I.**[c]	δ_{iso}[d] (±0.5)	C_Q[e] (±0.3)	η[f] (±0.1)	**Int. I.**[c] (±1)
Na-21	-12.6	4.0	100	—	—	—	—
Na-26	-9.8	4.2	96(3)	4.89	2.9	0.7	3(3)
Na-31	-8.7	4.3	88(5)	4.27	2.7	0.7	12(5)
Na-36	-6.2	4.0	64(5)	-1.4	2.0	0.7	35(5)
Na-41	-7.1	2.6	47(5)	-1.4	1.8	0.7	52(5)
Na-46	-3.6	1.3	30(5)	-1.1	1.1	0.6	70(5)

[a] Peak maximum (ppm)
[b] Full-width at half maximum (kHz)
[c] Integrated intensity (%)
[d] Isotropic shift (ppm)
[e] Quadrupolar coupling constant (MHz)
[f] Quadrupolar asymmetry parameter

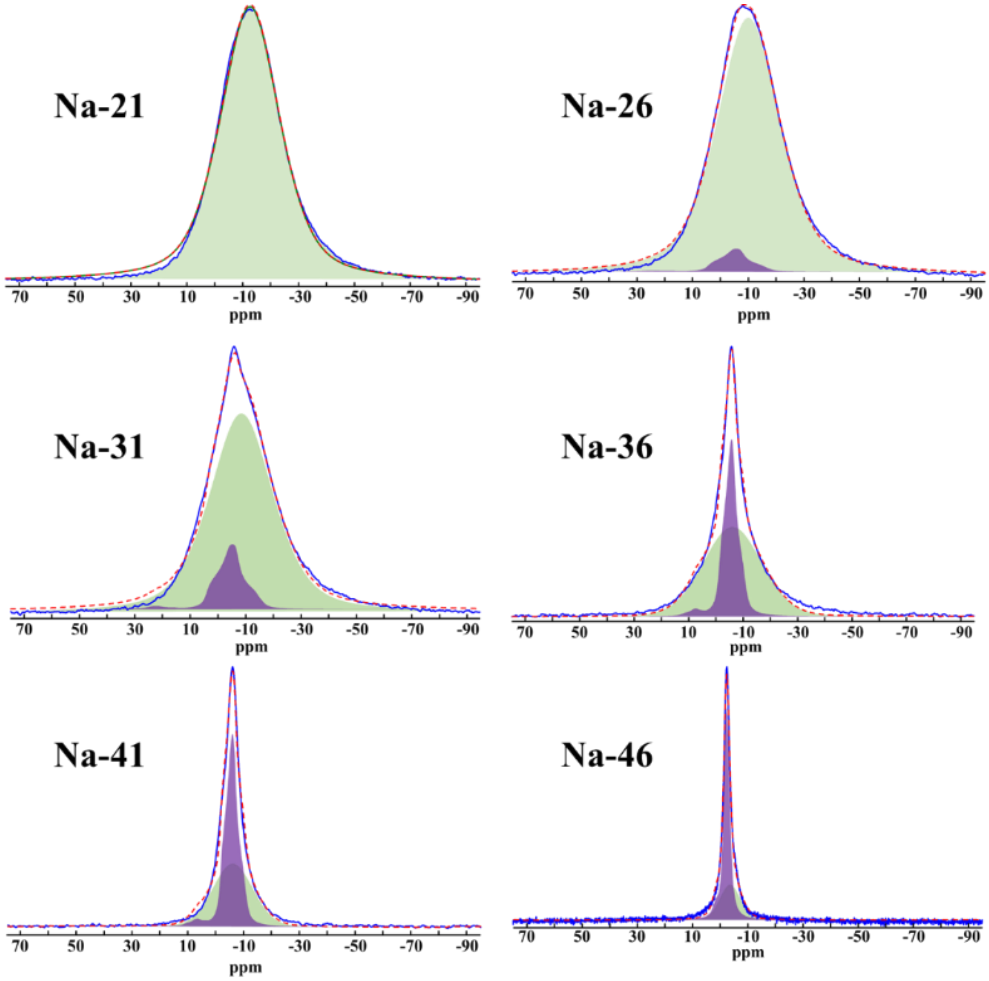

Figure 9.12. Deconvolution of the ^{23}Na MAS NMR spectra of altered samples. Green and purple peaks represent the glassy and crystalline phases, respectively.

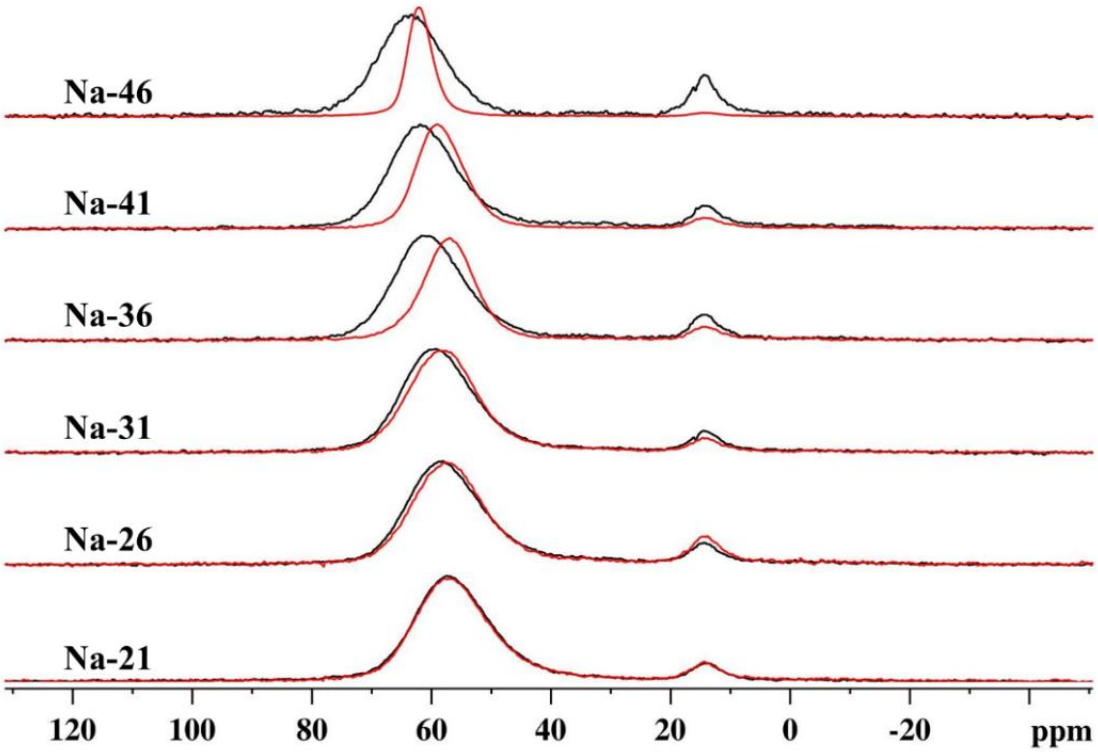

Figure 9.13. ^{27}Al MAS NMR spectra of pristine (black) and altered (red) samples plotted with intensities normalized to the $^{[4]}$Al peak. The apparent reduction in the $^{[5]}$Al peak intensity is due to the normalization of $^{[4]}$Al peak intensities.

^{29}Si MAS NMR spectra of pristine glasses and those chemically altered through aqueous degradation are compared in **Figure 9.14**. Except for Na-21, significant changes are observed in the spectral features, highlighting the drastic modification of the silicate network due to dissolution. Keeping in mind that these post-dissolution spectra represent the juxtaposition of silicon speciation in both the altered and unaltered portions of the glasses, the observed changes highlight the extensive degree to which silicon is involved in the alteration behaviour. The ^{29}Si NMR spectrum of Na-21 is little changed, either because it is not appreciably altered under these conditions or because the silicon speciation is generally retained in the alteration layer. However, Na-26 and Na-31 both show what appears to be an unaltered silicate glass core and a significant fraction of altered silicate in the Q^4 region. This is supported by the ^{29}Si{^{1}H} cross-polarization (CP) MAS spectra of these glasses, in which the silicon nuclei in the Q^4 chemical shift region are

polarized by nearby protons, whereas no peaks appear in the Q^3 region. This leads to the conclusion that alteration by hydration results in the formation of Q^4 with structural hydrogen, possibly as silanol groups, or interstitial water, while there remains a significant portion of the pristine glass untouched by hydration. The presence of a small $^{29}Si\{^1H\}$ CP-MAS signal in the Q^4 region of Na-21 reinforces this interpretation, indicating that alteration by hydration occurs to a lesser degree in this more-durable glass.

In the altered Na-36, Na-41 and Na-46 samples, the peaks shift completely into the Q^4 region, resolving in the latter case into a characteristic zeolite pattern. The progressive increase in resolution indicates an increase in the crystallinity of the zeolite. In Na-46, the chemical shifts of ca. -84, -89, -94 and, -99 ppm are assigned to Si units with four (Q^4_{4Al}), three (Q^4_{3Al}), two (Q^4_{2Al}), and one (Q^4_{1Al}) tetrahedral Al neighbours, respectively [65,66], as expected for faujasite-type zeolites [65]. Assuming that Si are bonded only to Al without any silanol groups, and that aluminum avoidance is obeyed [67], the Si/Al ratio in the recrystallized zeolite phase can be calculated using **equation 9.1** [68].

$$\mathrm{Si/Al} = \frac{\sum_1^4 I_{Si(nAl)}}{\sum_1^4 (n/4) I_{Si(nAl)}} \qquad (9.1)$$

where, n and $I_{Si(nAl)}$ refer to the number of tetrahedral Al neighbours and the intensity of Q^4_{nAl} peak, respectively. The calculated Si/Al ratio and the ratio in the phase identified by XRD ($Na_2Al_2Si_{3.3}O_{10.6}{\cdot}7H_2O$) are 1.76 and 1.65, respectively, which are in close agreement. The high degree of correspondence between the ^{29}Si CP and DP spectra confirms that the zeolites are hydrated, as expected for a process that is essentially hydrothermal synthesis.

$^{29}Si\{^1H\}$ CP-MAS NMR spectra of altered samples are compared to the direct-polarization (DP) spectra of pristine and altered samples in **Figure 9.14**. This experiment involves the transfer of ^1H polarization to ^{29}Si through the direct dipolar interaction, which is possible in a silanol group (Si−OH) originating in the alteration layer and the hydrated surface of the glass, and siloxane groups (Si−O−Si) which are dipolar-coupled to protons on interstitial water molecules [56,69–73]. The signal intensity is related to the proximity of these two nuclei, which provides information on the extent of glass hydration and the alteration of the surface [13,70,71], albeit qualitatively. Because the signal intensity depends on the dipolar coupling

between ^{1}H and ^{29}Si nuclei, a single mixing time generally does not produce quantitative peak intensities [56,69], hence, Q^3 and Q^2 units may not be easily distinguished by this method.

In Na-21, the CP peak overlaps on the lower-frequency side of the DP spectrum, accounting for the intensity difference between the DP spectra of pristine and altered samples. In Na-26 and Na-31, the CP peak overlaps only with the lower-frequency portion of the DP signal, substantiating the presence of at least two distinct Si species, one in close proximity to protons. In altered Na-36 and Na-41 samples, the CP spectra and post-dissolution DP spectra are identical, implying the complete transformation of the glass into a Si-rich amorphous phase consisting of Si−OH groups. The CP and the DP spectra of altered Na-46 overlap, which confirms the presence of a hydrated aluminosilicate zeolite phase. The position of the CP peak changes with Na/Si ratio wherein the peak from high-Na glasses is observed at higher frequencies (*ca.* -90 ppm) compared to low-Na samples (*ca.* -100 ppm). These chemical shifts correspond to Si units with two and one silanol groups, respectively [56,72,73], which are typically Q^2 and Q^3 species.

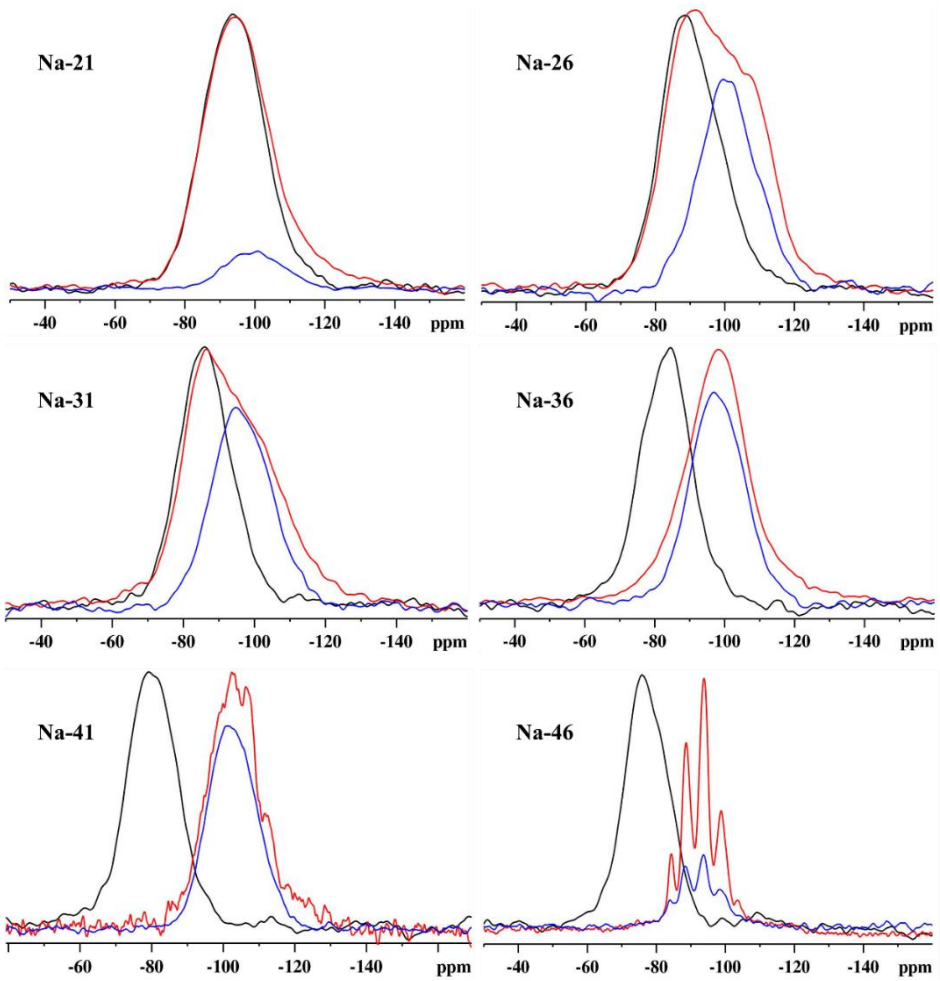

Figure 9.14. ^{29}Si MAS NMR spectra of pristine (black) and altered (red) samples. The ^{29}Si{^{1}H} CP-MAS NMR spectra of corresponding glasses post-dissolution are plotted in blue.

9.3.3 Dissolution behaviour

MCC-1 type [30] dissolution studies were carried out in polytetrafluoroethylene vessels housed in hermetically sealed stainless-steel vessels for 28 days with periodic leachate collection. Photographs of the glass monoliths after 28 days of dissolution are shown in **Figure 9.15**. **Table 9.8** lists the pH of the leachates after day 28 and the mass loss observed for each glass sample. The mass loss increases with the Na/Si ratio, underscoring the strong dependence of the chemical durability of glasses and the composition of the leachate on the glass composition. While the appearance of the Na-21 sample did not change during dissolution, the opacity of other glasses gradually increased, and the monoliths of the highest Na/Si ratios turned white. In fact, Na-41

and Na-46 were deliquescent after preparation and absorbed moisture already when briefly exposed to air during cutting and transferring them into the dissolution vessels. After dissolution, Na-36 and Na-41 exhibited poor mechanical properties in addition to a greater mass loss, whereas Na-46 lost the most mass and its structural integrity.

Table 9.8. pH of the leachate and measured mass losses of glass monoliths on day 28 of dissolution study.

Samples	pH (±0.1)	Mass loss (%)
Na-21	9.5	3
Na-26	10.5	15
Na-31	11.1	19
Na-36	11.9	53
Na-41	12.3	61
Na-46	12.6	69

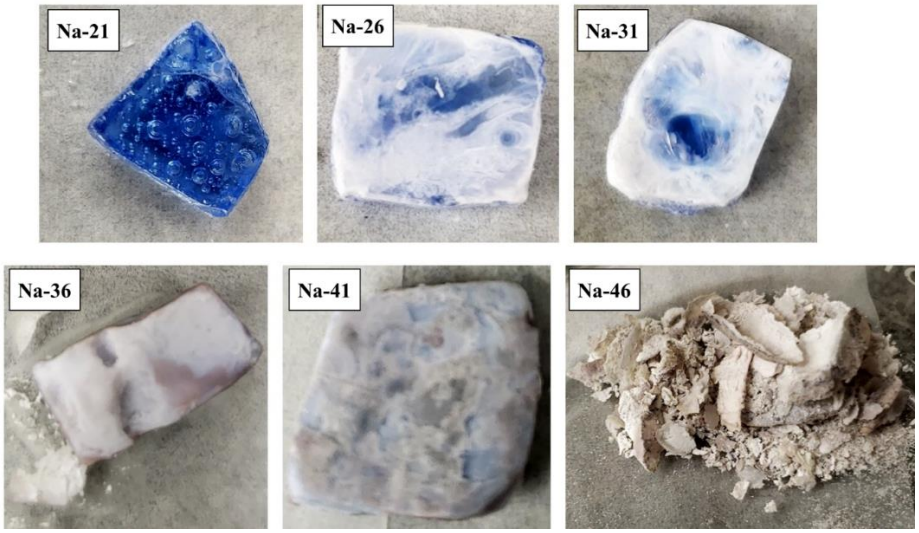

Figure 9.15. Pictures of the specimens retrieved after immersion in water for 28 days at 90° C in Parr® digestion vessels. Indentations on Na-36 are from an attempt to hold the monolith using tweezers, which emphasizes the mechanical fragility of the glass piece.

9.3.3.1 Normalized release of elements

The leachate aliquots collected at regular time intervals were subjected to ICP-OES analysis to quantify the elements released over the duration of the dissolution study (**Figure 9.16)**. The concentrations of elements are normalized to their mass fraction in the glass using **Equation 8.1** [5]. The B, Na, and Si leaching profiles are similar and correlate positively with the Na fractions in the pristine glasses: lower Na loading produces more durable glasses. Interestingly, their release profiles divide the series into two groups, those with lower Na fractions (Na-21−Na-31) and those with higher Na fraction (Na-36−Na-46) glasses. While the effect of Na/Si ratio on the B, Na, and Si release from the lower-Na group is persistent over the timescale of dissolution, the higher-Na group shows a dependence on the Na/Si ratio only during the first week of dissolution, beyond which the concentrations of these elements reach a steady state. Furthermore, Na uptake from the solution is observed in samples Na-41 and Na-46 by the end of the dissolution study, as evidenced by the slight downturn in the curves. The uptake of Na and Al in these samples can be attributed to the formation of the aluminosilicate zeolite as a secondary alteration product. In the Si release plots of the higher-Na glasses, the Si concentration in the leachate follows the Si mole fraction of glasses but exhibits different steady-state concentrations. As the mole fraction of Al in these glasses is very low (4 mol%) and the difference in Al release between the samples is small (*ca.* 10 gm^{-2}), no strong conclusions can be made regarding the Al release trends in relation to the Na/Si ratios. However, higher Al release is observed for Na-41 and Na-46, and a sharp decline in the Al release is observed as the dissolution progresses, suggesting the resorption of Al as the zeolite crystallizes.

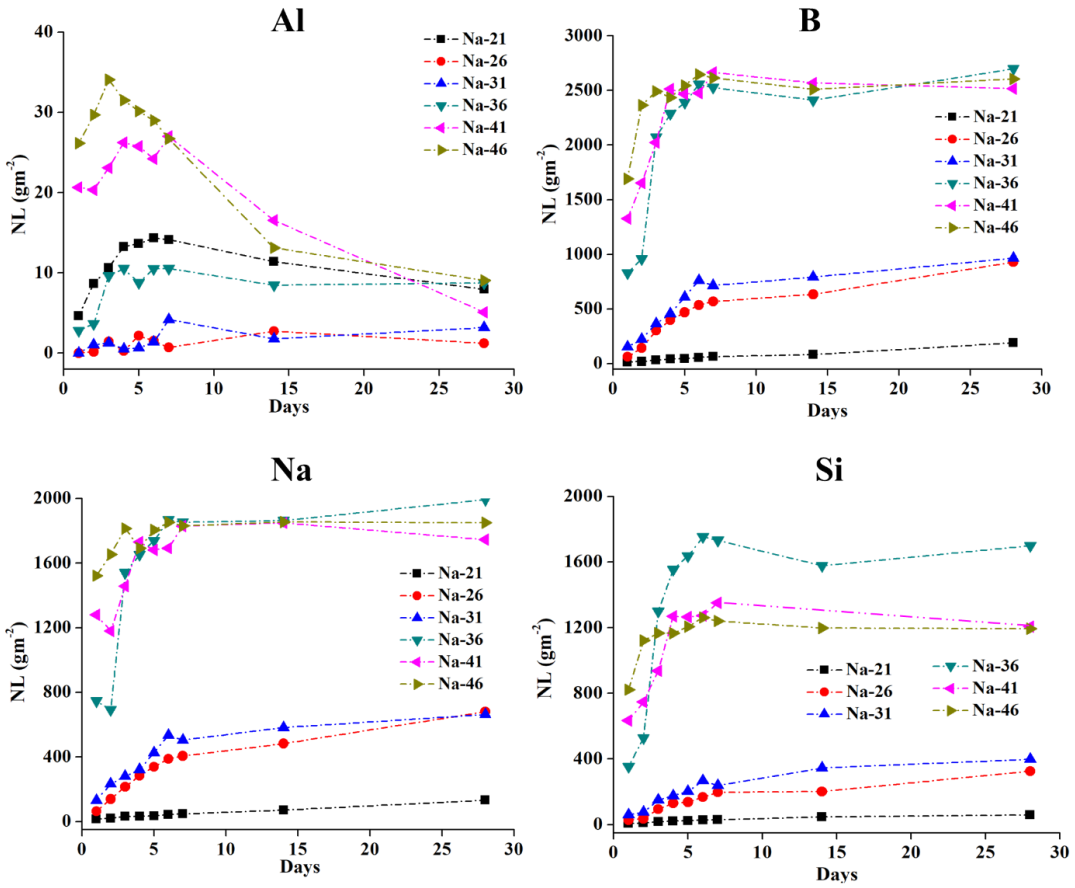

Figure 9.16. Release of elements from glasses over 28 days of dissolution normalized to their mass fractions, as measured by ICP-OES (The Si concentration of Na-41 on day 14 is not plotted as it was corrupted by an instrumental error).

The same data are presented in **Figure 9.17** for each glass separately to facilitate the comparison of element release within each sample. This representation reveals more clearly the effect of Na/Si ratio on the initiation of different dissolution stages. All of the glasses undergo incongruent dissolution, with B preferentially dissolved over Na and Si. Elemental release continues even after 28 days of dissolution in samples Na-21 and Na-26, placing these glasses in the forward-rate regime and suggesting these glasses are in stage 1 of glass dissolution. The concentrations of leached elements in Na-31 appears to be approaching a quasi-steady state (i.e., nearing saturation), indicating the progression of dissolution from stage 1 to stage 2. In the samples with higher Na content, a sharp increase in the elemental release is observed during the

first week, and the concentrations of elements plateau for the duration of the study. In these glasses, the rise in elemental concentration during the first week can be classified as the forward-rate regime and the observed plateau, which represents the steady-state concentration of elements (i.e., saturation), marks the onset of the second stage.

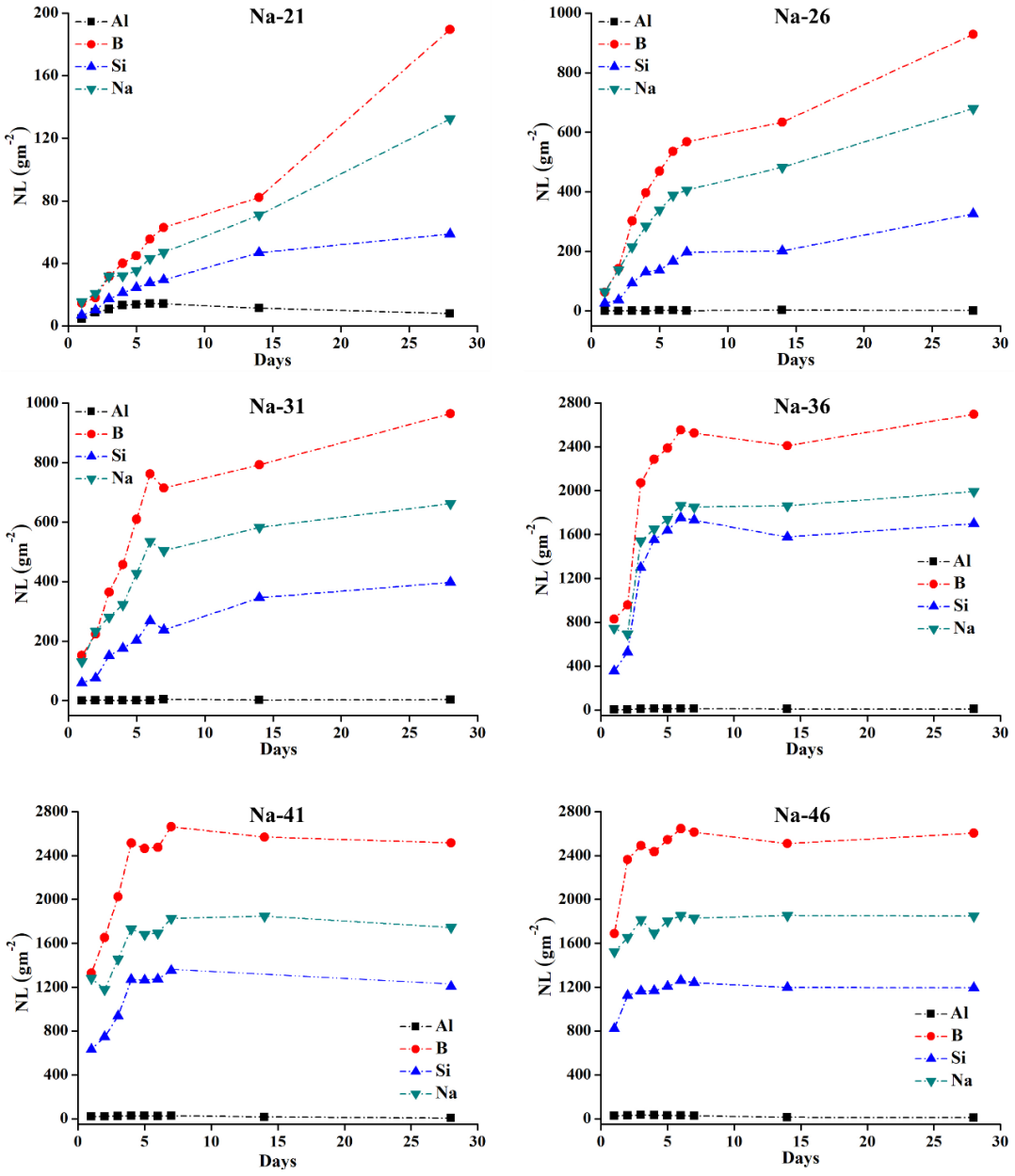

Figure 9.17. Normalized release of elements from glasses Na-21−Na-46 over 28 days of dissolution, as measured by ICP-OES.

9.4 Discussion

9.4.1 Network structure of pristine glasses

The boron and silicon speciation in the sodium aluminoborosilicate glasses studied here follow the structural models proposed for sodium borosilicate systems [42–44], which show a strong dependence on the alkali oxide content of glasses. With an increase in the Na fraction of glasses, N_4 declines sharply and the local chemical environment of the remaining $^{[4]}$B changes from Si to $^{[3]}$B, with a concomitant change in its speciation in the order: $^{[4]}B_{4Si} \rightarrow {}^{[4]}B_{3Si} \rightarrow {}^{[4]}B_{2Si}$. A recent investigation has pointed out that energetically unfavourable $^{[4]}$B−O−$^{[4]}$B linkages can be found in borosilicate glasses [74], which are generally not expected as per Lowenstein's aluminum avoidance principle [67]. Due to high fractions of $^{[3]}$B units present in these glasses, such linkages are expected not to be present. Charge calculations and N_{3A} vs. R plots from borosilicate structural models indicate that many $^{[3]}$B possess NBO, the fraction of which increases linearly with the alkali fraction of glasses. However, the calculated N_{3A} fraction is much lower than that of anionic Si units, Q^3 and Q^2 (**Tables 9.3 and 9.4**), consistent with the observation that NBO first appear on Si and eventually on $^{[3]}$B in borosilicate glasses [44]. The alkali oxide fraction has a profound effect on the silicate speciation as well, wherein increasing the fraction of the alkali oxide depolymerizes the silicate network in the order: $Q^4 \rightarrow Q^3 \rightarrow Q^2$, consistent with the binary distribution model observed in silicate glasses [21,49,54]. Due to the formation of anionic Q^3 and Q^2 species at higher alkali oxide contents, the number of NBO per Si tetrahedron increases, leading to a drastic reduction in the network connectivity.

In an aluminoborosilicate network, Al units are bonded to both Si and $^{[3]}$B, but preferentially to the latter [24]. As the $^{[3]}$B fraction increases with the Si→Na substitution, the $^{[4]}$Al units may be expected to have high numbers of next-nearest $^{[3]}$B neighbours, but this change should not affect the shielding at the nucleus as both Q^4 and $^{[3]}$B are comparable in their bond overlap populations [52]. Hence the high-frequency shift observed for the $^{[4]}$Al signal could be due to the formation of NBO bonded to $^{[3]}$B and Si. These NBO demand a higher bond strength contribution from the central cation (B^{3+} and Si^{4+}), decreasing the contribution of the cation to its other BO in the process. The bond strength deficits at the BO are suitably compensated by Al^{3+}, therefore the mean Al−O bond length decreases, which manifests in the spectrum as a high-frequency shift of the peak. The observed changes in the ^{23}Na MAS NMR peak positions provide indirect evidence of the presence of NBO in the network. An increase in the NBO fraction tends

to shorten the mean Na−O bond lengths and hence, the average coordination number of Na due to their higher charge densities, which are observed as high-frequency shifts in the ^{23}Na MAS NMR spectra [75].

9.4.2 Dissolution-mediated structural modifications

The multinuclear MAS NMR results of the glass samples after dissolution establish a clear relationship between the glass durability and its alkali content, emphasizing the need for considering alkali loading limits when designing glass compositions for HLW vitrification. The Si speciation transforms significantly in all glasses as a consequence of alteration except for Na-21, where the low-intensity CP signal and marginal changes in the DP spectra after dissolution suggest that only a small fraction of the silicon is near a source of protons. These results suggest that there has been very little penetration by water into the glass network (hydration), or the formation of an alteration layer. In contrast, the peakwidths in the DP spectra of altered Na-26 and Na-31 increase due to the appearance of a second overlapping peak, which match with the corresponding CP spectra of these samples. Hence, the new peaks in these spectra are attributed to Q^3 units with silanol groups, the characteristic isotropic shift of which is *ca.* -100 ppm [56,72,73]. Because long contact times must be used to achieve polarization transfer from water molecules to siloxane linkages [56], the presence of water molecules, and therefore the hydrated region, could not be confirmed. Hence, the additional intensity in the DP spectra represents the residual glass that is still pristine. In broad strokes, the MAS NMR spectra of these two samples identify two different regions in the glass, one that has not undergone any alteration and the other which is in the process of reorganization with a significant number of Si−OH groups.

In the altered Na-36 and Na-41 samples, the CP and DP spectra are identical, suggesting complete degradation of the glass network and its reorganization into a pre-zeolitic silica-gel phase comprising Si−OH groups. In the DP spectrum of altered Na-41, a broad peak overlaps with a characteristic zeolite pattern, the intensity of which increases in Na-46. The sharp resonances observed in the MAS spectrum of Na-46 persist in the CP spectrum as well, suggesting the hydrated nature of the Si sites and the presence of Si−OH groups, justifying the slight difference observed in the calculated Si/Al ratio of the zeolite and the ratio obtained from XRD phase identification (1.65 and 1.76, respectively). The interpretation of ^{29}Si MAS NMR

results is represented schematically in **Figure 9.18**, showing glass monoliths in different stages of restructuring.

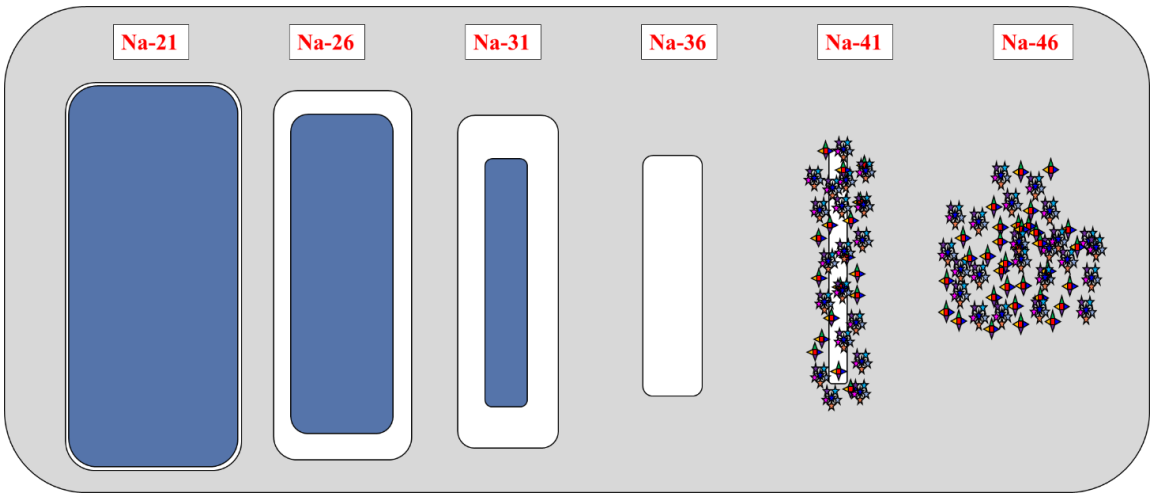

Figure 9.18. Pictorial representation of the dissolution-induced morphological changes in glass monoliths. The blue and white rectangles represent pristine and altered/reorganized regions of glass monoliths. The crystallinity in Na-41 and Na-46 samples is represented using custom graphics. The size of the monolith is shown to decrease with increasing Na content, simulating the mass loss observed for these compositions.

Although B release increases significantly with the Na/Si ratio, no preferential leaching of $^{[3]}$B or $^{[4]}$B units is observed up to a Na fraction of 31 mol%, beyond which the fraction of $^{[3]}$B decreases, increasing the N_4 ratio compared to pristine glasses. This marks either a preferential release of $^{[3]}$B into solution or its transformation into $^{[4]}$B due to glass alteration. Since the Si−O$^-$ is the second-most basic site in the network after $^{[4]}$B−O−$^{[4]}$B [76], the higher fractions of Q^3 and Q^2 lead to extensive H↔Na ion exchange and protonation of these sites [76,77]. Interstitial molecular H_2O coordinates to BO through thermally labile hydrogen bonds. Further, these H_2O molecules bond noncovalently to $^{[3]}$B through lone-pair electrons on the oxygen (O_3B−:OH_2). The adsorbed H_2O dissociates in the presence of another water molecule, leading to B−OH and silanol group formation [77]. Therefore, the presence of $^{[3]}$B units, and more importantly the

$^{[3]}B_A$ units, enhances the dissolution rates of the glasses, leading to the preferential release of $^{[3]}B$ from the glass in high-Na glasses.

The increase in N_4 in the altered samples may also be attributed to the possible incorporation of B into the alteration layers [1,40,78] or in the glass that has undergone restructuring. Since the borate speciation in the alteration layer has not been studied, this is only speculation. The shift of the $^{[4]}B$ peak towards lower frequency in Na-41 suggests an increase in the Si neighbours, which would be consistent with the incorporation of B in the newly-formed Si-rich phase. If B were incorporated, it might be present as tetrahedral units charge-balanced by Na^+ ions, low levels of which are known to be entrapped in the alteration layers [79]. The pronounced narrowing of the $^{[4]}B_{2Si}$ peak in altered Na-46 suggests increased structural ordering, hinting that $^{[4]}B$ might substitute for $^{[4]}Al$ in the nascent zeolite.

While no changes are observed in the ^{23}Na NMR spectrum of the altered Na-21 glass specimen, a broad shoulder begins to appear in Na-26 at *ca.* 6 ppm, which increases in intensity and shifts to lower frequencies along with a reduction in the C_Q as the alkali content of the glass increases. A relative reduction of the C_Q with increasing Na fraction suggests either a gradual increase in the crystallinity of the phase these Na^+ ions reside in, or the hydration of such Na^+ sites or some combination thereof. As Bragg peaks were observed only in the diffractograms of Na-41 and Na-46, the presence of Na-bearing crystalline phases in glasses with lower Na fractions can be ruled out. However, the reduction in C_Q might suggest the formation of zeolite precursors and progressive evolution in their crystallinity, ultimately leading to the formation of zeolite in the high-Na sample. Alternately, the observed changes in the NMR parameters may be due to the Na^+ ions in a hydrated environment, as these Na^+ ions are characterized by small C_Q and isotropic shifts closer to 0 ppm [80]. Molecular dynamics simulations have shown the affinity of Na^+ for water molecules, wherein the Na^+ exchanged with H^+ in the network are coordinated to 3−4 water molecules [77]. In a recent study of glasses with similar compositions, a narrow peak with a C_Q of 1.9 MHz and δ_{iso} of -3.3 ppm observed in the ^{23}Na MQMAS spectrum of an altered glass was assigned to $Na_2SiO_3{\cdot}5H_2O$, a hydrated sodium silicate product [71]. However, based on our analysis of the ^{23}Na NMR spectra and the possibility of Na^+ being present simultaneously in hydrated and poorly crystalline environments, such assignments are ambiguous. Similar changes are observed in the ^{27}Al MAS NMR spectra, wherein the $^{[4]}Al$ peak

shifts to lower frequencies and its width narrows. The inferences made for Na about its presence in a maturing crystalline phase or a hydrated environment can be extended to Al as well as the presence of Al in a hydrated environment leads to similar spectroscopic changes [4].

The physical appearance of the samples changed markedly upon dissolution: the glass monoliths became opaque, and the opacity increased with the Na-fraction. Except for Na-21 and Na-26, the monoliths became soft and crumbly, marking the drastic reduction in their mechanical properties upon alteration. When the percent mass loss (**Table 9.8**) and the fractions of $^{[3]}B_A$, Q^4, $Q^{3,}$ and Q^2 obtained from charge calculation (**Tables 9.3, 9.4 and 9.5**) and ^{29}Si spectral deconvolution are compared (**Figure 9.19**), a strong correlation is observed between the Q^4 fraction and the extent of glass degradation. The Na-21 specimen has a high Q^4/Q^3 ratio and negligible $^{[3]}B_A$ and hence, the degradation is minimal. However, with an increase in the Na fraction of glasses (Na-26 and Na-31), the Q^4/Q^3 ratios decrease, leading to a higher mass loss. The Si speciation shifts to Q^3 and Q^2 in the second group of glasses (Na-36−Na-46), which also contain a significant fraction of $^{[3]}B_A$, which further enhances the dissolution rate. Although Si−O−Si linkages are highly stable and the activation barrier for their hydrolysis is very high (vide infra), they are readily hydrolyzable in alkaline pH. Since the leachates are highly alkaline (**Table 9.8**), the Si−O−Si bonds of Q^3 and Q^2 units are hydrolyzed to a greater extent.

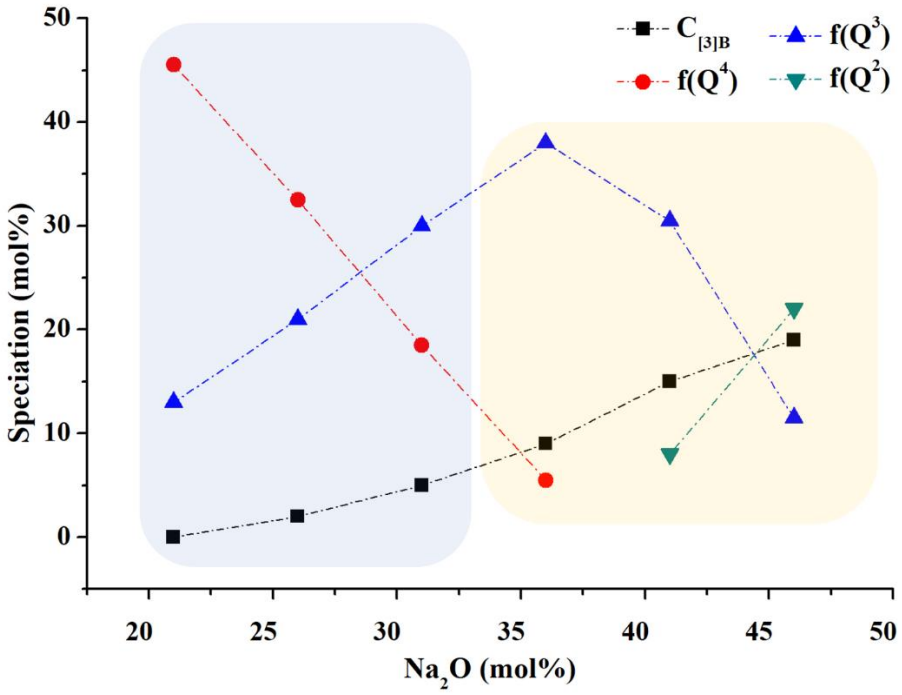

Figure 9.19. Fractions of $^{[3]}B_A$ ($C_{[3]B}$), Q^4 ($f(Q^4)$), Q^3 ($f(Q^3)$), and Q^2 ($f(Q^2)$) species in glasses plotted as a function of Na_2O mol%. The data points of glasses belonging to two subgroups are highlighted in blue and yellow.

The pH of the leachate obtained on day 28 of the dissolution and the mass loss increase with the Na fraction. The increase in pH is attributed to a higher release of Na^+, consistent with the Na mole fraction of the glasses. The pH has a significant impact on the hydrolysis of Si−O−T linkages in silicate glasses. The stability against hydrolysis for T−O−T linkages follows the order: Si−O−Si > Si−O−B > B−O−B in acidic and neutral conditions [81]. In basic conditions, the hydrolysis of B−O−Si bonds is considered to be rate-limiting [1] and the activation barriers for the hydrolysis of B−O−B and B−O−Si bonds are higher [82]. On the other hand, Si−O−Si linkages are unstable at high pH and undergo extensive hydrolysis, releasing H_4SiO_4. Furthermore, H_4SiO_4 dissociates into $H_3SiO_4^-$ and $H_2SiO_4^{2-}$, increasing the Si solubility in the leachate and raising the concentration required to reach the steady-state [11]. Although the hydrolysis energies of B-bearing linkages are higher in alkaline conditions, an opposite trend is observed in glasses studied here wherein the B leached extensively as the Na fraction of glasses increased. This observation suggests that if the linkages involving B have

NBO in their short-range chemical environment, i.e., linkages like $^{[3]}B_A-O-Si$, $^{[3]}B_A-O-^{[4]}B$, $^{[4]}B-O-Si(Q^{2/3})$, the expected trends in hydrolysis energy change. These linkages can be considered highly basic as the Na^+ ions charge-balancing the NBO are readily exchanged for H^+, leading to a higher diffusion of water into the network and therefore to extensive degradation of the glass network.

9.4.3 The effect of glass composition on dissolution stages

The network structure of sodium borosilicate glasses meant for HLW immobilization has been extensively explored and their chemical durability under the influence of several factors such as pH, glass composition, temperature and dissolved Si content has been investigated [1,2,11–13,3–10]. However, the influence of Na_2O content on the initiation of different dissolution stages has not been documented. A strong dependence of the kinetics of different dissolution stages on the Na content of glasses has been shown here. The concentration of leached elements is on the rise even after 28 days in Na-21, which suggests that the glass is still in stage 1 of dissolution, with ion exchange, hydrolysis, and dissolution reactions still prominent. In Na-26 and Na-31, the concentrations plateau by the end of the 28-day period, which marks the transient residual rate regime. In Na-36, the element concentration profiles plateau after only a week of dissolution, suggesting that the leachate is saturated, and the element concentrations have reached a steady state. The observed trend in the element release profiles corresponds to stage 2, the residual-rate regime of glass dissolution. Finally, the element release profiles in Na-41 and Na-46 are similar to Na-36 but approach a steady-state concentration within a week, suggesting a greater extent of degradation vis-à-vis other samples in the series. The x-ray diffraction and NMR analyses of these samples confirm the formation of secondary zeolite phases which are formed under the hydrothermal conditions of the dissolution vessels, with various dissolution products acting as templates [83]. From the trends in the elemental release profiles and the structural and morphological changes observed, it can be concluded that the glasses in this series illustrate the transitions between the first two conventional stages of glass dissolution.

9.5 Conclusion

The network structures and dissolution properties of sodium borosilicate glasses covering a wide compositional space were probed in this study. The network topology of pristine glasses agree well with the structural models developed for alkali borosilicate glasses wherein a depolymerization of the glass network is observed with increasing alkali oxide content. With the $SiO_2 \rightarrow Na_2O$ substitution, the fraction of $^{[4]}B_{nSi}$ decreases and the NBO-bearing $^{[3]}B_A$ species dominate the borate portion of the glass network. A similar effect is observed in Si speciation wherein the Q^4/Q^3 reduces, and the network becomes populated by anionic Q^3 and Q^2 species at high alkali oxide contents. Post-dissolution structural analysis reveals significant alteration of the glass network, which becomes more extensive with increases in Na/Si. A strong dependence of the kinetics of glass degradation on the fraction of NBO in the network is observed. The presence of NBO on $^{[3]}B$ expedites the dissolution process, which suggests that the trends in bond hydrolysis energies calculated or measured for B−O−T linkages in fully reticulated glass networks are vastly different compared to linkages consisting of $^{[3]}B$ bearing NBO. While the glass with the lowest Na fraction was resistant to aqueous corrosion, glasses with higher Na fractions corroded severely, became mechanically fragile and lost their structural integrity. The ^{29}Si DP- and $^{29}Si\{^1H\}$ CP-MAS NMR experiments have proven effective in determining the extent of glass dissolution, with distinct signals appearing from the altered and pristine regions of the glass. The alkali oxide content of glasses has a profound influence on the kinetics of different glass-dissolution stages and their onset. We have demonstrated the onset of two dissolution stages within a simple compositional series, wherein the glasses with low alkali oxide contents are found to be in the forward and residual rate regimes depending on the Na fraction, and glasses with high alkali contents show extensive degradation with reaching residual rate regimes in a very short time frame. Our results underscore the importance of considering both the alkali content of the calcine and the final wasteform for proper waste remediation.

9.6 References

[1] S. Gin, X. Guo, J.-M. Delaye, F. Angeli, K. Damodaran, V. Testud, J. Du, S. Kerisit, S.H. Kim, Insights into the mechanisms controlling the residual corrosion rate of borosilicate glasses, Npj Mater. Degrad. 4 (2020) 1–9.

[2] T.L. Gout, M.T. Harrison, I. Farnan, Evaluating the temperature dependence of Magnox waste glass dissolution, J. Non-Cryst. Solids. 518 (2019) 75–84.

[3] P. Frugier, S. Gin, Y. Minet, T. Chave, B. Bonin, N. Godon, J.E. Lartigue, P. Jollivet, A. Ayral, L. De Windt, G. Santarini, SON68 nuclear glass dissolution kinetics: Current state of knowledge and basis of the new GRAAL model, J. Nucl. Mater. 380 (2008) 8–21.

[4] M. Collin, M. Fournier, P. Frugier, T. Charpentier, M. Moskura, L. Deng, M. Ren, J. Du, S. Gin, Structure of International Simple Glass and properties of passivating layer formed in circumneutral pH conditions, Npj Mater. Degrad. 2 (2018) 1–13.

[5] T.L. Goût, M.T. Harrison, I. Farnan, Relating Magnox and international waste glasses, J. Non-Cryst. Solids. 524 (2019) 119647.

[6] J.D. Vienna, J.J. Neeway, J. V. Ryan, S.N. Kerisit, Impacts of glass composition, pH, and temperature on glass forward dissolution rate, Npj Mater. Degrad. 2 (2018) 1–12.

[7] M. Fournier, T. Ducasse, A. Pérez, A. Barchouchi, D. Daval, S. Gin, Effect of pH on the stability of passivating gel layers formed on International Simple Glass, J. Nucl. Mater. 524 (2019) 21–38.

[8] H. Arena, D. Rebiscoul, R. Podor, E. Garces, M. Cabie, J.-P. Mestre, N. Godon, Impact of Fe, Mg and Ca elements on glass alteration: Interconnected processes, Geochim. Cosmochim. Acta. 239 (2018) 420–445.

[9] T.L. Gout, M.T. Harrison, I. Farnan, Impacts of lithium on magnox waste glass dissolution, J. Non-Cryst. Solids. 51 (2019) 96–105.

[10] B. Parruzot, J. V. Ryan, J.L. George, R.K. Motkuri, J.F. Bonnett, L.M. Seymour, M.A. Derewinski, Multi-glass investigation of stage-III glass dissolution behavior from 22 to 90 °C triggered by the addition of zeolite phases, J. Nucl. Mater. 523 (2019) 490–501.

[11] N. Cassingham, C.L. Corkhill, D.J. Backhouse, R.J. Hand, J.V. Ryan, J.D. Vienna, N.C. Hyatt, The initial dissolution rates of simulated UK Magnox–ThORP blend nuclear waste glass as a function of pH, temperature and waste loading, Mineral. Mag. 79 (2015) 1529–1542.

[12] R.U. Farooqi, P. Hrma, Effect of Na_2O on aqueous dissolution of nuclear waste glasses, J. Nucl. Mater. 487 (2017) 210–219.

[13] S. Gin, P. Jollivet, M. Fournier, F. Angeli, P. Frugier, T. Charpentier, Origin and consequences of silicate glass passivation by surface layers, Nat. Commun. 6 (2015) 1–8.

[14] S. Gin, C. Guittonneau, N. Godon, D. Neff, D. Rebiscoul, M. Cabí, S. Mostefaoui, Nuclear glass durability: New insight into alteration layer properties, J. Phys. Chem. C. 115 (2011) 18696–18706.

[15] G.S. Frankel, J.D. Vienna, J. Lian, J.R. Scully, S. Gin, J. V Ryan, J. Wang, S.H. Kim, W. Windl, J. Du, A comparative review of the aqueous corrosion of glasses, crystalline ceramics, and metals, Mater. Degrad. 2 (2018).

[16] T. Geisler, A. Janssen, D. Scheiter, T. Stephan, J. Berndt, A. Putnis, Aqueous corrosion of borosilicate glass under acidic conditions: A new corrosion mechanism, J. Non-Cryst. Solids. 356 (2010) 1458–1465.

[17] L. Trotignon, J.C. Petit, G. Della Mea, J.C. Dran, The compared aqueous corrosion of four simple borosilicate glasses: Influence of Al, Ca and Fe on the formation and nature of secondary phases, J. Nucl. Mater. 190 (1992) 228–246.

[18] S. Gin, X. Beaudoux, F. Angéli, C. Jégou, N. Godon, Effect of composition on the short-term and long-term dissolution rates of ten borosilicate glasses of increasing complexity from 3 to 30 oxides, J. Non-Cryst. Solids. 358 (2012) 2559–2570.

[19] Donald I.W. et. al, Review: The immobilization of high level radioactive wastes using ceramics and glasses, J. Mater. Sci. 32 (1997) 5851–5887.

[20] J.E. Shelby, Structures of glasses, in: *Introduction to glass science and technology*, Royal Society of Chemistry, 2005: pp. 72–110.

[21] H. Maekawa, T. Maekawa, K. Kawamura, T. Yokokawa, The structural groups of alkali silicate glasses determined from ^{29}Si MAS-NMR, J. Non-Cryst. Solids. 127 (1991) 53–64.

[22] F. Angeli, O. Villain, S. Schuller, S. Ispas, T. Charpentier, Insight into sodium silicate glass structural organization by multinuclear NMR combined with first-principles calculations, Geochim. Cosmochim. Acta. 75 (2011) 2453–2469.

[23] H. Doweidar, Consideration of the boron oxide anomaly, J. Mater. Sci. 25 (1990) 253–258.

[24] A. Krishnamurthy, V.K. Michaelis, S. Kroeker, Network formation in borosilicate glasses with aluminum or gallium: implications for nepheline crystallization, J. Phys. Chem. C. 125 (2021) 8815–8824.

[25] M.G. Krzhizhanovskaya, P. Paufler, S.K. Filatov, R.S. Bubnova, Density and refractive indices of alkali borate and borosilicate crystals and glasses: A comparative analysis, Phys. Chem. Glas. Eur. J. Glas. Sci. Technol. Part B. 56 (2015) 183–188.

[26] H.A. Robinson, Physical properties and structure of silicate glasses: I, additive relations in alkali binary glasses, J. Am. Ceram. Soc. 52 (1969) 392–399.

[27] H.F. Shermer, Thermal expansion of binary alkali silicate glasses, J. Res. Natl. Bur. Stand. (1934). 57 (1956) 97.

[28] J.E. Shelby, Property/morphology relations in alkali silicate glasses, J. Am. Ceram. Soc. 66 (1983) 754–757.

[29] H. Jabraoui, Y. Vaills, A. Hasnaoui, M. Badawi, S. Ouaskit, Effect of sodium oxide modifier on structural and elastic properties of silicate glass, J. Phys. Chem. B. 120 (2016) 13193–13205.

[30] D.M. Strachan, Results from long-term use of the MCC-1 static leach test method, Nucl. Chem. Waste Manag. 4 (1983) 177–188.

[31] W. Haller, D.H. Blackburn, F.E. Wagstaff, R.J. Charles, Metastable immiscibility surface in system Na_2O-B_2O_3-SiO_2, J. Am. Ceram. Soc. 53 (1970) 34–39.

[32] M.H. Bartl, K. Gatterer, H.P. Fritzer, S. Arafa, Investigation of phase separation in Nd^{3+}

doped ternary sodium borosilicate glasses by optical spectroscopy, Spectrochim. Acta - Part A Mol. Biomol. Spectrosc. 57 (2001) 1991–1999.

[33] F. Bloch, W.W. Hansen, M. Packard, The nuclear induction experiment, Phys. Rev. 70 (1946) 460–474.

[34] C. Martineau, V.K. Michaelis, S. Schuller, S. Kroeker, Liquid-liquid phase separation in model nuclear waste glasses: A solid-state double-resonance NMR study, Chem. Mater. 22 (2010) 4896–4903.

[35] S. Prasad, T.M. Clark, T.H. Sefzik, H.T. Kwak, Z. Gan, P.J. Grandinetti, Solid-state multinuclear magnetic resonance investigation of Pyrex®, J. Non-Cryst. Solids. 352 (2006) 2834–2840.

[36] L.S. Du, J.F. Stebbins, Site preference and Si/B mixing in mixed-alkali borosilicate glasses: A high-resolution ^{11}B and ^{17}O NMR study, Chem. Mater. 15 (2003) 3913–3921.

[37] L.S. Du, J.F. Stebbins, Solid-state NMR study of metastable immiscibility in alkali borosilicate glasses, J. Non-Cryst. Solids. 315 (2003) 239–255.

[38] S. Kroeker, J.F. Stebbins, Three-coordinated boron-11 chemical shifts in borates, Inorg. Chem. 40 (2001) 6239–6246.

[39] S. Kroeker, Nuclear Waste Glasses: Insights from Solid-State NMR, Encycl. Magn. Reson. (2011) 453–466.

[40] A. Krishnamurthy, T. Nguyen, M. Fayek, B. Shabaga, S. Kroeker, Network Structure and Dissolution Properties of Phosphate-Doped Borosilicate Glasses, J. Phys. Chem. C. 124 (2020) 21184–21196.

[41] L.S. Du, J.F. Stebbins, Nature of Silicon-Boron Mixing in Sodium Borosilicate Glasses: A High-Resolution ^{11}B and ^{17}O NMR Study, J. Phys. Chem. B. 107 (2003) 10063–10076.

[42] Y.H. Yun, S.A. Feller, P.J. Bray, Correction and addendum to “Nuclear magnetic resonance studies of the glasses in the system Na_2O-B_2O_3-SiO_2,” J. Non-Cryst. Solids. 33 (1979) 273–277.

[43] Y.H. Yun, P.J. Bray, Nuclear magnetic resonance studies of the glasses in the system

K_2O-B_2O_3-P_2O_5, J. Non-Cryst. Solids. 30 (1978) 45–60.

[44] W.J. Dell, P.J. Bray, S.Z. Xiao, ^{11}B NMR studies and structural modeling of Na_2O-B_2O_3-SiO_2 glasses of high soda content, J. Non-Cryst. Solids. 58 (1983) 1–16.

[45] P.M. Aguiar, S. Kroeker, Boron speciation and non-bridging oxygens in high-alkali borate glasses, J. Non-Cryst. Solids. 353 (2007) 1834–1839.

[46] J.C.C. Chan, M. Bertmer, H. Eckert, Site connectivities in amorphous materials studied by double-resonance NMR-of quadrupolar nuclei: High-resolution $^{11}B \leftrightarrow 27Al$ spectroscopy of aluminoborate glasses, J. Am. Chem. Soc. 121 (1999) 5238–5248.

[47] M. Edén, ^{27}Al NMR Studies of Aluminosilicate Glasses, 1st ed., Elsevier Ltd., 2015.

[48] R. Youngman, NMR spectroscopy in glass science: A review of the elements, Materials (Basel). 11 (2018) 476.

[49] R. Dupree, D. Holland, D.S. Williams, The structure of binary alkali silicate glasses, J. Non-Cryst. Solids. 81 (1986) 185–200.

[50] M.S. Bødker, S.S. Sørensen, J.C. Mauro, M.M. Smedskjaer, Predicting composition-structure relations in alkali borosilicate glasses using statistical mechanics, Front. Mater. 6 (2019).

[51] J.F. Stebbins, Anionic speciation in sodium and potassium silicate glasses near the metasilicate ($[Na,K]_2SiO_3$) composition: ^{29}Si, ^{17}O, and ^{23}Na MAS NMR, J. Non-Cryst. Solids X. 6 (2020) 100049. doi:10.1016/j.nocx.2020.100049.

[52] T. Nanba, M. Nishimura, Y. Miura, A theoretical interpretation of the chemical shift of ^{29}Si NMR peaks in alkali borosilicate glasses, Geochim. Cosmochim. Acta. 68 (2004) 5103–5111.

[53] S. Prabakar, K.J. Rao, C.N.R. Rao, ^{29}Si NMR chemical shifts in silicates, Chem. Phys. Lett. 183 (1991) 176–182.

[54] R. Dupree, D. Holland, P.W. McMillan, R.F. Pettifer, The structure of soda-silica glasses: A mas NMR study, J. Non-Cryst. Solids. 68 (1984) 399–410.

[55] N. Janes, E. Oldfield, Prediction of Silicon-29 Nuclear magnetic resonance chemical shifts using a group electronegativity approach: applications to silicate and aluminosilicate structures, J. Am. Chem. Soc. 107 (1985) 6769–6775.

[56] G.D. Cody, B.O. Mysen, S.K. Lee, Structure vs. composition: A solid-state ^{1}H and ^{29}Si NMR study of quenched glasses along the Na_2O-SiO_2-H_2O join, Geochim. Cosmochim. Acta. 69 (2005) 2373–2384.

[57] R. Martens, W. Müller-Warmuth, Structural groups and their mixing in borosilicate glasses of various compositions - an NMR study, J. Non-Cryst. Solids. 265 (2000) 167–175.

[58] E. Nicoleau, S. Schuller, F. Angeli, T. Charpentier, P. Jollivet, A. Le Gac, M. Fournier, A. Mesbah, F. Vasconcelos, Phase separation and crystallization effects on the structure and durability of molybdenum borosilicate glass, J. Non-Cryst. Solids. 427 (2015) 120–133.

[59] D. Caurant, O. Majérus, E. Fadel, A. Quintas, C. Gervais, T. Charpentier, D. Neuville, Structural investigations of borosilicate glasses containing MoO_3 by MAS NMR and Raman spectroscopies, J. Nucl. Mater. 396 (2010) 94–101.

[60] L.S. Du, J.F. Stebbins, Network connectivity in aluminoborosilicate glasses: A High-Resolution ^{11}B, ^{27}Al and ^{17}O NMR Study, J. Non-Cryst. Solids. 351 (2005) 3508–3520.

[61] T. Degen, M. Sadki, E. Bron, U. König, G. Nénert, The high score suite, Powder Diffr. 29 (2014) S13–S18.

[62] K.J.D. Mackenzie, M.E. Smith, NMR of other commonly studied nuclei, in: R.W. Cahn (Ed.), *Multinuclear solid-state NMR of inorganic materials*, Pergamon materials series, 2002: pp. 400–402.

[63] S. Caldarelli, A. Buchholz, M. Hunger, Investigation of sodium cations in dehydrated zeolites LSX, X, and Y by ^{23}Na off-resonance RIACT triple-quantum and high-speed MAS NMR spectroscopy, J. Am. Chem. Soc. 123 (2001) 7118–7123.

[64] K.H. Lim, C.P. Grey, Characterization of extra-framework cation positions in zeolites NaX and NaY with very fast ^{23}Na MAS and multiple quantum MAS NMR spectroscopy, J. Am. Chem. Soc. 122 (2000) 9768–9780.

[65] S. Greiser, M. Hunger, C. Jäger, ^{29}Si{^{27}Al} TRAPDOR MAS NMR to distinguish Qn(mAl) sites in aluminosilicates. Test case: Faujasite-type zeolites, Solid State Nucl. Magn. Reson. 79 (2016) 6–10.

[66] R.J. Kirkpatrick, K.A. Smith, S. Schramm, G. Turner, W.-H. Yang, Solid-state nuclear magnetic resonance spectroscopy of minerals, Annu. Rev. Earth Planet. Sci. 13 (1985) 29–47.

[67] W. Loewenstein, M. Lowenstein, The distribution of aluminum in the tetrahedra of silicates and aluminates, Am. Mineral. 39 (1954) 92–96.

[68] J. Van Bokhoven, A.L. Roest, D.C. Koningsberger, J.T. Miller, G.H. Nachtegaal, A.P.M. Kentgens, Changes in structural and electronic properties of the zeolite framework induced by extraframework Al and La in H-USY and La(x)NaY: A ^{29}Si and ^{27}Al MAS NMR, J. Phys. Chem. B. 104 (2000) 6743–6754.

[69] J. V. Oglesby, J.F. Stebbins, ^{29}Si CPMAS NMR investigations of silanol-group minerals and hydrous aluminosilicate glasses, Am. Mineral. 85 (2000) 722–731.

[70] K.A. Murphy, N.M. Washton, J. V. Ryan, C.G. Pantano, K.T. Mueller, Solid-state NMR examination of alteration layers on nuclear waste glasses, J. Non-Cryst. Solids. 369 (2013) 44–54.

[71] T. Ohkubo, Y. Iwadate, K. Deguchi, S. Ohki, T. Shimizu, Changes in surface structure of sodium aluminoborosilicate glasses during aqueous corrosion analyzed by using NMR, J. Phys. Chem. Solids. 77 (2015) 164–171. doi:10.1016/j.jpcs.2014.10.018.

[72] X. Xue, M. Kanzaki, Dissolution mechanisms of water in depolymerized silicate melts: Constraints from ^{1}H and ^{29}Si NMR spectroscopy and ab initio calculations, Geochim. Cosmochim. Acta. 68 (2004) 5027–5057.

[73] S. Léonardelli, L. Facchini, C. Fretigny, P. Tougne, A.P. Legrand, Silicon-29 nuclear magnetic resonance study of silica, J. Am. Chem. Soc. 114 (1992) 6412–6418.

[74] Y. Yu, B. Stevensson, M. Edén, Medium-range structural organization of phosphorus-bearing borosilicate glasses revealed by advanced solid-state nmr experiments and md simulations: consequences of B/Si substitutions, J. Phys. Chem. B. 121 (2017) 9737–

9752.

[75] Q.J. Zheng, R.E. Youngman, C.L. Hogue, J.C. Mauro, M. Potuzak, M.M. Smedskjaer, Y.Z. Yue, Structure of boroaluminosilicate glasses: Impact of [Al_2O_3]/[SiO_2] ratio on the structural role of sodium, Phys. Rev. B - Condens. Matter Mater. Phys. 86 (2012).

[76] G. Geneste, F. Bouyer, S. Gin, Hydrogen-sodium interdiffusion in borosilicate glasses investigated from first principles, J. Non-Cryst. Solids. 352 (2006) 3147–3152.

[77] H. Jabraoui, T. Charpentier, S. Gin, J.M. Delaye, R. Pollet, Atomic insights into the events governing the borosilicate glass-water interface, J. Phys. Chem. C. 125 (2021) 7919–7931.

[78] H. Zhang, T. Suzuki-Muresan, Y. Morizet, S. Gin, A. Abdelouas, Investigation on boron and iodine behavior during nuclear glass vapor hydration, Npj Mater. Degrad. 5 (2021) 1–9.

[79] L. Dohmen, C. Lenting, R.O.C. Fonseca, T. Nagel, A. Heuser, T. Geisler, R. Denkler, Pattern formation in silicate glass corrosion zones, Int. J. Appl. Glas. Sci. 4 (2013) 357–370.

[80] X. Ai, L. Chen, J. Dong, C. Ye, F. Deng, Variation of sodium coordination during the hydration processes of layered sodium disilicates as studied by ^{23}Na MQMAS and ^{1}H↔^{23}Na CP/MAS NMR spectroscopy, J. Mater. Chem. 13 (2003) 614–621.

[81] B.C. Bunker, G.W. Arnold, D.E. Day, P.J. Bray, The effect of molecular structure on borosilicate glass leaching, J. Non-Cryst. Solids. 87 (1986) 226–253.

[82] P. Zapol, H. He, K.D. Kwon, L.J. Criscenti, First-principles study of hydrolysis reaction barriers in a sodium borosilicate glass, Int. J. Appl. Glas. Sci. 4 (2013) 395–407.

[83] C.S. Cundy, P.A. Cox, The hydrothermal synthesis of zeolites: history and development from the earliest days to the present time, Chem. Rev. 103 (2003) 663–702

10 Conclusions and Future Directions

10.1 Conclusions

The projects presented in this thesis encompass multicomponent phosphate and silicate glasses with wide compositional ranges, and focus on addressing important and long-standing questions in the area of nuclear-waste vitrification. This work draws strength from diverse state-of-art analytical tools such as nuclear magnetic resonance spectroscopy, x-ray diffraction, electron microscopy, energy-dispersive x-ray spectroscopy, and elemental analysis by inductively-coupled plasma optical emission spectroscopy/mass spectrometry, which have been successful in providing a wealth of information on the structural and chemical homogeneity, and the durability of glasses. Multinuclear solid-state NMR spectroscopy is the primary analytical tool in this work, which is known for its efficacy in probing the network connectivity of both amorphous and crystalline systems. Moreover, the concept of Pauling bond strength (PBS), a well-known theoretical approach routinely used in crystallography to calculate bond valence contributions of cations to the network, has been exploited in great depth to substantiate the interpretation of NMR results and to explain the bonding environments in multicomponent glasses.

Interpreting the network structure of aluminoborophosphate glasses is a challenge even for specialized double-resonance NMR experiments due to the strong intermixing of B, Al, and P structural units. Evaluation of the network structure of these glasses using both solid-state NMR experiments and PBS models of crystalline borophosphates and glassy clusters has allowed some degree of discrimination amongst possible bonding configurations, which helps visualize the glass network as a function of glass composition. Contrary to other borophosphate systems studied in the literature, our results highlight the presence of a high fraction of energetically unfavourable $^{[4]}B-O-^{[4]}B$ linkages with underbonded bridging oxygens (BO). These linkages are stabilized by Na^{+} and P^{5+} through their ability to contribute different bond strengths to the BO through charge delocalization.

The nuclear-waste-vitrification process was simulated using aluminoborophosphate glasses as glass frit and Mo as the waste component. Changes in the network structure upon Mo addition and its mode of incorporation were discerned using solid-state NMR and PBS modeling. A thorough bond-strength analysis of crystalline and glassy phosphomolybdate systems reveals

that Mo exists in an octahedral coordination environment and incorporates into the phosphate network by interacting with the non-bridging oxygens (NBO) on phosphate units functioning as anchoring sites, effectively forming P−O−Mo linkages. The efficacy of the formation of such linkages is attributed to the similar field strengths of P^{5+} and Mo^{6+} cations, which results in comparable ordering on the oxygens, favouring their formation and hence, the incorporation of Mo into the phosphate network. Our ^{95}Mo MAS NMR results and PBS analysis of the phosphomolybdate systems agree well and indicate that Mo resides in a distorted octahedral environment with NBO ($Mo-O^-$) charge-compensated by alkali cations and BO shared with neighbouring phosphate tetrahedra (P−O−Mo). Although Mo interacts with P exclusively, an indirect effect on the B and Al speciation is observed, which has been explained using bond strength distribution maps. Whether or not B−O−Mo linkages exist in Mo-doped borophosphate glasses is a topic of debate in the literature, as there is no spectroscopic handle to directly track its presence. We have provided an alternate rationale for the observed $^{[4]}$B chemical shifts that does not invoke B−O−Mo bonds, using the bond-strength contributions of B, P and Mo. Being a multicomponent system, aluminoborophosphate glasses exhibit lower Mo solubility vis-à-vis binary phosphate glasses due to the competition between Al, B, and Mo for phosphate units. This more closely models the actual scenario of Mo-rich waste immobilization, as pure phosphate glasses are seldom used for waste immobilization due to their poor chemical properties.

The *in-situ* high-temperature MAS NMR (HT-NMR) analysis of glasses, used to simulate the radiolytic heating of glasses, suggests negligible changes in the structure of glasses studied, implying an increase in the glass-transition temperature (T_g) of glasses and their resistance to devitrification due to increased network reticulation by the formation of B−O−P and Al−O−P linkages. This work also demonstrates the applicability of HT-NMR as a viable technique to estimate the T_gs of glasses.

Some of the more complex NMR results in this research are interpreted with the aid of simple, yet effective Pauling bond strength principles, highlighting their value in obtaining a preliminary understanding of complicated network structures in multicomponent glasses. The network structure of aluminoborophosphate glasses proposed using the multinuclear NMR studies and the PBS model will serve a key role in understanding their chemical and physical properties.

Inspired by the capability of phosphate glasses to immobilize high fractions of Mo, which we call the *cation-field-strength matching principle*, due to the similar field strengths of P and Mo and their similar ordering effect on oxygens, borosilicate glasses were doped with small fractions of phosphate to test for improved retention of high field strength cations, Mo^{6+} and S^{6+}. At least a four-fold increase in Mo and S solubility is observed with respect to the P-free aluminoborosilicate nuclear glasses currently in use worldwide, validating the CFS matching principle and underscoring the utility of phosphate-doping for the simultaneous incorporation of multiple high-field-strength cations. Multinuclear NMR results provide clues about the specific bonding locations of Mo^{6+} and S^{6+} within the glassy network, indicating that phosphate chains are key to their enhanced solubility. This work establishes the idea of matching cation field-strengths with appropriate additives to optimize the assimilation of selected cations into the glassy network, proving to be a valuable design principle in the development of better materials for radioactive waste immobilization. It may be further extended to studies focused on improving certain physical and chemical properties of glasses.

Since P^{5+} is also a high-field-strength cation, its effect on the network structure and chemical durability of aluminoborosilicate glasses were studied. Phosphate incorporation in borosilicate glasses is observed to be limited to 3 mol%, beyond which clustering of phosphate eventually leads to the separation of crystalline sodium phosphate phases. Nevertheless, this low fraction is found to be sufficient to improve Mo incorporation, wherein P bonds to Mo through NBO, significantly improving the Mo solubility but at the expense of the segregation of an amorphous alkali-phosphate phase containing most of the Mo. Chemical durability tests showed an increased resistance of glasses to aqueous corrosion with phosphate content, attributed to the alkali-scavenging property of phosphate, which increases the silicate network reticulation in the process. In addition, formation of an alteration layer is observed in all phosphate-doped glasses, confirming that the addition of phosphate does not ultimately compromise the durability of the waste-loaded materials. Since phosphate-doping permits a significant increase in the overall waste loading and does not compromise the chemical durability of glasses, minor compositional adjustments may serve to permit improved waste-loading capacities within existing industrial process streams, providing economic and ecological benefits. The high waste-loading feature brought about by doping borosilicate glasses with phosphate would lower the volume of the final wasteform that is generated, significantly reducing the stress on the limited repository space.

The effect of alkali oxide content, a major component of all waste streams, on the network structure and dissolution properties of sodium borosilicate glasses covering a wide compositional space was probed with the aim of determining the maximum alkali oxide loading in candidate glasses. With increasing Na/Si ratio, formation of NBO on silicate and three-coordinate boron units is observed at low and high Na_2O contents, respectively. While these structural changes are already documented in the literature, information on the effect of the fraction of NBO on the chemical durability of glasses and its effect on the stages of glass dissolution is scant. Our results show that with increasing Na/Si, the fraction of NBO in the glass network increases, resulting in greater degradation of the glass and an increase in the rate of glass dissolution. The presence of NBO on $^{[3]}B$ units enhances the dissolution process, which suggests that arguments about glass durability based on the energetics of B−O−T (T = Al, Si and, B) bond hydrolysis are incomplete, and must be corrected for the presence of NBO in the glass network, which become prominent species in high-Na glasses. Our results from the dissolution studies demonstrate the effect of alkali content on the kinetics of glass dissolution and the initiation of all three dissolution stages, underscoring the importance of considering alkali content of the calcine and the final wasteform for reliable waste remediation and in designing high-performance wasteforms. Our results define the limit of alkali loading to 21 mol%, as the glasses with alkali oxide beyond this level are poor candidates for long-term waste disposal due to their compromised chemical durability.

10.2 Future directions

Following our work on the incorporation of Mo into aluminoborophosphate glasses, a comparably detailed study of the integration of sulfur would be of interest. Although phosphate glasses have been shown to incorporate a high fraction of sulfate [1], the exact mechanism of incorporation remains unexplored. Since S and Mo are both hexavalent and have high CFS, the developed structural models for Mo-incorporated aluminoborophosphate glasses can be extended to sulfate-doped glasses to predict the mode of S incorporation.

New insights obtained from the structural and chemical-durability studies of glasses presented in this work open a window of opportunity for further exploration of radioactive waste vitrification. Although the doping of borosilicate glasses with phosphate improves the

incorporation of Mo^{6+} and S^{6+} on the laboratory scale, the mass of glasses tested is very small (*ca.* 3 g), which is minute compared to the volume of glass poured into each canister (*ca.* 330 L) [2] during industrial-scale vitrification. While such large volumes of glasses cannot be synthesized in a research lab setting, increasing the batch size to a maximum reasonable volume that can be synthesized with the available infrastructure (typically 50−100 mL) will contribute toward understanding how our results scale up to realistic vitrification volumes, and will further in fine-tuning the synthetic conditions.

High-level waste (HLW) is very chemically heterogeneous, with more than thirty elements typically present in their oxide forms. The work presented in this thesis focuses mainly on certain troublesome cations with high phase-separation tendencies (Mo^{6+} and S^{6+}), with the expectation that other elements in the waste will be completely integrated into the network. Most HLW streams include other elements in high oxidation states, such as Cr^{6+} [3] and Tc^{7+} (Re^{7+} is used as a surrogate in waste-immobilization studies as Tc is radioactive) [4], which are also known to phase-separate into crystalline phases in a similar fashion. The CFS matching principle can be extended to these cations as well to see if phosphate doping would improve their retention in the glassy phase. Furthermore, realistic waste streams generally include metals such as Ru, Pd, and Rh, which are known to nucleate and phase-separate from the glass in their elemental or oxide forms (for example, RuO_4) [5]. Vitrification of these elements in phosphate-doped glasses should be tested.

Our studies have shown that phosphate-doped borosilicate glasses often separate into two distinct glassy phases, wherein a less-durable alkali-phosphate phase containing the high field-strength cations is encapsulated in a highly-durable silicate-rich matrix. Although phase-separation is not generally considered to be desirable in waste vitrification, standard leach tests suggest that their chemical durability is on-par with homogeneous borosilicate glasses, albeit with an initial loss of any low-durability phase initially present on the glass surface. Nevertheless, phosphate-doped glasses improve the incorporation of high-CFS cations by three to four times relative to conventional borosilicate glasses, which increases the waste-loading capacity of glasses and decreases the volume of waste-glass generated, imparting huge economic and ecological benefits. Moreover, the effect of the heterogeneous chemical composition of high-

level waste streams on this type of phase separation must be tested by synthesizing glasses loaded with a simulated calcined waste which represents more realistic chemical compositions.

The glass-in-glass phase separation observed in phosphate-doped borosilicate glasses might be controlled by further extending the CFS approach to modifier cations in the glass network. The Mo-incorporated phosphate-rich region includes a significant fraction of Na^+, suggesting that these phosphomolybdate clusters consist of NBO which are charge-balanced by Na^+. A few alkaline-earth cations, such as Mg^{2+} and Ca^{2+}, are known to have a strong influence on the physical and chemical properties of glasses, likely brought about by their strong interaction with the NBO due to their high charge density [6–8]. Evidence of cation field strength at work comes from Mo-incorporated sodium-calcium borosilicate glasses wherein molybdate units preferentially sequester Ca^{2+} and phase-separate as powellite ($CaMoO_4$) [9]. In principle, substituting Na^+ by Mg^{2+} in phosphate-doped borosilicate glasses in varying ratios should have a pronounced influence on the modifier-scavenging property of phosphate, thereby frustrating the phase separation of phosphomolybdate clusters. Due to its higher field strength, Mg^{2+} might interact more strongly with the NBO on the silicate units vis-à-vis Na^+ ions, therefore limiting the modifier-scavenging property of phosphate and retarding the phase separation of phosphate-rich regions. This idea stems from the *mixed-alkali effect* observed in glasses consisting of two different modifiers, where the properties of mixed-alkali glasses deviate significantly from the trends expected based on glasses with either one of the cations alone [10–12].

The formation of alkali-phosphate-rich clusters might also be circumvented by increasing the boron fraction in the glass network. Since tetrahedral borate units are anionic and need modifier cations for charge compensation, a higher boron fraction may induce competition for modifier cations between the borate and phosphate units, limiting the modifier cations available for the phosphate clusters to form. Moreover, the high fraction of boron might promote the formation of B−O−P linkages [13], thereby functioning as anchoring sites for phosphomolybdate clusters to integrate with the borosilicate matrix of the bulk.

Although the standard leach tests provide a good estimate of the chemical durability of glasses and help assess their suitability for long-term waste disposal, the test conditions rarely represent those in actual repositories. For example, leaching tests are often carried out in distilled water as minerals dissolved in the groundwater interfere with the quantification of elements

leached from glasses. These tests are partially skewed as the dissolved minerals in the groundwater may have a significant impact on the mechanism through which the glasses corrode, and the extent of their dissolution. The pH of the dissolution medium is known to significantly influence glass dissolution [14,15], however most leach tests are carried out without any pH control of the solution, and involve the exploration of glass dissolution at one pH setting. The acidity or alkalinity of the groundwater is a major variable in repository conditions due to several natural factors. Hence, tests carried out in acidic or alkaline conditions for a particular wasteform might be irrelevant if the test conditions do not reflect those of geological repositories. Therefore the effect of pH on the dissolution of phosphate-doped silicate glasses should be further explored.

Canisters loaded with waste-immobilized glass are stored in repositories and backfilled with bentonite clay due to its swelling properties and low water permeability [5]. The clay consists predominantly of montmorillonite, a phyllosilicate mineral belonging to the smectite group [16]. Even aluminosilicate minerals are susceptible to hydrolysis in both acidic and alkaline conditions [17,18] and can introduce Si, Al, and other cations into the water, changing its composition, attenuating the steady-state concentrations of these elements in water and affecting glass dissolution rates. Moreover, the presence of natural components in the water such as olivine, a magnesium-bearing silicate mineral, has been shown to alter the dissolution rate of glasses [19,20]. Hence, leach tests must be performed in groundwater and bentonite-treated water to simulate the repository conditions. Along these lines, a recent study focused on the interactions between waste-immobilized glasses and the canister alloys shows that glass surfaces exposed to the alloy exhibit increased corrosion rates and morphological differences compared to the bulk of the glass, significantly impacting the formation of the alteration layer [21]. Studies designed to better simulate long-term geological repository conditions, including canister-wasteform interactions, would expand the applicability of this lab-based research.

In the final stage of glass dissolution, the alteration layer is lost to crystalline aluminosilicate minerals, which are considered secondary alteration products [20]. Due to the long time-scale of different dissolution stages, the crystallization of aluminosilicate minerals from the alteration layers has not been well explored. The silica-rich alteration layer is known to incorporate cations such as K^+, Cs^+, Na^+, Ca^{2+}, and B^{3+} leached from the bulk glass [22–24]. Our

ongoing attempts to study the chemical composition of the alteration layer suggest that its chemical makeup resembles the glass composition more closely than previously thought [25]. Since the secondary alteration products precipitate from the layer, their chemical compositions should match the latter and ultimately, the glass composition. Studies so far provide scant interpretation of the types of crystalline phases formed, and have failed to establish the chemical relationship between the altered surface layer and the crystalline products [26]. Aluminosilicate sol-gels [27], and the alteration layer bear similar chemical characteristics in terms of the structural species present and their interconnectivity. Sol-gel glasses are synthesized via a solution route whereby organic precursors of the network-forming cations are hydrolyzed and condensed into a three-dimensional network to form a hydrated gel. Hence, silicate-based sol-gel glasses with compositions matching that of the glassy matrices used for waste vitrification can be synthesized, and their conversion to crystalline products can be tracked through hydrothermal synthesis. This will help in identifying the types of crystalline products that might form from targeted glass compositions, providing insight useful for predicting their overall performance. Moreover, this study may provide further information on the incorporation of leached radionuclides into the secondary products if the sol-gel glasses are doped with radionuclide surrogates.

10.3 References

[1] P.A. Bingham, R.J. Hand, Sulphate incorporation and glass formation in phosphate systems for nuclear and toxic waste immobilization, Mater. Res. Bull. 43 (2008) 1679–1693.

[2] Design and operation of high level waste vitrification and storage facilities, Technical Report Series No. 339, International Atomic Energy Agency, Vienna, 1992.

[3] B.J. Greer, S. Kroeker, Characterisation of heterogeneous molybdate and chromate phase assemblages in model nuclear waste glasses by multinuclear magnetic resonance spectroscopy, Phys. Chem. Chem. Phys. 14 (2012) 7375–7383.

[4] J.S. McCloy, B.J. Riley, A. Goel, M. Liezers, M.J. Schweiger, C.P. Rodriguez, P. Hrma, D.S. Kim, W.W. Lukens, A.A. Kruger, Rhenium solubility in borosilicate nuclear waste glass: Implications for the processing and immobilization of technetium-99, Environ. Sci. Technol. 46 (2012) 12616–12622.

[5] J.E. Mendel, The Fixation of high-level wastes in glasses, Philos. Trans. R. Soc. London. Ser. A, Math. Phys. Sci. 319 (1986) 49–62.

[6] M.C. Eckersley, P.H. Gaskell, A.C. Barnes, Structural ordering in a calcium silicate, Nature. 335 (1988) 525–527.

[7] R.G. Kuryaeva, The state of magnesium in silicate glasses and melts, Glas. Phys. Chem. 35 (2009) 378–383.

[8] K. Shimoda, T. Nemoto, K. Saito, Local structure of magnesium in silicate glasses: A25Mg 3QMAS NMR study, J. Phys. Chem. B. 112 (2008) 6747–6752.

[9] T. Taurines, B. Boizot, Microstructure of powellite-rich glass-ceramics: a model system for high level waste immobilization, J. Am. Ceram. Soc. 95 (2012) 1105–1111.

[10] C.J. Wilkinson, A.R. Potter, R.S. Welch, C. Bragatto, Q. Zheng, M. Bauchy, M. Affatigato, S.A. Feller, J.C. Mauro, Topological origins of the mixed alkali effect in glass, J. Phys. Chem. B. 123 (2019) 7482–7489.

[11] Y. Onodera, Y. Takimoto, H. Hijiya, T. Taniguchi, S. Urata, S. Inaba, S. Fujita, I.

Obayashi, Y. Hiraoka, S. Kohara, Origin of the mixed alkali effect in silicate glass, NPG Asia Mater. 11 (2019).

[12] R.J. Charles, The mixed alkali effect in glasses, J. Am. Ceram. Soc. 48 (1965) 432–433.

[13] M.T. Rinke, H. Eckert, The mixed network former effect in glasses: solid state NMR and XPS structural studies of the glass system $(Na_2O)_x(BPO_4)_{1-x}$, Phys. Chem. Chem. Phys. 13 (2011) 6552.

[14] M. Fournier, T. Ducasse, A. Pérez, A. Barchouchi, D. Daval, S. Gin, Effect of pH on the stability of passivating gel layers formed on international simple glass, J. Nucl. Mater. 524 (2019) 21–38.

[15] J.D. Vienna, J.J. Neeway, J. V Ryan, S.N. Kerisit, Impacts of glass composition, pH, and temperature on glass forward dissolution rate, Npj Mater. Degrad. 2 (2018) 1–12.

[16] C.S. Ross, E.V. Shannon, The minerals of bentonite and related clays and their physical properties, J. Am. Ceram. Soc. 9 (1926) 77–96.

[17] G.R. Holdren, J.E. Adams, Parabolic dissolution kinetics of silicate minerals: an artifact of nonequilibrium precipitation processes., Geology. 10 (1982) 186–190.

[18] C.P. Morrow, S. Nangia, B.J. Garrison, Ab initio investigation of dissolution mechanisms in aluminosilicate minerals, J. Phys. Chem. A. 113 (2009) 1343–1352.

[19] J.C. Sang, A. Barkatt, J.A. O'Keefe, Attenuation of glass dissolution in the presence of natural additives, J. Non-Cryst. Solids. 208 (1996) 170–180.

[20] G.S. Frankel, J.D. Vienna, J. Lian, J.R. Scully, S. Gin, J. V Ryan, J. Wang, S.H. Kim, W. Windl, J. Du, A comparative review of the aqueous corrosion of glasses, crystalline ceramics, and metals, Mater. Degrad. 2 (2018).

[21] X. Guo, S. Gin, H. Liu, D. Ngo, J. Luo, S.H. Kim, C. Mohanty, J.D. Vienna, J. V. Ryan, G.S. Frankel, Near-field corrosion interactions between glass and corrosion resistant alloys, Npj Mater. Degrad. 4 (2020) 1–15.

[22] H. Aréna, D. Rébiscoul, E. Garcès, N. Godon, Comparative effect of alkaline elements and calcium on alteration of international simple glass, Npj Mater. Degrad. 3 (2019) 1–11.

[23] S. Gin, X. Guo, J.-M. Delaye, F. Angeli, K. Damodaran, V. Testud, J. Du, S. Kerisit, S.H. Kim, Insights into the mechanisms controlling the residual corrosion rate of borosilicate glasses, Npj Mater. Degrad. 4 (2020) 1–9.

[24] H. Zhang, T. Suzuki-Muresan, Y. Morizet, S. Gin, A. Abdelouas, Investigation on boron and iodine behavior during nuclear glass vapor hydration, Npj Mater. Degrad. 5 (2021) 1–9.

[25] A. Krishnamurthy, A. Farrant, M. Fayek, S. Kroeker, Structure and boron content of model nuclear sodium aluminoborosilicate glass alteration layers, Manuscript in Preparation, University of Manitoba, Canada, 2021.

[26] C.L. Trivelpiece, J.A. Rice, C.G. Pantano, Glass composition and solution speciation effects on stage III dissolution, No. DOE/NEUP-13-4926, Pennsylvania State Univ., University Park, PA (United States), 2017.

[27] R.R. Deshpande, H. Eckert, Sol-gel preparation of mesoporous sodium aluminosilicate glasses: Mechanistic and structural investigations by solid state nuclear magnetic resonance, J. Mater. Chem. 19 (2009) 3419–3426.